

**Design, Synthesis, Biological Characterization and *In Vivo*
Validation of Histone Deacetylase – 3 Inhibitors as
Anti-cancer Agents**

THESIS

Submitted in partial fulfilment
of the requirements for the degree of

DOCTOR OF PHILOSOPHY

by

PULYA SRAVANI

ID No. 2018PHXF0043H

Under the Supervision of

Prof. Balaram Ghosh



BITS Pilani
Pilani | Dubai | Goa | Hyderabad

BIRLA INSTITUTE OF TECHNOLOGY AND SCIENCE, PILANI

2023

BIRLA INSTITUTE OF TECHNOLOGY AND SCIENCE, PILANI

CERTIFICATE

This is to certify that the thesis titled “**Design, Synthesis, Biological Characterization and *In Vivo* Validation of Histone Deacetylase – 3 Inhibitors as Anti-cancer Agents**” submitted by **PULYA SRAVANI** ID No **2018PHXF0043H** for the award of Ph.D. of the Institute embodies original work done by him/her under my supervision.

Balaram Ghosh

Signature of the Supervisor:

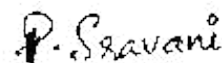
Name in capital letters: BALARAM GHOSH

Designation: Associate Professor, Department of Pharmacy.

Date: 09-11-2023

DECLARATION

I hereby declare that the research work presented in this thesis entitled “**Design, Synthesis, Biological Characterization and *In Vivo* Validation of Histone Deacetylase – 3 Inhibitors as Anti-cancer Agents**” is original and has been carried out by myself under the supervision of Prof. Balam Ghosh, Associate Professor, Department of Pharmacy, BITS-Pilani, Hyderabad Campus, Hyderabad, India. All prior work this thesis is built on, is cited at appropriate places. I further declare that this work has not been submitted in part or full for the award of any degree of this or any other university.



Pulya Sravani
Research Scholar
Department of Pharmacy
BITS-Pilani, Hyderabad Campus

*I dedicate this thesis to my beloved grandmother and
my parents.*

Acknowledgement

I would like to express my deepest gratitude and appreciation to all the people who have been instrumental in the successful completion of this dissertation. This thesis would not have been possible without the support, blessings and best wishes of several individuals who contributed in one way or the other.

My first and foremost gratitude to my esteemed supervisor Dr. Balaram Ghosh, Associate Professor, Department of Pharmacy, BITS Pilani, Hyderabad campus for his continuous support and encouragement from day 1 of my PhD journey. His constant guidance, wide knowledge and experience along with his intellectual and logical way of thinking have been of great value to me. Words fall short to explain my deepest appreciation to my supervisor. His ability to think out of the box, scientific temperament along with his personal traits of confidence, determination, strong moral and ethical values has inspired me to grow personally as well. The extensive discussions around my research, and the mentorship that he has provided during my PhD has been extremely invaluable. His understanding nature and personal guidance has been of extreme support during this journey.

I am whole heartedly thankful to Prof. Swati Biswas, Department of Pharmacy, BITS Pilani, Hyderabad Campus, who acted as Doctoral Advisory Committee (DAC) member, for her valuable suggestions, kind words of support and the discussions around my work. Her immense expertise in the field, enthusiasm and extreme passion for research will always be a source of inspiration to me.

I also express my sincere gratitude to Prof. Onkar Kulkarni, Department of Pharmacy, BITS Pilani Hyderabad who acted as a DAC member, for his timely suggestions, kind support and words of encouragement throughout my PhD.

I extend my profound sense of respect to Prof. V. Ramgopal Rao, Vice-Chancellor; Prof. G. Sundar, Director, BITS Pilani, Hyderabad Campus; Col Soumyabrata Chakraborty (Retd), Registrar; Prof. M. B. Srinivas, Dean, Academic Graduate Studies Research; and Prof. V. V. Vamsi Krishna, Associate Dean, Academic Graduate Studies Research Division for providing me with the required facilities and infrastructure for my research work.

I would extend my deepest appreciation to the former Head of the department Prof. D. Sriram for his invaluable support during my admission and during my tenure as Senior research fellow.

I would like to express my special thanks to the current HOD, Prof. Sajeli Begum, Department of Pharmacy, BITS Pilani, Hyderabad campus for her invaluable support to accomplish my research work.

I am also grateful to Dr. Nirmal J, Assistant Professor, Convener, Departmental Research Committee (DRC) for his constant support.

I will always be thankful to all the faculty members of Department of Pharmacy, Prof. P. Yogeewari, Prof. Ahmed Kamal, Prof. Punna Rao Ravi, Prof. Arti Dhar, Dr. Akash Chaurasiya, Dr Srinivas Prasad K, Dr. Abhijeet Rajendra Joshi for always being a source of support and inspiration.

I sincerely acknowledge the support through financial assistance from Council of Scientific and Industrial Research under Senior Research Fellowship scheme to pursue my PhD research work. Further, I would also like to thank BITS Pilani, Hyderabad for providing me with the Institute fellowship towards the completion of my doctoral studies.

I am sincerely thankful to all my seniors and lab mates Dr. Prakruti Trivedi, Dr. Yamini Bobde, Dr. Himanshu, Mr. Ganesh, Mrs. Soniya, Mr. Tarun, Mr. Milan, Mr. Sanjay, Mrs. Sri Ganga, Mr. Asif, Ms. Himaja Ambati, Ms. Darakhshan, Ms. Nikhita, Mr. Sanjeev and Dr. Goverdhan.

Thanks are due to Dr. Shubham, Dr. Nikhila, Dr. Kalyani, Kavita, Dr. Kirti, Dr. Chandra Teja, Dr. Avantika, Dr. Jaspreet Kalra, Ms. Pragya, Mr. Pravesh, Mr. Sai, Mr. Srashti, Mr. Parmeshwar, Mr. Deepanjan, Mr. Lokesh, Mr. Raghu, Ms. Sony Priyanka, Mr. Girdhari, Ms. Manisha, Mr. Ashutosh, Ms. Tripti, Ms. Swagata, Ms. Purbali, Mrs. Soukya, Ms. Samrun.

I extend my heartfelt thanks to graduate students Shreya, Shraddha, Srividya, Srinidhi, Ranjani, Dhruv and Abhiram for being a great support in my work.

I also extend my sincere thanks to all the technical staff of Central analytical lab facility, especially Mr. Uppalaiah, Mr. Mallesh, Mr. Narasimha for their support and coordination during the conduct of research work.

I am thankful to the staff of BITS Pilani, Hyderabad campus, Mr. Praveen, Mrs. Bhagyalaxmi, Mrs. Saritha, Mr. Rajesh, Mrs. Rekha, and Mrs. Sunitha, for their kind support.

Further, I extend my sincere thanks to all my teachers, professors and mentors who laid the foundation of my educational and research work including but not limited to Dr. C.V.Ramana, Prof. M. Himaja, Dr. Kasi Shankar, Dr. Swaroop and Dr. Rajender for being a continuous source of support and inspiration.

I also express my special thanks to my friends and extended family members who are always there to support me either directly or indirectly and also for being a source of happiness.

I owe my special thanks to my husband Mr. Kartheek, for his invaluable support, encouragement and for always being there through my lows and highs during this journey. I extend my thanks to my parents-in-law for their support and belief in my capabilities.

Words fall short to express my immense sense of gratitude to my nanna Mr. Ramamurthy Pulya, amma Mrs. Visalakshi Pulya for always being there encouraging me at every step of my journey. Their blessings, love, patience, unwavering support, motivation and extreme belief in my capabilities has got me where I stand today. Special thanks to my lovely sister Ms. Sruthi for always being cheerful and be a source of happiness and support to me.

A very special mention to my son Master. Aditya for his unconditional support to me at the final stages of my PhD by being very cooperative during my pregnancy until now. His presence has made this journey more special.

Lastly, the omnipresent God and the superpower for giving me the strength and capabilities to undertake this challenging task and making my destiny to reach this most important aim and milestone of my life.

-----PULYA SRAVANI

Abstract

Epigenetic alterations leading to abnormal gene expression affecting several signaling pathways have been widely implicated in life-threatening disease such as cancer. Histone deacetylases (HDACs), one of the key epigenetic enzymes were found to be potential target for cancer treatment. Histone deacetylase inhibitors (HDACis), are the drugs that inhibit HDAC isoforms, modulate the genetic aberrations by preventing the deacetylation on the lysine residues of the histone proteins. HDACs are found to be overexpressed in different cancers and thus targeting HDACs by HDACis have garnered attention of the researchers worldwide as a promising therapeutic strategy for cancer treatment. HDACis, act by implicating various biological processes of the cell such as cell cycle regulation, proliferation, apoptosis, metastasis and differentiation. In the past decade, numerous reports have been published identifying a number of HDACis that are explored preclinically and clinically as anticancer agents. So far, only six HDACis were clinically approved for the treatment of haematological malignancies. Most of the HDACis known so far are non-selective towards various HDAC isoforms and this is one of the major limitations for the HDACis to be successful at the clinical level. The non-selectivity of the HDACis led to severe adverse effects, dose-limiting toxicities, off-target effects, poor bioavailability and therefore, poor clinical outcome. Therefore, the quest for identifying novel isoform selective HDACis is still an unmet need in the area of epigenetic drug discovery. Structural modifications over the canonical pharmacophore of the HDACis, were found to enhance potency and selectivity against different HDACs. In this direction, novel Zinc Binding Group, hydrazide has been identified to enhance the potency and selectivity towards class I HDACs. With this approach, we have designed and synthesized benzoyl and pyrazino hydrazide series of compounds and evaluated their biological evaluation *in vitro* and *in vivo*.

Firstly, we have designed and synthesized a series of small molecules with benzoyl hydrazide scaffold as ZBG including acetyl, aryl or aroyl cap group. Compound **4e**, having the highest HDAC3 inhibitory potency ($IC_{50} = 15.41$ nM) and a minimum of 18-fold selective over other HDAC isoforms have been selected as the lead compound in the series. **4e**, exhibited potent and selective anticancer efficacy against different cancer cell lines over normal cell lines tested. The *in vivo* pharmacokinetic profile demonstrated good bioavailability of the compounds at 15 mg/kg and 25 mg/kg doses much lower than the corresponding hydroxamates and benzamides. Further, the *in vivo* anticancer efficacy in the 4T1-Luc tumor xenograft model has been evaluated. The western blot analysis has revealed the upregulation of Ac-H3K9, Ac-H4K12 both *in vitro* and *in vivo* suggesting the primary modulation effects of **4e** as HDAC3 inhibitor. Further, our results demonstrated that treatment with **4e** caused significant apoptosis, cell cycle arrest leading to its cytotoxic effects. The potential of **4e** as cytotoxic, anti-proliferative with reduced metastatic potential has been evaluated. The *in vivo* treatment of female Balb/c mice implanted with 4T1-Luc tumors by **4e**, demonstrated significant reduction in the tumor volume accompanied with no general toxicity in major organs during the treatment period. Therefore, compound **4e** can be a promising inhibitor targeting HDAC3 with a significant antitumor activity that can be evaluated further in preclinical and clinical evaluation.

Next, we have designed and discovered a series of novel pyrazino hydrazide based HDAC3 inhibitors as anticancer agents particularly against triple-negative breast cancer. **4i**, has been identified as the highly potent and selective HDAC3 inhibitor among the series of 20 small molecule that are designed and synthesized in this series. **4i** has exhibited potency of 14 nM with at least 121-fold selectivity over HDAC1 and HDAC2. We also tested the compounds against different breast cancer cell lines and normal human cell lines for their cytotoxicity profile and the identified lead compound **4i** has exhibited IC_{50} values

of 0.55 μ M and 0.74 μ M over 4T1 and MDA-MB-231 cells with a high degree of selectivity over normal cell lines. **4i** when tested in oxaliplatin resistant MDA-MB-231 cells demonstrated chemosensitizing properties both by retaining its cytotoxicity in the resistant cell line as well by improving the cytotoxicity profile of oxaliplatin when treated in combination in the oxaliplatin resistant MDA-MB-231 cells. **4i** was found to be metabolically stable when tested in rat liver microsomes and also displayed superior pharmacokinetic profile with about 7.2 h $t_{1/2}$, which is much better than other hydroxamates and benzamides reported till date. We for the first time, tested the lead molecule **4i** *in vivo* with a much lower frequency dosage regimen once in 3 days for 21 days treatment period and we observed excellent tumor volume reduction with no general toxicity in major organs of the mice. With about 97.92% tumor inhibition growth rate percentage, **4i** treatment in the female Balb/c mice implanted with 4T1-Luc tumors, demonstrated excellent antitumor properties *in vivo*. The western blot analysis has evidenced the upregulation of the histone biomarkers Ac-H3K9, Ac-H4K12 and Ac-H3K27 *in vivo* indicating the HDAC3 selectivity of the compound **4i**. Further, the mechanism of cell death via apoptosis, and cell cycle phase arrest at G2/M phase was evaluated through the biomarker analysis with isolated tumor tissues of **4i** treated mice. The analysis of the tumor tissues by immunoblotting displayed the upregulation of apoptotic proteins caspase-3, caspase-7, cytochrome *c* and the downregulation of proliferation markers BCL2, CD44, EGFR, and Ki-67.

Altogether, the detailed study of the novel ZBG, hydrazide containing series of compounds as HDAC3 selective inhibitors, with demonstrated efficacy both *in vitro* and *in vivo* anticancer systems might provide significant insights in designing newer druggable small molecules with improved potency and selectivity to be developed as anticancer therapeutics in future.

Table of contents

Contents	Page number
<i>Certificate</i>	I
<i>Declaration</i>	II
<i>Dedication</i>	III
<i>Acknowledgement</i>	IV – VI
<i>Abstract</i>	VII – IX
<i>List of tables</i>	X – XI
<i>List of figures</i>	XII – XXIII
<i>List of schemes</i>	XXIV
<i>List of abbreviations</i>	XXV – XXVI
Chapter 1. Introduction	1 – 25
1.1. Epigenetics	2 – 3
1.2. Chromatin structure and modifications	3 – 5
1.3. Histone deacetylases and key features	5 – 11
1.4. Zinc dependent HDAC isoforms and cancer	11 – 15
1.5. HDAC inhibitors as anti-cancer agents	15 – 21
1.6. Isoform selective HDACis till date	21 – 24
1.7. Limitations of the existing HDACis	24 – 25
Chapter 2. Literature review	26 – 38
2.1. About HDAC3	27 – 29
2.2. HDAC3 and cancer	29
2.3. HDAC3 selective inhibitors	29 – 31
2.4. Hydrazone based HDAC inhibitors	31 – 36

2.5. Gaps in the existing research of HDAC inhibitors	36 – 37
Objectives	37 – 38
Chapter 3. Selective Inhibition of Histone deacetylase 3 by Novel Hydrazide Based Small Molecules as Therapeutic Intervention for the Treatment of Cancer.	39 – 133
3.1. Introduction	40 – 44
3.2. Results and discussion	44 – 89
3.3. Materials and methods	89 – 132
3.4. Conclusion	132 – 133
Chapter 4. Design, synthesis, biological evaluation, pharmacokinetic profiling, and binding mode of interaction analysis of novel pyrazino hydrazide chemotypes as selective HDAC3 inhibitors with potent <i>in vivo</i> antitumor efficacy against triple negative breast cancer.	134 – 270
4.1. Introduction	135 – 140
4.2. Results and discussion	140 – 190
4.3. Materials and methods	190 – 268
4.4. Conclusion	268 – 270
Chapter 5. Conclusion	271 – 275
Chapter 6. Future perspectives	276 – 278
Bibliography	279 – 311
Appendix	312 - 318
<i>List of publications</i>	313 – 316
<i>Biography of the candidate</i>	317
<i>Biography of the supervisor</i>	318

List of Tables

Table number	Table legend	Page number
Table 1.1.	Classification of HDAC isoforms, their cellular localization, substrates and physiological functions.	8
Table 1.2.	FDA approved HDAC inhibitors, their indication and details.	18
Table 1.3.	Details of isoform selective HDACis.	23
Table 2.1.	Details of few HDAC1 – 3 selective and preferentially HDAC3 selective inhibitors including their structures and corresponding IC ₅₀ values.	30
Table 2.2.	Lead compounds from the series of hydrazide based HDACis reported till including their structures, HDAC3 IC ₅₀ values, their selectivity over HDAC1 and HDAC2 and their biological indication.	35
Table 3.1.	Structures of the designed compounds.	48
Table 3.2.	<i>pan</i> -HDAC and HDAC 3 enzyme inhibition (%) data of the synthesized compounds with 10 μM concentration of compounds against Hela nuclear extract (<i>pan</i> -HDACs) and 1 μM and 0.0625 μM concentration of compounds against human recombinant HDAC 3 enzymes.	51
Table 3.3.	Data representing the HDAC3 IC ₅₀ values (nM) of selected compounds. Values represent mean ± S.D. (n = 2).	51
Table 3.4.	Inhibitory potency of compounds 4c, 4e and reference molecule UF010 against human recombinant class I and class II HDACs as compared with HDAC3 selective inhibitors previously reported from our group BG-45 and PT3.	53
Table 3.5.	IC ₅₀ (μM) values of all compounds towards various cancer cells and normal HEK-293, HCEC and Raw 264.7 cells.	60
Table 3.6.	Table indicates the % cell population in different phases of cell cycle in B16F10 and 4T1 cells respectively.	65
Table 3.7.	Plasma concentration (μg/ml)-time data of 4e following an intravenous administration to male wistar rat (Dose: 15 mg/kg and 25 mg/kg).	68

Table 3.8.	Plasma concentration ($\mu\text{g/ml}$)-time data of 4e (Dose: 15 mg/kg and 25 mg/kg). and UF010 (Dose: 25 mg/kg) following an i.p administration to male wistar rats.	69
Table 3.9.	Optimized chromatographic conditions in HPLC.	70
Table 3.10.	Calibration curve data of 4e and UF010 in rat plasma.	71
Table 3.11.	Pharmacokinetic parameters of compound 4e (i.v and i.p) and UF010 (i.p) in plasma following an intravenous and intraperitoneal administration in male Wistar rats.	72
Table 4.1	% inhibition values of the compounds at 5 μM (for HeLa nuclear extract) and 1 μM (for HDAC1, HDAC2 and HDAC3) concentration of the tested compounds.	147
Table 4.2.	HDAC inhibitory potency of the lead compound 4i against representative human recombinant class I and class II HDACs along with the previously reported reference molecule UF010 and HDAC3 selective inhibitors, BG-45 and PT3.	150
Table 4.3.	IC_{50} (μM) values of synthesized compounds against various breast cancer cells and normal HEK-293, MCF-10A and HCEC cells.	151
Table 4.4.	Table indicates the % cell population in different phases of cell cycle in MDA-MB-231 and 4T1 cells respectively ^a .	160
Table 4.5.	Table indicates the % cell population in different phases of cell cycle at different concentrations C1, C2 and C3 of 4i and UF010 in 4T1 cells respectively. ^a	163
Table 4.6.	<i>In vitro</i> microsomal stability profile of compound 4i and propranolol (internal standard).	167
Table 4.7.	Plasma concentration ($\mu\text{g/ml}$)-time data of 4i (Dose: 5 mg/kg and 15 mg/kg) and UF010 (Dose: 25 mg/kg) following an intraperitoneal administration to male wistar rats.	168
Table 4.8.	Optimized chromatographic conditions in HPLC.	169
Table 4.9.	Calibration curve data of 4i and UF010 in rat plasma.	170
Table 4.10.	The results obtained from the plasma pharmacokinetic analysis of the compound 4i (5 mg/kg and 15 mg/kg) and UF010 (15 mg/kg) following an intraperitoneal administration in male Wistar rats. ^a	172

List of Figures

Figure number	Figure legend	Page number
Figure 1.1	Epigenetic processes	3
Figure 1.2.	Chromatin structure and its modifications	5
Figure 1.3.	Proposed mechanism for histone deacetylase catalysis.	11
Figure 1.4.	Role of different HDAC isoforms in cancer pathogenesis.	15
Figure 1.5.	Structures of clinically approved HDAC inhibitors.	18
Figure 1.6.	Different mechanism of action of HDAC <i>s</i> in cancer.	21
Figure 2.1.	(A) Crystal structure of HDAC3 (PDB ID: 4A69); (B) HDAC3 domain structure, organization and functions.	28
Figure 2.2.	Role of HDAC3 overexpression in cancer pathogenesis.	29
Figure 3.1.	Design of the novel hydrazide ZBG containing compounds as potential HDAC3 inhibitors.	45
Figure 3.2.	Graph represents the % inhibitory activity of the novel synthesized compounds for their <i>pan</i> -HDAC inhibitory activity.	50
Figure 3.3.	Graph represents the % inhibitory activity of the novel synthesized compounds on recombinant HDAC3 enzyme.	50
Figure 3.4.	Graphs represent the % inhibitory activity of 4c, 4e and UF010 compounds on human recombinant (A) HDAC1; (B) HDAC2; (C) HDAC8; (D) HDAC6; (E) HDAC4; (F) HDAC5.	52
Figure 3.5.	Graphs used in the calculation of IC ₅₀ values of compounds 4c, 4e and UF010 against human recombinant HDAC isozymes (A) HDAC3; (B) HDAC1; (C) HDAC2; (D) HDAC8; (E) HDAC6.	53
Figure 3.6.	Cytotoxicity of the synthesized compounds in murine melanoma cells (B16F10) were treated with compounds at 100 μ M and 10 μ M in duplicate for 72 h.	56
Figure 3.7.	Cytotoxicity of the synthesized compounds in Human breast cancer cells (MCF-7) were treated with compounds at 100 μ M and 10 μ M in duplicate for 72 h.	56

Figure 3.8.	Cytotoxicity of the synthesized compounds in human non-small cell lung cancer cells (A549). Cells were treated with compounds at 100 μ M and 10 μ M in duplicate for 72 h.	57
Figure 3.9.	Cytotoxicity of the synthesized compounds in mouse breast cancer cells (4T1). Cells were treated with compounds at 100 μ M and 10 μ M in duplicate for 72 h.	57
Figure 3.10.	Graph (A), (B), (C), (D) represents the IC ₅₀ results of the synthesized compounds by MTT assay in B16F10, MCF-7, A549 and 4T1 cells respectively.	58
Figure 3.11.	Cytotoxicity of the synthesized compounds in Human embryonic kidney cells (HEK-293). Cells were treated with compounds at 100 μ M and 10 μ M in duplicate for 72 h.	58
Figure 3.12.	Cytotoxicity of the synthesized compounds in Human corneal epithelial cells (HCEC). Cells were treated with compounds at 100 μ M and 10 μ M in duplicate for 72 h.	59
Figure 3.13.	Cytotoxicity of the synthesized compounds in Raw 264.7 cells. Cells were treated with compounds at 100 μ M and 10 μ M in duplicate for 72 h.	59
Figure 3.14.	Graph (A), (B) and (C) represents the IC ₅₀ results of the selected compounds for their toxicity by MTT assay against normal human cells (HEK-293), human corneal epithelial cells and Raw 264.7 cells respectively, and the cells were treated with the compounds at the concentration range from 7.81 μ M to 2000 μ M (n=2) for 72 h.	60
Figure 3.15	(A) Western blot analysis of Ac-H3K9 and Ac-H4K12 in the whole-cell lysate of B16F10-treated cells and Ac-H3K27 in the whole-cell lysate of 4T1-treated cells with compound 4e at two different doses (5 μ M and 10 μ M); (B) Western blot analysis of Ac-Tubulin and Ac-SMC3 in the whole-cell lysate of 4T1-treated cells with compound 4e at two different doses (5 μ M and 10 μ M); and (C), (D), (E), (F) and (G) Graphs representing the analysis of the blots obtained for Ac-H3K9, Ac-H4K12, Ac-H3K27, Ac-SMC3 and Ac-Tubulin respectively.	63
Figure 3.16.	(A) Apoptosis analysis using Annexin V/PI assay double staining by flow cytometry. B16F10 and 4T1 cells from the same cultures were treated with vehicle Control, UF010, 4c and 4e at their respective <i>in vitro</i> IC ₅₀	65

concentrations for 72 h (X and Y-axis represent the intensities of annexin V and propidium iodide respectively); (B) Graphical representation of the total apoptotic percentage analysis in B16F10 and 4T1 cells; (C) Cell cycle analysis in B16F10 and 4T1 cells treated with vehicle Control, reference compound UF010, 4c and 4e at 5 μ M for 48 h. After the indicated treatment times, cell cycle analysis was carried out and subsequently analysed by Flow cytometer (BD Aria III) [®]; (D) Graphical representation of the % cell population at various stages of the cell cycle in B16F10 and 4T1 cells, i.e., G1, S and G2/M phases.

Figure 3.17. Analysis of nuclear morphology in 4T1 cells based on DAPI and Acridine Orange staining following treatment by vehicle Control, UF010 (8.40 μ M) and 4e (1.92 μ M) for 48 h. The stained nuclei were visualized employing a fluorescence microscope (Leica microsystems, Germany) on 20x Magnification.

67

Figure 3.18. (A) Calibration curve of 4e in rat plasma; (B) Calibration curve of UF010 in rat plasma; (C) Representative chromatogram of blank in rat plasma (blank sample); (D) Representative chromatogram of 4e in rat plasma (standard); (E) Representative chromatogram of 4e in rat plasma (intravenous sample); (F) Representative chromatogram of 4e in rat plasma (intraperitoneal sample); (G) Representative chromatogram of UF010 in rat plasma (standard); (H) Representative chromatogram of UF010 in rat plasma (intraperitoneal sample).

71

Figure 3.19. (A) Mean plasma concentration-time profiles of compound 4e following a single intravenous administration to male wistar rats (n = 3; dose, 25 mg/kg, 15 mg/kg). (B) Mean plasma concentration-time profiles of compound 4e and UF010 following a single intraperitoneal administration to male Wistar rats (n = 3; dose, 4e: 25 mg/kg, 15 mg/kg and UF010: 25 mg/kg).

72

Figure 3.20. *In vivo* therapeutic efficacy of 4e and UF010 (reference compound) in 4T1-Luc tumor implanted Balb/C female mice treated with Control, UF010 (25 mg/kg) and 4e, 15 mg/kg, and 25 mg/kg (n=5) for 21 days (5 days/week). (A) Tumor volume reduced over the treatment period; (B) Body weight measurement over treatment period; (C) Representative *in*

76

vivo bioluminescence images of UF010 (25 mg/kg) and 4e treated mice with doses 15 mg/kg and 25 mg/kg in 4T1 Luc tumor-bearing mice on the day 10 and day 21 (n=2) after i.p administration of luciferin-D (100 μ l, 100 mg/kg) by IVIS® Lumina III, PerkinElmer, USA; (D) Representative tumors surgically isolated from mice post 21 days of treatment (n=5); (E) % survival analysis using Kaplan-Meier survival curve for 21 days post tumor resection.

Figure 3.21. (A) Reactive oxygen species generation and imaging on day 21 in female Balb/c mice implanted with 4T1-Luc tumor treated with Control, positive control (UF010, 25 mg/kg) and 4e (Dose:15 mg/kg and 25 mg/kg) (n=2) after Intratumoral injection of DCFH-DA probe (100 μ l, 25 μ M) by IVIS® Lumina III, PerkinElmer, USA; (B) Graph represents, florescence intensity found on Y-axis and day 21 of treatment on X-axis; (C) Images of tumor sections representing ROS levels; (D) Images representing TUNEL positive cells in the tumor sections from treated mice tumors; (E) fluorescent images of Ki-67 staining; (F) H & E staining of several organs and tumor sections isolated from treated mice; (Scale bar is 20 μ m) All the images visualized and obtained under a fluorescence microscope (Leica microsystems, Germany).

79

Figure 3.22. (A) Western blot analysis of caspase-3, caspase-7, BCL2, cytochrome *c*, CD44, EGFR, Ac-H3K9 and Ac-H4K12 in the tumor tissue collected from the 4e treated mice at two different doses (25 mg/kg and 15 mg/kg) in 4T1-Luc implanted tumor xenograft model. Lanes 1, 2: vehicle, lanes 3, 4: 25 mg/kg of 4e and lanes 5, 6: 15 mg/kg of 4e; (B) Graph representing the analysis of the blots obtained. Results obtained were normalized to the housekeeping protein β -actin.

82

Figure 3.23. Docking conformations of synthesized hydrazide derivatives with UF010 (In magenta) (A); Binding mode of interactions of compound UF010 (B); 4c (C) and 4e (D) at the HDAC3 active site of (PDB ID: 4A69).

84

Figure 3.24. Ligand binding interaction of (A) UF010 (B) 4c and (C) 4e with HDAC1 (PDB ID: 4BKX).

84

Figure 3.25. (A) Alignment of inbound ligand (green), redocked ligand (magenta), UF010 (orange), 4c (yellow) and 4e (cyan) at the HDAC2 active site

85

	(PDB ID: 3MAX); (B) Binding interaction of UF010 at the HDAC2 active site; (C) Binding interaction of 4c at the HDAC2 active site; (D) Binding interaction of 4e at the HDAC2 active site.	
Figure 3.26.	(A) Alignment of inbound ligand (green), redocked ligand (magenta), UF010 (orange), 4c (yellow) and 4e (cyan) at the HDAC8 active site (PDB ID: 1T69); (B) Binding interaction of UF010 at the HDAC8 active site; (C) Binding interaction of 4c at the HDAC8 active site; (D) Binding interaction of 4e at the HDAC8 active site.	86
Figure 3.27.	(A) Alignment of inbound ligand (green), redocked ligand (magenta), UF010 (orange), 4c (yellow) and 4e (cyan) at the HDAC6 active site (PDB ID: 5EDU); (B) Binding interaction of UF010 at the HDAC6 active site; (C) Binding interaction of 4c at the HDAC6 active site; (D) Binding interaction of 4e at the HDAC6 active site.	87
Figure 4.1.	(A) Structures of the lead compounds of HDAC3 selective inhibitors previously reported from our group and their HDAC3 IC ₅₀ values; (B) Design of the pyrazino hydrazide series of compounds.	142
Figure 4.2.	The graph represents the % inhibitory activity of the novel synthesized compounds for their <i>pan</i> -HDAC inhibitory activity. All novel compounds were screened at 5 μM concentrations for HeLa nuclear extract enzyme.	146
Figure 4.3.	The graph represents the % inhibitory activity of the novel synthesized compounds for their HDAC3 inhibitory activity. All novel compounds were screened at 1 μM concentrations for human recombinant HDAC3 enzyme.	146
Figure 4.4.	Graphs represent the % inhibitory activity of 4h, 4i, 4n and 4o compounds on human recombinant (A) HDAC1; (B) HDAC2; (C) HDAC8; (D) HDAC6; (E) HDAC4; (F) HDAC5.	147
Figure 4.5.	IC ₅₀ curves of the compounds 4i, BG-45, UF010, and PT3 when assayed with the human recombinant HDAC isozymes of (A) HDAC3; (B) HDAC1; (C) HDAC2; (D) HDAC8; and (E) HDAC6.	149
Figure 4.6.	Graphs (A), (B), (C), (D) represents the IC ₅₀ results of the synthesized compounds by MTT assay against MCF-7, 4T1, MDA-MB-231 and MDA-MB-453 cells respectively. Cells were treated with the compounds at concentration range of 0.048 μM to 50 μM (n=3) for 72 h.	152

Figure 4.7. Graphs (A), (B) and (C) represents the IC₅₀ results of all the synthesized compounds by MTT assay against normal human cells (HEK-293), human corneal epithelial cells (HCEC) and normal human breast cells (MCF-10A) respectively, and here cells were treated with the compounds at the concentration range from 1.95 μM to 4000 μM (n=3) for 72 h. Data represents mean ± SD.

152

Figure 4.8. Western blot analysis of various histone biomarkers in the protein samples extracted from the cell lysates that is obtained from the 4T1 cells treated with control, 4i (1 μM), UF010 (1 μM), BG-45 (1 μM) and SAHA (1 μM) for 72 h. The blots and the corresponding quantification of the blots were plotted as the graphs represented above. (A) Image representing the blots of Ac-H3K9, Ac-H4K12 levels in the treated 4T1 cell lysate samples and the corresponding quantification plotted as a graph below; (B) Western blot analysis of various apoptotic biomarkers in the protein samples extracted from the cell lysates that is obtained from the 4T1 cells treated with control, 4i (500 nM, 2 μM); Image representing the blots of caspase-7, caspase-3, cleaved caspase-3 and cytochrome *c* levels in the treated 4T1 cell lysate samples and the corresponding quantification plotted as a graph below. β-actin was used as an internal control and the graphs were plotted by normalizing the protein expression levels compared to the control group values analyzed in *Image J* software. Significance was analyzed using one-way ANOVA analysis and the graphs were plotted in GraphPad Prism™ version 8.0.1. Data represents the values of mean ± the standard error of the mean (SEM, n=2); *p < 0.05, **p < 0.01, ***p < 0.001, ****p < 0.0001, significantly different from the control group.

156

Figure 4.9. Image representing the blots of caspase-7, caspase-3, cleaved caspase-3 and cytochrome *c* levels in the UF010 treated 4T1 cell lysate samples and the corresponding quantification plotted as a graph below. β-actin was used as an internal control and the graphs were plotted by normalizing the protein expression levels compared to the control group values analyzed in *Image J* software. Significance was analyzed using one-way ANOVA analysis and the graphs were plotted in GraphPad Prism™ version 8.0.1.

157

Data represents the values of mean \pm the standard error of the mean (SEM); *** $p < 0.001$ significantly different from the control group.

Figure 4.10. Caspase3/7 activation levels of 4i and UF010 in 4T1 cells compared to control. Compound treatment shows significant difference from control indicates increased apoptosis in cells. Significance was analyzed using one-way ANOVA analysis and the graphs were plotted in GraphPad Prism™ version 8.0.1. Data represents mean \pm SD (n=2); *** $p < 0.001$, significantly different from the control group.

157

Figure 4.11. Different cultures of MDA-MB-231 and 4T1 cells were treated with the *in vitro* IC₅₀ concentrations of UF010 and 4i in the respective cell lines along with control for 72 h. (A) Annexin V/PI apoptosis assay by flow cytometer (BD Aria III) ® (where X and Y-axis represent the intensities of annexin V and propidium iodide respectively); (B) Graph representing the percentage of the total apoptotic population in MDA-MB-231 and 4T1 cells; (C) Cell cycle analysis by Flow cytometer (BD Aria III) ®; (D) Graph representing the percentage of cell population at different phases of the cell cycle in MDA-MB-231 and 4T1 cells. The data was analysed using *Flow Jo* software and the graphs were plotted using GraphPad Prism™ version 8.0.1.

159

Figure 4.12. Different cultures of MDA-MB-231 and 4T1 cells were treated with the *in vitro* IC₅₀ concentrations of UF010 and 4i in the respective cell lines along with control for 72 h. Analysis of nuclear morphology by nuclear staining experiment in (A) MDA-MB-231 and (B) 4T1 cells using the staining solutions of DAPI and Acridine Orange after the treatment period. NF represents nuclear fragmentation and CS represents cell shrinkage. A fluorescence microscope (Leica microsystems, Germany) on 20x Magnification was used for the visualization of the stained nuclei.

160

Figure 4.13 Different cultures of 4T1 cells were treated with three different concentrations including the IC₅₀ concentration of UF010 and 4i along with control (no treatment) for 72 h. (A) Annexin V/PI apoptosis assay by flow cytometer (BD Aria III) ® (where X and Y-axis represent the intensities of annexin V and propidium iodide respectively); (B) Graph representing the percentage of the total apoptotic population in 4T1 cells;

161

(C) Cell cycle analysis by Flow cytometer (BD Aria III) ®; (D) Graph representing the percentage of cell population at different phases of the cell cycle in 4T1 cells. The data was analyzed using *FlowJo* software and the graphs were plotted using GraphPad Prism™ version 8.0.1. Data represents, mean±SD (n=3).

Figure 4.14 Different cultures of 4T1 cells were treated with the *in vitro* IC₅₀ concentrations of UF010 and 4i along with control for 72 h. Analysis of nuclear morphology by nuclear staining experiment in (A) 4T1 cells using the staining solutions of DAPI and Acridine Orange after the treatment period and (B) Graph representing the % apoptosis data quantified by *Image J* software. **NF** represents nuclear fragmentation and **CS** represents cell shrinkage. A Laser Scanning Confocal Microscope (LSCM) DMI8 (Leica microsystems, Germany) on 63X Magnification was used for the visualization of the stained nuclei. The obtained values represent the mean±SD (n=3); ***p < 0.001. The quantification of the % apoptosis was done using *ImageJ* software. Significance was analyzed using one-way ANOVA analysis and the graph was plotted in GraphPad Prism™ version 8.0.1.

162

Figure 4.15. Graphs (A) and (B) represents the dose-response curves obtained by the MTT assay with the compounds oxaliplatin, UF010, 4i and the combination of 4i and oxaliplatin (equimolar concentration) for 72 h in MDA-MB-231 wild type and MDA-MB-231 oxaliplatin resistant cell lines respectively. Here, the cultured cells were treated with the compounds at the concentration range from 0.048 µM to 400 µM (n = 3) for 72 h. The graphs were plotted using GraphPad Prism™ version 8.0.1. Data represents, mean±SD (n=3).

165

Figure 4.16. Time course of 4i and propranolol depletion in rat liver microsomes. 4i and propranolol (100 µM) were incubated with 0.5 mg/mL of pooled rat liver microsomes in the presence of NADPH. Each data point represents the mean±SD (n=3). The degradation half-life ($t_{1/2}$) was calculated using the equation: $t_{1/2}=0.693/k$, where k is the first-order elimination rate constant that was estimated by one-phase exponential decay using nonlinear regression analysis of the degradation time course data in

166

GraphPad Prism™ version 8.0.1. Intrinsic clearance (Cl_{int} , $\mu\text{L}/\text{min}/\text{mg}$) was calculated using the equation: $Cl_{int} = V \cdot 0.693/t_{1/2}$. [where V = volume of incubation (μL)/ microsomal mass (mg)].

Figure 4.17. (A) Calibration curve of 4i in rat plasma; (B) Calibration curve of UF010 in rat plasma; (C) Representative chromatogram of blank in rat plasma (blank sample); (D) Representative chromatogram of 4i in rat plasma (standard); (E) Representative chromatogram of UF010 in rat plasma (standard); (F) Representative chromatogram of 4i in rat plasma (intraperitoneal sample); (G) Representative chromatogram of UF010 in rat plasma (intraperitoneal sample). 171

Figure 4.18. Graph representing mean plasma concentration vs time parameters of the compound 4i and UF010. 4 groups of Male Wistar rats ($n = 3$ mice per group) were intraperitoneally administered a single dose of 4i: 5 mg/kg, 15 mg/kg, and UF010: 15 mg/kg of 20 mg/mL concentration of compounds using 5% DMSO in saline as the vehicle. The graph was plotted using GraphPad Prism™ version 8.0.1. 171

Figure 4.19. Schematic representation of the experimental protocol followed for the *in vivo* antitumor therapeutic efficacy of 4i in the 4T1-Luc tumor xenograft mouse model. 173

Figure 4.20. *In vivo* antitumor therapeutic efficacy studies in a 4T1-Luc tumor bearing mouse model in female Balb/c mice treated intraperitoneally with control, UF010 (15 mg/kg) and 4i, 5 mg/kg, and 15 mg/kg ($n=12$) on every 3rd day for 21 days total period. (A) Representative whole animal bioluminescence imaging of luciferin induced (i.p administration of luciferin–D, 100 μL , 100 mg/kg) 4T1-Luc tumor-bearing mice on days 0, 5, 10, 15, and 21 by IVIS® Lumina III, PerkinElmer, USA; (B) Quantification of bioluminescence of the tumors; (C) Tumour volume growth over the treatment period; (D) Body weight changes in mice during the treatment period; (E) Representative images of 4T1-Luc tumors dissected from the mice after 21 days of treatment ($n=4$); (F) Average weight of the isolated tumors from each group ($n= 3$); (G) Tumour growth inhibition rate percentage (TGI rate %) calculated from the dissected tumor tissue weight collected from 3 mice of each treatment 175

group (total n = 12), at 0th, 7th, 14th, and 21st day of the treatment period. The TGI rate percentage was calculated with the formula $= 1 - \left(\frac{W_{T,t} - W_{T,0}}{W_{C,t} - W_{C,0}} \right) * 100$, where $W_{T,t}$ and $W_{T,0}$ represent the mean tumor weight of the treatment group at the time t and time 0 respectively, $W_{C,t}$ and $W_{C,0}$ represent the mean tumor weight of the control group at the time t and time 0 respectively. The obtained values represent the mean±the standard error of the mean (SEM); ***p < 0.001. Significance was analyzed using one-way ANOVA analysis and all the graphs were plotted in GraphPad Prism™ version 8.0.1.

Figure 4.21. (A) Bioluminescence images representing the reactive oxygen species (ROS) generation on day 21 after injecting DCFH-DA intratumorally (100 μL, 25 μM) in 4 mice from all the treated groups including control group in 4T1-Luc tumor xenograft mouse model, the images were recorded for their fluorescence intensity by IVIS® Lumina III, PerkinElmer, USA; (B) Images of tumor sections recorded after the surgical isolation of tumors, 10 min post-treatment with DCFH-DA; (C) Graph representing the fluorescence intensities recorded corresponding to the ROS levels; (D) Representative images of TUNEL assay in the sections of isolated tumors; and (E) Corresponding graph denoting the percentage of TUNEL positive cells; (F) Images representing the Ki-67 stained tumor sections; and (G) corresponding graph representing the percentage of Ki-67 positive cells in different groups of mice; Fluorescence microscope from Leica microsystems, Germany was used to obtain the images and the quantification was carried out using *Image J* software and the graphs were plotted in GraphPad Prism™ version 8.0.1.

178

Figure 4.22. Images depicting the H&E staining of tissue sections of various major organs of mice from all the groups isolated after the treatment period. A fluorescence microscope from Leica microsystems, Germany was used to obtain the images.

180

Figure 4.23. Analysis of *in vivo* tumor metastasis in the 4T1-Luc tumor bearing mouse model. (A) Tumor metastasis was assessed at the indicated time points by whole animal bioluminescence imaging of 4T1-Luc tumors using IVIS® Lumina III, PerkinElmer, USA; (B) Representative images of the lungs

182

isolated showing metastatic nodules; (C) Bioluminescence imaging of the isolated lungs containing metastatic 4T1-Luc tumors using IVIS® Lumina III, PerkinElmer, USA; (D) Graph representing the luminescence intensities recorded; (E) Mean number of tumor nodules as shown in the images of isolated lungs; (F) Graph representing the weight of the isolated lungs; (G) Detailed pictorial representation of the isolated lungs one from each group and the tumor nodules were marked with circles along with the H&E staining images of the lungs detecting tumor metastasis; (H) The graph represents the percentage affected area of the lungs after metastasis in different treatment groups. A fluorescence microscope from Leica microsystems, Germany was used to obtain the images. Representation of lung metastasis is expressed as the affected area with respect to the total area of the lung. Reduction in metastasis was observed in the lungs of 4i treated animals compared to that of UF010 ($t = 5.94$; $n = 170$; $* 0.001$). These differences are also significant between the lungs of 4i treatment animals with respect to untreated animal lungs. The quantification was carried out using *Image J* software, and the graphs were plotted in GraphPad Prism™ version 8.0.1. Data represents the values of mean \pm the standard error of the mean (SEM, $n=3$); $*p < 0.05$, $**p < 0.01$, $***p < 0.001$, $****p < 0.0001$, significantly different from the control group.

Figure 4.24. Western blot analysis of various biomarkers in the protein samples extracted from the tumor tissue that is isolated from the control, UF010 (15 mg/kg) and 4i (5 mg/kg and 15 mg/kg) treated mice in the 4T1-Luc tumor xenograft mouse model. The blots and the corresponding quantification of the blots were plotted as the graphs represented above. (A) Image representing the blots of *Ac*-H3K9, *Ac*-H3K27, *Ac*-H4K12, *Ac*-tubulin, and *Ac*-SMC3 levels in 4T1-Luc tumor tissue samples and the corresponding quantification plotted as a graph in the right; (B) Image representing the blots of caspase-3, caspase-7, and cytochrome *c* levels in the 4T1-Luc tumor tissue samples and the corresponding quantification plotted as a graph below; (C) Image representing the blots of CD44, BCL2, EGFR and Ki-67 levels in the 4T1-Luc tumor tissue samples and the corresponding quantification plotted as a graph below. β -actin was

	used as an internal control and the graphs were plotted by normalizing the protein expression levels compared to the control group values analyzed in <i>Image J</i> software. Significance was analyzed using one-way ANOVA analysis and the graphs were plotted in GraphPad Prism™ version 8.0.1.	
Figure 4.25.	Aligned structures of all these hydrazides at the HDAC3 active site (PDB: 4A69).	188
Figure 4.26.	Molecular docking interaction of the best active and selective HDAC3 inhibitor 4i at the active site of (A) HDAC3 (PDB: 4A69); (B) HDAC2 (PDB: 3MAX); (C) HDAC8 (PDB: 1T69); and (D) HDAC6 (PDB: 5EDU).	188
Figure 5.1.	Structure of the lead compound 4e from the series of benzoyl hydrazides as HDAC3 selective inhibitors. (Chapter 3)	276
Figure 5.2.	Structure of the lead compound 4i from the series of pyrazino hydrazides as HDAC3 selective inhibitors. (Chapter 4)	277

List of Schemes

Scheme number	Scheme legend	Page number
Scheme 3.1.	<i>Reagents and conditions:</i> (i) (a) acetic anhydride, dry DCM, 2 – 4 h, rt; (b) benzoyl chloride, NaHCO ₃ , THF, 10 h, rt; (c) phenylacetyl chloride, Et ₃ N, dry DCM, 8 h, rt; (ii) NH ₂ NH ₂ .H ₂ O, MeOH, 6 h, reflux; (iii) (a) propionaldehyde (or) butyraldehyde, catalytic PTSA, MeOH, 2 – 3 h, rt; (b) NaBH ₃ CN, MeOH, pH 5, 10 mins, rt.	45
Scheme 3.2.	<i>Reagents and conditions:</i> (i) (a) benzaldehyde, EtOH, 6 h, rt; (b) NaBH ₄ , 2 h, rt; (ii) NH ₂ NH ₂ .H ₂ O, MeOH, reflux, 6 h; (iii) (a) propionaldehyde (or) butyraldehyde, catalytic PTSA, MeOH, 2 – 3 h, rt; (b) NaBH ₃ CN, MeOH, pH 5, 10 mins, rt.	46
Scheme 3.3.	<i>Reagents and conditions:</i> (i) aniline, Pd ₂ (dba) ₃ , XPhos, DIPEA, K ₂ CO ₃ , 12 h, reflux; (ii) NH ₂ NH ₂ .H ₂ O, MeOH, reflux, 6 h; (iii) (a) propionaldehyde (or) butyraldehyde, catalytic PTSA, MeOH, 2 – 3 h, rt; (b) NaBH ₃ CN, MeOH, pH 5, 10 mins, rt.	46
Scheme 4.1.	<i>Reagents and conditions:</i> (i) Conc. H ₂ SO ₄ , MeOH, 3 h; (ii) NH ₂ NH ₂ .H ₂ O, MeOH, 6 h, reflux; (iii) (a) propionaldehyde (or) butyraldehyde, MgSO ₄ , EtOH, 2 – 3 h, rt; (b) NaBH ₃ CN, MeOH, pH 5, 30 min, rt.	143
Scheme 4.2.	<i>Reagents and conditions:</i> (i) (g) aniline, PTSA, 1,4-dioxane, 110 °C, 12 h, reflux; (h) benzylamine, PTSA, 1,4-dioxane, 110 °C, 12 h, reflux; (i) <i>p</i> -methoxybenzylamine, THF, 12 h, reflux; (j) naphthyl-1-amine, PTSA, 1,4-dioxane, 110 °C, 18 h, reflux; (k) piperidine, DIPEA, DMF, 5 h, rt; (ii) NH ₂ NH ₂ .H ₂ O, MeOH, 6 h, reflux; (iii) (a) propionaldehyde (or) butyraldehyde, MgSO ₄ , EtOH, 2 – 3 h, rt; (b) NaBH ₃ CN, MeOH, pH 5, 10 min, rt.	143
Scheme 4.3.	<i>Reagents and conditions:</i> (i) CF ₃ COOH, 60 °C, 2 h; (ii) (a) CH ₃ COCl, NEt ₃ , DCM, 3 – 5 h, rt; (b) indole-5-carboxylic acid or quinoline-6-carboxylic acid, EDC, HOBt, NEt ₃ , DCM, 16 h, 0 °C – rt.	144

List of Abbreviations

- ALK - Anaplastic lymphoma kinase
- AMPK- AMP Activated Protein Kinase
- AO- Acridine Orange
- BLI- Bioluminescence imaging
- cAMP- Cyclic Adenosine Monophosphate
- CCND1- Cyclin D1
- CdLS- Cornelia de Lange Syndrome
- CRBN- Cereblon
- DAPI- 4',6-diamidino-2-phenylindole
- DCM- Dichloromethane
- DIPEA- *N, N*-Diisopropylethylamine
- DMAP- 4-Dimethylaminopyridine
- EDC- 1-Ethyl-3-(3-dimethylaminopropyl) carbodiimide
- EMT- Epithelial Mesenchymal Transition
- ERK- Extracellular signal-regulated kinase
- ERR α - Estrogen Related Receptor Alpha
- FBS- Fetal bovine serum
- GSK-3 β - Glycogen synthase Kinase - 3 Beta
- HAT- Histone acetyltransferase
- HDAC- Histone deacetylase
- HOX-A5- Homeobox Protein A5
- MMP- Matrix Metalloproteinase
- MTT- 3-(4,5-dimethylthiazol-2-yl)-2,5-diphenyltetrazolium bromide
- NAD- Nicotinamide Adenine Dinucleotide
- NF- Nuclear fragmentation
- NMP- *N*-methyl 2-pyrrolidone;
- PD-L1- Programmed Death-1 Ligand-1
- PI- Propidium iodide

PI3K- Phosphatidylinositol 3-kinase
PKA- Protein Kinase A
PLC β 1- Phospholipase-C-Beta-1
PPAR γ - Peroxisome Proliferator Activated Receptor Gamma
PROTAC- Proteolysis Targeting Chimeras
PTEN- Phosphatase and Tensin Homolog deleted on Chromosome 10
PTM- Post Translational Modifications
PTP4A2- Protein Tyrosine Phosphatase Type IVA-2
ROS- Reactive oxygen species;
Rpd3- Reduced Potassium Dependency-3
RTK- Receptor Tyrosine Kinase
SMAD-3- Suppressor of Mothers Against Decapentaplegic
SMC3- Structural Maintenance Chromosomes 3
STAT- Signal Transducers and Activators of Transcription
TGF- β 3- Transforming Growth Factor Beta-3
TLC- Thin layer chromatography
TMS- Tetramethylsilane
TNBC- Triple-negative breast cancer.
VHL- Von Hippel Lindau
WNT- Wingless-related integration site
YAP- Yes-Associated Protein
ZBG- Zinc binding group

Chapter 1
Introduction

1.1. Epigenetics

“Epigenetics” was born in early 1940s and historically, it describes the events that could not be explained by genetic principles. The word epigenetics was first coined by Conrad Waddington in 1942 and he defined epigenetics as “the branch of biology which studies the causal interactions between genes and their products, that bring the phenotype into being” (Jablonka and Lamb, 2002). Since then, several biological phenomena have been included into the category of epigenetics. Much later in 1996, Riggs and colleagues defined epigenetics as “the study of mitotically and/or meiotically heritable changes in gene function that cannot be explained by changes in the DNA sequence” (Goldberg et al., 2007). Altogether, epigenetics is defined as the changes in the genetic code without changes in the DNA sequence. The term “Epi-” means on or above in Greek and therefore epigenetics is described as the factors above the genetic code (Dupont et al., 2009). More often, these epigenetic changes describe the way our genes work, caused by the changes in the lifestyle and environment around us and are reversible as they do not affect the underlying DNA sequence but influence the way the DNA is encoded. Epigenetic changes are known to regulate the gene expression and they are governed by the modifications that are attached to the DNA (Biel et al., 2005). These alterations in the gene expression influence the production of proteins in the cells. The transfer of genetic information includes various stages such as transcription, translation and subsequent protein modification leading to the required protein production. Each cell differs in its function due to the differences in their respective gene expression and thus the regulation of gene expression is the fundamental process of differentiation and development (Quina et al., 2006). Several epigenetic processes are known that includes covalent modifications on the DNA, post-translational modifications (PTMs) of histones and other RNA-mediated processes, chromatin remodeling complexes that modulate gene expression at the transcription level (Portela and

Esteller, 2010). The pictorial representation of the epigenetic processes is given in **Figure 1.1**. Therefore, any epigenetic alteration or aberrant mutation will eventually lead to the dysregulation of the proteins and their expression that play an important role in several human diseases including different types of cancer, cardiovascular diseases, several infections, inflammatory diseases and neurological disorders and their pathogenesis (Portela and Esteller, 2010). This understanding and application of epigenetics will be more effective in the discovery of novel therapeutic treatments in the form of personalized medicine for different diseases.

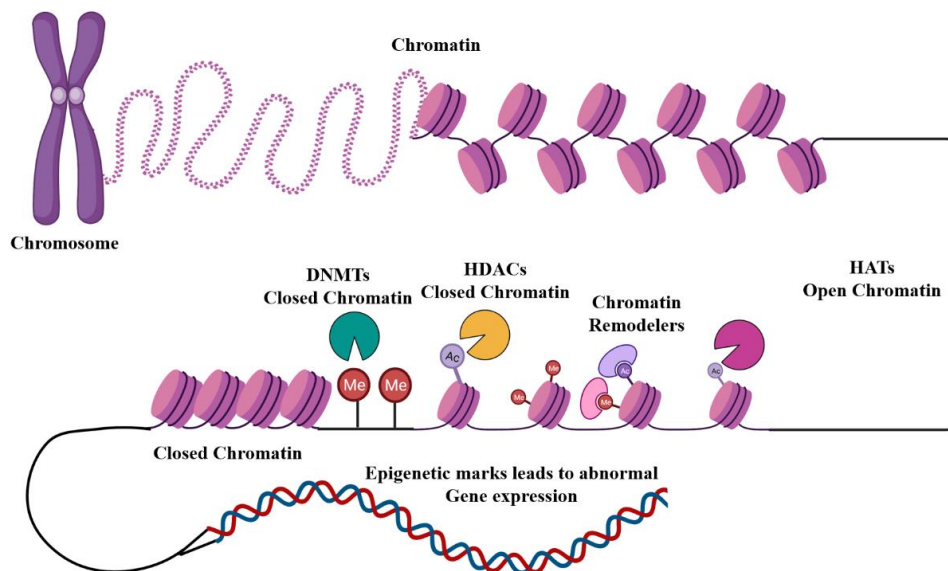


Figure 1.1. Epigenetic processes [redrawn from (Conboy et al., 2021)].

1.2. Chromatin structure and modifications

Eukaryotic chromatin consists of a basic unit called nucleosome that contains 147 base pairs of DNA tightly wrapped around an octamer of core histone proteins (Kornberg, 1974). The positively charged histone proteins (H1, H2A, H2B, H3 and H4) and the negatively charged DNA (due to the phosphate groups in the backbone) are tightly packed into each other due to the electrostatic interactions between them. The core octamer of histones consists of a heterotetramer of H3 and H4 and two heterodimers of H2A and H2B.

Chapter 1: Introduction

These nucleosomes are connected by a linker DNA consisting of H1 histone protein and all these together known as chromatosome. Nucleosomes upon several foldings into chromatin hinders the accessibility of DNA for further transcriptional processes (Luger et al., 1997). Chromatin exists in two different states namely, heterochromatin which is the transcriptionally inactive and highly compact structure of nucleosome and another being euchromatin which forms the open nucleosome associated with transcriptional activation (Ng and Adrian, 1999). These altered structures of chromatin are regulated by several factors that involve the presence of activators, repressors, chromatin remodelling complexes along with and also due to the covalent modifications of DNA as well as PTMs of the histone proteins (Turner, 2000). The accessibility of DNA towards regulatory proteins and thus, gene expression depends on the PTMs of the *N*-terminal of histone tails consisting of lysine residues. Several PTMs of histone proteins are known that include acetylation, phosphorylation, methylation, ubiquitylation, ADP ribosylation, sumoylation, deamination, proline isomerization, crotonylation, hydroxylation and *O*-GlcNAcylation. These PTMs affect the interactions between nucleosomes, thus affecting the overall chromatin structure and remodelling (Jenuwein and Allis, 2001).

Among various PTMs of histones, histone acetylation and deacetylation are the most extensively studied (**Figure 1.2**). Histone acetyl transferases (HATs) acetylate the terminal lysine residues and function as coactivators whereas Histone deacetylases (HDACs) deacetylate and function as corepressors and this balanced activity of HATs and HDACs is required for the epigenetic control of gene transcriptional regulation (Tr et al., 1988). The imbalance between the activities of HATs and HDACs eventually lead to abnormal gene expression thus leading to various epigenetic disorders or diseases (Timmermann et al., 2001). The inhibition of HAT leads to the inexpression of targeted gene whereas, HDAC inhibition leads to continuous expression of the targeted gene (Park

and Kim, 2020). The overexpression of HDACs is a well-known fact that leads to various types of cancers such as pancreatic, colorectal, breast, lung, colon and liver cancers as well as leukemia, hepatocellular carcinoma, prostate cancer and also other neurological disorders, autoimmune disorders, inflammatory diseases, cardiac along with pulmonary diseases (Sarkar et al., 2020). Apart from histone modifications caused by HATs and HDACs, several other epigenetic changes of non-histone targets lead to the altered gene expression of important regulator genes, many of which are involved in regulating cell growth and proliferation as well as DNA repair or in maintaining genome stability (Das and Kundu, 2005; Glozak et al., 2005). Thus, the application of epigenetic modulators might regulate the alterations in the gene expression which may ultimately aid in the treatment of life-threatening diseases.

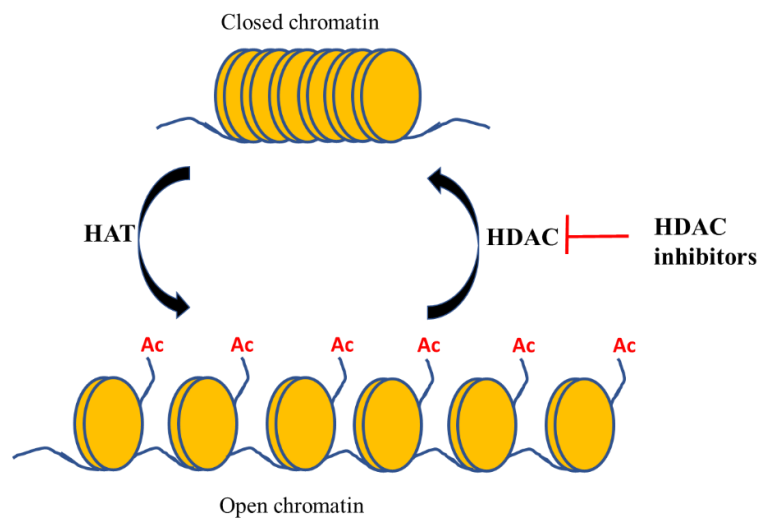


Figure 1.2. Chromatin structure and its modifications (Pulya et al., 2020).

1.3. Histone deacetylases and key features

Mammalian HDACs consists of 18 isoforms that are classified into 4 different classes based on their on their homology with yeast protein and their mechanism of action. All the four classes are distinct in terms of their structure, enzymatic function, subcellular localization and expression patterns (Gray and Ekström, 2001). The numbering of HDAC isozymes was according to their chronological order of discovery. Four different classes of

HDACs known are Class I (HDACs 1, 2, 3 and 8), Class II (further subdivided into class IIA consisting of HDACs 4, 5, 7 and 9 whereas, class IIB consisting of HDACs 6, 10), Class III (called as Sirtuins) and Class IV (HDAC 11) (Pulya et al., 2020).

➤ **Class I HDACs:** HDAC1 (Taunton et al., 1996), HDAC2 (Yang et al., 1996), HDAC3 (Yang et al., 1997), and HDAC8 (Hu et al., 2000) show a sequence similarity to reduced potassium dependency (Rpd3) like proteins of the yeast. They are predominantly located in the nucleus and primarily act through histone proteins as their substrates. They are ubiquitously expressed.

➤ **Class II HDACs:** These HDAC isoforms show a sequence similarity to yeast Histone deacetylase 1 (Hda1) like protein. Further, they are classified into two sub-classes, i.e., Iia (HDAC4, HDAC5, HDAC7 and HDAC9) and Iib (HDAC6 and HDAC10) based on their sequence homology and domain organization (Grozinger et al., 1999; Kao et al., 2002; Zhou et al., 2000). Class Iia HDACs are found in nucleus and following phosphorylation by kinases they shuttle to cytoplasm. On the other hand, Class Iib HDACs are predominantly cytoplasmic and hence, they are known to act through various non-histone proteins as their substrates for the deacetylase activity.

➤ **Class III HDACs or Sirtuins:** This class consists of SIRT1, 2, 3, 4, 5, 6, 7 named such, as they show similarity to yeast Sir2 silencing proteins (Seto and Yoshida, 2014).

➤ **Class IV HDAC:** This class consists of only HDAC11 that is known to share catalytic domain similarity to both Class I and II HDACs (Gao et al., 2002).

All the four classes are also distinct in terms of their mechanism of action in which Class I, II and IV HDACs are affiliated to zinc-dependent HDAC isoforms where Zn^{+2} metal ion acts as the co-factor for the hydrolysis of acetylated substrates. Besides, Class III is a NAD^+ dependent HDAC where NAD^+ acts as the cofactor for their enzymatic activity (Gray and Ekström, 2001). The detailed classification of HDAC isoforms along with their

cellular localization, substrates and physiological functions are highlighted in **Table 1.1**.

HDACs are basically transcriptional corepressors that are involved in the epigenetic regulation in the form of complexes with co-repressors such as Sin3, NCoR (nuclear receptor co-repressor), CoREST (co-repressor for element-1-silencing transcription factor), NuRD (nucleosome remodeling and deacetylation) and SMRT (silencing mediator of retinoid and thyroid receptors) (Kao et al., 2000). These complexes effect the downstream signaling pathways in various disease pathogenesis. Physiologically HDACs are found to play a critical role in the normal developmental processes and also in the differentiation of cells (Haberland et al., 2009). Several knockout studies in mice revealed different phenotypes and also sometimes resulting in the embryonic death. These animals were found to develop variety of abnormalities such as hypertrophy, cardiac disorders, aberrant bone mineral densities etc (Witt et al., 2009). Studies have also reported that HDACs are widely implicated in various life-threatening diseases such as different cancers, Alzheimer's disease, Huntington's disease, Parkinson's disease, other cardiovascular and inflammatory diseases (Rosato and Grant, 2005).

1.3.1. Key structural features of zinc dependent HDACs

In 1999, Finnin *et al*, for the first time described the HDAC catalytic activity and they reported the key structural features of the HDACs when inhibited by Trichostatin A (TSA) and Vorinostat (SAHA) from their crystal structures bound to HDAC related protein named as HDLP (Histone deacetylase like protein) (Finnin et al., 1999). This crystal structure study identified the presence of a tube-like 11Å hydrophobic pocket that accommodates the inhibitors. The Zinc ion (Zn^{+2}) was found to be placed at the bottom end of the hydrophobic channel to which the hydroxamic acid end of the HDAC inhibitors (HDACis) is bound. Alongside, a deep internal cavity made up by arginine, tyrosine and cysteine residues was also revealed (Finnin et al., 1999).

Table 1.1. Classification of HDAC isoforms, their cellular localization, substrates and physiological functions.

Class	HDAC Isoform	Chromosomal location	Amino acids No.	Substrates	Physiological function
I	HDAC1	1p35 – p35.1	483	Histones, GATA, YY1, NF-kB, ATM, Myo D, p53, BRCA1,	Cell growth & proliferation, apoptosis, transcriptional regulation, cell survival.
	HDAC2	6q21	488	Histones, HOP, GATA2, BRCA1, MEC IRS-1,	Proliferation control and apoptosis, transcriptional repressor.
	HDAC3	5q31.3	428	Histones, HDAC4, GATA1, NF-kB, pRb	Cell growth & proliferation, differentiation, a transcriptional repressor, Fox3 deacetylation.
II	HDAC8	Xq13.1	377	Histones, SMC3, α -tubulin, cortactin, p53, ERR- α	Proliferation, differentiation, and cell survival.
	HDAC4	2q37.3	1084	Histones. p53, p21, GATA, FOXO, HPI, CaM, MEF2,	Differentiation, angiogenesis, cytoskeletal dynamics, and cell motility.
	HDAC5	17q21.31	1122	Histones, YY1, MEF2, CaM	Differentiation, lymphocyte activation, endothelial cell function.
HDAC7	12q13.11	912	Histones, PML, Runx2, HIF-1 α , MEF2	Angiogenesis, Lymphocyte activation, thrombocyte differentiation.	
III	HDAC9	7p21	1069	Histones, MEF2, CaM	Deacetylates FoxP3, Immunosuppressive activity.
	HDAC6	Xp11.23	1215	Cortactin, α -tubulin, HSP90, PP1, LcoR, SHP	Regulation of protein degradation through aggresome pathway, Hsp90 chaperone activity, cytoskeletal dynamics, cell motility, Angiogenesis.
	HDAC10	2q13.33	669	PP1, SHP	Angiogenesis.
III	SIRT1	10q21.3	747	Histones, FOXO, NF-kB,	DNA repair, cell survival, autoimmunity.
	SIRT2	19q13.2	389	SREBP-1c, p53, p300, p73,	DNA repair, cell survival, cell invasion.
	SIRT3	11p15.5	399	cortactin, α -tubulin, histones	DNA repair, cell signalling apoptosis.

Chapter 1: Introduction

In case of Class I HDACs, they share a common feature of the presence of 11Å deep channel alongside 14Å cavity bound to the catalytic active site of Zn^{+2} ion. The carbonyl group of glycine and the side chain of tyrosine point inwards to the 11Å channel and the Zn^{+2} ion is situated near the bottom of the pocket. The Zn^{+2} ion exists in penta-coordination with the histidine and asparagine amino acid side-chains along with the carbonyl group of the inhibitor and a molecule of water (Manal et al., 2016). The structural features of HDAC8 are distinct from other class I HDACs. HDAC8 is found to have a bigger surface opening and larger active site pocket and also lacks in protein binding domain at the C-terminal end as that of other class I HDACs. The presence of L1 loop of amino acid residues 30 to 36 at the N-terminal end of the protein, and the formation of L1 to L7 loops in the catalytic domain with the Zn^{+2} ion located between loop 7 and loop 4 were considered to be distinct structural features of HDAC8 (Gantt et al., 2006).

Class IIa HDACs are made up of C-terminal catalytic domain and N-terminal domain of 600 amino acid residues that are responsible for their localization and shuttling between both cytoplasm and nucleus and also for their catalytic activity. HDAC4 and HDAC7 are distinct in their functional properties to that of other class II HDACs and are structurally similar to class I HDACs (Yang and Grégoire, 2005). A second Zn^{+2} binding motif was found in HDAC4 and HDAC7 with an extended groove adjacent to the active site of the hydrophobic pocket. The Zn^{+2} ion of the catalytic active site is found to coordinate with cysteine and histidine residues which form the exclusive feature for class IIa HDACs (Zhou et al., 2000). The presence of hydroxyl group of tyrosine 306 that is known to play a critical role in the stabilization of the transition state yielding an oxyanion intermediate for class I and IIb HDACs is absent and replaced with histidine 976 and histidine 843 in HDAC4 and HDAC7 thus rendering them with diminished enzymatic activity of class IIa HDACs

(Manal et al., 2016). On the other hand, class IIb HDACs possess two catalytic domains and are the lengthiest of all HDAC isoforms. The presence of leucine rich region in HDAC10 and the structural homology of C and N – terminal regions suggest a second catalytic domain (Kao et al., 2002). Moreover, the presence of SE-14 domain as the linker between two domains of the protein consisting of 8 successive tetradecapeptide repeats were found to be essential for the cytoplasmic retention of HDAC6. The unique ZnF-UBP domain at the C-terminal end is involved in ubiquitination, a modification that is involved in protein clearance and degradation via aggresome pathway (Pulya et al., 2020).

HDAC11 is the smallest HDAC known with only 347 amino acids present and 80% of its protein sequence encodes the HDAC catalytic domain leaving very small N and C-terminal residues (Gao et al., 2002). HDAC11 also has the catalytic channel similar to other HDACs and it is found to be enlarged by other amino acid substitutions thus accommodating larger acyl groups like in HDAC8. HDAC11 was found to possess the loop L2 with asparagine 101 positioned at the entrance of the tunnel and this L2 loop has a key role in the function of substrate recognition and catalysis while fixing the substrate conformation (Liu et al., 2020).

1.3.2. Catalytic mechanism of action of HDACs

The catalytic mechanism of action of HDACs for the lysine deacetylase activity was first described by Finnin *et al* in 1999 when studied with the HDACis, TSA and SAHA bound HDAC homologue structures (**Figure 1.3.**) (Finnin et al., 1999). The mechanism started with the chelation of the carbonyl group of the acetyl lysine to the catalytic bidentate Zn^{+2} ion and the necessary water molecule thus protonating histidine 132 leading to the polarization of the carbonyl group followed by the activation of elevated electrophilic carbon. Following which the water gets deprotonated and the subsequent protonation of histidine 131 leading to the production of a hydroxide ion

attacking the carbonyl group of the acetyl. This results in the production of a tetrahedral acyloxyanion which is further stabilized by the hydroxyl group of tyrosine 297. The final step involves the proton transfer from the histidine 131 to the acyloxyanion which led to the generation of the acetate and the terminal ammonium on the lysine as byproducts thus completing the deacetylation reaction (Finnin et al., 1999).

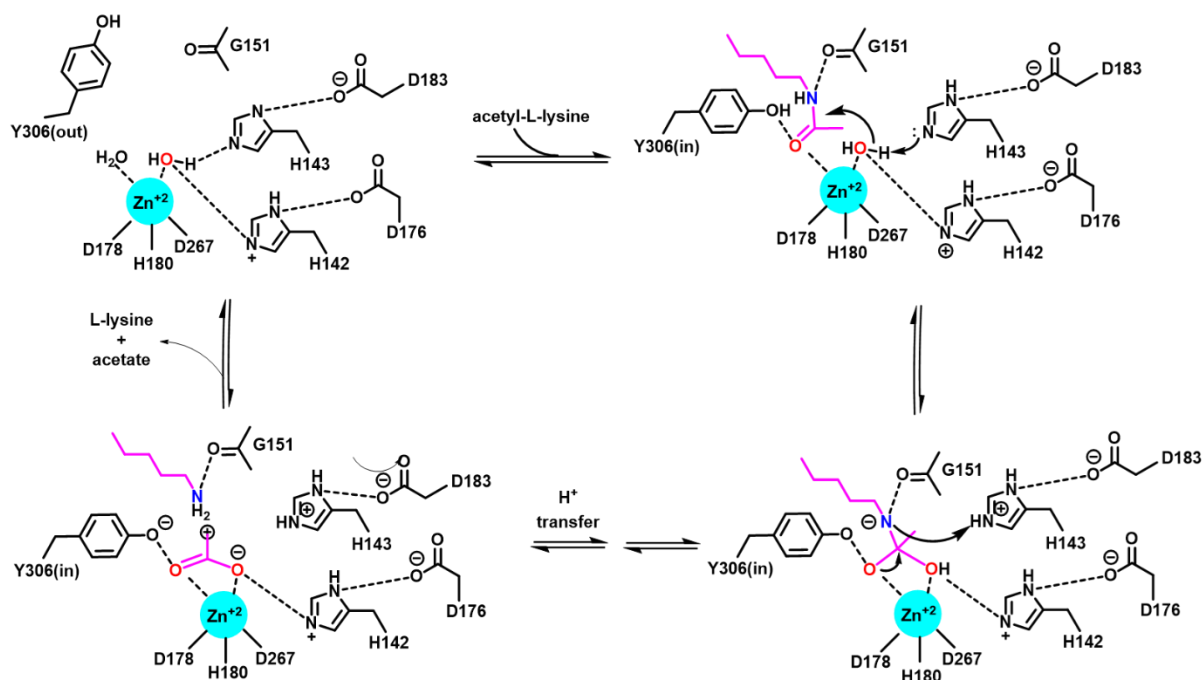


Figure 1.3. Proposed mechanism for histone deacetylase catalysis (Finnin et al., 1999).

1.4. Zinc dependent HDAC isoforms and cancer

One of the first identified hallmarks of cancer is the hypoacetylation and hypomethylation of K16 and K20 residues of H4 histone protein (Fraga et al., 2005). While forming the complexes with the various co-repressors, HDACs exhibit transcriptional repression activity thus causing their implications in different types of cancer (**Figure 1.4.**) (Ramaiah et al., 2021). These histone modifications resulted in unregulated growth potential in tumor cells and the HDAC overexpression is directly correlated to various advanced cancers and their etiology. Abnormal expression of HDACs often leads to different proliferative and non-proliferative signalling pathways and hence, HDAC inhibition is correlated with cell cycle arrest and apoptosis (Brancolini et al., 2022). HDACs

are also found to regulate tumor suppressor genes and oncogenes at the transcription level playing a critical role at various stages of cancer disease progression such as apoptosis, cell cycle, DNA damage and repair, metastasis, angiogenesis, cancer cell proliferation and stemness properties of tumor cells (Hai et al., 2022). Along with targeting histones, the deacetylation activity of HDACs affecting various non-histone proteins such as p53, E2F, α -tubulin and MyoD thus resulting in the execution of more complicated functions of HDACs in many cellular processes (Hai et al., 2021).

1.4.1. Class I HDACs

Class I HDACs (HDAC1 – 3 and 8) are the first and the most widely implicated in different cancers and many HDACs are also identified targeting these isoforms at the preclinical level. HDAC1 is mainly oncogenic in various tumor cells but literature has also reported its dual role in case of acute promyelocytic leukaemia (APL) by functioning as the tumor suppressor. HDAC1 and 2 exhibited high similarity in their binding sites thus indicating functional redundancy. They often together with other protein complexes exert their activity through the regulation of transcription, DNA repair. One of the main target proteins of HDAC1/2 is p53 which affects several downstream pathways by p53. Several HDAC1/2 corepressor complexes are known such as SIN3A (switch-independent protein 3A), MiDAC (Mitotic deacetylase), NuRD, MIER (mesoderm induction early response), CoREST, RERE (arginine-glutamic acid dipeptide repeats). These complexes were found to play key role in inhibiting the activity of tumor suppressor genes and also were found to be highly expressed in different tumor malignancies (Ropero and Esteller, 2007). HDAC3 forms the active complex with NCoR1/2 and modify histones and thus silence transcription. HDAC3 promotes cancer cell proliferation by regulating the transcription factors I and II thus inhibiting nuclear receptor transporting activity (Guenther et al., 2001). HDAC3 is proved to be associated with various cancers due to its overexpression. HDAC3 is known

to play a vital role in cell cycle progression, DNA damage and repair, apoptosis and also in regulating cancer cell proliferation (Karagianni and Wong, 2007). Overexpressed HDAC3 is found in the pathogenesis of various cancer progression such as breast cancer, colon cancer, pancreatic cancer, prostate cancer, colorectal cancer, lymphoma, myeloma, leukemia, melanoma and glioma, Ewing's sarcoma, and cholangiocarcinoma (Routholla et al., 2021b). HDAC8 is found to be overexpressed in various cancers such as colon, cervical, lung, breast cancers as well as in T cell lymphoma, acute lymphocytic leukemia (ALL), acute myeloid leukemia (AML) and also in neuroblastoma conditions. HDAC8 with its unique structural aspects and also due to deacetylating both histone and non-histone substrates present in both nucleus and the cytoplasm such as p53, estrogen related receptor alpha (ERR α), structural maintenance of chromosomes 3 (SMC3), cortactin, inv (16) fusion protein thus leading to different physiological functions such as cell cycle regulation, tumorigenesis, muscle contraction (Kim et al., 2022).

1.4.2. Class II HDACs

Class II HDACs due to their unique structural and functional aspects exert various functions due to their association with different binding proteins such as NCoR/SMRT, thus executing the epigenetic modulations (Yang and Grégoire, 2005). Class IIa HDACs retain in the nucleus due to their association with a transcription factor MEF2, and on the other hand 14-3-3 protein retains the HDACs in the cytoplasm thus avoiding their transport to the nucleus upon binding to MEF2. HDAC4 upon deacetylation of transcription factors such as SP1 (specificity protein 1) and Kruppel-like factor-5 promotes cancer cell invasion and proliferation in case of glioma (Parra, 2015). HDAC4 was also found to play a crucial role in promoting drug resistance via inhibiting pro-apoptotic genes. HDAC4 overexpression was found in hepatocellular carcinoma, breast cancer, gastric cancer, high-grade tumors like lymphoma or leukemia. HDAC4 through the regulation of proteostasis

and autophagy has a key role in multiple myeloma (Cuttini et al., 2023). HDAC4 and also HDAC5 are investigated in the development and aggressiveness of various solid tumors such as lung cancer, nasopharyngeal cancer and esophageal cancer through promoting epithelial mesenchymal transition (EMT) and metastasis. HDAC5 primarily functions in cell proliferation, invasion, immune responses and the cancer stemness maintenance in different cancers. HDAC5 via the deacetylation of p65, known to promote cancer progression and therapeutic resistance in case of pancreatic cancer. HDAC5 is widely overexpressed in case of breast cancer, hepatocellular cancer, lung cancer, melanoma, lymphoma, ovarian cancer, pancreatic cancer, colorectal cancer, glioma and osteosarcoma (Yang et al., 2021). HDAC9, found to enhance cell proliferation and drug resistance in lymphoblastic leukemia. Overexpression of HDAC9 downregulates the activity of melatonin, thus playing a key role in lung cancer (Parra, 2015).

Being majorly localized in the cytoplasm, HDAC6 has rare functions in gene transcriptional regulation. Rather, it has exerted its main functions in maintaining cell division, migration, angiogenesis, cell motility and adhesion. High levels of HDAC6 are implicated in case of triple negative breast cancer, estrogen receptor positive breast cancer, primary melanoma, hepatocellular carcinoma functioning via cortactin/F-actin binding pathway, estrogen receptor regulator, alpha-tubulin deacetylation, PD-L1 upregulation, p53 deacetylation, PTPN1/ERK1/2 pathways (Pulya et al., 2020). HDAC10, was found to be primarily overexpressed in case of lung cancer, ovarian cancer and on the other hand, HDAC10 was found to exhibit tumor suppressor property in case of cervical cancer (Kao et al., 2002).

1.4.3. Class IV HDAC

HDAC11, the only class IV HDAC isoform, was found to be overexpressed in case of breast, colon, lung, liver, prostate, testicular, colon and ovarian cancers. HDAC11 was

found to promote cancer proliferation via inhibiting the p53 transcription thus exerting its anti-apoptotic activity of cancer cells. High levels of HDAC11 are correlated with cancer cell stemness causing their self-renewal and inducing drug resistance. On the contrary, HDAC11 expression is anticorrelated in case of uveal melanomas and gliomas and HDAC11 knockout mice have exhibited an increase in the lymphoma tumor growth. Therefore, HDAC11 role is not fully elucidated and is complex in its nature (Núñez-Álvarez and Suelves, 2022).

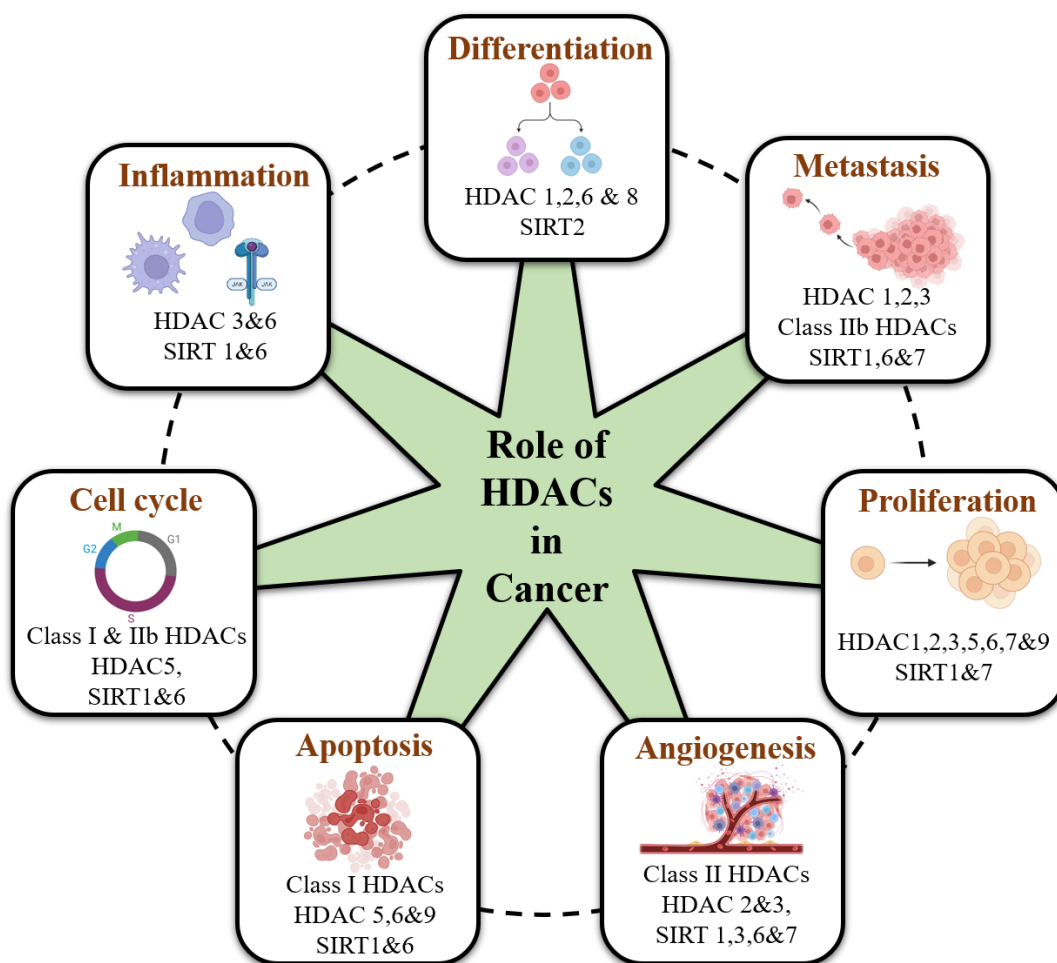


Figure 1.4. Role of different HDAC isoforms in cancer pathogenesis.

1.5. HDAC inhibitors as anticancer agents

Given the critical role of different HDAC isoforms in the prognosis of different cancers and targeting HDACs by using histone deacetylase inhibitors (HDACis) have increasingly gained attention in the recent years at both preclinical and clinical therapeutic

level. HDAC*is*, upon inhibiting the HDACs, suppress their deacetylase activity thus attaining the balanced state of acetylation. HDAC inhibition occurs by various mechanisms mostly by promoting cell death. HDAC inhibition upregulates cell cycle gene p21 which leads to cell cycle arrest and inhibiting differentiation, and also upregulates the intrinsic and extrinsic apoptosis pathways through the induction of pro apoptotic genes (Sambucetti et al., 1999). On the other hand, hyperacetylation stabilizes the p53 protein, promoting cell cycle arrest (Li et al., 2011). HDAC*is* thus affect various underlying pathways and regulate the gene expression thus exerting their therapeutic efficacy. HDAC*is* commonly possess a basic pharmacophoric model that consists of a cap group that interacts with the surface of the enzyme, a zinc binding group (ZBG) that interacts with the zinc ion at the catalytic pocket and a linker that serves as a bridge between the cap and ZBG (Johnstone, 2002). The first few identified HDAC*is* are non-selective HDAC*is* which bind to different HDAC isoforms non-specifically and cause various off-target activities and toxicities. Later, modifications around the pharmacophore of the HDAC*is* have been carried out extensively to develop isoform-selective HDAC*is*. As the anticancer effect of HDAC inhibition is well established by now, there is a growing interest in the research area of HDAC*is* and since past few years numerous HDAC*is* have been extensively studied preclinically and clinically (Patel et al., 2023).

1.5.1. Classification of HDAC inhibitors

Based on the chemical structure of ZBGs, HDAC*is* were further divided into four major classes of:

1. Hydroxamates: such as vorinostat (SAHA), belinostat, panobinostat, abexinostat, givinostat.
2. Benzamides: such as BG-45, CI-994 (tacedenaline), entinostat, mocetinostat, chidamide etc.

3. Short chain fatty acids: such as valproic acid, phenyl butyrate etc.
4. Cyclic tetrapeptide: such as romidepsin etc.

Along with the above mentioned HDACis, there are several other identified HDACis with various other ZBGs such as thiols, esters, hydrazides, electrophilic ketones, thioacetyl groups, sulfonamides etc, that have gained attention during recent times due to enhanced potency and selectivity towards individual HDAC isoforms (Frühauf and Meyer-Almes, 2021).

1.5.2. FDA approved HDAC inhibitors

Despite the rigorous studies on numerous HDACis, so far only 6 have been clinically approved namely vorinostat (SAHA), romidepsin (FK228), belinostat (PXD101), panobinostat (LBH589), pracinostat approved by U.S. Food and Drug Administration (FDA) and chidamide (approved by China FDA) for the treatment of different hematological cancers. The structures and details of the FDA approved HDACis are represented in **Figure 1.5** and **Table 1.2**. Vorinostat (SAHA), is the first FDA approved HDACi for the treatment of patients with relapsed and refractory cutaneous T-cell lymphoma (CTCL), marketed by Merck & Co. Inc. in 2006 (Mann et al., 2007). In 2009, romidepsin (FK228, a natural product), was FDA approved for CTCL treatment by Gloucester Pharmaceuticals (Celgene). Later, in 2011, romidepsin was also approved for peripheral T-cell lymphoma (PTCL) therapy (Barbarotta and Hurley, 2015). Belinostat (PXD101), in 2014 was FDA approved for the treatment of patients with relapsed or refractory peripheral T-cell lymphoma (PTCL) by Spectrum Pharmaceuticals (Lee et al., 2015). Later in 2015, panobinostat (LBH589) was approved for the treatment of multiple myeloma developed by Novartis Pharmaceutical Company (Raedler, 2016). Pracinostat (SB939), was approved in the year 2014 by FDA and given the orphan drug designation for the treatment of acute myeloid leukemia (AML) by Helsinn group and MEI pharma

companies (Novotny-Diermayr et al., 2012). China FDA in the year 2015, approved chidamide for the treatment of relapsed or refractory PTCL and pancreatic cancer discovered and developed by Chipscreen Biosciences (Lu et al., 2016).

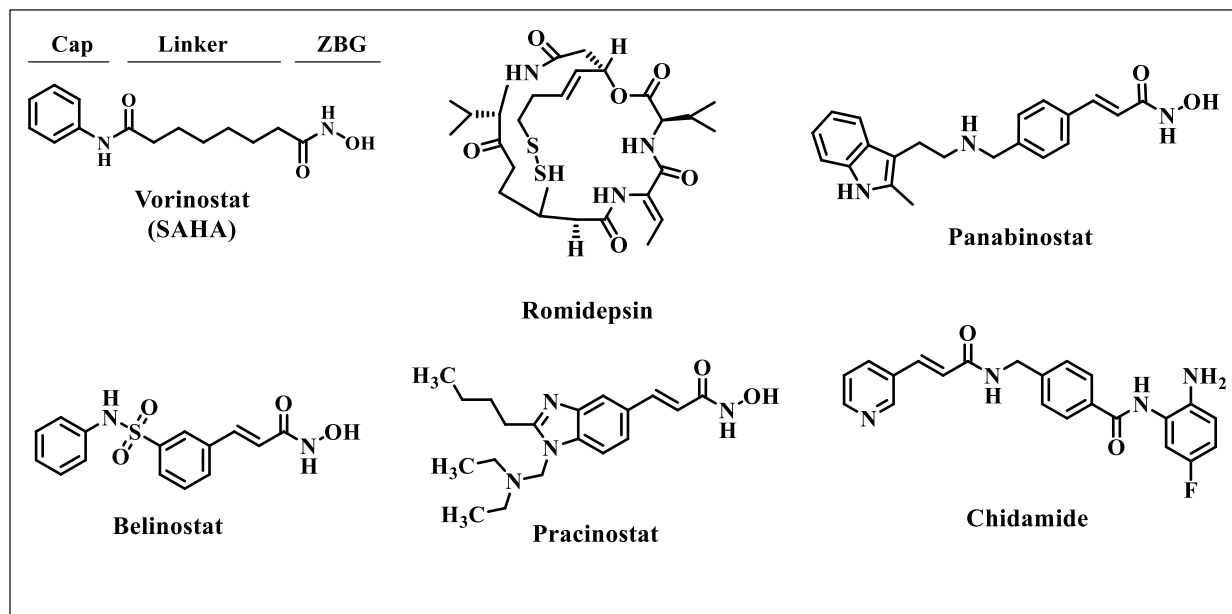


Figure 1.5. Structures of clinically approved HDAC inhibitors.

Table 1.2. FDA approved HDAC inhibitors, their indication and details. (Pulya et al., 2020)

Drug name	Trade name	Class of inhibitor	Indication	Year approved, Company
Vorinostat (SAHA)	Zolinza	Hydroxamate	Cutaneous T-cell lymphoma	2006, Merck
Belinostat (PXD101)	Belidaq	Hydroxamate	Relapsed peripheral T-cell lymphoma	2014, Spectrum
Panabinostat (LBH589)	Farydak	Hydroxamate	Relapsed multiple myeloma	2015, Novartis
Romidepsin (FK228)	Istodax	Cyclic peptide	Peripheral T-cell lymphoma	2009, Celgene
Chidamide (HBI8000)	Epidaza	Benzamide	Relapsed peripheral T-cell lymphoma	2015, Shenzhen core biotechnology
Pracinostat (SB939)	-	Hydroxamate	Acute myeloid leukemia	2016, Helsinn and MEI pharma

1.5.3. Mechanism of action of HDAC inhibitors

HDAC inhibitors (HDAC*is*) are a class of epigenetic modulators or drugs that exert various biological activities by modulating histone acetylation at specific lysine residues

Chapter 1: Introduction

on histone proteins. Particularly, HDACs have major application as antitumor agents both at preclinical and clinical level (Johnstone, 2002). Apart from modulating histone acetylation over histone proteins and regulating gene expression at the transcription level, HDACs also target several non-histone proteins thus governing various cellular and physiological processes such as DNA damage and repair, cell division, signal transduction, oxidative stress, apoptosis, cytotoxicity, anti-proliferative activities, autophagy. The treatment with SAHA induces DNA double strand damage and oxidative stress, causes cell differentiation, cell cycle arrest at G2/M phase due to the repression of *cyclin D* and *cyclin A* genes, thus reducing CDK2 and CDK4 kinase activities and also cause the apoptosis of tumor cells via promoting various protein acetylation and modulating the gene expression (Ruefli et al., 2001). Further, SAHA inhibits mTOR (mammalian target of rapamycin), accumulates the reactive oxygen species (ROS), upregulates the p21 CIP/WAF1 by inducing CDKN1A, causes the hyperacetylation of transcription factors such as NF- κ B, p53, STAT1, STAT3, E2F1 thus affecting the cell cycle progression, DNA-damage response, and apoptosis (Saito et al., 2017). Treatment with panobinostat induced the hyperacetylation of H3 and H4, increased the level of p21, caused apoptosome inactivation, and apoptosis mediated cell death (Prince et al., 2009). The treatment with romidepsin was found to induce apoptosis in chemoresistant cells via modulating c-MYC, HSP90 and p53 thus enabling their accessibility for its target genes and also inducing protein degradation, cell growth inhibition and eventual cell death. Romidepsin treatment leads to the accumulation of ROS, causing translocation of AIF (apoptosis inducing factor) to the nucleus leading to apoptosis caused by ROS mediated cell death (Karthik et al., 2014). Belinostat, is known to inhibit all the classes of HDAC isoforms thus facilitating various mechanisms leading to cell cycle arrest, inhibiting cell proliferation and inducing apoptosis, therefore, exerting its potent antitumor activities (Manal et al., 2016). Chidamide, a

benzamide HDACi, upon treatment was found to induce the expression of apoptosis related genes such as EMP1, EPLIN, T-cell receptor, and death receptor 6 causing apoptosis. Further, it is also reported to induce cell cycle arrest and apoptosis along with reversing the EMT and drug resistance of tumor cells (Ning et al., 2012).

HDACis, via targeting histones H3 and H4 induce apoptosis via both extrinsic and intrinsic pathways. They induce caspase-mediated apoptosis, also downregulate the c-FLIP protein, upregulate TRAIL, DR5, TNF- α thus activating caspase 8 and caspase 10. Further, they also induce mitochondrial mediated apoptosis via intrinsic pathways such as upregulating the expression of pro-apoptotic proteins of BCL2 family (Bid, Bim, Bmf etc) and also downregulate the expression of anti-apoptotic proteins of BCL2 family (BCL2, BCL-XL, BCL-w), MCL-1 and XIAP. They also cause the gene induction for Caspase 9, Apaf1, Cytochrome *c* causing mitochondrial damage leading to apoptosis (Brancolini et al., 2022). HDACis via modulating various non-histone proteins cause the activation of the aggresome pathway leading to the degradation of misfolded protein aggregates. HDACis also cause cell migration and motility via hyperacetylating cortactin, blocking F-actin association and thus impairing cell periphery translocation and motility. The hyperacetylation of tubulin decreases the microtubule dynamics thus obstructing the fibroblast invasion and motility. Further, HDACis treatment affect the cell motility and metastasis via the downregulation of matrix metalloproteinases such as MMP-1, MMP-2, MMP-9 and also cause the overexpression of TIMP-1, TIMP-3 proteins. They also act via the gene repression of RAD51, BRAC1, BRAC2, Ku70 genes causing oxidative stress and subsequent DNA damage (Boyault et al., 2007). The different mechanism of action of HDACis in various stages of cancer is depicted in the **Figure 1.6**.

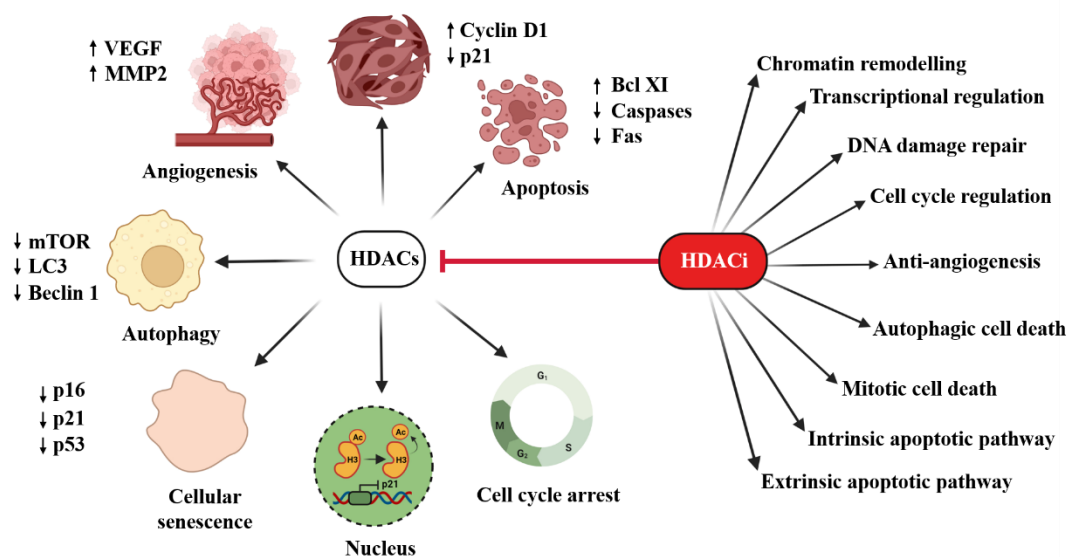


Figure 1.6. Different mechanism of action of HDAC*is* in cancer.

1.6. Isoform selective HDAC inhibitors

As mentioned above, so far only six HDAC*is* are clinically approved till date and all of them are non-selective towards HDAC isoforms and therefore named as *pan*-HDAC inhibitors. Apart from the *pan*-HDAC*is*, several other HDAC*is* have been evaluated in various phases of clinical and preclinical trials for their potential anticancer properties (Ho et al., 2020). Though HDAC*is* are well-recognized as anticancer agents, their non-specific mechanism of action towards different HDAC isoforms may lead to unwanted off-target adverse effects as well as dose-related toxicities (Ramaiah et al., 2021). Hence, there is a pressing need for identifying and developing isoform-selective HDAC*is* to understand the underlying mechanisms of the specific HDAC isozyme in the disease progression and downstream pathways. The isoform-selectivity might be achieved through the structural modification of any of the pharmacophore region such as cap region, linker or ZBG.

Several advantages of isoform selectivity can be achieved by inhibiting class I HDACs that are predominantly located in the nucleus, in particular HDACs1-3. This might target specifically transcriptional regulation and subsequently, the underlying gene

expression (Xu et al., 2007). Furthermore, inhibiting HDAC6 selectively might offer other therapeutic interventions other than the class I HDACs as HDAC6 is predominantly cytoplasmic in nature and inhibiting HDAC6 might affect various other non-histone proteins and cause related biological effects (Pulya et al., 2020). Selective inhibition of HDAC8 might offer a unique therapeutic implication other than modulating histones due to its different structural features to that of other class I HDACs (M et al., 2022).

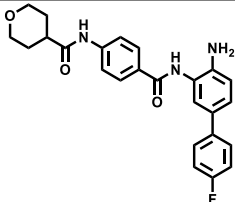
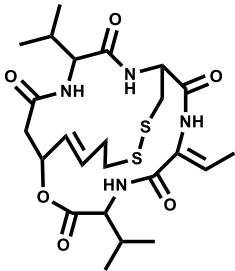
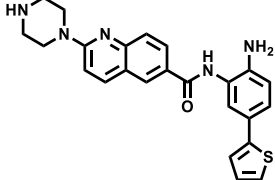
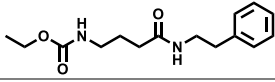
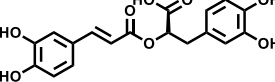
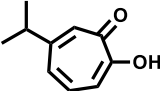
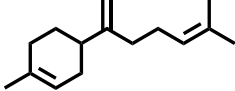
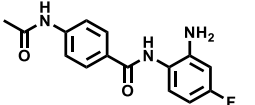
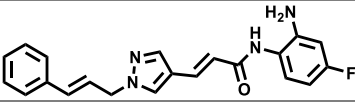
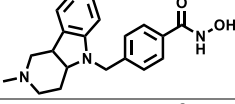
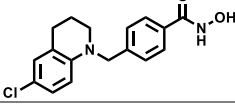
The existing FDA approved *pan*-HDACis exhibit a wide range of toxicities such as fatigue, nausea, liver damage, thrombocytopenia and cardiotoxicity. These compounds due to their non-specific mechanism of action and thus effect multiple cellular processes and signalling pathways of normal physiological function other than the desired site of action in cancers (Karagiannis and Rampias, 2021).

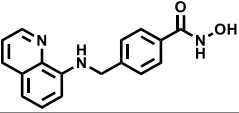
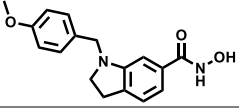
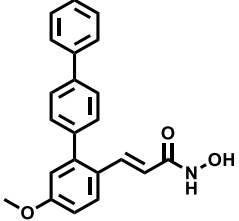
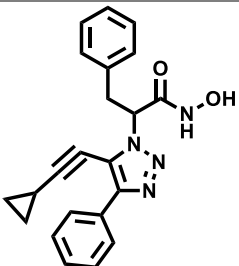
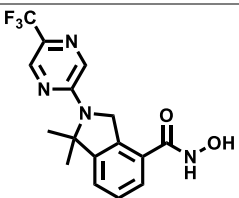
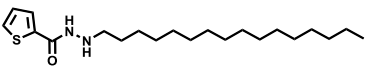
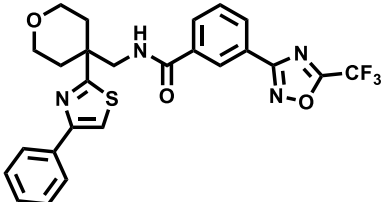
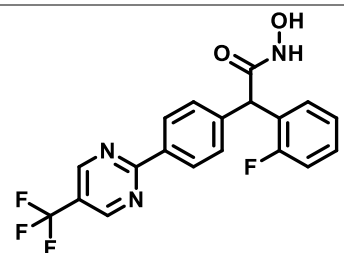
On the other hand, isoform selective HDACis offer advantages in reducing the side-effects by targeting specifically and also can be employed as chemical probes or tools in understanding the individual role of HDAC isoforms as well as to elucidate their detailed mechanism of action in the cancer disease progression. They might also provide targeted therapies for different malignancies thus providing insights into future drug development based on HDACis.

Designing and identifying the isoform selective HDACis is the most challenging task right now for the researchers worldwide, owing to their numerous advantages over *pan*-HDACis. But it is a difficult task, due to high sequential homology in the structures of HDAC isoforms and in order to design the isoform selective inhibitors, the detail information about the structural features of individual HDAC isoforms need to be elucidated. Recently, studies have also emerged identifying the crystal structures of HDAC isoforms bound to their selective ligands at the active site, thus providing the valuable insights of the differences among the active sites of the individual HDAC isoform that helps

researchers to design and develop highly potent and selective HDACis (Thaler and Mercurio, 2014).

Table 1.3. Details of isoform selective HDACis.

Inhibitor	Structure	Isoform	Clinical status	Indication
BRD4884			Preclinical	Neurodegenerative disorders
FK228		HDAC1&2	Phase II	Peripheral T-cell lymphoma
ACY-957			Preclinical	Acute Myeloid Leukemia
Santacruzamate A			Preclinical	Hepatocellular carcinoma
Rosmarinic acid			Preclinical	Prostate cancer
B-Thujaplicin		HDAC2	Preclinical	T-cell lymphoma
Gamma-Bisabolene			Preclinical	Oral squamous cell carcinoma
BRD3308			Preclinical	Type 1 Diabetes
RGFP996		HDAC3	Preclinical	Neurodegenerative disorders
Tubastatin A		HDAC6 & 10	Preclinical	Neurodegenerative disorders
SW-100		HDAC6	Preclinical	Neurodegenerative disorders

MPT0G211		Preclinical	Multiple myeloma
PCI-34051		Preclinical	T-cell lymphoma
WK2-16		Preclinical	Neurodegenerative disorders
Beeler's phenylalanine derived hydroxamic acid		Preclinical	Cancer
FT895		Preclinical	Cancer
N'-hexadecylthiophene-2-carbohydrazide		Preclinical	Cancer
TMP269		Preclinical	Neurodegenerative disorders
CHDI-390576		Preclinical	Neurodegenerative disorders

1.7. Limitations of the existing HDAC inhibitors

Although HDACis have proven to be promising anticancer agents both preclinically and clinically, only six have been FDA approved, that too for only haematological

malignancies. None of the HDAC*s* so far were approved for solid tumors. At the clinical level, many HDAC*s* have displayed severe side-effects and dose related toxicities. There are several limitations identified for the existing HDAC*s* and they are listed below:

- Lack of HDAC isoform selectivity causing poor therapeutic efficacy and other non-specific toxicities.
- At the clinical level, HDAC*s* were found to cause severe side-effects such as anaemia, fatigue, cardiotoxicity, thrombocytopenia, neutropenia and also diarrhoea and sometimes even death of the patient.
- Poor pharmacokinetic profile, leading to larger therapeutic window and higher dosage regimen causing several dose-related toxicities.
- The induction of chemoresistance during the clinical therapy.
- HDAC*s* suffer through extensive metabolism mainly through glucuronidation thus affecting the bioavailability of the drug.

Therefore, further studies must be done to focus on addressing these limitations and towards that direction, the discovery and development of highly potent and isoform selective HDAC*s* might offer promising therapeutic efficacy at the clinical level as anticancer drugs.

Chapter 2
Literature review

2.1 About HDAC3

Among class I HDACs, HDAC3 has been well established as a potential target due to its overexpression in different cancers. HDAC3 has a molecular weight of about 48kDa and is primarily localized in the nucleus thus acting via deacetylating histones such as H3, H4, H2A, H2B (Guenther et al., 2001). HDAC3 has been correlated with various stages of cancer progression such as cell cycle regulation, apoptosis, metastasis, signal transduction, angiogenesis along with other metabolic processes. HDAC3 has been found to be highly expressed in different body tissues including different regions of brain thus exerting its deacetylation function ubiquitously (Bhaskara et al., 2010). In particular, HDAC3 acts on the increased cellular histone during DNA replication and thus play a very important role in the gene transcriptional regulation. Recently, HDAC3 activity over other non-histone proteins has also been reported, extending its role in the deacetylation activity over other proteins (Adhikari et al., 2021; Bhaskara et al., 2010).

Structurally, HDAC3, a repressive chromatin modifying enzyme is found to form a stable multi-protein complex with NCoR/SMRT (nuclear receptor co-repressor and silencing mediator of retinoic and thyroid receptors) corepressor complex thus exerting its gene repressive properties. HDAC3 acts as the catalytic component in the HDAC3/NCoR/SMRT complex, leading to the repressive activity of target genes (Guenther et al., 2001). HDAC3 when recruited into the corepressor complex leads to enhanced deacetylation activity of HDAC3. DAD, the deacetylase activating domain, which is generally placed in the *N*-terminus of SMRT and NCoR, activates the SMRT upon activation of HDAC3. Two tightly spaced motifs SANT1 and SANT2 are included in the DAD complex and among them SANT2 functions as histone interacting domain (HID) that interacts with the histone following the binding and the activation of HDAC3 enzyme (Karagianni and Wong, 2007). HDAC3 markedly differs from other class I HDACs in its

Chapter 2: Literature Review

C-terminal domain. HDAC3/SMRT complex crystal structure revealed the presence of two monovalent cations of potassium ions one of which is closer to the active site Zn^{+2} ion with the second one situated ≥ 20 Å from the active site Zn^{2+} ion. Apart from SMRT/NCoR/HDAC3 complex, a WD40 repeat protein is present known as TBL1X (Transducin β -like 1X). This complex altogether exerts the deacetylase activity and without the co-repressor complex, HDAC3 alone has no role in the deacetylation process (Sarkar et al., 2020). Inositol phosphate 4 (Ins(1,4,5,6)P4) also involved in the activation of HDAC3 by acting as a bridge between HDAC3 and SMRT/DAD complex. HDAC3, is a protein made up of eight parallel beta sheets that is arranged in the form of loops and are composed of several amino acid residues that play a key role in determining the substrate selectivity. The amino acid residue, Arginine 265 associated with the Ins(1,4,5,6)P4 and Leucine 266 of the loop L6 plays the significant role in the substrate accessibility towards the active site of HDAC3. The loop L5 contains a tyrosine residue 198 on the enzyme surface along with the phenylalanine residue 199 that participates in the substrate specificity adjacent to the active site tunnel (Watson et al., 2012). The key structural features including the domain organisation of HDAC3 are represented in **Figure 2.1**.

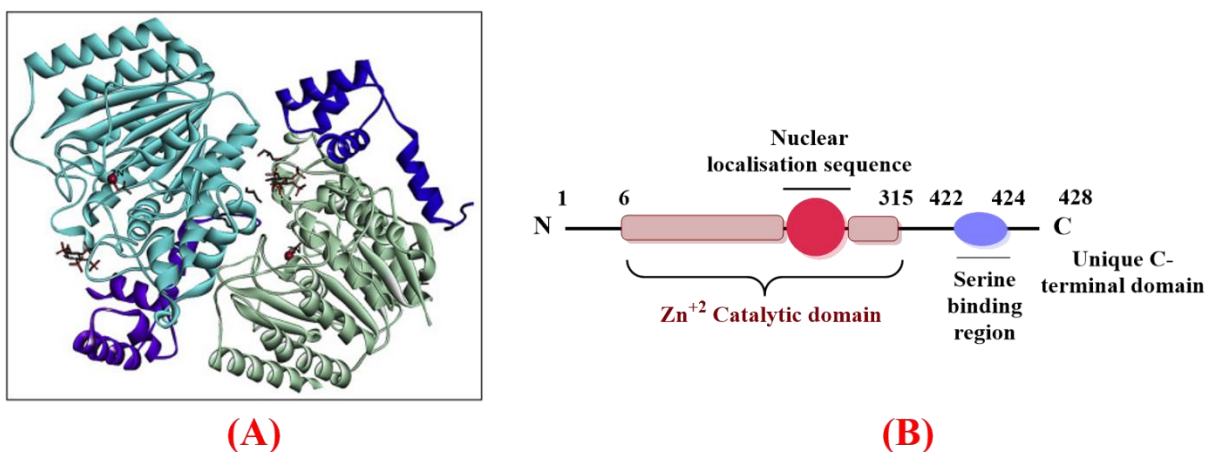


Figure 2.1. (A) Crystal structure of HDAC3 (PDB ID: 4A69) (Sarkar et al., 2020); (B) HDAC3 domain structure, organization and functions.

2.2 HDAC3 and cancer

Over time, among all other class I HDACs, HDAC3 has emerged as a crucial regulator of various stages of cancer progression and its pathogenesis. Studies reported the crucial role of HDAC3 overexpression in several downstream signaling pathways thus affecting the gene expression regulation and resulting in variety of pathogenetic conditions of not only cancer but also various other disease conditions such as inflammation and several neurological disorders (Adhikari et al., 2021). Given its significant role in cancer progression, specific HDAC3 inhibition would be a promising therapeutic strategy for combating various cancers like breast cancer, pancreatic cancer, colorectal cancer, prostate cancer, colon cancer, lymphoma, leukemia, glioma, myeloma, melanoma and Ewing's sarcoma (Adhikari et al., 2018).

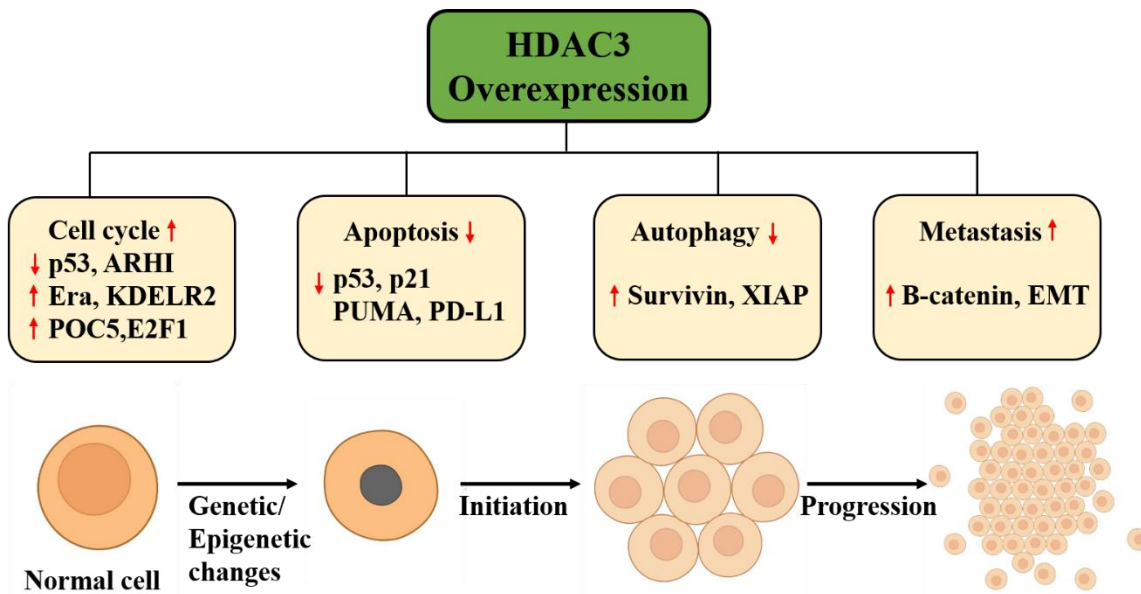


Figure 2.2. Role of HDAC3 overexpression in cancer pathogenesis.

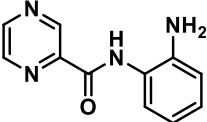
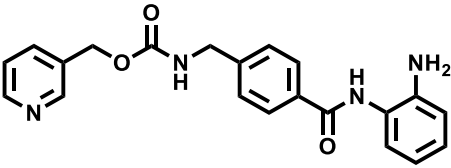
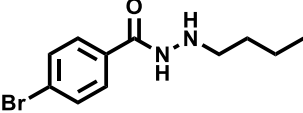
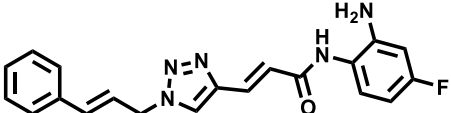
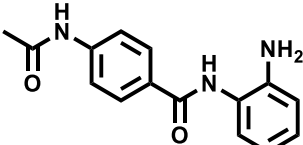
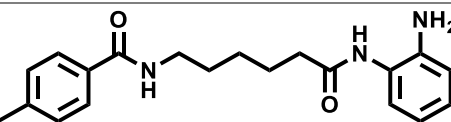
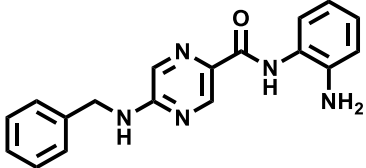
2.3 HDAC3 selective inhibitors

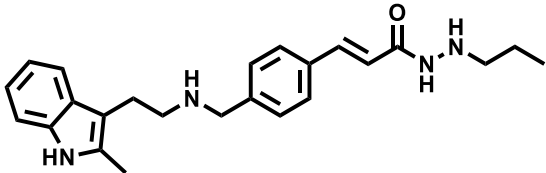
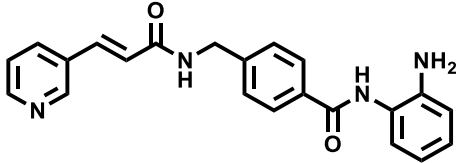
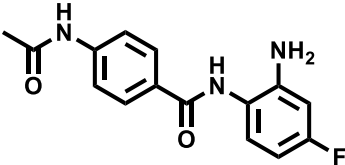
A lot of research has been taken up to date towards the exploration of HDAC3 selective inhibitors for various disease conditions. Given the flexibility of designing novel HDACis over the basic pharmacophore model, numerous pieces of literature have been reported up to the preclinical level but none of them have passed clinical trials. Many of the existing

Chapter 2: Literature Review

HDAC3is have exhibited preferential selectivity towards HDAC3 but not exclusive selectivity. As the structural and mechanistic aspects of HDAC3 are widely reported, it has been a sought-after challenge to design novel molecules as HDAC3 inhibitors. The reported HDAC3is belong to different classes of HDACis with varied ZBGs such as hydroxamates, benzamides, thiols, ketones, etc but very few of them have achieved promising preclinical outcomes (Cao et al., 2018). The list of some promising HDAC3is is tabulated in **Table 2.1**.

Table 2.1. Details of few HDAC1 – 3 selective and preferentially HDAC3 selective inhibitors including their structures and corresponding IC₅₀ values.

S. No	Name	Structure	IC ₅₀ (nM)		
			HDAC1	HDAC2	HDAC3
1	BG-45		2000	2200	289
2	MS-275		190	410	950
3	UF010		500	100	60
4	RGFP966		28670	17680	80
5	CI-994		929	930	902
6	RGFP109		60	-	50
7	PT-3		1053	2083	245

8	13a		4.69	46	0.28
9	Chidamide		95	160	67
10	BRD3308		1260	1340	64

2.4 Hydrazide-based HDAC inhibitors

So far most of the HDACis belong to either hydroxamates or benzamides as ZBG. Out of these, hydroxamates have been non-selective in terms of their HDAC inhibitory activity, whereas preferential selectivity has been exhibited by benzamide-based HDACis towards different classes, particularly class I HDACs. All the FDA-approved HDACis are *pan*-HDACis and due to their non-selective nature, their treatment has led to a high dosage regimen to produce the required effect. The limitations of hydroxamates being low bioavailability, poor metabolic stability and their strong metal chelating properties that caused undesirable clinical toxicities. Though hydroxamates are highly potent, due to their inactivation by glucuronidation-based metabolism, they were administered mostly in large doses, ultimately leading to poor pharmacokinetic profiles and dose-limiting toxicities (Yue et al., 2022).

Notably, benzamide-based HDACis were also well explored at both preclinical and clinical levels either alone or in combination with other drugs due to their preferential selectivity and druggable properties. Nevertheless, benzamides are also either non-selective or class-selective HDACis displaying little or no isoform-selectivity. Benzamide-based HDACis are in general less potent than hydroxamates, but they displayed preferential isoform selectivity and improved pharmacokinetics than hydroxamates (Frühaufer and

Chapter 2: Literature Review

Meyer-Almes, 2021). Whereas, they also did not cross the phase II level of the clinical trial may be due to their low metabolic stability and poor bioavailability *in vivo* causing adverse effects and in some cases death of the patients during the treatment (Adhikari et al., 2018). These limitations of both hydroxamates and benzamides urged the researchers to look out for novel chemotypes for ZBGs as HDACis. In this direction, recently hydrazide-based HDACis have gained major attention and very few reports are published with this ZBG, showing promising results and excellent potency as well as HDAC isoform selectivity (Wang et al., 2015). Firstly, Wang and colleagues in 2015, identified a novel chemotype benzoyl hydrazide as ZBG which they found to be impervious to glucuronidation, also exhibiting high potency and improved metabolic stability and pharmacokinetic profile. They identified a lead compound UF010 from their high-throughput screening experiments and reported the altered histone acetylation levels correlated with their *in vitro* cytotoxic activities. These hydrazides were particularly found to be HDAC1, 2 and 3 selective and therefore, they acted particularly through the activation of tumor suppressor genes causing significant anticancer potential (Wang et al., 2015). Later, few reports (**Table 2.2.**) have been published with hydrazide scaffold suggested they are impervious to glucuronidation based metabolism and also, they primarily act through modulating p53, tumor suppressor gene, thus displaying excellent properties as anticancer agents. In this direction, several modifications were reported over the cap region and linker region, keeping the hydrazide scaffold as ZBG to generate potent HDACis with improved HDAC1, 2 and 3 selectivity and pharmacological properties.

Wang and colleagues reported a series of benzoyl hydrazides as potent class I HDACis, and from the series **UF010** was identified as the lead compound with 60 nM HDAC3 inhibition, 500 and 100 nM for HDACs 1 and 2, respectively, and displaying 20-fold selectivity for class I HDACs compared to HDAC6. These compounds were found to

Chapter 2: Literature Review

activate tumor suppressor mechanisms and also inhibit oncogenic pathways. Structurally, this class of compounds contains a -CO-NH-NH- group as ZBG with a linker on one hand and an aliphatic chain that is attached to the amino group that is crucial for HDAC inhibition. This central unit of hydrazide might provide hydrogen bonding along with weak Zn^{+2} chelation with the hydrophobic groups at the cap region interacting with the hydrophobic pockets in the HDAC catalytic core. These weak Zn^{+2} chelating properties might be the reason for reduced off-target activities. The chain length of four carbons was found to produce activity and any change in the chain length reduced the class I selectivity of the compounds. **UF010** was found to cause the induction of cell death and suppress the cell-cycle progression at the G1 phase via the activation of p53 and Rb tumor suppressor pathways, and through the suppression of MYC, MYCN, KRAS oncogenic pathways (Mahmud and Liao, 2015; Wang et al., 2015).

Later, McClure and colleagues reported a series of hydrazide-based HDACis, that displayed highly potent HDAC inhibitory activities in acute myeloid leukemia disease conditions. These inhibitors were also impervious to glucuronidation-based metabolism as they possess little anionic charge thus displaying mixed or non-competitive inhibition. They have demonstrated that these compounds might be acting through an allosteric site of inhibition and thus indicating the presence of a non-catalytic metal-center target of these compounds (McClure et al., 2016). The hydrazide motif along with the carbonyl group serves as the hydrogen bond donor with weak Zn^{+2} chelation. The SAR of this series of compounds suggested an optimum chain length of either 3 or 4 carbons for HDAC3 selective inhibition and any change in the chain length has reduced HDAC3 selectivity. The lead compound from this series **3e** has exhibited HDAC3 IC_{50} potency of 0.95 nM with ~100-fold selectivity over HDAC2 and ~12.4-fold selectivity over HDAC1. The *in vitro* and *ex vivo* studies of the lead compounds displayed low nanomolar activity against the

Chapter 2: Literature Review

models of AML and are about 100-fold selective over normal human cells such as HEK-293 (McClure et al., 2016).

Further, the same group reported a series of compounds, in which they replaced their previously synthesized *o*-amino benzamide derivatives with the novel hydrazide class as ZBG and designed some indole moiety as the cap group (Li et al., 2018). They were found to be preferentially HDAC3 inhibitors over HDAC1, 2, and 6, and also their studies have demonstrated that they are highly resistant to glucuronidation, thus reducing the associated toxicities and also a possibility to overcome the high therapeutic window challenge of hydroxamates and benzamides scaffold. All these compounds were found to be potent against human acute myeloid leukemia (AML) cell line MV4-11. The most potent HDAC3 inhibitor (**13e**) was known to be potent against the human prostate cancer cell line and has no effect against normal cell line HEK229. They identified that hydrazide-based HDAC*is* act with a different mechanism of action in different cell lines (Li et al., 2018). (IC₅₀ values)

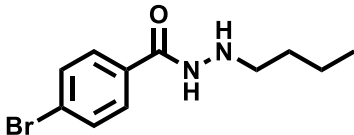
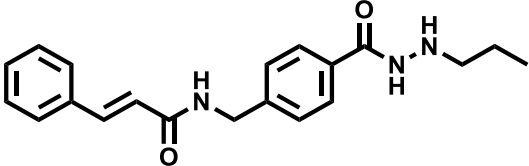
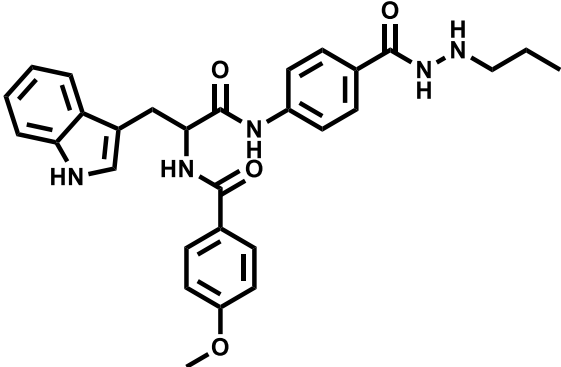
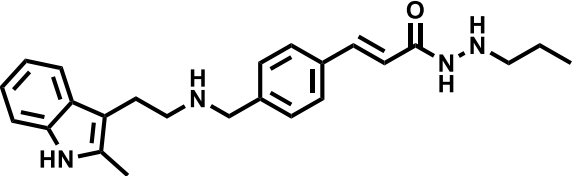
Recently, Li and co-workers reported a series of hydrazide based HDAC*is* with modifications on panobinostat at all the three pharmacophoric regions (Li et al., 2020). The lead compound of the series, **13a** has exhibited HDAC3 IC₅₀ potency of 0.28 nM with ~150-fold selectivity over HDAC2 and ~18.7-fold selectivity over HDAC1 and was found to retain the potency of panobinostat. The lead compound was found to indirectly inhibit the FLT3 pathway via the downregulation of FLT3, STAT5 and pERK thus offering a promising therapeutic strategy for the treatment of FLT3 mutation induced AML. Further, the downregulation of antiapoptotic proteins such as c-Flip, XIAP, caspase proteins was observed. The results indicated that the presence of functional p53 is required for the selective toxicity in the AML model. They have reported that **13a** causes class I HDAC inhibition induced cytotoxicity in AML model based on their p53 and FLT3 status. With

Chapter 2: Literature Review

encouraging pharmacokinetics *in vivo*, they have suggested the possibility of using lower doses with longer intervals in between the dosing (Li et al., 2020).

The most recent work by Jiang and co-workers, reported the first *in vivo* antitumor activity of the hydrazide based HDACis by identifying a lead molecule **11h**, as an orally active anti AML agent with a tumor growth inhibition percentage of 78.9% after 21 days of treatment in the mouse model of AML. Compound **11h** has demonstrated high HDAC3 IC₅₀ potency of 0.435 nM with ~42.6-fold selectivity over HDAC2 and ~6.89-fold selectivity over HDAC1 (Jiang et al., 2022).

Table 2.2. Lead compounds from the series of hydrazide based HDACis reported till including their structures, HDAC3 IC₅₀ values, their selectivity over HDAC1 and HDAC2 and their biological indication.

Cpd code	Structure	HDAC3 IC ₅₀ (nM)	Selectivity over HDAC1 and HDAC2	Biological Indication
UF010		60	~8 fold over HDAC1&2	Different cancer cell lines
3c		0.95	~100-fold (HDAC2); ~12.4-fold (HDAC1).	Acute myeloid leukemia
13e		1.41	~19.88-fold (HDAC2); ~6.76-fold (HDAC1).	Acute myeloid leukemia
13a		0.28	~150-fold (HDAC2); ~18.7-fold (HDAC1).	Acute myeloid leukemia

11h		0.44	~42.6-fold (HDAC2); ~6.89-fold (HDAC1).	Acute myeloid leukemia
-----	--	------	--	------------------------

2.5 Gaps in the existing research of HDACis

- Challenge to develop potent and isoform selective inhibitors for different HDAC isozymes as most of the available inhibitors are *pan*-HDACs or class I selective HDACs.
- So far only five reports have identified hydrazide based HDACis as anticancer agents, particularly in acute myeloid leukemia conditions and none in other haematological as well as solid tumor malignancies.
- Extensive research in the structure activity relationships needs to be done in case of hydrazide based HDACis.
- The detailed pharmacokinetic analysis, metabolic stability analysis needs to be explored and studied of hydrazide based HDACis to understand their pharmacological properties and explore its clinical application.
- Identification of more isoform specific HDACis in order to exploit the pathological implications of individual HDACs and to understand their role in different cancer pathology. Further, the detailed mechanism of action of causing the anticancer activity needs to be studied.
- Optimisation of the *in vivo* dosage regimen of the hydrazide based HDACis, in order to reduce the unwanted effects during their clinical application.

Objectives

The main objective of our research is to identify and develop potent and selective histone deacetylase 3 inhibitors with promising anticancer therapeutic efficacy following hybrid structure strategy. Histone deacetylase inhibitors have garnered much attention as promising anticancer therapeutics with increased preclinical and clinical applications. Nevertheless, they have exhibited several side-effects, toxicities and poor clinical efficacy at the clinical trials due to their non-selective histone deacetylase inhibitory activity. Recently, the main focus of HDAC inhibitor discovery has been towards the identification of isoform-selective HDAC*is* and few of them are in preclinical and clinical level either alone or in combination. In this direction, we now aim to study the effect of a novel zinc binding group, hydrazide in the design of isoform selective HDAC*is* with various modifications incorporated in the cap region and linker region. We further studied their potent anticancer activity *in vitro* as well as in the *in vivo* tumor xenograft mouse model.

Objective I

To identify novel benzoyl hydrazides based small molecules as HDAC3 selective inhibitors as promising anticancer agents.

Specific aims:

1. To design and synthesize a series of novel benzoyl hydrazides with hydrazide as ZBG followed by their characterization using ^1H NMR, ^{13}C NMR, HPLC/LC-MS, HRMS spectroscopy.
2. Assessment of HDAC3 inhibitory potency and isoform selectivity of the synthesized small molecules using fluorophore coupled biochemical HDAC enzyme inhibition assays.

3. To evaluate their *in vitro* cytotoxicity by using MTT assay protocol in different cancer cell lines and normal human cell lines.
4. To determine the mechanism and extent of cell death via various studies *in vitro*.
5. To evaluate pharmacokinetic properties of the lead molecule from the series.
6. To evaluate the therapeutic efficacy of the lead molecule in tumor xenograft mouse model using various studies.

Objective II

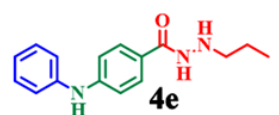
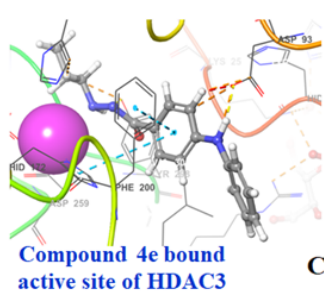
To identify and develop novel chemotypes of *pyrazino*-hydrazide based small molecules as HDAC3 selective inhibitors as promising anti-breast cancer agents.

Specific aims:

1. To design and synthesize a series of novel *pyrazino*-hydrazides with hydrazide as ZBG followed by their characterization using ^1H NMR, ^{13}C NMR, HPLC/LC-MS, HRMS spectroscopy.
2. Assessment of HDAC3 inhibitory potency and isoform selectivity of the synthesized small molecules using fluorophore coupled biochemical HDAC enzyme inhibition assays.
3. To evaluate their *in vitro* cytotoxicity by using MTT assay protocol in different breast cancer cell lines and normal human cell lines.
4. To determine the mechanism and extent of cell death via various studies *in vitro*.
5. To determine the metabolic stability of the lead molecule by microsomal assay.
6. To evaluate pharmacokinetic properties of the lead molecule from the series.
7. To evaluate the therapeutic efficacy of the lead molecule in 4T1-Luc tumor xenograft mouse model using various studies.

Chapter 3

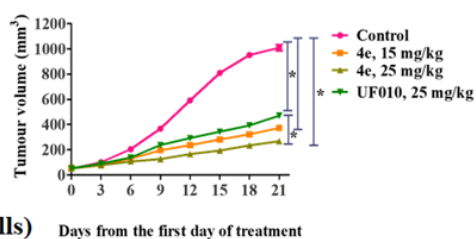
Selective Inhibition of Histone deacetylase 3 by Novel Hydrazide Based Small Molecules as Therapeutic Intervention for the Treatment of Cancer



Cap Linker ZBG
HDAC3 IC_{50} = 15.41 nM
(Selectivity > 18-fold)

(>80-fold selective for 4T1 cells)

C_{max} : 119.2 μ M (i.v) & 44.93 μ M (i.p)
[25 mg/kg]



3.1. INTRODUCTION

Epigenetic modifications regulating the gene expression has been strongly linked to cancer and several other diseases (Barter and Foster, 2018; Biswas and Rao, 2017). In particular, the modifications targeting the histone proteins have been widely explored and are found to be a promising target for drug discovery associated with epigenetic research (Berger, 2002; Strahl and Allis, 2000). Among PTMs of histones, the histone acetylation has been studied most extensively and it is found to be highly correlated with different types of cancers, neurodegenerative disorders and inflammatory diseases (Gräff and Tsai, 2013; Lawrence et al., 2016; Shahbazian and Grunstein, 2007). The reversible process of acetylation is modulated and balanced by the activity of HATs and HDACs. HATs and HDACs are involved in the acetylation and deacetylation of the lysine residues at the *N*-terminal region of histones, respectively (Bannister and Kouzarides, 2011; Yang and Seto, 2007). Due to acetylation, the open state of chromatin leads to gene expression whereas the closed or compact state of chromatin upon deacetylation leads to repression in transcription and expression of genes (Bannister and Kouzarides, 2011; Grunstein, 1997; Gryder et al., 2019a, 2019b; Kornberg, 1974).

HDACs are widely explored for their critical roles in various diseases including cancer (Adhikari et al., 2021; Li and Seto, 2016; Pulya et al., 2020). HDACs are known to target not only H3 and H4 histone proteins but also several non-histone proteins having effects on various downstream pathways and thus, influencing several cellular mechanisms including apoptosis, cell proliferation, cell differentiation and survival (Adhikari et al., 2021; Carew et al., 2008; Rosato et al., 2003; Sambucetti et al., 1999; Schölz et al., 2015; Telles and Seto, 2012). HDACs are found to be overexpressed in several cancers and the overexpression may be associated with the alteration activity of various oncogenes including tumor suppressor genes, leading to disease progression (Spurling et al., 2008;

Chapter 3: Benzoyl hydrazides as HDAC3 inhibitors

Yin et al., 2017). Therefore, inhibiting HDACs is believed to be one of the most promising approaches in anticancer drug discovery. The therapeutic potential of HDACis has already been proven as anticancer agents. A variety of HDACis have been approved clinically such as SAHA (vorinostat), FK228 (romidepsin), PXD-101 (belinostat), LBH589 (panobinostat) and chidamide for the management of several cancers like cutaneous T-cell lymphoma (CTCL), multiple myeloma (MM) and peripheral T-cell lymphoma (PTCL) (Banerjee et al., 2019; Barbarotta and Hurley, 2015; Lee et al., 2015; Lu et al., 2016; Mann et al., 2007; Raedler, 2016). Apart from that, several HDACis have been evaluated in various phases of clinical and preclinical trials for their potential anticancer properties (Adhikari et al., 2021; Connolly et al., 2017; Khan and Thangue, 2012; Li et al., 2020; Li and Seto, 2016; Minami et al., 2014; Wang et al., 2015). Though HDACis are well-recognized as anticancer agents, their non-specific mechanism of action towards different HDAC isoforms may lead to unwanted off-target adverse effects as well as dose-related toxicities (Balasubramanian et al., 2009). Hence, there is a pressing need for identifying and developing isoform-selective HDACis to understand the underlying mechanisms of the specific HDAC isozyme in the disease progression and downstream pathways.

Among the 18 different classical human HDAC isoforms, HDAC3 has emerged as a crucial regulator of various stages of cancer progression and its related pathogenesis (Adhikari et al., 2018, 2021; Minami et al., 2014; Spurling et al., 2008; Wilson et al., 2006; Yin et al., 2017). Various studies reported the crucial role of HDAC3 overexpression in several pathways and downstream signalling cascades in variety of cancers and other disease conditions such as inflammation and several neurological disorders (Adhikari et al., 2021; Amin et al., 2019; Bhaskara et al., 2010; Spurling et al., 2008; Yin et al., 2017). Moreover, HDAC3 is structurally well-characterized and is found to remain as a steady complex with NCoR and SMRT, thus modulating the repression of various receptors and transcriptional

Chapter 3: Benzoyl hydrazides as HDAC3 inhibitors

regulators (Adhikari et al., 2018; Watson et al., 2012). Interestingly, HDAC3 is unique compared to other HDACs regarding the substrate specificity as well as for its differences in the amino acid residues located in the foot pocket thus providing a rationale for designing HDAC3-selective inhibitors (Cao et al., 2018). Therefore, specific HDAC3 inhibition would be a promising therapeutic strategy for combating various cancers like breast cancer, pancreatic cancer, colorectal cancer, prostate cancer, colon cancer, lymphoma, leukemia, glioma, myeloma, melanoma and Ewing's sarcoma (Adhikari et al., 2021; Routholla et al., 2021b).

HDAC*s* consist of a general pharmacophoric structure containing a cap region acting as a surface binding region, a linker function interacting with the hydrophobic pocket/groove including the internal cavity, and a zinc-binding group (ZBG) that binds to the catalytic site of these enzymes (Trivedi et al., 2019). Depending on the type of ZBGs, HDAC*s* are classified into four major chemical classes, i.e., hydroxamates, benzamides, short-chain fatty acids and cyclic tetrapeptides (Routholla et al., 2021a). Most of the HDAC*s* including those approved by USFDA namely vorinostat, belinostat and panobinostat belong to the hydroxamate class. Hydroxamates have very strong Zn^{2+} metal chelating properties which also renders it non-specific towards almost all HDAC isoforms leading to unwanted off-target side effects along with undesirable clinical toxicities (Subramanian et al., 2010). Despite their potent inhibitory activities, these are being administered mostly in large doses clinically because of their inactivation during metabolism caused by the glucuronidation of the hydroxamate function *in vivo* (Kang et al., 2010; McClure et al., 2016; Shah, 2019; Wang et al., 2013). This might be the reason for their poor pharmacokinetic profiles in clinical applications. With the literature reports claiming the increase of isoform specificity reduces the unwanted toxicities and off-target activities, a variety of highly selective Class I HDAC*s* with aminobenzamide as ZBG were identified and evaluated in preclinical and

Chapter 3: Benzoyl hydrazides as HDAC3 inhibitors

clinical studies (Adhikari et al., 2018; Balasubramanian et al., 2009; Cao et al., 2018; Kashyap and Kakkar, 2020). Several small molecule inhibitors of benzamide class such as MS-275, CI-994, RGFP966, BG-45, BRD3308 were extensively studied for their clinical utility against different cancers and were selective towards class I HDACs preferentially towards HDAC 1/2 or HDAC3 (Hess-Stumpp et al., 2007; LoRusso et al., 1996; Minami et al., 2014; Sarkar et al., 2020; X. Yu et al., 2020). Nevertheless, modifications over these lead compounds at either cap or linker region along with various substitutions on benzamide moiety have further enhanced their isoform specificity and potency (Adhikari et al., 2018; Hamoud et al., 2020; Hsieh et al., 2017; Nepali et al., 2020; Routholla et al., 2021a; Singh et al., 2021; Trivedi et al., 2019). Though several benzamide-based HDACis are reported to date, these are mostly limited to preclinical studies and most of them did not achieve clinical utility due to their metabolic instability caused by the glucuronidation of the aminobenzamide moiety (Acharya et al., 2006; Kummar et al., 2007; Suresh et al., 2017; Thomas et al., 2008). Therefore, all these limitations with hydroxamates and other ZBG motifs have led to the need for the identification and development of novel chemotypes which can overcome these metabolic instabilities as well as enhance the isoform specificity leading to much potent and selective HDACis with enhanced clinical properties *in vivo*. Towards this end, novel molecules comprising hydrazide as ZBG were identified recently by Wang and group (Wang et al., 2015) showing enhanced potency and selectivity towards class I HDAC isoforms particularly HDAC 1, 2 and 3. They identified a lead compound **UF010** from their high throughput screening experiments that were found to alter histone acetylation levels correlating with the *in vitro* cytotoxic activities. **UF010** was found to activate tumor suppressor genes causing significant anticancer potential (Wang et al., 2015). Furthermore, reports on HDACis with hydrazide scaffold have suggested that this novel hydrazide ZBG is impervious to glucuronidation-dependent inactivation and may

Chapter 3: Benzoyl hydrazides as HDAC3 inhibitors

offer a better pharmacokinetic profile (Jiang et al., 2022; Li et al., 2020, 2018; Mahmud and Liao, 2015; McClure et al., 2016; Son et al., 2019).

In this chapter, a series of compounds comprising benzoyl hydrazide scaffold (hydrazide as the ZBG) with various modifications on the cap region have been designed and synthesized. For the first time ever, we demonstrated the antitumor properties in the 4T1-Luc tumor xenograft model. From various reports on class I HDAC selectivity (namely HDAC1, HDAC2 and HDAC3) of hydrazide analogues, we envisioned that further substitution with acetyl, aryl or aroyl moieties on the cap region may contribute to the selectivity among the class I HDACs, particularly HDAC3. Here, in this study, such type of hydrazide compounds were evaluated for HDAC3 inhibition and selectivity assessment was performed over other HDAC isoforms. The lead compound was subjected to rigorous *in vitro* and *in vivo* biological assessments with the evaluation of pharmacokinetic properties. The expression of apoptotic markers along with several proliferative markers upon treatment of the lead compound was also studied by western blot analysis.

3.2. RESULTS AND DISCUSSION

3.2.1. Designing novel benzoyl hydrazide analogues.

In our quest to explore HDAC3-selective inhibitors, we started with a goal of designing and synthesizing potent and selective hydrazide-based HDACis with preferential HDAC3 isoform selectivity. Previous studies indicated that the 3-carbon chain on the hydrazide resulted in an excellent inhibitory profile when compared to *n*-butyl or di-*N*-substituted hydrazides (Li et al., 2018; McClure et al., 2016). Considering **UF010** (Wang et al., 2015) as the reference compound, here, we designed and synthesized some benzoyl hydrazide-based analogues with either *n*-butyl or *n*-propyl aliphatic carbon chain attached with the hydrazide motif and incorporating different amino substituents at the *para* position of the benzoyl hydrazide moiety in the cap region. The design of the compounds is represented in

Figure 3.1.

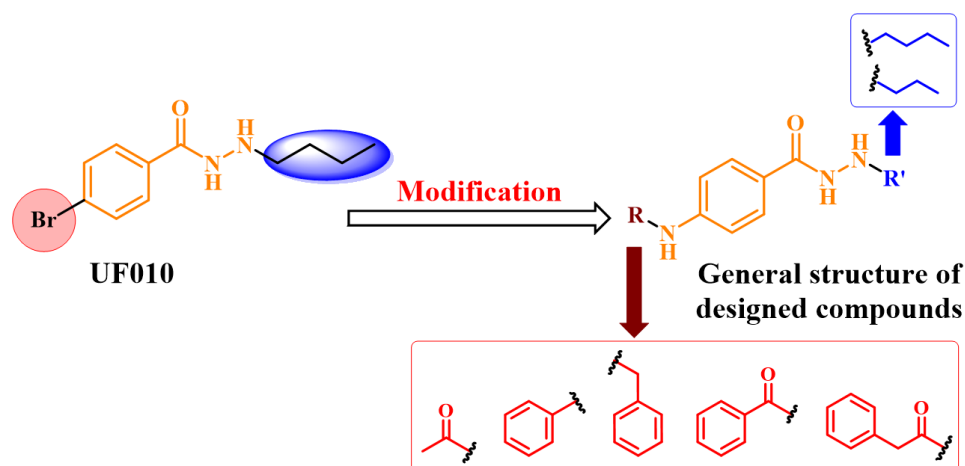
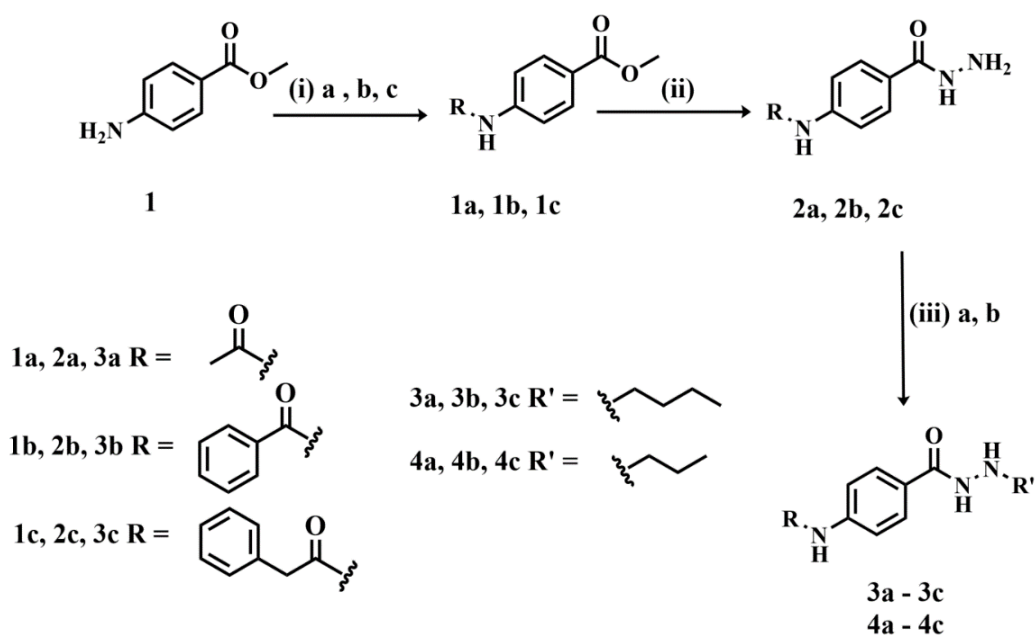


Figure 3.1. Design of the novel hydrazide ZBG containing compounds as potential HDAC3 inhibitors.

3.2.2. Synthesis of the designed compounds

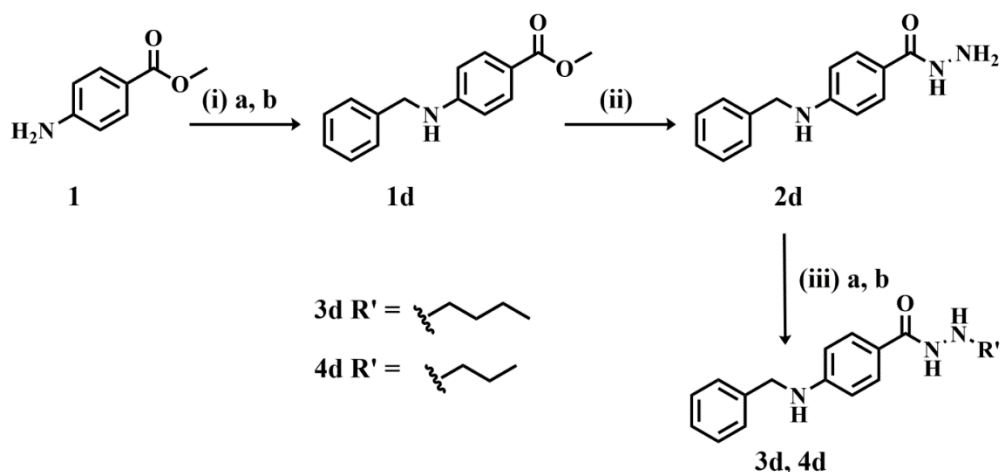
The synthesis of the designed compounds (**3a – 3e**, **4a – 4e**) is represented in Schemes **3.1** to **3.3**. The starting materials were directly procured from the commercial source and were used directly without further purification. The corresponding esters (**1a – 1e**) were synthesized following reactions **a**, **b**, **c**, **d** and **e** under different reaction conditions.



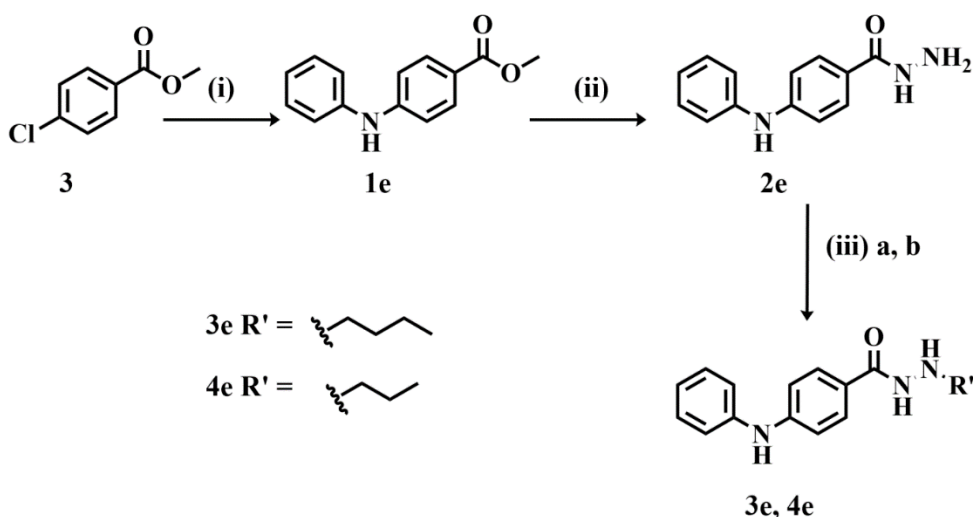
Scheme 3.1. Synthesis of **3a – 3c** and **4a – 4c** (*Reagents and conditions*): (i) (a) acetic

Chapter 3: Benzoyl hydrazides as HDAC3 inhibitors

anhydride, dry DCM, 2 – 4 h, rt; (b) benzoyl chloride, NaHCO₃, THF, 10 h, rt; (c) phenylacetyl chloride, Et₃N, dry DCM, 8 h, rt; (ii) NH₂NH₂·H₂O, MeOH, 6 h, reflux; (iii) (a) propionaldehyde (or) butyraldehyde, catalytic PTSA, MeOH, 2 – 3 h, rt; (b) NaBH₃CN, MeOH, pH 5, 10 mins, rt.



Scheme 3.2. Synthesis of **3d** and **4d** (*Reagents and conditions*): (i) (a) benzaldehyde, EtOH, 6 h, rt; (b) NaBH₄, 2 h, rt; (ii) NH₂NH₂·H₂O, MeOH, reflux, 6 h; (iii) (a) propionaldehyde (or) butyraldehyde, catalytic PTSA, MeOH, 2 – 3 h, rt; (b) NaBH₃CN, MeOH, pH 5, 10 mins, rt.



Scheme 3.3. Synthesis of **3e** and **4e** (*Reagents and conditions*): (i) aniline, Pd₂(dba)₃, XPhos, DIPEA, K₂CO₃, 12 h, reflux; (ii) NH₂NH₂·H₂O, MeOH, reflux, 6 h; (iii) (a) propionaldehyde (or) butyraldehyde, catalytic PTSA, MeOH, 2 – 3 h, rt; (b) NaBH₃CN,

Chapter 3: Benzoyl hydrazides as HDAC3 inhibitors

MeOH, pH 5, 10 mins, rt.

The obtained methyl esters (**1a** – **1e**) were reacted with the excess of hydrazine monohydrate to obtain the respective hydrazides (**2a** - **2e**). These hydrazides (**2a** - **2e**) were further reacted with either butyraldehyde or propionaldehyde and eventually reduced with sodium cyanoborohydride under acidic conditions to obtain target final compounds (**3a** - **3e**, **4a** - **4e**).

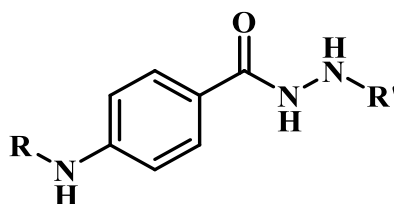
The synthesis of acetyl, benzoyl and phenyl acetyl protected amino esters was carried out by using commercially available methyl 4-amino benzoate (**1**) as per **Scheme 3.1**. Acetylation was facilitated by reacting (**1**) with acetyl chloride using dry dichloromethane (DCM) as solvent at room temperature to obtain **1a**. Compound **1b** was obtained by treating (**1**) with benzoyl chloride using sodium bicarbonate as the base and tetrahydrofuran as solvent. Treating (**1**) with phenylacetyl chloride using triethylamine as a base and dry DCM as solvent yielded compound **1c**. Similarly, compound **1d** was synthesized by treating (**1**) with benzaldehyde in the presence of ethanol, subsequently followed by reduction using sodium borohydride (NaBH₄) at room temperature for 2 hours as represented in **Scheme 3.2**. Another starting material, methyl 4-chloro benzoate (**3**) was reacted with aniline as per Buchwald-Hartwig reaction conditions to obtain **1e** as shown in **Scheme 3.3**.

The resulting methyl esters (**1a** - **1e**) were treated with hydrazine monohydrate and refluxed in the solvent methanol to obtain corresponding hydrazides **2a** – **2e**, which were carried for the next reaction without further purification. The resultant hydrazides (**2a** – **2e**) were reacted with butyraldehyde or propionaldehyde in the presence of *p*-toulenesulphonic acid (PTSA) as the catalyst in methanol for 2 – 3 h at room temperature and the obtained imine intermediate was further reduced using 1.5 equivalents of sodium cyanoborohydride for about 10 mins under acidic conditions to obtain the target compounds (**3a** – **3e** and **4a** – **4e**). The detailed experimental procedure was described in the chemistry experimental

Chapter 3: Benzoyl hydrazides as HDAC3 inhibitors

section. All the novel compounds were confirmed for their purity percentage using HPLC analysis and all the compounds were found to be >95% pure as per our HPLC reports. The final compounds were further characterized by ^1H , ^{13}C NMR and HRMS and all the obtained spectra are provided in the supporting information section (**Spectra 3.1 – 3.49**). Structures of the designed compounds (**3a – 3e** and **4a – 4e**) are listed in **Table 3.1**.

Table 3.1. Structures of the designed compounds.



Compound	R	R'
3a	CH ₃ CO	<i>n</i> -Butyl
4a	CH ₃ CO	<i>n</i> -Propyl
3b	PhCO	<i>n</i> -Butyl
4b	PhCO	<i>n</i> -Propyl
3c	PhCH ₂ CO	<i>n</i> -Butyl
4c	PhCH ₂ CO	<i>n</i> -Propyl
3d	Benzyl	<i>n</i> -Butyl
4d	Benzyl	<i>n</i> -Propyl
3e	Ph	<i>n</i> -Butyl
4e	Ph	<i>n</i> -Propyl

3.2.3. Inhibition of Class I and Class II HDACs.

With the primary goal of identifying HDAC3-selective inhibitors, initially, all these synthesized compounds of the series (**3a – 3e** and **4a – 4e**) were screened against HeLa nuclear extract for % *pan*-HDAC inhibition (at 10 μM concentration) as well as recombinant HDAC3/NCoR1 enzyme for % HDAC3 inhibition (at 1 μM and 0.0625 μM compound concentration), keeping **UF010** as the reference molecule in duplicate (**Figure 3.2 & 3.3, Table 3.2**). Testing these compounds at two different doses for their % inhibition

Chapter 3: Benzoyl hydrazides as HDAC3 inhibitors

of HDAC3 activity, further helped us to identify the most potent compounds from the series for the determination of their IC₅₀ values and subsequent other biological and pharmacological characterizations. From the results obtained, it was found that all the tested compounds except **3b**, exhibited more than 50% and 10% HDAC3 activity inhibition at 1 μ M and 0.0625 μ M concentrations, respectively. The compounds that were found to inhibit HDAC3 activity with more than 80% enzyme inhibition at 1 μ M concentration and more than 30% enzyme inhibition at 0.0625 μ M concentration and showed more than ~10-fold HDAC3 selectivity over *pan*-HDAC, were further evaluated for their IC₅₀ determination (**Table 3.2**) against HDAC3. All the compounds exhibited nanomolar potency towards HDAC3 inhibition with **4c** and **4e** being the most potent among them, possessing HDAC3 IC₅₀ values of 30.67 nM and 15.41 nM, respectively. It was noticed that compounds **4c**, **4d** and **4e** with the *n*-propyl group attached to the hydrazide moiety displayed a comparatively better HDAC3 inhibitory profile than the compounds **3c** and **3d** with the *n*-butyl group associated with the hydrazide moiety (**Table 3.3**). These results reaffirmed the idea previously reported, that *n*-propyl substitution attached to the hydrazide function is more favourable for enhancing efficacy as well as selectivity towards HDAC3 isozyme (Li et al., 2020; McClure et al., 2016). Considering the higher inhibitory profiles of **4c** and **4e** against HDAC3 compared to the reference compound **UF010** (IC₅₀ = 256.7 nM) as depicted in **Figure 3.5A**, their selectivity profiles against different HDAC isoforms was determined. Further, two most potent compounds (**4c** and **4e**) against several HDAC isoforms, i.e., class I HDACs (HDAC1, HDAC2 and HDAC8), class IIa HDACs (HDAC4 and HDAC5) as well as class IIb HDAC (HDAC6) were evaluated to determine their selectivity profiles towards HDAC3 isoform. The initial screening of the compounds was done with a single concentration as per the Vendor's recommendation (**Figure 3.4**). The IC₅₀ values obtained by the dose-response curves against HDAC1, HDAC2, HDAC8 and

Chapter 3: Benzoyl hydrazides as HDAC3 inhibitors

HDAC6 are represented in **Figure 3.5B – 3.5E** and the IC₅₀ values against different HDAC isoforms are tabulated in **Table 3.4**.

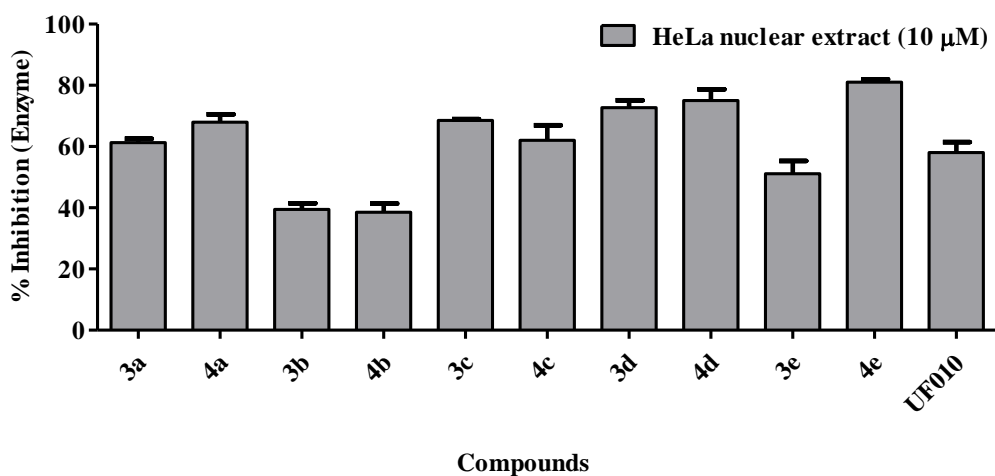


Figure 3.2. Graph represents the % inhibitory activity of the novel synthesized compounds for their *pan*-HDAC inhibitory activity. All novel compounds were screened at 10 μ M concentrations for Hela nuclear extract enzyme. [Data represents mean \pm SD (n=2)].

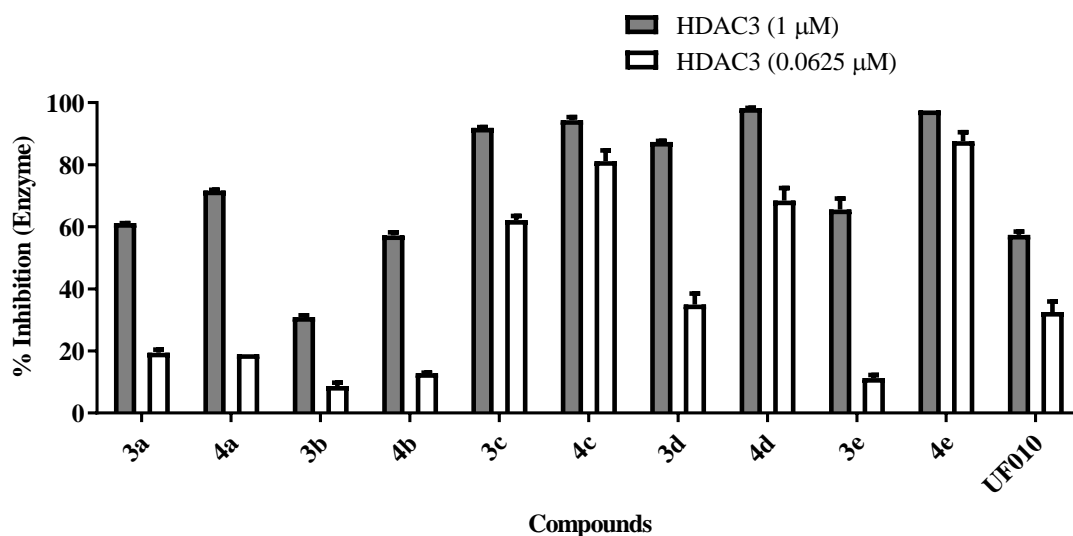


Figure 3.3. Graph represents the % inhibitory activity of the novel synthesized compounds on recombinant HDAC3 enzyme. All compounds were screened at 1 μ M and 0.0625 μ M concentrations for HDAC3 enzyme. [Data represents mean \pm SD (n=2)].

Table 3.2. *pan*-HDAC and HDAC3 enzyme inhibition (%) data of the synthesized

Chapter 3: Benzoyl hydrazides as HDAC3 inhibitors

compounds with 10 μM concentration of compounds against Hela nuclear extract (*pan*-HDACs) and 1 μM and 0.0625 μM concentration of compounds against human recombinant HDAC3 enzymes. Data represents mean \pm SD (n = 2).

Compound code	% Inhibition		
	<i>Pan</i> -HDAC (10 μM)	HDAC3 (1 μM)	HDAC3 (0.0625 μM)
3a	61.32 \pm 1.22	61.15 \pm 0.06	19.43 \pm 0.96
4a	67.97 \pm 2.60	71.68 \pm 0.26	18.92 \pm 0.01
3b	39.42 \pm 1.99	30.91 \pm 0.57	8.72 \pm 1.04
4b	38.58 \pm 0.42	57.22 \pm 0.26	12.81 \pm 0.17
3c	68.53 \pm 2.78	91.88 \pm 0.97	62.19 \pm 1.32
4c	62.03 \pm 4.90	94.35 \pm 0.99	81.18 \pm 3.43
3d	72.71 \pm 2.38	87.37 \pm 0.27	34.98 \pm 3.47
4d	75.01 \pm 3.68	98.21 \pm 0.27	68.43 \pm 4.07
3e	51.11 \pm 4.19	65.53 \pm 3.55	11.25 \pm 0.97
4e	81.06 \pm 0.85	97.48 \pm 0.04	87.59 \pm 2.87
UF010	58.06 \pm 3.43	57.39 \pm 1.09	32.52 \pm 3.41

Table 3.3. Data representing the HDAC3 IC₅₀ values (nM) of selected compounds.

S. No	Compound code	HDAC3 IC ₅₀ (nM)
1	3c	36.67 \pm 0.99
2	4c	30.67 \pm 0.78
3	3d	212 \pm 1.98
4	4d	32.88 \pm 1.25
5	4e	15.41 \pm 0.57
6	UF010	256.7 \pm 2.69

*Values represent mean \pm S.D. (n = 2).

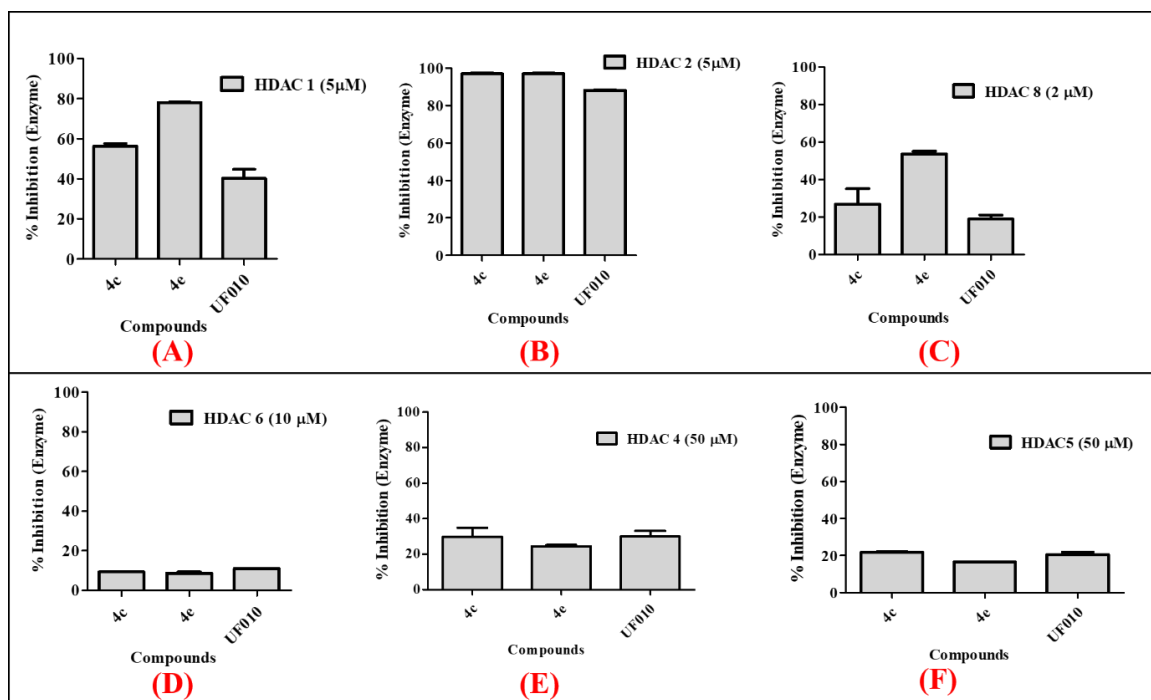


Figure 3.4. Graphs represent the % inhibitory activity of **4c**, **4e** and **UF010** compounds on human recombinant (A) HDAC1 isozyme with 5 μM compound concentration; (B) HDAC2 isozyme with 5 μM compound concentration; (C) HDAC8 isozyme with 2 μM compound concentration; (D) HDAC6 isozyme with 10 μM compound concentration; (E) HDAC4 isozyme with 50 μM compound concentration; (F) HDAC5 isozyme with 50 μM compound concentration. The initial screening was done as per the vendor's recommended concentration. [Data represents mean \pm SD (n=2)].

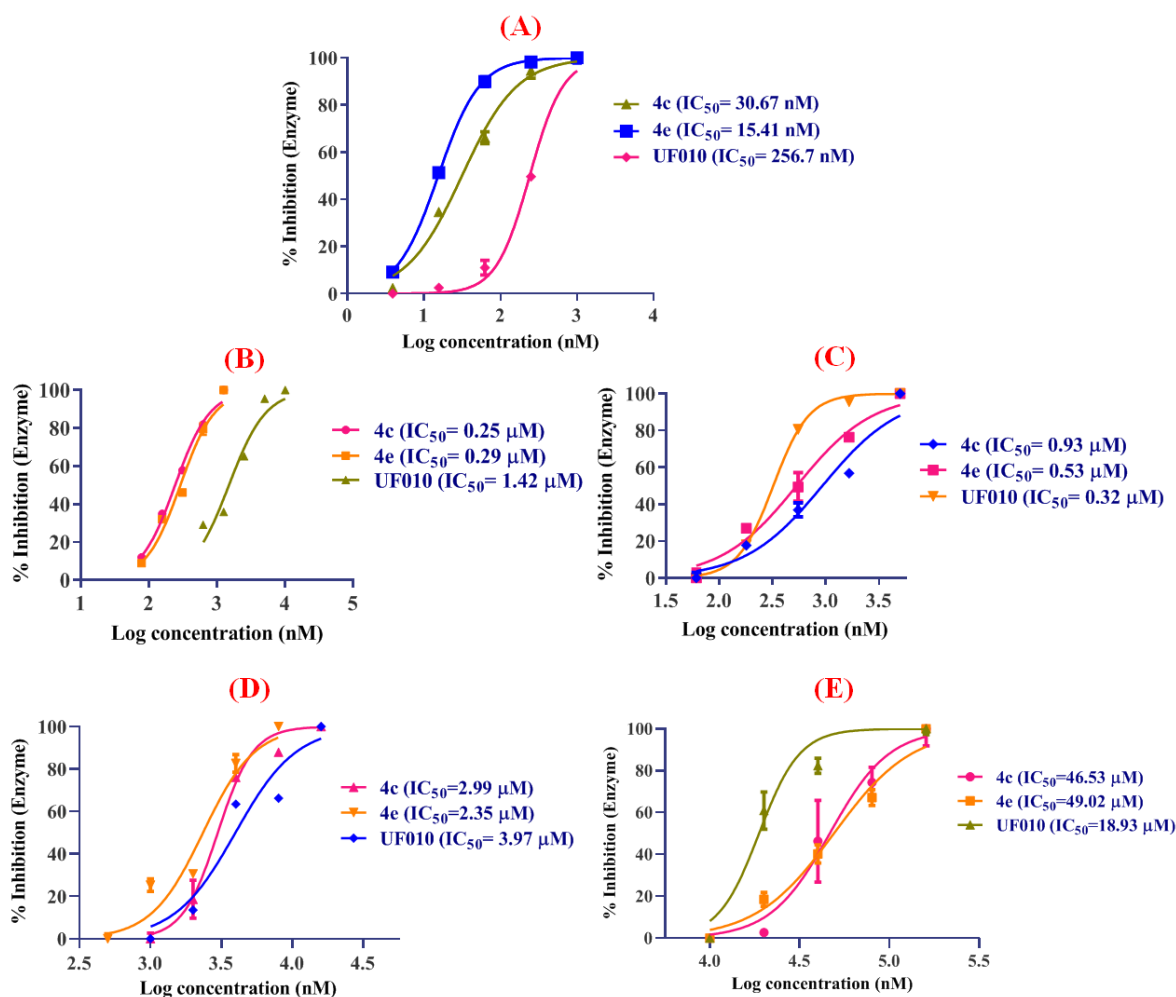


Figure 3.5. Graphs used in the calculation of IC₅₀ values of compounds **4c**, **4e** and **UF010** against human recombinant HDAC isozymes (A) HDAC3; (B) HDAC1; (C) HDAC2; (D) HDAC8; (E) HDAC6. [Determination of IC₅₀ was performed at the varied concentration range of 0.005 μ M – 160 μ M of these compounds in duplicate according to the protocol described. The IC₅₀ values were estimated with the help of the nonlinear regression analysis method by Graph Pad Prism 8.0.1. Data represent mean \pm SD (n = 2)].

Table 3.4. Inhibitory potency of compounds **4c**, **4e** and reference molecule **UF010** against human recombinant class I and class II HDACs as compared with HDAC3 selective inhibitors previously reported from our group BG-45 (Minami et al., 2014) and PT3 (Pulya et al., 2021).

Chapter 3: Benzoyl hydrazides as HDAC3 inhibitors

HDAC class	Isoforms	IC ₅₀ ^a (nM)				
		4c	4e	UF010	BG-45 ^b	PT3 ^c
I	HDAC1	249.3	288.5	1420	2302 ±	1053 ± 98
		±11.2	±12.6	±77.9	62.3	
	HDAC2	931 ±28.8	534 ±22.6	322 ±39.5	2362 ±	2083 ± 129
					156	
	HDAC3	30.67	15.41	256.7	566 ± 12	245 ± 16
		±2.58	±1.04	±28.6		
HDAC8	2991	2352	3970	2850 ±	1561 ± 165	
	±39.5	±169.8	±99.7	198		
IIa	HDAC4	>50000	>50000	>50000	ND	ND
	HDAC5	>50000	>50000	>50000	ND	ND
IIb	HDAC6	46534	49022	18935	34152 ±	37182 ± 268
		±268	±567	±143	123	

^aIC₅₀ values are represented as the mean of duplicate values ± standard deviation (n = 2). ^b

and ^c; values previously obtained in our lab.

Both these compounds (**4c** and **4e**) were found to be highly promising and excellent HDAC3-selective inhibitors compared to the other HDACs (**Figure 3.5**). Compound **4e** was the most potent HDAC3-selective inhibitor having an HDAC3 IC₅₀ value of 15.41 nM and with IC₅₀ values of 288.5 nM, 534 nM, 2352 nM and 49.02 μM towards HDAC1, HDAC2, HDAC8 and HDAC6, respectively with no inhibitory activity against HDAC4 and HDAC5 up to 30 μM concentration. Compound **4e** displayed about ~18.72, 34.65, >100, >1000, >1000, >1000 - fold selectivity over HDAC1, HDAC2, HDAC8, HDAC6, HDAC4 and HDAC5, respectively. Similarly, compound **4c** exhibited the HDAC3 IC₅₀ value of 30.67 nM and with IC₅₀ values of 249.3 nM, 931 nM, 2991 nM and 46.53 μM towards HDAC1, HDAC2, HDAC8 and HDAC6, respectively with no inhibition against HDAC4 and HDAC5 up to 30 μM concentration with an HDAC3 selectivity profile over

Chapter 3: Benzoyl hydrazides as HDAC3 inhibitors

~8.12, 30.35, 97.52, >1000, >1000, >1000 – fold over HDAC1, HDAC2, HDAC8, HDAC6, HDAC4 and HDAC5, respectively. Interestingly, both the compounds (**4e** and **4c**) displayed preferential HDAC3-selectivity when compared to the reference compound **UF010** and also HDAC3 selective positive controls **BG-45** and **PT3** (Minami et al., 2014; Pulya et al., 2021; Wang et al., 2015). These compounds (**4e** and **4c**) also exhibited 16.65 and 8.36 times higher IC₅₀ values (potency) for HDAC3 compared to the reference molecule **UF010**. Overall, the novel series of hydrazide compounds except **3b** with different aromatic cap group substitutions exhibited higher % inhibition values than the reference compound **UF010**. Among these, compounds containing phenylacetyl (**4c**) and phenyl (**4e**) substitution at the *para*-amino group of the benzoyl hydrazide scaffold with *n*-propyl substituted hydrazide analogue are the most active and selective towards HDAC3 compared to other class I HDACs and the representative class II HDACs.

3.2.4. *In vitro* cytotoxic efficacy of the novel series of compounds.

The *in vitro* screening of these synthesized molecules against a variety of cancer cell lines was conducted to assess the cytotoxic effects. Considering the implication of HDAC3 in different cancers (Hsieh et al., 2017; Sarkar et al., 2020; Spurling et al., 2008), these compounds including the reference molecule **UF010** were screened against the diverse cancer cell lines such as murine breast cancer cell line 4T1, human breast cancer cell line MCF-7, murine melanoma cell line B16F10 and non-small cell lung cancer cell line A549 with the help of MTT assay. The initial evaluation of these compounds and the reference compound **UF010** was performed at two distinct concentrations (10 µM and 100 µM, **Figure 3.6 – 3.9**) followed by their IC₅₀ value determination against the same set of cell lines suggested their significant cytotoxic activity (**Figure 3.10A – 3.10D**). It is noteworthy that all these compounds were found to be potent with less than 25 µM of IC₅₀ value towards all the cancer cell lines tested. Again, these compounds also exhibited comparable

cytotoxicity to that of UF010 (Table 3.5).

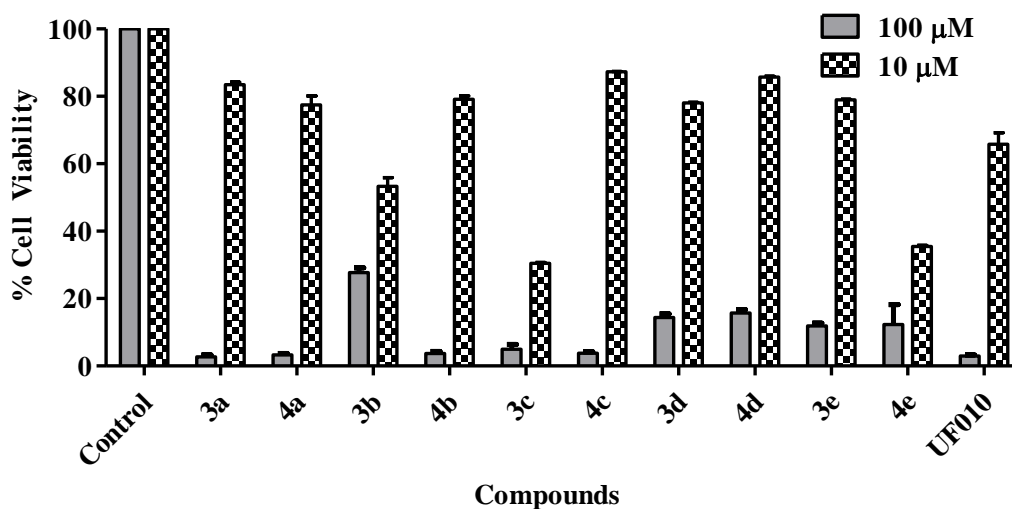


Figure 3.6. Cytotoxicity of the synthesized compounds in murine melanoma cells (B16F10) when treated with compounds at 100 μ M and 10 μ M in duplicate for 72 h. Cell viability was measured by MTT reagent. Data represents mean \pm SD (n=2).

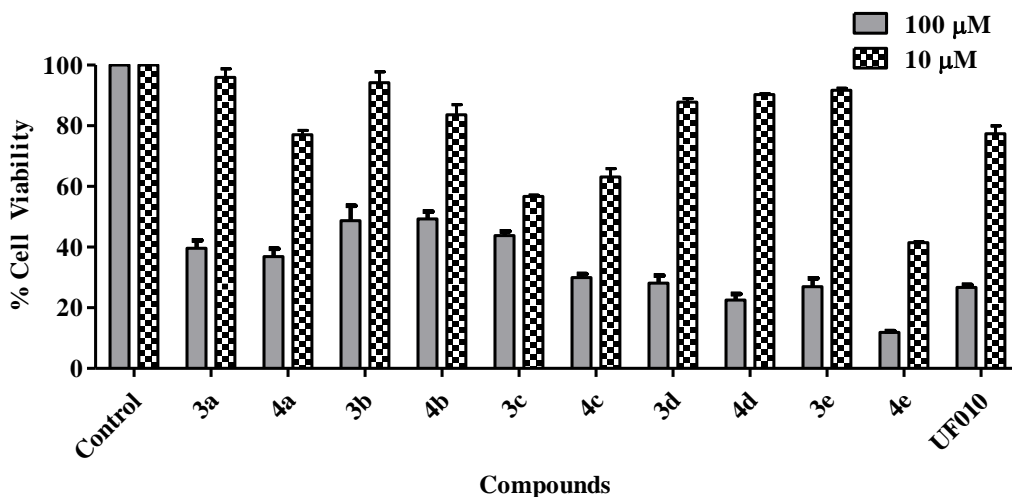


Figure 3.7. Cytotoxicity of the synthesized compounds in Human breast cancer cells (MCF-7) when treated with compounds at 100 μ M and 10 μ M in duplicate for 72 h. Cell viability was measured by MTT reagent. Data represents mean \pm SD (n=2).

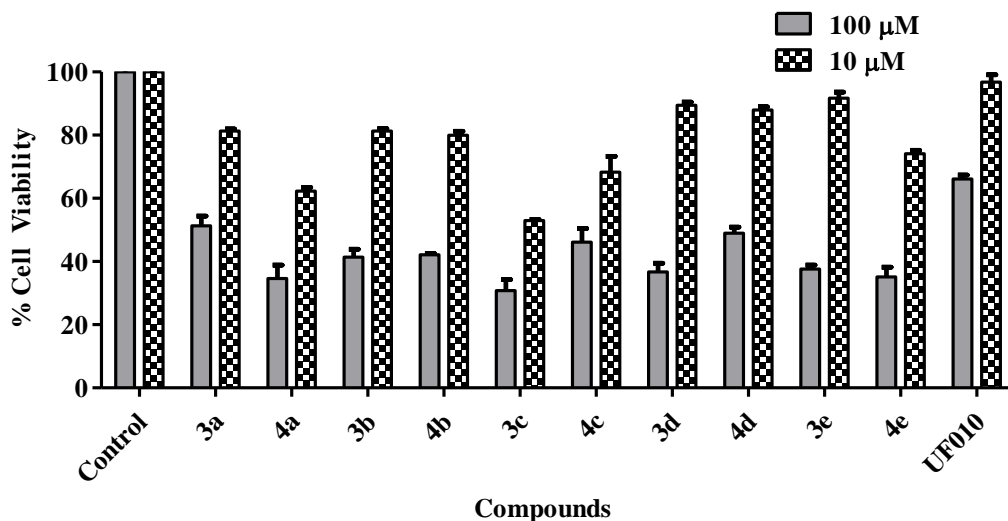


Figure 3.8. Cytotoxicity of the synthesized compounds in human non-small cell lung cancer cells (A549). Cells were treated with compounds at 100 μ M and 10 μ M in duplicate for 72 h. Cell viability was measured by MTT reagent. Data represents mean \pm SD (n=2).

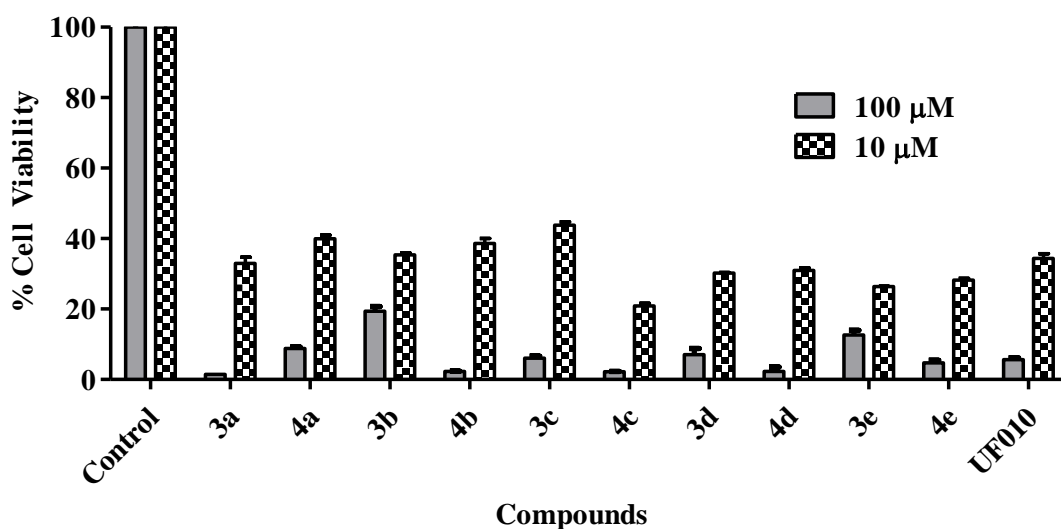


Figure 3.9. Cytotoxicity of the synthesized compounds in mouse breast cancer cells (4T1). Cells were treated with compounds at 100 μ M and 10 μ M in duplicate for 72 h. Cell viability was measured by MTT reagent. Data represents mean \pm SD (n=2).

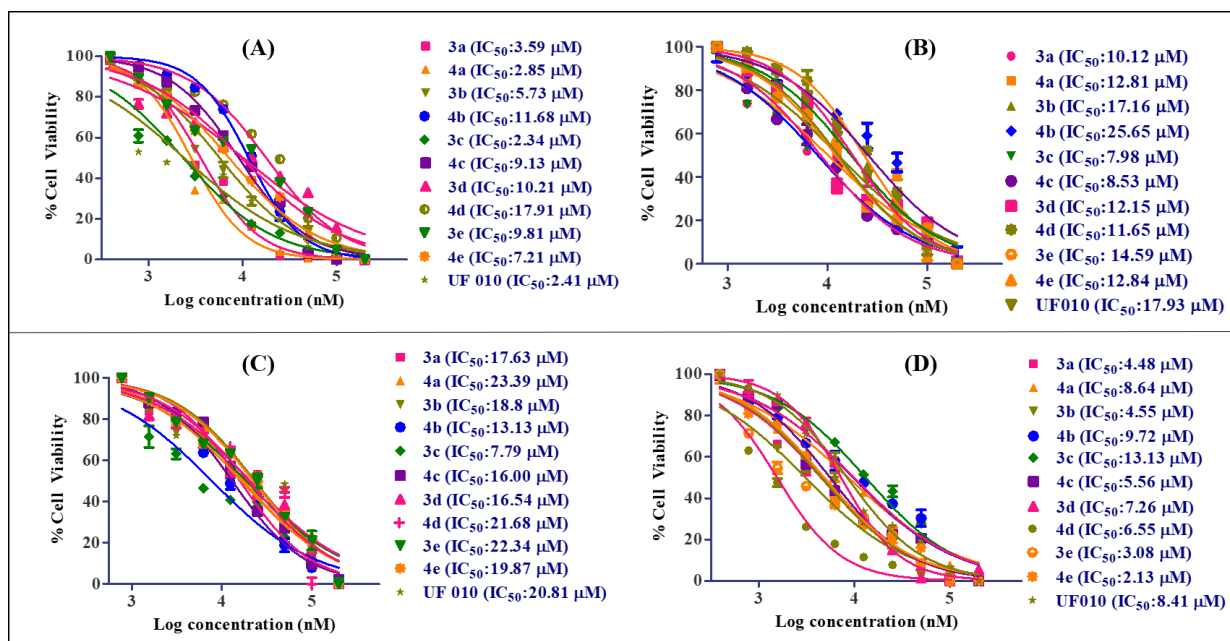


Figure 3.10. Graph (A), (B), (C), (D) represents the IC₅₀ results of the synthesized compounds by MTT assay in B16F10, MCF-7, A549 and 4T1 cells respectively. Cells were treated with the compounds at concentration range of 0.097 μM to 100 μM (n=2) for 72 h. Data represents mean ± SD.

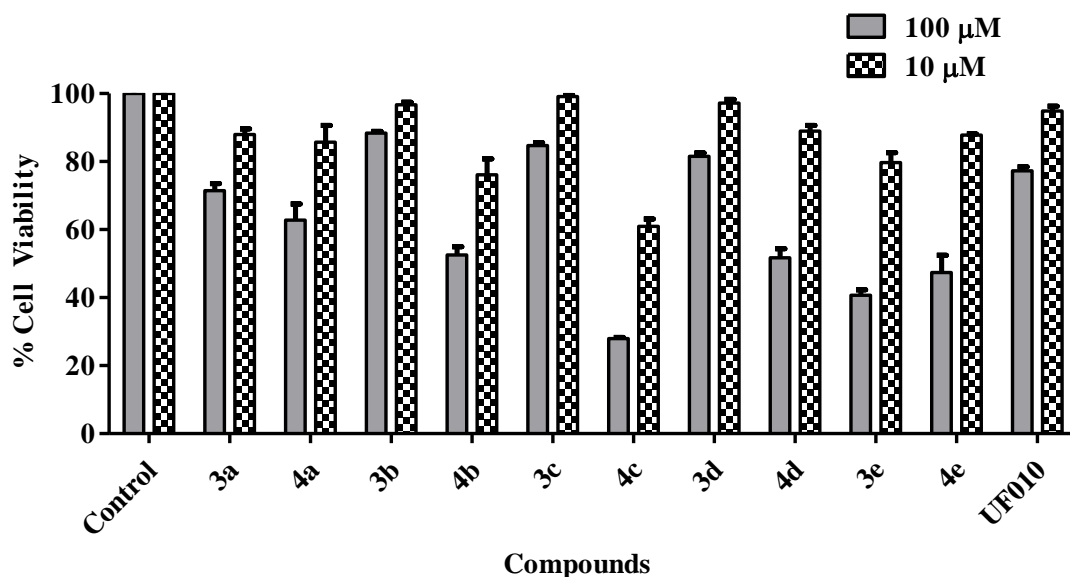


Figure 3.11. Cytotoxicity of the synthesized compounds in Human embryonic kidney cells (HEK-293). Cells were treated with compounds at 100 μM and 10 μM in duplicate for 72 h. Cell viability was measured by MTT reagent. Data represents mean ± SD (n=2).

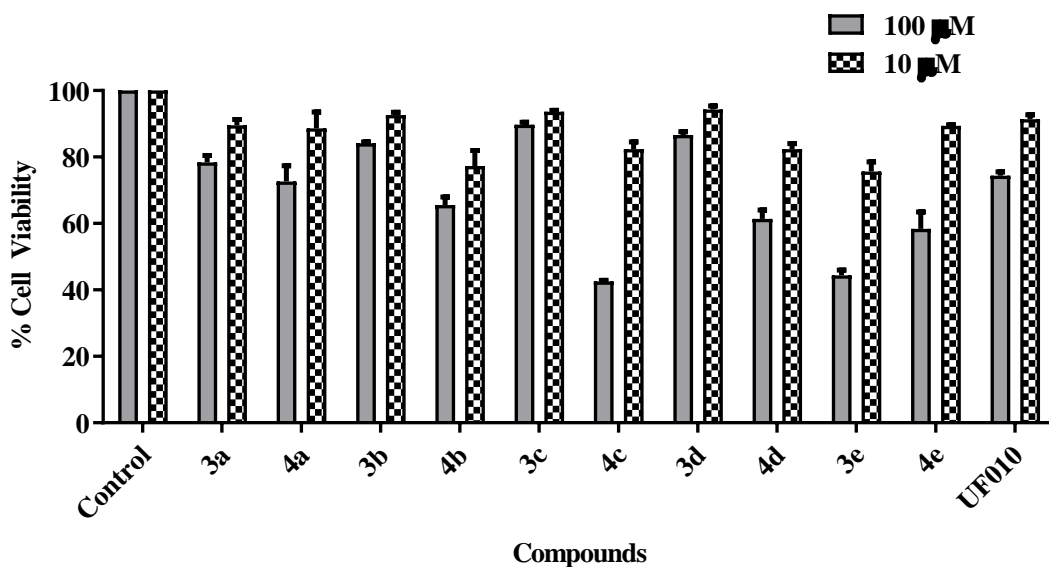


Figure 3.12. Cytotoxicity of the synthesized compounds in Human corneal epithelial cells (HCEC). Cells were treated with compounds at 100 μM and 10 μM in duplicate for 72 h. Cell viability was measured by MTT reagent. Data represents mean ± SD (n=2).

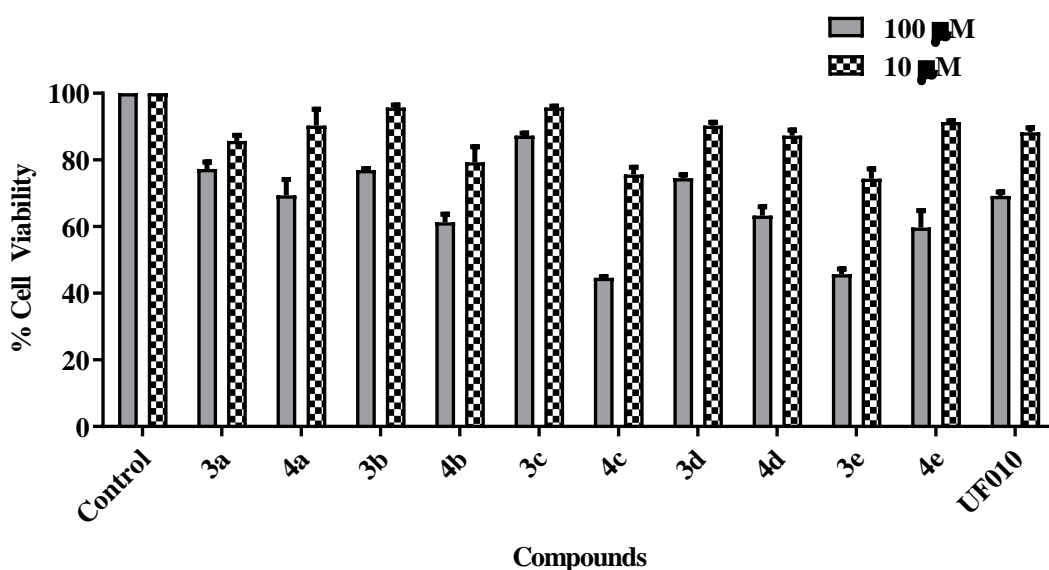


Figure 3.13. Cytotoxicity of the synthesized compounds in Raw 264.7 cells. Cells were treated with compounds at 100 μM and 10 μM in duplicate for 72 h. Cell viability was measured by MTT reagent. Data represents mean ± SD (n=2).

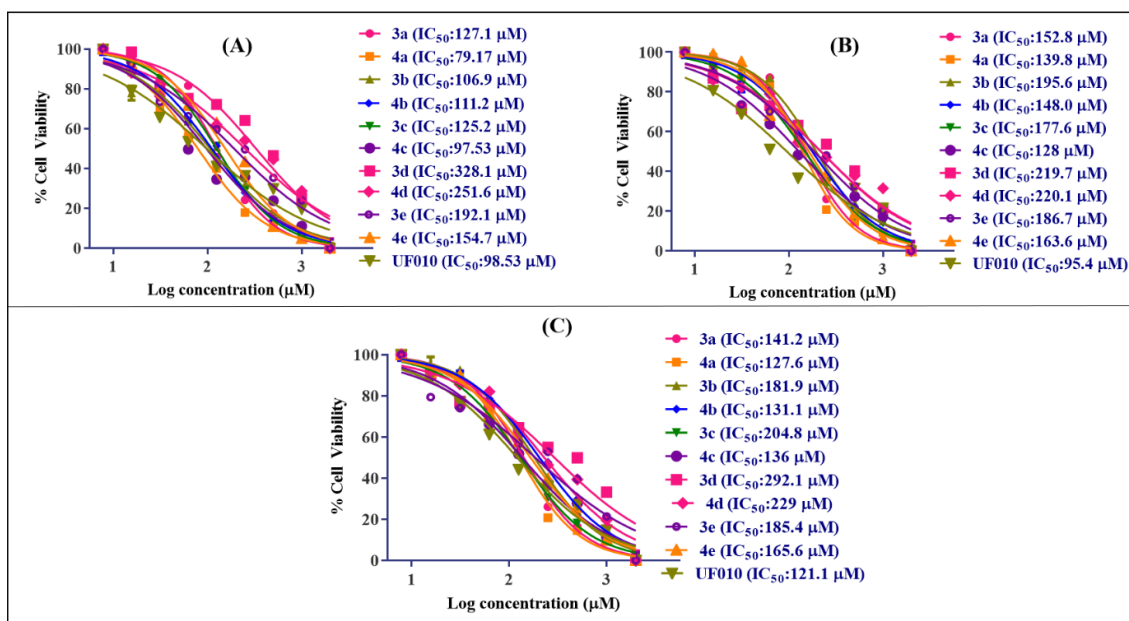


Figure 3.14. Graph (A), (B) and (C) represents the IC₅₀ results of the selected compounds for their toxicity by MTT assay against normal human cells (HEK-293), human corneal epithelial cells and Raw 264.7 cells respectively, and the here cells were treated with the compounds at the concentration range from 7.81 µM to 2000 µM (n=2) for 72 h. Data represents mean ± SD.

Table 3.5. IC₅₀ (µM) values of all compounds towards various cancer cells and normal HEK-293, HCEC and Raw 264.7 cells.

Cpd ^a	IC ₅₀ (µM)						
	<i>In vitro</i> cytotoxicity						
	B16F10	A549	MCF-7	4T1	HEK-293	HCEC	Raw 264.7
3a	3.59 ±	17.63 ±	10.12 ±	4.48 ±	127.1 ±	152.8 ±	141.2 ± 15.6
	0.51	2.69	1.24	0.64	11.5	13.5	
4a	2.85 ±	23.39 ±	12.81 ±	8.64 ±	79.17 ±	139.8 ±	127.6 ± 14.6
	0.06	3.87	3.48	1.68	9.89	8.64	
3b	5.73 ±	18.80 ±	17.16 ±	4.55 ±	106.9 ±	195.6 ±	181.9 ± 12.9
	0.56	4.56	2.98	0.87	23.2	11.6	
4b	11.68 ±	13.13 ±	25.65 ±	9.74 ±	111.2 ±	148.0 ±	131.1 ± 9.89
	1.24	3.68	4.06	1.25	28.9	7.69	
3c	2.34 ±	7.79 ±	7.98 ±	13.13 ±	125.2 ±	177.6 ±	204.8 ± 21.8
	0.98	1.96	0.57	2.16	27.9	15.8	

Chapter 3: Benzoyl hydrazides as HDAC3 inhibitors

4c	9.13 ±	16.00 ±	8.53 ±	5.56 ±	97.53 ±	128.0 ±	136.0 ± 11.8
	1.06	2.88	1.68	0.82	15.9	9.67	
3d	10.21 ±	16.54 ±	12.15 ±	7.25 ±	328.1 ±	219.7 ±	292.1 ± 34.6
	1.24	3.89	2.88	1.66	32.7	24.6	
4d	17.91 ±	21.68 ±	11.65 ±	1.55 ±	251.6 ±	220.1 ±	229.0 ± 19.6
	2.59	4.87	1.49	0.64	21.9	6.8	
3e	9.81 ±	22.34 ±	14.59 ±	3.08 ±	192.1 ±	186.7 ±	185.4 ± 10.6
	1.58	4.66	4.06	0.77	17.8	9.16	
4e	7.21 ±	19.87 ±	12.84 ±	1.92 ±	154.7 ±	163.6 ±	165.6 ± 15.4
	1.67	1.99	2.58	0.28	24.8	19.5	
UF010	2.41 ±	20.81 ±	17.93 ±	8.40 ±	98.52 ±	95.4 ±	121.1 ± 11.3
	0.76	4.99	3.24	1.65	11.9	6.98	

^aCompound; IC₅₀ values were determined by the MTT assay and are the mean of duplicate values (from the same cultures) ± the standard deviation (n = 2).

These compounds were found to be most potent in 4T1 cells having IC₅₀ in the range of 1.55 µM – 13.13 µM followed by B16F10 cells with IC₅₀ in the range of 2.34 µM – 17.91 µM among the cell lines tested. It was also noticed that these compounds were comparatively moderately active towards the A549 cell line with IC₅₀ in the range of 7.79 µM – 23.39 µM and MCF-7 cell line with IC₅₀ in the range of 7.98 µM – 25.65 µM. The results obtained suggested a higher inhibitory effect for the murine cancer cell lines when compared to that of the human cancer cell lines used. Interestingly, the HDAC inhibitory potency of the compounds correlated with their cytotoxic activity *in vitro*. The compounds with *N*-acetyl substitution (**3a** and **4a**) were the least active among all with higher IC₅₀ values when compared to the compounds containing *N*-aryl/royl substitution further suggesting that the presence of aromatic substitution is essential for the cytotoxic activity. This observation is well correlated with that of our molecular docking results described in the following section. The most potent and HDAC3-selective compounds **4c** and **4e** exhibited significant cytotoxicity; compound **4c** with IC₅₀ values of 9.13 µM, 16 µM, 8.53 µM, 5.56 µM against B16F10, A549, MCF-7 and 4T1 cell lines, respectively whereas compound **4e** with IC₅₀ values of 7.21 µM, 19.87 µM, 12.84 µM, 1.92 µM against the same

Chapter 3: Benzoyl hydrazides as HDAC3 inhibitors

set of cell lines, B16F10, A549, MCF-7 and 4T1 cell lines, respectively. Further, we have also tested the compounds for their *in vitro* cytotoxicity against normal human embryonic cell line (HEK-293), human corneal epithelial cells (HCEC) and Raw 264.7 (murine macrophage) cells. Interestingly, all the tested compounds were preferentially selective towards cancer cell lines, and the compounds exhibited less cytotoxicity towards normal cell lines used [Table 3.5 and Figure 3.11 – 3.13 and 3.14A – 3.14C]. The lead compound **4e** exhibited more than 80-fold selectivity towards 4T1 cells and overall, more than 10-fold selectivity towards other cancer cell lines tested (except A549) over HEK-293, HCEC and Raw 264.7 cell lines.

3.2.5. Selective inhibition of HDAC3 by compound 4e by western blot analysis of Ac-H3K9, Ac-H4K12, Ac-H3K27 and Ac-Tubulin and Ac-SMC3.

HDACs are known to target canonical H3 and H4 histones and enhance the cellular acetylation levels of specific lysine residues in particular H3K9, H4K12 and H3K27 through the inhibition of HDACs (Grunstein, 1997). From the *in vitro* studies, compound **4e** was found to be the most effective HDAC3 inhibitor among other molecules of the series and it displayed significant cytotoxic activity against B16F10 and 4T1 cell lines. Therefore, the evaluation of the potential cellular acetylation levels of H3K9, H4K12 and H3K27 was carried out by treating cells with compound **4e** and **UF010** (as reference) in a dose-dependent manner (5 μ M and 10 μ M) in B16F10 and 4T1 cells. It was observed from the results, that the compound **4e** caused significant hyperacetylation on H3K9, H4K12 and H3K27 residues in a similar fashion to the reference compound **UF010**, well correlating with its HDAC3 inhibition results (Figure 3.15A, 3.15C – 3.15E). Tubulin and SMC3 are known acetylation substrates of the HDAC6 and HDAC8 histone deacetylase isoforms, respectively (Dasgupta et al., 2016; Zhang et al., 2003). For the purpose, we have used **Tubastatin A** (Butler et al., 2010), a selective HDAC6 inhibitor and **PT5e** (Trivedi et al.,

Chapter 3: Benzoyl hydrazides as HDAC3 inhibitors

2019), a selective HDAC8 inhibitor previously reported by our group as the positive control along with the compound **4e** and **UF010** in a dose-dependent manner (5 μ M and 10 μ M). The results are depicted in **Figure 3.15B, 3.15F** and **3.15G**. From the results obtained, it can be inferred that the compound **4e** selectively inhibited HDAC3 through the hyperacetylation of H3K9, H4K12 and H3K27 and also no significant acetylation of tubulin and SMC3 was seen at 5 μ M and 10 μ M compound treatment concentration when compared to the positive controls.

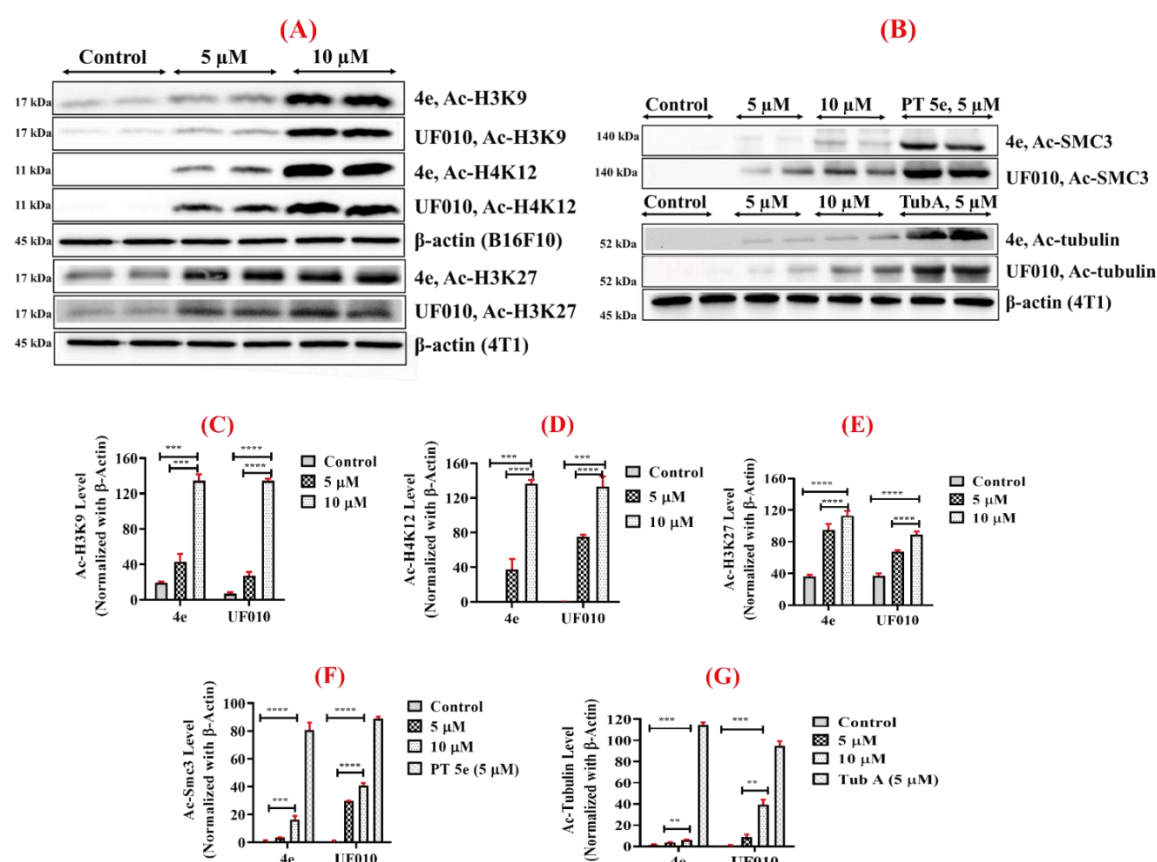


Figure 3.15 (A) Western blot analysis of Ac-H3K9 and Ac-H4K12 in the whole-cell lysate of B16F10-treated cells and Ac-H3K27 in the whole-cell lysate of 4T1-treated cells with compound **4e** at two different doses (5 μ M and 10 μ M). Lanes 1, 2: vehicle, lanes 3, 4: 5 μ M of **4e** and **UF010** and lanes 5, 6: 10 μ M of **4e** and **UF010**; **(B)** Western blot analysis of Ac-Tubulin and Ac-SMC3 in the whole-cell lysate of 4T1-treated cells with compound **4e** at two different doses (5 μ M and 10 μ M). Lanes 1, 2: vehicle, lanes 3, 4: 5 μ M of **4e** and

Chapter 3: Benzoyl hydrazides as HDAC3 inhibitors

UF010 and lanes 5, 6: 10 μ M of **4e** and **UF010** and lanes 7,8: 5 μ M of **PT5e** in case of *Ac*-SMC3 and 5 μ M of **Tubastatin A** in case of *Ac*-Tubulin and (C), (D), (E), (F) and (G) Graphs representing the analysis of the blots obtained for *Ac*-H3K9, *Ac*-H4K12, *Ac*-H3K27, *Ac*-SMC3 and *Ac*-Tubulin respectively. Results obtained were normalized to the housekeeping protein β -actin. [Image J software was used for the quantification of the results. Graph plotted and data analysed using one-way ANOVA analysis. Data represents mean \pm the standard error of the mean of the respective proteins. **p <0.01***p <0.001, ****p=0.0001].

3.2.6. Apoptosis and cell cycle analysis of 4c and 4e in B16F10 and 4T1 cells.

The cytotoxic effects of HDACis were found to be mediated by cell cycle arrest, in particular, G1 and G2/M phase arrest and apoptosis (Carew et al., 2008; Marks et al., 2000; Marks and Jiang, 2005; Sambucetti et al., 1999; Telles and Seto, 2012; Xu et al., 2007). The cytotoxic activity of the lead compounds (**4c** and **4e**) was also been explored in apoptosis and cell cycle arrest experiments using flow cytometry analysis and nuclear staining assay with B16F10 and 4T1 cells. The results demonstrated significant apoptotic activity and G2/M phase arrest of the cell cycle when B16F10 and 4T1 cells were treated with **4c**, **4e** and **UF010** for a specified time gap. Cells were given treatment with the IC₅₀ concentration of these compounds as per the given protocol. Both these compounds (**4c** and **4e**) exhibited significant early and late apoptotic activity compared to the reference molecule **UF010**. **Figure 3.16A** and **3.16B** indicates the % total apoptotic cell population in both B16F10 and 4T1 cells as denoted in the figures.

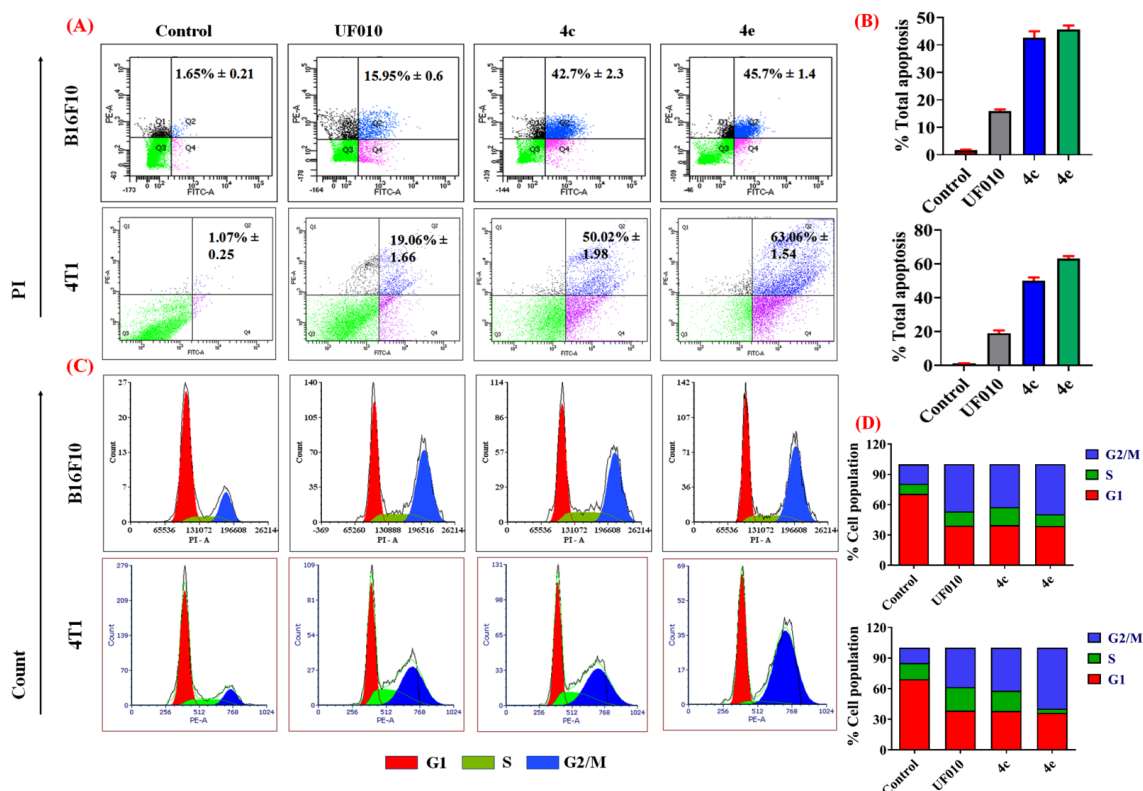


Figure 3.16. (A) Apoptosis analysis using Annexin V/PI assay double staining by flow cytometry. B16F10 and 4T1 cells from the same cultures were treated with vehicle **Control**, **UF010**, **4c** and **4e** at their respective *in vitro* IC₅₀ concentrations for 72 h (X and Y-axis represent the intensities of annexin V and propidium iodide respectively); (B) Graphical representation of the total apoptotic percentage analysis in B16F10 and 4T1 cells; (C) Cell cycle analysis in B16F10 and 4T1 cells treated with vehicle **Control**, reference compound **UF010**, **4c** and **4e** at 5 μM for 48 h. After the indicated treatment times, cell cycle analysis was carried out and subsequently analysed by Flow cytometer (BD Aria III) ®; (D) Graphical representation of the % cell population at various stages of the cell cycle in B16F10 and 4T1 cells, i.e., G1, S and G2/M phases.

Table 3.6. Table indicates the % cell population in different phases of cell cycle in B16F10 and 4T1 cells respectively.^a

Chapter 3: Benzoyl hydrazides as HDAC3 inhibitors

Cycle phase	% Cell population							
	B16F10 cells				4T1 cells			
	Control	UF010	4c	4e	Control	UF010	4c	4e
G1	70.66	39.20	39.76	38.95	69.29	38.48	38.17	36.22
S	10.08	14.18	17.76	11.62	15.74	22.97	19.81	4.13
G2/M	19.26	46.62	42.48	49.43	14.97	38.55	42.02	59.65

^a Data represents n = 3 experiments.

The lead compounds **4c** and **4e** induced 42.7% and 45.7% apoptotic B16F10 cells in Annexin-V apoptosis assay, and 50.02% and 63.06% apoptotic 4T1 cells in the same assay. The results indicated that both the compounds are more active in both B16F10 and 4T1 cell lines in the said assay when compared with the same activity of the reference compound **UF010** (15.95% apoptotic B16F10 cells, and 19% apoptotic 4T1 cells). Cell cycle analysis using B16F10 and 4T1 cells when exposed to **4c**, **4e** and **UF010** at a defined concentration of 5 μ M indicated that these compounds mainly blocked the G2/M transition phase showing an accumulation of G2/M phase cell population compared to control (**Figure 3.16C and 3.16D** and **Table 3.6**). There is an exceptional decrease in the G1 phase population in the treated cells from 70.66% in control to 39.20%, 39.76% and 38.95% in B16F10 cells and from 69.29% in control to 38.48%, 38.17% and 36.22% in 4T1 cells in the case of **UF010**, **4c** and **4e**, respectively. The simultaneous increase was noticed in the G2/M phase % cell population from 19.26% in control group cells to 46.62%, 42.48% and 49.43% in B16F10 cells and from 14.97% in control group cells to 38.55%, 42.02% and 59.65% in 4T1 cells in the case of **UF010**, **4c** and **4e** respectively causing cell cycle arrest at the G2/M phase. Nuclear staining assay was performed for one of the promising compounds **4e** along with the reference compound **UF010** to examine the cytotoxicity caused by the treatment in 4T1 cells (**Figure 3.17**).

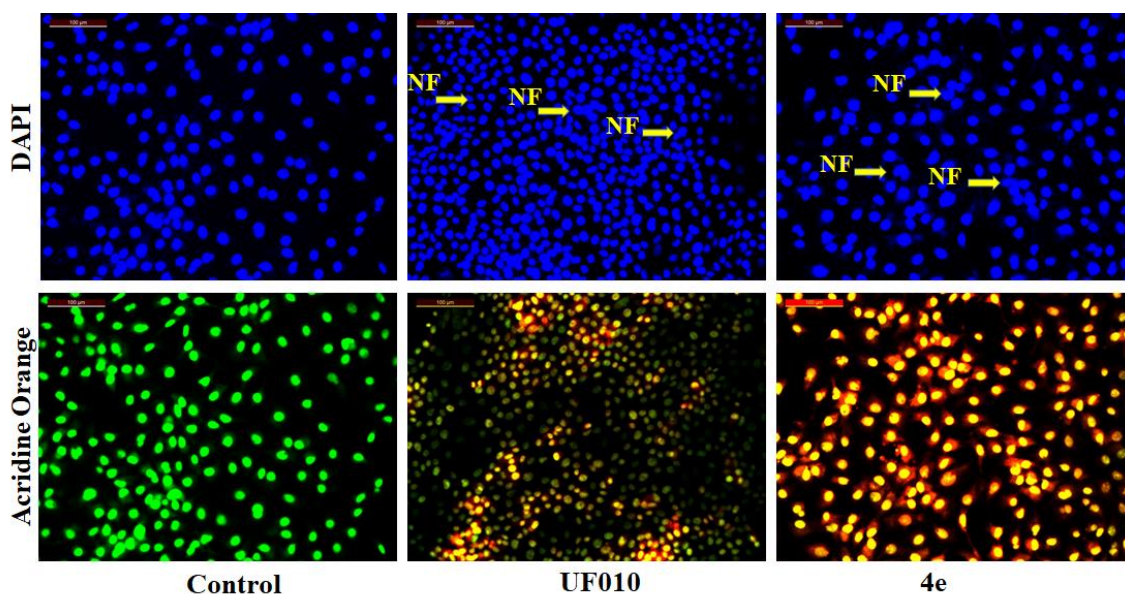


Figure 3.17. Analysis of nuclear morphology in 4T1 cells based on DAPI and Acridine Orange staining following treatment by vehicle **Control**, **UF010** (8.40 μM) and **4e** (1.92 μM) for 48 h. There was more nuclear fragmentation (NF) in **4e** treated cells compared to **UF010** as indicated by arrows whereas there were mostly intact nuclei in vehicle treated control cells. The stained nuclei were visualized employing a fluorescence microscope (Leica microsystems, Germany) on 20x Magnification. Data represent mean \pm standard deviation, n=3.

Here, 4T1 cells were treated for 48 h followed by double staining using DAPI/ AO. AO staining result showed a change in the fluorescence pattern from green (normal cellular DNA) to orange (nicked cellular DNA). Increased fluorescence of AO in **4e** treated cells revealed that chromosomal condensation occurred significantly compared to untreated cells, suggesting the cytotoxicity of the compound. A greater degree of apoptosis was observed in the cells treated with **4e** than the reference compound **UF010**. Altogether, these results suggested the cytotoxic effects of this HDAC3 inhibitor (**4e**) that also made cell cycle arrest in G2/M phase. These *in vitro* results further encouraged studying the *in vivo* antitumor activity of the most potent compound, **4e**.

3.2.7. **4e** displayed promising pharmacokinetic profile in i.v and i.p routes of

Chapter 3: Benzoyl hydrazides as HDAC3 inhibitors

administration.

One of the major limitations of the existing HDACis in the clinic is their poor pharmacokinetic (PK) profile followed by lower bioavailability and undesirable toxicities. To overcome these limitations, novel compounds with good PK properties along with reduced clinical toxicities are in need. Due to the promising *in vitro* cytotoxic activity results, the lead compound (**4e**) was subjected to detailed pharmacokinetic analysis after intravenous and intraperitoneal routes of administration. Most of the reported benzamides and hydroxamates were found to be administered at 50 mg/kg and 100 mg/kg doses in tumor xenograft models (Hess-Stumpp et al., 2007; Konsoula et al., 2009; LoRusso et al., 1996; Minami et al., 2014; Prince et al., 2009; Saito et al., 1999). Given the better stability of compounds containing hydrazide moiety as ZBG (Jiang et al., 2022; Li et al., 2020; Wang et al., 2015), two doses (15 mg/kg and 25 mg/kg) were tried for the pharmacokinetic studies in male Wistar rats by intravenous (i.v.) administration of **4e** and intraperitoneal administration of **4e** and **UF010** (Figure 3.18, Table 3.7 – 3.10). Compound **4e** was dissolved in saline along with 5% DMSO and was administered intravenously and intraperitoneally at 15 mg/kg and 25 mg/kg body weight doses (n = 3) along with the reference compound **UF010** at 25 mg/kg in the intraperitoneal route of administration. The mean plasma concentrations and time profiles of the resultant PK parameters are depicted in Figure 3.19 and Table 3.11.

Table 3.7. Plasma concentration ($\mu\text{g/ml}$)-time data of **4e** following an intravenous administration to male wistar rat (Dose: 15 mg/kg and 25 mg/kg).

Time Point (h)	15 mg/kg				25 mg/kg			
	AUC	Conc. ($\mu\text{g/ml}$)	Average	STDev	AUC	Conc. ($\mu\text{g/ml}$)	Average	STDev
0.25	708960	28.8314	24.4187	4.0477	804020	32.7337	30.2706	4.23768
	580220	23.5465			803216	32.7007		
	515220	20.8782			624820	25.3774		

Chapter 3: Benzoyl hydrazides as HDAC3 inhibitors

0.5	79285 6	32.2754	26.7413	5.2052	85366 8	34.771 8	32.1237	2.8198 5
	64011 2	26.0052			79687 2	32.440 3		
	54116 8	21.9434			71693 6	29.158 9		
1	49110 8	19.8884	18.0399	1.6025 3	70624 4	28.719 9	26.3676	2.3930 2
	42532 8	17.1881			58970 4	23.935 9		
	42179 6	17.0431			65087 2	26.446 9		
2	41231 2	16.6538	13.855	2.4238 5	64520 8	26.214 4	21.7312	3.9002 8
	31032 0	12.4669			49045 2	19.861 5		
	30976 8	12.4442			47233 6	19.117 8		
4	30954 4	12.435	11.8088	0.6897 3	44974 8	18.190 5	17.2835	0.8904 7
	29704 0	11.9217			42682 4	17.249 5		
	27628 0	11.0695			40638 8	16.410 6		
6	28062 4	11.2478	10.9683	0.4515 3	39033 2	15.751 5	15.6689	5.3183
	27969 2	11.2096			25777 2	10.309 8		
	26112 4	10.4474			51685 6	20.945 4		
8	26302 0	10.5252	9.41189	1.4654 5	29290 8	11.752 1	9.49136	2.131
	24922 4	9.95885			23079 6	9.2023 6		
	19545 6	7.75163			18980 4	7.5196 1		
12	17727 6	7.00532	3.96224	3.1275 6	15453 6	6.0718 2	3.61868	2.1993 8
	10710 8	4.12486			78760	2.9611 5		
	25056	0.75655			51036	1.8230 5		
24	10164	0.14522	0.06684	0.0694	12200	0.2288	0.1363	0.0803 9
	7652	0.0421			8984	0.0967 8		
	6948	0.0132			8656	0.0833 2		

Table 3.8. Plasma concentration ($\mu\text{g/ml}$)-time data of **4e** (Dose: 15 mg/kg and 25 mg/kg) and **UF010** (Dose: 25 mg/kg) following an i.p administration to male wistar rats.

Time Point	4e						UF010		
	15 mg/kg			25 mg/kg			25 mg/kg		
	AUC	Conc. ($\mu\text{g/ml}$)	Average (STDev)	AUC	Conc. ($\mu\text{g/ml}$)	Average (STDev)	AUC	Conc. ($\mu\text{g/ml}$)	Average (STDev)

Chapter 3: Benzoyl hydrazides as HDAC3 inhibitors

0.25	1740	0.156366	0.173189 (0.07573)	2486	0.25049	0.176343 (0.076428)	2771	0.092926	0.09877 (0.035837)
	2529	0.255916		1276	0.097822		2544	0.066214	
	1351	0.107285		1933	0.180717		3147	0.13717	
0.5	7875	0.93043	0.988974 (0.123898)	6151	0.71291	0.544008 (0.191045)	8268	0.739768	0.737925 (0.144216)
	9467	1.131296		5117	0.582448		7019	0.592796	
	7675	0.905196		3169	0.336666		9470	0.88121	
1	13977	1.700331	1.734691 (0.443043)	29045	3.601488	3.18613 (0.565855)	33061	3.65721	3.798455 (0.655243)
	17889	2.193915		27569	3.415258		40332	4.512803	
	10882	1.309829		20645	2.541644		29391	3.225354	
2	58416	7.30728	8.34437 (0.899476)	79797	10.00496	11.09336 (1.050764)	75376	8.636499	8.562327 (0.323163)
	70358	8.814024		89056	11.17318		77122	8.841955	
	71133	8.911807		96417	12.10194		71739	8.208527	
4	24806	3.066645	4.276843 (1.883081)	19759	2.429856	2.742426 (0.346945)	8710	0.791779	0.817824 (0.030463)
	26794	3.317475		21755	2.681695		9216	0.851321	
	51593	6.44641		25195	3.115726		8868	0.810372	
6	18155	2.227476	1.518601 (0.635651)	7795	0.920336	0.900612 (0.132388)	6581	0.541256	0.608878 (0.066851)
	8421	0.99932		8601	1.022031		7169	0.610447	
	11034	1.329007		6520	0.759467		7717	0.674931	
8	7696	0.907845	0.451692 (0.400808)	3365	0.361395	0.437939 (0.072063)	5150	0.372867	0.415896 (0.055847)
	1736	0.155861		4051	0.447949		6052	0.479007	
	2810	0.29137		4499	0.504474		5345	0.395813	
12	2079	0.199138	0.147155 (0.048453)	1777	0.161034	0.152118 (0.023391)	3295	0.154586	0.161411 (0.033011)
	1603	0.13908		1846	0.16974		3658	0.197301	
	1319	0.103248		1496	0.12558		3106	0.132346	
24	1303	0.101229	0.08756 (0.01395)	995	0.062368	0.067373 (0.007093)	2433	0.053152	0.056761 (0.017694)
	1082	0.073345		1010	0.064261		2627	0.075981	
	1199	0.088107		1099	0.07549		2331	0.04115	

Bioanalytical Summary

Table 3.9. Optimized chromatographic conditions in HPLC.

HPLC: Optimized chromatographic conditions		
Compound	4e	UF010
Column	Phenomenex C18 (150nmX4.4nm,5µm)	Phenomenex C18 (150nmX4.4nm,5µm)
Mobile phase	Water: Methanol (40:60)	Water: Methanol (30:70)
Injection volume	10 µl	10 µl
Run time	10 min	10 min

Chapter 3: Benzoyl hydrazides as HDAC3 inhibitors

Flow rate	1 ml/min	1 ml/min
Column temp	25 °C	25 °C
Retention time	6.8 min	7.3 min

Table 3.10. Calibration curve data of **4e** and **UF010** in rat plasma.

4e			UF010		
Nominal Conc. (µg/ml)	Calculated Conc.(µg/ml)	% Accuracy	Nominal Conc. (µg/ml)	Calculated Conc.(µg/ml)	% Accuracy
0.25	0.2404128	91.32699463	50	49.62823892	99.25647784
0.5	0.44722394	99.48739148	25	25.17047139	100.6818856
1	1.02352941	100.8433237	12.5	13.20464334	105.6371467
2	2.08260062	103.4518396	6.25	6.468040291	103.4886447
4	4.14138287	103.2699463	3.125	2.992363089	95.75561884
8	7.72070175	96.44119471	1.5625	1.40732155	90.06857923
16	16.0944066	100.631976	0.78125	0.769068744	98.44079923
Regression equation	$y = 24190.1x + 8498.8$		Regression equation	$y = 8465.9x + 2648.6$	
Slope	24190.1		Slope	8465.9	
Intercept	8498.8		Intercept	2648	
R ²	0.999		R ²	0.999	

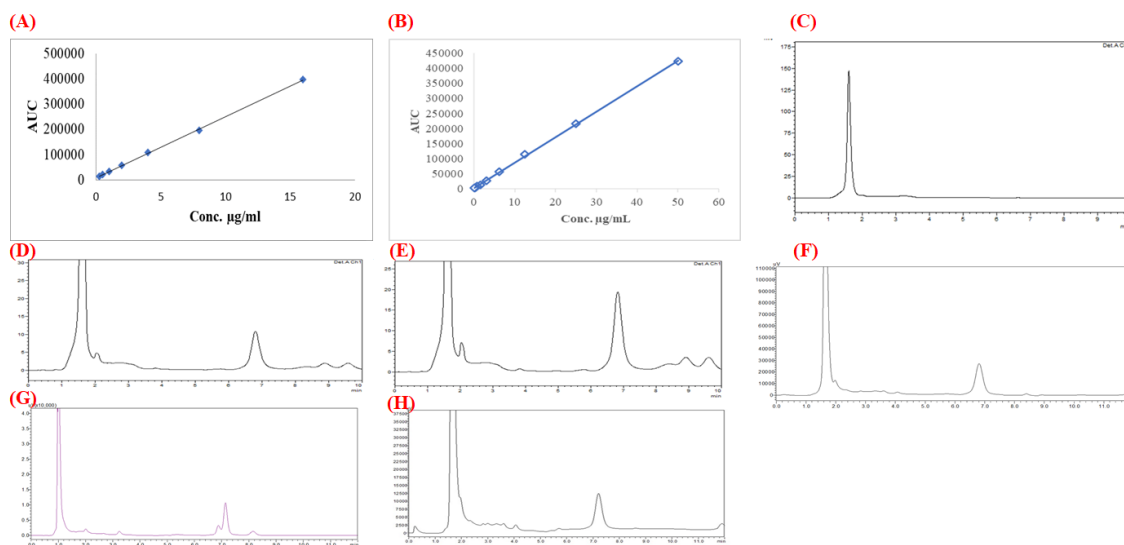


Figure 3.18. (A) Calibration curve of **4e** in rat plasma; (B) Calibration curve of **UF010** in rat plasma; (C) Representative chromatogram of blank in rat plasma (blank sample); (D) Representative chromatogram of **4e** in rat plasma (standard); (E) Representative chromatogram of **4e** in rat plasma (intravenous sample); (F) Representative chromatogram of **4e** in rat plasma (intravenous sample); (G) Representative chromatogram of **4e** in rat plasma (intravenous sample); (H) Representative chromatogram of **4e** in rat plasma (intravenous sample).

of **4e** in rat plasma (intraperitoneal sample); (G) Representative chromatogram of **UF010** in rat plasma (standard); (H) Representative chromatogram of **UF010** in rat plasma (intraperitoneal sample).

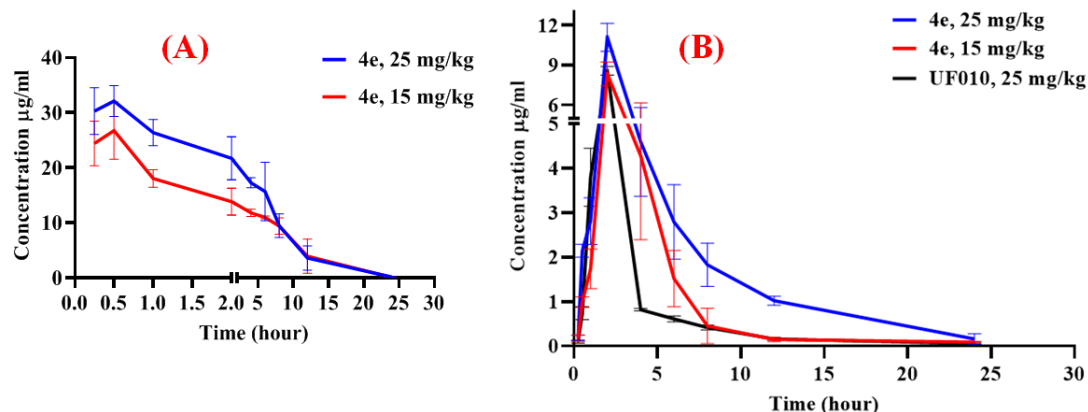


Figure 3.19. (A) Mean plasma concentration-time profiles of compound **4e** following a single intravenous administration to male wistar rats ($n = 3$; dose, 25 mg/kg, 15 mg/kg). (B) Mean plasma concentration-time profiles of compound **4e** and **UF010** following a single intraperitoneal administration to male Wistar rats ($n = 3$; dose, **4e**: 25 mg/kg, 15 mg/kg and **UF010**: 25 mg/kg).

Table 3.11. Pharmacokinetic parameters of compound **4e** (i.v and i.p) and **UF010** (i.p) in plasma following an intravenous and intraperitoneal administration in male Wistar rats.^a

Parameters	Data obtained				
	4e (i.v)		4e (i.p)		UF010 (i.p)
Dose (mg/kg)	15	25	15	25	25
Tmax (h)	0.5	0.5	2	2	2
C _{max} (µg/ml)	26.74 ± 5.21	32.12 ± 2.84	8.34 ± 0.29	12.10 ± 0.34	8.56 ± 3.84
[C _{max} (µM)]	(99.28 ± 19.32)	(119.58 ± 10.53)	(30.97 ± 3.33)	(44.93 ± 3.90)	(31.58 ± 1.19)
AUC _{0-t} [(µg/ml).h]	159.38 ± 39.37	199.91 ± 35.78	28.88 ± 1.28	48.95 ± 0.50	21.73 ± 13.45
[AUC _{0-t} [(µM).h]]	(591.74 ± 146.17)	(742.26 ± 126.54)	(107.22 ± 12.27)	(187.36 ± 6.68)	(80.13 ± 5.17)
AUC _{0-inf} [(µg/ml).h]	159.59 ± 39.61	200.43 ± 36.11	29.31 ± 1.29	49.99 ± 0.85	22.15 ± 11.89
[AUC _{0-inf} [(µM).h]]					

Chapter 3: Benzoyl hydrazides as HDAC3 inhibitors

	(592.57 ± 147.06)	(744.17 ± 127.79)	(108.82 ± 10.55)	(191.25 ± 6.67)	(81.69 ± 5.84)
AUMC_{0-inf} [(µg/ml).h²]	909.34 ± 368.72	1028.3 ± 306.1	137 ± 6.3	302.67 ± 18.45	89.52 ± 13.24
[AUMC_{0-inf} [(µM).h²]]	(3377.5 ± 1368.91)	(3817.8 ± 1089.09)	(478.96 ± 46.95)	(1134.96 ± 20.19)	(330.13 ± 52.98)
MRT_{0-inf} (h)	5.69 ± 1.01	5.13 ± 0.58	4.16 ± 0.53	4.03 ± 0.65	4.04 ± 1.36
t_{1/2} (h)	2.19 ± 0.34	2.62 ± 0.18	3.41 ± 0.09	4.54 ± 0.84	5.18 ± 3.09
Vz/F [(mg/kg)/(µg/ml)]	0.29 ± 0.04	0.47 ± 0.12	2.16 ± 1.44	3.27 ± 4.13	8.43 ± 2.29
[Vz/F [(mg/kg)/(µM)]]	(0.077 ± 0.009)	(0.13 ± 0.01)	(1.44 ± 0.68)	(2.01 ± 0.30)	(2.29 ± 0.13)
Cl/F [[(mg/kg)/(µg/ml)].h]	0.09 ± 0.03	0.12 ± 0.04	0.51 ± 0.33	0.79 ± 0.04	1.13 ± 0.06
[Cl/F [[(mg/kg)/(µM)].h]	(0.026 ± 0.006)	(0.034 ± 0.005)	(0.138 ± 0.012)	(0.224 ± 0.01)	(0.306 ± 0.02)

4e was injected intravenously (n = 3) and in another experiment, **4e** along with **UF010** were injected intraperitoneally (n = 3) and the blood sample was collected at fixed intervals and different time points for the duration of 24 h. The plasma concentrations of **4e** and **UF010** were estimated by the HPLC method. Linear trapezoidal rule was used for the calculation of area under the concentration and time curve (AUC values). Non-compartmental analysis was used to obtain the PK parameters. The clearance was estimated as $CL = \text{Dose}/AUC_{inf}$; $MRT = AUMC_{inf}/AUC_{inf}$, n=3, data represent mean ± standard deviation, dose; **4e**: 25 mg/kg and 15 mg/kg, **UF010**: 25 mg/kg. Data represented in µg/ml or µM units in the table.

In the i.v route of administration, the *in vivo* half-life ($t_{1/2}$) of **4e** was found to be 2.19 h and 2.62 h with the peak plasma levels (C_{max}) of 26.74 µg/ml (99.28 µM) and 32.12 µg/ml (119.58 µM) shortly after 0.5 h (T_{max}) for 15 mg/kg and 25 mg/kg dose respectively. The AUC_{0-inf} values were 159.59 µg. h/ml and 200.43 µg. h/ml for 15 mg/kg and 25 mg/kg dose, respectively. In the case of i.p route of administration, the *in vivo* half-life ($t_{1/2}$) of **4e** was found to be 3.41 h and 4.54 h, and 5.18 h for **UF010** with the peak plasma levels (C_{max}) of 8.34 µg/ml (30.97 µM) and 12.10 µg/ml (44.93 µM) for **4e** and 8.16 µg/ml (31.58 µM)

Chapter 3: Benzoyl hydrazides as HDAC3 inhibitors

for **UF010** after 2 h (T_{max}) for the given doses respectively. The AUC_{0-inf} values for the compound **4e** were 159.59 $\mu\text{g. h/ml}$ and 200.43 $\mu\text{g. h/ml}$ for 15 mg/kg and 25 mg/kg dose in the i.v route, whereas in case of i.p route of administration, the obtained AUC_{0-inf} values were 29.31 $\mu\text{g. h/ml}$ and 49.99 $\mu\text{g. h/ml}$ for 15 mg/kg and 25 mg/kg dose respectively. All these results with the sufficient residence time and better AUC levels suggested the good bioavailability and PK profile of **4e** at low doses (15 mg/kg and 25 mg/kg) when compared to the earlier reported benzamides and hydroxamates at comparatively higher doses (50 and 100 mg/kg) (Thakur et al., 2020; Zhao et al., 2018). These results further encouraged to study of the antitumor properties of **4e** in the 4T1-Luc tumor xenograft model in mice.

3.2.8. *In vivo* antitumor activity of **4e** in the xenograft mouse model of 4T1-Luc cell line.

Given the excellent *in vitro* cytotoxicity, its potent and selective HDAC3 inhibition and *in vivo* PK properties, the lead compound **4e** was then evaluated along with **UF010** as a positive control in the 4T1-Luc breast cancer tumor-xenograft mouse model in female Balb/c mice for its *in vivo* antitumor activity. **As per our knowledge, this is the first study reporting the *in vivo* antitumor study in a 4T1-Luc tumor xenograft mouse model evaluating a lead compound containing hydrazide moiety as ZBG.** From the obtained *in vitro* results, it was observed that the compound **4e** exhibited potent cytotoxicity against the 4T1 cell line with IC_{50} of 1.92 μM with about ~80.57-fold selectivity for 4T1 cells over normal cell line with significant HDAC3 inhibition potency as shown from the *in vitro* enzymatic assay and also the cellular western blot analysis. Henceforth, we evaluated its *in vivo* antitumor potential in the 4T1-Luc tumor xenograft mouse model. Based on the literature reports, the standard dosing regimen of HDAC inhibitors was reported as 5 days/week cycle for 3 to 4 weeks that caused significant antitumor activity (Khan and Thangue, 2012; LoRusso et al., 1996; Minami et al., 2014; Nepali et al., 2020; Saito et al.,

Chapter 3: Benzoyl hydrazides as HDAC3 inhibitors

1999; Sanderson et al., 2004). Based on the plasma PK profile of **4e** at 15 mg/kg and 25 mg/kg, these two doses were chosen for the *in vivo* antitumor study for 21 days, and 25 mg/kg was the administered dose for the reference compound **UF010**. Female Balb/c mice of about 5 to 6 weeks old were subcutaneously inoculated with 4T1–Luc cells with PBS suspension containing 1.5×10^6 cells for each implantation. Once the tumor volumes reached about 50 mm^3 , approximately 10 days after inoculation, mice were clubbed into four groups containing 5 mice in each group and were provided with treatment with vehicle alone, **UF010** at 25 mg/kg and **4e** at 15 mg/kg and 25 mg/kg dose (dosing solution was prepared as the protocol described in experimental method section) intraperitoneally with a dosage regimen of 5 days/week for 3 weeks. The tumor growth inhibition resulted in different groups at different time points after treatment were recorded (**Figure 3.20**).

The tumor growth curve for 21 days with tumor volume was measured once in 3 days from the beginning of the treatment in all the mice of different groups (**Figure 3.20A**). The group treated with the reference compound **UF010** exhibited the tumor volume growth from 52.33 ± 3.14 to $470.00 \pm 32.24 \text{ mm}^3$ whereas mice treated with **4e** at 15 mg/kg exhibited the tumor volume growth from 55.66 ± 5.57 to $372.00 \pm 15.75 \text{ mm}^3$ and, those treated with 25 mg/kg has shown the tumor growth volume from 51.83 ± 2.71 to $267.50 \pm 6.37 \text{ mm}^3$ as against the rapid increase in tumor volume growth in the control group from 49.16 ± 2.04 to $1032.50 \pm 65.43 \text{ mm}^3$.

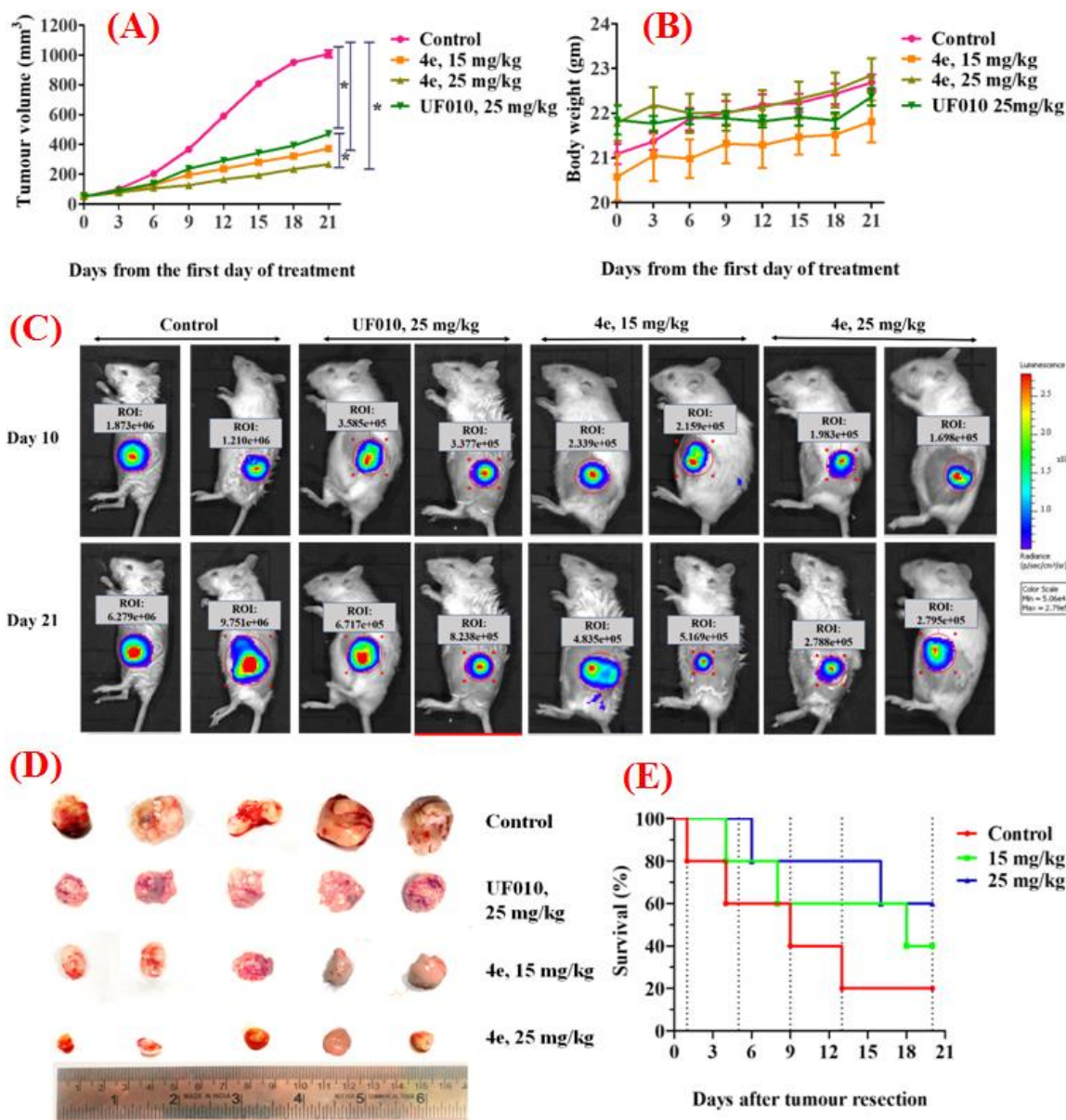


Figure 3.20. *In vivo* therapeutic efficacy of **4e** and **UF010** (reference compound) in 4T1-Luc tumor implanted Balb/C female mice treated with Control, **UF010** (25 mg/kg) and **4e**, 15 mg/kg, and 25 mg/kg (n=5) for 21 days (5 days/week). **(A)** Tumor volume reduced over the treatment period; **(B)** Body weight measurement over treatment period; **(C)** Representative *in vivo* bioluminescence images of **UF010** (25 mg/kg) and **4e** treated mice with doses 15 mg/kg and 25 mg/kg in 4T1 Luc tumor-bearing mice on the day 10 and day 21 (n=2) after i.p administration of luciferin-D (100 μ l, 100 mg/kg) by IVIS® Lumina III, PerkinElmer, USA; **(D)** Representative tumors surgically isolated from mice post 21 days

Chapter 3: Benzoyl hydrazides as HDAC3 inhibitors

of treatment (n=5); **(E)** % survival analysis using Kaplan-Meier survival curve for 21 days post tumor resection. Data represents the values of mean \pm the standard error of the mean (SEM), n =5; *p < 0.05.

Simultaneously, the toxicity of **4e** was assessed by monitoring the mice body weight at equal intervals once in 3 days (**Figure 3.20B**). Interestingly, the body weight was maintained consistent with no weight loss in all the groups, indicating compound **4e** was well-tolerated at all doses with no general toxicity and no mortality. These results were further evidenced by performing the bio-luminescence imaging in the treated mice by randomly selecting one from each group. The whole body NIRF images were taken on days 10 and 21 of the treatment after i.p. administration of Luciferin – D (100 μ l, 100 mg/kg) for the representative mice (n=2) from each group (**Figure 3.20C**). The obtained bio-luminescence intensities around the region of interest are provided in **Figure 3.20C**. Correlating with the tumor volume reduction values, the increase in the intensities were also found to be the highest in the case of control group mice whereas, the treated mice with **UF010** and **4e** (lower dose), showed a moderate increase compared to **4e** (25 mg/kg) treated mice that showed the least increase in the bio-luminescence. After 21 days of treatment, the survival study on **4e**-treated mice for another 21 days was performed. The tumors were collected by surgery and the mice were kept in individual cages for 21 days continuously monitoring for their survival. The images of the tumors collected on day 21 are represented in **Figure 3.20D**. It was found that the survival percentage was the lowest in the case of the untreated group of mice followed by 15 mg/kg (lower dose) and the highest survival percentage was found in the mice treated with 25 mg/kg (higher dose). The results indicated the improved survival rate in treated mice post-surgical excision of tumor compared to the control group (**Figure 3.20E**). This might be due to the reduced metastasis of the tumor in the treated mice.

3.2.9. Compound 4e caused significant ROS generation leading to apoptosis in treated mice.

From the preliminary *in vitro* studies, it was found that the lead compound **4e** caused cytotoxic effects through apoptosis as well as cell cycle arrest. The *in vivo* antitumor study also exhibited a significant reduction in the tumor volume in treated mice when compared to the vehicle control group. It is documented in the literature that HDACis induce tumor cell death by the generation of reactive oxygen species (ROS) causing oxidative stress eventually leading to apoptosis through several intrinsic pathways (Carew et al., 2008; Liao et al., 2020; Richa et al., 2020; Rosato et al., 2003; Ruefli et al., 2001). Further, to explore the mechanism of apoptosis we evaluated the ROS generation in the tumor implanted mice. DCFH-DA probe was injected intratumorally on the day 21 to randomly selected mice (n=2) from each group. The fluorescence intensity of the ROS generation was obtained from the IVIS Lumina III. The images were captured at 10 mins post-DCFH-DA injection into the mice (**Figure 3.21A**).

It can be inferred from the images that the mice treated with **4e** (25 mg/kg) showed the highest fluorescence intensity followed by **4e** (15 mg/kg) and **UF010** (25 mg/kg) with no fluorescence detected in the control group mice. The quantified fluorescence signals obtained were depicted in the graph in **Figure 3.21B**. These results indicated that **4e** caused significant ROS generation *in vivo* and thus, led to apoptosis which was further represented by DAPI staining of the cryosections of the isolated tumors collected from the mice sacrificed 30 mins post-DCFH-DA treatment (**Figure 3.21C**).

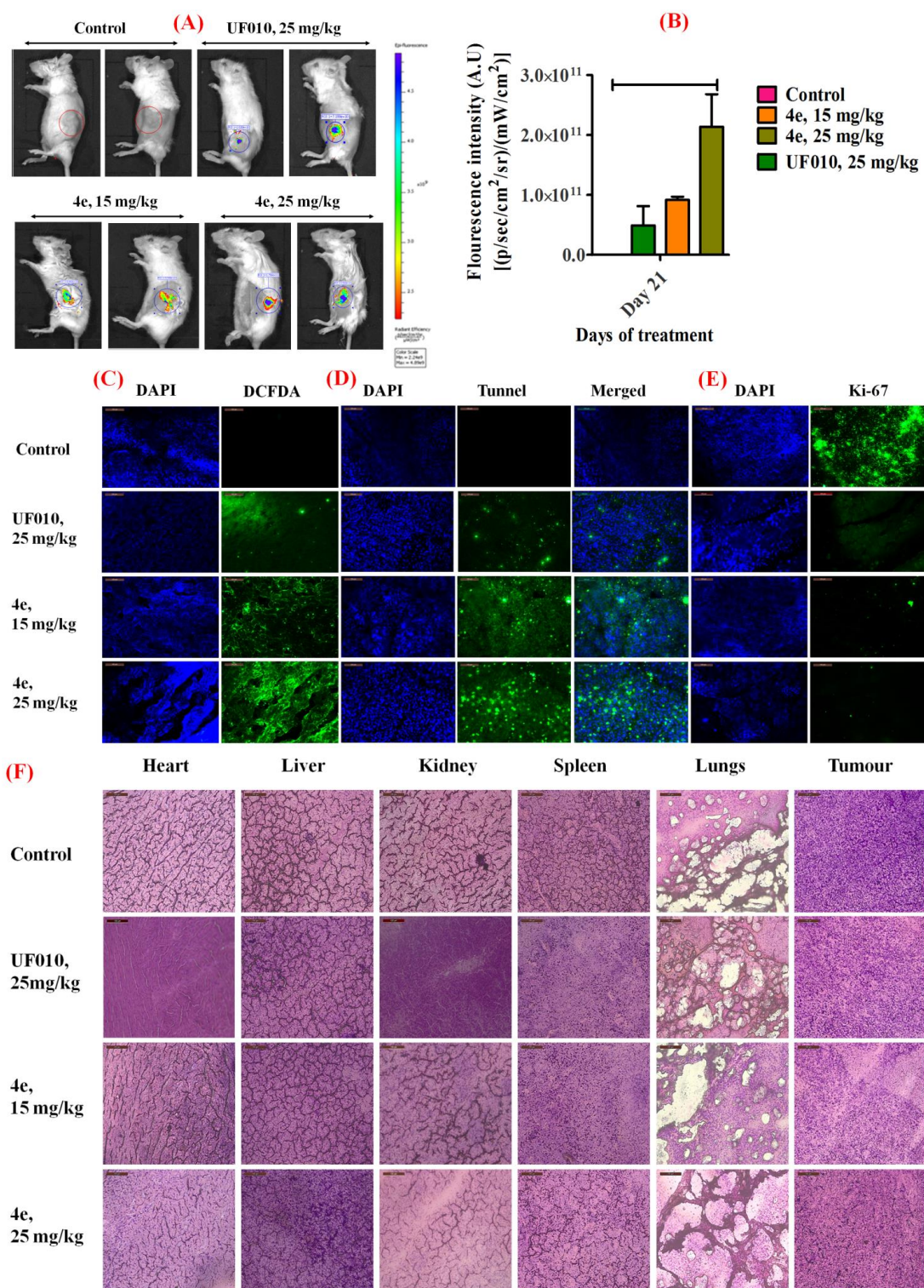


Figure 3.21. (A) Reactive oxygen species generation and imaging on day 21 in female Balb/c mice implanted with 4T1-Luc tumor treated with **Control**, positive control (**UF010**, 25 mg/kg) and **4e** (Dose:15 mg/kg and 25 mg/kg) (n=2) after Intratumoral injection of DCFH-DA probe (100 μ l, 25 μ M) by IVIS® Lumina III, PerkinElmer, USA; (B) Graph

Chapter 3: Benzoyl hydrazides as HDAC3 inhibitors

represents, fluorescence intensity found on Y-axis and day 21 of treatment on X-axis; (C) Images of tumor sections representing ROS levels; (D) Images representing TUNEL positive cells in the tumor sections from treated mice tumors; (E) fluorescent images of Ki-67 staining; (F) H & E staining of several organs and tumor sections isolated from treated mice; (Scale bar is 20 μm) All the images visualized and obtained under a fluorescence microscope (Leica microsystems, Germany). Data represents the values of mean \pm the standard error of the mean, n =2; **p = 0.009.

The images under a fluorescence microscope indicated the increase in the ROS generation in the tumor sections of treated mice with **4e** (higher dose) contributing to more apoptotic activity than **4e** (lower dose) followed by **UF010** treated mice. TUNEL assay was then carried out on the collected cryosections of the tumors and obtained their fluorescence images (**Figure 3.21D**). TUNEL assay identified the fragmented nuclear DNA as suggested by TUNEL +ve cells in the form of green dots when visualised under a fluorescence microscope. The increase in the number of TUNEL +ve cells in the order **4e**, 25 mg/kg > **4e**, 15 mg/kg > **UF010**-treated tumor sections indicated that the compound **4e** is largely capable of inducing apoptotic cell death *in vivo*. Together with the visualization of apoptotic mechanisms from ROS generation and TUNEL assay, the tumor cryosections were characterized using immunostaining analysis by Ki-67, a proliferative marker. The tumor cryosections were incubated with Ki-67 primary antibody followed by secondary antibody and was visualized under the fluorescence microscope (**Figure 3.21E**). The percentage of Ki-67 positively stained cells was highest in the case of control group tissue sections. When compared in the treated cells, a marked significant decrease in the staining was observed in 25 mg/kg followed by 15 mg/kg tissue sections of the treated mice. The decrease in the Ki-67-stained cells in the treated mice as compared to the untreated group demonstrated the significant cytotoxic activity of **4e** *in vivo* in correlation with its potent *in*

Chapter 3: Benzoyl hydrazides as HDAC3 inhibitors

in vitro cytotoxic effects in 4T1 cells. H & E analysis was performed on the tissue sections of tumors and various organs obtained from control and treated mice and the images obtained were represented in **Figure 3.21F**. No tissue damage or toxicity was found in any of the major organs in contrast to the tumor sections, which showed significant tissue damage due to cell death. Altogether, these results indicate that compound **4e** causes significant apoptotic activity through ROS generation and is also highly anti-proliferative with no induced organ toxicity among the other major organs *in vivo* with the results well correlated with the *in vitro* studies.

3.2.10. Analysis of different proliferation biomarker by western blot with the isolated tumor tissue.

The treated tumor tissues were collected from the mice treated with **4e** at two doses (15 mg/kg and 25 mg/kg) and were further investigated for the protein expression levels of histone proteins, various apoptotic and proliferation markers. The western blots obtained are shown in **Figure 3.22A** and the quantification of the blot is represented in **Figure 3.22B**.

The *in vitro* western blot analysis with the lysate of **4e** treated cells indicated the enhanced cellular acetylation levels of H3K9, H4K12 in a dose-dependent manner. Similar results were observed in the western blot analysis of the isolated tumor tissue collected from **4e** treated mice. This hyperacetylation of H3K9 and H4K12 histone lysine residues by **4e** is possibly majorly due to its HDAC3 inhibition property. The next step was to study the mechanism of cell death causing antitumor activity of **4e**. Literature reports demonstrated that HDAC inhibitors are antiproliferative and they induce cell cycle arrest, apoptosis and cause cell differentiation (Carew et al., 2008; Czabotar et al., 2014; Rosato et al., 2003; Shao et al., 2004; Telles and Seto, 2012).

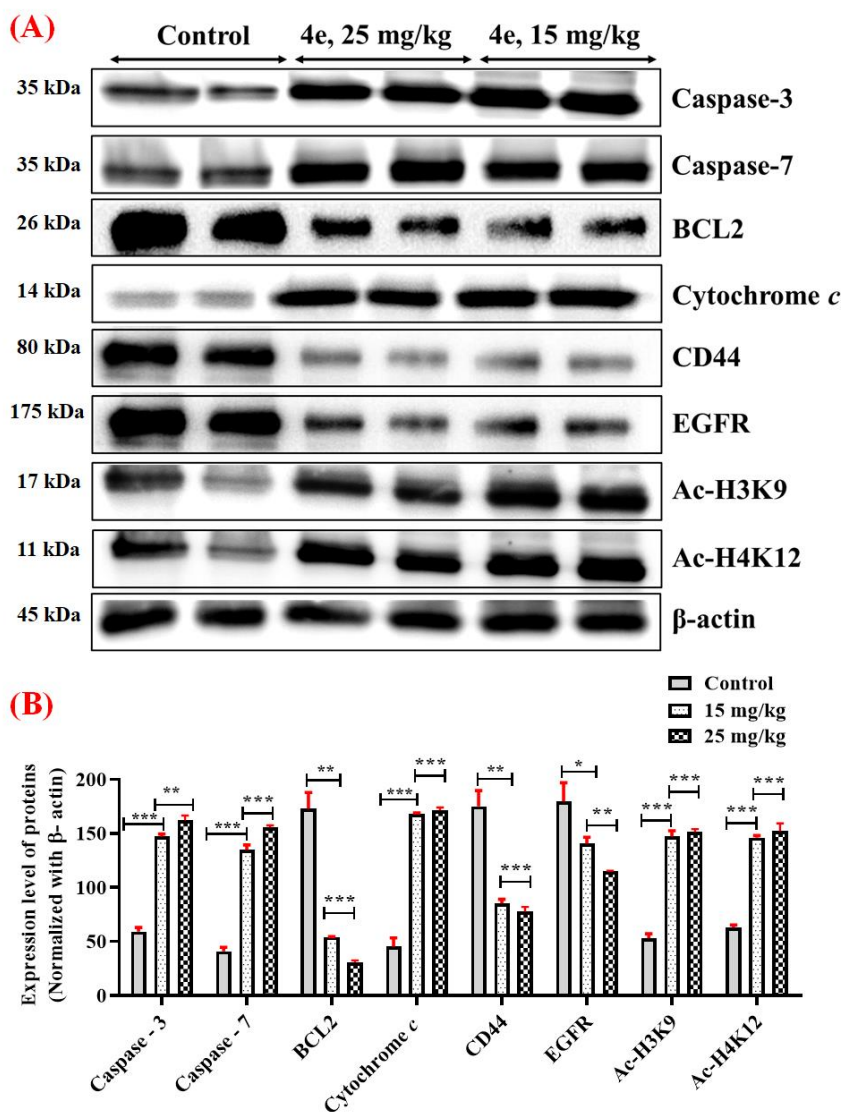


Figure 3.22. (A) Western blot analysis of caspase-3, caspase-7, BCL2, cytochrome c, CD44, EGFR, Ac-H3K9 and Ac-H4K12 in the tumor tissue collected from the **4e** treated mice at two different doses (25 mg/kg and 15 mg/kg) in 4T1-Luc implanted tumor xenograft model. Lanes 1, 2: vehicle, lanes 3, 4: 25 mg/kg of **4e** and lanes 5, 6: 15 mg/kg of **4e**; (B) Graph representing the analysis of the blots obtained. Results obtained were normalized to the housekeeping protein β -actin. Image J software was used for the quantification of the results. Graph plotted and data analysed using one-way ANOVA analysis. Data represents mean \pm the standard error of the mean of the respective proteins. *p < 0.05, **p < 0.01, ***p \leq 0.0005.

Chapter 3: Benzoyl hydrazides as HDAC3 inhibitors

These mechanisms are further regulated by various pro and anti-apoptotic markers namely caspase-3, caspase-7, cytochrome *c*, BCL2 and other metastatic and proliferative markers such as CD44 and EGFR. Caspase-3 and caspase-7 were upregulated in the treated samples against the control group resulting in cell apoptosis. It is well documented that caspase activation is mediated through the cytochrome *c* pathway following its release from mitochondria leading to apoptosis (Brentnall et al., 2013; Shao et al., 2004). In this regard, our results indicated the increased expression levels of cytochrome *c* which activates caspase-3 and caspase-7 thus mediating caspase activation-induced apoptosis. The experimental data also demonstrated the significant ROS production leading to oxidative stress together with the intrinsic upregulation of caspase-7 further contributed to the apoptotic cell death. The anti-apoptotic protein BCL2 was found to be downregulated in the treated *vs* the control group animals. From the survival plot displayed in **Figure 3.20E**, the % survival of the treated mice was found to be higher than the untreated mice up to 21 days post-tumor resection possibly due to reduced metastasis. In this regard, the protein levels of surface adhesion marker CD44 that is known to be involved in metastasis (Negi et al., 2012) has also been studied and the proliferation marker EGFR is known to be over expressed in cancer cells in particular breast cancer cells (Lo et al., 2006). The western blot analysis correlated with the cytotoxic results of **4e** demonstrating the reduced expression of CD44 and EGFR in the treated animal tumor tissue samples over control group samples. From the results, it was evident that HDAC3 inhibitor **4e** induced antitumor activity through the induction of several intrinsic pathways leading to apoptosis and also contributing to its cytotoxic activity.

3.2.11. Binding mode of interactions of the inhibitors into the HDAC enzymes by molecular docking analysis.

As far as our choice of target is concerned, the potent hydrazides (**4c** and **4e**) along with

Chapter 3: Benzoyl hydrazides as HDAC3 inhibitors

the reference molecule **UF010** were docked initially with the active site of HDAC3 (**PDB ID: 4A69**) following the protocol reported earlier (Routholla et al., 2021b, 2021a). The molecular docking studies conducted at the active site of HDAC3 revealed promising superimposed docked conformations of these synthesized molecules (**Figure 3.23**).

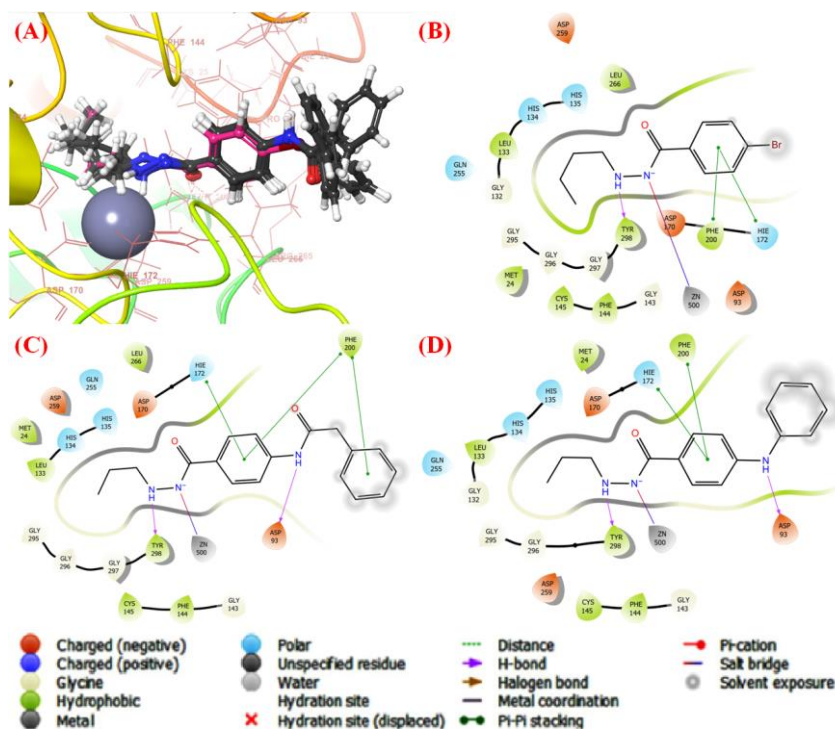


Figure 3.23. Docking conformations of synthesized hydrazone derivatives with **UF010** (In magenta) (A); Binding mode of interactions of compound **UF010** (B); **4c** (C) and **4e** (D) at the HDAC3 active site of (**PDB ID: 4A69**).

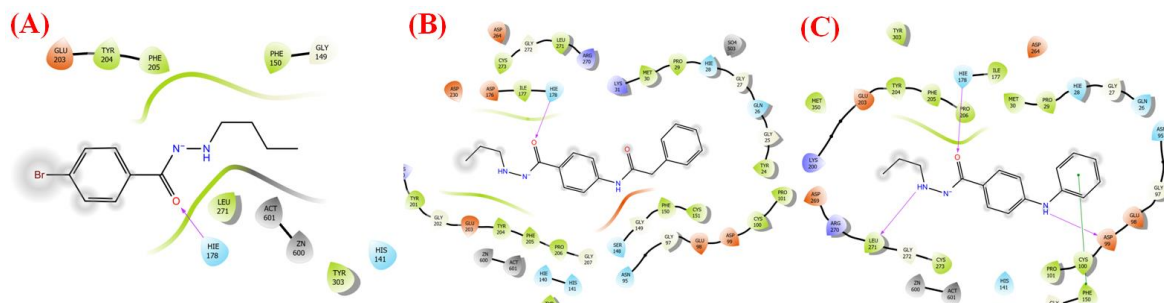


Figure 3.24. Ligand binding interaction of (A) **UF010** (B) **4c** and (C) **4e** with HDAC1 (**PDB ID: 4BKX**).

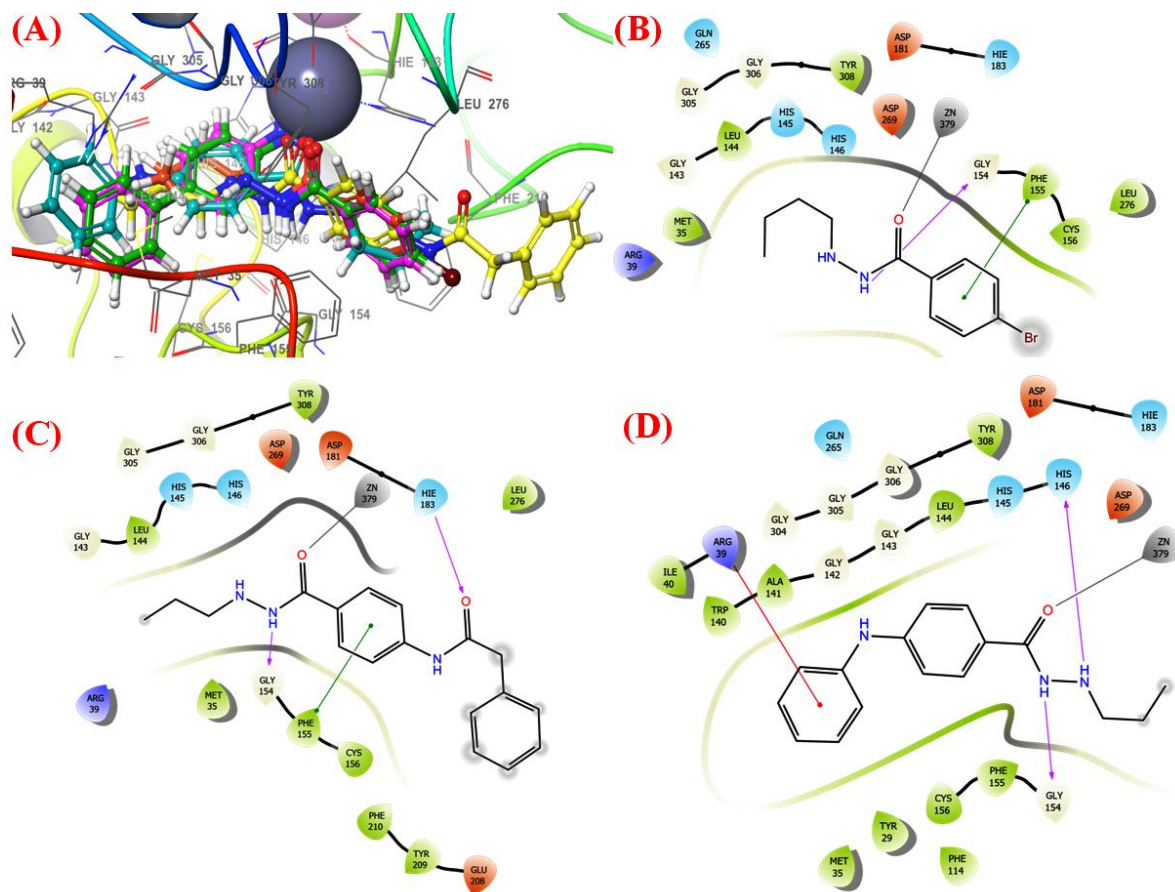


Figure 3.25. (A) Alignment of inbound ligand (green), redocked ligand (magenta), UF010 (orange), 4c (yellow) and 4e (cyan) at the HDAC2 active site (PDB ID: 3MAX); (B) Binding interaction of UF010 at the HDAC2 active site (PDB ID: 3MAX); (C) Binding interaction of 4c at the HDAC2 active site (PDB ID: 3MAX); (D) Binding interaction of 4e at the HDAC2 active site (PDB ID: 3MAX).

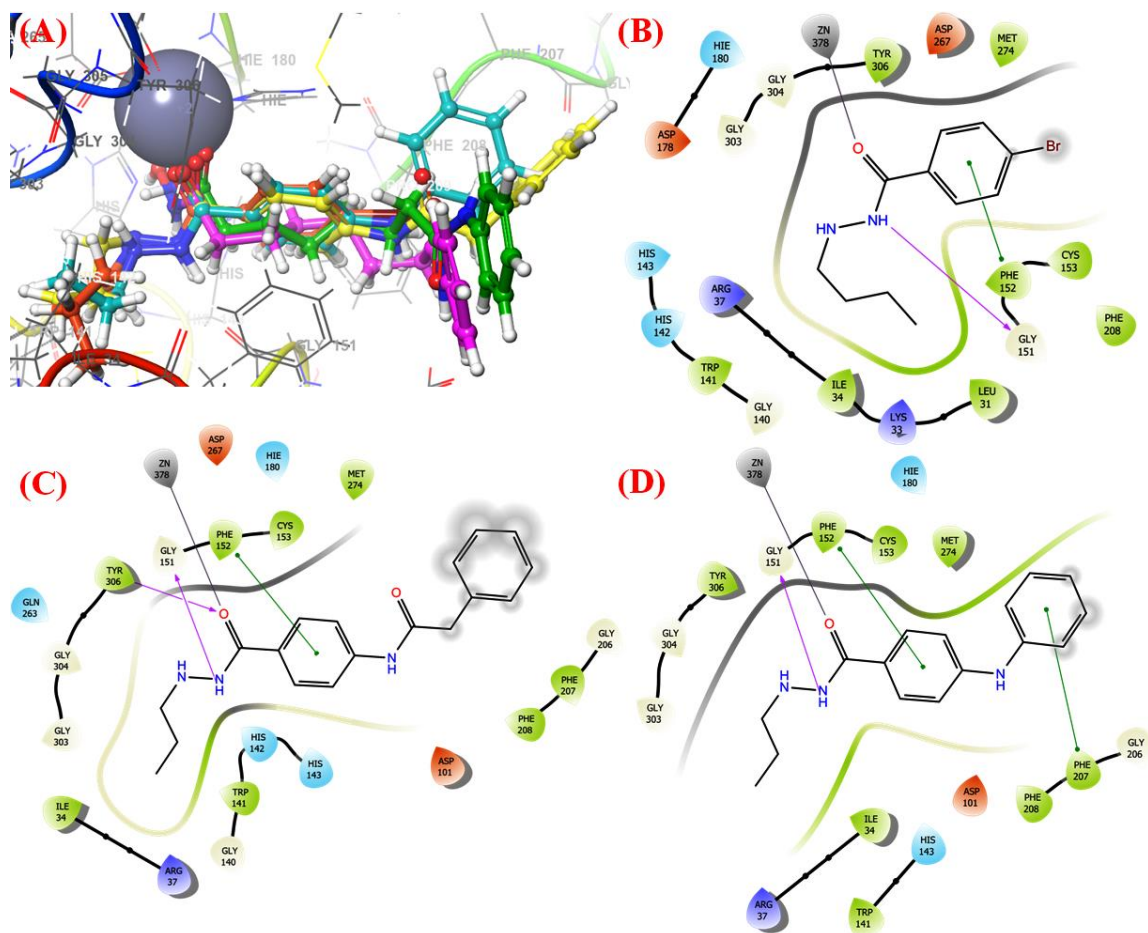


Figure 3.26. (A) Alignment of inbound ligand (green), redocked ligand (magenta), UF010 (orange), 4c (yellow) and 4e (cyan) at the HDAC8 active site (PDB ID: 1T69); (B) Binding interaction of UF010 at the HDAC8 active site (PDB ID: 1T69); (C) Binding interaction of 4c at the HDAC8 active site (PDB ID: 1T69); (D) Binding interaction of 4e at the HDAC8 active site (PDB ID: 1T69).

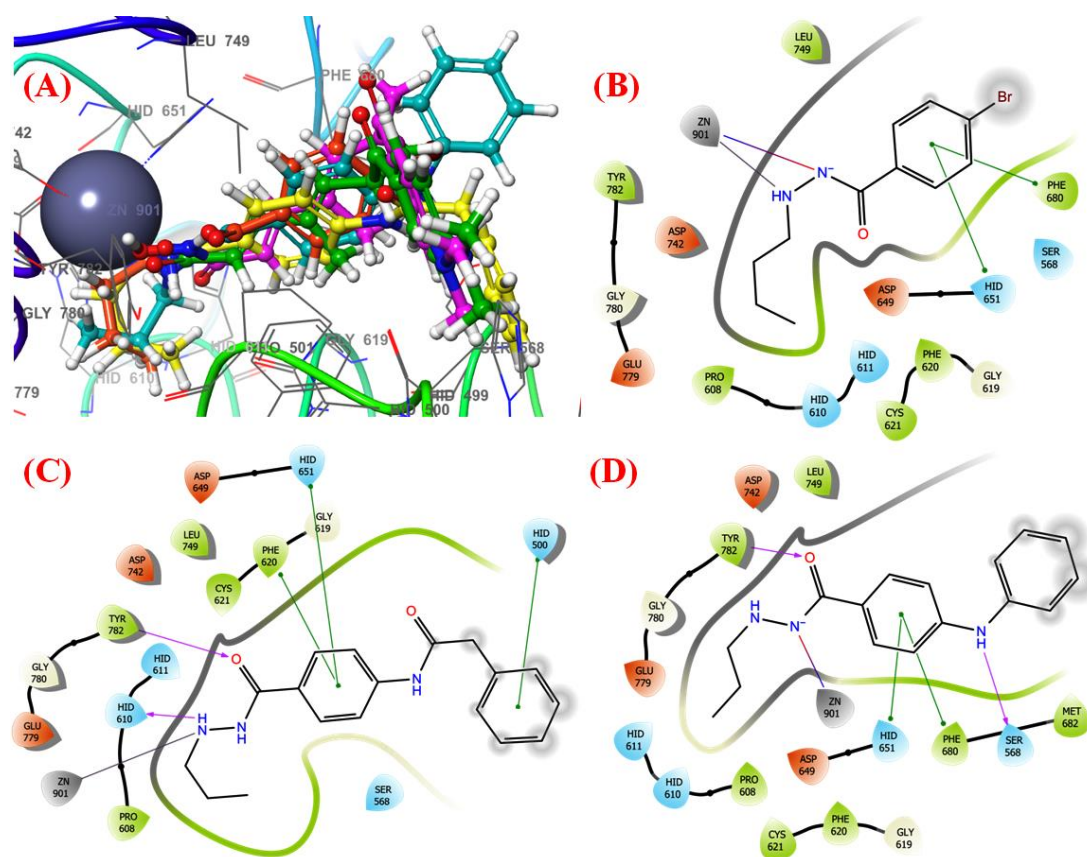


Figure 3.27. (A) Alignment of inbound ligand (green), redocked ligand (magenta), UF010 (orange), 4c (yellow) and 4e (cyan) at the HDAC6 active site (PDB ID: 5EDU); (B) Binding interaction of UF010 at the HDAC6 active site (PDB ID: 5EDU); (C) Binding interaction of 4c at the HDAC6 active site (PDB ID: 5EDU); (D) Binding interaction of 4e at the HDAC6 active site (PDB ID: 5EDU).

All of these docked molecules exhibited a similar binding pattern of their hydrazide zinc-binding motif with the catalytic Zn^{2+} ion present at the HDAC3 active site. The docking interactions of these compounds are displayed in **Figure 3.23**. From the analysis of the docking interactions at the HDAC3 active site, it was observed that the amide group adjacent to the carbonyl function involved a chelate through a salt-bridge interaction with the catalytic Zn^{2+} ion whereas the other amide group of the hydrazide moiety formed a hydrogen bonding with Tyr298 amino acid residue for all these molecules (**Figure 3.23**). Interestingly, the phenyl ring attached to the hydrazide moiety of all these molecules

Chapter 3: Benzoyl hydrazides as HDAC3 inhibitors

including **UF010** formed π - π stacking interactions with the amino acid residues His172 and Phe200 at the active site implicating the necessity of such interactions for potent HDAC3 inhibition (**Figure 3.23B – 3.23D**). Additionally, the amide function of the carboxamido benzyl moiety of compound **4c** and the amide function of the anilide moiety of compound **4e** formed hydrogen bond interaction with the negatively charged Asp93 amino acid residue that was missing in the case of **UF010** (**Figure 3.23C and 3.23D**). Probably, this may be the reason of higher *in vitro* HDAC3 inhibitory activity of **4c** (HDAC3 IC₅₀ = 30.67 nM) and **4e** (HDAC3 IC₅₀ = 15.41 nM) compared to the reference molecule **UF010** (HDAC3 IC₅₀ = 256.7 nM). Therefore, the amide function at the *para* position of the phenyl ring is required for higher HDAC3 inhibition. Though there is an additional π - π stacking interaction between the phenyl ring of the carboxamido benzyl moiety of compound **4c** and Phe200, this compound was less active compared to the compound **4e**. Therefore, it may be assumed that bulky, flexible and elongated functions are not suitable at this position as they may produce some unfavourable steric hindrance during enzyme-drug interaction.

Since lack of selectivity is one of the major issues in the development of isoform specific HDAC inhibitors, the molecular docking study of these same molecules with other class I HDACs such as HDAC1 (PDB ID:4BKX), HDAC2 (PDB ID:3MAX), and HDAC8 (PDB ID: 1T69) along with class II HDAC6 (PDB ID: 5EDU) were also analysed. The RMSD of the redocked ligands with the inbound ligands were also calculated. The RMSD of 0.24 Å, 1.46 Å and 1.23 Å was observed in case of the inbound and redocked ligand for HDAC2, HDAC8 and HDAC6, respectively. The low RMSD for all these cases suggested that the molecules mapped well at the respective HDAC sites and supports that the docking protocol was validated. Unlike HDAC3, these synthesized molecules due to the presence of smaller size, shape and hydrazide ZBG demonstrated variable binding conformations for other class-I and II HDAC isoforms but were unable to show any encouraging docked

Chapter 3: Benzoyl hydrazides as HDAC3 inhibitors

conformation (**Figure 3.24 – 3.27**). This observation is also in agreement with the HDAC3 selective nature of these hydrazide derivatives found during the *in vitro* experimentation. This current study can elucidate a preliminary concept regarding these hydrazides containing selective HDAC3 inhibitors that may encourage the further designing and development of selective hydrazide-based inhibitors of HDAC3.

3.3. MATERIALS AND METHODS

3.3.1. Chemistry

The starting materials, chemical reagents, solvents were procured from Sigma-Aldrich and other chemical suppliers and were used without further purification. UF010 was synthesized as per the published procedure (Wang et al., 2015). The completion of the reaction was monitored with the help of precoated silica gel plates with Merck 60 F254 silica gel bought from Merck Millipore Co., USA by using the TLC (Thin-layer chromatography) technique.

Purification and analysis

Column chromatography was carried out using silica gel (100-200 or 230-400 mesh size) using different polar and non-polar solvents. Compound purity was determined by the HPLC-UFLC Shimadzu model instrument and were analysed on LC-MS 8040 which was equipped with a photodiode array detector. The column used was Shiseido C18, 4.6 × 150 mm, 5 μ for reverse phase HPLC analysis. The flow rate was 1 ml/min, isocratic flow in the ratio of A20: B80 or A10: B90 (where solvents, A = water + 0.05% TFA, B = methanol).

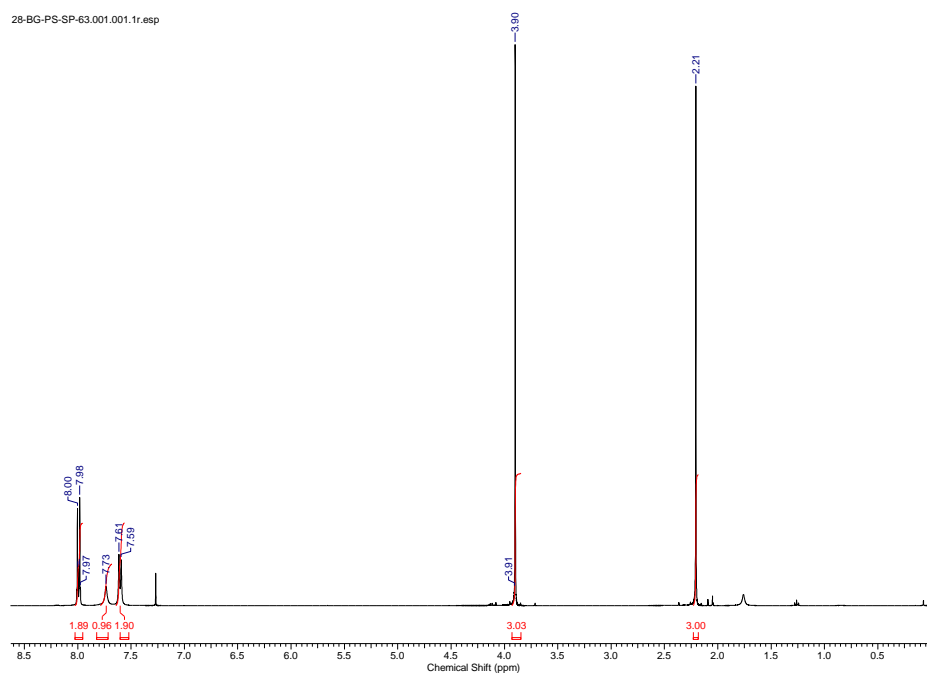
Characterization: All the synthesized final compounds were characterized using ¹H and ¹³C NMR, HPLC-LCMS and HRMS (high-resolution mass spectrometry). All the compounds were found to be >95% pure as per HPLC reports. Especially, the compounds **4c**, **4e** and **UF010** were found to be 96.8%, 98.6% and 97.5% pure. ¹H and ¹³C NMR were recorded on Bruker, ASCEND™ 400 MHz spectrometer, using deuterated solvents CDCl₃

Chapter 3: Benzoyl hydrazides as HDAC3 inhibitors

and methanol-d₄ referenced to trimethyl silane (TMS) as the internal standard or residual solvent peaks. Chemical shifts (δ) were given in parts per million, and the coupling constants (J) are reported in hertz (Hz). NMR data were processed using ACD/Lab's release 2D NMR software version 12.01. High-resolution mass spectroscopy was conducted in HRMS (6545 Q-TOF LC/MS, Agilent) at BITS-Pilani, Pilani campus. Our HRMS data suggested that the difference between the theoretical mass and obtained mass from HRMS analysis was ± 0.005 further confirming the purity of the final compounds synthesized.

3.3.1.1. Preparation of methyl 4-acetamidobenzoate (**1a**)

Methyl 4-amino benzoate (**1**) (1 g, 6.62 mmol) was dissolved in dry-dichloromethane and to this, excess of acetic anhydride (3.13 ml, 33.08 mmol) was added and stirred for 2 – 4 h at room temperature. The solvent was evaporated under a vacuum. The mixture was then neutralised with aqueous sodium bicarbonate solution and dissolved in ethyl acetate and washed with water three times. The organic part was then isolated, washed with brine solution, dried over anhydrous Na₂SO₄ and then concentrated *in vacuo*. The crude product was then purified using column chromatography and the pure compound **1a** is eluted using 50% hexane and 50% ethyl acetate as solvents in the form of a white powder of about 90% yield. ¹H NMR (400 MHz, CDCl₃) δ 7.99 (d, J = 8.8 Hz, 2H), 7.73 (s, 1H), 7.60 (d, J = 8.6 Hz, 2H), 3.90 (s, 3H), 2.21 (s, 3H).



Spectra 3.1: ^1H NMR Spectra for the compound **1a**.

3.3.1.2. Preparation of *N*-(4-(hydrazinecarbonyl) phenyl) acetamide (**2a**)

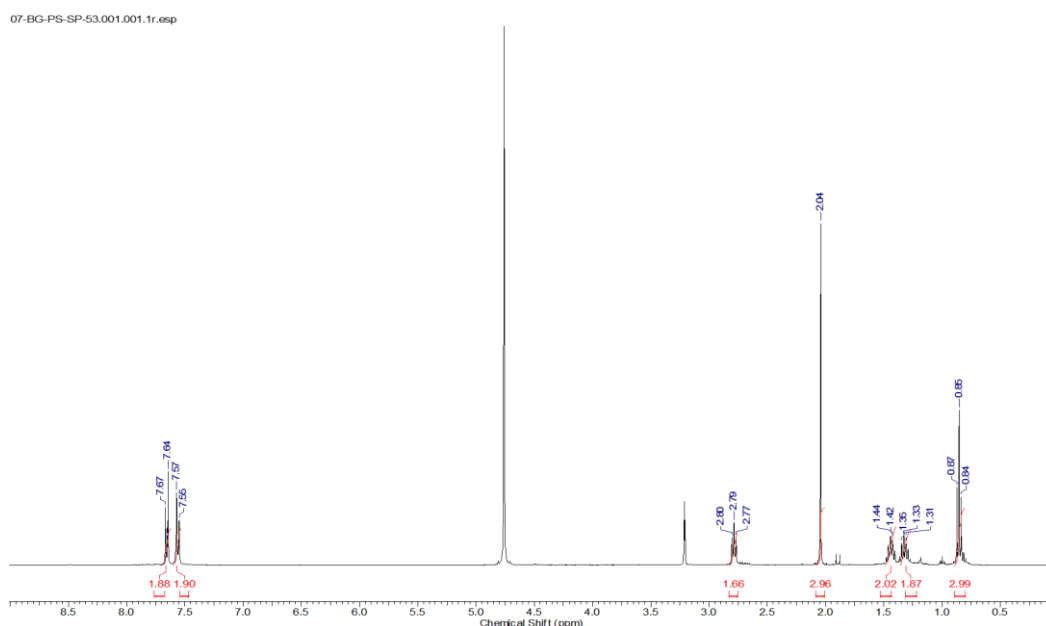
Methyl 4-acetamidobenzoate (**1a**) (150 mg, 0.776 mmol) was dissolved in 5 ml of methanol and to this hydrazine monohydrate (377 μl , 7.76 mmol) was added. The chemical reaction was carried out for 6 h at reflux conditions. After completion of the reaction, the reaction mixture was condensed *in vacuo* and dried under a vacuum oven. The crude material obtained was subjected to the next reaction without further purification.

3.3.1.3. Preparation of *N*-(4-(2-butylhydrazine-1-carbonyl) phenyl) acetamide (**3a**)

In a round-bottomed flask, *N*-(4-(hydrazinecarbonyl) phenyl) acetamide (**2a**, 100 mg, 0.25 mmol) dissolved in 1 ml of methanol was taken. To this, 46 μl of butyraldehyde (1 eq, 0.512 mmol) and catalytic *p*-toluenesulfonic acid were subsequently added. The resultant solution was stirred for 3 h at room temperature. After confirmation of the intermediate by TLC, sodium cyanoborohydride (39.03 mg, 1.2 eq, 0.62 mmol) was added and the reaction mixture was stirred for 10 mins at room temperature. The completion of the reaction was confirmed by TLC. The reaction mixture was quenched by using an aqueous sodium bicarbonate solution. The reaction mixture was then thickened *in vacuo*. The reaction

Chapter 3: Benzoyl hydrazides as HDAC3 inhibitors

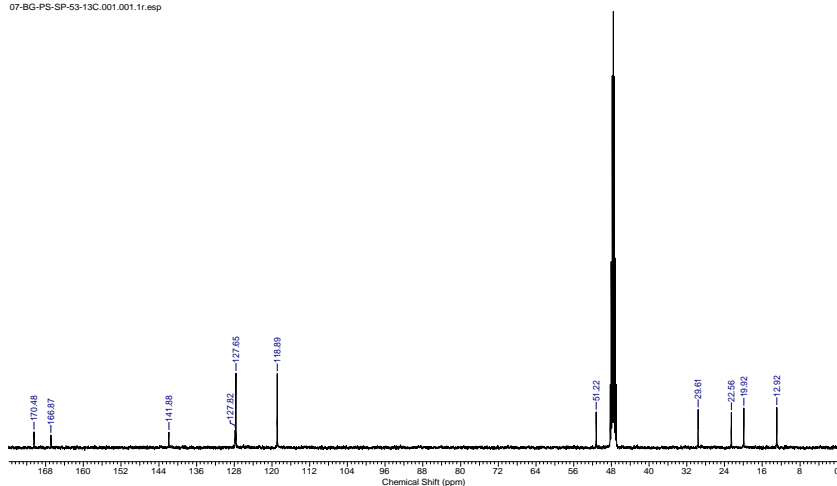
mixture was extracted three times using ethyl acetate into the organic layer using water. The organic layers were combined, dried and condensed on a rota evaporator. The resultant mixture was further purified by column chromatography using 40% hexane and 60% ethyl acetate solvent system to obtain the final product **3a** as white powder of about 46% yield. ^1H NMR (400 MHz, methanol- d_4) δ 7.64 - 7.67 (m, 2 H), 7.54 - 7.58 (m, 2 H), 2.77 - 2.80 (t, $J = 7.19$ Hz, 2 H), 2.04 (s, 3 H), 1.40 - 1.48 (m, 2 H), 1.28 - 1.37 (m, 2 H), 0.84 - 0.87 (t, $J = 7.25$ Hz, 3 H). ^{13}C NMR (101 MHz, methanol- d_4) δ 170.48, 166.87, 141.88, 127.82, 127.65, 118.89, 51.22, 29.61, 22.56, 19.92, 12.92. HRMS (APESI) m/z calcd for $\text{C}_{13}\text{H}_{19}\text{N}_3\text{O}_2$ $[\text{M}+\text{H}]^+$: 250.1515; found: 250.1519.



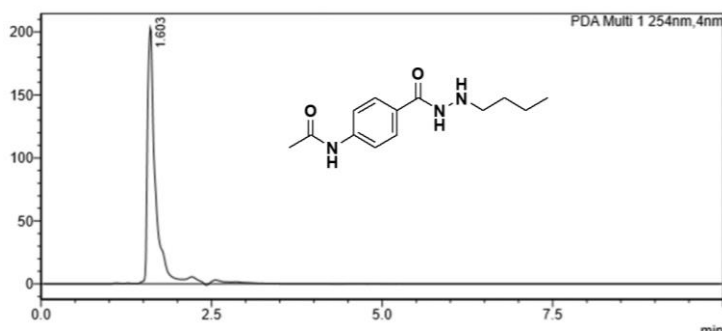
Spectra 3.2: ^1H NMR Spectra for the compound **3a**.

Chapter 3: Benzoyl hydrazides as HDAC3 inhibitors

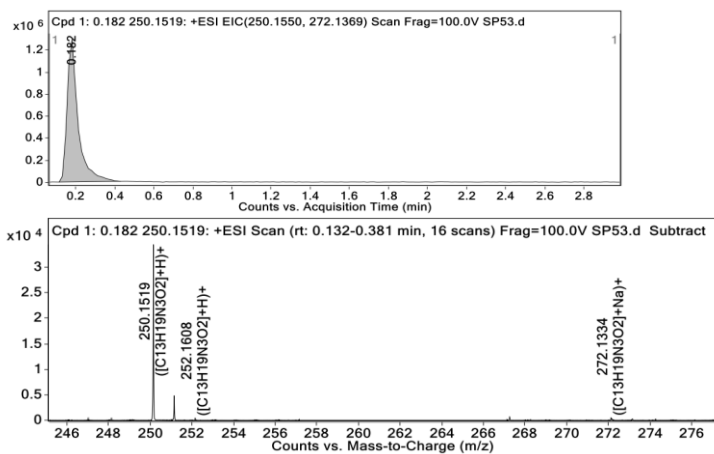
07-BG-PS-SP-53-13C.001.001.1r.esp



Spectra 3.3: ^{13}C NMR Spectra for compound 3a.



Spectra 3.4: HPLC traces of compound 3a.



Spectra 3.5: HRMS Spectra for the compound 3a.

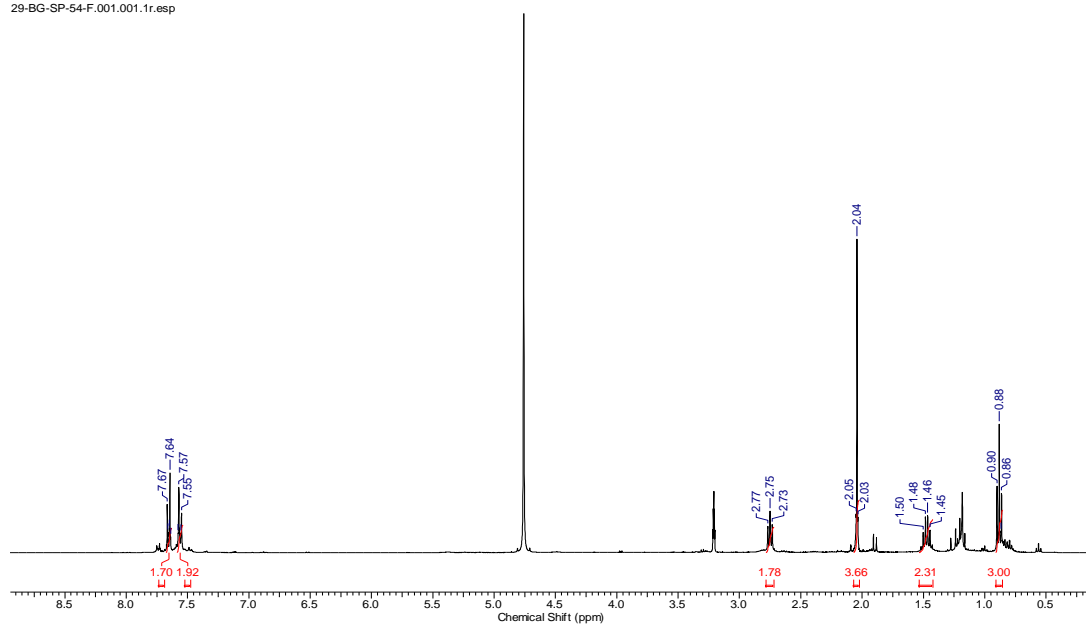
3.3.1.4. Preparation of *N*-(4-(2-propylhydrazine-1-carbonyl) phenyl) acetamide (4a)

In a round-bottomed flask, *N*-(4-(hydrazinecarbonyl) phenyl) acetamide (**2a**, 100 mg, 0.25

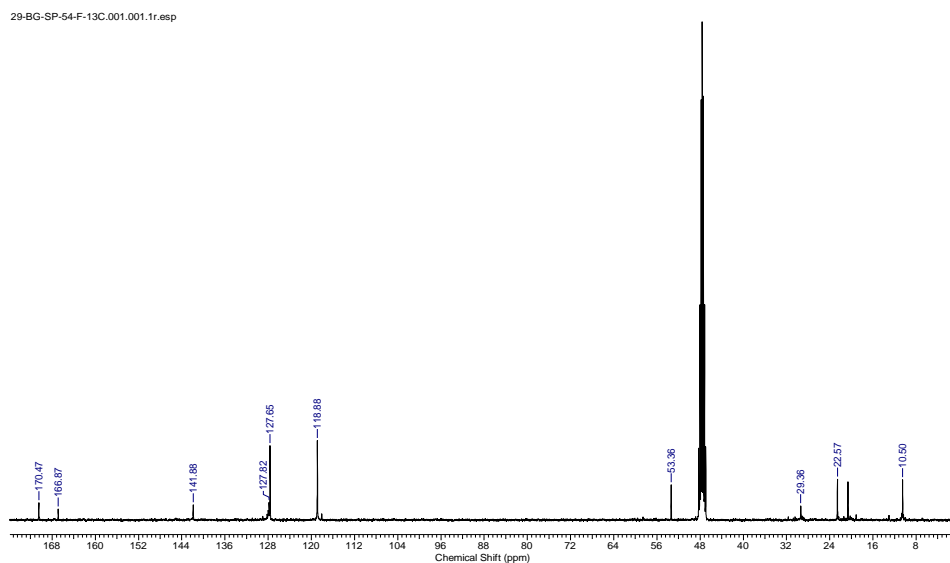
Chapter 3: Benzoyl hydrazides as HDAC3 inhibitors

mmol) dissolved in 1ml of methanol was taken. To this, 37 μ l of propionaldehyde (1 eq, 0.517 mmol) and catalytic *p*-toluenesulfonic acid were subsequently added. The resultant solution was allowed to stir for 3 h at room temperature. After confirmation of the intermediate by TLC, sodium cyanoborohydride (39.03 mg, 1.2 eq, 0.62 mmol) was added and the reaction mixture was allowed to stir for 10 mins at room temperature. The completion of the reaction was confirmed by TLC. The reaction mixture was quenched by using an aqueous sodium bicarbonate solution. The reaction mixture was then concentrated *in vacuo*. The reaction mixture was extracted three times using ethyl acetate into the organic layer using water. The organic layers were combined, dried and concentrated on a rota evaporator. The resultant mixture was further purified by column chromatography using 40% hexane and 60% ethyl acetate solvent system to obtain the final product **4a** as white powder of about 41% yield. ^1H NMR (400 MHz, methanol- d_4) δ 7.63 - 7.68 (m, 2H), 7.54 - 7.58 (m, 2H), 2.73 - 2.77 (t, $J = 7.32$ Hz, 2H), 2.04 (s, 3H), 1.43 - 1.50 (m, 2H) 0.86 - 0.90 (t, $J = 7.44$ Hz, 3H). ^{13}C NMR (101 MHz, methanol- d_4) δ 170.47, 66.87, 141.88, 127.82, 127.65, 118.88, 53.36, 22.57, 20.62, 10.50. HRMS (APESI) m/z calcd for $\text{C}_{12}\text{H}_{17}\text{N}_3\text{O}_2$. $[\text{M}+\text{H}]^+$:236.1394; found 236.1360.

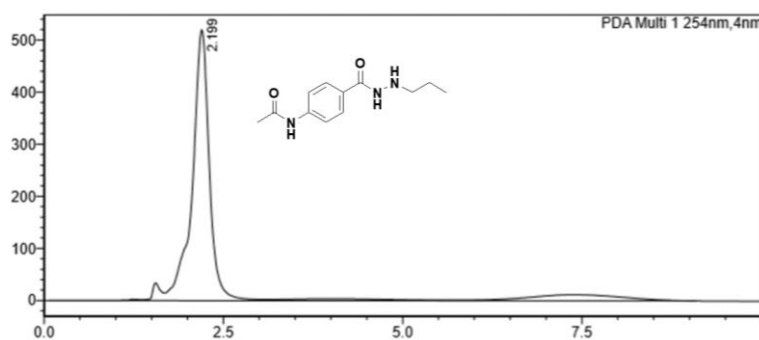
29-BG-SP-54-F.001.001.1r.esp



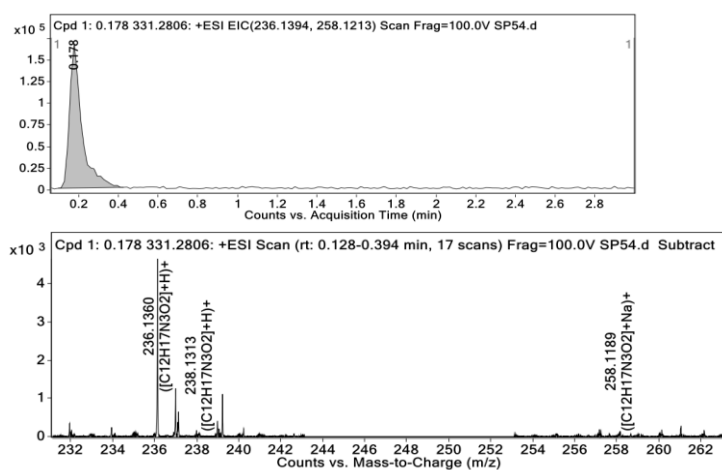
Spectra 3.6: ¹H NMR Spectra for the compound 4a.



Spectra 3.7: ¹³C NMR Spectra for the compound 4a.



Spectra 3.8: HPLC traces of compound 4a.

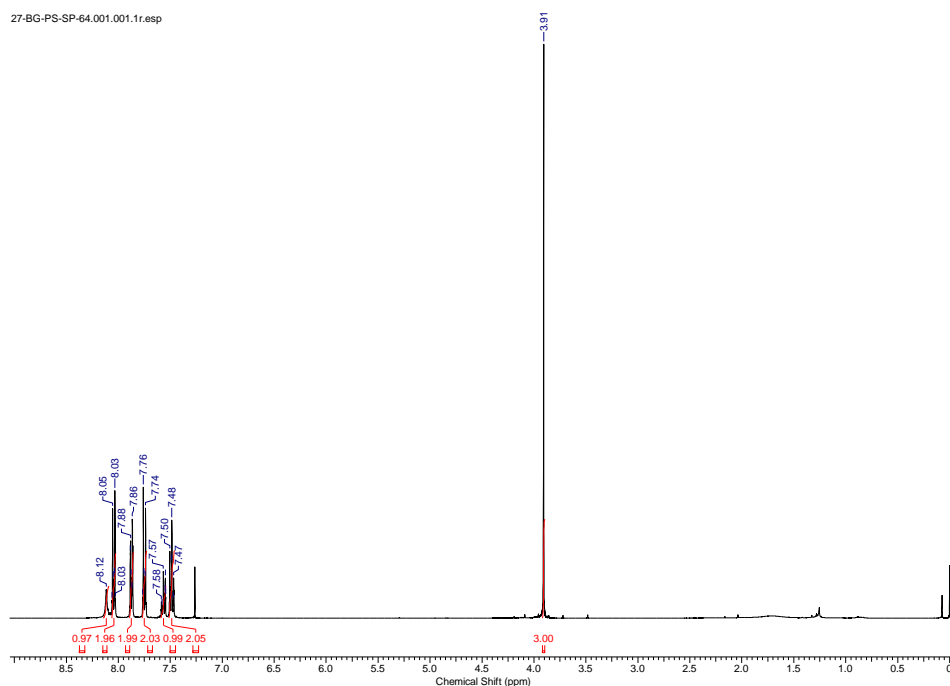


Spectra 3.9: HRMS Spectra for the compound 4a.

3.3.1.5. Preparation of methyl 4-benzamidobenzoate (1b)

Chapter 3: Benzoyl hydrazides as HDAC3 inhibitors

Methyl 4-amino benzoate (**1**) (200 mg, 1.32 mmol), sodium bi-carbonate (167 mg, 1.98 mmol) was stirred in tetrahydrofuran and to this benzoyl chloride (203 μ l, 1.59 mmol) was added dropwise and stirred for 10 h at room temperature. The excess solvent was evaporated *in vacuo*. The reaction mixture was extracted into the organic layer using ethyl acetate and water three times. The organic layer was then separated, washed with brine solution, dried over anhydrous Na₂SO₄ and then concentrated *in vacuo*. The crude product was then purified using column chromatography and the pure compound **1b** is eluted using 50% hexane and 50% ethyl acetate as solvents in the form of white powder of about 69% yield. ¹H NMR (400 MHz, CDCl₃) δ 8.12 (s, 1H), 8.04 (d, *J* = 8.8 Hz, 2H), 7.87 (d, *J* = 7.0 Hz, 2H), 7.75 (d, *J* = 8.8 Hz, 2H), 7.57 (t, *J* = 8.0 Hz, 1H), 7.48 (t, *J* = 7.9 Hz, 2H), 3.91 (s, 3H).



Spectra 3.10: ¹H NMR Spectra for the compound **1b**.

3.3.1.6. Preparation of *N*-(4-(hydrazinecarbonyl) phenyl) benzamide (**2b**)

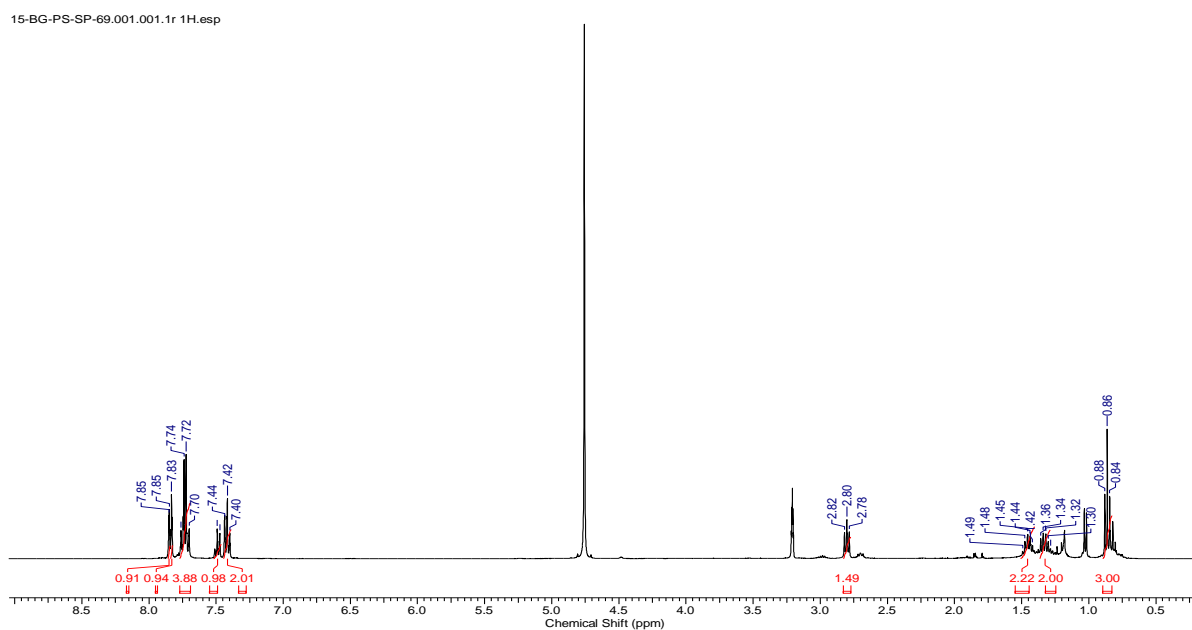
Methyl 4-benzamidobenzoate (**1b**) (150 mg, 0.587 mmol) was dissolved in 5 ml of methanol and to this hydrazine monohydrate (286 μ l, 5.88 mmol) was added. The reaction was carried out for 6 h at reflux conditions. Upon completion of the reaction, the reaction

Chapter 3: Benzoyl hydrazides as HDAC3 inhibitors

mixture was concentrated *in vacuo* and dried under a vacuum oven. The crude product obtained was used for the next reaction without purification.

3.3.1.7. Preparation of *N*-(4-(2-butylhydrazine-1-carbonyl) phenyl) benzamide (**3b**)

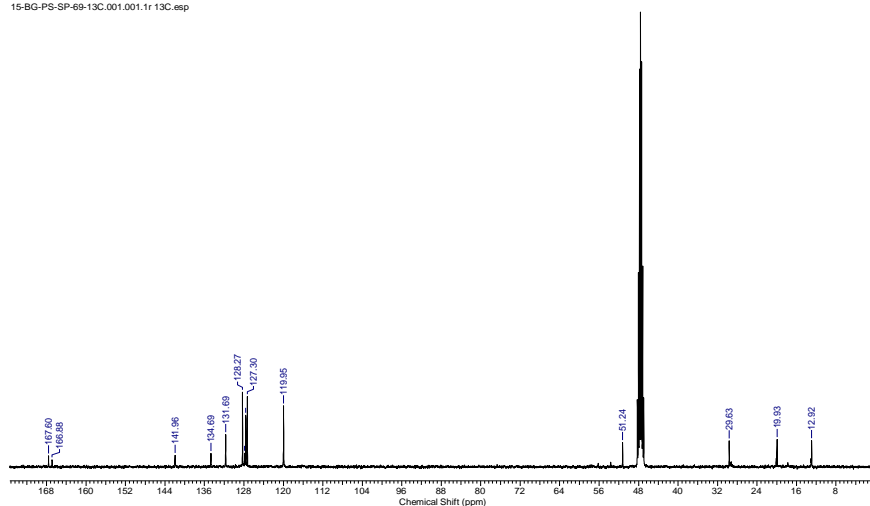
Using the synthetic procedure of **3a**, starting materials **2b** and butyraldehyde gave **3b** in 45% yield. ^1H NMR (400 MHz, methanol- d_4) δ 7.85 (d, $J = 1.13$ Hz, 1H), 7.82 - 7.84 (m, 1H), 7.69 - 7.77 (m, 4H), 7.46 - 7.52 (m, 1H), 7.39 - 7.45 (m, 2H), 2.78 - 2.82 (t, $J = 7.25$ Hz, 2H), 1.40 - 1.51 (m, 2H), 1.30 - 1.36 (m, 2H), 0.84 - 0.88 (t, $J = 7.32$ Hz, 3H). ^{13}C NMR (101 MHz, methanol- d_4) δ 167.60, 166.88, 141.96, 134.69, 131.69, 128.27, 127.62, 127.30, 119.95, 51.24, 29.63, 19.93, 12.92. HRMS (APESI) m/z calcd for $\text{C}_{18}\text{H}_{21}\text{N}_3\text{O}_2$. $[\text{M}+\text{H}]^+$: 312.1707; found 312.1658.



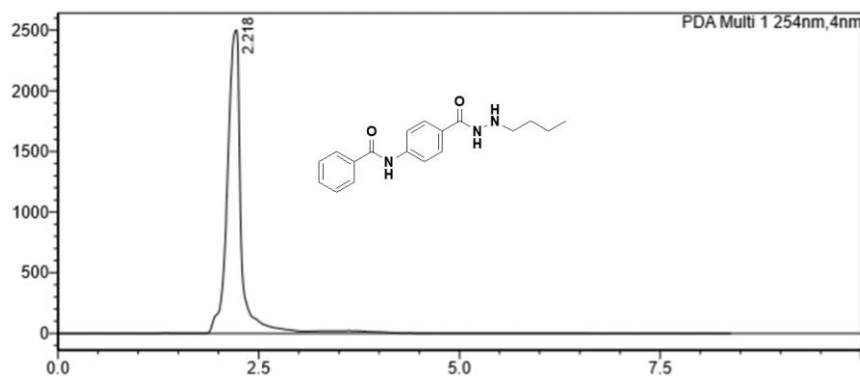
Spectra 3.11: ^1H NMR Spectra for the compound **3b**.

Chapter 3: Benzoyl hydrazides as HDAC3 inhibitors

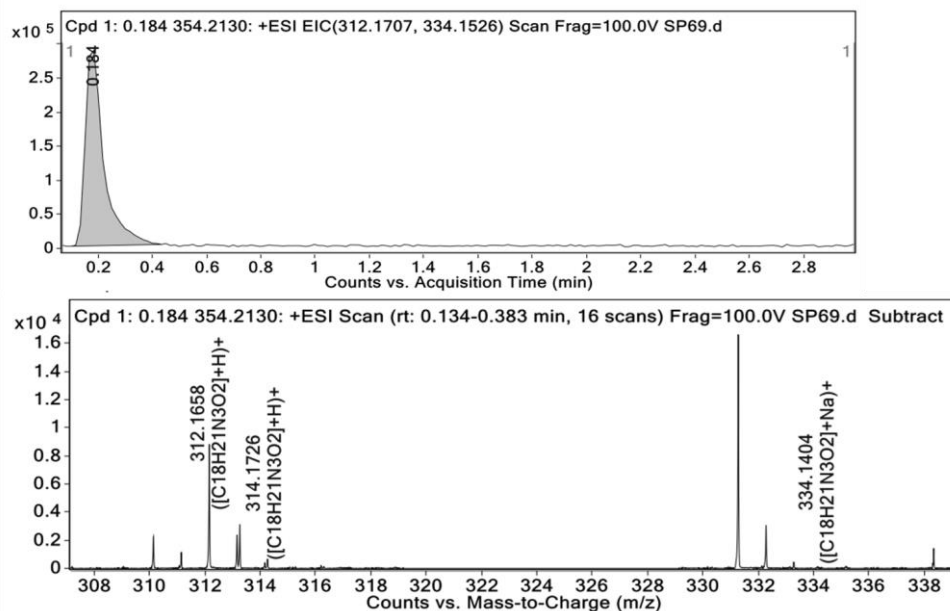
15-BG-PS-SP-69-13C.001.001.1r 13C.esp



Spectra 3.12: ^{13}C NMR Spectra for the compound 3b.



Spectra 3.13: HPLC traces of compound 3b.



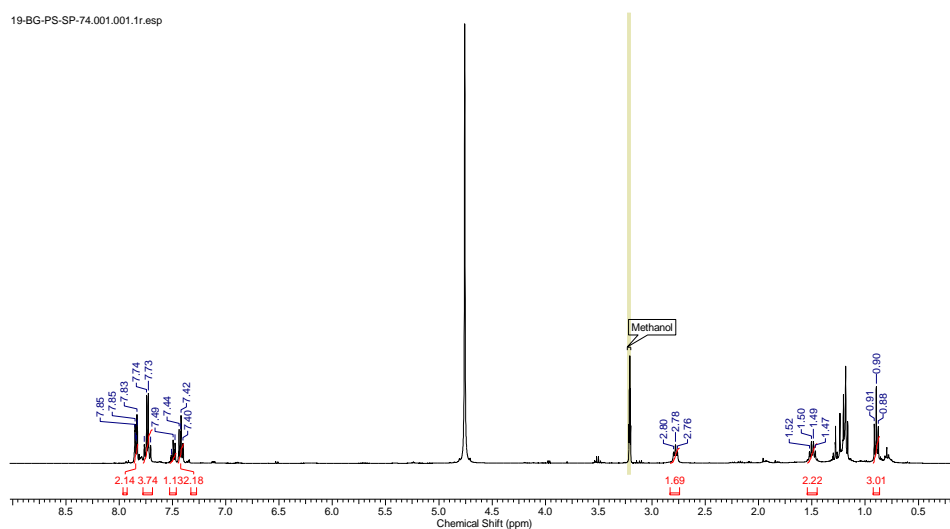
Spectra 3.14: HRMS Spectra for the compound 3b.

3.3.1.8. Preparation of *N*-(4-(2-propylhydrazine-1-carbonyl) phenyl) benzamide

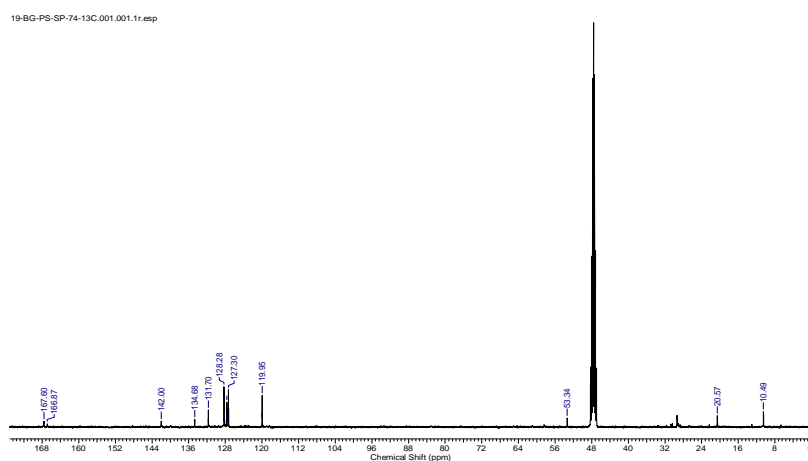
Chapter 3: Benzoyl hydrazides as HDAC3 inhibitors

(4b)

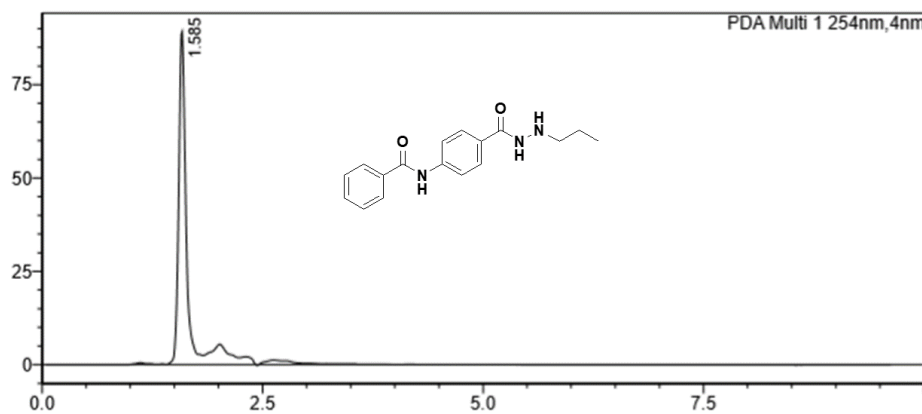
Using the synthetic procedure of **4a**, starting materials **2b** and propionaldehyde gave **4b** in 62% yield. ^1H NMR (400 MHz, methanol- d_4) δ 7.82 - 7.87 (m, 2H), 7.69 - 7.78 (m, 4H), 7.45 - 7.54 (m, 1H), 7.37 - 7.45 (m, 2H), 2.76 - 2.80 (t, $J = 7.19$ Hz, 2H), 1.45 - 1.52 (m, 2H), 0.88 - 0.91 (t, $J = 7.44$ Hz, 3H). ^{13}C NMR (101 MHz, methanol- d_4) δ 167.60, 166.87, 142.00, 134.68, 131.70, 128.28, 127.64, 127.30, 119.95, 53.34, 20.57, 10.49. HRMS (APESI) m/z calcd for $\text{C}_{17}\text{H}_{19}\text{N}_3\text{O}_2$. $[\text{M}+\text{H}]^+$: 298.1550; found 298.1508.



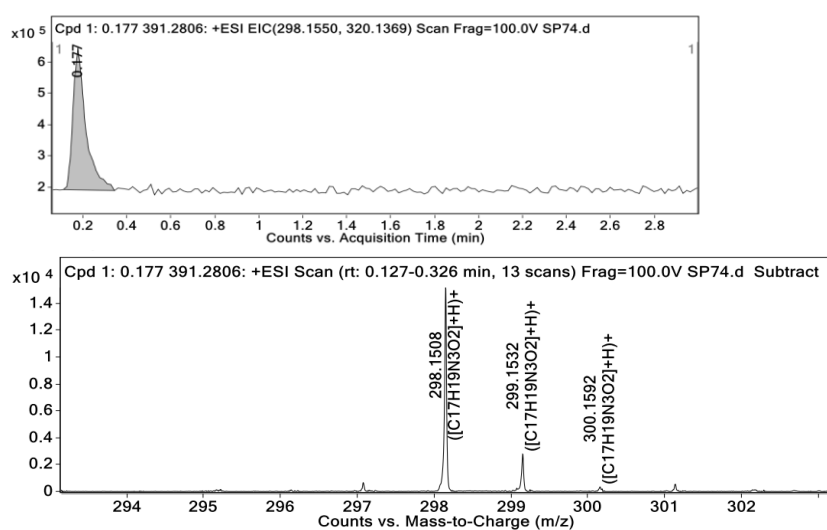
Spectra 3.15: ^1H NMR Spectra for the compound **4b**.



Spectra 3.16: ^{13}C NMR Spectra for the compound **4b**.



Spectra 3.17: HPLC traces of compound 4b.



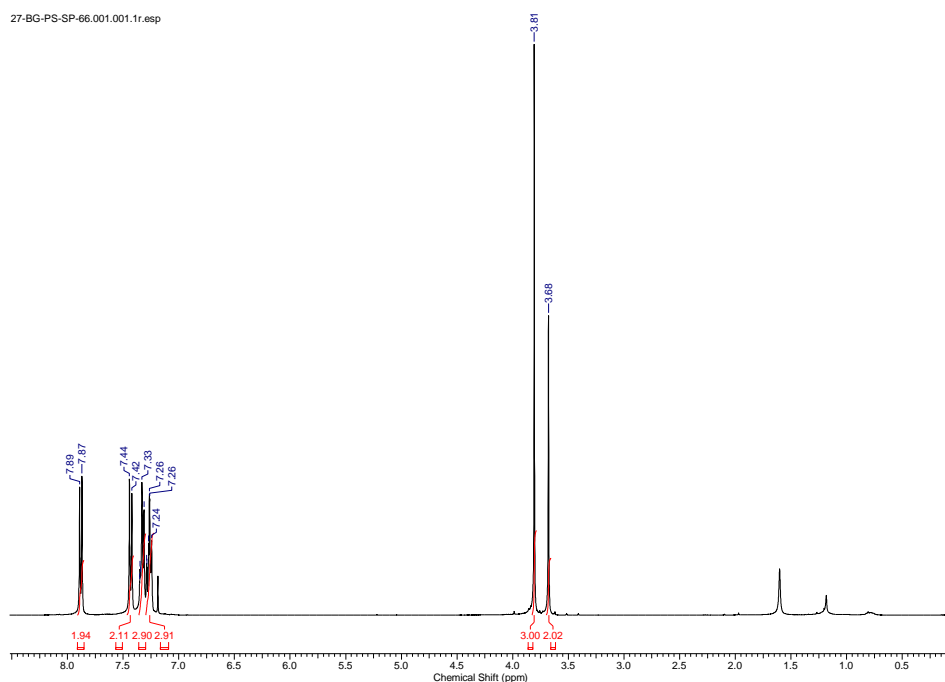
Spectra 3.18: HRMS Spectra for the compound 4b.

3.3.1.9. Preparation of methyl 4-(2-phenylacetamido) benzoate (1c)

Methyl 4-amino benzoate (**1**) (200 mg, 1.32 mmol), tri-ethylamine was dissolved in dry dichloromethane and to this phenylacetyl chloride (210 μ l, 1.59 mmol) was added and stirred for 8 h at room temperature. The solvent was evaporated *in vacuo*. The reaction mixture was extracted into the organic layer using ethyl acetate and water three times. The organic layer was then separated, washed with brine solution, dried over anhydrous Na_2SO_4 and then concentrated *in vacuo*. The crude product was then purified using column chromatography and the pure compound **1c** is eluted using 40% hexane and 60% ethyl acetate as solvents in the form of white powder of about 81% yield. ^1H NMR (400 MHz,

Chapter 3: Benzoyl hydrazides as HDAC3 inhibitors

CDCl₃) δ 7.88 (d, $J = 8.7$ Hz, 2H), 7.43 (d, $J = 8.7$ Hz, 2H), 7.32 (d, $J = 7.4$ Hz, 2H), 7.26 (t, $J = 8.9$ Hz, 3H), 3.81 (s, 3H), 3.68 (s, 2H), 1.60 (s, 1H).



Spectra 3.19: ¹H NMR Spectra for the compound **1c**.

3.3.1.10. Preparation of *N*-(4-(hydrazine carbonyl) phenyl)-2-phenylacetamide (**2c**)

Methyl 4-(2-phenylacetamido) benzoate (**1c**) (150 mg, 0.557 mmol) was dissolved in 5ml of methanol and to this hydrazine monohydrate (271 μ l, 5.57 mmol) was added. The reaction was carried out for 6 h at reflux conditions. Upon completion of the reaction, the reaction mixture was concentrated *in vacuo* and dried under a vacuum oven. The crude product obtained was used for the next reaction without purification.

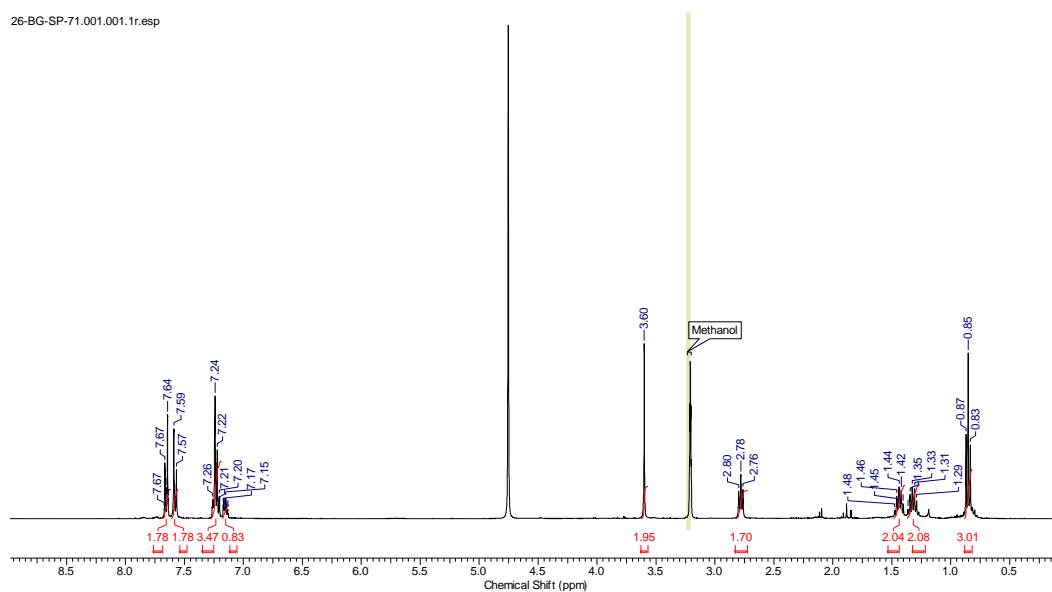
3.3.1.11. Preparation of *N*-(4-(2-butylhydrazine-1-carbonyl) phenyl)-2-phenylacetamide (**3c**)

Using the synthetic procedure of **3a**, starting materials **2c** and butyraldehyde gave **3c** in 56% yield. ¹H NMR (400 MHz, methanol-*d*₄) δ 7.62 - 7.69 (m, 2H), 7.55 - 7.61 (m, 2H), 7.19 - 7.28 (m, 4H), 7.12 - 7.18 (m, 1H), 3.60 (s, 2H), 2.76 - 2.80 (t, $J = 7.25$ Hz, 2H), 1.39 - 1.48 (m, 2H), 1.29 - 1.35 (m, 2H), 0.83 - 0.87 (t, $J = 7.25$ Hz, 3H). ¹³C NMR (101 MHz, methanol-*d*₄) δ 171.13, 141.85, 135.18, 128.76, 128.21, 127.67, 126.62, 119.03, 51.21,

Chapter 3: Benzoyl hydrazides as HDAC3 inhibitors

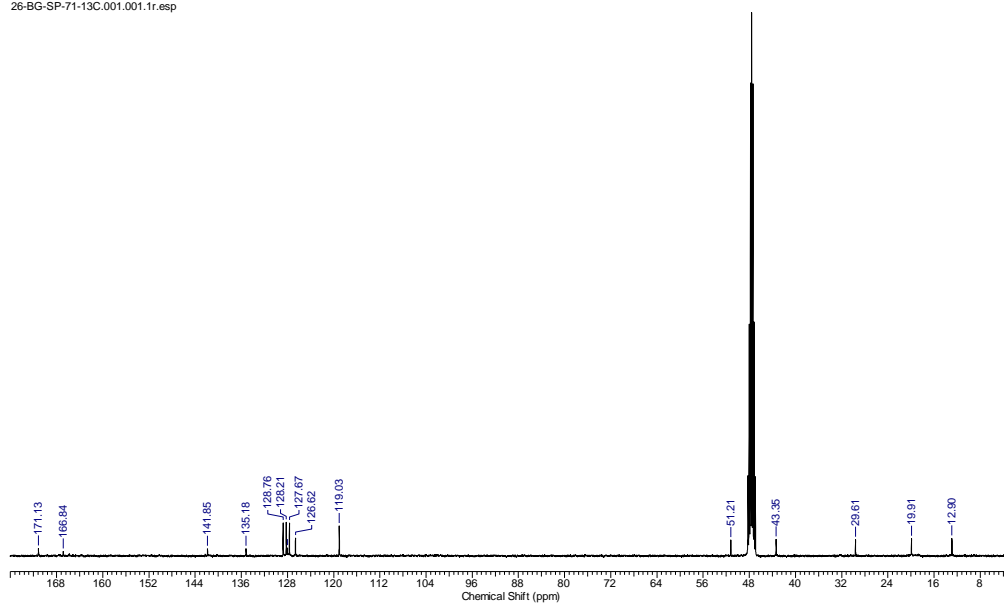
43.35, 29.61, 19.91, 12.90. HRMS (APESI) m/z calcd for $C_{19}H_{23}N_3O_2$. $[M+H]^+$: 326.1863; found 326.1824.

26-BG-SP-71.001.001.1r.esp

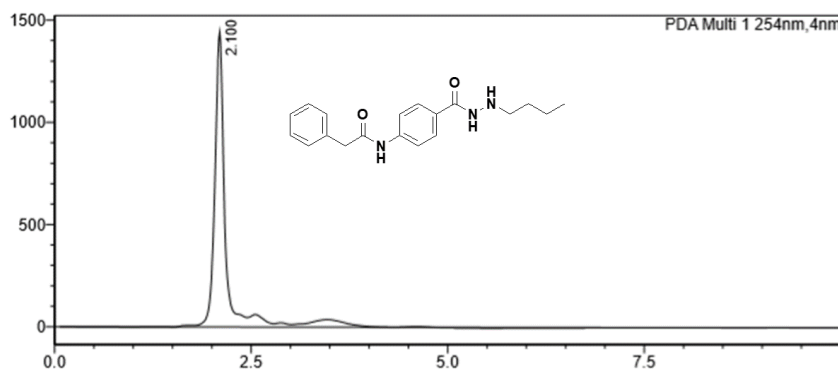


Spectra 3.20: 1H NMR Spectra for the compound 3c.

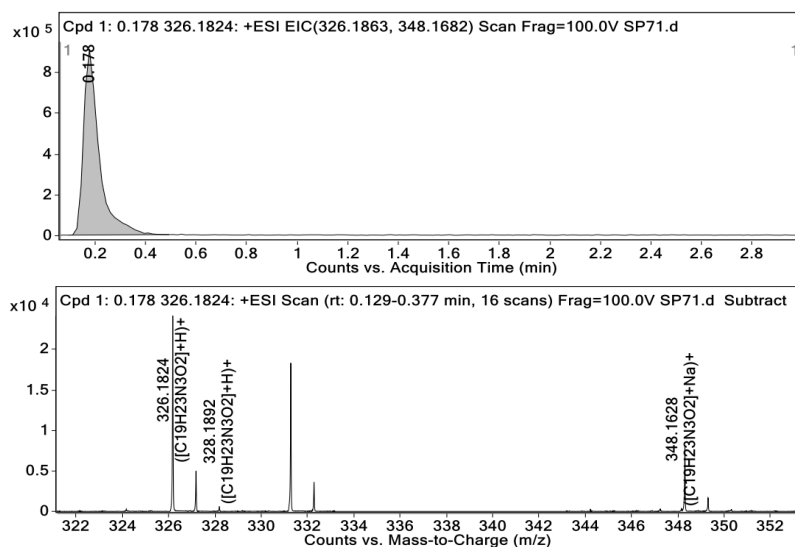
26-BG-SP-71-13C.001.001.1r.esp



Spectra 3.21: ^{13}C NMR Spectra for the compound 3c.



Spectra 3.22: HPLC traces of compound 3c.



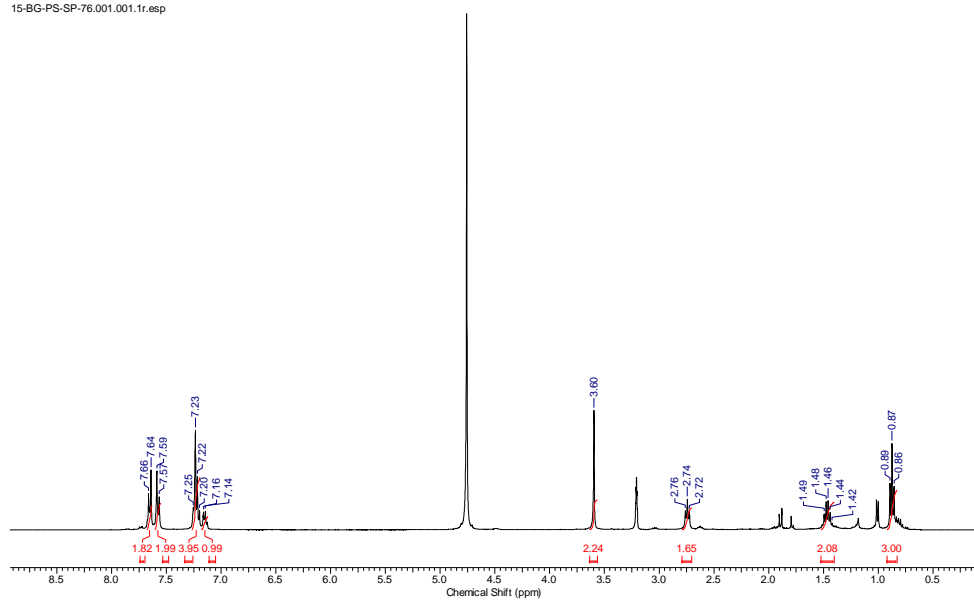
Spectra 3.23: HRMS Spectra for the compound 3c.

3.3.1.12. Preparation of 2-phenyl-N-(4-(2-propylhydrazine-1-carbonyl) phenyl) acetamide (4c)

Using the synthetic procedure of **4a**, starting materials **2c** and propionaldehyde gave **4c** in 62% yield. ^1H NMR (400 MHz, methanol- d_4) δ 7.65 (d, J = 8.76 Hz, 2H), 7.58 (d, J = 8.76 Hz, 2H), 7.23 (m, 4H), 7.15 (d, J = 6.75 Hz, 1H), 3.60 (s, 2H), 2.72 – 2.76 (t, J = 7.19 Hz, 2H), 1.42 - 1.49 (m, 2H), 0.86 – 0.89 (t, J = 7.44 Hz, 3H). ^{13}C NMR (101 MHz, methanol- d_4) δ 171.14, 166.85, 141.85, 135.18, 128.76, 128.22, 126.63, 119.04, 53.35, 43.36, 20.61, 10.50. HRMS (APESI) m/z calcd for $\text{C}_{18}\text{H}_{21}\text{N}_3\text{O}_2$. $[\text{M}+\text{H}]^+$: 312.1707; found 312.1672.

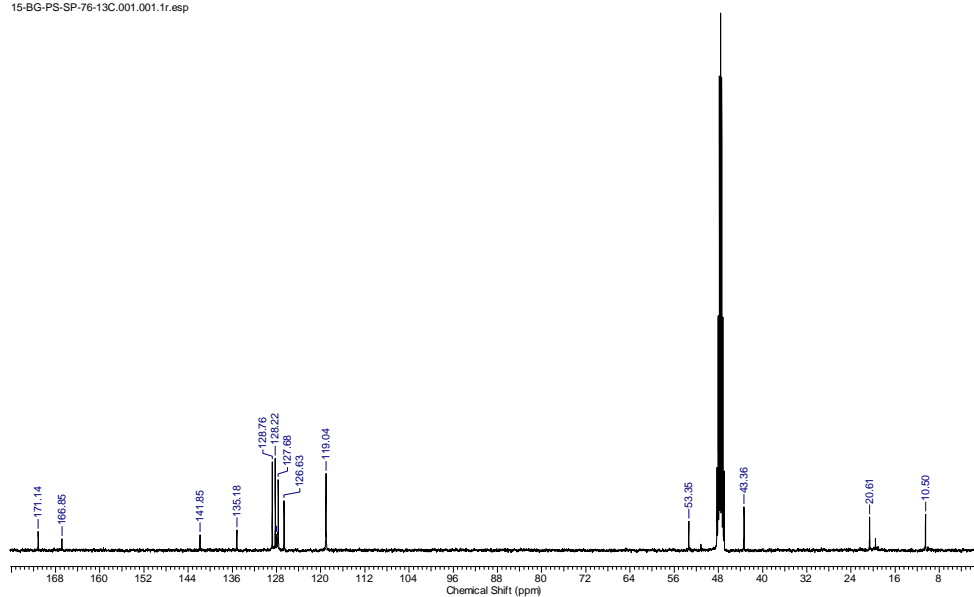
Chapter 3: Benzoyl hydrazides as HDAC3 inhibitors

15-BG-PS-SP-76.001.001.1r.esp

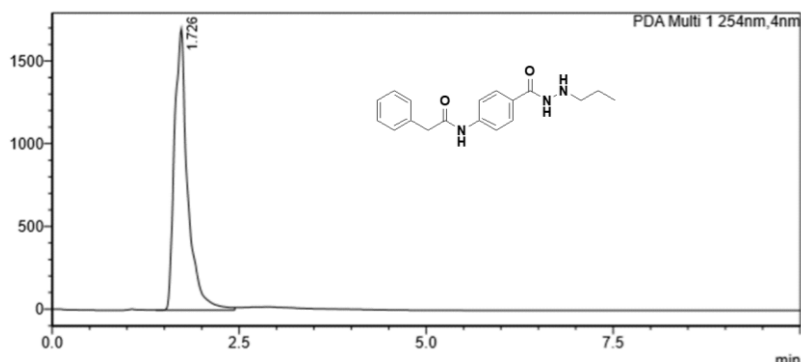


Spectra 3.24: ¹H NMR Spectra for the compound 4c.

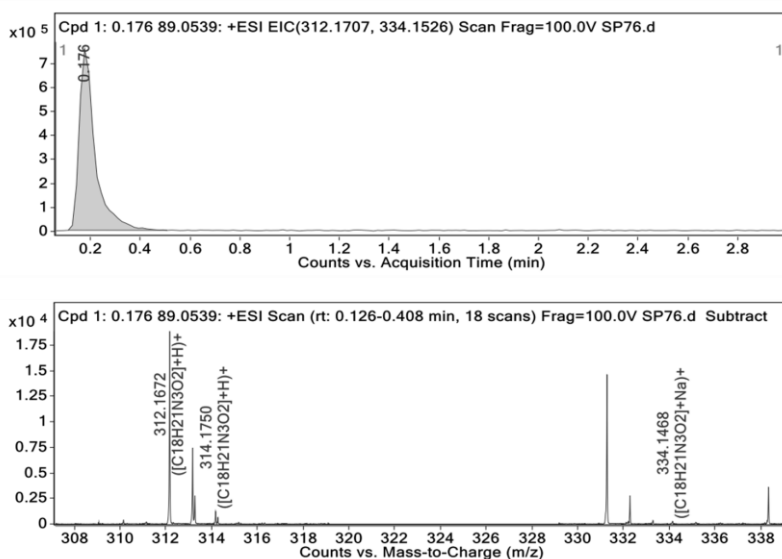
15-BG-PS-SP-76-13C.001.001.1r.esp



Spectra 3.25: ¹³C NMR Spectra for the compound 4c.



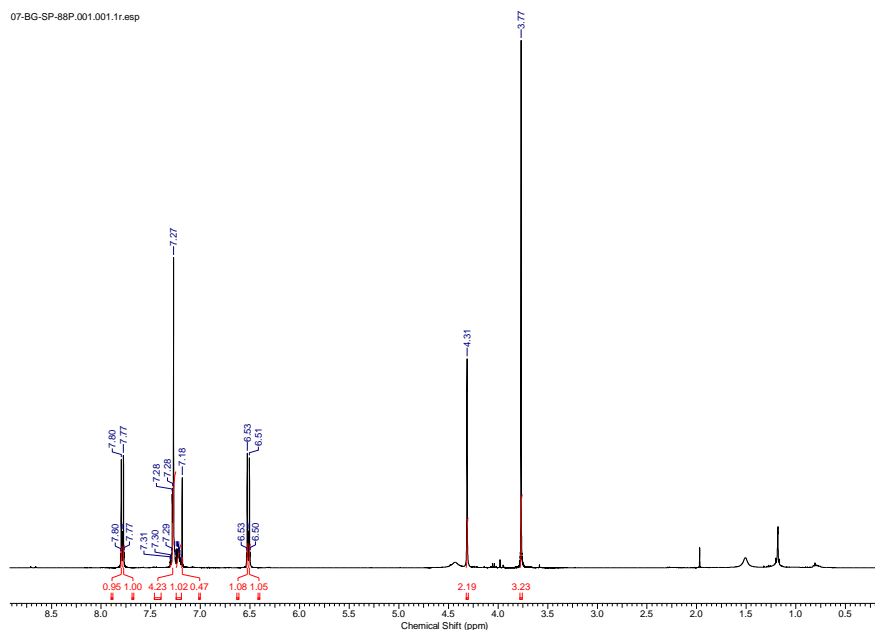
Spectra 3.26: HPLC traces of compound 4c.



Spectra 3.27: HRMS Spectra for the compound 4c.

3.3.1.13. Preparation of methyl 4-(benzyl amino) benzoate (1d)

Methyl 4-amino benzoate (**1**) (200 mg, 1.32 mmol) was dissolved in 2 ml of ethanol, to this benzaldehyde (135 μ l, 1.32 mmol) was added. The resultant solution was allowed to stir for 10 h at room temperature. After confirmation of the intermediate by TLC, Sodium borohydride (60 mg, 1.2 eq, 1.59 mmol) was added and the reaction mixture was allowed to stir for 2 h at room temperature. The completion of the reaction was confirmed by TLC. The reaction mixture was quenched using an aqueous sodium bicarbonate solution. The reaction mixture was then concentrated *in vacuo*. The crude reaction mixture was extracted into the organic layer three times using ethyl acetate and water. The organic layer was then separated, washed with brine solution, dried over anhydrous Na₂SO₄ and then concentrated *in vacuo*. The crude product was then purified using column chromatography and the pure compound **1d** is eluted using 40% hexane and 60% ethyl acetate as solvents in the form of white powder of about 71% yield. ¹H NMR (400 MHz, CDCl₃) δ 7.79 - 7.81 (m, 1H), 7.77 - 7.78 (m, 1H), 7.24 - 7.31 (m, 4H), 7.19 - 7.24 (m, 1H), 6.52 - 6.54 (m, 1H), 6.50 - 6.51 (m, 1H), 4.31 (s, 2H), 3.77 (s, 3H).



Spectra 3.28: ^1H NMR Spectra for the compound **1d**.

3.3.1.14. Preparation of 4-(benzylamino) benzohydrazide (**2d**)

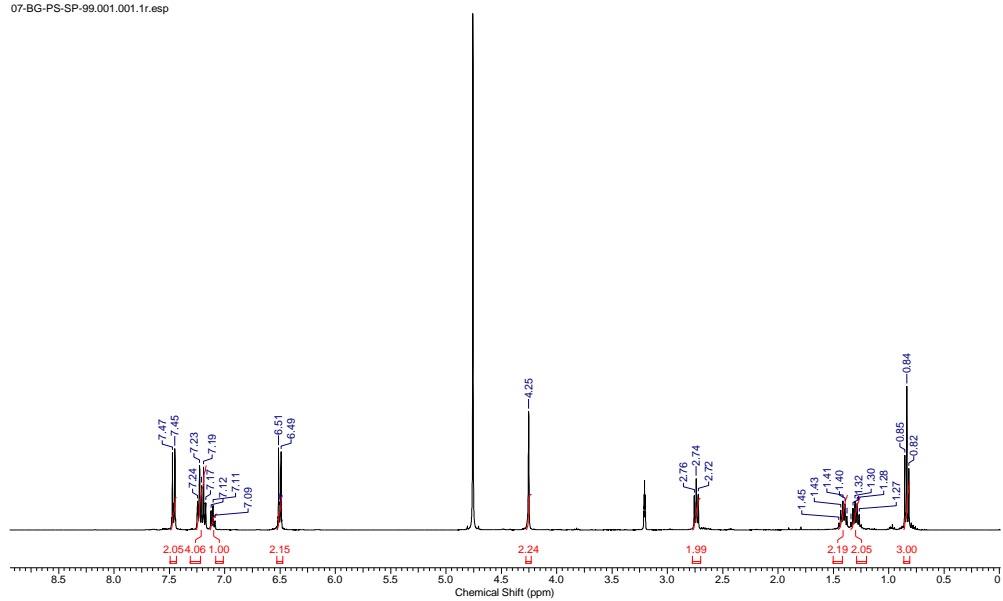
Methyl 4-(benzylamino) benzoate (**1d**) (150 mg, 0.62 mmol) was dissolved in 5 ml of methanol and to this hydrazine monohydrate (302 μl , 6.22 mmol) was added. The reaction was carried out for 6 h at reflux conditions. Upon completion of the reaction, the reaction mixture was concentrated *in vacuo* and dried under a vacuum oven. The crude product obtained was used for the next reaction without purification.

3.3.1.15. Preparation of 4-(benzylamino)-*N'*-butylbenzohydrazide (**3d**)

Using the synthetic procedure of **3a**, starting materials **2d** and butyraldehyde gave **3d** in 51% yield. ^1H NMR (400 MHz, methanol- d_4) δ 7.43 - 7.49 (m, 2H), 7.16 - 7.26 (m, 4H), 7.11 (s, 1H), 6.48 - 6.52 (m, 2H), 4.25 (s, 2H), 2.74 (t, $J = 7.25$ Hz, 2H), 1.36 - 1.45 (m, 2H), 1.27 - 1.32 (m, 2H), 0.82 - 0.85 (t, $J = 7.25$ Hz, 3H). ^{13}C NMR (101 MHz, methanol- d_4) δ 167.84, 151.96, 139.43, 128.30, 128.11, 126.81, 126.57, 119.51, 111.38, 51.37, 46.52, 29.60, 19.94, 12.93. HRMS (APESI) m/z calcd for $\text{C}_{18}\text{H}_{23}\text{N}_3\text{O}$. $[\text{M}+\text{H}]^+$: 298.1914; found 298.1880.

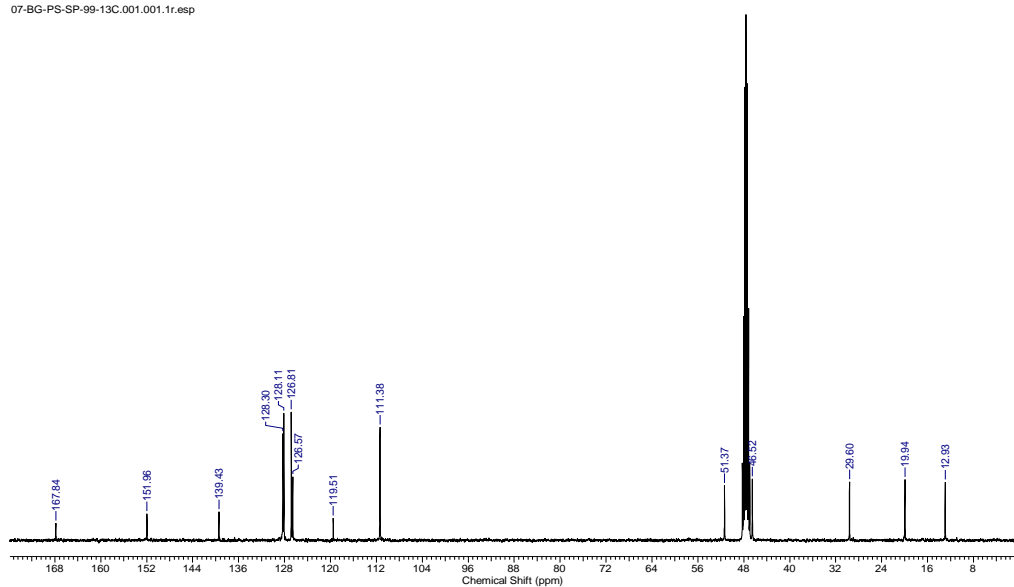
Chapter 3: Benzoyl hydrazides as HDAC3 inhibitors

07-BG-PS-SP-99.001.001.1r.esp

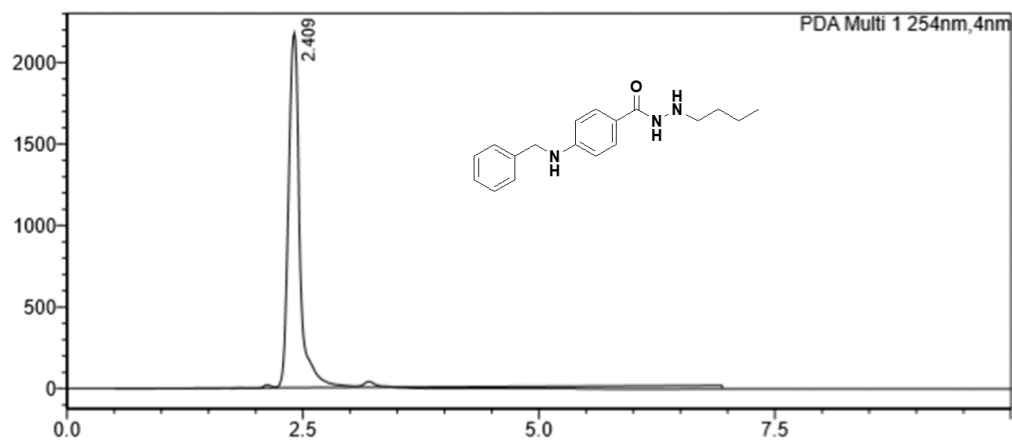


Spectra 3.29: ¹H NMR Spectra for the compound 3d.

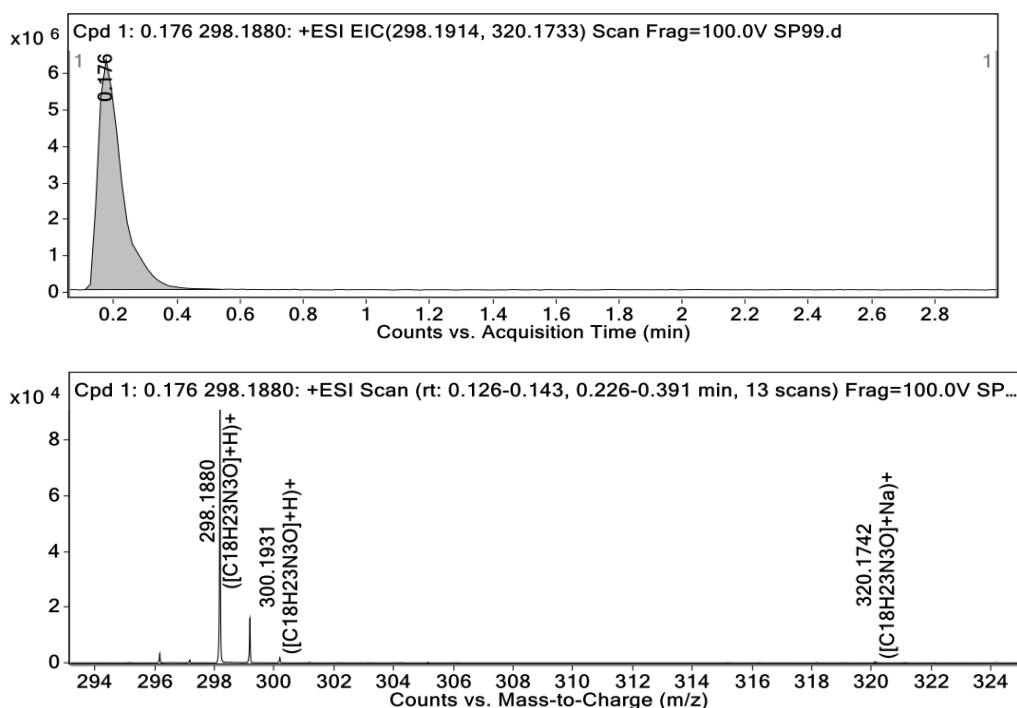
07-BG-PS-SP-99-13C.001.001.1r.esp



Spectra 3.30: ¹³C NMR Spectra for the compound 3d.



Spectra 3.31: HPLC traces of compound 3d.

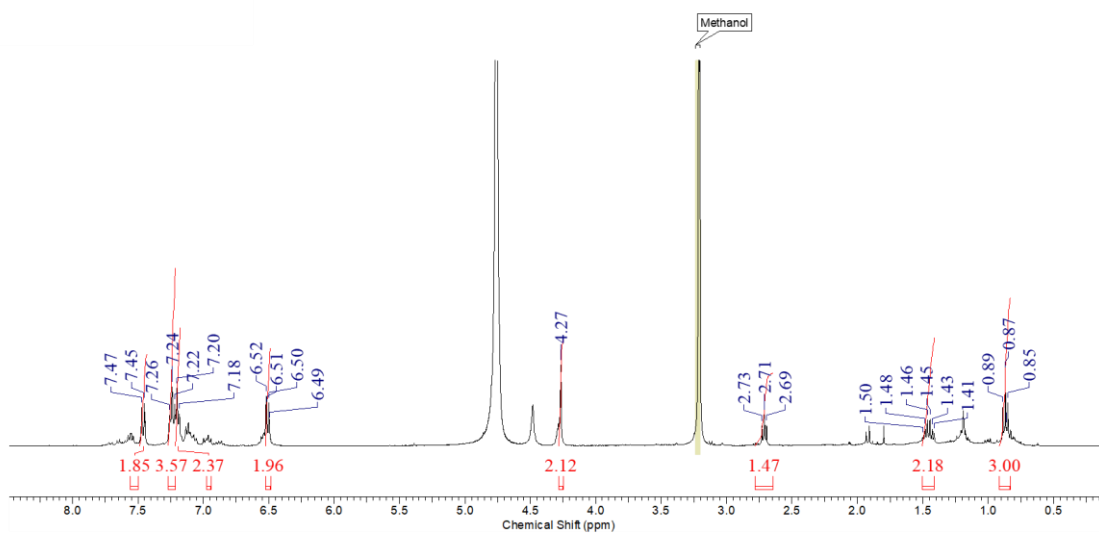


Spectra 3.32: HRMS Spectra for the compound 3d.

3.3.1.16. Preparation of 4-(benzylamino)-N'-propylbenzohydrazide (4d)

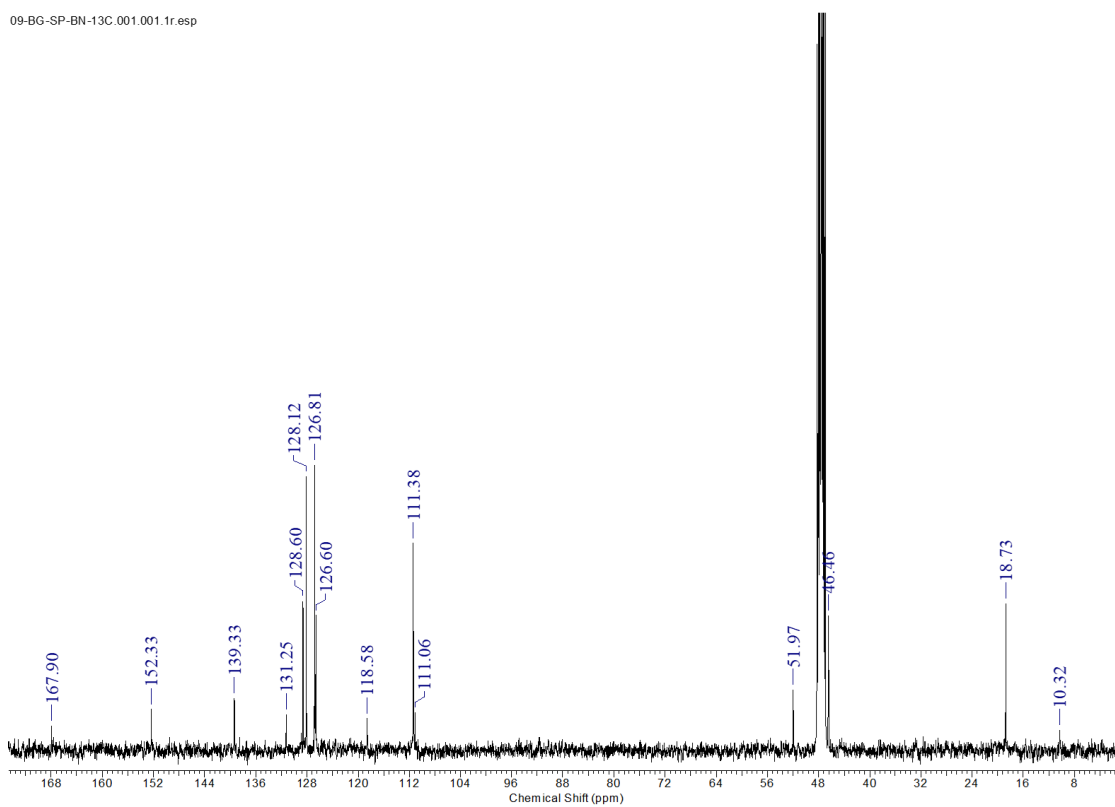
Using the synthetic procedure of **4a**, starting materials **2d** and propionaldehyde gave **4d** in 48% yield. ¹H NMR (400 MHz, methanol-*d*₄) δ 7.45 - 7.47 (m, 2H) 7.22 - 7.26 (m, 3H) 7.18 - 7.22 (m, 2H) 6.49 - 6.52 (m, 2H) 4.27 (s, 2H) 2.69 - 2.73 (t, *J* = 7.19 Hz, 2H) 1.40 - 1.52 (m, 2H) 0.85 - 0.89 (t, *J* = 7.44 Hz, 3H). ¹³C NMR (101 MHz, methanol-*d*₄) δ 167.90, 152.33, 139.33, 131.25, 128.60, 128.12, 126.81, 126.60, 118.58, 111.38, 51.97, 46.46, 18.73, 10.32. HRMS (APESI) *m/z* calcd for C₁₈H₂₃N₃O. [M+H]⁺: 284.1758; found 284.1722.

Chapter 3: Benzoyl hydrazides as HDAC3 inhibitors

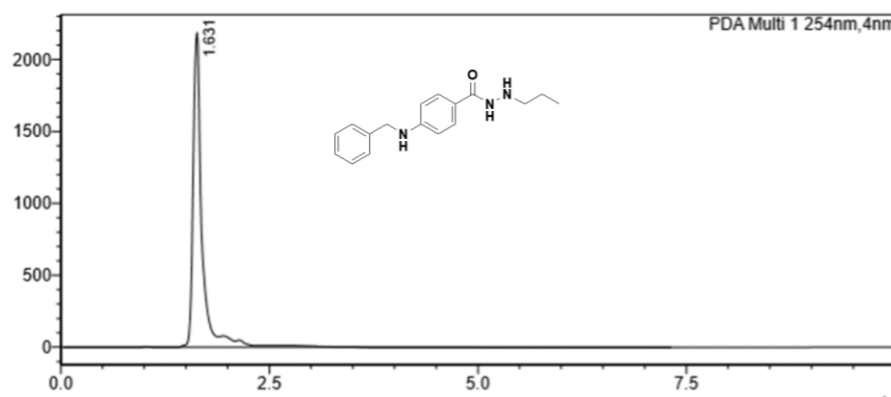


Spectra 3.33: ¹H NMR Spectra for the compound 4d.

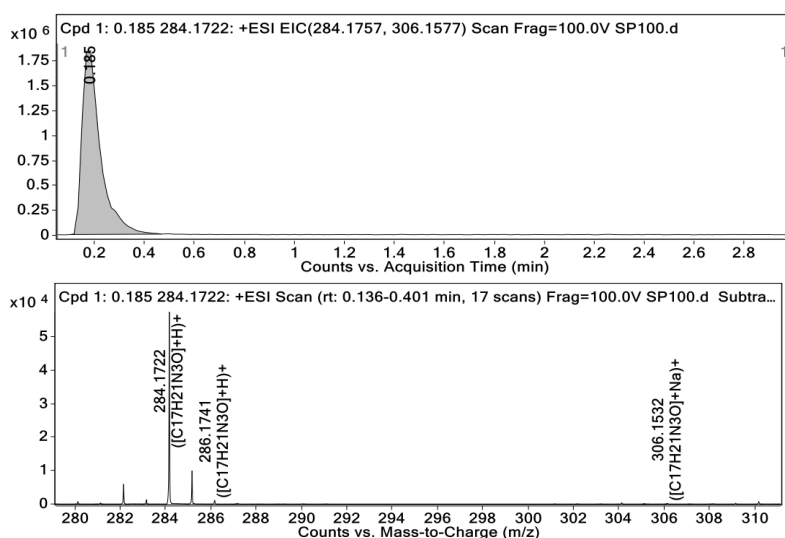
09-BG-SP-BN-13C.001.001.1r.esp



Spectra 3.34: ¹³C NMR Spectra for the compound 4d.



Spectra 3.35: HPLC traces of compound 4d.



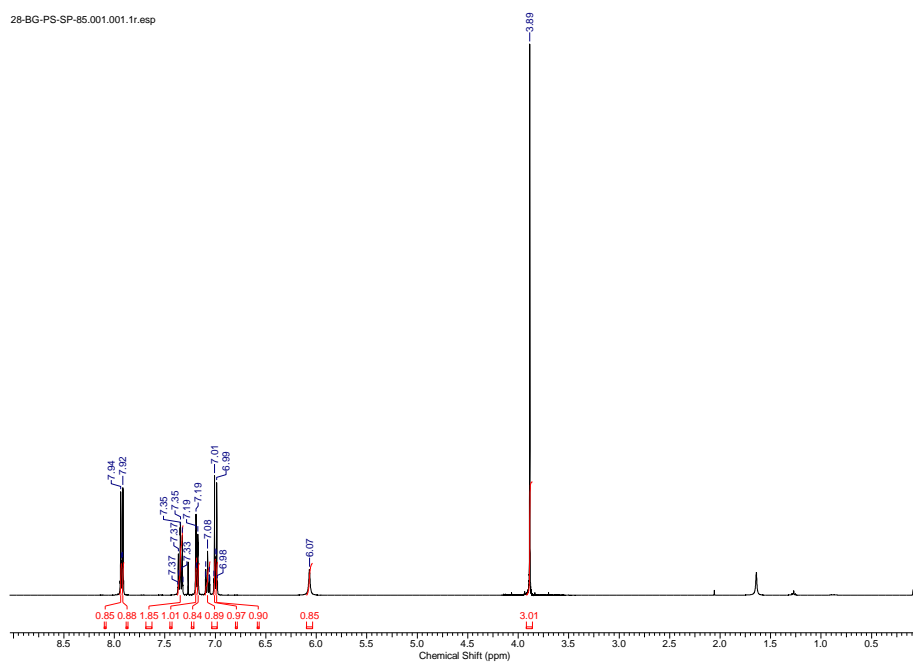
Spectra 3.36: HRMS Spectra for the compound 4d.

3.3.1.17. Preparation of methyl 4-(phenylamino)benzoate (1e)

A mixture of methyl 4-chlorobenzoate (**3**) (200 mg, 1.17 mmol), XPhos (5.6 mg, 0.011 mmol), K_2CO_3 (162 mg) catalytic $Pd_2(dba)_3$ in 3 ml of *N,N*-Di-isopropylethylamine were stirred and aniline (127 μ l, 1.41 mmol) was subsequently added and allowed to stirred for overnight at 110°C at reflux conditions. The reaction mixture was then concentrated *in vacuo*. The completion of the reaction was confirmed by TLC. The reaction mixture was quenched using an aqueous sodium bicarbonate solution. The crude reaction mixture was extracted into the organic layer three times using ethyl acetate and water. The organic layer was then separated, washed with brine solution, dried over anhydrous Na_2SO_4 and then

Chapter 3: Benzoyl hydrazides as HDAC3 inhibitors

concentrated *in vacuo*. The crude product was then purified using column chromatography and the pure compound **1d** is eluted using 80% hexane and 20% ethyl acetate as solvents in the form of brown powder of about 75% yield. $^1\text{H NMR}$ (400 MHz, CDCl_3) δ 7.93 - 7.95 (m, 1H), 7.91 - 7.92 (m, 1H), 7.32 - 7.38 (m, 2H), 7.18 - 7.20 (m, 1H), 7.16 - 7.18 (m, 1H), 7.05 - 7.10 (m, 1H), 7.00 - 7.02 (m, 1H), 6.98 - 7.00 (m, 1H), 6.07 (1H), 3.89 (s, 3H).



Spectra 3.37: $^1\text{H NMR}$ Spectra for the compound **1e**.

3.3.1.18. Preparation of 4-(phenylamino)benzohydrazide (**2e**)

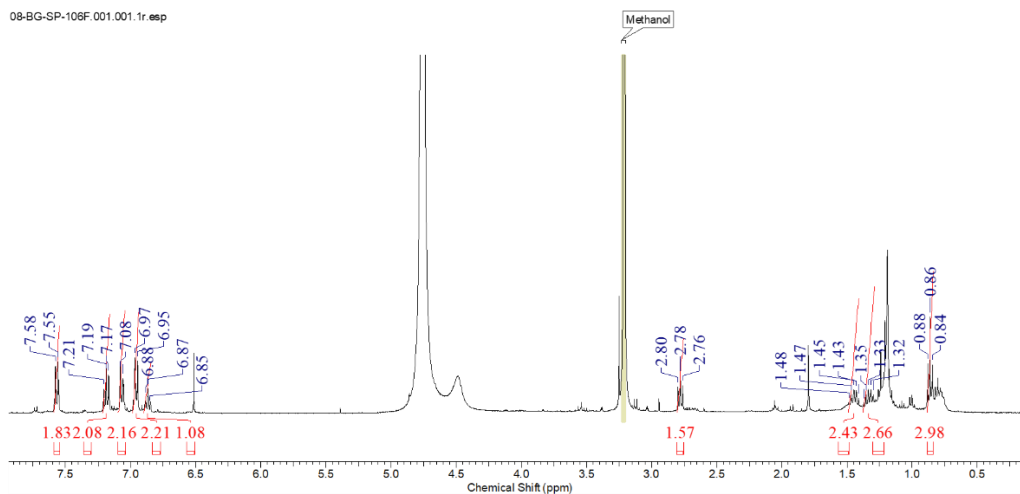
Methyl 4-(phenylamino) benzoate (**1e**) (150 mg, 0.66 mmol) was dissolved in 5ml of methanol and to this hydrazine monohydrate (321 μl , 6.60 mmol) was added. The reaction was carried out for 6 h at reflux conditions. Upon completion of the reaction, the reaction mixture was concentrated *in vacuo* and dried under a vacuum oven. The crude product obtained was used for the next reaction without purification.

3.3.1.19. Preparation of *N'*-butyl-4-(phenylamino)benzohydrazide (**3e**)

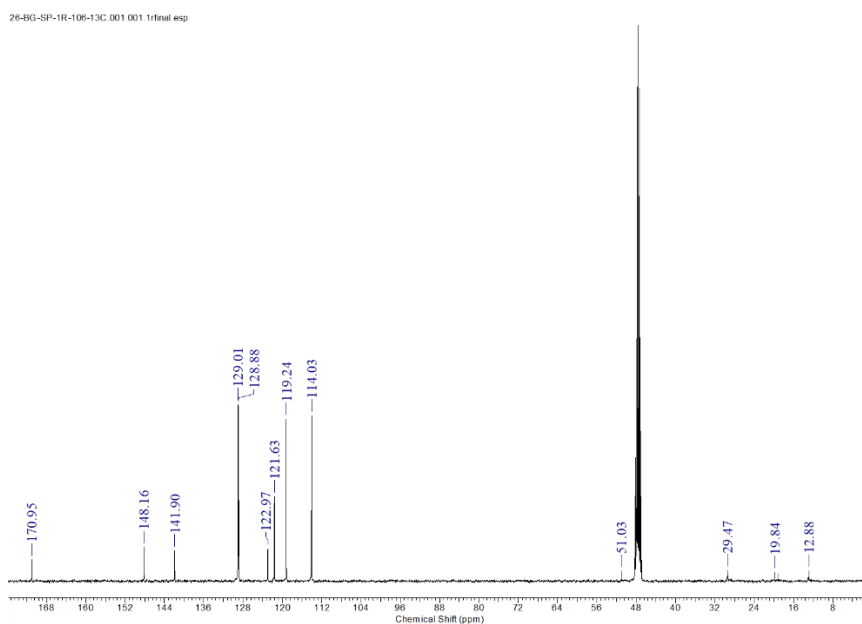
Using the synthetic method of **3a**, **2e** and butyraldehyde gave **3e** in 52% yield. $^1\text{H NMR}$ (400 MHz, methanol- d_4) δ 7.55 - 7.58 (m, 2H), 7.17 - 7.21 (m, 2H), 7.08 - 7.06 (m, 2H), 6.97 - 6.95 (m, 2H), 6.85 - 6.88 (m, 1H), 2.76 - 2.80 (t, $J = 7.32$ Hz, 2H), 1.41 - 1.48 (m,

Chapter 3: Benzoyl hydrazides as HDAC3 inhibitors

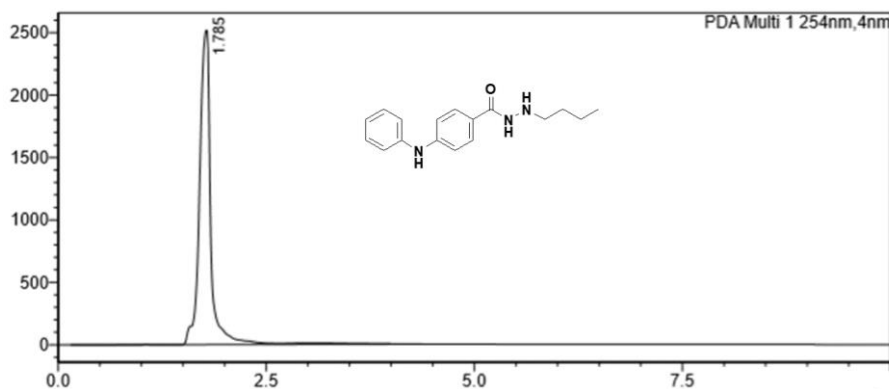
2H), 1.30 - 1.37 (m, 2H), 0.84 – 0.88 (t, $J = 7.44$ Hz, 3H). ^{13}C NMR (101 MHz, methanol- d_4) δ 170.95, 148.16, 141.90, 129.01, 128.88, 122.97, 121.63, 119.24, 114.03, 51.03, 29.47, 19.84, 12.88. HRMS (APESI) m/z calcd for $\text{C}_{17}\text{H}_{21}\text{N}_3\text{O}.[\text{M}+\text{H}]^+$: 284.1758; found 284.1718.



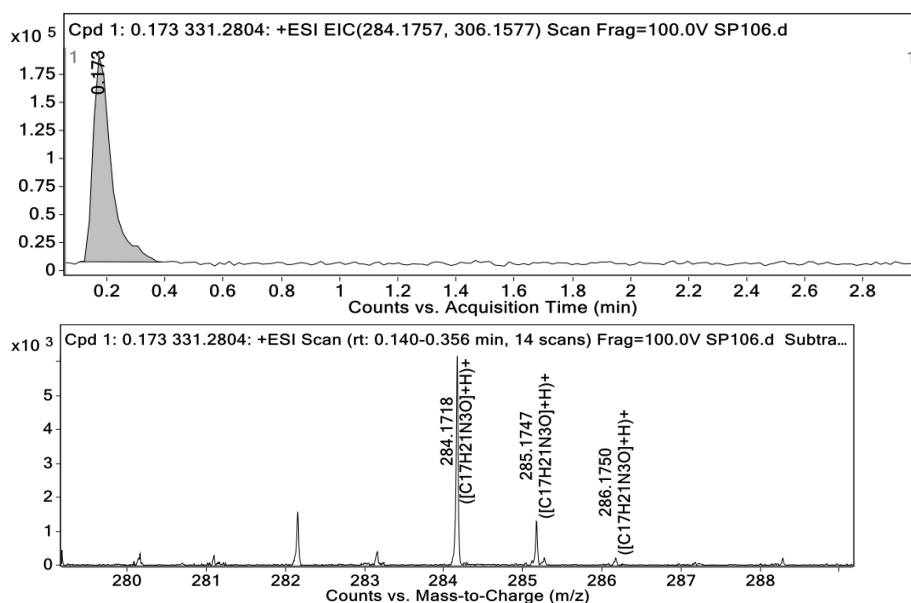
Spectra 3.38: ^1H NMR Spectra for the compound 3e.



Spectra 3.39: ^{13}C NMR Spectra for the compound 3e.



Spectra 3.40: HPLC traces of compound 3e.



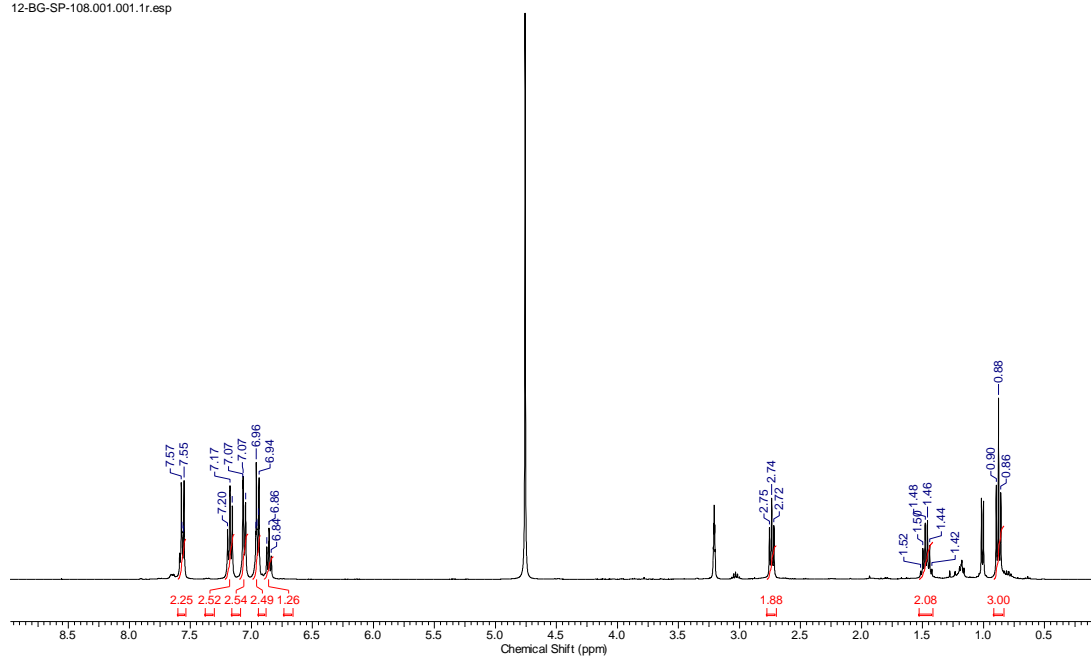
Spectra 3.41: HRMS Spectra for the compound 3e.

3.3.1.20. Preparation of 4-(phenylamino)-N'-propylbenzohydrazide (4e)

Using the synthetic method of **4a**, **2e** and propionaldehyde gave **4e** in 54% yield. ^1H NMR (400 MHz, methanol- d_4) δ 7.64 - 7.70 (m, 2H), 7.24 - 7.30 (m, 2H), 7.13 - 7.18 (m, 2H), 7.03 - 7.07 (m, 2H), 6.93 - 6.98 (m, 1H), 2.84 (t, $J = 7.32$ Hz, 2 H), 1.42 - 1.52 (m, 2H), 0.86 - 0.90 (t, $J = 7.44$ Hz, 3 H). ^{13}C NMR (101 MHz, methanol- d_4) δ 167.41, 147.98, 141.93, 128.89, 128.35, 122.37, 121.59, 119.17, 114.19, 53.48, 20.62, 10.53. HRMS (APESI) m/z calcd for $\text{C}_{16}\text{H}_{19}\text{N}_3\text{O}$. $[\text{M}+\text{H}]^+$: 270.1601; found 270.1574.

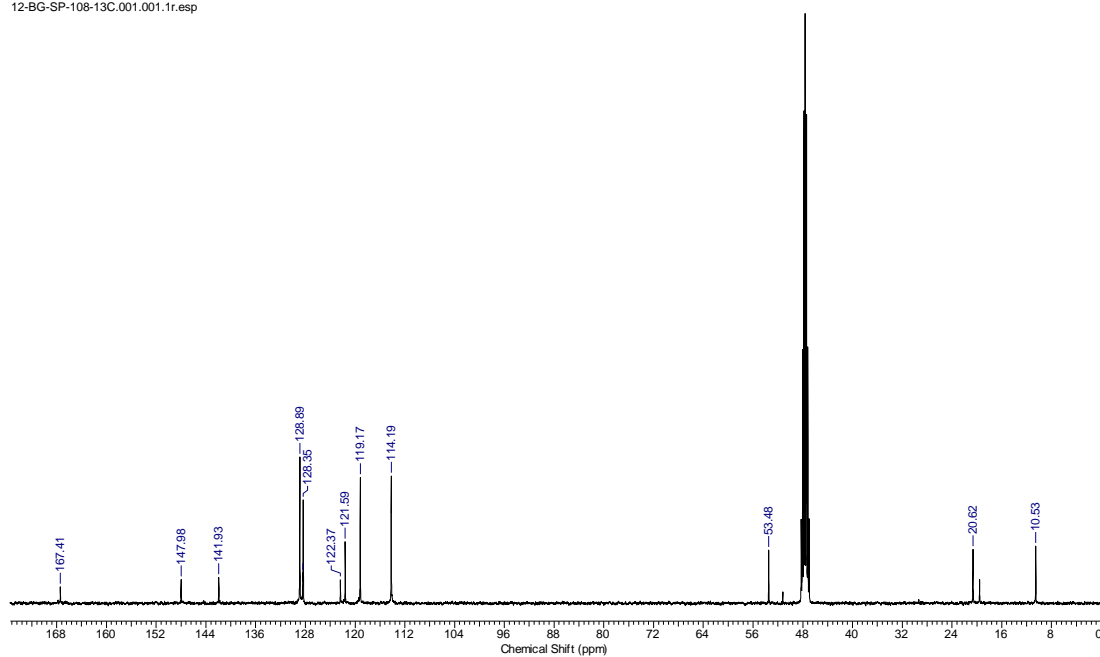
Chapter 3: Benzoyl hydrazides as HDAC3 inhibitors

12-BG-SP-108.001.001.1r.esp

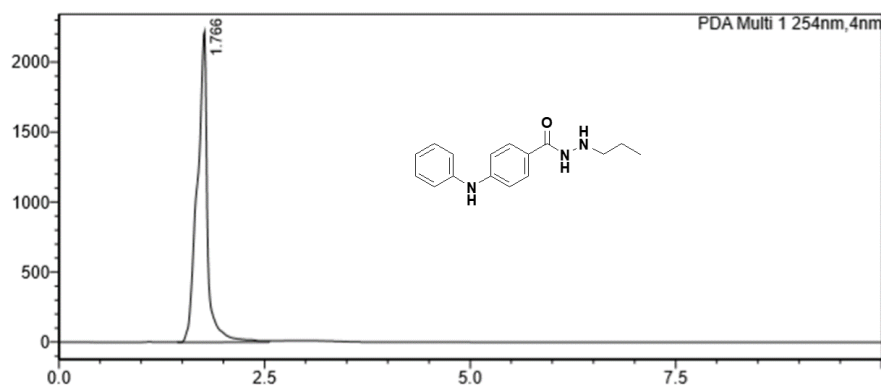


Spectra 3.42: ¹H NMR Spectra for the compound 4e.

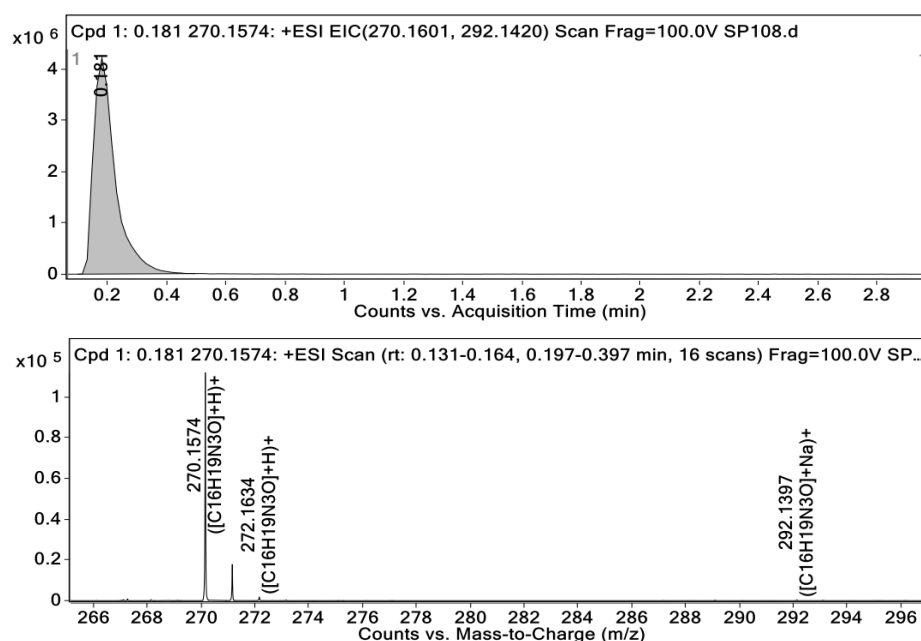
12-BG-SP-108-13C.001.001.1r.esp



Spectra 3.43: ¹³C NMR Spectra for the compound 4e.



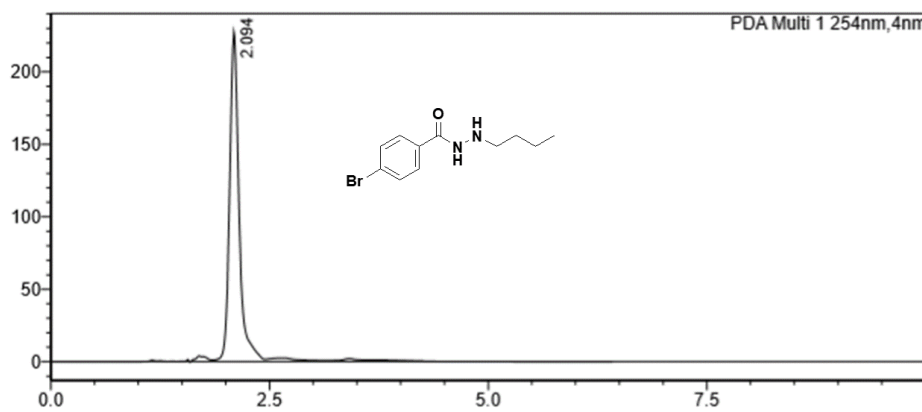
Spectra 3.44: HPLC traces of compound 4e.



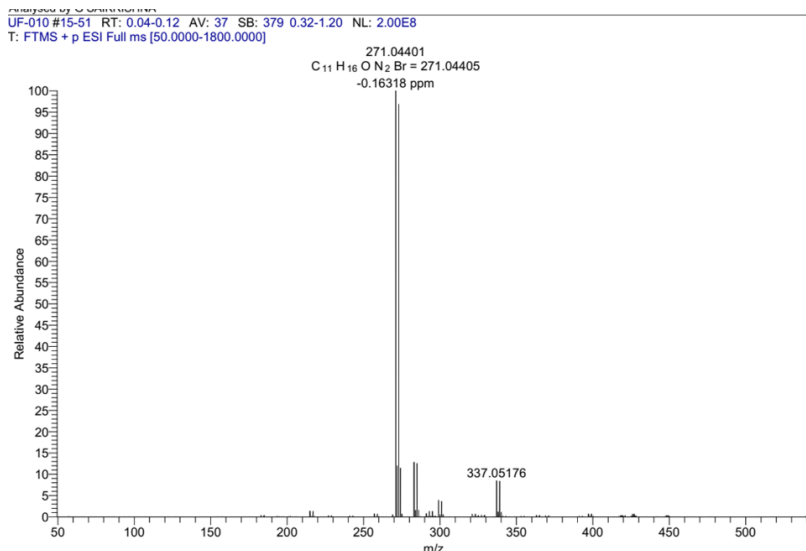
Spectra 3.45: HRMS Spectra for the compound 4e.

3.3.1.21. Preparation of UF010

The reference compound UF010 was synthesized as per the reported protocol (Wang et al., 2015). The percentage yield obtained was 57%. ^1H NMR (400 MHz, methanol- d_4) δ 7.57 - 7.64 (m, 4H), 2.91 - 2.95 (t, J = 7.32 Hz, 2 H), 1.48 - 1.56 (m, 2H), 1.35 - 1.44 (m, 2H), 0.92 - 0.95 (t, J = 7.44 Hz, 3 H). ^{13}C NMR (101 MHz, methanol- d_4) δ 166.33, 131.93, 128.42, 126.50, 52.02, 30.10, 20.22, 13.94. HRMS (APESI) m/z calcd for $\text{C}_{16}\text{H}_{19}\text{N}_3\text{O}$. $[\text{M}+\text{H}]^+$: 271.1580; found 271.0440.



Spectra 3.48: HPLC traces of compound UF010.



Spectra 3.49: HRMS Spectra for the compound 4e.

3.3.2. Cell culture studies

In vitro cell culture studies were carried out by using four cancer cell lines for determining the cytotoxic activity of these compounds as per our earlier reported methodologies (Routholla et al., 2021b, 2021a). MTT assay was conducted using mouse breast cancer cell line (4T1), murine melanoma cancer cell line (B16F10), human breast cancer (MCF-7) cell line, human non-small cell lung cancer cell line (A549), human embryonic kidney (HEK – 293) cell line, human corneal epithelial cell line (HCEC) and Raw 264.7 cell line (murine) that was collected from National Centre for Cell Science (NCCS, Pune, India). B16F10, MCF– 7, HEK – 293, HCEC and Raw 264.7 cell lines were cultured in DMEM (high

Chapter 3: Benzoyl hydrazides as HDAC3 inhibitors

glucose media: AL007S, Dulbecco's modified eagle medium) and 4T1 cell line was cultured in MEM (AT154, Minimum essential medium) and A549 cell line was cultured in DMEM/F-12 (AT140A, Dulbecco's Modified Eagle Medium /Nutrient Mixture F12 Ham, DMEM/F-12, 1:1 mixture) with 10% fetal bovine serum (FBS) and 1% antibiotic (Pen strep: A001) and was incubated at 37 °C under 5% CO₂ atmosphere. MTT [3-(4,5-dimethylthiazol-2-yl)-2,5-diphenyltetrazolium bromide], a yellow dye was considered for the assay. All the reagents were directly procured from Himedia Laboratories Pvt. Ltd., Mumbai, India.

3.3.3. Chemicals and antibodies

The synthesized compounds were dissolved in a DMSO stock solution and were stored for further experiments. The positive controls, **Tubastatin A** (Butler et al., 2010) and **PT5e** (Trivedi et al., 2019) were synthesised in-house with the reported protocols. HDAC fluorimetric drug discovery kits for HDAC1, 2, 3, 6 and 8 were purchased from Enzo life sciences, Delhi and HDAC4 and 5 were purchased from Invenio Biosciences, Mumbai. DAPI and Acridine Orange, propidium iodide and RNase were purchased from Sigma-Aldrich. TACs Annexin-V/FITC – PI assay kit was purchased from Bio-legend and was used as per the protocol provided in the kit. For western blot analysis, all the antibodies were purchased from cell signalling technology except Ac-SMC3 purchased from Merck sigma. The details are provided below. Primary antibodies used were rabbit mAb H3K9 acetylated histone H3 (#9649), H4K12 acetylated histone H4 (#13944), H3K27 acetylated histone H3 (#4353), alpha- Tubulin K40 acetylated (3971), acetylated SMC3 (Lys105/106), clone 21A7 (MABE1073), Caspase-3 (#9662), Caspase-7 (#12827), BCL-2 (#3498), EGFR (#2132), CD44 (#3578), cytochrome *c* (#4280), Ki-67 (#9129S) and mouse mAb beta-actin primary antibodies (#58169) and the secondary antibodies – anti-rabbit HRP linked antibody and anti-mouse IgG HRP-Linked antibody.

Chapter 3: Benzoyl hydrazides as HDAC3 inhibitors

3.3.4. *Pan-HDAC inhibition assay with HeLa nuclear extract*

HDAC colorimetric assay kit (BML-AK500-0001) was used for the enzyme inhibition assay for *pan*-HDAC inhibition of the compounds as per the protocol reported earlier (Routholla et al., 2021b, 2021a). Each well of the microtiter plate was added with 5 μ l of HeLa nuclear extract, 10 μ l of assay buffer and 10 μ l of 10 μ M final concentration of the sample solution to be assayed. 25 μ l of the Color de Lys® substrate solution was added subsequently to initiate the reaction and the microtiter plate was incubated for 30 mins at room temperature. 50 μ l of the developer and stop solution were added towards the termination of the reaction. Further incubation of 15 mins at 37°C was facilitated and the absorbance was measured at 405 nm. The assay was carried out in duplicate and the results were analysed using Graph Pad Prism 8.0.1.

3.3.5. *HDAC1 inhibition assay*

HDAC1 fluorimetric drug discovery kit (BML-AK511-0001) was used for the enzyme inhibition assay for HDAC1 isozyme inhibition of the promising compounds following the protocol reported earlier (Routholla et al., 2021b, 2021a). Each well of the microtiter plate were added with 15 μ l of diluted HDAC1 complex solution, 10 μ l of 10 μ M final concentration of the sample solution to be assayed. 25 μ l of the Fluor de Lys® substrate solution was added subsequently to initiate the reaction and the microtiter plate was incubated for 15 mins at room temperature. 50 μ l of Fluor de Lys® developer II and Trichostatin A solution were added towards the termination of the reaction. Further incubation of 45 mins at 37 °C was facilitated and the fluorescence intensity was recorded at excitation wavelength 360 nm and emission wavelength 460 nm. The same procedure was followed for the estimation of IC₅₀ values using the concentration range of 0.0781 μ M – 1.25 μ M for **4c**, **4e** and 0.625 μ M – 10 μ M for **UF010** in duplicate. Analysis was done using the non-linear regression analysis method using Graph Pad Prism 8.0.1.

Chapter 3: Benzoyl hydrazides as HDAC3 inhibitors

3.3.6. HDAC2 inhibition assay

HDAC2 fluorimetric drug discovery kit (BML-AK512-0001) was used for the enzyme inhibition assay for HDAC2 isozyme inhibition of the promising compounds according to the protocol reported earlier (Routholla et al., 2021b, 2021a). Each well of the microtiter plate was added with 15 μ l of diluted HDAC2 complex solution, 10 μ l of 10 μ M final concentration of the sample solution to be assayed. 25 μ l of the Fluor de Lys® substrate solution was added subsequently to initiate the reaction and the microtiter plate was incubated for 30 mins at room temperature. 50 μ l of Fluor de Lys® developer II and Trichostatin A solution were added towards the termination of the reaction. Further incubation of 15 mins at 37 °C was facilitated and the fluorescence intensity was recorded at excitation wavelength 485 nm and emission wavelength 530 nm. The same procedure was followed for determining IC₅₀ values using the concentration range of 0.625 μ M to 5 μ M for **4c**, **4e** and **UF010** in duplicate. Analysis was done using the non-linear regression analysis method using Graph Pad Prism 8.0.1.

3.3.7. HDAC3/NCOR1 inhibition assay

HDAC3/NCOR1 fluorimetric drug discovery kit (BML-AK531-0001) was used for the enzyme inhibition assay for HDAC3 isozyme inhibition of the promising compounds as per the protocol reported earlier (Routholla et al., 2021b, 2021a). Each well of the microtiter plate was added with 15 μ l of diluted HDAC3 complex solution, 10 μ l of 1 μ M and 0.625 μ M final concentration of the sample solution to be assayed. 25 μ l of the Fluor de Lys® substrate solution was added subsequently to initiate the reaction and the microtiter plate was incubated for 15 mins at room temperature. 50 μ l of Fluor de Lys® developer II and Trichostatin A solution were added towards the termination of the reaction. Further incubation of 45 mins at 37 °C was facilitated and the fluorescence intensity was recorded at excitation wavelength 360 nm and emission wavelength 460 nm. The same procedure

Chapter 3: Benzoyl hydrazides as HDAC3 inhibitors

was followed for determining IC₅₀ values using the concentration range of 3.9 nM to 1000 nM for **4c**, **4e** and **UF010** in duplicate. Analysis was done using the non-linear regression analysis method using Graph Pad Prism 8.0.1.

3.3.8. HDAC8 inhibition assay

HDAC8 fluorimetric drug discovery kit (BML-AK518-0001) was used for the enzyme inhibition assay for HDAC8 isozyme inhibition of the promising compounds following the protocol reported earlier (Routholla et al., 2021b, 2021a). Each well of the microtiter plate were added with 15 µl of diluted HDAC8 complex solution, 10 µl of 5 µM final concentration of the sample solution to be assayed. 25 µl of the Fluor de Lys® substrate solution was added subsequently to initiate the reaction and the microtiter plate was incubated for 10 mins at room temperature. 50 µl of Fluor de Lys® developer II and Trichostatin A solution were added towards the termination of the reaction. Further incubation of 45 mins at 37°C was facilitated and the fluorescence intensity was recorded at excitation wavelength 360 nm and emission wavelength 460 nm. The same procedure was followed for determining IC₅₀ values using the concentration range of 0.005 µM to 1 µM for **4c**, **4e** and **UF010** in duplicate. Analysis was done using the non-linear regression analysis method using Graph Pad Prism 8.0.1.

3.3.9. HDAC6 inhibition assay

HDAC6 fluorimetric inhibitor screening kit (BML-AK516-0001) was used for the enzyme inhibition assay for HDAC6 isozyme inhibition of the promising compounds as per the protocol reported earlier (Routholla et al., 2021b, 2021a). Each well of the microtiter plate were added with 50 µl of diluted HDAC6 complex solution, 2 µl of 20 µM final concentration of the sample solution to be assayed. 48 µl of the Fluor de Lys® substrate solution was added subsequently to initiate the reaction and the microtiter plate was incubated for 30 mins at room temperature. 10 µl of Fluor de Lys® developer II was added

Chapter 3: Benzoyl hydrazides as HDAC3 inhibitors

towards the termination of the reaction. Further incubation of 10 mins at 37 °C was facilitated and the fluorescence intensity was recorded at excitation wavelength 380 nm and emission wavelength 490 nm. The same procedure was followed for determining IC₅₀ values using the concentration range of 5 µM to 80 µM for **4c**, **4e** and **UF010** in duplicate. Analysis was done using the non-linear regression analysis method using Graph Pad Prism 8.0.1.

3.3.10. HDAC4 inhibition assay

HDAC4 fluorogenic kit was used for the enzyme inhibition assay for HDAC4 isozyme inhibition of the promising compounds. Each well of the microtiter plate was added with 5 µl of 20 µM substrate solution, 5 µl of 1mg/ml BSA solution, 30 µl of HDAC buffer, 5 µl of 50 µM final concentration of the sample solution of **4c**, **4e** and **UF010** in duplicate, to be assayed and 5 µl of HDAC4 enzyme of 0.012 ng/µl concentration. All the required components were prepared as per the protocol given. The microtiter plate was incubated for 30 mins at room temperature in a shaker. 50 µl of undiluted developer (2x) was added towards the termination of the reaction. Further incubation of 15 mins at 37 °C was facilitated and the fluorescence intensity was recorded at excitation wavelength 380 nm and emission wavelength 480 nm. Graphs were plotted using Graph Pad Prism 8.0.1.

3.3.11. HDAC5 inhibition assay

HDAC5 fluorogenic kit was used for the enzyme inhibition assay for HDAC5 isozyme inhibition of the promising compounds. Each well of the microtiter plate was added with 5 µl of 20 µM substrate solution, 5 µl of 1mg/ml BSA solution, 30 µl of HDAC buffer, 5 µl of 50 µM final concentration of the sample solution of **4c**, **4e** and **UF010** in duplicate, to be assayed and 5 µl of HDAC5 enzyme of 0.6 ng/µl concentration. All the required components were prepared as per the protocol given. The microtiter plate was incubated for 30 mins at room temperature in a shaker. 50 µl of undiluted developer (2x) was added

Chapter 3: Benzoyl hydrazides as HDAC3 inhibitors

towards the termination of the reaction. Further incubation of 15 mins at 37 °C was facilitated and the fluorescence intensity was recorded at excitation wavelength 380 nm and emission wavelength 480 nm. Graphs were plotted using Graph Pad Prism 8.0.1.

3.3.12. Cell culture and drug treatment in MTT assay

The *in vitro* cytotoxicity of the synthesized molecules over different cancer cell lines and their selectivity over normal HEK–293, HCEC and Raw 264.7 cell lines were carried out by MTT assay procedure (Routholla et al., 2021b, 2021a). Cells were cultured as per the ATCC protocol in the specified media and were plated in a sterile 96-well plate with about 100 µL/well of cell suspension in their respective media with a cell density of about 1 x 10⁴ cells per well and were incubated overnight for the cell attachment. The following day, the medium was aspirated and the cells were treated with two different concentrations at 10 and 100 µM of the DMSO dissolved compounds in 150 µl of the respective media and were incubated for 72 h with 1% DMSO final concentration in the growth medium. The experiment was conducted in duplicate for every concentration. Post-treatment period, the media was aspirated and to this 50 µl of 5 mg/ml of MTT solution in phenol red-free media was added and incubated for about 3 h. The formation of formazan crystals was confirmed under a microscope. 150 µl of DMSO was added to each well after the removal of MTT solution for the dissolution of the formed crystals. The absorbance was measured at 570 nm and 650 nm wavelengths. The % cell viability was calculated as follows:

$$\frac{\text{Absorbance of treated cells}}{\text{Absorbance of untreated cells}} \times 100$$

The same procedure was followed for the determination of IC₅₀ values of the compounds to be assayed. Dilutions at different concentrations were prepared from the DMSO stock solutions of the compounds using the respective media as per the cell line. Dilutions were prepared of the concentrations, 200 µM, 100 µM, 50 µM, 25 µM, 12.5 µM, 6.25 µM, 3.125 µM, 1.562 µM and 0.781 µM and also a blank control with 1% DMSO in media. The cells

Chapter 3: Benzoyl hydrazides as HDAC3 inhibitors

were subsequently treated with these freshly prepared dilutions and were incubated for 72 h. MTT assay was followed and the % cell viability was determined and the obtained results were depicted in the dose-response curve for the IC₅₀ determination using Graph Pad Prism 8.0.1.

In the case of the HEK-293, HCEC and Raw 264.7 cell lines, the MTT assay was followed the same as previously described (Routholla et al., 2021b, 2021a). The dilutions of the compounds were prepared from their DMSO stock solutions into 2 mM, 1 mM, 500 μ M, 250 μ M, 125 μ M, 62.5 μ M, 31.25 μ M, 15.62 μ M and 7.81 μ M with the DMEM complete media and the IC₅₀ values were determined from the dose-response curve analysed from the % cell viability values obtained from the MTT assay procedure.

3.3.13. Nuclear staining assay

The extent of disintegration of the cancer cells post-treatment with the promising compounds was found by performing nuclear staining assay (Routholla et al., 2021b, 2021a). For this purpose, 4T1 cells were seeded into flat bottom 12 well plates and were incubated overnight for proper attachment. The following day, the media was aspirated and the cells were treated with control (1% DMSO solution), **4e** (1.92 μ M) and **UF010** (8.40 μ M) and further incubated for 48 h. After the treatment, the cells were fixed by using 4% paraformaldehyde followed by staining with DAPI and Acridine Orange. The extent of nuclear staining in both control and treated cells was subsequently visualised under a fluorescence microscope (Leica microsystems, Germany) on 20x Magnification.

3.3.14. Apoptosis assay

Apoptosis assay was performed over B16F10 and 4T1 cells using TACs/ Annexin V kit purchased from Biolegend US (Routholla et al., 2021b, 2021a). In a flat bottomed 12 well plate, 0.5 million/well B16F10 and 4T1 cells were seeded and incubated overnight. The following day, the media was aspirated and the cells were treated with the compounds **4c**,

Chapter 3: Benzoyl hydrazides as HDAC3 inhibitors

4e and **UF010** in duplicate as per their IC₅₀ values for 72 h. Following the treatment period, the cells were washed twice with ice-cold PBS followed by trypsinization. The trypsinized cells were collected and centrifuged to obtain the cell pellet. Further, the cell pellet was washed twice with ice-cold PBS and the obtained cell pellet is resuspended in 100 µl Annexin V incubation reagent freshly prepared including 10X binding buffer (10 µl), FITC (1 µl), PI (10 µl) making up to 100 µl using double distilled water. This is further kept for incubation for about 30 mins at room temperature in dark. To this, 400 µl of 1X binding buffer was added per 100 µl of cell suspension and was analysed by flow cytometry (BD Aria™ III), BD biosciences. The data was analysed into four quadrants in the form of a dot plot. Each quadrant represents as follows: Q1 – necrotic cells, Q2 – late apoptosis cells, Q3 – live cells, Q4 – early apoptotic cells. The data together in Q2 and Q4 is considered as the total apoptotic population.

3.3.15. Cell cycle analysis

Cell cycle analysis was carried out by using flow cytometry and was analysed using FCS Express software (Routholla et al., 2021b, 2021a). For this assay, B16F10 and 4T1 cells were seeded in a flat bottomed 12 well plate with a cell density of 0.5 million cells/well and incubated overnight. The next day, the media was aspirated and the cells were treated with the compounds **4c**, **4e** and **UF010** dissolved in the DMEM complete media of 5 µM final concentration and further were incubated for about 48 h. Post-treatment, the cells were washed with ice-cold PBS, trypsinized and were collected in the form of a cell pellet. This cell pellet obtained is further washed twice with ice-cold PBS and the cells were subsequently fixed using dropwise addition of ice-cold 70% ethanol vortexing gently to avoid clumping. Finally, the single-cell suspension was achieved and was confirmed under a microscope and was left at -20 °C overnight. The following day, the cells were centrifuged and the obtained cell pellet was re-suspended in 500 µl of staining solution prepared by

Chapter 3: Benzoyl hydrazides as HDAC3 inhibitors

20% w/v RNase, 2% w/v PI in about 0.1% v/v of triton X 100 solution in PBS. The samples were incubated in dark for about 30 min at room temperature before the analysis. The cell cycle histograms were obtained and were analysed by flow cytometry (BD Aria™ III), BD biosciences. The data was obtained in the form of a dot plot with PI width on the X-axis and PI area on the Y-axis. The % cell population was analysed from the histogram plotted with PI area on the X-axis and counts on the Y-axis. The data were analysed using FCS Express software to measure the percentage of cells in each cell cycle phase.

3.3.16. Animals

All the *in vivo* experiments were conducted strictly adhering to the approved CPCSEA guidelines of the Institutional Animal Ethics Committee (IAEC), Department of Pharmacy, BITS Pilani, Hyderabad Campus, Hyderabad. For the pharmacokinetic study, male Wistar rats about 7 – 8 weeks old of weight 200 – 220 g were purchased and for *in vivo* antitumor study in a tumor xenograft model, female Balb/c mice of about 6 – 8 weeks of age weighing 18 – 22 g were procured from National Centre for Laboratory Animal Sciences, National Institute of Nutrition (Hyderabad, India). All the animals were housed according to grouping in the separate cages that were kept in a room with room temperature maintained at 23±2 °C and relative humidity at 60±10% in a 12 h light/ 12 h dark cycle. Animals were fed with standard laboratory food and water.

3.3.17. *In vivo* pharmacokinetic study

The pharmacokinetic study was carried out in male Wistar rats and was grouped into 3 groups of control, 15 mg/kg and 25 mg/kg of **4e** with 3 rats in each group. The rats were intravenously administered using **control** (vehicle alone) and **4e** (10 mg/ml) solution in saline. The compound was dissolved in saline containing 5% DMSO. After administration of **4e**, the blood samples of about 500 µl were collected at different time points (pre-dose, 0.25 h, 0.5 h, 1 h, 2 h, 4 h, 6 h, 8 h, 12 h and 24 h) from the retro-orbital plexus while

Chapter 3: Benzoyl hydrazides as HDAC3 inhibitors

placing rats under anaesthetic conditions. Once in 2 h, a fluid replacement was carried out by administering 1.5 ml of saline, USP. The obtained blood samples were centrifuged for collecting plasma and was stored at $-20\text{ }^{\circ}\text{C}$ for further analysis. **4e** was extracted from plasma by protein precipitation method and the samples were analysed by HPLC Shimadzu. Linear trapezoidal rule was used for the calculation of area under the concentration and time curve (AUC values). Non-compartmental analysis was used to obtain the pk parameters. The clearance was estimated as $\text{CL}=\text{Dose}/\text{AUC}_{\text{inf}}$; $\text{MRT}=\text{AUMC}_{\text{inf}}/\text{AUC}_{\text{inf}}$. A similar procedure was carried out for the intraperitoneal route of administration for the compound **4e** at 15 mg/kg and 25 mg/kg and the reference compound **UF010** at 25 mg/kg, respectively. Data obtained represents mean \pm standard deviation of the mean for $n = 3$.

3.3.18. *In vivo antitumor activity by the 4T1-Luc xenograft mouse model*

For the *in vivo* antitumor study of the compounds, 4T1-Luc cells cultured as per ATCC guidelines (in MEM complete media) of about 1.5 million cells that were suspended in 100 μl of sterile PBS were inoculated for the tumor implantation. The cells were subcutaneously injected into the dorsal flank region of the female Balb/c mice. Tumors started appearing after 10 days post-injection of the cells. Tumor volume was measured regularly using a vernier calliper and calculated as tumor volume = $[(\text{length} \times \text{width}^2) \div 2]$. Once, the tumor volume reached about 50 mm^3 , 12 mice were grouped into 3 groups with $n = 5$ mice in each group. Compound **UF010** and **4e** were dissolved in the vehicle consisting of 5% DMSO, 30% camphor and 65% saline. The treatment regimen was for 21 days (5 days/ week) and 4 groups of mice were treated with vehicle alone (control group), **UF010** as a positive control at 25 mg/kg, and 15 mg/kg and 25 mg/kg of **4e** for the treatment period. Every 3 days, the mice body weight and the tumor volume was recorded.

3.3.19. *In vivo Bioluminescence image analysis*

Bioluminescence analysis was carried out by using *in vivo* imaging technique to monitor

Chapter 3: Benzoyl hydrazides as HDAC3 inhibitors

the growth of tumors periodically using IVIS® Lumina III, PerkinElmer, USA. Mice were placed in the induction chamber with the flow of 2% isoflurane and O₂ continuously to anaesthetize them. Subsequently, Luciferin D (100 µl, 100 mg/kg dissolved in sterile PBS) was injected intraperitoneally. After 2 mins, mice were placed inside the imaging facility for bioluminescence imaging. Two from each group of mice was selected randomly and were monitored for tumor growth on day 10 and day 21 of the treatment period and the images were acquired. The region of interest around the tumor area was selected and the bioluminescence signals were analysed in the units of photons/sec/cm²/sr (maximum photons per second per centimetre square per steradian).

3.3.20. *Survival study post tumor resection*

After 21 days of treatment, mice were anaesthetized and the tumor area of the mice was cleaned, shaved and the tumor removal was performed surgically under sterile conditions following the reported protocols. Post-tumor resection, auto-clip applier was used and the surgical site was closed and the mice were placed in individual cages following strict adherence to the institutional guidelines for about 21 days. The mice were monitored for their survival and the data were analysed using Graph Pad Prism 8.0.1. and represented as Kaplan-Meier plots. The data represented in the graphs were calculated from at least four independent experiments and calculated as mean \pm SEM.

At the end of the study, the mice were sacrificed and the tumors were isolated and stored in a tissue freezing medium at -80 °C for further experiments. Other organs like the heart, kidney, spleen, liver and lungs were also isolated and stored further for immunohistochemical analysis. Tumor sections were further lysed in ice-cold 1X RIPA lysis buffer, 0.5 mM PMSF and protease inhibitor and stored at -80 °C for western blot analysis. Part of the tumors from the control group as well as the treated mice were sectioned into 5 µm thickness using cryotome (Leica Biosystems, Germany). These tumor

Chapter 3: Benzoyl hydrazides as HDAC3 inhibitors

and tissue sections were further used for immunohistochemical analysis.

3.3.21. *ROS generation in tumor tissues*

The production of ROS was evaluated by using the DCFH-DA probe. Mice were anaesthetized (n=2) and they were intratumorally injected with DCFH-DA (100 μ l, 25 μ M) on day 21 of the treatment. Images were obtained with IVIS® Lumina III, PerkinElmer, USA. The fluorescence intensity [(p/sec/cm²/sr)/ μ W/cm²] was quantified by choosing the region of interest. After 30 mins, the tumors were surgically isolated and the tumor sections were observed under a fluorescence microscope.

3.3.22. *TUNEL assay on tumor cryosections*

TUNEL assay was carried out in the tumor tissue sections as per the previous protocol. The tumor sections were placed onto the slides and were stained using a TUNEL reagent kit and were fixed using 4% paraformaldehyde solution. The stained tumor sections were imaged with the help of a fluorescent microscope using blue and green filters. Image J software was used to process and analyse the obtained images.

3.3.23. *Immunohistochemistry of tumor sections and H&E staining*

Immunohistochemical analysis was performed on tumor sections using the Ki-67 biomarker for the analysis of cell proliferation. The tissue sections were fixed with 4% paraformaldehyde onto the slides. The sections were further incubated with the primary antibody of Ki-67 with a dilution of 1: 500 at 4 °C. After overnight incubation, the tumor sections were washed using 1X PBS and were further incubated with secondary antibody conjugated with Alexa Fluor® 488 for 3 h. After washing the sections with 1X PBS twice, the coverslip was placed onto the sections and was visualised under a fluorescent microscope for the extent of proliferation indicated by Ki-67 positively stained cells.

Immunohistochemical analysis of various organ sections and tumor sections was done following the reported protocol (Routholla et al., 2021b, 2021a). The sections obtained

Chapter 3: Benzoyl hydrazides as HDAC3 inhibitors

from all the major organs isolated from mice were stained using H and E (Harris haematoxylin and eosin) reagent purchased. The images obtained after staining were visualised under a light microscope.

3.3.24. Western blot analysis *in vitro* and *in vivo*

For the western blotting of H3K9 acetylated histone H3(#9649S), H4K12 acetylated histone H4 (#13944S), in B16F10, murine melanoma cells were cultured in flat-bottom 96 well plates and allowed to grow 24 h, and then they were treated with the **4e**, and **UF010** as a reference at 5 μ M, 10 μ M final concentrations for 24 h. Similarly, for the western blotting of H3K27 acetylated histone H3 (#4353), alpha- Tubulin K40 acetylated (#3971), acetylated SMC3 (Lys105/106) (#MABE1073), in 4T1, murine breast cancer cells were cultured in flat-bottom 96 well plates and allowed to grow 24 h, and then they were treated with the **4e**, and **UF010** as a reference at 5 μ M, 10 μ M final concentrations for 24 h. After treatment, the whole cell lysate was prepared by using 100 μ l 1X RIPA lysis buffer (Millipore, Billerica, MA, USA), supplemented with 0.5 mM phenylmethylsulfonyl fluoride (PMSF) and protease inhibitor. Similarly, for the *in vivo* tumor tissue model 3 mg of tumor tissue from the tumor xenograft model from mice treated with **4e** at 15 mg/kg and 25 mg/kg was homogenised with 100 μ l 1X RIPA lysis buffer (Millipore, Billerica, MA, USA), supplemented with 0.5 mM phenylmethylsulfonyl fluoride (PMSF), protease inhibitor and separated the protein extract. The extracted protein was quantified using the BSA protein estimation kit. The whole-cell lysates 20 μ l and 20 μ l (15 ng) of tumor proteins were heated at 95 °C for 7 mins with 5 μ l of loading buffer (4X). Then, the denatured proteins were subjected to sodium dodecyl sulphate-polyacrylamide gel electrophoresis. Gels were transferred to the polyvinylidene fluoride membranes (Bio-Rad, Laboratories, Inc.) and membranes were blocked in 5% non-fat skimmed milk (Bio-Rad, Laboratories, Inc.) in tris-buffered saline with 1% Tween 20 (TBST), and incubated with Rabbit mAb

Chapter 3: Benzoyl hydrazides as HDAC3 inhibitors

H3K9 acetylated histone H3 (#9649S), H4K12 acetylated histone H4 (#13944S), Caspase-3 (#14220), Caspase-7 (#12827), BCL-2 (#3498), EGFR (#2132), CD44 (#3578), cytochrome *c* (#4280) and Mouse mAb beta-Actin as an internal control and primary antibodies (Cell Signalling Technology, Inc.), then used Horseradish peroxidase (HRP)-conjugated anti-rabbit secondary antibody (Cell Signalling Technology, Inc.), and visualized with a chemiluminescence kit (Bio-Rad, Laboratories, Inc.), and exposed using a Fusion plus 6 Imaging System (Vilber Lourmat, France).

3.3.25. Statistical analysis

All the data are reported as means \pm standard deviation or mean \pm standard error mean. Differences were analysed by Student's t-test and one-way ANOVA (with 95% confidence interval). p values < 0.05 , were considered statistically significant.

3.3.26. Molecular docking analysis

The crystallographic structures of the HDAC isoforms (i.e., HDAC1, HDAC2, HDAC3, HDAC6 and HDAC8) required for the molecular docking analysis were procured from the Protein Data Bank (Bank, n.d.). In this study, the *GLIDE* module of the Schrodinger Maestro v12.1 software (“Schrödinger Suite, Schrödinger, LLC, New York, USA, 2019. <http://www.schrodinger.com/glide.>,” n.d.) was used for the molecular docking study to know the enzyme-ligand interactions of these synthesized hydrazide compounds. At the inceptive step, the ‘*Protein Preparation Wizard*’ of Maestro v12.1 (Bank, n.d.) is used for the optimization and preparation of these HDACs including the addition of missing hydrogen atoms, generation of states and refinement (He et al., 2020; “Schrödinger Suite, Schrödinger, LLC, New York, USA, 2019. <http://www.schrodinger.com/glide.>,” n.d.). In this protein preparation process, the *OPLS_2005* force field has been utilized for the restrained minimization of the proteins. After the protein preparation, the ‘*Receptor Grid Generation*’ module from Maestro v12.1 is used to locate the active site and to prepare the

Chapter 3: Benzoyl hydrazides as HDAC3 inhibitors

receptor grid for the docking study (He et al., 2020; “Schrödinger Suite, Schrödinger, LLC, New York, USA, 2019. <http://www.schrodinger.com/glide>,” n.d.). The synthesized hydrazide molecules were prepared with the help of the *Ligprep* module of Maestro v12.1 using the *OPLS_2005* force field. Finally, the molecular docking was executed with the *extra precision (XP)* method using the *GLIDE* module (He et al., 2020; “Schrödinger Suite, Schrödinger, LLC, New York, USA, 2019. <http://www.schrodinger.com/glide>,” n.d.). The post-docking results executed different docking poses of these compounds with different docking scores. These docked conformations were studied and ranked depending on their docking scores and binding interactions at the active site of these HDACs.

3.4. CONCLUSION

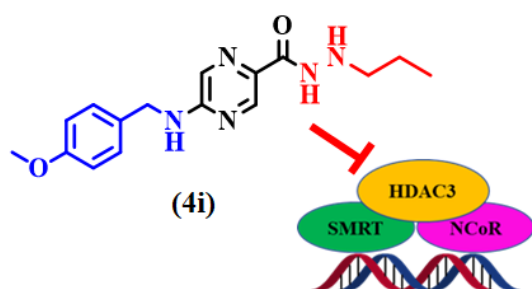
In this current study, some novel small molecule hydrazides with different acetyl, aryl or aroyl substituents as cap group was synthesized as potent HDAC3-selective inhibitors. Among the compounds of the series, compound **4e** was identified as the lead molecule having potent and selective HDAC3 inhibition ($IC_{50} = 15.41$ nM) with more than 18-fold HDAC3 isoform selectivity over other class I HDACs and more than 3000-fold selectivity over HDAC4, HDAC5 and HDAC6. All the compounds in the series possess significant cytotoxicity against various cancer cell lines such as 4T1, B16F10, MCF-7 but were found to be comparatively less potent against the A549 cell line. The result of *in vitro* cytotoxicity experiment suggested a higher inhibitory efficacy for the murine cancer cell lines when compared to that of the human cancer cell lines used. Notably, all the compounds were significantly less toxic when tested *in vitro* against the normal cell lines such as HEK-293, HCEC and Raw 264.7. Compound **4e** exhibited the highest potency against 4T1 cells ($IC_{50} = 1.92$ μ M) with more than 80-fold selectivity for cancer cells over normal cells. Further, the *in vivo* pharmacokinetic study of compound **4e** in rats revealed the $t_{1/2}$ of 2.19 h and 2.62 h when treated with 15 mg/kg and 25 mg/kg body weight dose when tested

Chapter 3: Benzoyl hydrazides as HDAC3 inhibitors

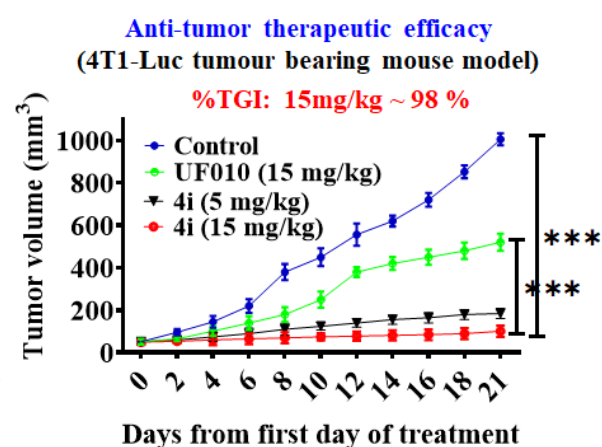
intravenously and with the $t_{1/2}$ of 3.41 h and 4.54 h when treated with 15 mg/kg and 25 mg/kg body weight dose respectively. For the first time in this study, compound **4e** being the lead molecule was subjected to evaluation for the *in vivo* antitumor potency at two different doses (15 mg/kg and 25 mg/kg) in the 4T1-Luc xenograft model in the female Balb/c mice. It was found that compound **4e** exhibited promising antitumor activity with reduced tumor volume after 21 days of treatment with **4e** when compared to the vehicle **control** group and reference compound **UF010** treated group, and with no general toxicity in the main organs which is evidenced by the H&E staining assay of treated organ tissues. Enhanced acetylation levels on H3K9 and H4K12 residues were found both *in vitro* and *in vivo* experiments when treated with compound **4e**. Significant apoptotic activity was noticed upon treatment with compound **4e** which was further evidenced by the upregulated levels of pro-apoptotic proteins caspase-3, caspase-7, cytochrome *c* and downregulated levels of BCL2 in treated tumor tissue isolated from the experimental mice. The reduced proliferation and metastasis and increased survival rate of the treated mice were found and was further supported by the downregulation of CD44, EGFR and Ki-67 in the tumor. Further, cell cycle arrest at G2/M in B16F10 cells and 4T1 cells reaffirmed the programmed cell death mechanism leading to apoptosis. Immunohistochemical analysis by TUNEL assay and ROS generation assay supported the findings that the mice treated with **4e** possessed significant apoptotic activity. Altogether, these results with promising antitumor activity in the *in vitro* as well as *in vivo* experiments suggested that compound **4e** is a selective and potent HDAC3 inhibitor and can be considered as a promising anticancer therapeutic for further development in preclinical and clinical evaluation.

Chapter 4

Design, synthesis, biological evaluation, pharmacokinetic profiling, and binding mode of interaction analysis of novel pyrazino hydrazide chemotypes as selective HDAC3 inhibitors with potent in vivo antitumor efficacy against triple negative breast cancer.



- HDAC3: IC_{50} = 14 nM (121-fold selective).
- 4T1 cancer cells: IC_{50} = 550 nM (385-fold selective over MCF-10A cells and 286-fold selective over HEK cells).
- Chemo sensitizing properties.



Chapter 4: Pyrazino hydrazides as HDAC3 selective inhibitors

4.1. INTRODUCTION

Breast cancer is one of the most commonly diagnosed cancer accounting for most cancer-related deaths in women worldwide (Harbeck et al., 2019; Siegel et al., 2022). Breast cancer is a heterogeneous disease that is caused due to both genetic and epigenetic changes (Harbeck et al., 2019). Based on their gene expression profiling and molecular characteristics, breast cancer can be divided into four subtypes, i.e., luminal A (an estrogen receptor (ER)/progesterone receptor (PR)-positive and human epidermal growth factor receptor 2-negative; ER+, PR+, HER2-), luminal B (ER+, PR+, HER2+), human epidermal growth factor receptor 2-positive (HER2+), and triple-negative breast cancer (ER-, PR-, HER2-) (Rahbari et al., 2022). Among these, triple-negative breast cancer (TNBC) accounts for almost 15% of all breast cancer types characterized by poor prognosis, and high rates of metastasis along with a high risk of relapse resulting in overall fewer survival rates (Bianchini et al., 2022). With limited targeted therapeutic interventions for TNBC treatment and the most common being chemotherapy, there is a higher incidence of chemotherapeutic resistance in TNBC patients overtime (Bianchini et al., 2022; Han et al., 2019; Maccallini et al., 2022). Different mechanisms of chemoresistance in the TNBC (Cao et al., 2021; Han et al., 2019; Ji et al., 2019; O'Reilly et al., 2015) include: a. Multi-drug resistance caused by efflux transporters such as ABC transporters that include P-glycoprotein (P-gp), multi-drug resistance-associated protein (MRP1), breast cancer resistance protein (BCRP); b. Signalling pathways that are implicated in the survival, growth, and invasion of cancer cells such as PTEN/ PI3K/ Akt/ mTOR (PAM), JAK/ STAT, NF- κ B, TGF- β ; c. Dysregulated micro RNAs such as miR-221/222, miR-873, miR-770, and miR-342-3p that lead to metastasis and chemoresistance; d. Pathways causing cancer stem cell self-renewal such as Wnt/ Frizzled/ β -catenin, Hippo, Notch, and Hedgehog pathways. Histone deacetylase inhibitors (HDAC*is*) such as trichostatin A (TSA) (H. Luo

Chapter 4: Pyrazino hydrazides as HDAC3 selective inhibitors

et al., 2021), vorinostat (SAHA) (Duan et al., 2017), belinostat (Chi et al., 2021), and CG200745 (Lee et al., 2017) were found to sensitize the resistant cancer cells to conventional chemotherapy bypassing or regulating the efflux transporter mechanism by ABC transporters, BCRP, MRP1 and also by cancer stem cell reprogramming (Asfaha et al., 2020; Fatma et al., 2022; Stenzel et al., 2017; Wang et al., 2016; You et al., 2020). Therefore, targeted therapies that overcome chemoresistance may provide a better opportunity for precision medicine and thus, offer improved treatment for patients suffering from breast cancer.

Epigenetic changes leading to the alteration in the gene expressions were established as one of the most important reasons for cancer development and progression (Sharma et al., 2010). Targeting these epigenetic modifications is one of the important strategies for cancer treatment (Arrowsmith et al., 2012). Among several post-translational modifications, the acetylation of histone proteins is most widely reported (Mai et al., 2005). Two different enzymes namely histone acetyltransferases (HATs) and histone deacetylases (HDACs) catalyze the acetylation and deacetylation processes of the *N*-terminal lysine residues of the histone proteins respectively leading to the regulation of gene expression. HDACs are known to be involved in the post-translational modification of both histone and non-histone proteins and thus, play a crucial role in various cellular and mechanistic pathways (Gallinari et al., 2007).

The deacetylation of the lysine residues by HDACs leads to the repression of gene expression (eg; tumor suppressor genes) and hence their overexpression is known to be associated with different types of cancers and their etiology (Mai et al., 2005). Therefore, targeting HDACs has widely been explored in the treatment of cancer, and in this direction, several HDAC*is* have been reported over the last two decades (Ahmad Ganai et al., 2016; De Simone and Milelli, 2019; He et al., 2022; Ho et al., 2020; Li and Seto, 2016; Pulya et

Chapter 4: Pyrazino hydrazides as HDAC3 selective inhibitors

al., 2020; Sarkar et al., 2020; Trivedi et al., 2019, 2018; Yang et al., 2019). Till date, 18 mammalian HDAC isoforms have been identified, and these are categorized into four classes namely, class I HDACs (HDAC1 – 3, and HDAC8), class II HDACs (HDAC4 – 7, HDAC9, and HDAC10), class III HDACs (Sirtuins) and class IV HDAC (HDAC11) (Bradner et al., 2010). So far, five HDACis (vorinostat, belinostat, romidepsin, panobinostat, and chidamide) have been clinically approved for the treatment of specific haematologic cancers (Manal et al., 2016). Further, several other small molecule HDACis are being explored for the treatment of a variety of haematological malignancies as well as solid tumors (Cui et al., 2022; He et al., 2022; M et al., 2022; Maccallini et al., 2022; Zhou et al., 2021). It is known that the clinical efficiency of the reported HDACis is known to be limited in haematologic tumors and also has a poor manifestation in solid tumors as there are no clinically approved HDACis for the treatment of solid tumors (Kim and Bae, 2011; Manal et al., 2016). Major limitations of the existing HDACis in solid tumors such as breast cancer, and colorectal cancer might be poor pharmacokinetic profile and less metabolic stability of the molecules (Cui et al., 2022; Maccallini et al., 2022; Rahbari et al., 2022; Zhou et al., 2021). Moreover, because of their non-specificity against different HDAC isoforms, the treatment with HDACis may often lead to several adverse effects and dose-related toxicities. Therefore, identifying and developing isoform-selective HDAC inhibitors with improved metabolic stability and pharmacokinetic profile has been the main objective of researchers in this area of epigenetic drug discovery.

HDAC3, a class I HDAC isoform, is well known to be involved in various phases of breast cancer development. HDAC3 overexpression leads to various stages of disease progression such as proliferation, apoptosis, angiogenesis, cell cycle regulation, and metastasis (Rahbari et al., 2022). Higher levels of HDAC3 expression were found particularly in TNBCs than non-TNBCs (Bianchini et al., 2022; Hanigan et al., 2017; Kwak

Chapter 4: Pyrazino hydrazides as HDAC3 selective inhibitors

et al., 2019). Literature reports established the key role of HDAC3 in various pathways where HDAC3 selective inhibition or knockdown led to the upregulated expression of p53 acetylation, enhanced p21 mRNA levels leading to cell cycle arrest, and eventually leading to apoptosis (Park et al., 2020; Yang et al., 2018). HDAC3 expression was found to be linked to cancer stem cell homeostasis by increased β -catenin expression via Akt/ GSK3 β pathway (Hsieh et al., 2017). HDAC3 inhibition or knockdown using *siRNAs* led to reduced Err α (estrogen-related receptor alpha) mRNA protein levels and stability leading to decreased proliferation in breast cancer cells (Oie et al., 2013; S. Yu et al., 2020). Many other recent reports using HDAC3 selective inhibitors have established the critical role of HDAC3 in the *in vitro* as well as *in vivo* models of breast cancer (Adhikari et al., 2021; Hanigan et al., 2017; Kwak et al., 2019; Rahbari et al., 2022; Su et al., 2021; Wei et al., n.d.; Yang et al., 2018). The structure and regulatory mechanisms of HDAC3 are well established and therefore, the discovery and development of selective HDAC3 inhibitors have become the most promising therapeutic strategy against various cancers (Watson et al., 2012).

The general pharmacophoric structure of the reported HDACis consists of a cap region, a linker region, and a zinc-binding group (ZBG) (Adhikari et al., 2018). Based on the chemical motif of ZBG that binds to the active catalytic site of the HDAC enzymes, HDACis have been classified into four major classes, such as hydroxamates, benzamides, cyclic tetrapeptides, and short-chain fatty acids, but recently several other ZBGs have been identified like phenols, thiols, hydrazides, etc (Chen et al., 2019; X. Luo et al., 2021; Melesina et al., 2021; Wagner et al., 2013; Yue et al., 2022; Zhang et al., 2018). Most of the HDACis with hydroxamates as the ZBGs are *pan*-HDACis with several off-target effects and poor bioavailability (Shah, 2019). On the other hand, HDACis with benzamides as ZBG were widely reported as somewhat specific HDACis and many of them have been

Chapter 4: Pyrazino hydrazides as HDAC3 selective inhibitors

studied preclinically. Unfortunately, none of them made it to the clinic so far, which may be owing to their poor pharmacokinetic profile and cardiotoxicity (Balasubramanian et al., 2009; Chen et al., 2009; Dokmanovic et al., 2007; Thomas et al., 2008). Therefore, there is an unmet need to identify highly specific HDACis with potent inhibitory activities possessing improved bioavailability and metabolic stability, particularly for the treatment of solid tumors. In this direction, recently HDACis with hydrazide ZBG have been reported to be the new-generation HDACis with high specificity as well as potency along with improved pharmacokinetic profile and *in vivo* antitumor potency exerting less off-target effects (Jiang et al., 2022; Li et al., 2020; Mahmud and Liao, 2015; McClure et al., 2016, 2017; Wang et al., 2015). Our group recently has reported a promising HDAC3 inhibitor, **4e**, with hydrazide as ZBG possessing HDAC3 inhibitory activity at the nanomolar level (HDAC3 IC₅₀ = 15.41 nM) and displaying significant antitumor potency *in vivo* in a 4T1-Luc tumor-bearing mouse model (Pulya et al., 2022). With those encouraging results, we now propose that modification in either cap and linker region of the reported lead molecule might offer improved HDAC3 selectivity and potency with improved druggable properties. With the established role of HDAC3 in breast cancer and its higher levels of expression in TNBCs, specific HDAC3 inhibition could provide targeted treatment for breast cancer, particularly TNBCs (Bianchini et al., 2022; Maccallini et al., 2022; Rahbari et al., 2022).

In this chapter, we have discussed and reported the design, synthesis, and biological evaluation of a small library of 20 molecules with a *pyrazino*-hydrazide scaffold having different modifications in the cap region and either *n*-butyl or *n*-propyl hydrazide as the ZBG. In this series, pyrazine has been included as the linker scaffold owing to its more drug-likeness nature and a high potential for protein interactions (Juhás and Zitko, 2020). We performed the *in vitro* biochemical HDAC enzyme inhibition assay for assessing their HDAC isoform inhibitory potency and selectivity. Further, all these compounds were tested

Chapter 4: Pyrazino hydrazides as HDAC3 selective inhibitors

for their *in vitro* cytotoxicity profiling against various subtypes of breast cancer cell lines and also studied their selectivity over normal human cell lines. The identified lead compound **4i** was then subjected to its detailed *in vitro* and *in vivo* biological evaluation. Further, compound **4i** was also studied for its chemosensitizing properties in chemotherapy (oxaliplatin) resistant MDA-MB-231 cells *in vitro*. Again, compound **4i** was subjected to *in vitro* metabolic stability assessment using rat liver microsomes as well as *in vivo* pharmacokinetic analysis. Lastly, the *in vivo* antitumor efficacy of compound **4i** was also assessed in the 4T1-Luc tumor xenograft mice model followed by rigorous mechanistic and immunohistochemical analysis of the tumor tissue.

4.2. RESULTS AND DISCUSSION

4.2.1. Design and the synthesis of the novel pyrazino-hydrazide derivatives as HDAC3 inhibitors.

In our quest of identifying selective and potent HDAC i s, so far, we have reported a few series of small molecule benzamides with preferential selectivity towards HDAC3 (Hamoud et al., 2020; Pulya et al., 2021; Routholla et al., 2021a, 2021b; Trivedi et al., 2018). Among those series of molecules, the lead compounds **PT3**, **5e**, **5f**, **11a**, and **12b** (**Figure 4.1**) with different cap groups have exhibited promising HDAC3 selective inhibition (Hamoud et al., 2020; Pulya et al., 2021; Routholla et al., 2021a, 2021b; Trivedi et al., 2018). Further, in this direction we have also recently reported a series of highly potent and selective HDAC3 inhibitors with hydrazide as ZBG of which, the lead compound **4e** (Pulya et al., 2022) has shown excellent HDAC3 selective inhibition at nanomolar potency (HDAC3 IC₅₀ = 15.41 nM) and potent *in vivo* antitumor potential when compared to the reference compound **UF010**, (Wang et al., 2015) a class I selective HDAC inhibitor. So far, compounds bearing hydrazide as ZBG were reported to be highly potent HDAC i s with preferential selectivity towards class I HDAC isoforms (Jiang et al., 2022;

Chapter 4: Pyrazino hydrazides as HDAC3 selective inhibitors

Li et al., 2020; McClure et al., 2016; Wang et al., 2015). Our recent report with benzoyl hydrazide scaffold exhibited excellent selectivity and potency at the nM level and also displayed promising *in vitro* and *in vivo* antitumor potential against the 4T1-Luc cell line (Pulya et al., 2022). In this direction, we further envisioned exploring hydrazide as ZBG with different modifications in the cap group as well as the linker region. This present work discloses the design and synthesis of novel pyrazino-hydrazide compounds employing a hybrid structure strategy. Keeping intact, the basic pharmacophore model of HDACis consisting of a cap region, linker, and ZBG, this new series of compounds was designed from the lead compounds reported previously by our group. **BG-45**, (Minami et al., 2014) a selective small molecule HDAC3 inhibitor with pyrazino-benzamide scaffold is the core of our design. Pyrazine fragment due to its heteroaromatic nature is capable of possessing several interactions with proteins, which makes it a potential aromatic isostere of biological importance (Juhás and Zitko, 2020). The introduction of a pyrazine fragment into the pharmacophoric structure of HDACis might lead to more metabolically stable compounds with improved pharmacokinetics (Subbaiah and Meanwell, 2021). We started our design by replacing the benzamide of **BG-45** with substituted hydrazide as the ZBG. Our next step was to introduce the amine group at the *para* position of the pyrazine moiety. We further started incorporating various substitutions at the *para*-amino group such as acetyl, aryl, aroyl, and also a few heteroaryl groups along with substituted hydrazide with *n*-butyl or *n*-propyl alkyl carbon chain as ZBG. For understanding the effect of the cap group, we strategically incorporated cap groups from our previous lead compounds into this design, such as the benzyl group from **PT3**, (Pulya et al., 2021) indole and quinoline groups from **5e**, **5f**, **11a**, and **12b** (Routholla et al., 2021a, 2021b) respectively, and the aniline group from **4e** (Pulya et al., 2022) along with few others cap groups such as naphthalene, piperidine, and *p*-methoxy benzylamine. With this design, we have synthesized and studied

Chapter 4: Pyrazino hydrazides as HDAC3 selective inhibitors

in detail the SAR of the series of 20 compounds in this report. The design of the pyrazino-hydrazide series of compounds including the inhibitory activity (IC_{50}) values of our previous lead compounds is represented in **Figure 4.1**.

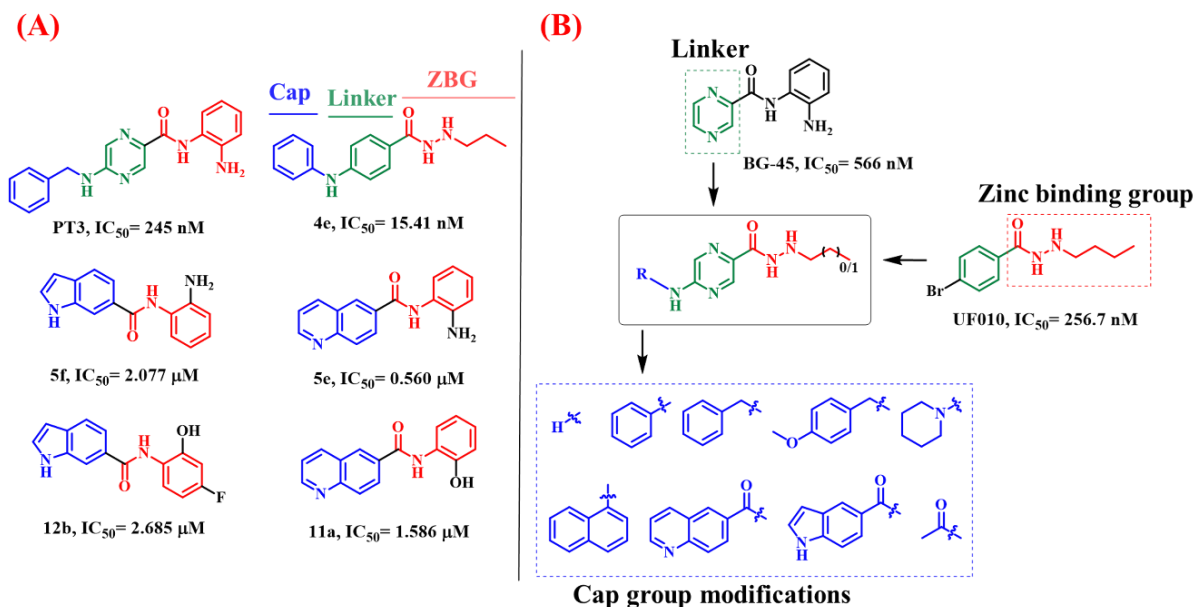
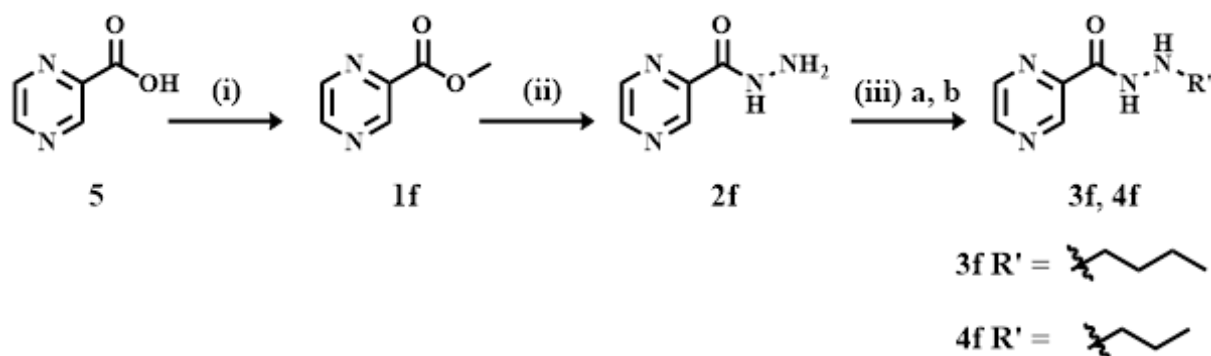


Figure 4.1. (A) Structures of the lead compounds of HDAC3 selective inhibitors previously reported from our group and their HDAC3 IC_{50} values; (B) Design of the pyrazino-hydrazide series of compounds.

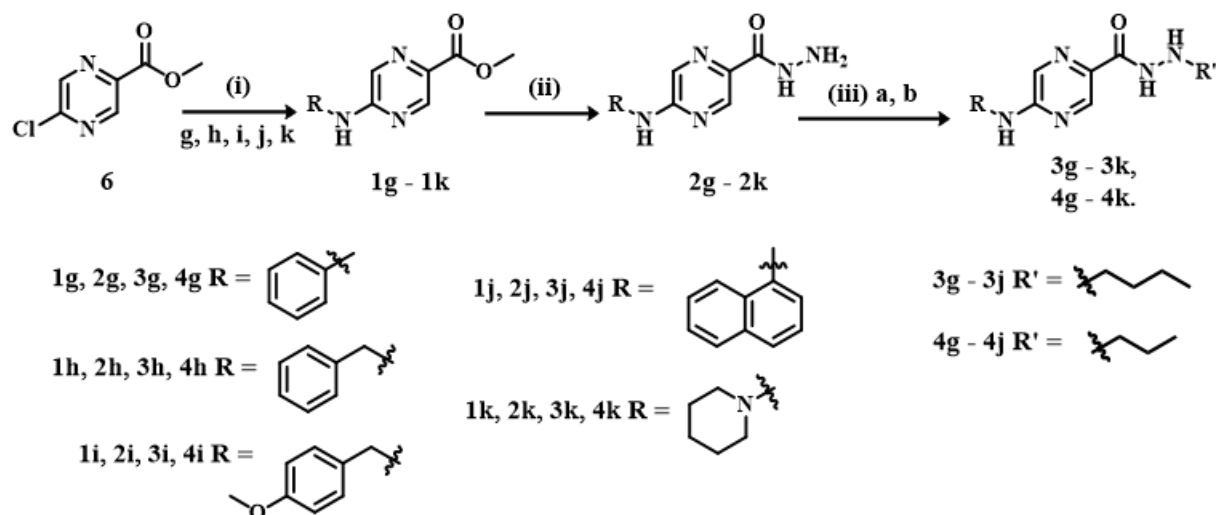
4.2.2. Synthesis of the designed compounds

Scheme 4.1 and **scheme 4.2** represents the synthesis of the final compounds **3f** to **3k** and **4f** to **4k**. The compounds **1f** to **1k** were synthesized from the starting materials directly purchased using the reaction conditions specified in **schemes 4.1** and **4.2**. Further reaction with an excess of hydrazine monohydrate under the reflux conditions gave the corresponding hydrazides **2f** to **2k**. The final compound synthesis involved a two-step reaction. First, the hydrazides were reacted with either butyraldehyde or propionaldehyde in the presence of $MgSO_4$ and ethanol. The crude intermediate was then subjected to imine reduction to obtain the final compounds **3f** to **3k** and **4f** to **4k**.

Chapter 4: Pyrazino hydrazides as HDAC3 selective inhibitors



Scheme 4.1. Reagents and conditions: (i) Conc. H₂SO₄, MeOH, 3 h; (ii) NH₂NH₂.H₂O, MeOH, 6 h, reflux; (iii) (a) propionaldehyde (or) butyraldehyde, MgSO₄, EtOH, 2 – 3 h, rt; (b) NaBH₃CN, MeOH, pH 5, 30 min, rt.

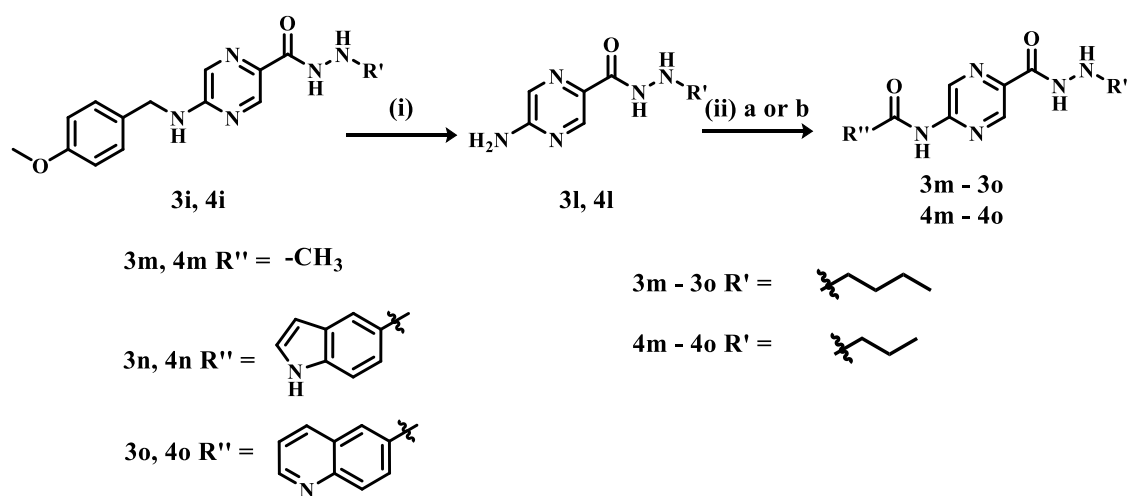


Scheme 4.2. Reagents and conditions: (i) (g) aniline, PTSA, 1,4-dioxane, 110 °C, 12 h, reflux; (h) benzylamine, PTSA, 1,4-dioxane, 110 °C, 12 h, reflux; (i) *p*-methoxybenzylamine, THF, 12 h, reflux; (j) naphthyl-1-amine, PTSA, 1,4-dioxane, 110 °C, 18 h, reflux; (k) piperidine, DIPEA, DMF, 5 h, rt; (ii) NH₂NH₂.H₂O, MeOH, 6 h, reflux; (iii) (a) propionaldehyde (or) butyraldehyde, MgSO₄, EtOH, 2 – 3 h, rt; (b) NaBH₃CN, MeOH, pH 5, 10 min, rt.

Scheme 4.3 depicts the synthesis of the final compounds **3i** to **3o** and **4i** to **4o**. For this purpose, the compounds **3i** and **4i** were subjected to the deprotection of the *p*-methoxy

Chapter 4: Pyrazino hydrazides as HDAC3 selective inhibitors

benzyl group using trifluoroacetic acid under heating conditions at 60 °C for 2 h to obtain **3l** and **4l** respectively. Acetylation at the free amino group of **3l** and **4l** by acetyl chloride in the presence of triethylamine and dichloromethane for 5–6 h at room temperature gave us the compounds **3m** and **4m**. Further, the synthesis of the compounds **3n**, **3o**, **4n**, and **4o** were carried out by the EDC-HOBt acid-amine coupling reaction for the amide formation for 16 h at room temperature using **3l** and **4l** with the 5-indole and 6-quinoline carboxylic acids respectively as represented in the **Scheme 4.3**. The experimental procedures followed for the synthesis are described in the chemistry experimental section. All the final compounds including **UF010** were confirmed for their percentage of purity using HPLC/LC-MS analysis and were found to be >95% pure. The physicochemical characterization of the final compounds was carried out by ¹H, ¹³C NMR, LC-MS, and HRMS analysis. All the obtained spectral data are given in the supporting information file (**Spectra 4.1 – 4.111**).



Scheme 4.3. Reagents and conditions: (i) CF₃COOH, 60 °C, 2 h; (ii) (a) CH₃COCl, NEt₃, DCM, 3 – 5 h, rt; (b) indole-5-carboxylic acid or quinoline-6-carboxylic acid, EDC, HOBt, NEt₃, DCM, 16 h, 0 °C – rt.

4.2.3. HDAC isoform enzyme inhibition assay.

As a first step, all the synthesized compounds (**3f – 3o**, **4f – 4o**) were evaluated for their

Chapter 4: Pyrazino hydrazides as HDAC3 selective inhibitors

pan-HDAC inhibitory activity (HeLa nuclear extract) at 5 μ M concentration (**Figure 4.2**) followed by their HDAC3 inhibitory activity at 1 μ M concentration (**Figure 4.3**) as per the given protocol. (Pulya et al., 2022) It was interesting to note that all of these compounds provided better HDAC3 inhibition (% inhibition) compared to *pan*-HDAC inhibition (% inhibition). However, the reference molecule **UF010** yielded more or less similar % inhibition data for both *pan*-HDAC (58.06%) and HDAC3 (57.39%). Nevertheless, all these compounds (except compound **3f**) resulted in better HDAC3 inhibition (inhibitory activity range = 59.61% to 99.48%) than **UF010**. Therefore, it pointed out clearly that all these compounds exhibited potent and selective HDAC3 inhibitory patterns over *pan*-HDAC inhibition. Among these compounds, compounds **4g**, **3h**, **4h**, **3i**, **4i**, **4n**, and **4o** yielded more than 75% HDAC3 inhibition. Most of the other remaining compounds (**4f**, **3g**, **3j**, **4j**, **4k**, **3l**, **4l**, **4m**, **3n** and **3o**) showed more than 60% HDAC3 inhibition. The compounds with greater than 75% HDAC3 inhibition were further screened for their % HDAC1 and HDAC2 inhibition at 1 μ M concentration to assess their selectivity among class I HDACs (**Figure 4.4A and 4.4B, Table 4.1**). It was noticed that the compounds **4h**, **4i**, **4n**, and **4o** have exhibited less than 17% of HDAC1 and HDAC2 inhibition at 1 μ M conc. Further, the compounds **4i**, **4n**, and **4o** have exhibited more than 9% selectivity towards HDAC3 than HDAC1 and HDAC2 as per their % inhibition values. It also reflected the higher HDAC3 inhibitory potency of these compounds over HDAC1 and HDAC2. Subsequently, we have also assayed these compounds for their % inhibition values over HDAC4, HDAC5, HDAC6, and HDAC8 (**Figure 4.4C – F**). From the obtained % HDAC3 inhibitory activity results of the compounds, it can be inferred that compounds with various cap groups have exhibited better selectivity than the ones with no cap group attached (**3f** and **4f**). Further, the compounds containing benzylamine (**4h**), *p*-methoxy benzylamine (**4i**), 5-indolyl (**4n**), and 6-quinolinoyl (**4o**) in the cap region with *n*-propyl

Chapter 4: Pyrazino hydrazides as HDAC3 selective inhibitors

hydrazide group as ZBG exhibited better potency towards HDAC3 over HDAC1 and HDAC2 isoforms than the remaining compounds.

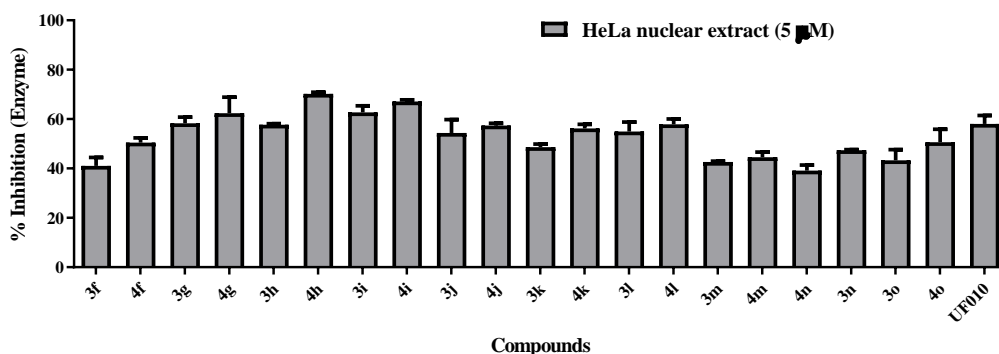


Figure 4.2. The graph represents the % inhibitory activity of the novel synthesized compounds for their *pan*-HDAC inhibitory activity. All novel compounds were screened at 5 μ M concentrations for HeLa nuclear extract enzyme. [Data represents mean \pm SD (n=2)].

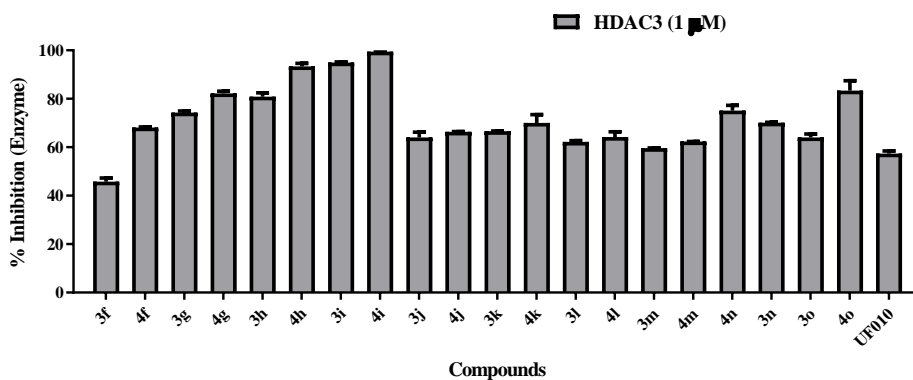


Figure 4.3. The graph represents the % inhibitory activity of the novel synthesized compounds for their HDAC3 inhibitory activity. All novel compounds were screened at 1 μ M concentrations for human recombinant HDAC3 enzyme. [Data represents mean \pm SD (n=2)].

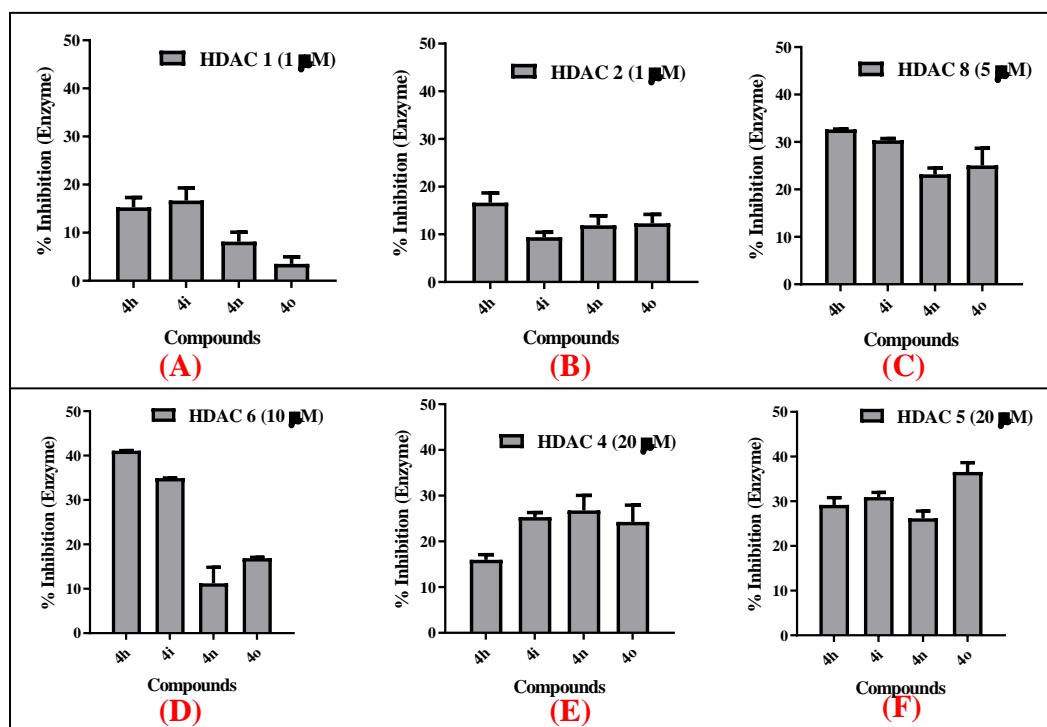


Figure 4.4. Graphs represent the % inhibitory activity of **4h**, **4i**, **4n** and **4o** compounds on human recombinant (A) HDAC1 isozyme with 1 μM compound concentration; (B) HDAC2 isozyme with 1 μM compound concentration; (C) HDAC8 isozyme with 5 μM compound concentration; (D) HDAC6 isozyme with 10 μM compound concentration; (E) HDAC4 isozyme with 20 μM compound concentration; (F) HDAC5 isozyme with 20 μM compound concentration. The initial screening was done as per the vendor's recommended concentration. [Data represents mean ± SD (n=2)].

Table 4.1: % inhibition values of the compounds at 5 μM (for HeLa nuclear extract) and 1 μM (for HDAC1, HDAC2 and HDAC3) concentration of the tested compounds:

Cpd No	<i>pan</i> -HDAC (5 μM)	HDA C3 (1 μM)	HDAC1 (1 μM)	HDA C2 (1 μM)
3f	41.08	45.8	ND	ND
4f	50.44	68.08	ND	ND
3g	58.29	74.25	ND	ND
4g	62.41	82.22	ND	ND
3h	57.7	80.85	ND	ND
4h	70.18	93.4	15.25	16.65
3i	62.73	94.96	ND	ND

Chapter 4: Pyrazino hydrazides as HDAC3 selective inhibitors

4i	67.09	99.48	16.69	9.39
3j	54.36	64.05	ND	ND
4j	57.36	66.33	ND	ND
3k	48.59	66.6	ND	ND
4k	56.22	70.01	ND	ND
3l	54.98	62.18	ND	ND
4l	57.85	64.2	ND	ND
3m	42.65	59.61	ND	ND
4m	44.53	62.35	ND	ND
4n	39.13	75.09	8.14	11.88
3n	47.37	70.09	ND	ND
3o	43.31	64.02	ND	ND
4o	50.58	83.36	3.52	12.31
UF010	58.06	57.39	ND	ND

[Data represents mean \pm SD (n=2)].

Among these compounds, the best potent HDAC3 inhibitor (**4i**) was further subjected to judge for its HDAC3 selectivity over other class I and class II HDAC isoforms. It was interesting to note that compound **4i** exhibited maximum inhibitory potency against HDAC3 ($IC_{50} = 14$ nM) with a minimum of 121-fold selectivity over HDAC1 ($IC_{50} = 1983$ nM) and HDAC2 ($IC_{50} = 1696$ nM) as well as sparing other HDACs including HDAC8 ($IC_{50} = 10744$ nM), HDAC6 ($IC_{50} = 25930$ nM), and HDAC4 ($IC_{50} > 20000$ nM) and HDAC5 ($IC_{50} > 20000$ nM). It was also interesting to note that compound **4i** was a better potent and selective HDAC3 inhibitor compared to the reference HDAC3 inhibitors namely **UF010** ($IC_{50} = 256.7$ nM),(Pulya et al., 2022) **BG-45** ($IC_{50} = 566$ nM)(Minami et al., 2014) and **PT3** ($IC_{50} = 245$ nM).(Pulya et al., 2021) It was noteworthy that compound **4i** resulted in a minimum of 17.5-fold better HDAC3 inhibitory potency than the reference HDAC3 inhibitors namely **UF010**, **BG-45** and **PT3**. The dose-response curves obtained from the analysis of IC_{50} values of **4i**, **BG-45**, **UF010**, and **PT3** have been represented in **Figure 4.5** and the values are tabulated in **Table 4.2**. Altogether, this series of pyrazino-hydrazide compounds with various cap groups attached to the amine at the *para* position of the

Chapter 4: Pyrazino hydrazides as HDAC3 selective inhibitors

pyrazine moiety has demonstrated an increase in the selectivity as well as potency towards HDAC3 over other HDAC isoforms tested.

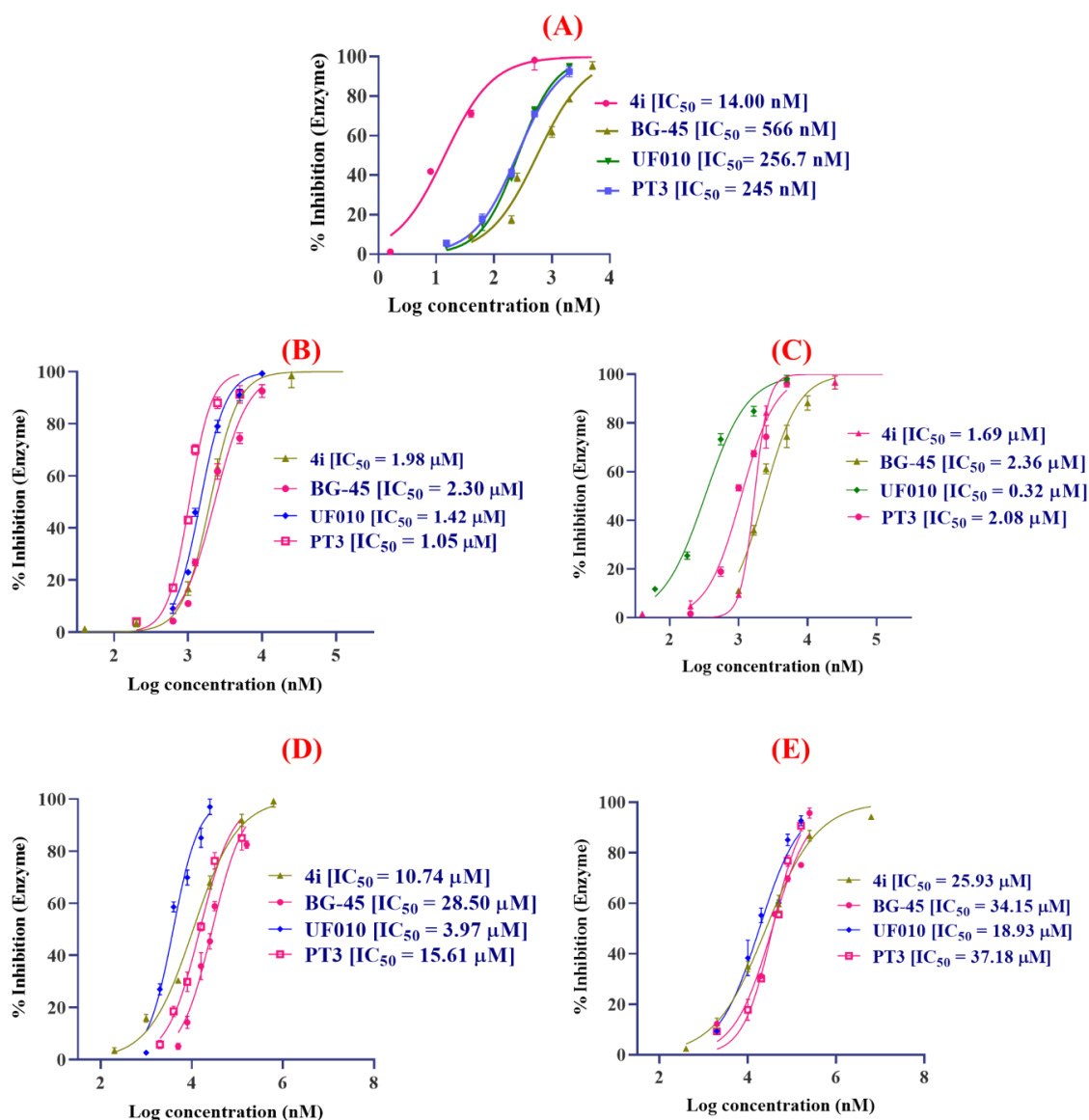


Figure 4.5. IC₅₀ curves of the compounds **4i**, **BG-45**, **UF010**, and **PT3** when assayed with the human recombinant HDAC isozymes of **(A)** HDAC3; **(B)** HDAC1; **(C)** HDAC2; **(D)** HDAC8; and **(E)** HDAC6. [The experiment was carried out as per the Vendor's protocol given in their respective recombinant HDAC assay kits. The compounds were tested at the varied concentration range of 0.005 μM – 125 μM in duplicate. The IC₅₀ values were determined with the help of the nonlinear regression analysis method by GraphPad Prism™ version 8.0.1. Data represent mean ± SD (n = 2)].

Chapter 4: Pyrazino hydrazides as HDAC3 selective inhibitors

Table 4.2. HDAC inhibitory potency of the lead compound **4i** against representative human recombinant class I and class II HDACs along with the previously reported reference molecule **UF010** (Pulya et al., 2022) and HDAC3 selective inhibitors, **BG-45** (Minami et al., 2014) and **PT3**. (Pulya et al., 2021)

HDAC isoforms inhibitory potency (IC ₅₀ values in nM)							
HDAC class	Class I				Class IIa		Class IIb
Isoforms	HDAC1	HDAC2	HDAC3	HDAC8	HDAC4	HDAC5	HDAC6
4i	1983 ±	1696 ±	14.00 ±	10744 ±	>20000	>20000	25930 ±
	19.68	16.87	1.68	145.3			478.2
UF010^b	1420 ±	322 ±	256.7 ±	3970 ±	>20000	>20000	18935 ±
	77.9	39.5	28.6	99.7			143
BG-45^c	2302 ±	2362 ±	566 ± 12	28501 ±	ND	ND	34152 ±
	62.3	156		198			123
PT3^d	1053 ±	2083 ±	245 ± 16	15613 ±	ND	ND	37182 ±
	98	129		165			268

^aIC₅₀ values are represented as the mean of duplicate values ± standard deviation (n = 2).

^{b, c} and ^d; values previously reported from our lab.

4.2.4. *In vitro* cytotoxicity profile over breast cancer cell lines and normal human cells.

As the compounds were found to be more HDAC3 selective and potent in terms of their HDAC3 enzyme inhibition profile, we further performed the *in vitro* cytotoxicity screening and their selectivity towards different subtypes of breast cancer cell lines over normal human cell lines including normal breast cell line MCF-10A, and the results are tabulated in **Table 4.3**.

Table 4.3. IC₅₀ (μM) values of synthesized compounds against various breast cancer cells and normal HEK-293, MCF-10A and HCEC cells.

<i>In vitro</i> cytotoxicity (IC ₅₀ values in μM)							
Cpd ^a	MCF-7	4T1	MDA-MB-231	MDA-MB-453	MCF-10A	HEK-293	HCEC

Chapter 4: Pyrazino hydrazides as HDAC3 selective inhibitors

3f	2.44 ± 0.56	0.88 ± 0.06	1.17 ± 0.03	2.52 ± 0.13	103.2 ± 2.1	100.7 ± 15.2	175.4 ± 24.5
4f	1.39 ± 0.27	1.14 ± 0.08	1.07 ± 0.08	2.49 ± 0.17	116.9 ± 1.2	134.5 ± 11.3	128 ± 10.6
3g	1.14 ± 0.12	2.17 ± 0.35	1.91 ± 0.11	5.18 ± 0.29	137.7 ± 0.9	207.4 ± 37.4	180 ± 44.6
4g	3.28 ± 0.98	2.76 ± 0.65	1.88 ± 0.11	5.44 ± 0.25	205 ± 3.1	217.6 ± 73.2	195.8 ± 22.5
3h	2.16 ± 0.09	1.60 ± 0.15	1.32 ± 0.09	3.33 ± 0.22	112.8 ± 1.7	133.1 ± 16.5	129.2 ± 26.5
4h	1.12 ± 0.07	1.15 ± 0.09	1.23 ± 0.07	2.76 ± 0.19	113.7 ± 0.6	110.3 ± 10.5	139.8 ± 16.9
3i	2.59 ± 0.69	0.93 ± 0.17	0.97 ± 0.05	2.68 ± 0.22	109.4 ± 1.3	107.2 ± 9.87	137.5 ± 11.6
4i	0.95 ± 0.08	0.55 ± 0.03	0.74 ± 0.04	1.72 ± 0.11	211.9 ± 4.5	238.7 ± 21.5	211.8 ± 15.6
3j	4.16 ± 0.98	0.98 ± 0.07	2.02 ± 0.19	4.67 ± 0.35	113.9 ± 1.6	188.9 ± 15.9	150.7 ± 32.5
4j	1.51 ± 0.22	0.94 ± 0.08	1.74 ± 0.11	2.89 ± 0.24	112 ± 6.1	115.9 ± 8.9	126.2 ± 5.8
3k	1.87 ± 0.05	3.86 ± 0.57	2.93 ± 0.12	6.79 ± 0.12	104.5 ± 2.6	101.3 ± 6.98	118.9 ± 12.6
4k	2.44 ± 0.17	0.89 ± 0.06	1.32 ± 0.11	2.87 ± 0.11	109.6 ± 1.7	117.6 ± 10.8	163.1 ± 16.2
3l	1.81 ± 0.19	1.27 ± 0.10	1.25 ± 0.09	3.33 ± 0.16	118.2 ± 2.3	133.2 ± 11.2	215 ± 15
4l	0.99 ± 0.05	1.08 ± 0.12	0.88 ± 0.03	2.43 ± 0.11	138.8 ± 5.8	141.4 ± 5.9	220.1 ± 5.6
3m	1.65 ± 0.07	2.74 ± 0.16	3.05 ± 0.22	7.94 ± 0.46	105.6 ± 0.8	228.8 ± 20.9	186.7 ± 11.8
4m	1.21 ± 0.11	0.92 ± 0.26	0.97 ± 0.07	1.93 ± 0.10	142 ± 4.2	118.5 ± 15.6	163.6 ± 40.8
3n	2.44 ± 0.11	1.43 ± 0.16	1.69 ± 0.17	4.05 ± 0.36	105.3 ± 0.7	107.2 ± 7.3	129.5 ± 12.8
4n	2.03 ± 0.39	0.71 ± 0.11	0.92 ± 0.02	2.19 ± 0.12	124.8 ± 3.5	137.9 ± 10.9	180.1 ± 7.6
3o	1.36 ± 0.25	2.92 ± 0.29	2.84 ± 0.23	4.92 ± 0.31	219.9 ± 1.7	264.3 ± 16.8	234.2 ± 48.9
4o	1.01 ± 0.12	0.59 ± 0.09	0.87 ± 0.02	1.82 ± 0.27	140.3 ± 1.9	126.1 ± 36.8	130.7 ± 40.3
UF010	15.36 ± 1.92	7.72 ± 0.58	24.74 ± 1.01	25.34 ± 5.12	99.3 ± 0.5	98.52 ± 11.9	95.4 ± 6.98

^aCompound number; IC₅₀ values were determined by the MTT assay procedure and are calculated as the mean (from the same cultures) ± the standard deviation (n = 3).

Chapter 4: Pyrazino hydrazides as HDAC3 selective inhibitors

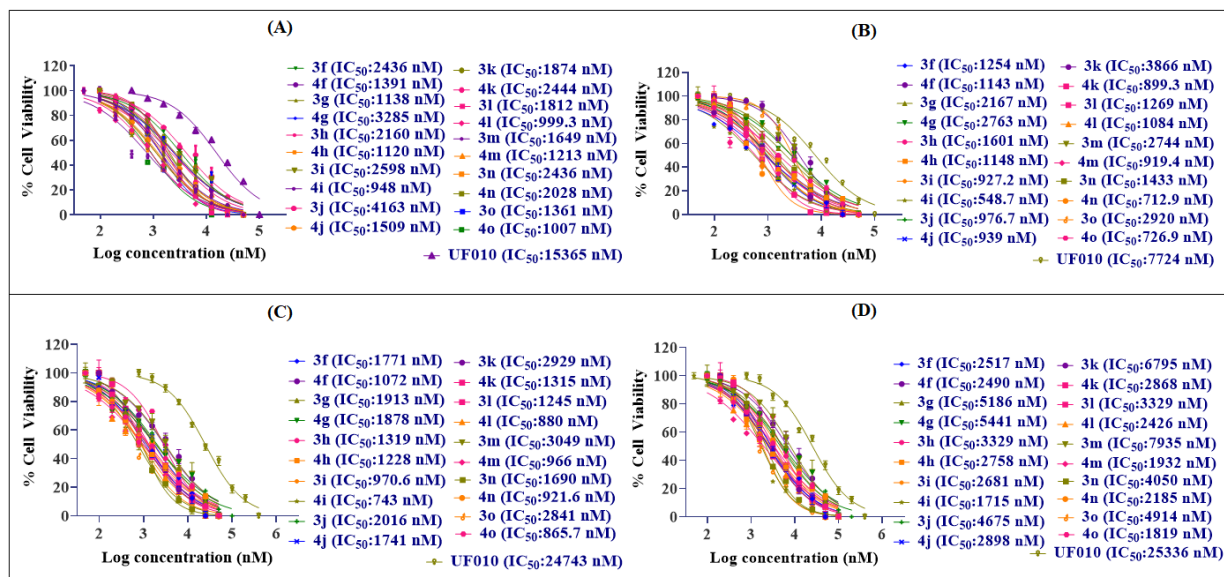


Figure 4.6. Graphs (A), (B), (C), (D) represents the IC₅₀ results of the synthesized compounds by MTT assay against MCF-7, 4T1, MDA-MB-231 and MDA-MB-453 cells respectively. Cells were treated with the compounds at concentration range of 0.048 μ M to 50 μ M (n=3) for 72 h. Data represents mean \pm SD.

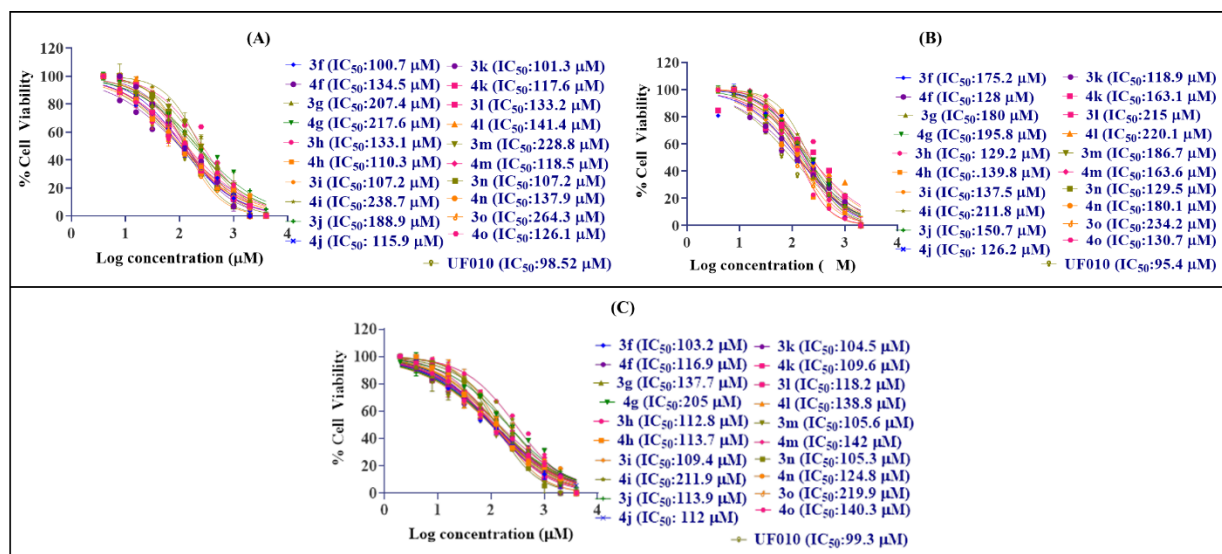


Figure 4.7. Graphs (A), (B) and (C) represents the IC₅₀ results of all the synthesized compounds by MTT assay against normal human cells (HEK-293), human corneal epithelial cells (HCEC) and normal human breast cells (MCF-10A) respectively, and here cells were treated with the compounds at the concentration range from 1.95 μ M to 4000 μ M (n=3) for 72 h. Data represents mean \pm SD.

Chapter 4: Pyrazino hydrazides as HDAC3 selective inhibitors

Several studies indicated the role of HDAC3 in the initiation and progression of various cancers and other malignancies and related disorders.(Amin et al., 2019; Hsieh et al., 2017; Ma et al., 2015; McLeod et al., 2018; Minami et al., 2014; Spurling et al., 2008) In particular, the role of HDAC3 in the case of breast cancer has been widely studied and a high level of HDAC3 is well correlated with various events in breast tumors.(Cui et al., 2018; Hsieh et al., 2017; Rahbari et al., 2022; Su et al., 2021) Thus, HDAC3 inhibition could be considered a promising target in breast cancer therapy. HDAC3 is more prominently overexpressed in TNBC cells than non-TNBC cells as per the reported literature.(Hanigan et al., 2017; Kwak et al., 2019) Therefore, we studied the synthesized compounds in breast cancer cell lines of various subtypes namely MCF-7 (Luminal A cell line), 4T1 (murine TNBC cell line), MDA-MB-231 (human TNBC - claudin-low cell line) and MDA-MB-453 (HER2+ cell line). We further evaluated their selectivity towards breast cancer cell lines over normal human cell lines such as MCF-10A (normal human breast cells), HEK-293 (human embryonic kidney-293) and HCEC (human corneal epithelial cells). The corresponding dose-response curves are represented in **Figure 4.6** and **Figure 4.7**. All these hydrazides were significantly cytotoxic (activity in lower μM) against the tested breast cancer cell lines and relatively less cytotoxic against normal cell lines (activity in higher μM). It was also observed from the IC_{50} values, that most of these compounds were more cytotoxic towards both murine and human TNBC cell lines 4T1 and MDA-MB-231 respectively than the MCF-7 cell line. Interestingly, all these compounds (except compounds **3k**, **3m**, and **3n**) exhibited a minimum of 40-fold selectivity towards breast cancer cell lines over normal human cell lines. All of these compounds exhibited better cytotoxic profile and higher selectivity towards breast cancer cell lines than the reference molecule **UF010**. It was also noticed that most of these compounds (like **3f**, **4f**, **3g**, **3h**, **4h**,

Chapter 4: Pyrazino hydrazides as HDAC3 selective inhibitors

4i, 4j, 4k, 3l, 4l, 4m, 3n, 4n, and **4o**) exhibited a lower IC₅₀ value (< 2.5 μM) against cancer cell lines MCF-7, 4T1, and MDA-MB-231. However, the remaining compounds (i.e., **4g, 3i, 3j, 3m, 3o**) exhibited comparatively lower cytotoxicity in the same breast cancer cell lines. Among these compounds, **4i**, the most potent and selective HDAC3 inhibitor was also the most cytotoxic (IC₅₀ value < 1 μM) and exhibited more than 286-fold selectivity towards cancer cell lines over normal cell lines and about 385-fold selectivity over normal breast cells (MCF-10A). Compound **4i** exhibited the IC₅₀ values of 950 nM, 550 nM and 741 nM against MCF-7, 4T1 and MDA-MB-231 cell lines. Apart from that, compounds **4l, 4m, 4n,** and **4o** exhibited a minimum of 60-fold selectivity towards breast cancer cell lines. It is interesting to note that, the most potent and selective compounds contain the propyl hydrazide moiety and also correlate well with their HDAC3 inhibitory activity. When compared with our recent report of benzoyl hydrazide HDAC3 inhibitors,(Pulya et al., 2022) this series of compounds with pyrazino-hydrazide scaffold exhibited better cytotoxicity profile. This might be attributed to the linker pyrazine which is known to possess better cellular penetration property due to its significant molecular interactions to proteins.(Juhás and Zitko, 2020) Overall, these results further suggest that selective HDAC3 inhibition might play a major role in breast cancer therapy.

4.2.5. Protein expression levels of various histone, apoptotic proliferative biomarkers by western blot analysis in vitro in 4T1 cells

Compound **4i** was found to be highly cytotoxic *in vitro*, particularly against 4T1 cells. We investigated the cellular acetylation levels of Ac-H3K9 and Ac-H4K12 induced by **4i** in comparison to the HDACis of different chemotypes such as **UF010** as a positive control, **BG-45** for the benzamide and **SAHA** for the hydroxamate chemical class of HDACis in the 4T1 cells following the treatment with 1 μM concentration *in vitro*. The obtained results as represented in the **Figure 4.8A**, indicated the significant upregulation of Ac-H3K9 and

Chapter 4: Pyrazino hydrazides as HDAC3 selective inhibitors

Ac-H4K12 by **4i** was much greater than that of **UF010**, **BG-45** and **SAHA** at the same dose. This signifies the excellent HDAC3 inhibitory potency of **4i** in cells. The induction of tumor cell death and the antiproliferative property has been linked to the therapeutic efficacy of HDACis. However, several intrinsic pathways such as activation of caspase cascade and increased levels of cytochrome *c* in the tumor cells are known to have a key role in regulating the antitumor effects of HDACis.⁸⁵ Therefore, we studied the protein expression levels of caspase-3, caspase-7, cleaved caspase-3 and cytochrome *c* in *in vitro* with **4i** and **UF010** (results represented in the **Figures 4.8B** and **4.9**) upon treatment of 4T1 cells in a dose-dependent manner at 500 nM and 2 μ M concentrations as per the protocol described in the experimental section. The results depicted in the **Figure 4.8B** for **4i** has clearly evidenced the elevated levels of cleaved caspase-3 and the released cytochrome *c* in a dose dependent manner in the cell lysate of **4i** treated 4T1 cells thus indicating apoptosis mediated cell death *in vitro*. Further, in order to assess the apoptosis activity *in vitro*, the quantitative analysis of caspases activity was performed using Apo-ONE® Homogeneous Caspase-3/7 Assay kit (Promega, USA) as per the protocol described in the experimental section. The compound **4i** and **UF010** were tested for their caspase3/7 activity in the 4T1 cells following the induction of apoptosis. Results are displayed in **Figure 4.10**. The obtained results demonstrated the significant increase in the caspase 3/7 activity in **4i** treated cells than **UF010** treated cells and control cells, which indicated the significant apoptosis induction in the cancer cells. Altogether, these results prove the *in vitro* anticancer potential of **4i**.

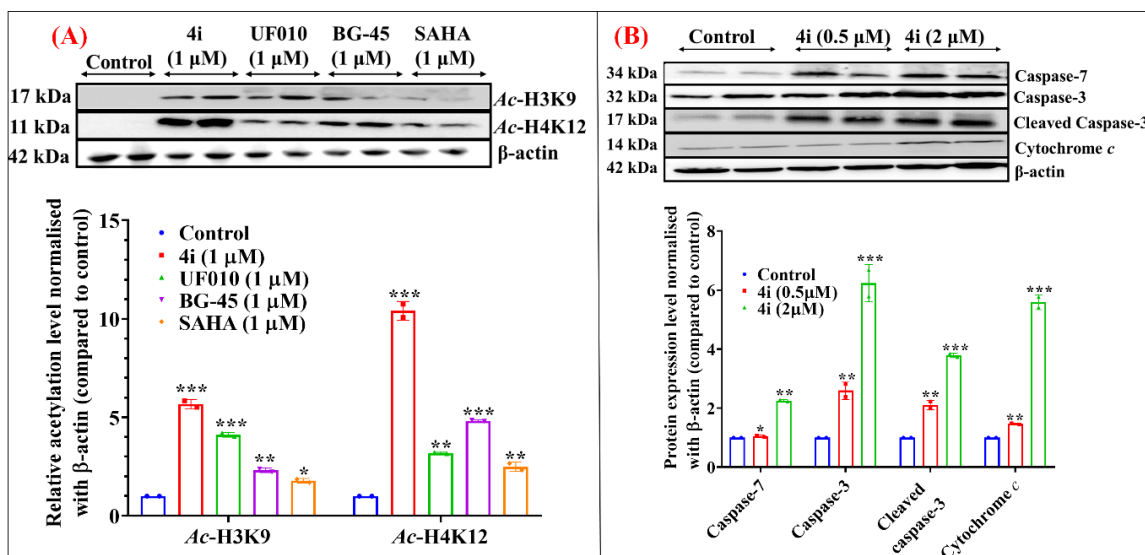


Figure 4.8. Western blot analysis of various histone biomarkers in the protein samples extracted from the cell lysates that is obtained from the 4T1 cells treated with control, **4i** (1 μ M), **UF010** (1 μ M), **BG-45** (1 μ M) and **SAHA** (1 μ M) for 72 h. The blots and the corresponding quantification of the blots were plotted as the graphs represented above. **(A)** Image representing the blots of *Ac-H3K9*, *Ac-H4K12* levels in the treated 4T1 cell lysate samples and the corresponding quantification plotted as a graph below; **(B)** Western blot analysis of various apoptotic biomarkers in the protein samples extracted from the cell lysates that is obtained from the 4T1 cells treated with control, **4i** (500 nM, 2 μ M); Image representing the blots of caspase-7, caspase-3, cleaved caspase-3 and cytochrome *c* levels in the treated 4T1 cell lysate samples and the corresponding quantification plotted as a graph below. β -actin was used as an internal control and the graphs were plotted by normalizing the protein expression levels compared to the control group values analyzed in *Image J* software. Significance was analyzed using one-way ANOVA analysis and the graphs were plotted in GraphPad Prism™ version 8.0.1. Data represents the values of mean \pm the standard error of the mean (SEM, n=2); *p < 0.05, **p < 0.01, ***p < 0.001, ****p < 0.0001, significantly different from the control group.

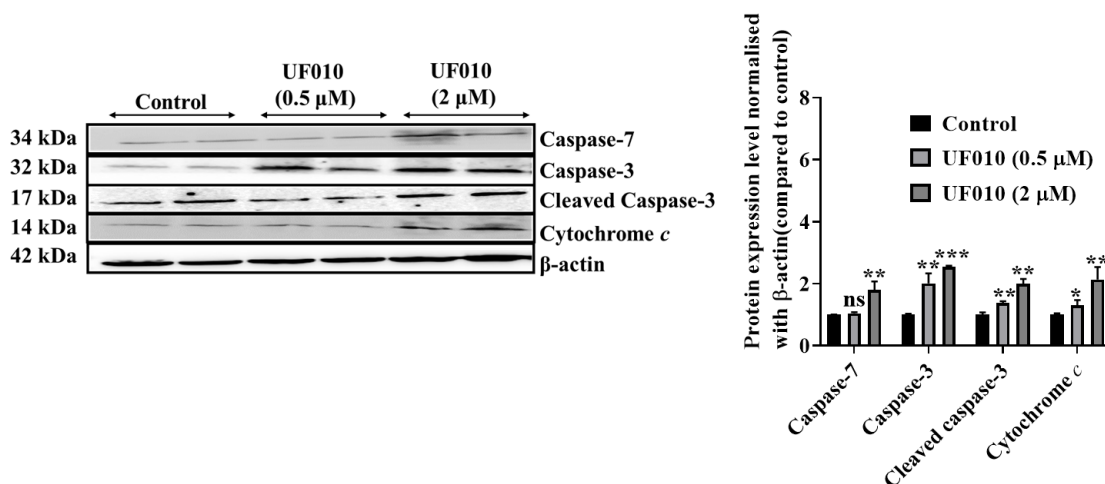


Figure 4.9. Image representing the blots of caspase-7, caspase-3, cleaved caspase-3 and cytochrome *c* levels in the **UF010** treated 4T1 cell lysate samples and the corresponding quantification plotted as a graph below. β-actin was used as an internal control and the graphs were plotted by normalizing the protein expression levels compared to the control group values analyzed in *Image J* software. Significance was analyzed using one-way ANOVA analysis and the graphs were plotted in GraphPad Prism™ version 8.0.1. Data represents the values of mean ± the standard error of the mean (SEM);***p < 0.001 significantly different from the control group.

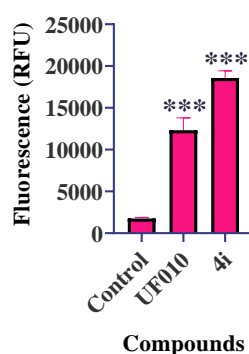


Figure 4.10. Caspase3/7 activation levels of **4i** and **UF010** in 4T1 cells compared to control. Compound treatment shows significant difference from control indicates increased apoptosis in cells. Significance was analyzed using one-way ANOVA analysis and the

Chapter 4: Pyrazino hydrazides as HDAC3 selective inhibitors

graphs were plotted in GraphPad Prism™ version 8.0.1. Data represents mean \pm SD (n=2); ***p < 0.001, significantly different from the control group.

4.2.6. **4i induced apoptosis and caused G2/M cell cycle arrest in TNBC cells.**

The *in vitro* cytotoxicity results against different subtypes of breast cancer cell lines suggested that the pyrazino-hydrazide series of compounds exhibited higher potency in the TNBC cell lines, 4T1 and MDA-MB-231. Overexpression of HDAC3 is known to be directly correlated with various events such as apoptotic cell death, cell cycle regulation, and metastasis that finally resulted in significant antiproliferative activity in breast cancer tumors.(Cui et al., 2018; Park et al., 2020; Rahbari et al., 2022; Singh et al., 2005) Hence, we performed apoptosis, cell cycle analysis, and nuclear staining assay of the lead compound **4i** and **UF010** (reference) in both 4T1 and MDA-MB-231 cells at their respective *in vitro* IC₅₀ values and the samples were processed as per the described experimental protocol.(Pulya et al., 2022) The results obtained as displayed in **Figure 4.11 and 4.12**). Further, to assess the apoptotic percentage and cell cycle arrest at different concentrations, we treated the 4T1 cells at three different concentrations of **4i** (C1: 110 nM, C2: 550 nM, C3: 2.75 μ M) and **UF010** (C1: 1.54 μ M, C2: 7.72 μ M, C3: 38.6 μ M) for 72 h. The results obtained as displayed in **Figure 4.13A and 4.13B**, showed significant apoptosis of 36.8%, 63.4% and 94.6% in **4i** treated samples and 30.4%, 46.9% and 82.7% in **UF010** treated samples at their respective three concentrations of C1, C2 and C3. Cell cycle analysis results as displayed in **Figure 4.13C and 4.13D, Tables 4.4 and 4.5**, indicated the G2/M phase cell cycle arrest with increased cell population in the G2/M phase for **4i** (38.8%, 52.6% and 63.4%). Whereas in case of **UF010**, at the lower concentration of C1, G1 phase cell cycle arrest was observed with increased cell population (50.4% of G1) and at higher concentrations, G2/M phase arrest was seen (41.4% and 52.3%).

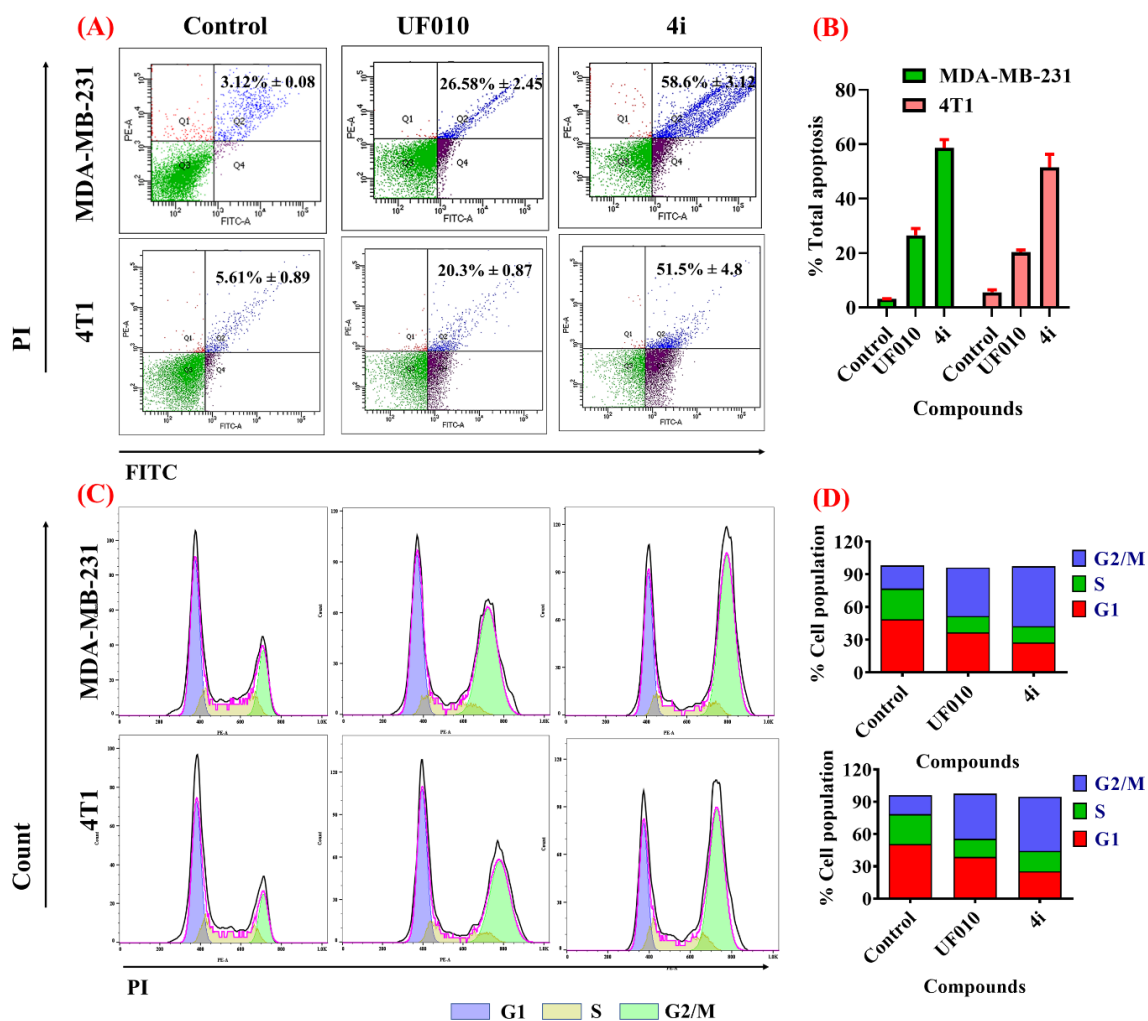


Figure 4.11. Different cultures of MDA-MB-231 and 4T1 cells were treated with the *in vitro* IC₅₀ concentrations of **UF010** and **4i** in the respective cell lines along with **control** for 72 h. **(A)** Annexin V/PI apoptosis assay by flow cytometer (BD Aria III) ® (where X and Y-axis represent the intensities of annexin V and propidium iodide respectively); **(B)** Graph representing the percentage of the total apoptotic population in MDA-MB-231 and 4T1 cells; **(C)** Cell cycle analysis by Flow cytometer (BD Aria III) ®; **(D)** Graph representing the percentage of cell population at different phases of the cell cycle in MDA-MB-231 and 4T1 cells. The data was analysed using *Flow Jo* software and the graphs were plotted using GraphPad Prism™ version 8.0.1. Data represents, mean±SD (n=3).

Table 4.4. Table indicates the % cell population in different phases of cell cycle in MDA-

Chapter 4: Pyrazino hydrazides as HDAC3 selective inhibitors

MB-231 and 4T1 cells respectively^a.

Cycle phase	% Cell population					
	MDA-MB-231 cells			4T1 cells		
	Control	UF010	4i	Control	UF010	4i
G1	48.7	36.7	27.3	50.6	38.7	25.3
S	28.1	14.8	15.1	27.8	16.6	19
G2/M	19.5	44.7	55	17.6	42	50.4

^aData represents n = 3 experiments.

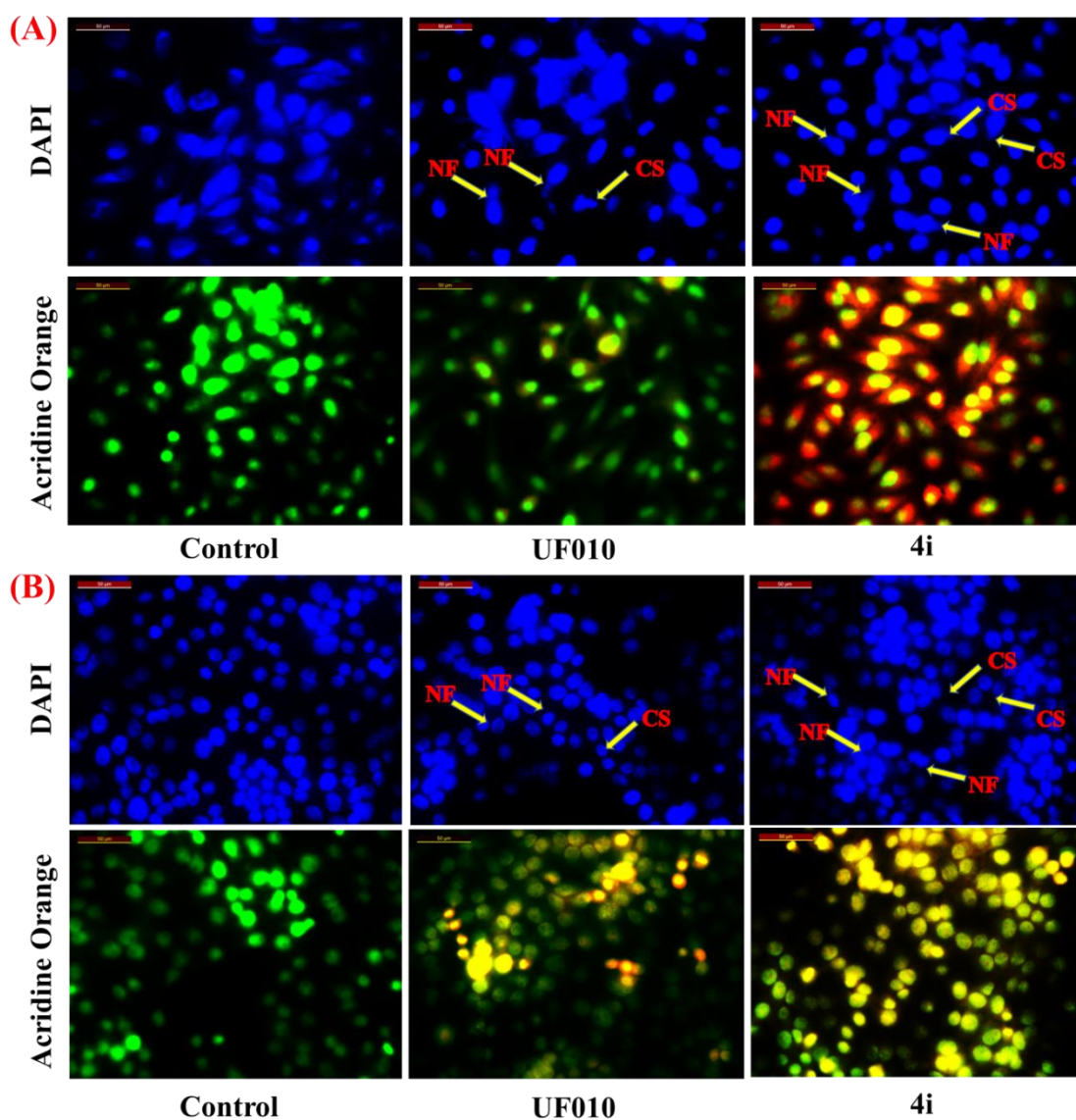


Figure 4.12. Different cultures of MDA-MB-231 and 4T1 cells were treated with the *in vitro* IC₅₀ concentrations of **UF010** and **4i** in the respective cell lines along with **control** for 72 h. Analysis of nuclear morphology by nuclear staining experiment in (A) MDA-MB-

Chapter 4: Pyrazino hydrazides as HDAC3 selective inhibitors

231 and (B) 4T1 cells using the staining solutions of DAPI and Acridine Orange after the treatment period. **NF** represents nuclear fragmentation and **CS** represents cell shrinkage. A fluorescence microscope (Leica microsystems, Germany) on 20x Magnification was used for the visualization of the stained nuclei. Data represents, mean \pm SD (n=3).

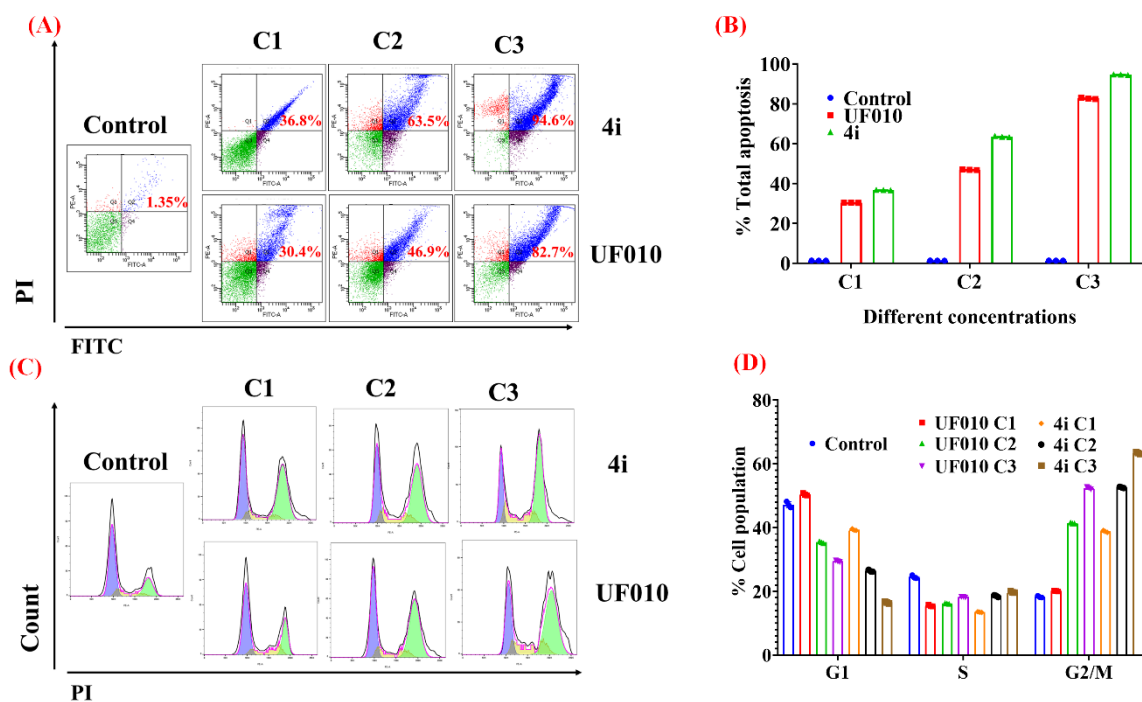


Figure 4.13. Different cultures of 4T1 cells were treated with three different concentrations including the IC₅₀ concentration of **UF010** and **4i** along with **control** (no treatment) for 72 h. (A) Annexin V/PI apoptosis assay by flow cytometer (BD Aria III) ® (where X and Y-axis represent the intensities of annexin V and propidium iodide respectively); (B) Graph representing the percentage of the total apoptotic population in 4T1 cells; (C) Cell cycle analysis by Flow cytometer (BD Aria III) ®; (D) Graph representing the percentage of cell population at different phases of the cell cycle in 4T1 cells. The data was analyzed using *FlowJo* software and the graphs were plotted using GraphPad Prism™ version 8.0.1. Data represents, mean \pm SD (n=3).

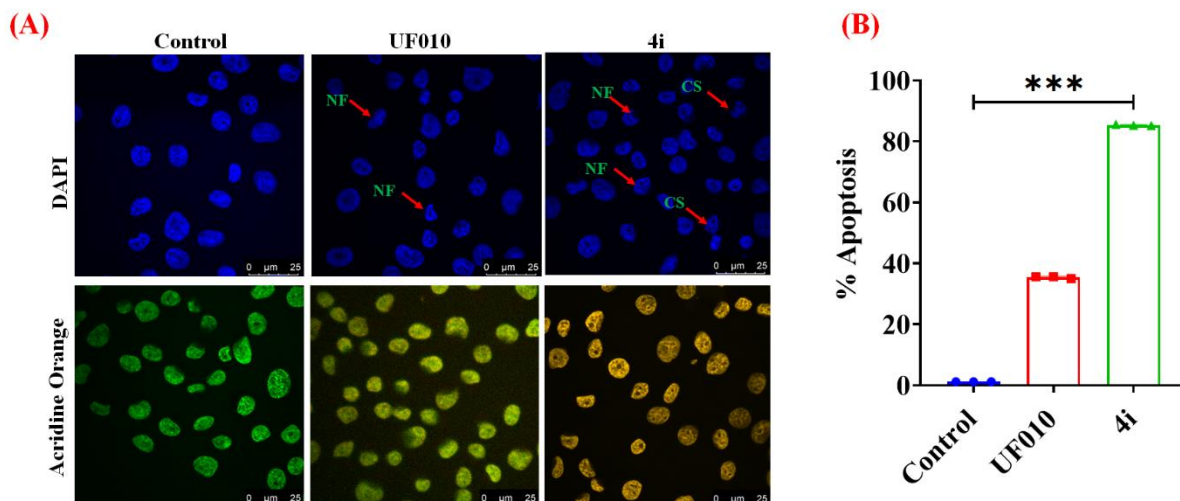


Figure 4.14. Different cultures of 4T1 cells were treated with the *in vitro* IC₅₀ concentrations of **UF010** and **4i** along with **control** for 72 h. Analysis of nuclear morphology by nuclear staining experiment in (A) 4T1 cells using the staining solutions of DAPI and Acridine Orange after the treatment period and (B) Graph representing the % apoptosis data quantified by *Image J* software. **NF** represents nuclear fragmentation and **CS** represents cell shrinkage. A Laser Scanning Confocal Microscope (LSCM) DMI8 (Leica microsystems, Germany) on 63X Magnification was used for the visualization of the stained nuclei. The obtained values represent the mean±SD (n=3); ***p < 0.001. The quantification of the % apoptosis was done using *ImageJ* software. Significance was analyzed using one-way ANOVA analysis and the graph was plotted in GraphPad Prism™ version 8.0.1.

Table 4.5. Table indicates the % cell population in different phases of cell cycle at different concentrations C1, C2 and C3 of **4i** and **UF010** in 4T1 cells respectively.^a

Chapter 4: Pyrazino hydrazides as HDAC3 selective inhibitors

Cycle phase	% Cell population						
	UF010				4i		
	Control	C1 (1.54 μM)	C2 (7.76 μM)	C3 (38.4 μM)	C1 (110 nM)	C2 (550 nM)	C3 (2.75 μM)
G1	47.2	50.4	35.4	29.4	39.3	26.4	16.5
S	24.5	15.5	16.2	18.2	13.5	18.5	19.8
G2/M	18.3	20.1	41.4	52.3	38.8	52.6	63.4

^aData represents n = 3 experiments.

These results suggest that the selective HDAC3 inhibitory activity of **4i** might have played a role in inducing the *in vitro* cytotoxicity in the TNBC cell lines, 4T1 and MDA-MB-231 with significant apoptosis activity and cell cycle arrest at G2/M phase. We then performed nuclear staining assay for **4i** and **UF010** along with the control group to visualise the cytotoxicity and the extent of apoptosis caused by their treatment. From the fluorescence images indicated in (**Figure 4.14A**), it can be seen that the cells treated with **4i** demonstrated increased fluorescence upon acridine orange (AO) staining indicating greater extent of nuclear fragmentation and cell shrinkage due to apoptosis when compared to UF010 and the control group in the 4T1 cells. The % apoptosis was found to be more in case of **4i** treated cells upon quantification and the results are depicted in the form of graph in the **Figure 4.14B**.

4.2.7. **4i** has exhibited chemosensitizing properties in oxaliplatin resistant MDA-MB-231 cells.

Considering the potent cytotoxicity of **4i** towards TNBC cell lines, initially we performed the *in vitro* cytotoxicity study in oxaliplatin (OXPt) resistant MDA-MB-231 vs wild type

Chapter 4: Pyrazino hydrazides as HDAC3 selective inhibitors

(WT) MDA-MB-231 cells to examine if the lead compound **4i** has retained its cytotoxicity in OXPt resistant MDA-MB-231 cells. It is well known that chemoresistance is one of the major causes of treatment failure in breast cancer patients.(Cao et al., 2021) Due to the absence of ER/PR/HER-2 receptors in TNBC cells, chemotherapy, and radiotherapy are the only effective treatments to date and this would eventually lead to chemoresistance in the patients thus causing poor prognosis and also a potential risk of relapse.(Cao et al., 2021; Han et al., 2019; Hsieh et al., 2017; Maccallini et al., 2022) Literature reports have indicated that HDACis such as SAHA, TSA, entinostat, and several other HDACis with different ZBGs have overcome chemoresistance in different cancer cell lines including TNBC cell line, MDA-MB-231.(Asfaha et al., 2020; Han et al., 2019; Jin et al., 2017; Marek et al., 2013; RHODES et al., 2012; Stenzel et al., 2017; Sun et al., 2019; Wawruszak et al., 2019; Zhou et al., 2021) In this direction, we have now performed the *in vitro* cytotoxicity study in OXPt resistant and WT MDA-MB-231 cells. The oxaliplatin-resistant MDA-MB-231 cell line was developed as per the protocol described previously.(Itoo et al., 2022) MTT assay was performed on both the cell lines with **4i**, **UF010**, **oxaliplatin** and a combination of **4i** and **oxaliplatin** in the equimolar ratio. The results obtained are depicted in **Figure 4.15A and 4.15B**. It can be seen that both **4i** and **UF010** have retained their cytotoxicity in the MDA-MB-231OXPtR cells as against the WT MDA-MB-231 cells when treated for 72 h. Further, the combination of **4i** and **oxaliplatin** in equimolar ratio has also exhibited much lower IC₅₀ of 403 nM and 447 nM in WT and OXPtR MDA-MB-231 cells, than their respective individual IC₅₀ values. The significantly less IC₅₀ values of the combination (**4i+oxaliplatin**) than that of their individual potency indicated the synergistic interaction of these two compounds when used in combination in both wildtype and oxaliplatin resistant cells. Altogether, the increased and the retained potency in case of the combination of **4i** and **oxaliplatin** in both WT and OXPtR MDA-MB-231 cells might also

Chapter 4: Pyrazino hydrazides as HDAC3 selective inhibitors

be attributed to the chemosensitizing properties of **4i** in overcoming the oxaliplatin resistance in TNBC cell line, MDA-MB-231.

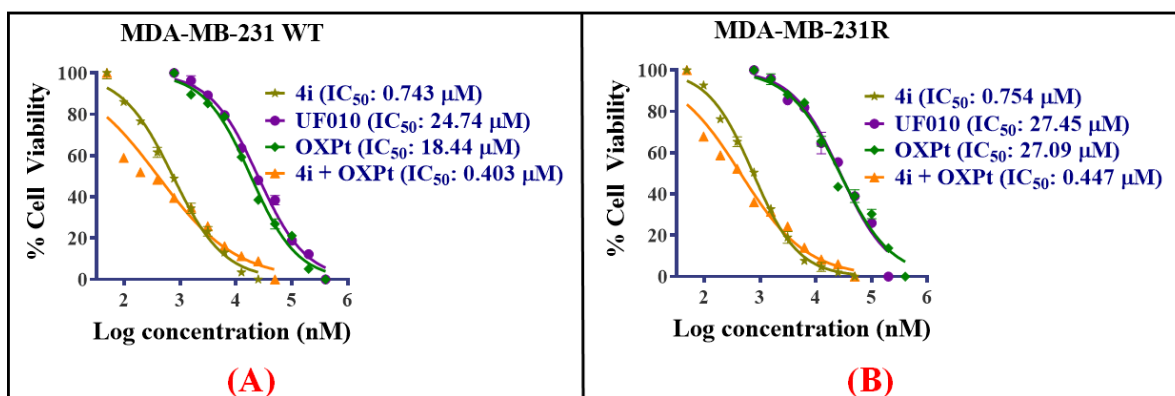


Figure 4.15. Graphs (A) and (B) represents the dose-response curves obtained by the MTT assay with the compounds **oxaliplatin**, **UF010**, **4i** and the combination of **4i** and **oxaliplatin** (equimolar concentration) for 72 h in MDA-MB-231 wild type and MDA-MB-231 oxaliplatin resistant cell lines respectively. Here, the cultured cells were treated with the compounds at the concentration range from 0.048 μM to 400 μM (n = 3) for 72 h. The graphs were plotted using GraphPad Prism™ version 8.0.1. Data represents, mean ± SD (n=3).

4.2.8. *In vitro* metabolic stability study of 4i in rat liver microsomes.

We further investigated the *in vitro* metabolic stability of the most potent and HDAC3 selective inhibitor **4i** in rat liver microsomes as per the protocol described in the experimental section. One of the major limitations of HDACis containing hydroxamates and benzamides as the ZBG is their poor metabolic stability due to their ability to be sulphated or glucuronidated by UDP glucuronosyltransferase. (Kang et al., 2010; Mulder and Meerman, 1983) This process of glucuronidation lead to the inactivation of these compounds due to the loss of their HDAC inhibitory activity. (McClure et al., 2016) Recent reports have shown that HDACis having hydrazides as ZBG are impervious to glucuronidation, hence were found to be metabolically more stable. (Li et al., 2018;

Chapter 4: Pyrazino hydrazides as HDAC3 selective inhibitors

McClure et al., 2016) In this report, a preliminary investigation was carried out to determine the *in vitro* half-life and intrinsic clearance in the rat liver microsomes. The obtained results are depicted in **Figure 4.16** and **Table 4.6**. The $t_{1/2}$ value of **4i** was 38.33 min and the intrinsic clearance was obtained as 36.18 $\mu\text{L}/\text{min}/\text{mg}$. The obtained results suggest optimal half-life and intrinsic clearance suggesting good metabolic stability of the lead compound **4i**. These results indicate better metabolic stability of hydrazides as ZBG than that of other hydroxamate and benzamide ZBG-containing HDAC inhibitors at the same dose as compared to the literature reference in rat liver microsomes. (Chen et al., 2019; Cho et al., 2013; Lehrmann et al., 2002; Liu et al., 2017; Mai et al., 2005; Shultz et al., 2011; Wang et al., 2021) The better and optimal metabolic stability of the pyrazino-hydrazide-containing compound **4i** has further inspired us to conduct pharmacokinetic profiling of **4i**.

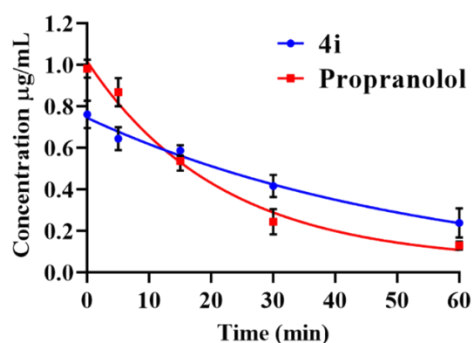


Figure 4.16. Time course of **4i** and **propranolol** depletion in rat liver microsomes. **4i** and **propranolol** (100 μM) were incubated with 0.5 mg/mL of pooled rat liver microsomes in the presence of NADPH. Each data point represents the mean \pm SD ($n=3$). The degradation half-life ($t_{1/2}$) was calculated using the equation: $t_{1/2}=0.693/k$, where k is the first-order elimination rate constant that was estimated by one-phase exponential decay using nonlinear regression analysis of the degradation time course data in GraphPad Prism™ version 8.0.1. Intrinsic clearance (Cl_{int} , $\mu\text{L}/\text{min}/\text{mg}$) was calculated using the equation: $Cl_{\text{int}} = V*0.693/t_{1/2}$. [where V = volume of incubation (μL)/ microsomal mass (mg)].

Table 4.6. *In vitro* microsomal stability profile of compound **4i** and **propranolol** (internal

Chapter 4: Pyrazino hydrazides as HDAC3 selective inhibitors

standard).

Compound	Intrinsic Clearance (CL _{int}) (μL/min/mg)	Elimination constant (k)	t _{1/2} (min)
4i	36.18	0.01808	38.33
Belinostat	-	-	18
Mocetinostat	-	-	31.3
Propranolol	92.77	0.04639	14.94

4.2.9. *In vivo* pharmacokinetic properties of 4i.

Poor pharmacokinetic profiles with lower bioavailability and dose-limiting toxicities have always been the major limitations for the majority of the existing HDACis in the clinic to date. (Pulya et al., 2022) In our recent report the lead compound **4e** displayed better pharmacokinetic profile at comparatively lower doses of 15 mg/kg and 25 mg/kg as against the other reports of hydroxamates and benzamides at comparatively higher doses of 50 mg/kg and 100 mg/kg. (Pulya et al., 2022) In this report, we evaluated the detailed pharmacokinetic analysis of our lead compound **4i** via the intraperitoneal route of administration at lesser doses of 5 mg/kg and 15 mg/kg body weight (n=3) in male Wistar rats (**Figure 4.17, Tables 4.7 – 4.9**). The reference compound **UF010** was also tested at 15 mg/kg intraperitoneally along with **4i** following the experimental protocol described previously. (Pulya et al., 2022) The obtained results and the PK parameters are displayed in **Figure 4.18** and the values are tabulated in **Table 4.10**.

Table 4.7. Plasma concentration (μg/ml)-time data of **4i** (Dose: 5 mg/kg and 15 mg/kg) and **UF010** (Dose: 25 mg/kg) following an intraperitoneal administration to male wistar rats.

Ti	4i	UF010

Chapter 4: Pyrazino hydrazides as HDAC3 selective inhibitors

Time Point (h)	5 mg/kg			15 mg/kg			15 mg/kg		
	Conc. (µg/ml)	Average	STDev	Conc. (µg/ml)	Average	STDev	Conc. (µg/ml)	Average	STDev
0.25	0.106	0.107	0.002	0.150	0.138	0.012	0.170	0.170	0.001
	0.109			0.138			0.168		
	0.105			0.125			0.171		
0.5	0.170	0.171	0.007	0.502	0.416	0.085	0.304	0.347	0.043
	0.178			0.332			0.389		
	0.165			0.415			0.348		
1	0.912	0.860	0.111	4.137	4.775	1.227	4.137	3.559	0.506
	0.732			3.998			3.348		
	0.936			6.189			3.192		
2	0.982	1.109	0.183	8.322	7.178	1.079	4.122	4.734	0.547
	1.319			6.177			4.902		
	1.028			7.036			5.177		
4	0.173	0.181	0.009	0.912	0.822	0.182	0.997	1.218	0.280
	0.190			0.612			1.533		
	0.180			0.942			1.123		
6	0.160	0.148	0.011	0.628	0.628	0.111	0.234	0.266	0.028
	0.138			0.739			0.279		
	0.145			0.517			0.284		
8	0.102	0.111	0.009	0.501	0.413	0.090	0.228	0.215	0.014
	0.119			0.322			0.199		
	0.112			0.415			0.217		
12	0.051	0.063	0.029	0.224	0.263	0.034	0.113	0.098	0.013
	0.095			0.279			0.094		
	0.041			0.286			0.087		
24	0.012	0.028	0.027	0.113	0.087	0.032	0.012	0.025	0.023

Chapter 4: Pyrazino hydrazides as HDAC3 selective inhibitors

	0.059			0.095			0.051	
	0.011			0.051			0.011	

Bioanalytical Summary

Table 4.8. Optimized chromatographic conditions in HPLC.

HPLC: Optimized chromatographic conditions		
Compounds	4i	UF010
Column	phenomenex C18 (150 nm X 4.4 nm, 5 μ)	phenomenex C18 (150 nm X 4.4 nm, 5 μ)
Mobile phase	Water: Methanol (40:60)	Water: Methanol (30:70)
Injection volume	10 μL	10 μL
Run time	10 min	10 min
Flow rate	0.9 mL/min	1 mL/min
Column temp	25 °C	25 °C
Retention time	6.96 min	7.3 min

Table 4.9. Calibration curve data of **4i** and **UF010** in rat plasma.

4i			UF010		
Nominal Conc. (μg/ml)	Calculated Conc.(μg/ml)	% Accuracy	Nominal Conc. (μg/ml)	Calculated Conc.(μg/ml)	% Accuracy
50	50.108	100.216	50	49.63	99.25
25	24.711	98.844	25	25.17	100.68
12.5	12.58	100.641	12.5	13.20	105.63
6.25	6.389	102.238	6.25	6.47	103.48

Chapter 4: Pyrazino hydrazides as HDAC3 selective inhibitors

3.125	3.169	101.408	3.125	2.99	95.75
1.5625	1.483	94.938	1.5625	1.41	90.07
0.78125	0.781	100.03	0.78125	0.77	98.44
0.390625	0.394	100.981	0.390625	0.38	96.89
0.1953125	0.182	93.687	0.1953125	0.19	100.35
0.09765625	0.099	102.299	0.09765625	0.09	95.39
0.04882812	0.05	102.646	0.04882812	49.63	99.26
5			5		
0.02441406	0.027	111.234	0.02441406	25.17	100.68
3			3		
Regression equation	$y = 17898x - 68.052$		Regression equation	$y = 8465.9x + 2648.6$	
Slope	17898		Slope	8465.9	
Intercept	68.052		Intercept	2648	
R ²	0.999		R ²	0.999	

Chapter 4: Pyrazino hydrazides as HDAC3 selective inhibitors

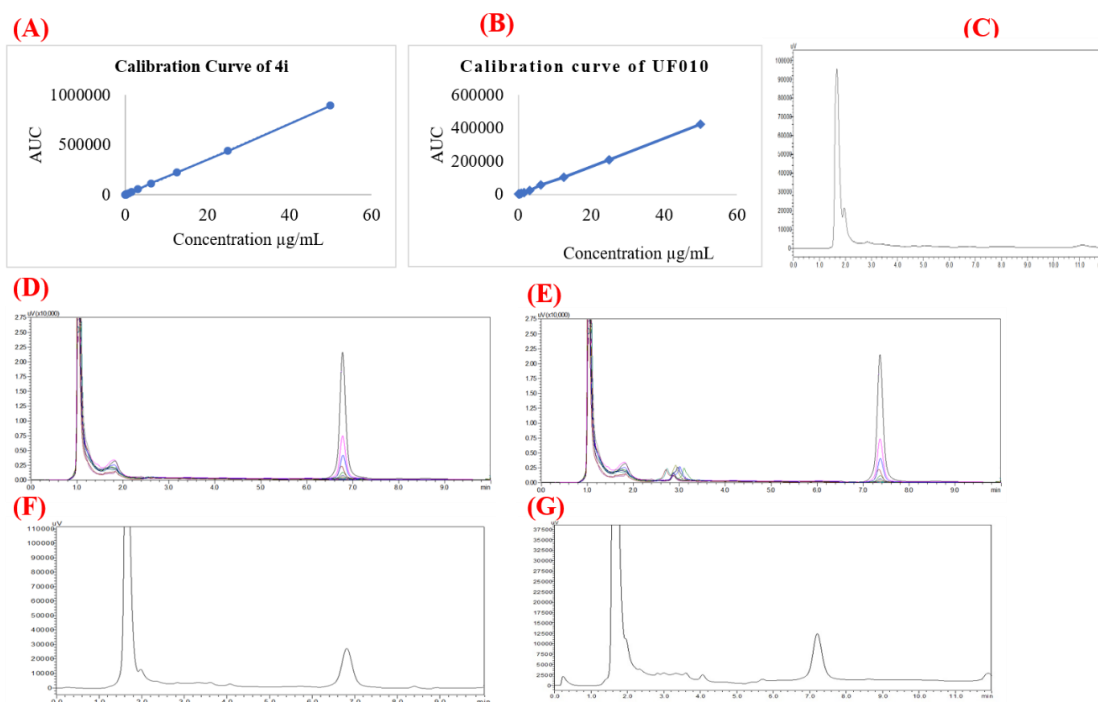


Figure 4.17. (A) Calibration curve of **4i** in rat plasma; (B) Calibration curve of **UF010** in rat plasma; (C) Representative chromatogram of blank in rat plasma (blank sample); (D) Representative chromatogram of **4i** in rat plasma (standard); (E) Representative chromatogram of **UF010** in rat plasma (standard); (F) Representative chromatogram of **4i** in rat plasma (intraperitoneal sample); (G) Representative chromatogram of **UF010** in rat plasma (intraperitoneal sample).

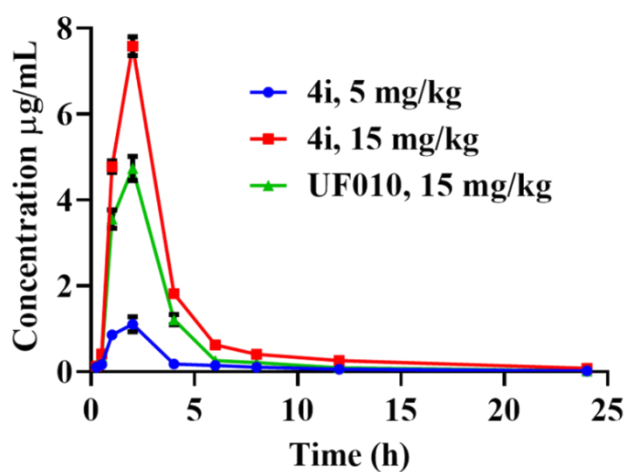


Figure 4.18. Graph representing mean plasma concentration vs time parameters of the

Chapter 4: Pyrazino hydrazides as HDAC3 selective inhibitors

compound **4i** and **UF010**. 4 groups of Male Wistar rats (n = 3 mice per group) were intraperitoneally administered a single dose of **4i**: 5 mg/kg, 15 mg/kg, and **UF010**: 15 mg/kg of 20 mg/mL concentration of compounds using 5% DMSO in saline as the vehicle. The graph was plotted using GraphPad Prism™ version 8.0.1. Data represents, mean±SD (n=3).

Table 4.10. The results obtained from the plasma pharmacokinetic analysis of the compound **4i** (5 mg/kg and 15 mg/kg) and **UF010** (15 mg/kg) following an intraperitoneal administration in male Wistar rats.^a

Parameters	Data obtained		
	4i		UF010
	5	15	15
Dose (mg/kg)			
t _{1/2} (h)	7.19 ± 0.67	7.20 ± 0.84	5.18 ± 0.17
T _{max} (h)	2	2	2
C _{max} (µg/mL)	1.11 ± 0.13	9.58 ± 0.04	5.24 ± 0.42
AUC _{0-t} [(µg/mL).h]	4.05 ± 0.12	19.65 ± 0.27	14.48 ± 0.18
AUC _{0-inf} [(µg/mL).h]	4.32 ± 0.19	20.55 ± 0.54	14.66 ± 0.27
AUMC _{0-inf} [(µg/mL).h ²]	29.08 ± 4.09	114.50 ± 19.40	53.64 ± 4.72
MRT _{0-inf} (h)	5.73 ± 0.72	6.57 ± 2.62	3.66 ± 0.37
V _z /F [(mg/kg)/(µg/mL)]	7.01 ± 0.54	12.57 ± 0.18	7.65 ± 0.46
Cl/F [(mg/kg)/(µg/mL).h]	1.15 ± 0.09	1.30 ± 0.33	1.03 ± 0.11

^a**4i** and **UF010** were injected intraperitoneally into male Wistar rats (n = 3) and the blood sample was collected for a period of 24 h at a predetermined time points. The plasma concentrations of **4i** and **UF010** were determined via the HPLC method. The linear trapezoidal rule was used for the calculation of the area under the concentration and time curve (AUC values). Non-compartmental analysis was used to obtain the pk parameters.

Chapter 4: Pyrazino hydrazides as HDAC3 selective inhibitors

The clearance was estimated as $CL = \text{Dose}/AUC_{\text{inf}}$; $MRT = AUMC_{\text{inf}}/AUC_{\text{inf}}$. Data obtained represents mean \pm standard deviation of the mean for $n = 3$.

Interestingly, our lead compound **4i** displayed an improved pharmacokinetic profile than our previously reported hydrazide **4e** (Pulya et al., 2022) at comparatively lower doses as well as the reference compound **UF010**. The half-life ($t_{1/2}$) of **4i** was found to be 7.19 h and 7.20 h at 5 mg/kg and 15 mg/kg doses respectively and 5.18 h for **UF010** at 15 mg/kg dose. The C_{max} values were 1.11 $\mu\text{g/mL}$, 9.58 $\mu\text{g/mL}$ at 5 mg/kg and 15 mg/kg dose of **4i**, and 5.24 $\mu\text{g/mL}$ for **UF010** at 15 mg/kg dose after 2 h (T_{max}) of the dose given. The obtained results have displayed sufficient mean residence time of the compound in the plasma and better volume of distribution thus indicating the good bioavailability of the lead compound **4i** at much lower doses 5 mg/kg and 15 mg/kg.

4.2.10. **4i** inhibits 4T1 cell proliferation and tumor growth in the 4T1-Luc tumor xenograft model.

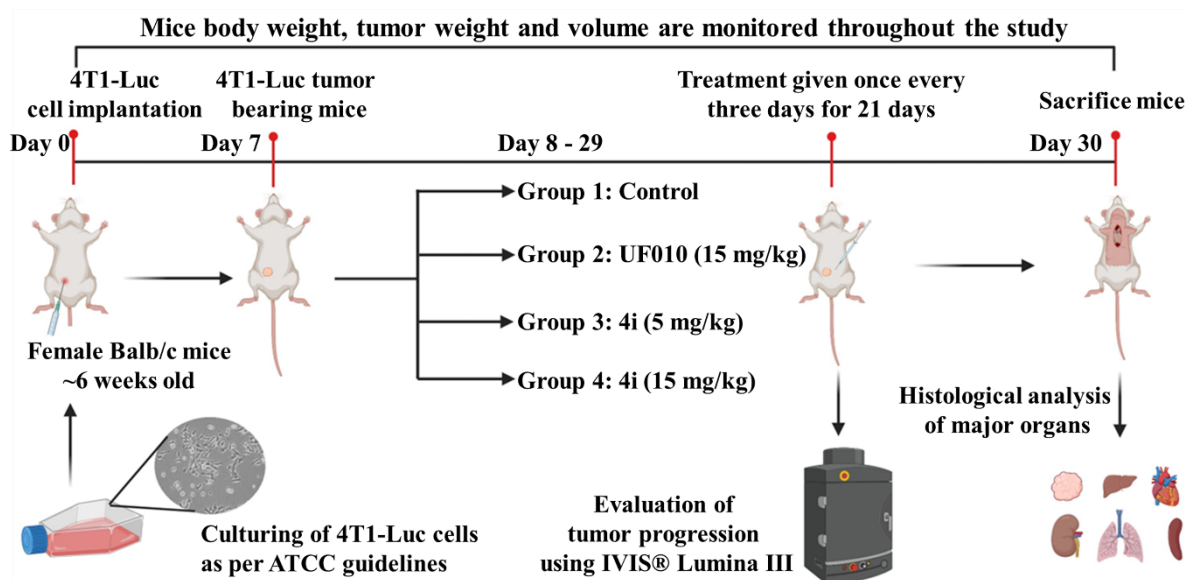


Figure 4.19. Schematic representation of the experimental protocol followed for the *in vivo* antitumor therapeutic efficacy of **4i** in the 4T1-Luc tumor xenograft mouse model.

With the encouraging pharmacokinetic results of **4i** at the doses of 5 mg/kg and 15 mg/kg,

Chapter 4: Pyrazino hydrazides as HDAC3 selective inhibitors

we further accessed the antitumor efficacy of **4i** *in vivo*. For this study, we have implanted 4T1-Luc tumors in female Balb/c mice of about 6 weeks old following the protocol represented schematically in **Figure 4.19**.(Pulya et al., 2022)

As we found the suitable dosage for **4i** and **UF010**, from our pharmacokinetic study, we took 5 mg/kg and 15 mg/kg for **4i** and 15 mg/kg for **UF010** as the dosage regimen following the intraperitoneal route of administration once in every 3 days for 7 administrations for a total treatment period of 21 days. The formulations were prepared using 5% DMSO, 20% PEG and 75% saline as the vehicle. To the best of our knowledge, this is the first report with a dosage regimen of only 7 doses in total for 21 days at a lower dose of 5 mg/kg and 15 mg/kg in a 4T1-Luc tumor bearing mouse model used for the therapeutic evaluation of HDAC*is*. The literature reports so far indicated the treatment period as 5 days per week for 21 days or more while administrating benzamides or hydroxamate-based HDAC*is* at comparatively higher doses of 50 mg/kg or 100 mg/kg intraperitoneally.(Buckley et al., 2007; Hubeek et al., 2008; Leoni et al., 2002; Saito et al., 1999; Spiller et al., 2006) In this study, **4i** could potentially reduce the tumor volume and tumor weight of the 4T1-Luc tumors in the xenograft mice model. Four mice from each group were also subjected to luciferin-mediated bioluminescence imaging analysis for evaluating the tumor growth post-treatment on days 0, 5, 10, 15, and 21. The obtained NIRF images were depicted in **Figure 4.20A**.

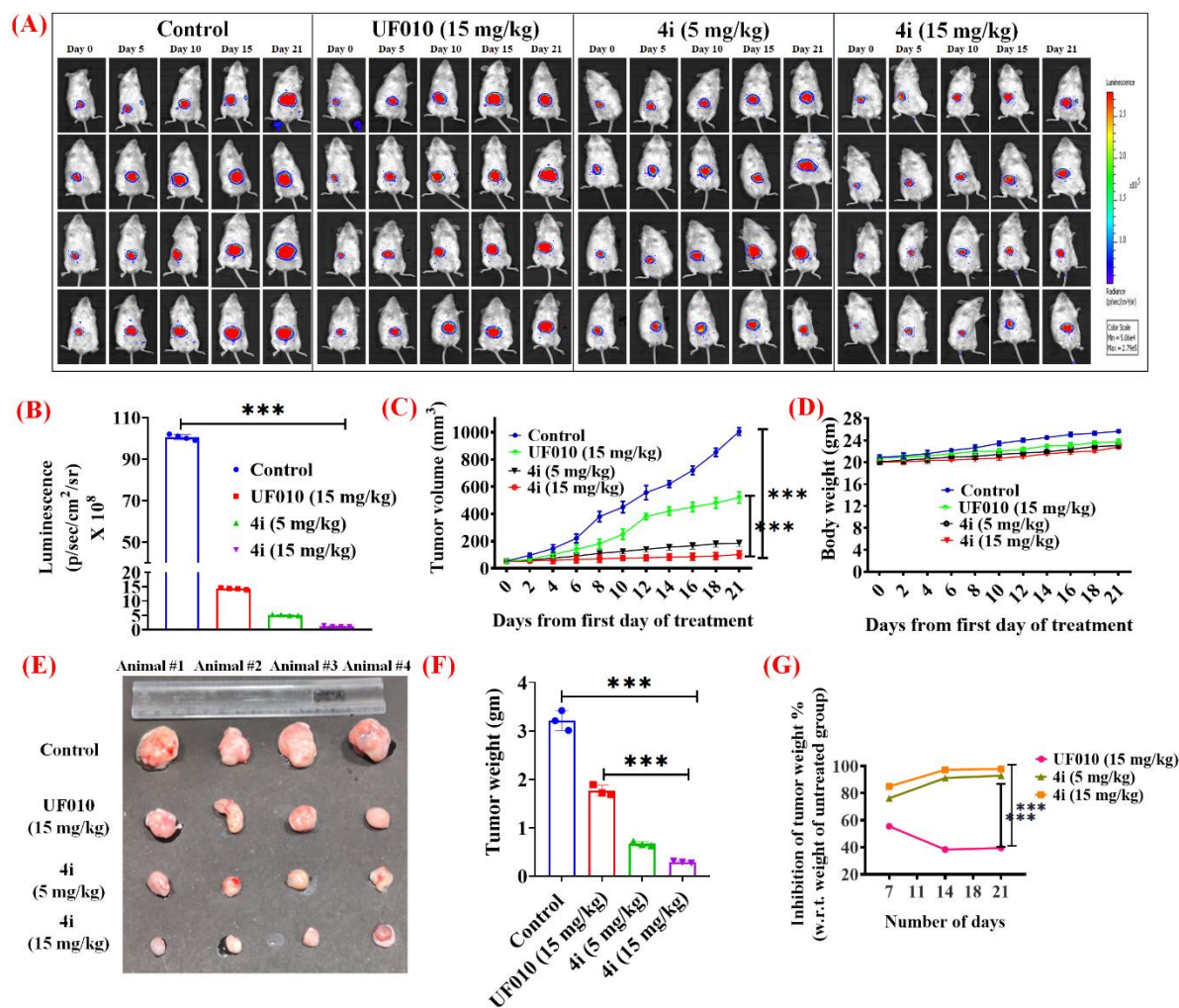


Figure 4.20. *In vivo* antitumor therapeutic efficacy studies in a 4T1-Luc tumor bearing mouse model in female Balb/c mice treated intraperitoneally with control, **UF010** (15 mg/kg) and **4i**, 5 mg/kg, and 15 mg/kg (n=12) on every 3rd day for 21 days total period. **(A)** Representative whole animal bioluminescence imaging of luciferin induced (i.p administration of luciferin-D, 100 µL, 100 mg/kg) 4T1-Luc tumor-bearing mice on days 0, 5, 10, 15, and 21 by IVIS® Lumina III, PerkinElmer, USA; **(B)** Quantification of bioluminescence of the tumors; **(C)** Tumor volume growth over the treatment period; **(D)** Body weight changes in mice during the treatment period; **(E)** Representative images of 4T1-Luc tumors dissected from the mice after 21 days of treatment (n=4); **(F)** Average weight of the isolated tumors from each group (n= 3); **(G)** Tumor growth inhibition rate percentage (TGI rate %) calculated from the dissected tumor tissue weight collected from

Chapter 4: Pyrazino hydrazides as HDAC3 selective inhibitors

3 mice of each treatment group (total n = 12), at 0th, 7th, 14th, and 21st day of the treatment period. The TGI rate percentage was calculated with the formula $= 1 - \left(\frac{W_{T,t} - W_{T,0}}{W_{C,t} - W_{C,0}} \right) * 100$, where $W_{T,t}$ and $W_{T,0}$ represent the mean tumor weight of the treatment group at the time t and time 0 respectively, $W_{C,t}$ and $W_{C,0}$ represent the mean tumor weight of the control group at the time t and time 0 respectively. The obtained values represent the mean ± the standard error of the mean (SEM); ***p < 0.001. Significance was analyzed using one-way ANOVA analysis and all the graphs were plotted in GraphPad Prism™ version 8.0.1.

The tumor growth was quantified and the obtained luminescence intensities around the region of interest of tumors were plotted as a graph as shown in **Figure 4.20B**. It can be observed that a constant and substantial increase in the luminescence signal was observed in the untreated control group indicating the high tumor growth and the significantly lower luminescence signals were observed in **4i** treated groups even in comparison with the reference compound **UF010** treated group. From the results depicted in **Figure 4.20C**, it was found that the tumor growth volume of the mice treated with **4i** at 5 mg/kg exhibited the growth from 52.05 ± 13.23 to 185.23 ± 24.14 mm³ and those treated with 15 mg/kg has shown the lowest increase in the tumor growth volume from 50.25 ± 12.35 to 101.23 ± 26.56 mm³ when compared to that of the **UF010** at 15 mg/kg with a tumor volume growth of 52.25 ± 13.24 to 520.32 ± 40.25 mm³ and also the huge increase in the tumor volume was seen in the control group mice from 51.91 ± 7.45 to 1005.32 ± 28.32 mm³ by the end of the treatment period. Notably, no significant body weight loss/gain was observed for the treatment groups mice throughout the experiment suggesting good general biosafety of **4i** (**Figure 4.20D**). The final tumor images at the end of the treatment period were represented in **Figure 4.20E** and the corresponding average tumor weights as 3.23 g, 1.78 g, 0.65 g, and 0.29 g for the control, **UF010**, **4i** (5 mg/kg), and **4i** (15 mg/kg) respectively were plotted as a graph in the **Figure 4.20F**. Simultaneously, the tumor growth inhibition rate percentage

Chapter 4: Pyrazino hydrazides as HDAC3 selective inhibitors

(TGI% rate) was assessed following the dissection of tumors from 3 mice of each group on the 0th, 7th, 14th, and 21st day of the treatment. The TGI% rate was found to be 76.24%, 91.23%, 92.87%, and 84.94%, 97.32%, 97.92% for compound **4i** at 5 mg/kg and 15 mg/kg respectively when compared to 55.56%, 38.36%, 39.52% for **UF010** at day 7, 14 and 21 respectively (**Figure 4.20G**). Both the results obtained from the tumor volume reduction and TGI% rate demonstrated excellent *in vivo* antitumor efficacy of the lead compound **4i** in the 4T1-Luc murine triple-negative breast cancer animal model.

4.2.11. **4i induced ROS generation causing apoptosis-mediated tumor cell death.**

The induction of tumor cell death by activating tumor suppressive mechanisms involving ROS (reactive oxygen species) generation is a well-known fact in the case of HDAC inhibitor-mediated cell death mechanisms. (Rosato and Grant, 2005) One of the first studies using the *pan*-HDACi, SAHA has identified that the induction of ROS generation led to apoptotic cell death. (Ruefli et al., 2001) In brief, the mechanism involved the mitochondrial damage subsequently releasing cytochrome *c*, also activating caspase cascade along with the degradation of various apoptotic proteins such as Bcl-2. (Newbold et al., 2016) Hence, we quantified the ROS generation in mice on day 21 (n = 4) by measuring the DCFH-DA fluorescence. DCFH-DA was injected intratumorally and after 10 min, the fluorescence intensity was detected using IVIS® Lumina III, PerkinElmer, USA. The images obtained were depicted in **Figure 4.21A**. From the obtained results it can be seen that high levels of ROS generation were detected in the 15 mg/kg dose of **4i** treated group of animals followed by 5 mg/kg of **4i** and 15 mg/kg of **UF010** treated group of mice. Post-treatment period, the tumors were surgically isolated, sectioned into slices, and analyzed microscopically within 1 h of the treatment with DCFH-DA. Similar levels of ROS generation were observed in all the isolated tumor sections from different groups respectively as shown in **Figure 4.21B** and the quantified fluorescence intensities were graphically represented in **Figure 4.21C**.

Chapter 4: Pyrazino hydrazides as HDAC3 selective inhibitors

The highest level of intensities was seen in 15 mg/kg and 5 mg/kg of **4i** followed by **UF010** and control group tumors.

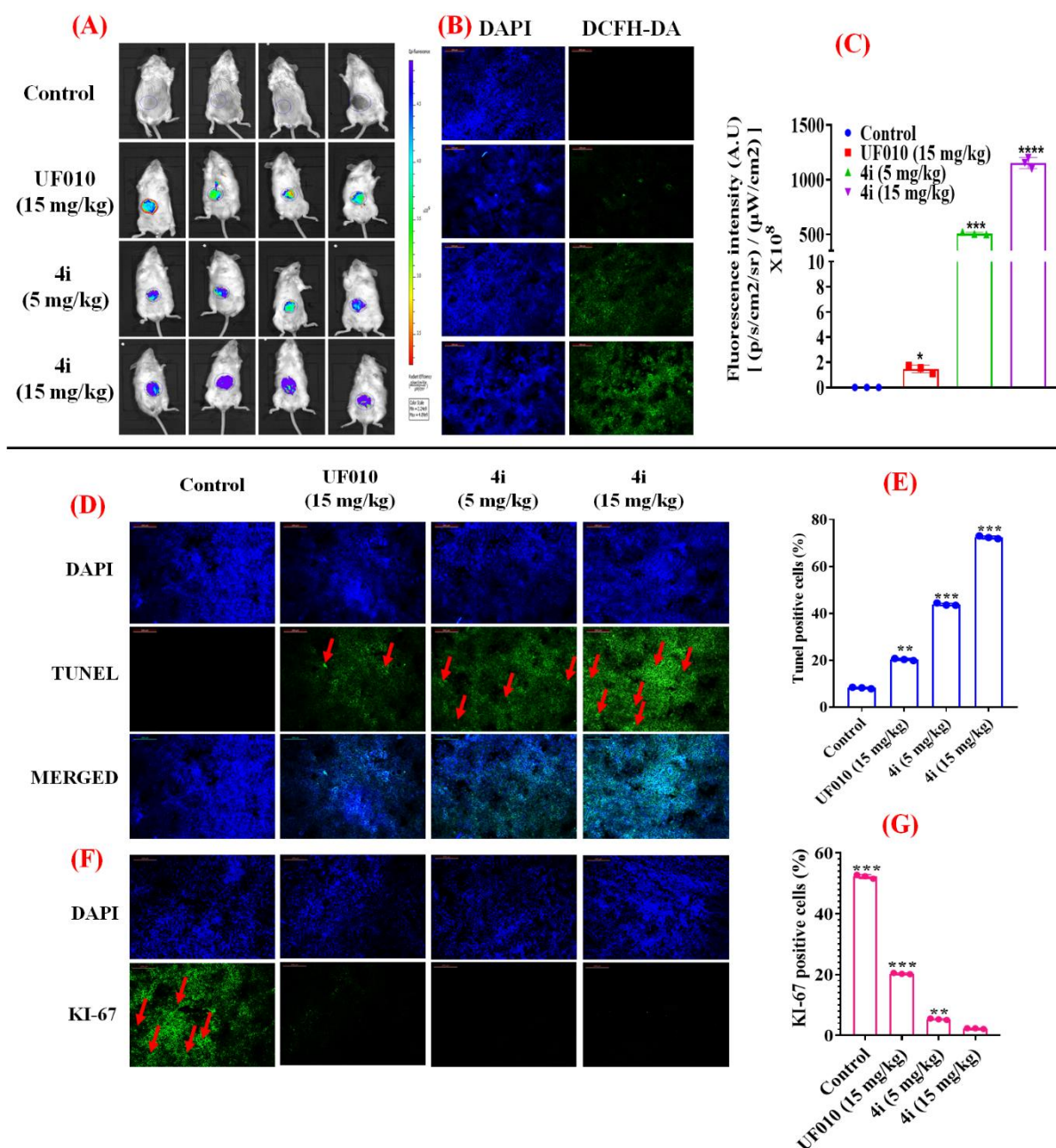


Figure 4.21. (A) Bioluminescence images representing the reactive oxygen species (ROS) generation on day 21 after injecting DCFH-DA intratumorally (100 μ L, 25 μ M) in 4 mice from all the treated groups including control group in 4T1-Luc tumor xenograft mouse model, the images were recorded for their fluorescence intensity by IVIS® Lumina III, PerkinElmer, USA; (B) Images of tumor sections recorded after the surgical isolation of

Chapter 4: Pyrazino hydrazides as HDAC3 selective inhibitors

tumors, 10 min post-treatment with DCFH-DA; **(C)** Graph representing the fluorescence intensities recorded corresponding to the ROS levels; **(D)** Representative images of TUNEL assay in the sections of isolated tumors; and **(E)** Corresponding graph denoting the percentage of TUNEL positive cells; **(F)** Images representing the Ki-67 stained tumor sections; and **(G)** corresponding graph representing the percentage of Ki-67 positive cells in different groups of mice; Fluorescence microscope from Leica microsystems, Germany was used to obtain the images and the quantification was carried out using *Image J* software and the graphs were plotted in GraphPad Prism™ version 8.0.1. Data represents the values of mean \pm the standard error of the mean (SEM); * $p < 0.05$, ** $p < 0.01$, *** $p < 0.001$, **** $p < 0.0001$, significantly different from the control group.

4.2.12. Effect of 4i on apoptosis and tumor cell proliferation by TUNEL assay and Ki-67 staining.

TUNEL assay was then performed to confirm the role of ROS in the induction of apoptosis. The obtained microscopic images and the percentage of TUNEL-positive cells were represented in **Figures 4.21D** and **4.21E**. It is visible clearly from the microscopic images of the sectioned tumors of different treated groups that the percentage of TUNEL-positive cells was found to be the highest in the case of **4i** (15 mg/kg) tumors followed by **4i** (5 mg/kg) and **UF010** (15 mg/kg). We have also examined the extent of cell proliferation by quantifying the percentage of Ki-67-positive cells in the tumor sections from the treatment groups. Cancers are well characterized by uncontrolled proliferation and Ki-67 is one of the most widely used proliferation markers in routine pathological investigations of various cancers.(Inwald et al., 2013) Moreover, Ki-67 is also an important prognostic factor for breast cancer detection.(Soliman and Yussif, 2016) Particularly in TNBC patients, a higher incidence of Ki-67 (>15%) was detected which clinically correlated with the metastasis and clinical stage of cancer detection.(Soliman and Yussif, 2016) Therefore, we have analyzed the expression of Ki-67 in the tumor sections of the tumors isolated after 21 days of treatment using immuno-histofluorescence analysis.

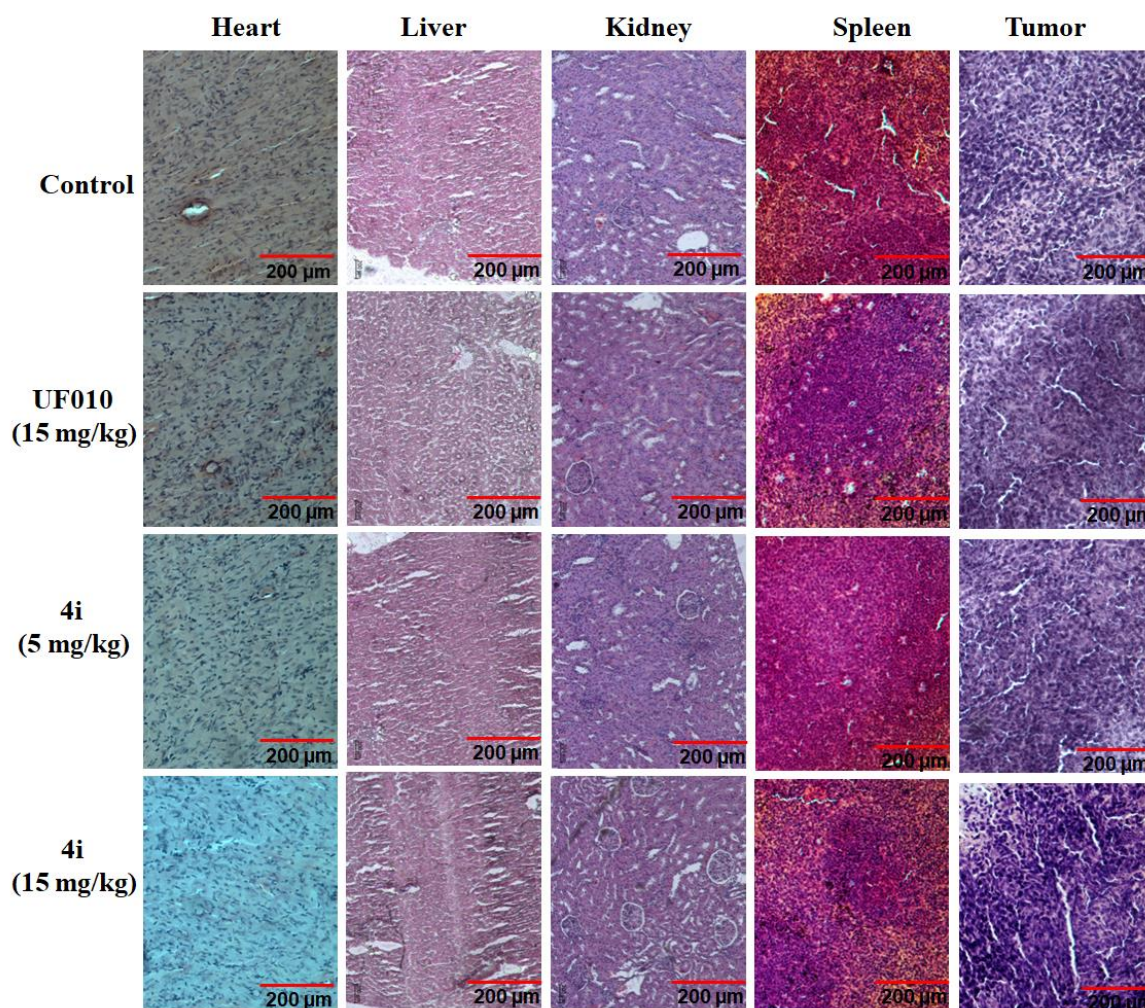


Figure 4.22. Images depicting the H&E staining of tissue sections of various major organs of mice from all the groups isolated after the treatment period. A fluorescence microscope from Leica microsystems, Germany was used to obtain the images.

. The images of the tumor sections were depicted in **Figure 4.21F** and the percentage of Ki-67 positive cells was graphically plotted in **Figure 4.21G**. It can be seen that Ki-67 expression in both **4i** (15 mg/kg) and **4i** (5 mg/kg) treated animals was very low compared to **UF010** (15 mg/kg). The histological analysis by H&E staining of the tissue sections of various major organs including tumors isolated from the mice after their sacrifice was performed to find out the extent of tissue damage in the respective organs. From the fluorescence images represented in **Figure 4.22**, no tissue damage or toxicity was observed in any of the major organs. Further, it was clear that the cell shape and size were not

Chapter 4: Pyrazino hydrazides as HDAC3 selective inhibitors

disturbed by the **4i** treatment. There was no evidence of myocardial hypertrophy in the heart tissues of the control and the **4i** treated groups. The liver, kidney, and spleen images in control and **4i** treatment indicates no tissue fibrosis. The neutrophile infiltration was also not observed. These observations indicate the good biosafety of **4i**. Altogether, these results indicate that the treatment with **4i** has caused significant apoptosis in tumors possibly due to ROS generation, and also significantly reduced tumor cell proliferation *in vivo*.

4.2.13. 4i treatment significantly reduced the metastatic potential of 4T1-Luc tumors.

One of the leading causes of breast cancer-related deaths is metastasis.(Park et al., 2022) Particularly, TNBC accounts for most breast cancer deaths at the advanced stage due to metastasis to various parts of the body.(Jin and Mu, 2015) Breast cancer most commonly metastasizes to major organs of the body mainly the lungs.(André and Zielinski, 2012) In order to test the effect of **4i** on the metastatic potential of the tumors *in vivo*, post-treatment period, after the surgical tumor isolation from different groups of mice on day 22, all the mice were left for 7 more days to observe metastasis. Metastasis was first detected by measuring the luciferin-mediated bioluminescence from the 4T1-Luc tumors. From the images obtained as depicted in **Figure 4.23A**, it was observed that severe metastasis to the lungs was seen in the control group, and a considerable amount of signal was found in **UF010**-treated mice, whereas little signal was found in both the treatment groups of **4i** (5 mg/kg and 15 mg/kg).

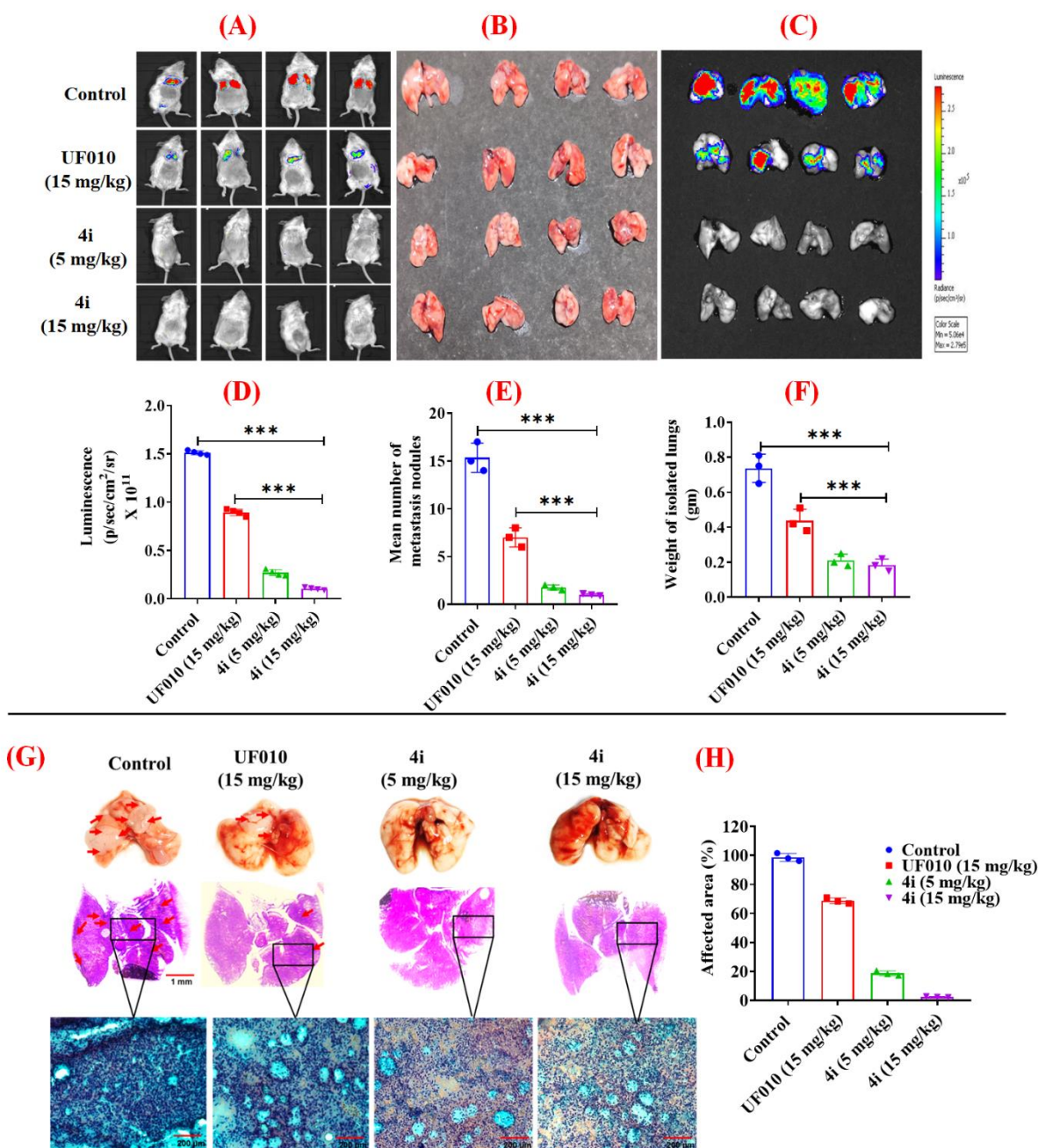


Figure 4.23. Analysis of *in vivo* tumor metastasis in the 4T1-Luc tumor bearing mouse model. (A) Tumor metastasis was assessed at the indicated time points by whole animal bioluminescence imaging of 4T1-Luc tumors using IVIS® Lumina III, PerkinElmer, USA; (B) Representative images of the lungs isolated showing metastatic nodules; (C) Bioluminescence imaging of the isolated lungs containing metastatic 4T1-Luc tumors using IVIS® Lumina III, PerkinElmer, USA; (D) Graph representing the luminescence intensities recorded; (E) Mean number of tumor nodules as shown in the images of isolated lungs; (F) Graph representing the

Chapter 4: Pyrazino hydrazides as HDAC3 selective inhibitors

weight of the isolated lungs; **(G)** Detailed pictorial representation of the isolated lungs one from each group and the tumor nodules were marked with circles along with the H&E staining images of the lungs detecting tumor metastasis; **(H)** The graph represents the percentage affected area of the lungs after metastasis in different treatment groups. A fluorescence microscope from Leica microsystems, Germany was used to obtain the images. Representation of lung metastasis is expressed as the affected area with respect to the total area of the lung. Reduction in metastasis was observed in the lungs of **4i** treated animals compared to that of **UF010** ($t = 5.94$; $n = 170$; $* t0.001$). These differences are also significant between the lungs of **4i** treatment animals with respect to untreated animal lungs. The quantification was carried out using *Image J* software, and the graphs were plotted in GraphPad Prism™ version 8.0.1. Data represents the values of mean \pm the standard error of the mean (SEM, $n=3$); $*p < 0.05$, $**p < 0.01$, $***p < 0.001$, $****p < 0.0001$, significantly different from the control group.

The corresponding luminescence intensities were plotted as a graph in **Figure 4.23D**. Further, the animals were sacrificed on day 30 and the lungs were isolated, weighed and the luminescence was measured. The isolated lungs of different groups of mice were represented in **Figure 4.23B** and their luminescence was measured and shown in **Figure 4.23C**. The average number of tumor nodules was observed in the lungs and from the resulting graph (**Figure 4.23E**) it can be seen that a higher number of nodules was found in the control that also correlated with the increased weight of the isolated lungs when compared to the treatment groups where **4i** (15 mg/kg) treated mice lungs weighed the least (**Figure 4.23F**). The detailed pictorial representation of the isolated lungs along with the H&E staining of the whole lungs has been shown in the **Figure 4.23G**, where larger and a greater number of nodules were found in the lungs of the control group mice followed by **UF010** while the smaller or negligible nodules in **4i** treated mice lungs as indicated by the

Chapter 4: Pyrazino hydrazides as HDAC3 selective inhibitors

arrows. The higher number of hematoxyline-positive cells aggregated in certain areas of the lungs indicated tumor nodules. The number of aggregated cells in **4i** treated groups decreased significantly. Upon quantification (**Figure 4.23H**) of the affected area in lungs by metastasis, about ~90% reduction of the affected area was observed in **4i** treated group when compared to the mice treated with **UF010**. It is noteworthy that these results showed significant reduction of metastasis in the 4T1-Luc tumor bearing mouse model upon treatment with a selective HDAC3 inhibitor **4i**.

4.2.14. Protein expression levels of various histone, apoptotic and proliferative biomarkers by western blot analysis in the isolated tumor tissue.

Taking into consideration, the potent and selective HDAC3 inhibition of **4i** along with its excellent antitumor efficacy in the breast cancer model, as per the *in vitro* and *in vivo* evaluation, we next wanted to investigate the relative acetylation levels of canonical histone markers along with *ac*- tubulin and *ac*-SMC3, and also the protein expression levels of various apoptotic proteins such as caspase-3/7, cytochrome *c*, Bcl-2, proliferative marker proteins such as EGFR and Ki-67 and also a metastatic surface adhesion marker CD44 by western blot analysis. The blots obtained and their corresponding graphical representation of the quantified blots are represented in **Figure 4.24A–C**.

The tumor tissue lysate from the isolated tumors from the mice were subjected to the western blot analysis following the protocol previously described.(Pulya et al., 2022). From the results obtained, hyperacetylation of the canonical histone lysine residues *Ac*-H3K9, *Ac*-H3K27, and *Ac*-H4K12 was found in the treated tissue blots and significantly higher levels in **4i** blots in a dose dependant manner at both the doses treated. Same time, no significant increase of acetylation on tubulin (*Ac*-tubulin) and on SMC3 (*Ac*-SMC3) was observed in **4i** blots compared to the control. Tubulin and SMC3 are known to be acetylation substrates of HDAC6 and HDAC8 respectively.

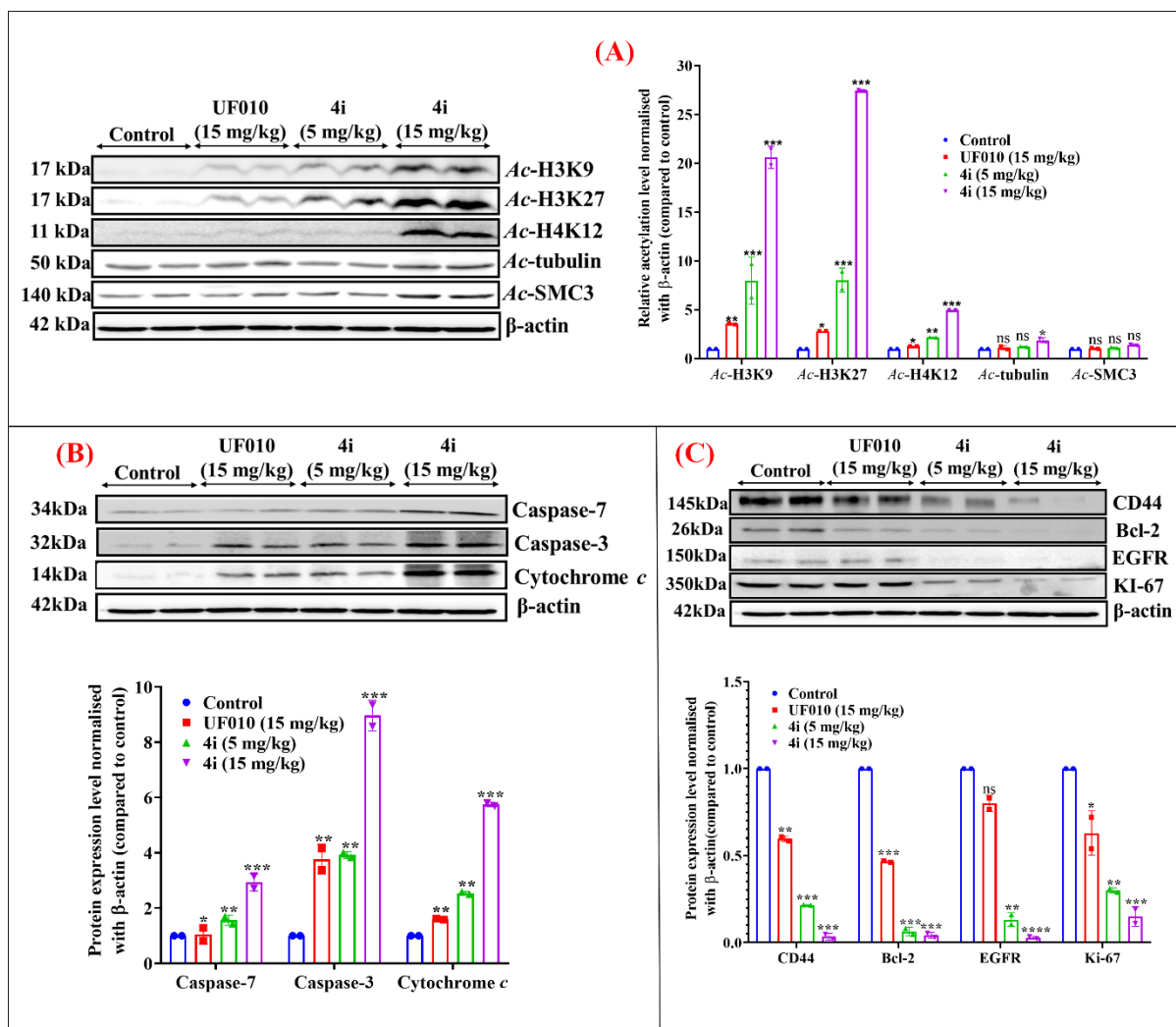


Figure 4.24. Western blot analysis of various biomarkers in the protein samples extracted from the tumor tissue that is isolated from the control, **UF010** (15 mg/kg) and **4i** (5 mg/kg and 15 mg/kg) treated mice in the 4T1-Luc tumor xenograft mouse model. The blots and the corresponding quantification of the blots were plotted as the graphs represented above. **(A)** Image representing the blots of *Ac*-H3K9, *Ac*-H3K27, *Ac*-H4K12, *Ac*-tubulin, and *Ac*-SMC3 levels in 4T1-Luc tumor tissue samples and the corresponding quantification plotted as a graph in the right; **(B)** Image representing the blots of caspase-3, caspase-7, and cytochrome *c* levels in the 4T1-Luc tumor tissue samples and the corresponding quantification plotted as a graph below; **(C)** Image representing the blots of CD44, Bcl-2, EGFR and Ki-67 levels in the 4T1-Luc tumor tissue samples and the corresponding quantification plotted as a graph below. β -actin was used as an internal control and the

Chapter 4: Pyrazino hydrazides as HDAC3 selective inhibitors

graphs were plotted by normalizing the protein expression levels compared to the control group values analyzed in *Image J* software. Significance was analyzed using one-way ANOVA analysis and the graphs were plotted in GraphPad Prism™ version 8.0.1. Data represents the values of mean \pm the standard error of the mean (SEM); * $p < 0.05$, ** $p < 0.01$, *** $p < 0.001$, **** $p < 0.0001$, significantly different from the control group.

These findings represented in **Figure 4.24A** correlate with our *in vitro* HDAC isoform enzyme inhibition assay results, that **4i** is a highly selective HDAC3 inhibitor and demonstrates a greater extent of selectivity over HDAC6 and HDAC8. All the *in vitro* and *in vivo* results demonstrated excellent cytotoxic and antitumor properties of **4i** through different mechanisms such as apoptosis, ROS generation, reduced metastatic potential, and also its excellent antiproliferative property. However, several intrinsic pathways in the tumor cells are known to have a key role in regulating the antitumor effects of HDACis.(Newbold et al., 2016) We have seen from our results that apoptosis induction is due to ROS generation in the tumor cells in response to the treatment by HDAC3 inhibitor, **4i**. This mechanism of HDAC inhibitor-mediated ROS generation and accumulation in response to oxidative stress leads to the loss of mitochondrial membrane potential thus releasing cytochrome *c* along with caspase activation, particularly in the cancer cells over normal cells.(Brentnall et al., 2013; Rosato et al., 2003; Rosato and Grant, 2005) Hence, we studied the protein expression levels of caspase-3, caspase-7, and cytochrome *c* through western blot analysis. The results represented in **Figure 4.24B** have revealed significant upregulation of the studied apoptotic markers further affirming the cell death mechanism in the tumor cells. Moreover, the downregulation of antiapoptotic marker Bcl-2 was observed consistent with the literature reports stating the HDAC inhibitor-mediated downregulation of Bcl-2 subsequently led to apoptosis.(Bolden et al., 2013) Further, the

Chapter 4: Pyrazino hydrazides as HDAC3 selective inhibitors

antiproliferative and reduced metastasis in the **4i** treated mice was significantly higher than the **UF010** and the control group mice. In this regard, EGFR and Ki-67, the proliferative markers that are especially known to be overexpressed in breast cancer cells were studied. (Kwak et al., 2019; Lo et al., 2006; Soliman and Yussif, 2016) From the blots obtained and analyzed (**Figure 4.24C**), we can see a huge reduction in the protein levels in the **4i** treated tumor tissue against **UF010** and control group, indicating a higher antiproliferative potential of **4i** in the *in vivo* mouse model. One of the key regulators of metastasis is the cell surface adhesion receptor, CD44, which is found to be over expressed in various cancers and its attachment to the cell surface regulates metastasis via interacting with various extracellular ligands thus promoting tumor cell invasion and progression into the blood circulation. (Negi et al., 2012; Park et al., 2022) Our results clearly demonstrated the significant reduction in the CD44 protein expression levels in the **4i** treated samples over **UF010** and the control group samples, thus correlating with our *in vivo* therapeutic efficacy data. The western blot analysis of the various markers indicated the significant HDAC3 isoform selectivity and also evidenced the HDAC inhibitor-induced tumor cell death and the antiproliferative property is majorly through the regulation of various intrinsic pathways thus contributing to the therapeutic efficacy of the lead compound **4i** in the 4T1-Luc TNBC tumors *in vivo*.

4.2.15. Binding mode of interactions analysis of lead compound 4i.

All these compounds were docked into the active site of HDAC3 (PDB: 4A69). It was noticed that all these compounds aligned closely at the HDAC3 active site in an almost overlapping fashion (**Figure 4.25**). The hydrazide amide groups of all these compounds were located close to the catalytic Zn²⁺ ion.

Chapter 4: Pyrazino hydrazides as HDAC3 selective inhibitors

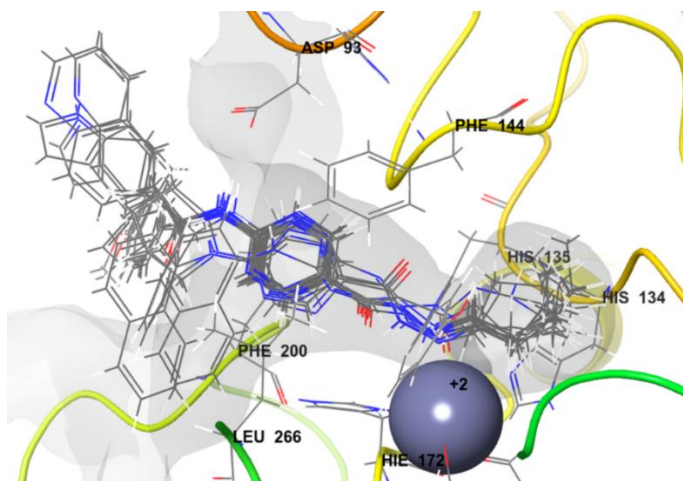


Figure 4.25. Aligned structures of all these hydrazides at the HDAC3 active site (PDB: 4A69)

The most potent and selective HDAC3 inhibitor (**4i**) was docked into the active site of several HDAC isoforms (namely HDAC3, HDAC2, HDAC8, and HDAC6) to know the exact binding mode of action regulating the activity profile (**Figure 4.26A - D**).

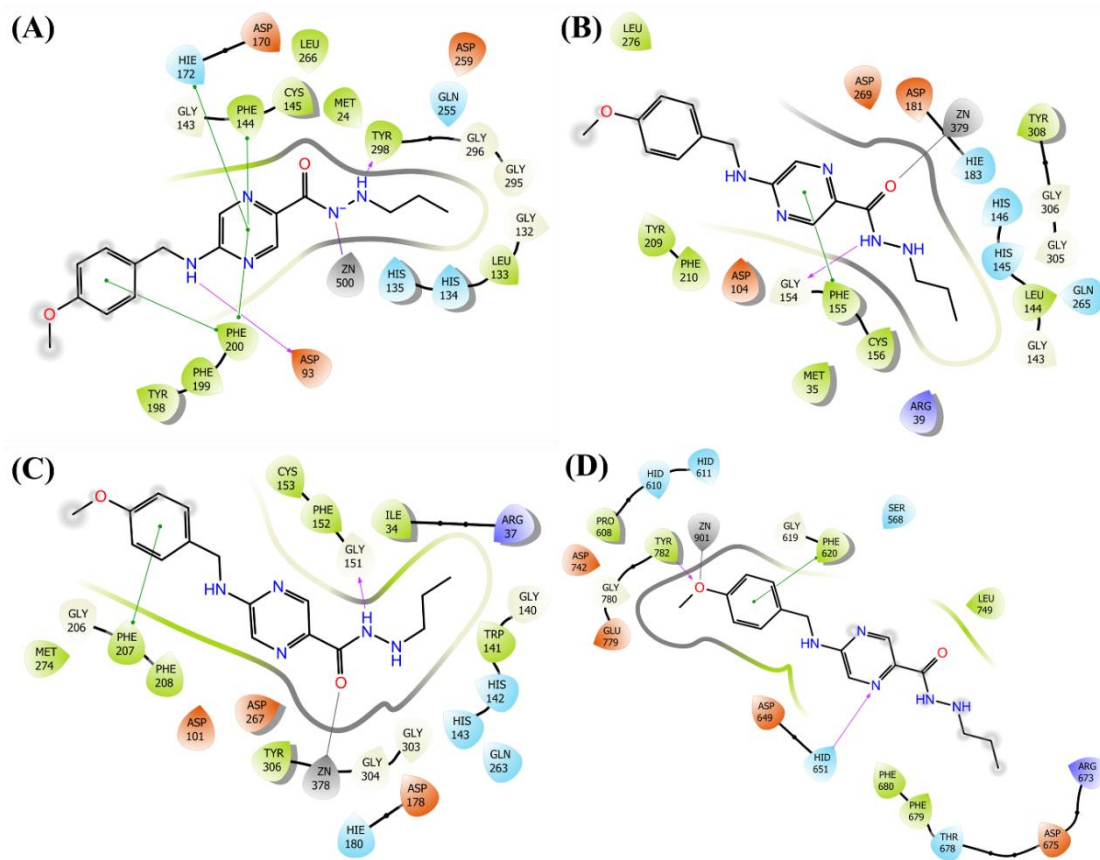


Figure 4.26. Molecular docking interaction of the best active and selective HDAC3

Chapter 4: Pyrazino hydrazides as HDAC3 selective inhibitors

inhibitor **4i** at the active site of (A) HDAC3 (PDB: 4A69); (B) HDAC2 (PDB: 3MAX); (C) HDAC8 (PDB: 1T69); and (D) HDAC6 (PDB: 5EDU).

It was noticed that compound **4i** perfectly fitted into the active site of HDAC3 executing several interactions that were comparatively higher than the binding of other respective HDAC isoforms (Figure 4.26). It was also in agreement with the enzyme inhibitory results obtained for compound **4i**. Regarding the binding mode of interaction at the HDAC3 active site (Figure 4.26A), it was noticed that the amide group adjacent to the carbonyl group formed a salt bridge interaction with the catalytic Zn²⁺ ion. The other amide group formed a hydrogen bonding interaction with Tyr298 amino acid residue. The other hydrogen bonding interaction between the amide group adjacent to the pyrazine scaffold and Asp93 was found to be the most crucial one because such type of interaction was not observed while binding with other HDAC isoforms (Figure 4.26). Similarly, in the case of binding with HDAC3, the pyrazine scaffold was found to be involved with three π - π stacking interactions with amino acid residues Phe144, Phe200, and His172. Apart from that, the terminal phenyl group also formed a π - π stacking interaction with Phe200. On the other hand, during binding with HDAC2, the carbonyl group was found to form Zn²⁺ metal coordination (Figure 4.26B). Though compound **4i** fitted properly at the HDAC2 active site, it formed only a few interactions (a π - π stacking interaction between the pyrazine ring and Phe155 and a hydrogen bonding interaction between the amide group and amino acid residue Gly154). It properly justified the HDAC3-selective character over HDAC2 of compound **4i**. Again, while binding to the active site of HDAC8 (PDB: 1T69), few interactions were noticed but there was no such involvement of the pyrazine ring (Figure 4.26C). It also speculated a comparatively lower HDAC8 inhibitory activity of **4i** than in HDAC3. Interestingly, it was noticed that while binding to the active site of HDAC6 (PDB: 5EDU), compound **4i** displayed a completely different orientation than the other HDACs

Chapter 4: Pyrazino hydrazides as HDAC3 selective inhibitors

mentioned above (**Figure 4.26D**). It justified the HDAC6-sparing character of compound **4i**. Therefore, in a nutshell, the binding mode of interaction analysis completely correlated with the enzyme inhibitory activity and explained the HDAC3-selective character of compound **4i**.

4.3. MATERIALS AND METHODS

4.3.1. Chemistry

The required starting materials, solvents, and chemical reagents were procured from different vendors, and make such as Sigma-Aldrich was used directly without further purification. The reference compound, **UF010** was synthesized as per the reported protocol and was also physicochemically characterized for its purity and structural confirmation. (Wang et al., 2015) Thin-layer chromatography technique was used to monitor the reaction progress and completion, by using precoated silica gel plates with Merck 60 F254 silica gel bought from Merck Millipore Co., USA.

Purification and analysis: The obtained reaction products were purified using the column chromatography technique and for this purpose different mesh sizes (100-200 or 230-400) of silica gel were used. The desired product was eluted using different polar and non-polar solvents. Further, the compounds were subjected to purity determination using HPLC/LC-MS analysis. For this purpose, the HPLC-UFLC Shimadzu instrument was used coupled with LC-MS 8040 and a photodiode array detector. The reverse phase column of C18, 4.6×150 mm, of 5 μ was used for HPLC analysis at a flow rate of 1 mL/min for 10 min. The isocratic flow was maintained by using the ratio of A20: B80 or A10: B90 (A is water + 0.05% TFA, B is methanol were used as solvents). About 0.6 mL/min flow rate was maintained for LC-MS for about 10 min run.

Characterization: The physicochemical characterization of the final compounds was carried out by using proton (^1H) and carbon-13 (^{13}C) NMR techniques along with high-

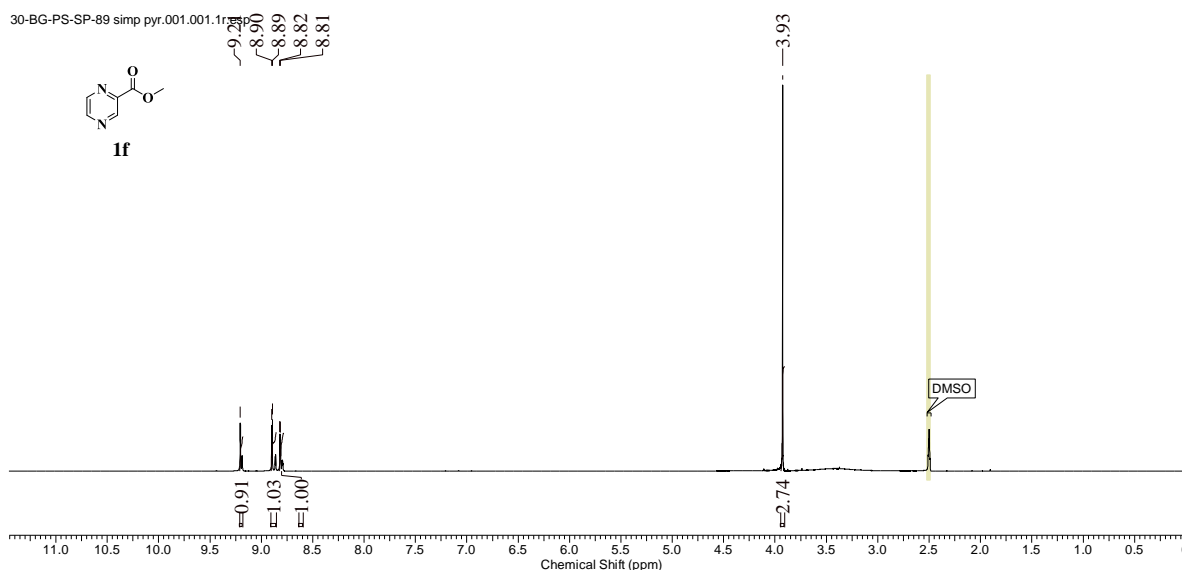
Chapter 4: Pyrazino hydrazides as HDAC3 selective inhibitors

resolution mass spectroscopy (HRMS) along with HPLC/LC-MS for purity analysis. >95% purity was found for all the final compounds as per the HPLC analysis and the lead compound **4i**, and the reference compound, **UF010** were found to be 99.16% and 100% pure. The NMR data including both ^1H and ^{13}C NMR were recorded on 400 MHz Bruker, ASCEND™ spectrometer. Deuterated solvents such as chloroform-*d* (CDCl_3), dimethylsulfoxide- d_6 ($\text{DMSO-}d_6$), and methanol- d_4 (CD_3OD) were used for the purpose. Trimethyl silane (TMS) was used as the internal standard. The data was recorded as chemical shifts (δ) in ppm (parts per million) units and the corresponding coupling constants (J) were reported in Hz (hertz) units. ACD/Lab's 2D NMR software of version 12.01 was used for NMR data analysis. HRMS analysis was conducted using the HRMS instrument of make 6545 Q-TOF LC/MS, Agilent, the facility at BITS-Pilani, Pilani campus. The data obtained from the HRMS analysis confirmed the purity of the final compounds synthesized as the data indicated a difference of ± 0.005 between the obtained mass and the theoretical mass of the compounds.

4.3.1.1. Preparation of methyl pyrazine-2-carboxylate (1f)

Pyrazine 2-carboxylic acid (**5**) (1 g, 8.06 mmol) was dissolved in methanol and to this catalytic amount of concentrated hydrochloric acid was added dropwise and refluxed for 2 – 4 h. The excess solvent was evaporated and the crude reaction mixture was dissolved in ethyl acetate and washed with water three times and the organic layer was separated. The obtained organic layer was then dried over anhydrous sodium sulphate and the excess solvent was removed under vacuum using a rota evaporator. The crude reaction mixture was then column purified and the pure compound **1f** was eluted from the column using a 40% ethyl acetate and 60% hexane solvent mixture. The compound **1f** was obtained as a light brown powder of about 81% yield. ^1H NMR (400 MHz, $\text{DMSO-}d_6$) δ 9.19 - 9.22 (m, 1H), 8.86 - 8.92 (m, 1H), 8.80 - 8.84 (m, 1H), 3.93 (s, 3H).

Chapter 4: Pyrazino hydrazides as HDAC3 selective inhibitors



Spectra 4.1: ^1H NMR Spectra for the compound **1f**.

4.3.1.2. Preparation of pyrazine-2-carbohydrazide (**2f**)

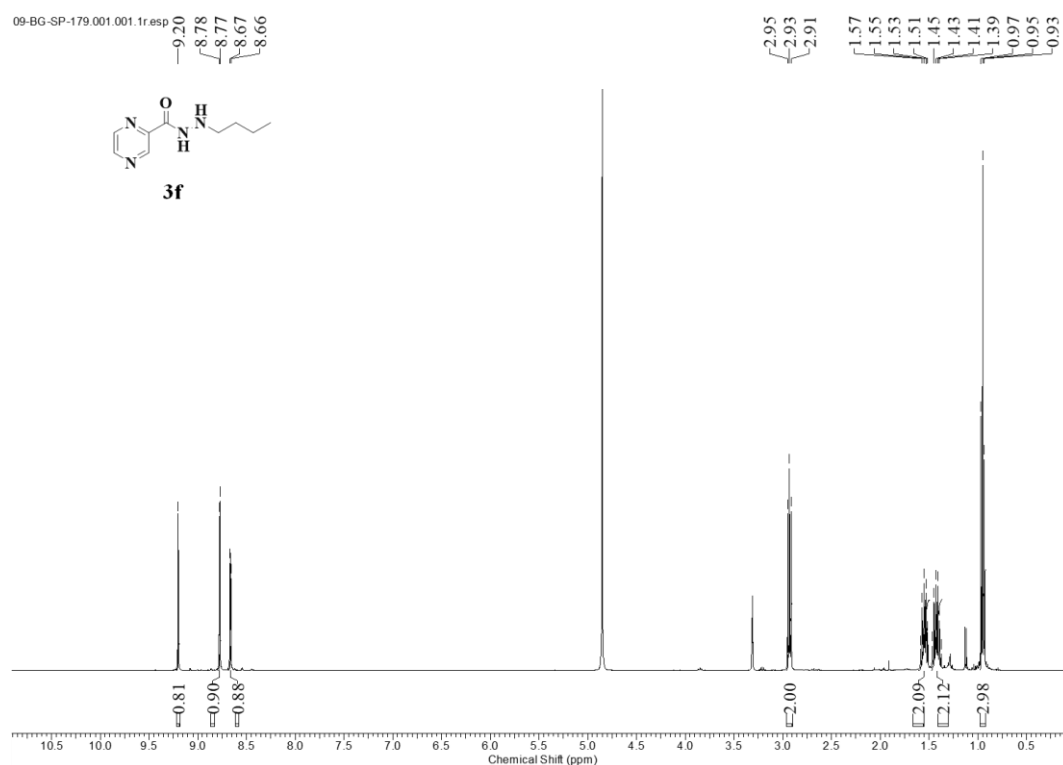
Methyl pyrazine-2-carboxylate (**1f**) (500 mg, 3.62 mmol) was dissolved in 10 mL of methanol, and to these 10 equivalents of hydrazine monohydrate (1.12 mL, 36.2 mmol) was added and the reaction was refluxed for 6 h. The reaction completion was confirmed by TLC and the crude reaction mixture was rota-evaporated and vacuum dried and was carried to the next reaction without any further purification.

4.3.1.3. Preparation of *N'*-butylpyrazine-2-carbohydrazide (**3f**)

Pyrazine-2-carbohydrazide (**2f**, 100 mg, 0.723 mmol) was taken in a round-bottomed flask and to this 5 mL of ethanol was added. To this, 78.3 μL of butyraldehyde (1 eq, 0.868 mmol) and 200 mg of anhydrous MgSO_4 were added and left for stirring overnight and the reaction completion was monitored by TLC. After the reaction is complete, MgSO_4 was filtered and the excess ethanol was removed and dried completely. The obtained crude reaction mixture was then dissolved in 2 mL of methanol and to this 68.24 mg, 1.09 mmol of sodium cyanoborohydride was added as a reducing agent. Then a 1:1 mixture of methanol and concentrated hydrochloric acid was added dropwise and left for stirring until the reaction completion was confirmed by TLC. The reaction mixture was then neutralized

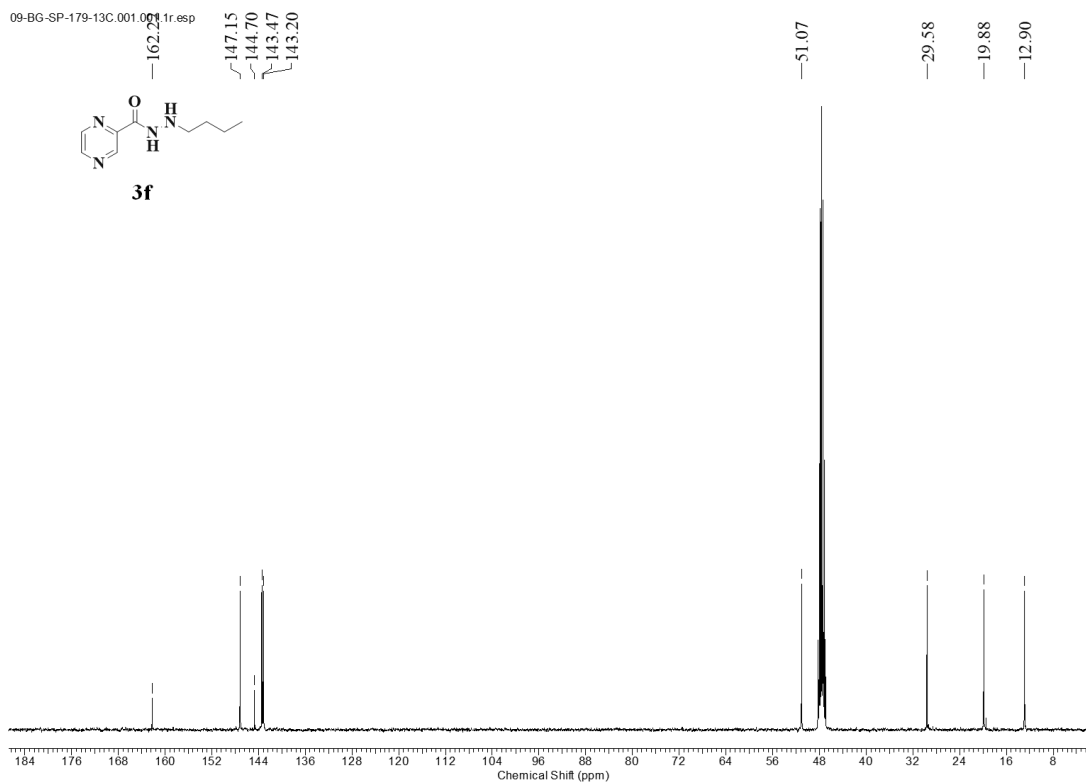
Chapter 4: Pyrazino hydrazides as HDAC3 selective inhibitors

by an aqueous sodium bicarbonate solution and concentrated under vacuum. The crude reaction mixture was extracted into the ethyl acetate layer three times from the aqueous layer. The organic layer was all combined and then dried under a rota evaporator. The resultant reaction mixture was then column purified using 30% hexane and 70% ethyl acetate as solvent system to obtain the final product **3f** as a light brown powder of about 52% yield. ^1H NMR (400 MHz, methanol- d_4) δ 9.20 (d, $J = 1.50$ Hz, 1H), 8.77 (d, $J = 2.38$ Hz, 1H), 8.66 (dd, $J = 1.56, 2.44$ Hz, 1H), 2.90 - 2.96 (m, 2H), 1.49 - 1.60 (m, 2H), 1.36 - 1.47 (m, 2H), 0.93 - 0.97 (t, $J = 7.32$ Hz, 3H). ^{13}C NMR (101 MHz, methanol- d_4) δ 162.2, 147.2, 144.7, 143.5, 143.2, 51.1, 29.6, 19.9, 12.9 HRMS (APESI) m/z calcd for $\text{C}_9\text{H}_{14}\text{N}_4\text{O}$. $[\text{M}+\text{H}]^+$: 195.1188; found 195.1242.

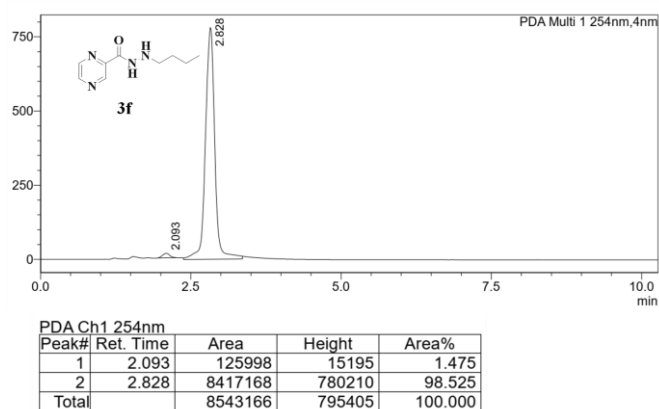


Spectra 4.2: ^1H NMR Spectra for the compound **3f**.

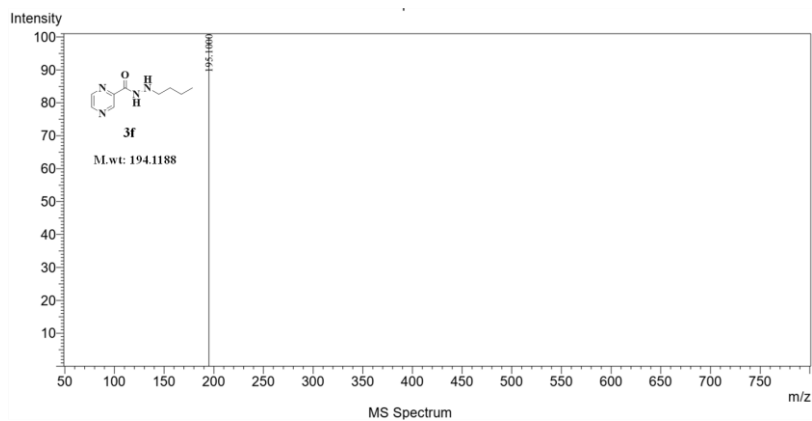
Chapter 4: Pyrazino hydrazides as HDAC3 selective inhibitors



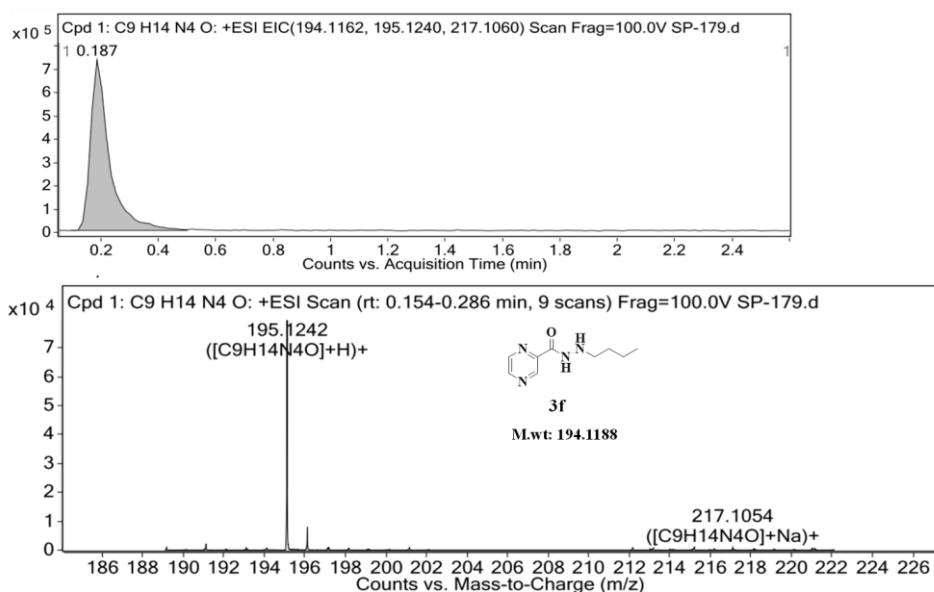
Spectra 4.3: ¹³C NMR Spectra for compound **3f**.



Spectra 4.4: HPLC traces of compound **3f**.



Spectra 4.5: LC-MS Spectra for the compound 3f.



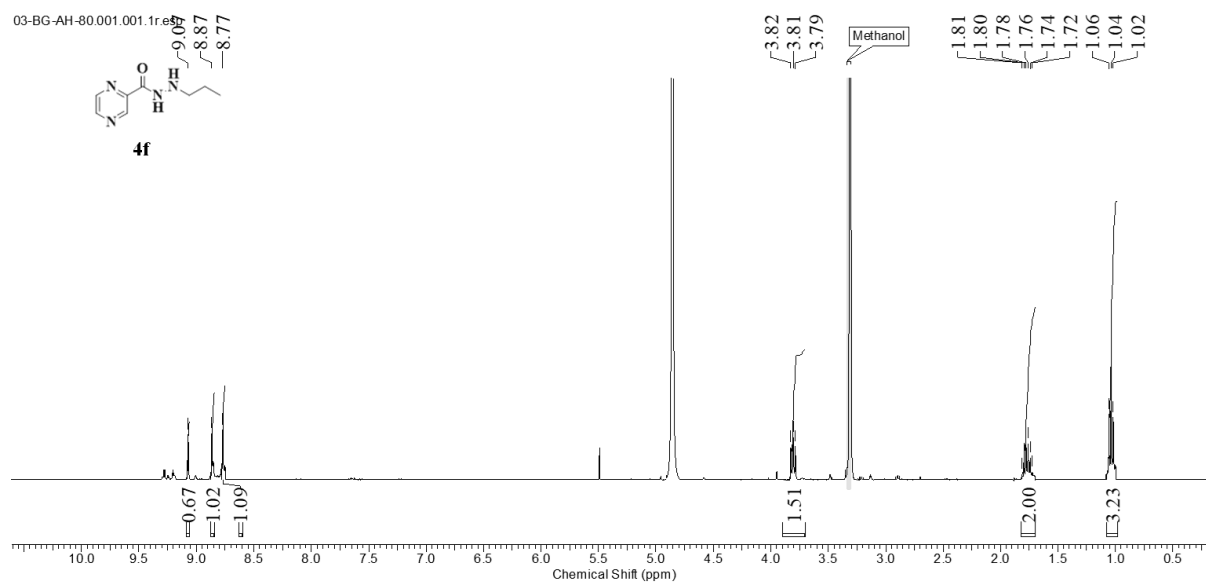
Spectra 4.6: HRMS Spectra for the compound 3f.

4.3.1.4. Preparation of *N'*-propylpyrazine-2-carbohydrazide (4f)

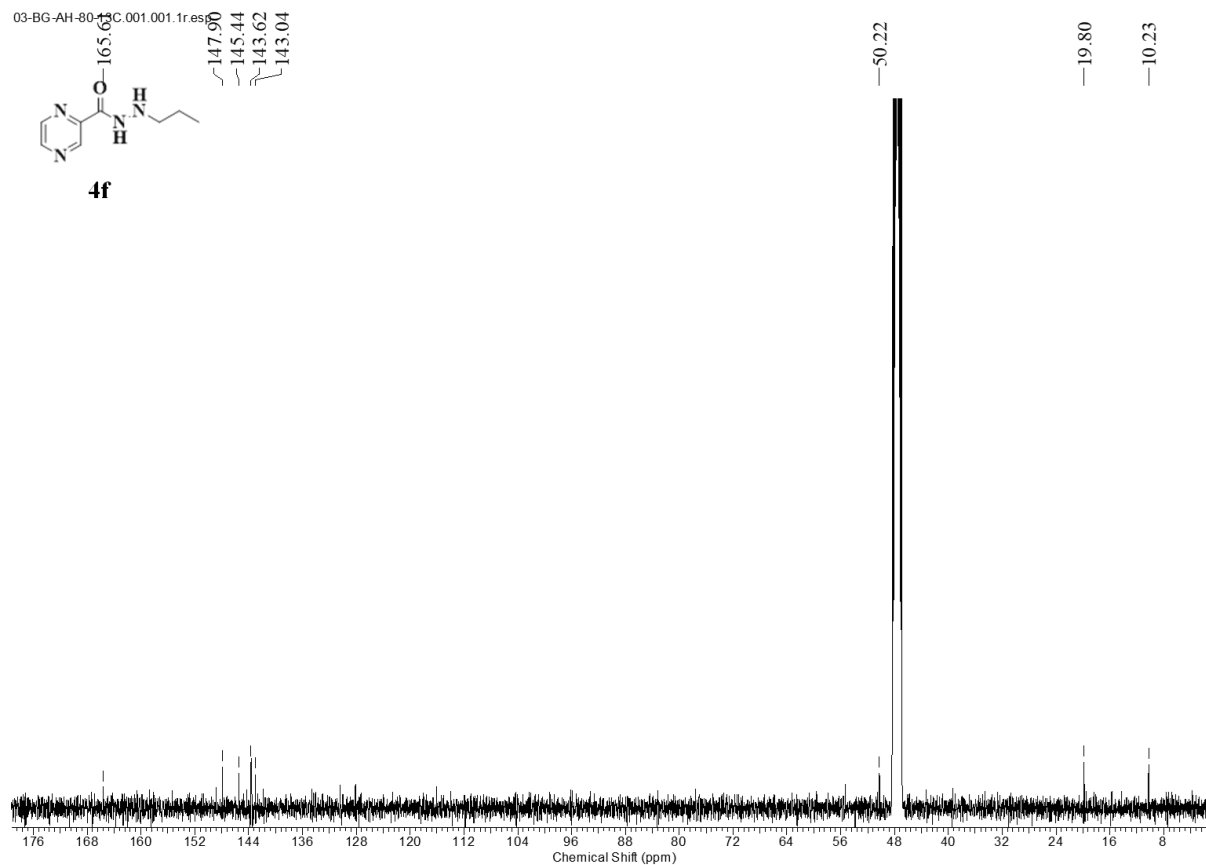
Pyrazine-2-carbohydrazide (**2f**, 100 mg, 0.723 mmol) was taken in a round-bottomed flask and to this 5 mL of ethanol was added. To this reaction mixture, 62.5 μ L of butyraldehyde (1 eq, 0.868 mmol) and 200 mg of anhydrous MgSO₄ were added and left for stirring overnight and the reaction completion was monitored by TLC. After the reaction is complete, MgSO₄ was filtered and the excess ethanol was removed and dried completely. The obtained crude reaction mixture was then dissolved in 2 mL of methanol and to this 68.24 mg, 1.09 mmol of sodium cyanoborohydride was added as a reducing agent. Then a 1:1 mixture of methanol and concentrated hydrochloric acid was added dropwise and left for stirring until the reaction completion was confirmed by TLC. The reaction mixture was then neutralized by an aqueous sodium bicarbonate solution and concentrated under vacuum. The crude reaction mixture was extracted into the ethyl acetate layer three times from the aqueous layer. The organic layer was all combined and then dried under a rota evaporator. The resultant reaction mixture was then column purified using 30% hexane and 70% ethyl acetate as solvent system to obtain the final product **4f** as a light brown powder

Chapter 4: Pyrazino hydrazides as HDAC3 selective inhibitors

about 63% yield. ^1H NMR (400 MHz, methanol- d_4) δ 9.07 (s, 1H), 8.87 (s, 1H), 8.77 (s, 1H), 3.79 - 3.82 (m, 2H), 1.72 - 1.81 (m, 2H), 1.02 - 1.06 (t, $J = 7.44$ Hz, 3H). ^{13}C NMR (101 MHz, methanol- d_4) δ 165.6, 147.9, 145.4, 143.6, 143.0, 50.2, 19.8, 10.2. HRMS (APESI) m/z calcd for $\text{C}_8\text{H}_{12}\text{N}_4\text{O}$. $[\text{M}+\text{H}]^+$: 181.1031; found 181.1081.

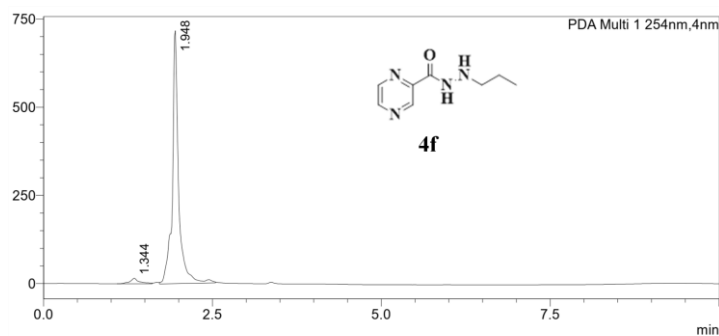


Spectra 4.7: ^1H NMR Spectra for the compound 4f.



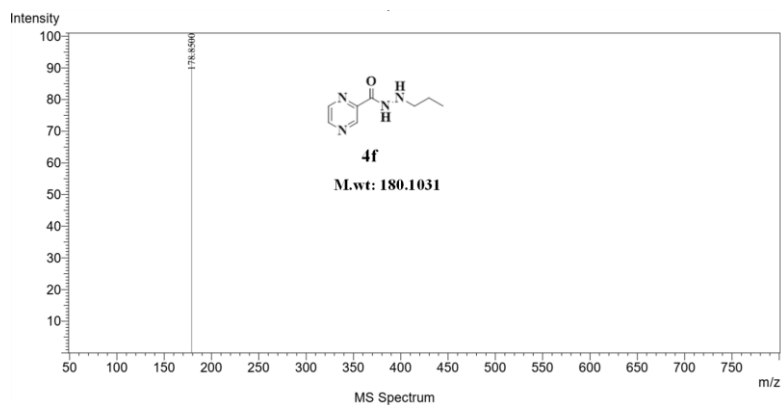
Chapter 4: Pyrazino hydrazides as HDAC3 selective inhibitors

Spectra 4.8: ¹³C NMR Spectra for compound 4f.

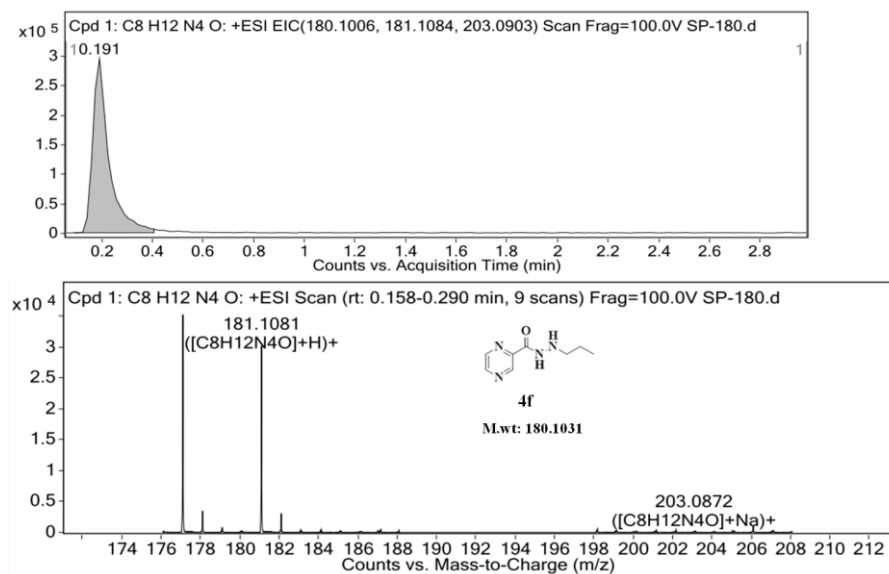


Peak#	Ret. Time	Area	Height	Area%
1	1.344	152735	15839	3.174
2	1.948	4658855	717003	96.826
Total		4811590	732842	100.000

Spectra 4.9: HPLC traces of compound 4f.



Spectra 4.10: LC-MS Spectra for the compound 4f.

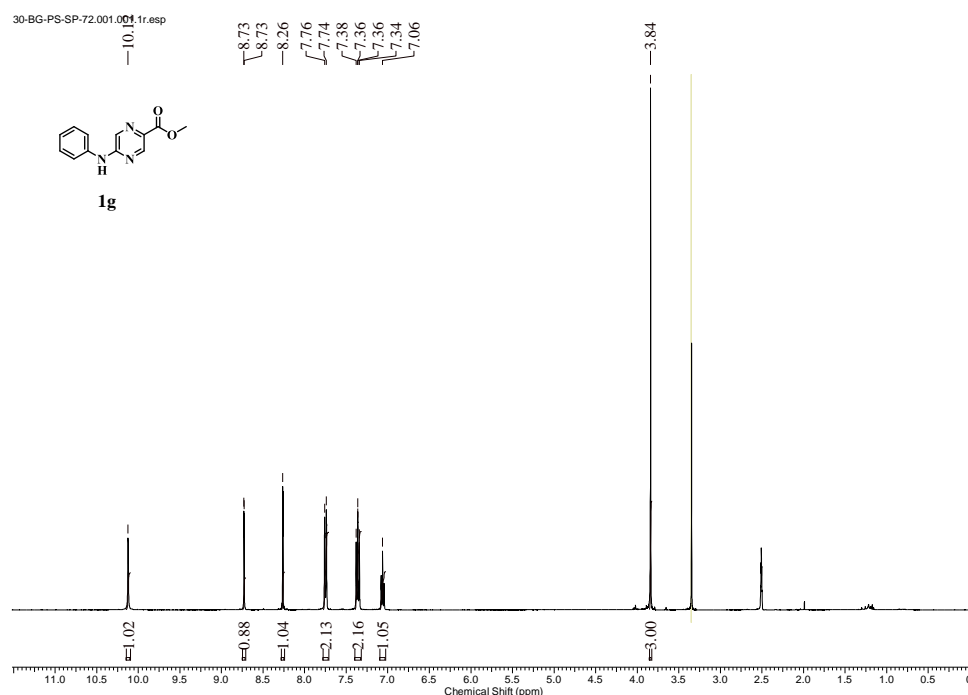


Spectra 4.11: HRMS Spectra for the compound 4f.

Chapter 4: Pyrazino hydrazides as HDAC3 selective inhibitors

4.3.1.5. Preparation of methyl 5-(phenylamino)pyrazine-2-carboxylate (**1g**)

Methyl 5-chloro pyrazine 2-carboxylate (**6**) (1 g, 5.79 mmol) was dissolved in 30 mL of 1,4-dioxane and to this, 2 equivalents of *para* toluene sulphonic acid (2 g, 11.59 mmol) and aniline (0.793 mL, 8.69 mmol) was added and refluxed for 16 h. The reaction completion was monitored by TLC and once the reaction is complete, the excess solvent was evaporated under a rota evaporator. The crude reaction mixture was dissolved in ethyl acetate and washed with water three times and the organic layer was separated. The organic layer containing the compound was then dried over anhydrous sodium sulphate and the excess solvent was removed under vacuum. The crude reaction mixture was then column purified and the pure compound **1g** was eluted from the column using 25% ethyl acetate and 75% hexane as solvents. The obtained compound **1g** in the form of brown powder of about 76% yield. ^1H NMR (400 MHz, DMSO- d_6) δ 10.12 (s, 1H), 8.73 (s, 1H), 8.26 (s, 1H), 7.74 – 7.76 (d, $J = 9.63$ Hz, 2H), 7.34 – 7.38 (t, $J = 7.57$, Hz, 2H), 7.06 (s, 1H), 3.84 (s, 3H).



Spectra 4.12: ^1H NMR Spectra for the compound **1g**.

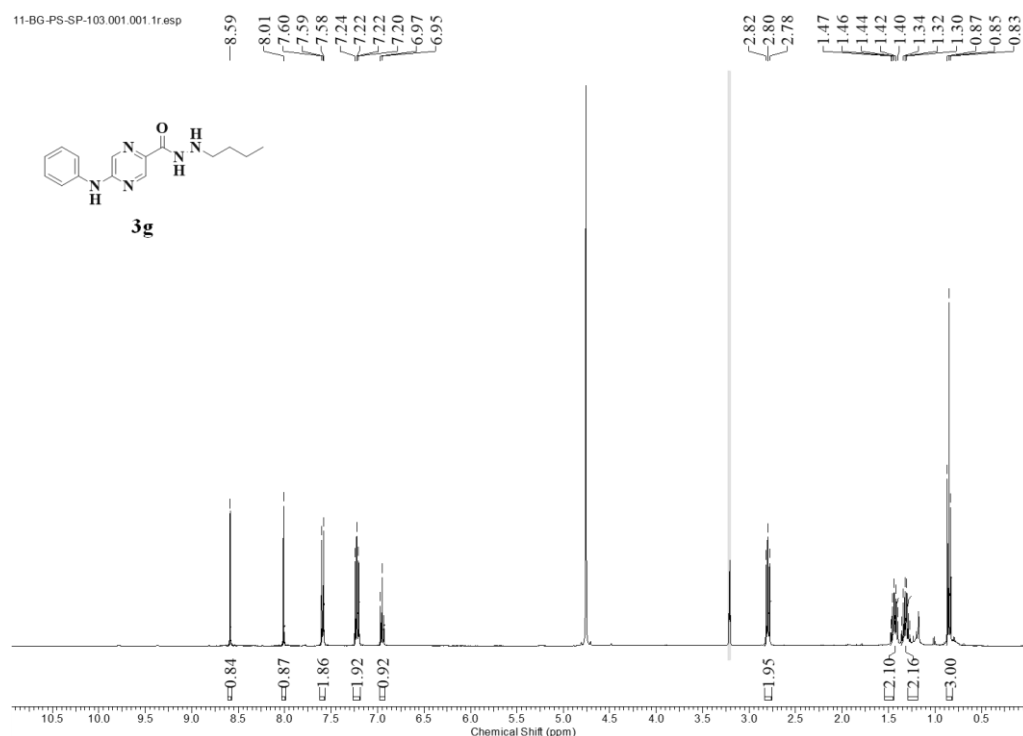
Chapter 4: Pyrazino hydrazides as HDAC3 selective inhibitors

4.3.1.6. Preparation of 5-(phenylamino)pyrazine-2-carbohydrazide (2g)

Following the synthetic procedure of **2f**, compound **1f** and the excess of hydrazine monohydrate gave **2g** as brown solid. The crude reaction mixture was carried for next reaction without further purification.

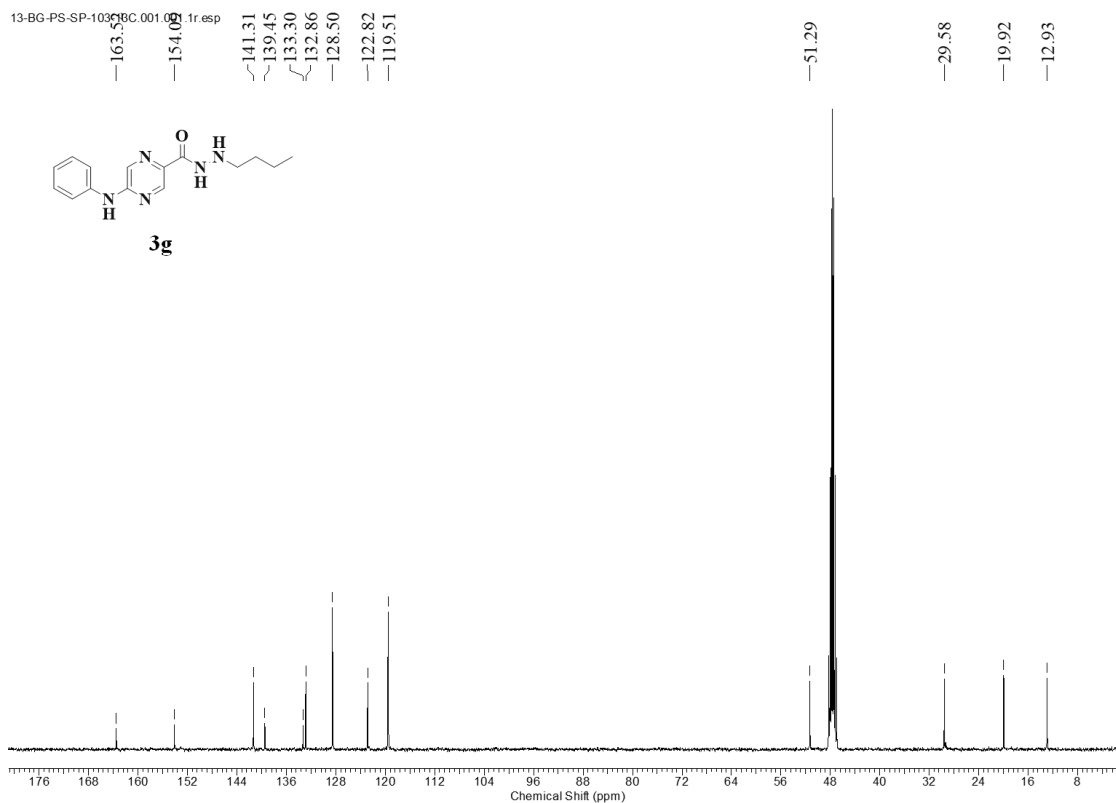
4.3.1.7. Preparation of N'-butyl-5-(phenylamino)pyrazine-2-carbohydrazide (3g)

Following the synthetic procedure of **3f**, starting materials **2g** and butyraldehyde gave **3g** as a white powder in 42% yield. ^1H NMR (400 MHz, methanol- d_4) δ 8.59 (d, $J = 1.25$ Hz, 1H), 8.01 (d, $J = 1.38$ Hz, 1H), 7.59 (d, $J = 7.63$ Hz, 2H), 7.21 - 7.25 (m, 2H), 6.93 - 6.97 (m, 1H), 2.78 - 2.82 (m, 2H), 1.39 - 1.49 (m, 2H), 1.27 - 1.36 (m, 2H), 0.83 - 0.87 (t, $J = 7.32$ Hz, 3H). ^{13}C NMR (101 MHz, methanol- d_4) δ 163.5, 154.1, 141.3, 139.4, 133.3, 132.9, 128.5, 122.8, 119.5, 51.3, 29.6, 19.9, 12.9. HRMS (APESI) m/z calcd for $\text{C}_{15}\text{H}_{19}\text{N}_5\text{O}$. $[\text{M}+\text{H}]^+$: 286.162; found 286.1663.

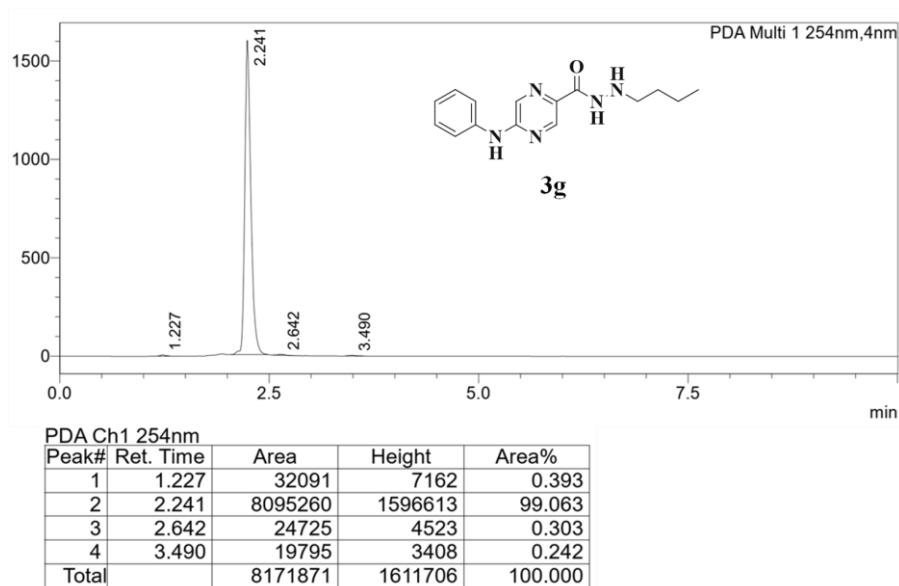


Spectra 4.13: ^1H NMR Spectra for the compound **3g**.

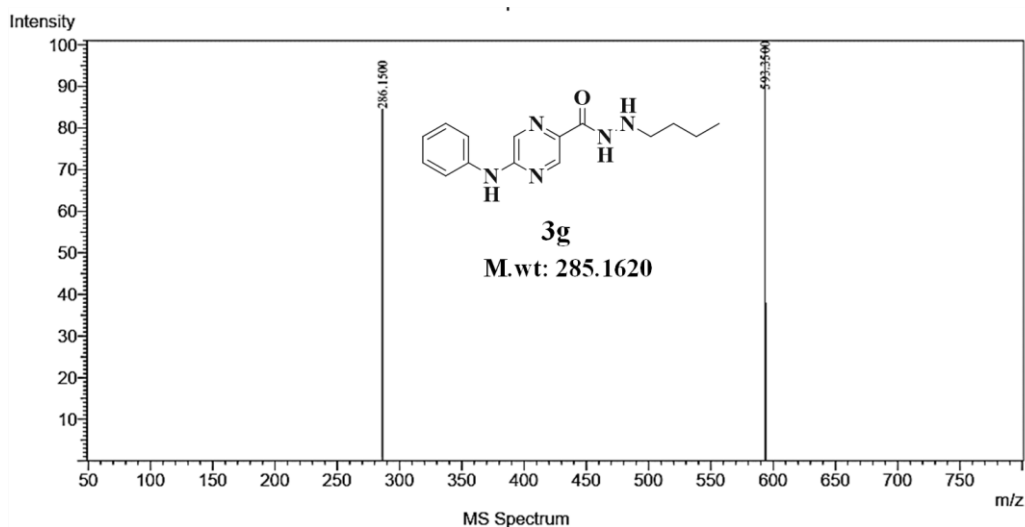
Chapter 4: Pyrazino hydrazides as HDAC3 selective inhibitors



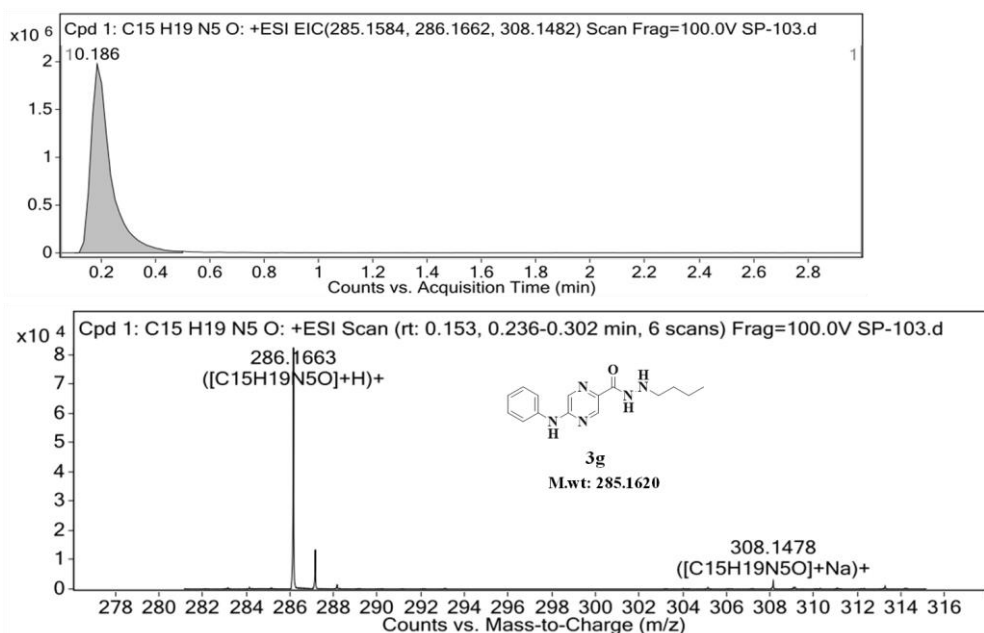
Spectra 4.14: ¹³C NMR Spectra for compound **3g**.



Spectra 4.15: HPLC traces of compound **3g**.



Spectra 4.16: LC-MS Spectra for the compound 3g.



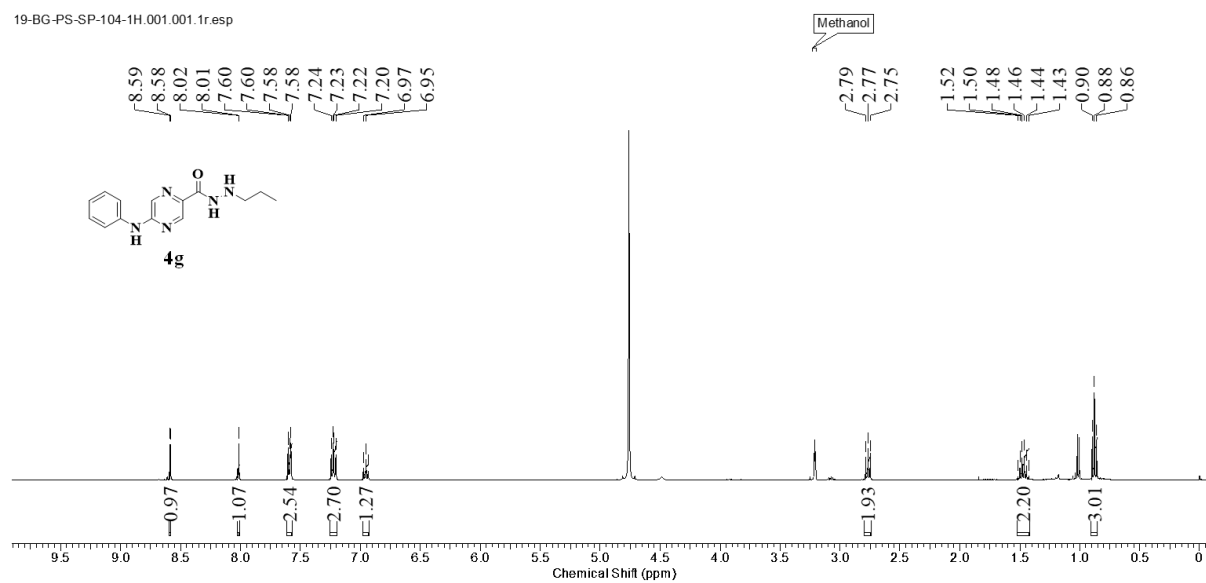
Spectra 4.17: HRMS Spectra for the compound 3g.

4.3.1.8. Preparation of *N'*-propyl-5-(phenylamino)pyrazine-2-carbohydrazide (4g)

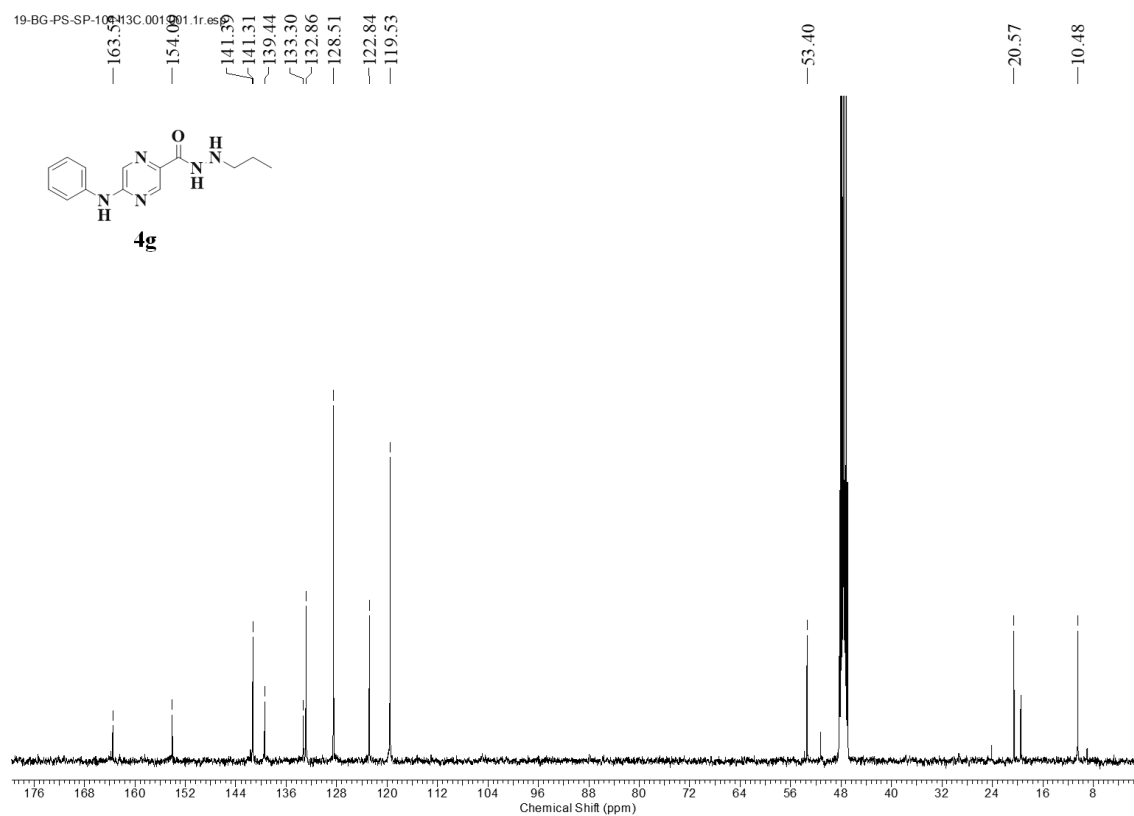
Following the synthetic procedure of **4f**, starting materials **2g** and propionaldehyde gave **4g** as a white powder in 47% yield. ¹H NMR (400 MHz, methanol-*d*₄) δ 8.69 (d, *J* = 1.38 Hz, 1H), 8.12 (d, *J* = 1.38 Hz, 1H), 7.69 - 7.71 (m, 2H), 7.31 - 7.35 (m, 2H), 7.04 - 7.08 (m, 1H), 2.86 - 2.89 (m, 2H), 1.53 - 1.63 (m, 2H), 0.97 - 1.01 (t, *J* = 7.44 Hz, 3H). ¹³C NMR (101 MHz, methanol-*d*₄) δ 163.5, 154.1, 141.4, 141.3, 139.4, 133.3, 132.9, 128.5, 122.8, 119.5, 53.4, 20.6, 10.5. HRMS (APESI) *m/z* calcd for C₁₄H₁₇N₅O. [M+H]⁺:

Chapter 4: Pyrazino hydrazides as HDAC3 selective inhibitors

272.1463; found 272.1505.

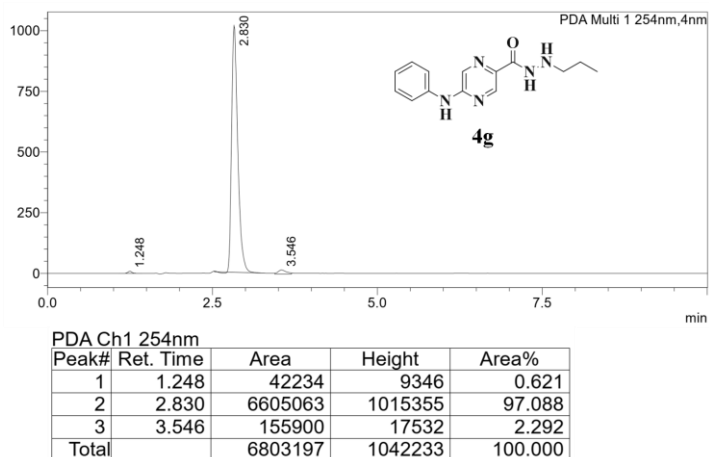


Spectra 4.18: ¹H NMR Spectra for the compound **4g**.

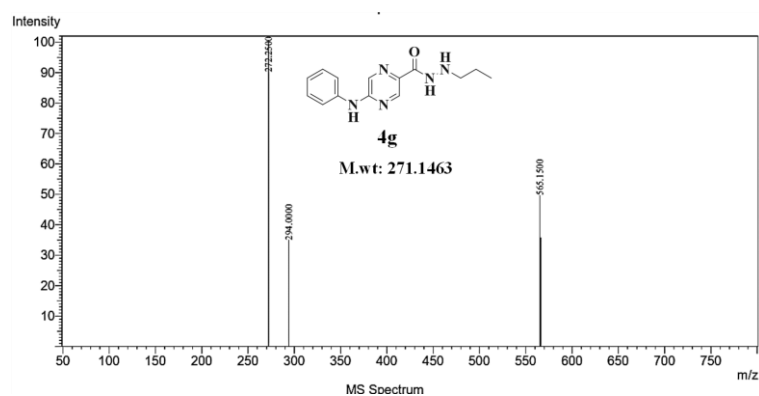


Spectra 4.19: ¹³C NMR Spectra for compound **4g**.

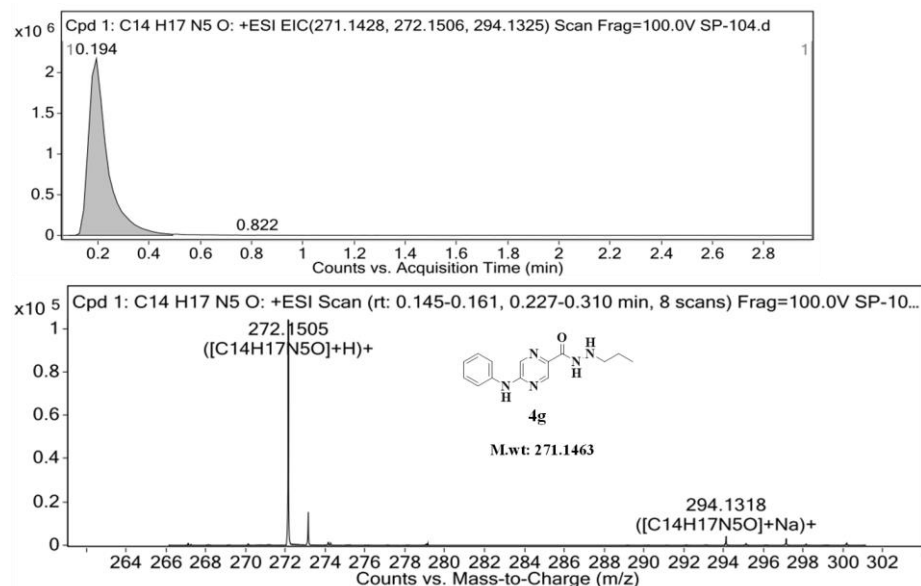
Chapter 4: Pyrazino hydrazides as HDAC3 selective inhibitors



Spectra 4.20: HPLC traces of compound 4g.



Spectra 4.21: LC-MS Spectra for the compound 4g.

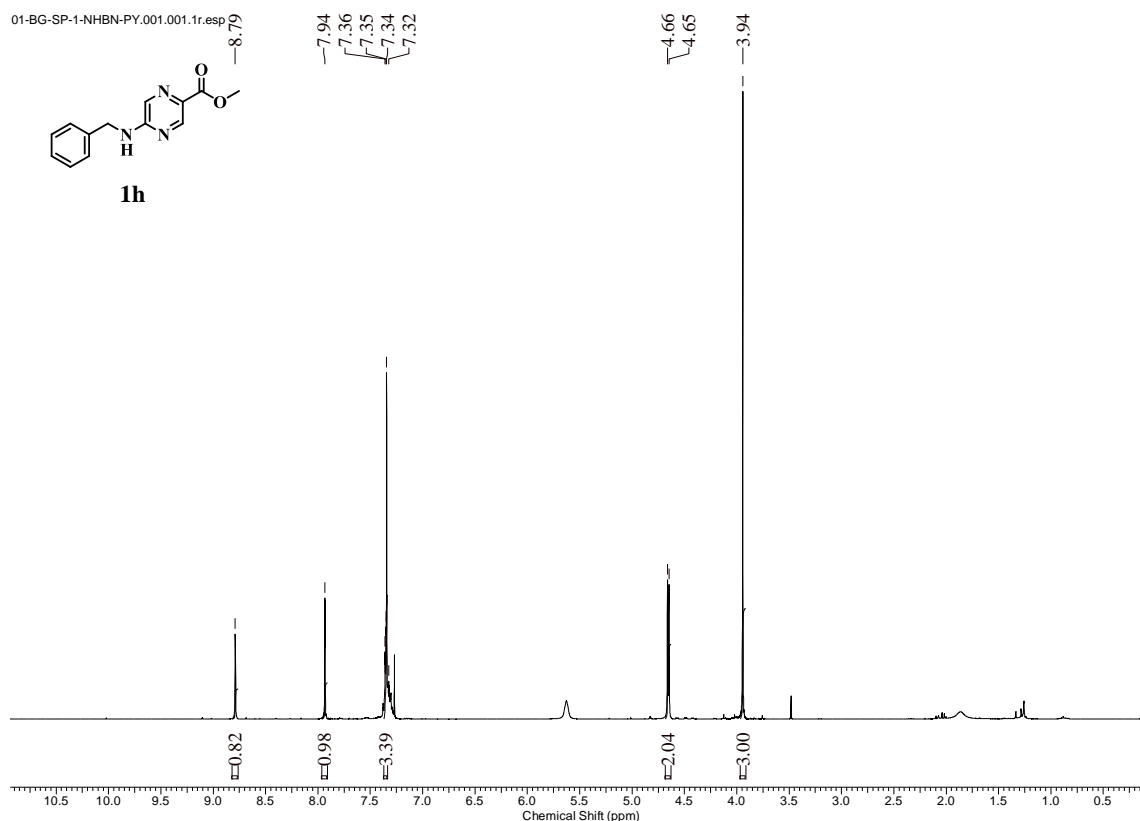


Spectra 4.22: HRMS Spectra for the compound 4g.

4.3.1.9. Preparation of methyl 5-(benzylamino)pyrazine-2-carboxylate (1h)

Chapter 4: Pyrazino hydrazides as HDAC3 selective inhibitors

Methyl 5-chloro pyrazine 2-carboxylate (**6**) (1 g, 5.79 mmol) was dissolved in 30 mL of 1,4-dioxane, and to these 2 equivalents of *para* toluene sulphonic acid (2 g, 11.59 mmol) and benzylamine (0.950 mL, 8.69 mmol) was added and refluxed for 12 h. The reaction completion was monitored by TLC and once the reaction is complete, the excess solvent was evaporated under rota evaporator. The crude reaction mixture was dissolved in ethyl acetate and washed with water three times and the organic layer was separated. The organic layer containing the compound was then dried over anhydrous sodium sulphate and the excess solvent was removed under vacuum. The crude reaction mixture was then column purified and the pure compound **1h** was eluted from the column using 35% ethyl acetate and 65% hexane as solvents. The obtained compound **1h** in the form of light brown powder of about 76% yield. $^1\text{H NMR}$ (400 MHz, CDCl_3) δ 8.79 (s, 1H), 7.94 (s, 1H), 7.32 - 7.36 (m, 3H), 4.65 (d, $J = 5.63$ Hz, 2H), 3.94 (s, 3H).



Spectra 4.23: $^1\text{H NMR}$ Spectra for the compound **1h**.

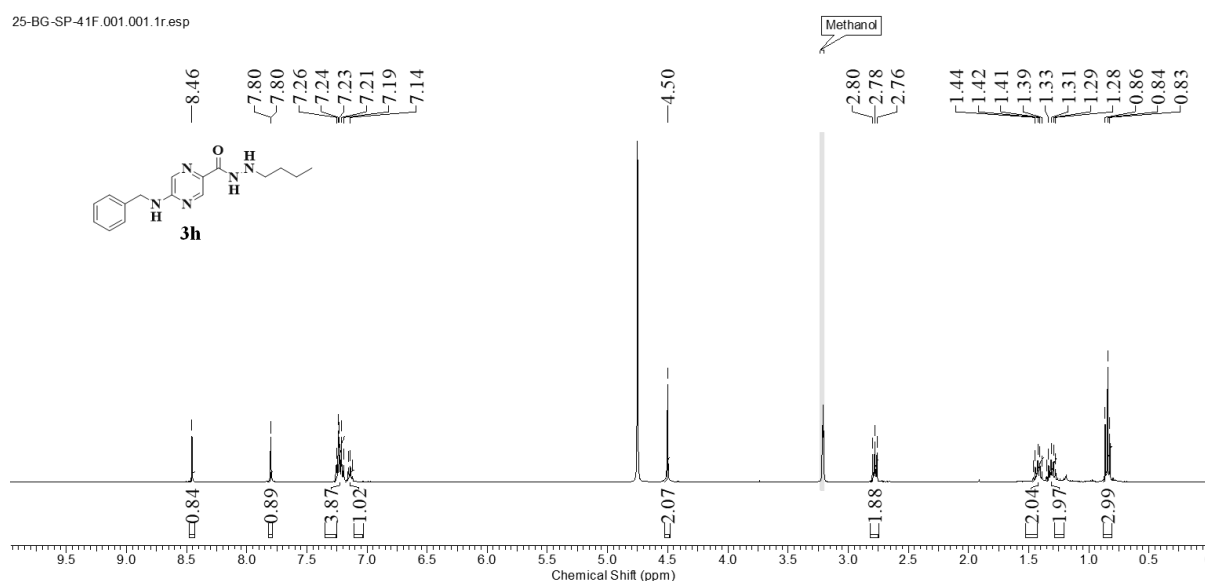
4.3.1.10. Preparation of 5-(benzylamino)pyrazine-2-carbohydrazide (**2h**)

Chapter 4: Pyrazino hydrazides as HDAC3 selective inhibitors

Following the synthetic procedure of **2f**, compound **1h** and excess of hydrazine monohydrate gave **2h** as a light brown solid. The crude reaction mixture was carried out for the next reaction without further purification.

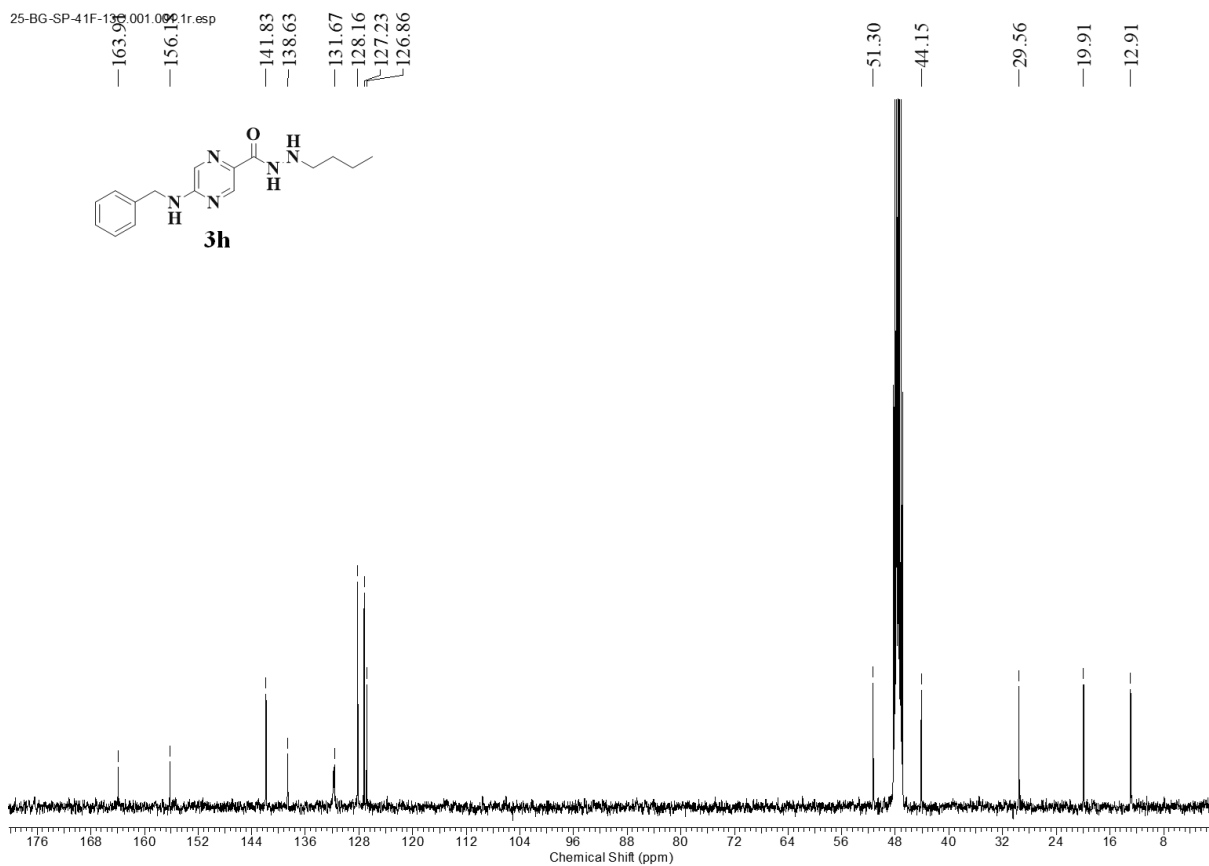
4.3.1.11. Preparation of 5-(benzylamino)-N'-butylpyrazine-2-carbohydrazide (**3h**)

Following the synthetic procedure of **3f**, starting materials **2h** and butyraldehyde gave **3h** as a brown solid in 56% yield. ^1H NMR (400 MHz, methanol- d_4) δ 8.46 (d, $J = 1.38$ Hz, 1H), 7.80 (d, $J = 1.38$ Hz, 1H), 7.19 - 7.26 (m, 4H), 7.12 - 7.16 (m, 1H), 4.50 (s, 2H), 2.76 - 2.80 (t, $J = 7.25$ Hz, 2H), 1.39 - 1.46 (m, 2H), 1.28 - 1.35 (m, 2H), 0.83 - 0.86 (t, $J = 7.32$ Hz, 3H). ^{13}C NMR (101 MHz, methanol- d_4) δ 163.9, 156.2, 141.8, 138.6, 131.8, 131.7, 128.2, 127.2, 126.9, 51.3, 44.1, 29.6, 19.9, 12.9. HRMS (APESI) m/z calcd for $\text{C}_{16}\text{H}_{21}\text{N}_5\text{O}$. $[\text{M}+\text{H}]^+$: 300.1766; found 300.1818.

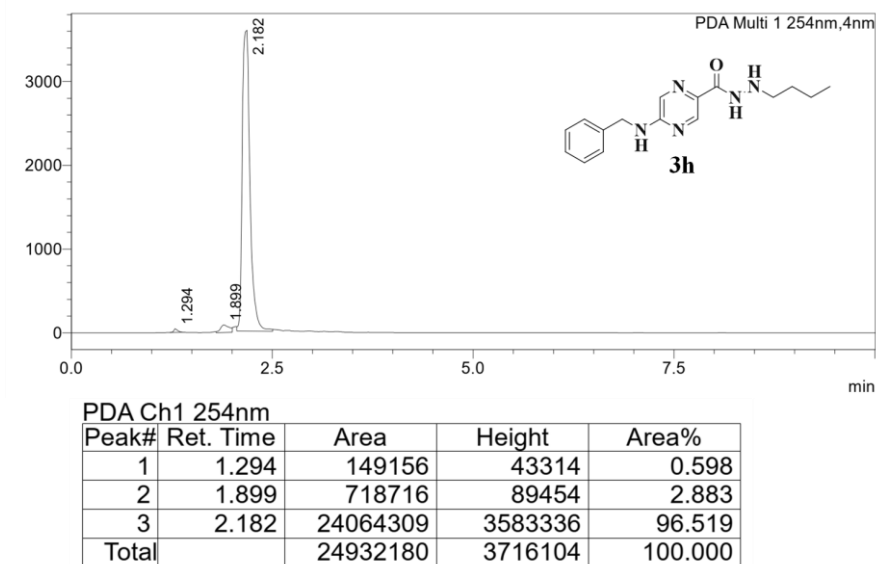


Spectra 4.24: ^1H NMR Spectra for the compound **3h**.

Chapter 4: Pyrazino hydrazides as HDAC3 selective inhibitors

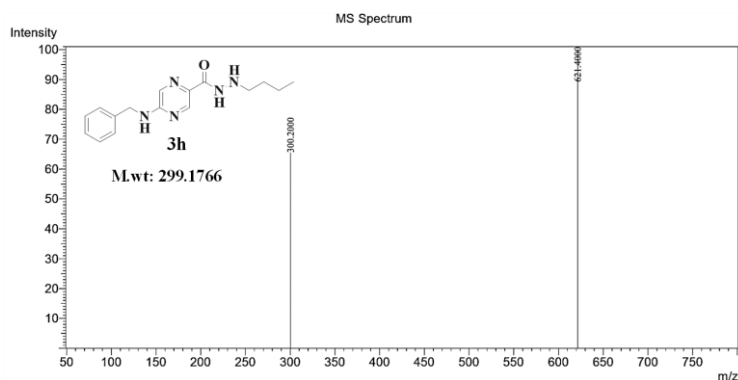


Spectra 4.25: ^{13}C NMR Spectra for compound 3h.

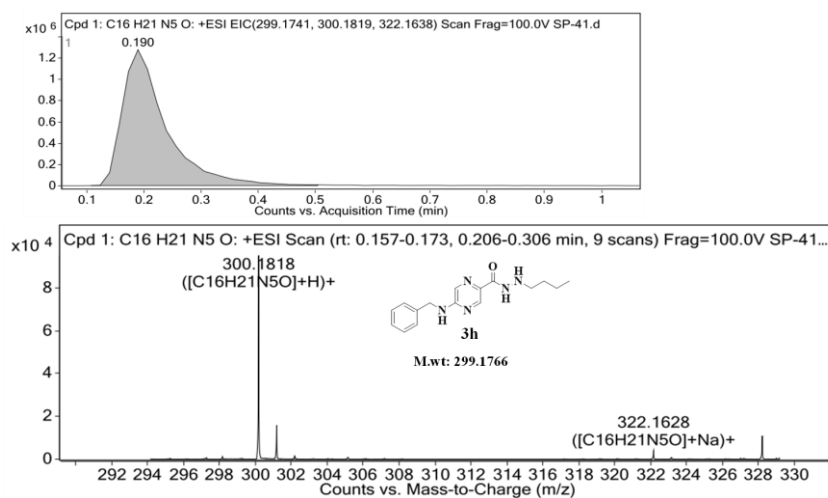


Spectra 4.26: HPLC traces of compound 3h.

Chapter 4: Pyrazino hydrazides as HDAC3 selective inhibitors



Spectra 4.27: LC-MS Spectra for the compound 3h.

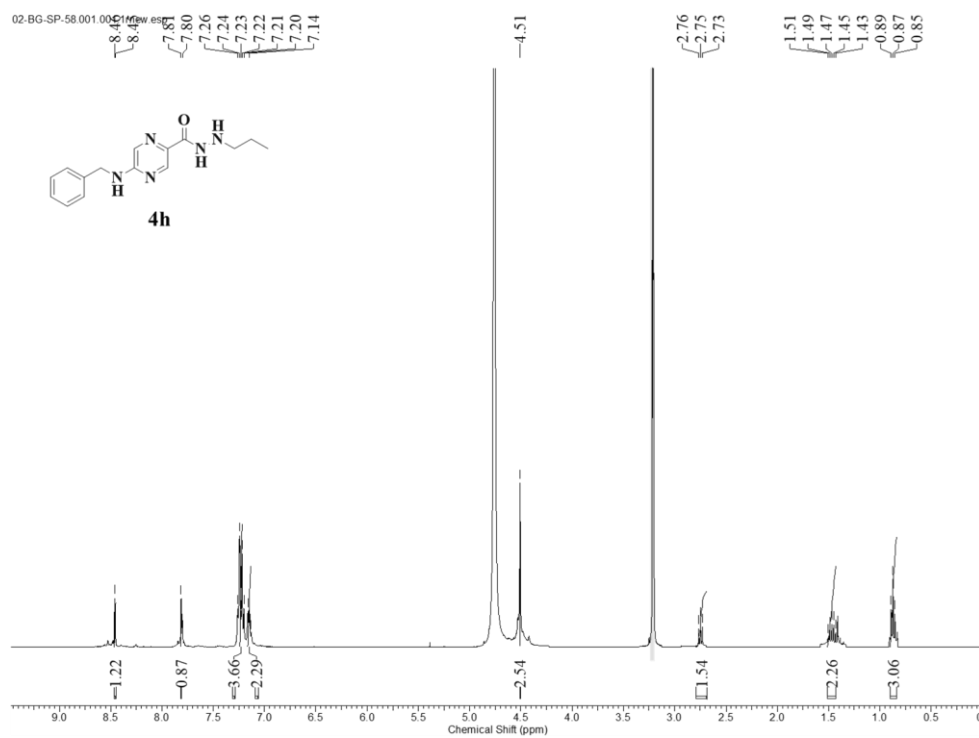


Spectra 4.28: HRMS Spectra for the compound 3h.

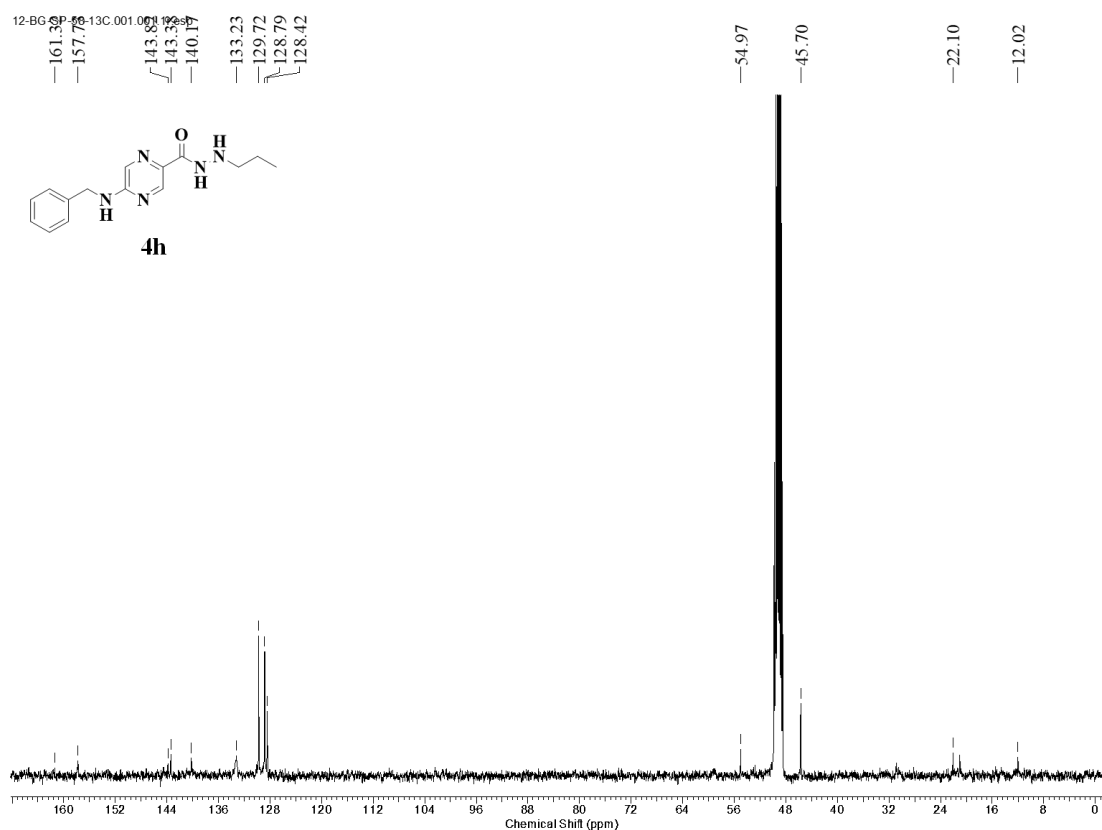
4.3.1.12. Preparation of 5-(benzylamino)-N'-propylpyrazine-2-carbohydrazide (4h)

Following the synthetic procedure of **4f**, the starting materials **2h** and propionaldehyde gave **4h** as a brown solid in 49% yield. ^1H NMR (400 MHz, methanol- d_4) δ 8.46 (s, 1H), 7.81 (s, 1H), 7.24 - 7.26 (m, 3H), 7.14 - 7.17 (m, 2H), 4.51 (s, 2H), 2.73 - 2.76 (m, 1H), 1.43 - 1.51 (m, 2H), 0.85 - 0.89 (t, $J = 7.44$ Hz, 3H). ^{13}C NMR (101 MHz, methanol- d_4) δ 161.3, 157.7, 143.8, 143.4, 140.2, 133.2, 129.7, 128.8, 128.4, 55.0, 45.7, 22.1, 12.0. HRMS (APESI) m/z calcd for $C_{15}H_{19}N_5O$. $[M+H]^+$: 286.161; found 286.1659.

Chapter 4: Pyrazino hydrazides as HDAC3 selective inhibitors

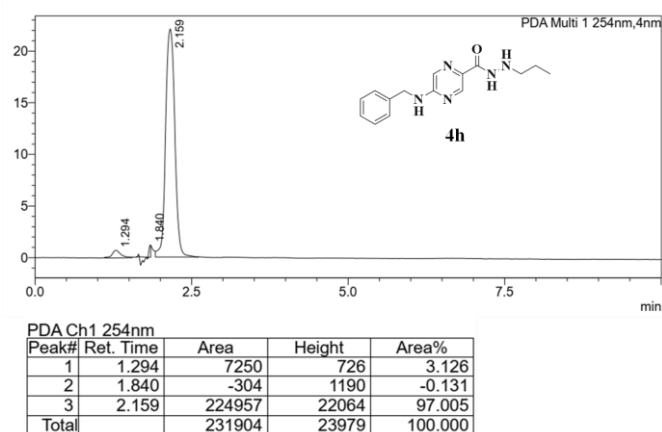


Spectra 4.29: ^1H NMR Spectra for the compound **4h**.

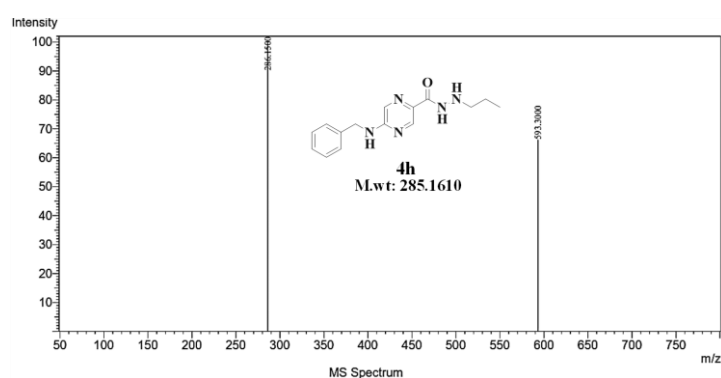


Spectra 4.30: ^{13}C NMR Spectra for compound **4h**.

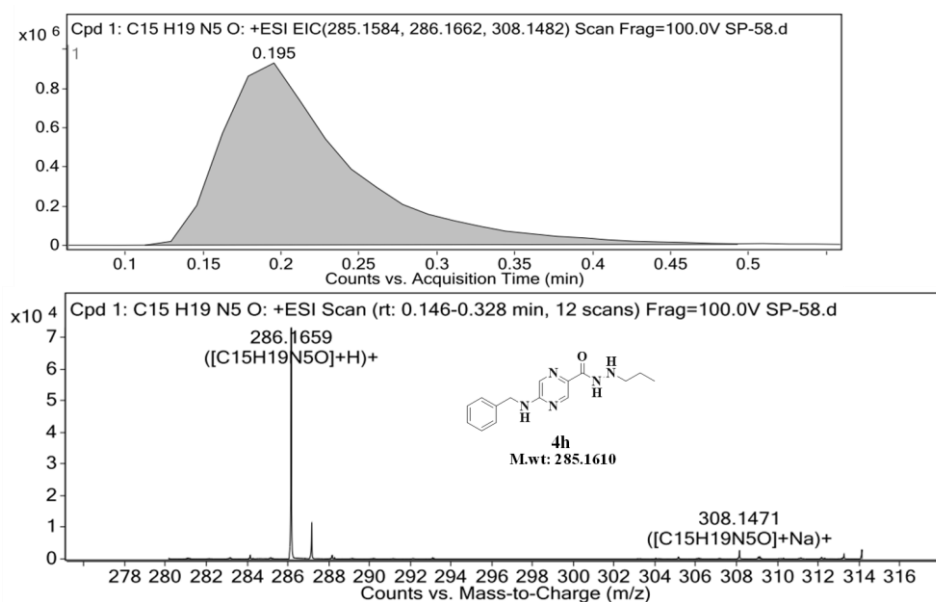
Chapter 4: Pyrazino hydrazides as HDAC3 selective inhibitors



Spectra 4.31: HPLC traces of compound 4h.



Spectra 4.32: LC-MS Spectra for the compound 4h.



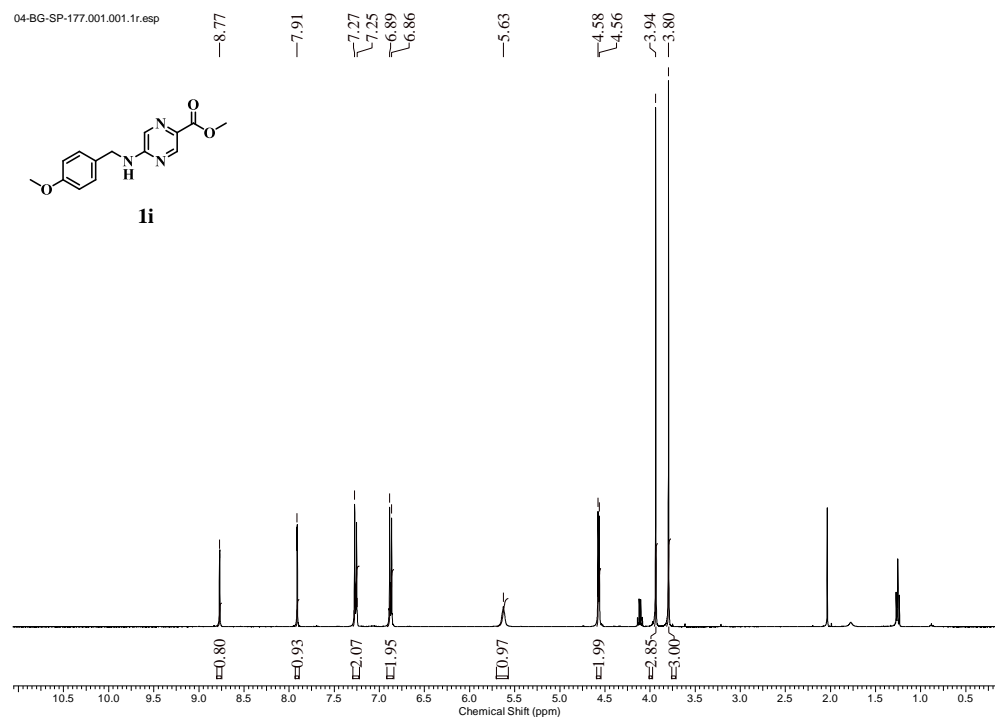
Spectra 4.33: HRMS Spectra for the compound 4h.

4.3.1.13. Preparation of methyl 5-((4-methoxybenzyl)amino)pyrazine-2-carboxylate (1i)

Methyl 5-chloro pyrazine 2-carboxylate (**6**) (3 g, 17.38 mmol) was dissolved in 30 mL of

Chapter 4: Pyrazino hydrazides as HDAC3 selective inhibitors

THF, and to these 2 equivalents of *para* methoxy benzylamine (4.54 mL, 34.77 mmol) was added, and stirred for 18 h at room temperature. The reaction completion was monitored by TLC and once the reaction is complete, the excess solvent was evaporated under a rota evaporator. The crude reaction mixture was dissolved in ethyl acetate and washed with water three times and the organic layer was separated. The organic layer containing the compound was then dried over anhydrous sodium sulphate and the excess solvent was removed under vacuum. The crude reaction mixture was then column purified and the pure compound **1i** was eluted from the column using 15% ethyl acetate and 85% hexane as solvents. The obtained compound **1i** in the form of a white powder of about 89% yield. ^1H NMR (400 MHz, CDCl_3) δ 8.77 (s, 1H), 7.91 (s, 1H), 7.25 – 7.27 (d, $J = 8.50$ Hz, 2H), 6.86 – 6.89 (d, $J = 8.63$ Hz, 2H), 5.63 (br. s., 1H), 4.56 – 4.58 (d, $J = 5.50$ Hz, 2H), 3.94 (s, 3H), 3.80 (s, 3H).



Spectra 4.34: ^1H NMR Spectra for the compound **1i**.

4.3.1.14. Preparation of 5-((4-methoxybenzyl)amino)pyrazine-2-carbohydrazide (**2i**)

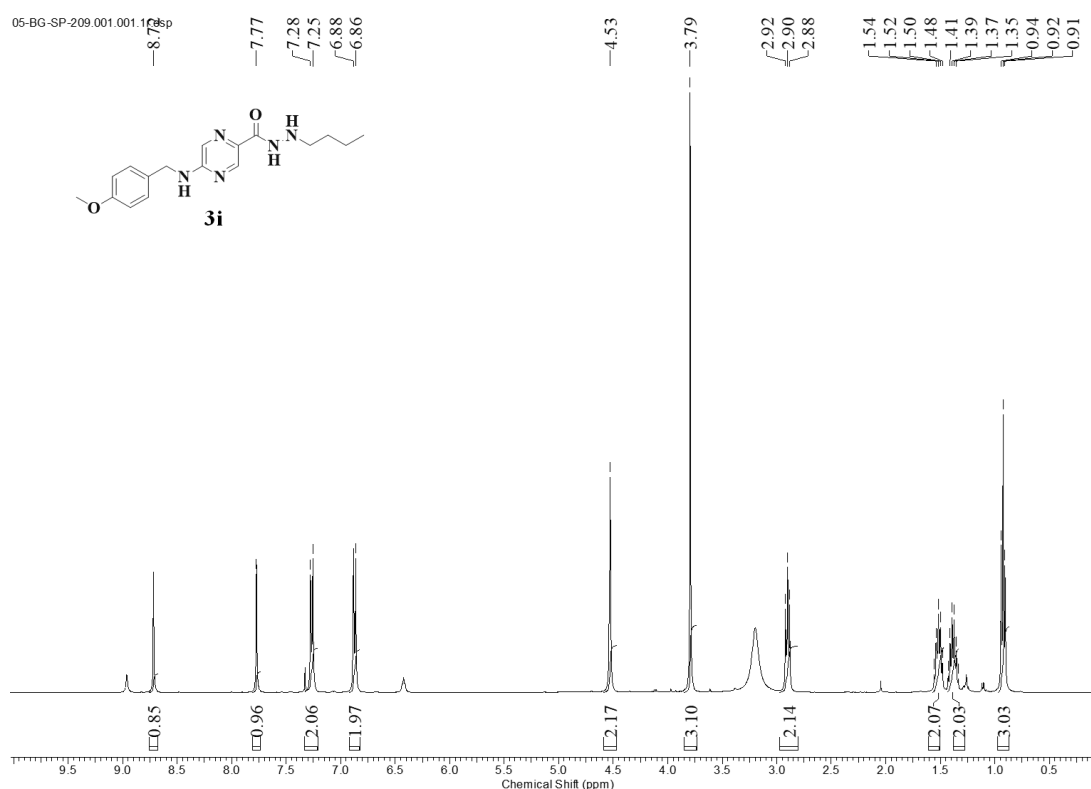
Following the synthetic procedure of **2f**, compound **1i** and excess of hydrazine

Chapter 4: Pyrazino hydrazides as HDAC3 selective inhibitors

monohydrate gave **2i** as a white solid. The crude reaction mixture was carried out for the next reaction without further purification.

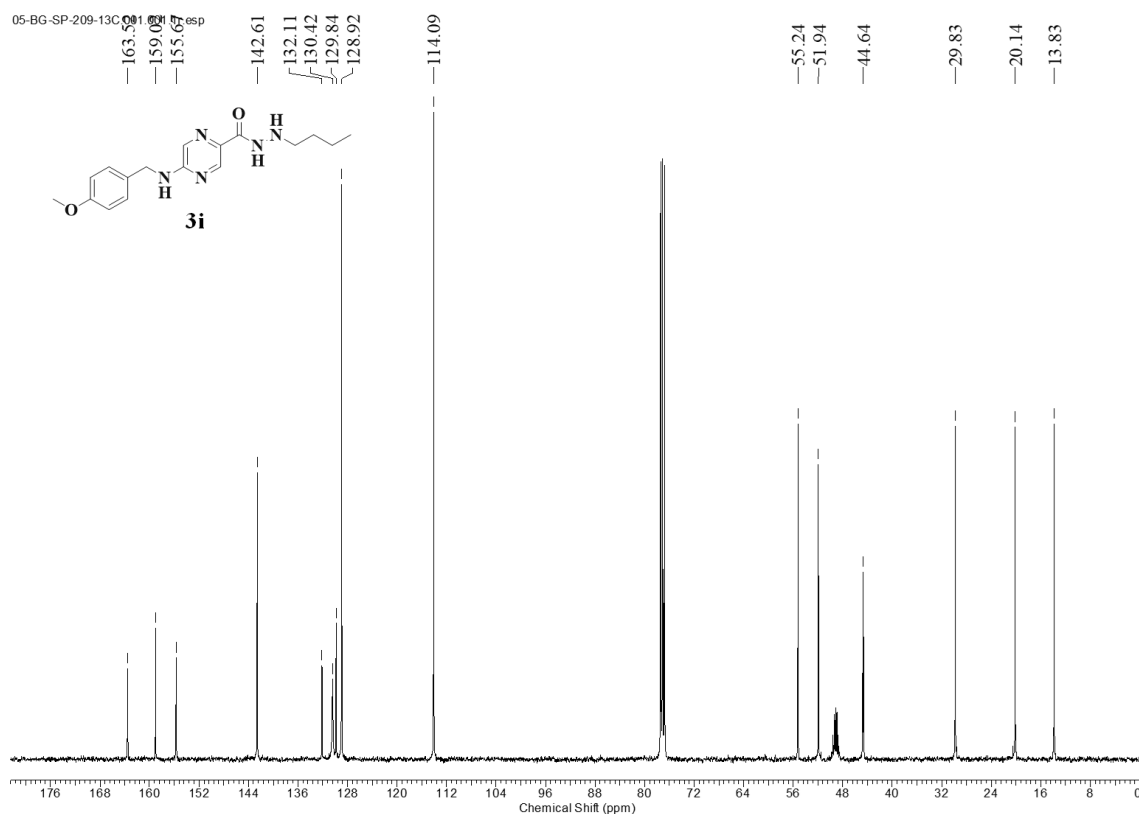
4.3.1.15. Preparation of *N'*-butyl-5-((4-methoxybenzyl)amino)pyrazine-2-carbohydrazide (**3i**)

Following the synthetic procedure of **3f**, starting materials **2i** and butyraldehyde gave **3i** as a white powder in 71% yield. ^1H NMR (400 MHz, CDCl_3) δ 8.72 (d, $J = 1.25$ Hz, 1H), 7.77 (d, $J = 1.25$ Hz, 1H), 7.21 - 7.33 (m, 2H), 6.82 - 6.92 (m, 2H), 4.53 (s, 2H), 3.79 (s, 3H), 2.88 - 2.92 (t, $J = 7.32$ Hz, 2H), 1.48 - 1.55 (m, 2H), 1.34 - 1.43 (m, 2H), 0.91 - 0.95 (t, $J = 7.25$ Hz, 3H). ^{13}C NMR (101 MHz, CDCl_3) δ 163.5, 159.0, 155.7, 142.6, 132.1, 130.4, 129.8, 128.9, 114.1, 55.2, 51.9, 44.6, 29.8, 20.1, 13.8. HRMS (APESI) m/z calcd for $\text{C}_{17}\text{H}_{23}\text{N}_5\text{O}$. $[\text{M}+\text{H}]^+$: 330.1872; found 330.1911.

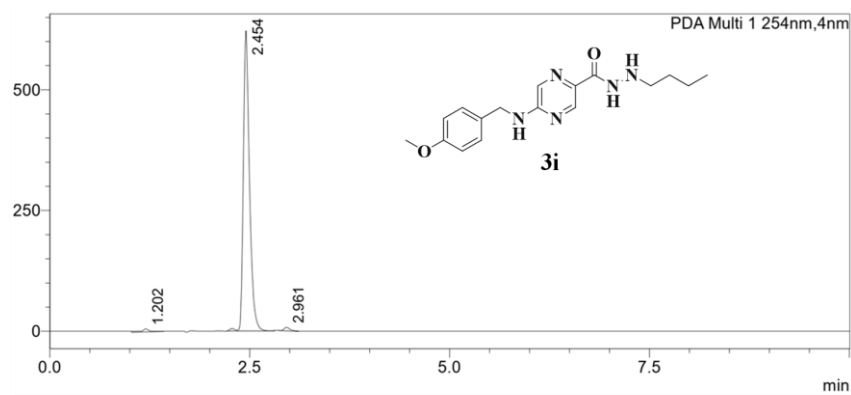


Spectra 4.35: ^1H NMR Spectra for the compound **3i**.

Chapter 4: Pyrazino hydrazides as HDAC3 selective inhibitors



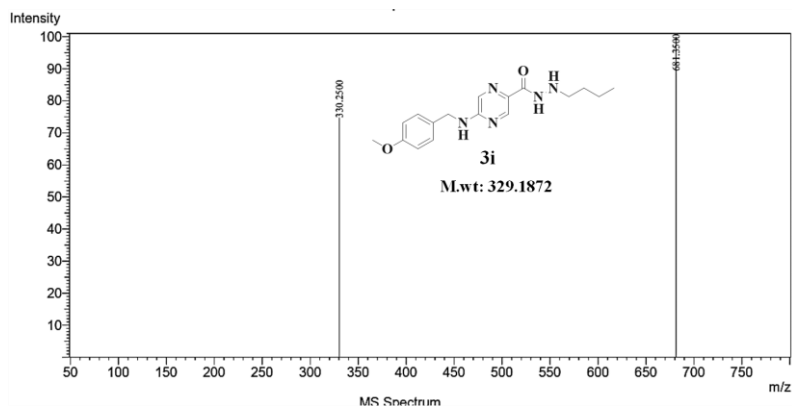
Spectra 4.36: ¹³C NMR Spectra for compound 3i.



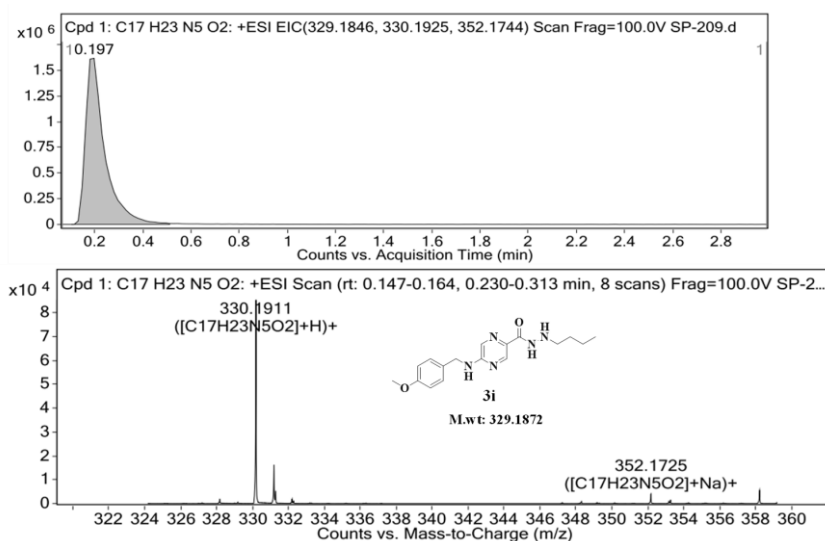
Peak#	Ret. Time	Area	Height	Area%
1	1.202	47147	6255	1.379
2	2.454	3331381	621726	97.424
3	2.961	40947	7182	1.197
Total		3419475	635163	100.000

Spectra 4.37: HPLC traces of compound 3i.

Chapter 4: Pyrazino hydrazides as HDAC3 selective inhibitors



Spectra 4.38: LC-MS Spectra for the compound 3i.

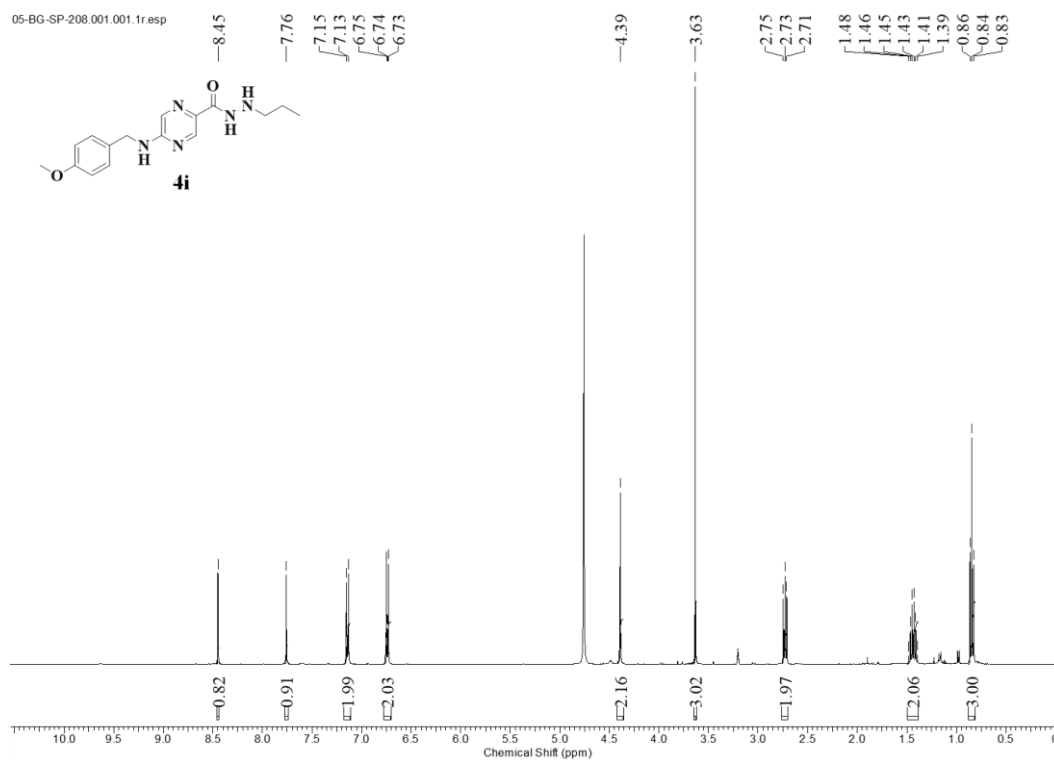


Spectra 4.39: HRMS Spectra for the compound 3i.

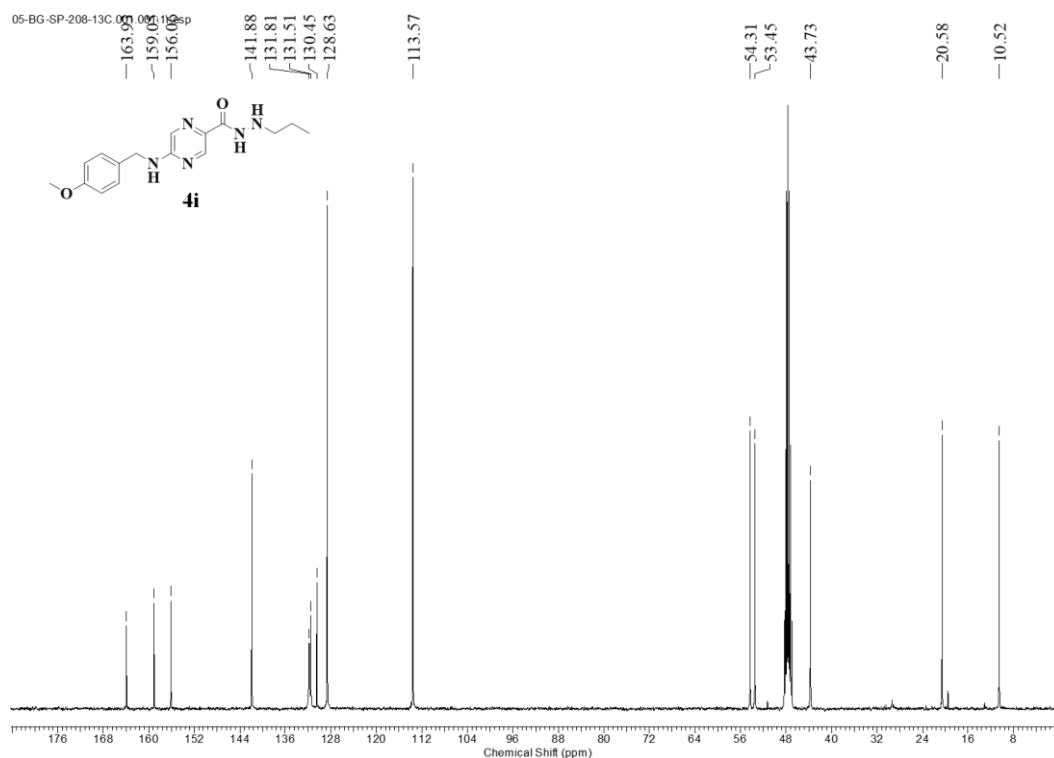
4.3.1.16. Preparation of *N'*-propyl-5-((4-methoxybenzyl)amino)pyrazine-2-carbohydrazide (**4i**)

Following the synthetic procedure of **4f**, starting materials **2i** and propionaldehyde gave **4i** as a white powder in 73% yield. ^1H NMR (400 MHz, methanol- d_4) δ 8.45 (d, $J = 1.38$ Hz, 1H), 7.76 (d, $J = 1.38$ Hz, 1H), 7.13 - 7.15 (m, 2H), 6.73 - 6.75 (m, 2H), 4.39 (s, 2H), 3.63 (s, 3H), 2.71 - 2.75 (m, 2H), 1.39 - 1.48 (m, 2H), 0.83 - 0.86 (t, $J = 7.44$ Hz, 3H). ^{13}C NMR (101 MHz, methanol- d_4) δ 163.9, 159.1, 156.1, 141.9, 131.8, 131.5, 130.4, 128.6, 113.6, 54.3, 53.5, 43.7, 20.6, 10.5. HRMS (APESI) m/z calcd for $C_{16}H_{21}N_5O$. $[M+H]^+$: 316.1695; found 316.1745.

Chapter 4: Pyrazino hydrazides as HDAC3 selective inhibitors

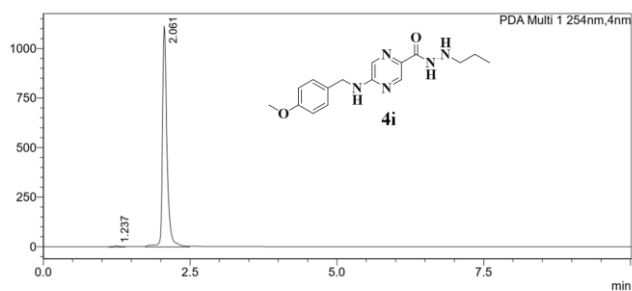


Spectra 4.40: ^1H NMR Spectra for the compound **4i**.



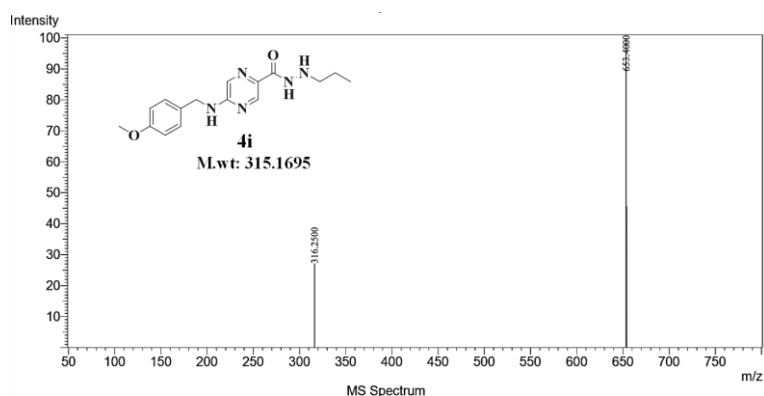
Spectra 4.41: ^{13}C NMR Spectra for compound **4i**.

Chapter 4: Pyrazino hydrazides as HDAC3 selective inhibitors

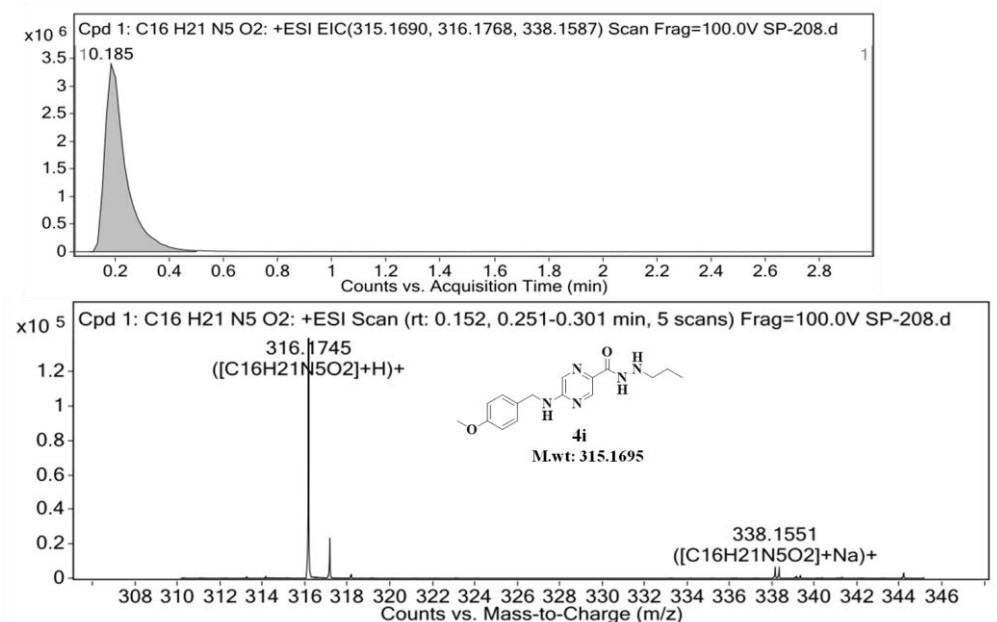


Peak#	Ret. Time	Area	Height	Area%
1	1.237	50182	6142	0.833
2	2.061	5973815	1115133	99.167
Total		6023997	1121275	100.000

Spectra 4.42: HPLC traces of compound 4i.



Spectra 4.43: LC-MS Spectra for the compound 4i.

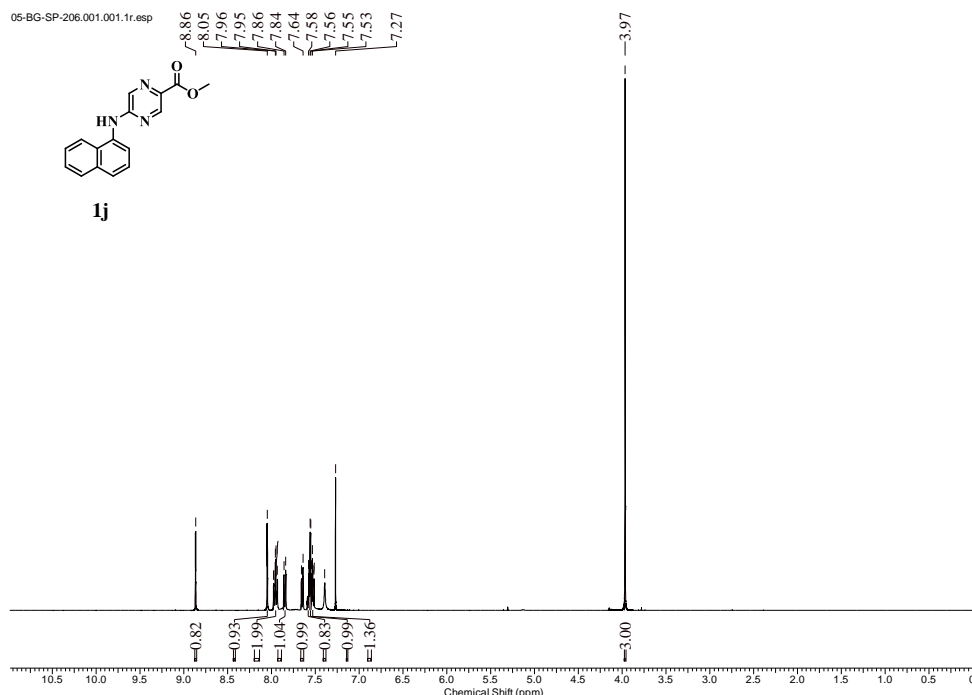


Spectra 4.44: HRMS Spectra for the compound 4i.

4.3.1.17. Preparation of methyl 5-(naphthalen-1-ylamino)pyrazine-2-carboxylate (1j)

Chapter 4: Pyrazino hydrazides as HDAC3 selective inhibitors

Methyl 5-chloro pyrazine 2-carboxylate (**6**) (1 g, 5.79 mmol) was dissolved in 30 mL of 1,4-dioxane, and to these 2 equivalents of *para* toluene sulphonic acid (2 g, 11.59 mmol) and naphthylamine (995.70 mg, 6.95 mmol) was added and refluxed for 24 h. The reaction completion was monitored by TLC and once the reaction is complete, the excess solvent was evaporated under a rota evaporator. The crude reaction mixture was dissolved in ethyl acetate and washed with water three times and the organic layer was separated. The organic layer containing the compound was then dried over anhydrous sodium sulphate and the excess solvent was removed under vacuum. The crude reaction mixture was then column purified and the pure compound **1j** was eluted from the column using 15% ethyl acetate and 85% hexane as solvents. The obtained compound **1i** in the form of dark brown powder of about 48% yield. $^1\text{H NMR}$ (400 MHz, CDCl_3) δ 8.86 (d, $J = 1.38$ Hz, 1H), 8.05 (d, $J = 1.38$ Hz, 1H), 7.93 - 7.98 (m, 2H), 7.85 (d, $J = 8.25$ Hz, 1H), 7.65 (d, $J = 7.13$ Hz, 1H), 7.50 - 7.60 (m, 3H), 7.39 (s, 1H), 3.97 (s, 3H).



Spectra 4.45: $^1\text{H NMR}$ Spectra for the compound **1j**.

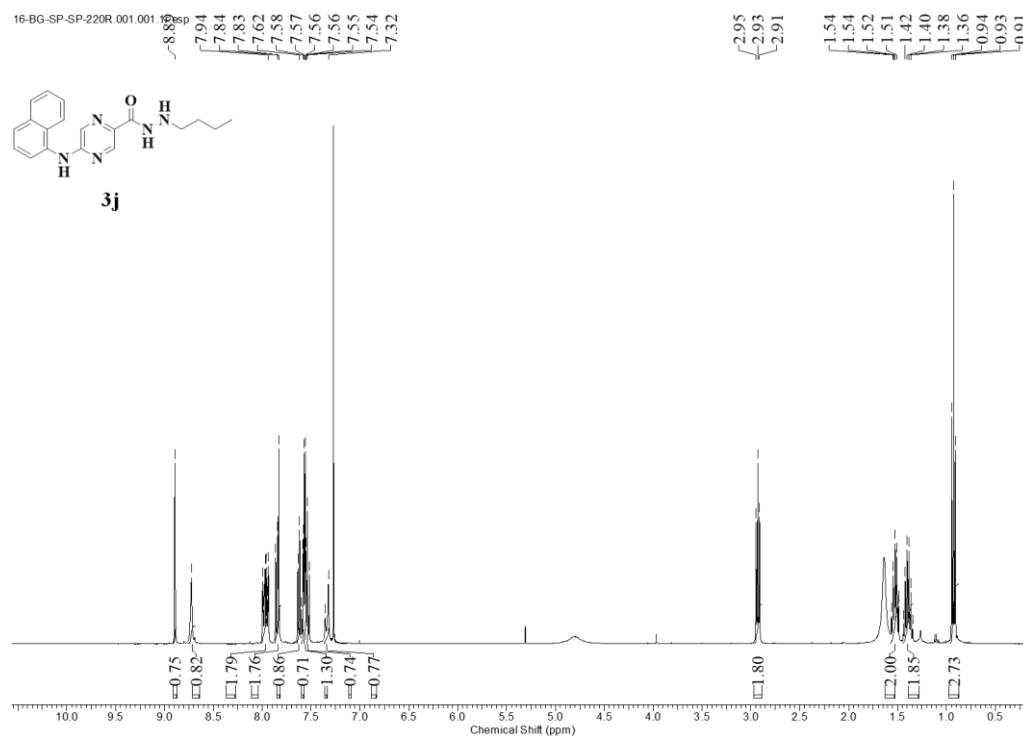
4.3.1.18. Preparation of 5-(naphthalen-1-ylamino)pyrazine-2-carbohydrazide (**2j**)

Chapter 4: Pyrazino hydrazides as HDAC3 selective inhibitors

Following the synthetic procedure of **2f**, compound **1j** and excess of hydrazine monohydrate gave **2j** as a dark brown solid. The crude reaction mixture was carried out for the next reaction without further purification.

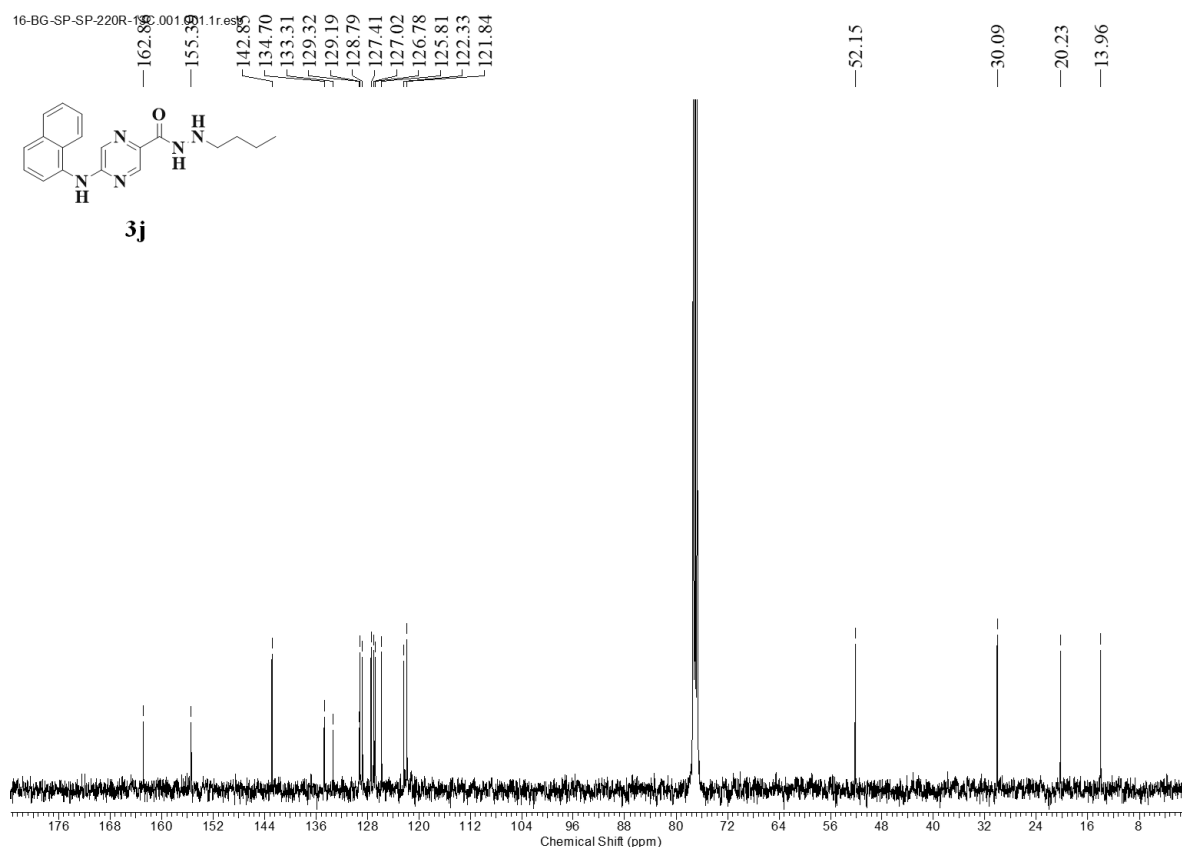
4.3.1.19. Preparation of *N'*-butyl-5-(naphthalen-1-ylamino)pyrazine-2-carbohydrazide (**3j**)

Following the synthetic procedure of **3f**, starting materials **2j** and butyraldehyde gave **3j** as a dark brown powder in 59% yield. ^1H NMR (400 MHz, CDCl_3) δ 8.89 (d, $J = 1.25$ Hz, 1H), 8.72 (br. s., 1H), 7.93 - 8.01 (m, 2H), 7.82 - 7.87 (m, 2H), 7.61 - 7.65 (m, 1H), 7.51 - 7.60 (m, 3H), 7.31 - 7.37 (m, 1H), 2.91 - 2.95 (t, $J = 7.25$ Hz, 2H), 1.64 (br. s., 2H), 1.47 - 1.58 (m, 2H), 1.35 - 1.44 (m, 2H), 0.91 - 0.94 (t, $J = 7.32$ Hz, 3H). ^{13}C NMR (101 MHz, CDCl_3) δ 162.9, 155.4, 142.9, 134.7, 133.3, 129.3, 129.2, 128.8, 127.4, 127.0, 126.8, 125.8, 122.3, 121.8, 52.2, 30.1, 20.2, 14.0. HRMS (APESI) m/z calcd for $\text{C}_{19}\text{H}_{21}\text{N}_5\text{O}$. $[\text{M}+\text{H}]^+$: 336.1780; found 336.1810.

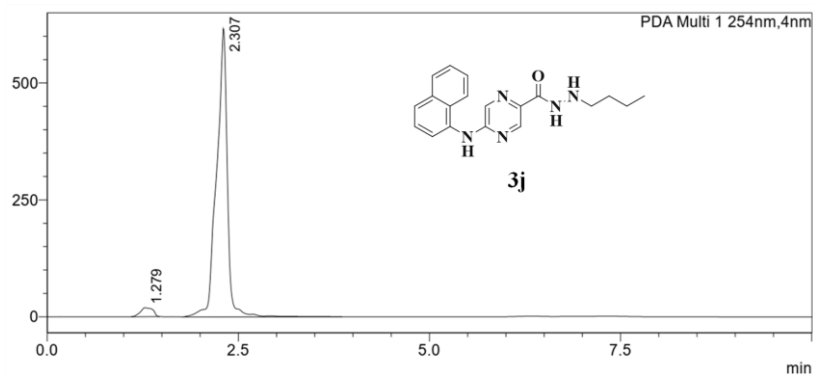


Spectra 4.46: ^1H NMR Spectra for the compound **3j**.

Chapter 4: Pyrazino hydrazides as HDAC3 selective inhibitors



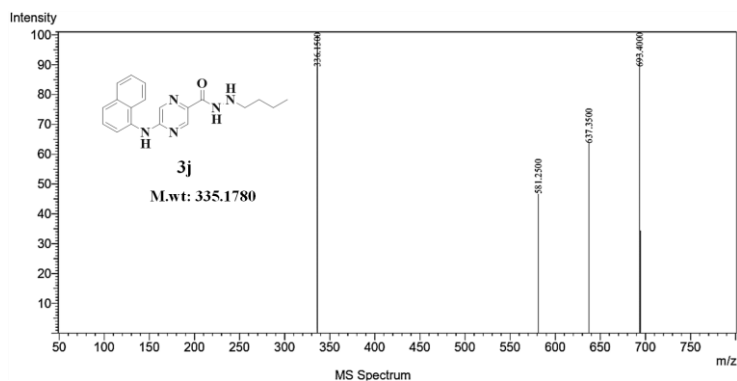
Spectra 4.47: ¹³C NMR Spectra for compound **3j**.



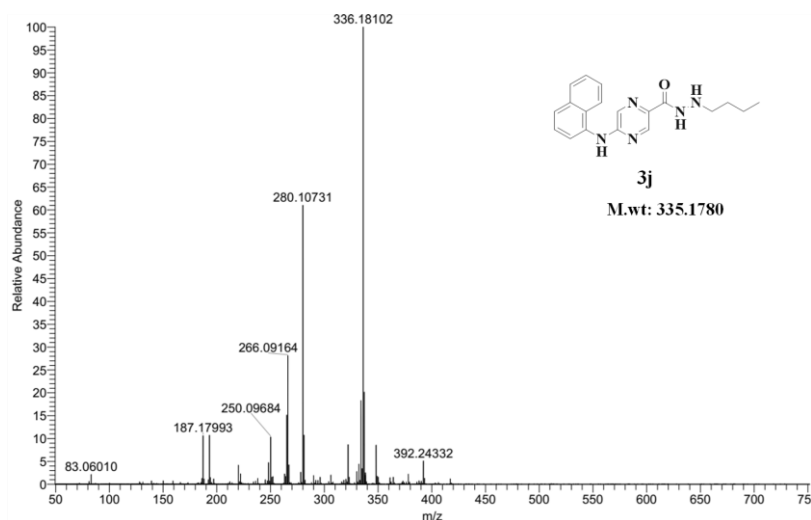
Peak#	Ret. Time	Area	Height	Area%
1	1.279	218469	19276	3.492
2	2.307	6037044	615971	96.508
Total		6255513	635247	100.000

Spectra 4.48: HPLC traces of compound **3j**.

Chapter 4: Pyrazino hydrazides as HDAC3 selective inhibitors



Spectra 4.49: LC-MS Spectra for the compound 3j.

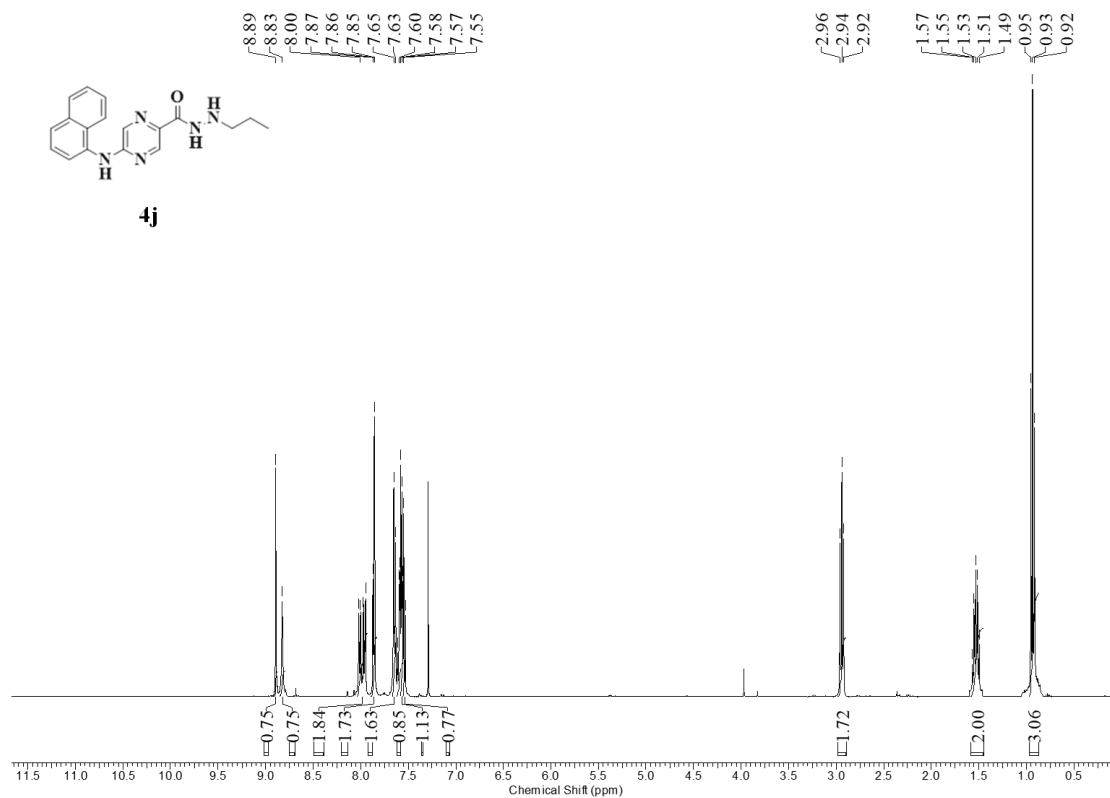


Spectra 4.50: HRMS Spectra for the compound 3j.

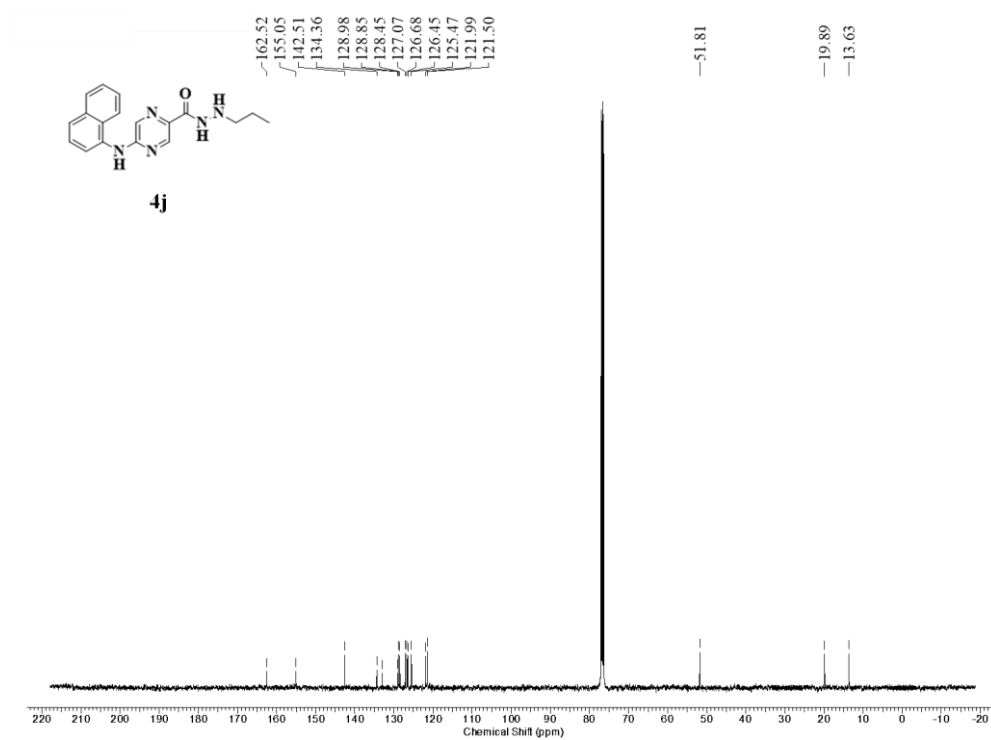
4.3.1.20. Preparation of *N'*-propyl-5-(naphthalen-1-ylamino)pyrazine-2-carbohydrazide (**4j**)

Following the synthetic procedure of **4f**, starting materials **2j** and propionaldehyde gave **4j** as a dark brown solid in 37% yield. ^1H NMR (400 MHz, CDCl_3) δ 8.89 (d, $J = 1.25$ Hz, 1H), 8.72 (br. s., 1H), 7.93 - 8.01 (m, 2H), 7.82 - 7.87 (m, 2H), 7.61 - 7.65 (m, 1H), 7.51 - 7.60 (m, 3H), 7.31 - 7.37 (m, 1H), 2.91 - 2.95 (t, $J = 7.25$ Hz, 2H), 1.64 (br. s., 2H), 1.35 - 1.44 (m, 2H), 0.91 - 0.94 (t, $J = 7.32$ Hz, 3H). ^{13}C NMR (101 MHz, CDCl_3) δ 161.56, 154.10, 141.46, 133.23, 132.04, 127.97, 127.43, 126.02, 126.01, 125.52, 124.47, 120.93, 120.55, 50.78, 18.87, 12.93. HRMS (APESI) m/z calcd for $\text{C}_{18}\text{H}_{19}\text{N}_5\text{O}$. $[\text{M}+\text{H}]^+$: 322.1600; found 322.1653.

Chapter 4: Pyrazino hydrazides as HDAC3 selective inhibitors

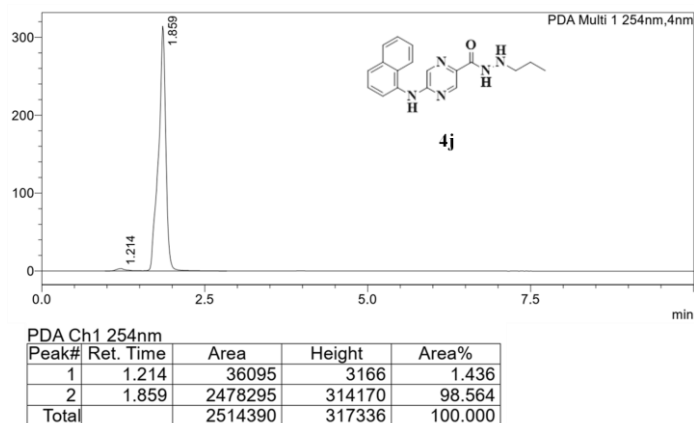


Spectra 4.51: ^1H NMR Spectra for the compound **4j**.

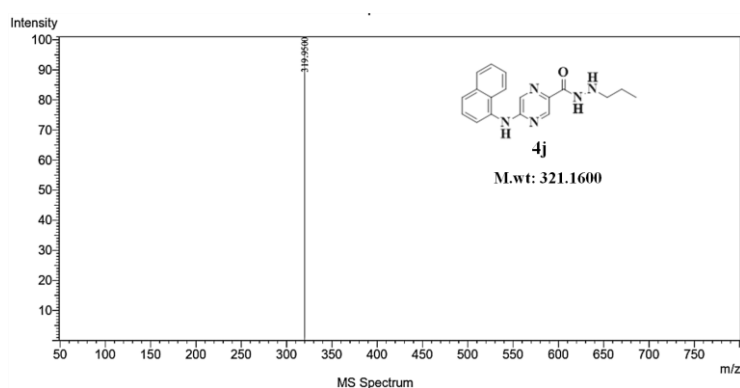


Spectra 4.52: ^{13}C NMR Spectra for compound **4j**.

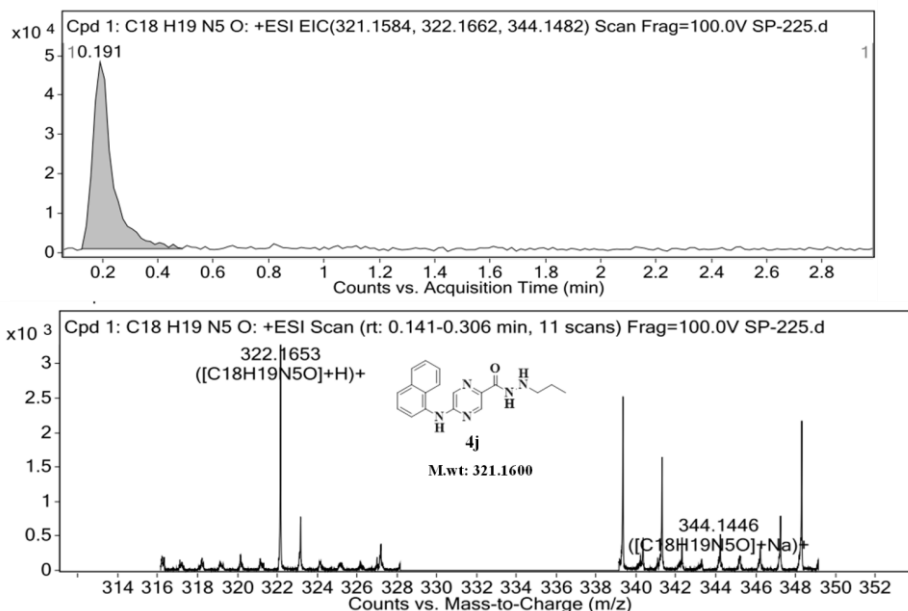
Chapter 4: Pyrazino hydrazides as HDAC3 selective inhibitors



Spectra 4.53: HPLC traces of compound 4j.



Spectra 4.54: LC-MS Spectra for the compound 4j.

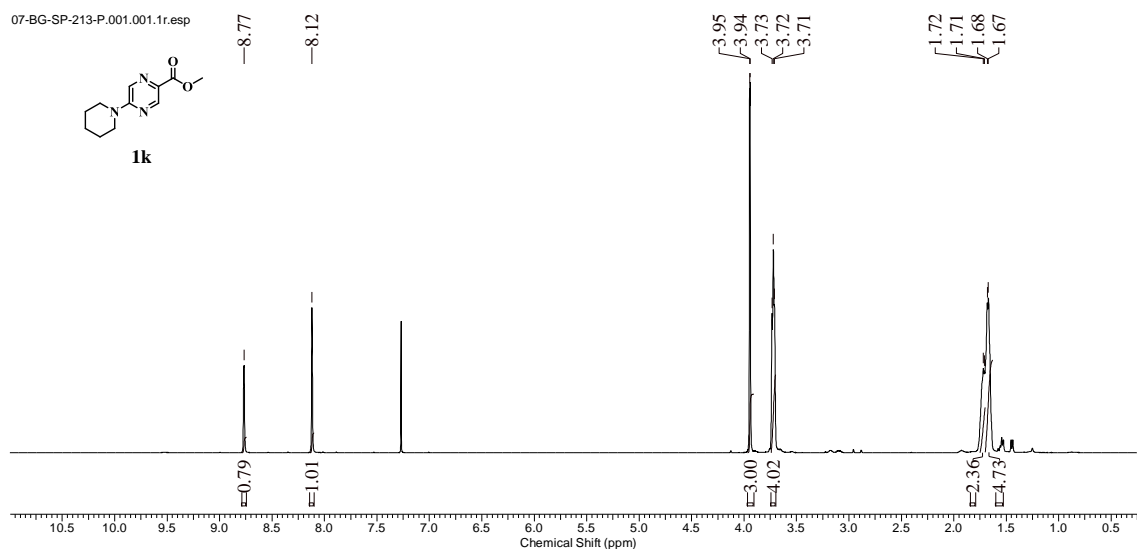


Spectra 4.55: HRMS Spectra for the compound 4j.

4.3.1.21. Preparation of methyl 5-(piperidin-1-yl)pyrazine-2-carboxylate (1k)

Chapter 4: Pyrazino hydrazides as HDAC3 selective inhibitors

Methyl 5-chloro pyrazine 2-carboxylate (**6**) (1 g, 5.79 mmol) was dissolved in 10 mL of DMF and to these 1.5 equivalents of DIPEA (1.51 mL, 8.69 mmol) and piperidine (0.686 mL, 6.95 mmol) was added and stirred at room temperature overnight. The reaction completion was monitored by TLC and once the reaction is complete, the excess solvent was evaporated under a rota evaporator. The crude reaction mixture was dissolved in ethyl acetate and washed with water three times and the organic layer was separated. The organic layer containing the compound was then dried over anhydrous sodium sulphate and the excess solvent was removed under vacuum. The crude reaction mixture was then column purified and the pure compound **1k** was eluted from the column using 20% ethyl acetate and 80% hexane as solvents. The obtained compound **1k** in the form of a white powder of about 65% yield. $^1\text{H NMR}$ (400 MHz, CDCl_3) δ 8.77 (s, 1H), 8.12 (s, 1H), 3.94 - 3.95 (m, 3H), 3.71 - 3.73 (t, $J = 4.38$ Hz, 4H), 1.70 - 1.72 (m, 2H), 1.66 - 1.70 (m, 4H).



Spectra 4.56: $^1\text{H NMR}$ Spectra for the compound **1k**.

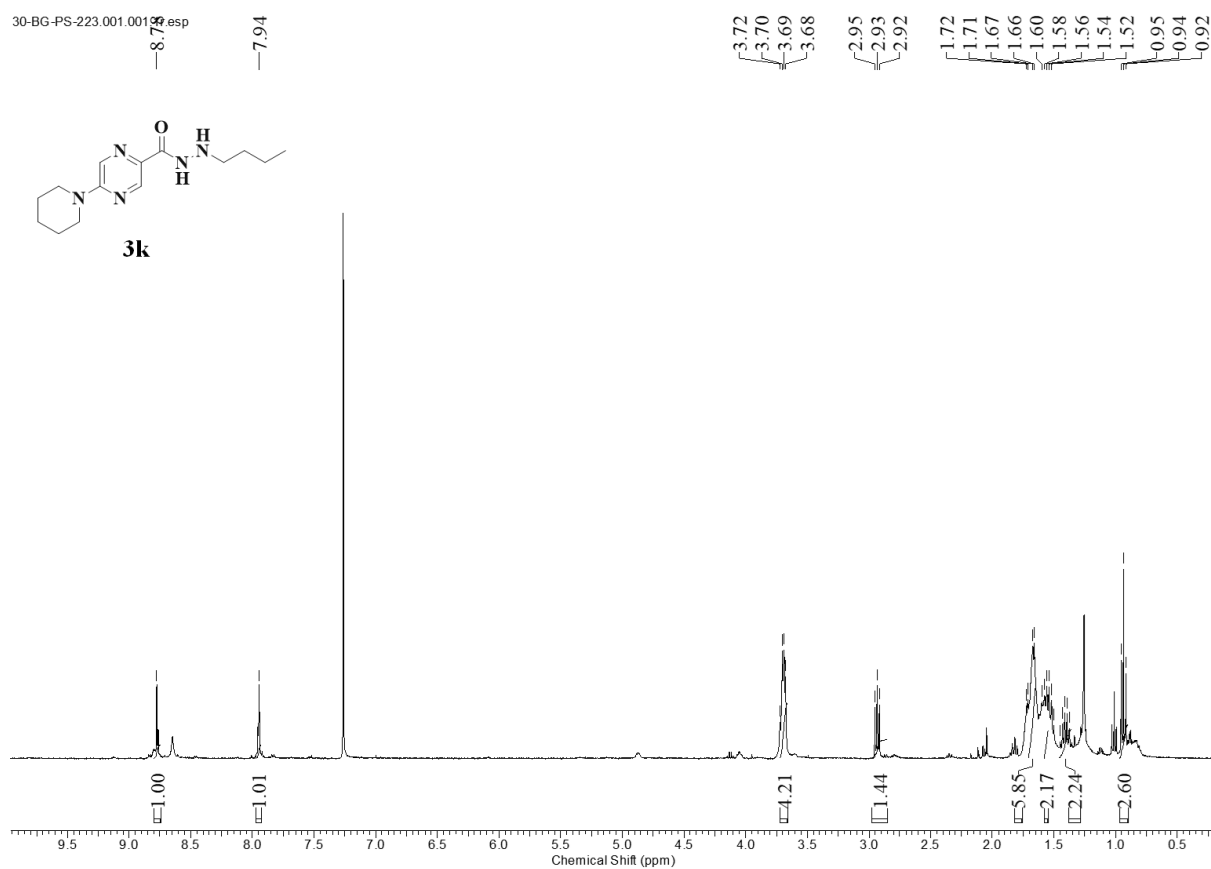
4.3.1.22. Preparation of 5-(piperidin-1-yl)pyrazine-2-carbohydrazide (**2k**)

Following the synthetic procedure of **2f**, compound **1k** and excess of hydrazine monohydrate gave **2k** as a light brown solid. The crude reaction mixture was carried out for the next reaction without further purification.

Chapter 4: Pyrazino hydrazides as HDAC3 selective inhibitors

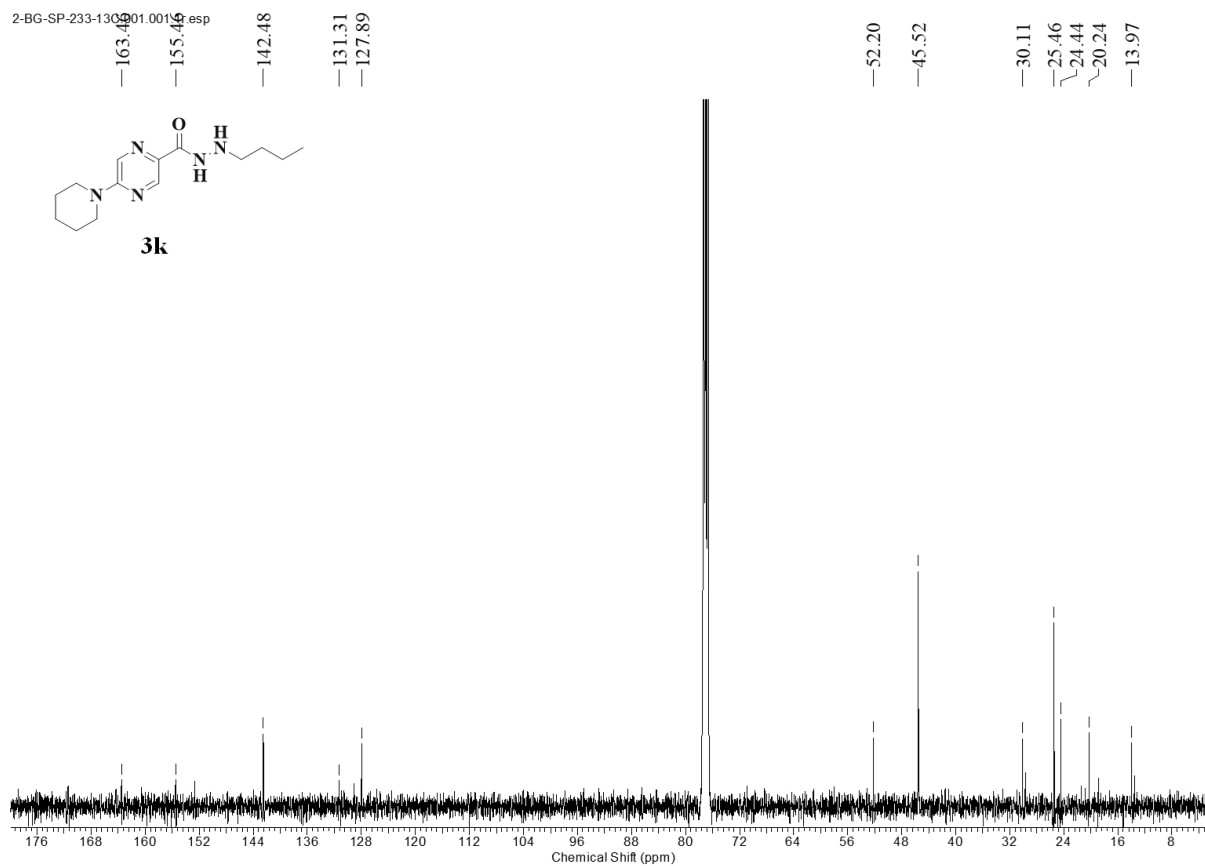
4.3.1.23. Preparation of *N'*-butyl-5-(piperidin-1-yl)pyrazine-2-carbohydrazide (**3k**)

Following the synthetic procedure of **3f**, starting materials **2k** and butyraldehyde gave **3k** as a brown powder in 65% yield. ^1H NMR (400 MHz, CDCl_3) δ 8.78 (s, 1H), 7.94 (s, 1H), 3.66 - 3.72 (m, 4H), 2.92 - 2.95 (m, 2H), 1.67 - 1.72 (m, 6H), 1.52 - 1.58 (m, 2H), 1.37 - 1.45 (m, 2H), 0.92 - 0.95 (t, $J = 7.25$ Hz, 3H). ^{13}C NMR (101 MHz, CDCl_3) δ 163.5, 155.5, 142.5, 131.3, 127.9, 52.2, 45.5, 30.1, 25.5, 24.4, 20.2, 14.0. HRMS (APESI) m/z calcd for $\text{C}_{14}\text{H}_{23}\text{N}_5\text{O}$. $[\text{M}+\text{H}]^+$: 278.1933; found 278.1976.

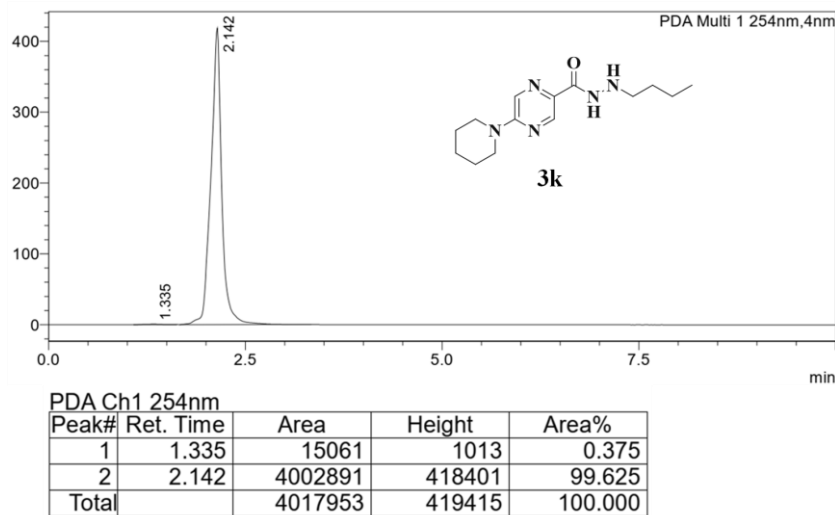


Spectra 4.57: ^1H NMR Spectra for the compound **3k**.

Chapter 4: Pyrazino hydrazides as HDAC3 selective inhibitors

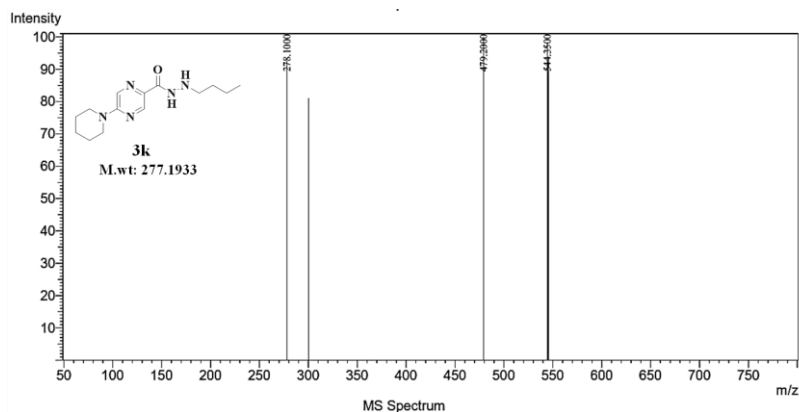


Spectra 4.58: ^{13}C NMR Spectra for compound **3k**.

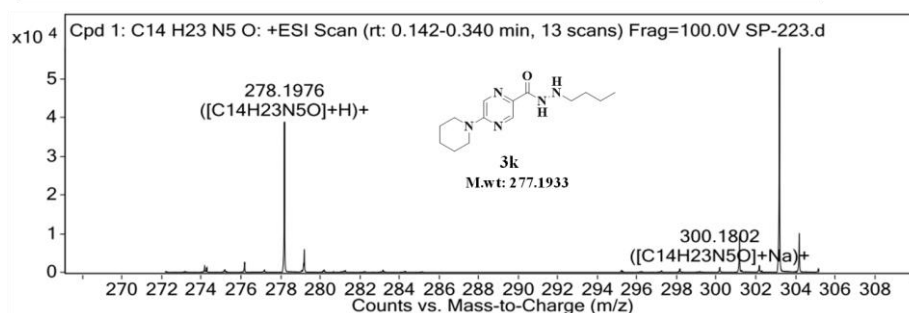
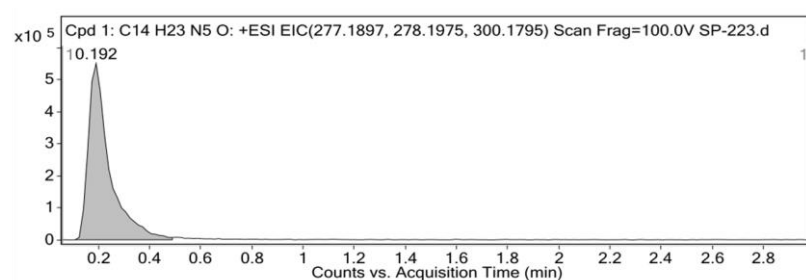


Spectra 4.59: HPLC traces of compound **3k**.

Chapter 4: Pyrazino hydrazides as HDAC3 selective inhibitors



Spectra 4.60: LC-MS Spectra for the compound 3k.

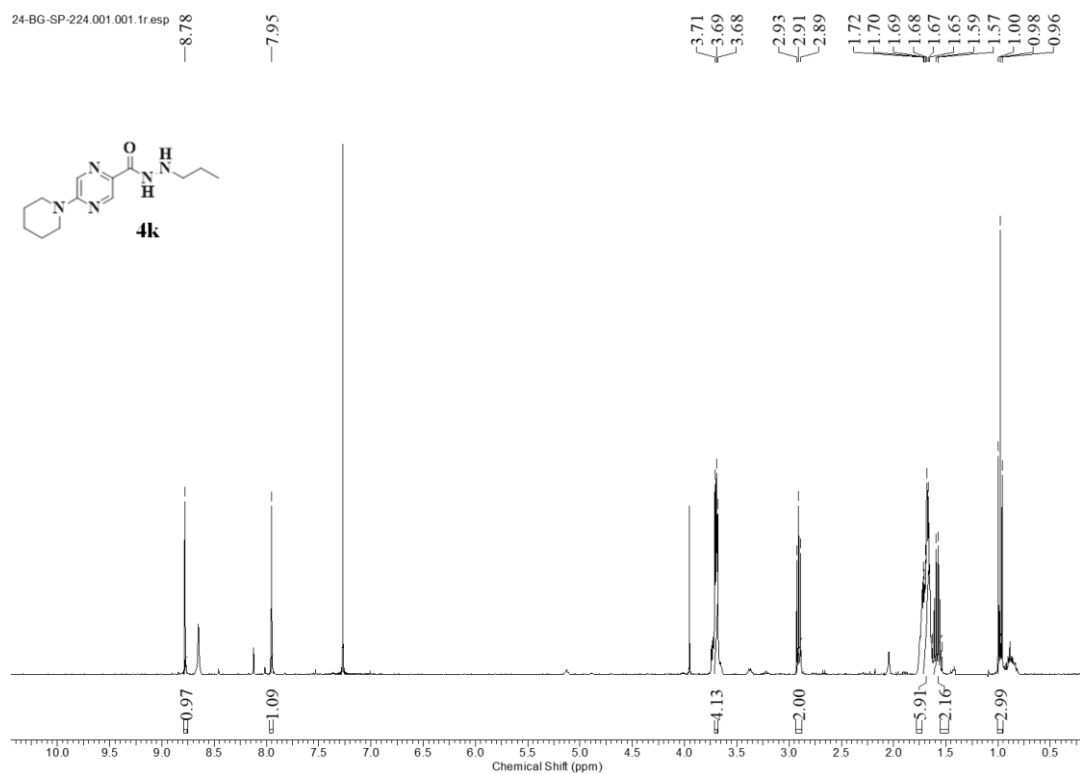


Spectra 4.61: HRMS Spectra for the compound 3k.

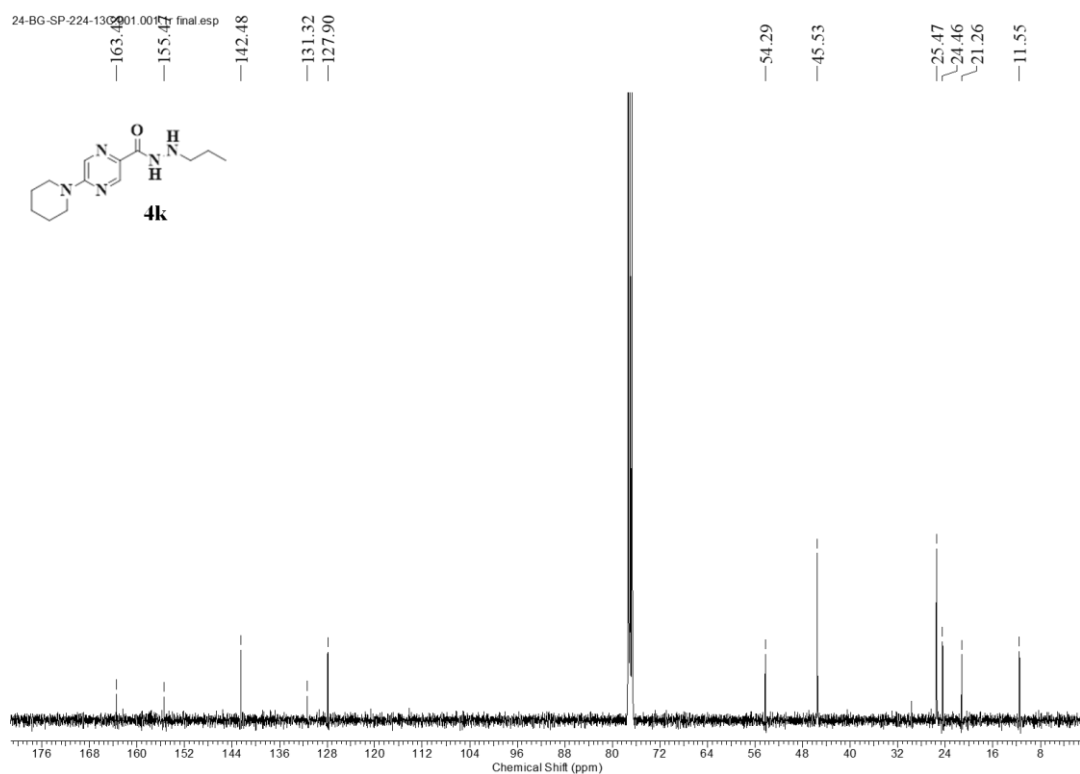
4.3.1.24. Preparation of *N'*-propyl-5-(piperidin-1-yl)pyrazine-2-carbohydrazide (**4k**)

Following the synthetic procedure of **4f**, starting materials **2k** and propionaldehyde gave **4k** as a light brown powder in 69% yield. ¹H NMR (400 MHz, CDCl₃) δ 8.78 (s, 1H), 7.95 (s, 1H), 3.68 - 3.71 (m, 4H), 2.89 - 2.93 (t, *J* = 7.25 Hz, 2H), 1.67 - 1.70 (m, 6H), 1.56 - 1.62 (m, 2H), 0.96 - 1.00 (t, *J* = 7.44 Hz, 3H). ¹³C NMR (101 MHz, CDCl₃) δ 163.5, 155.5, 142.5, 131.3, 127.9, 54.3, 45.5, 25.5, 24.5, 21.3, 11.6. HRMS (APESI) *m/z* calcd for C₁₃H₂₁N₅O. [M+H]⁺: 264.1786; found 264.1821.

Chapter 4: Pyrazino hydrazides as HDAC3 selective inhibitors

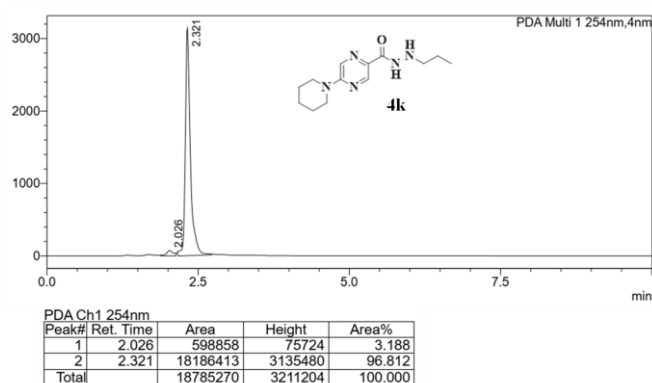


Spectra 4.62: ¹H NMR Spectra for the compound 4k.

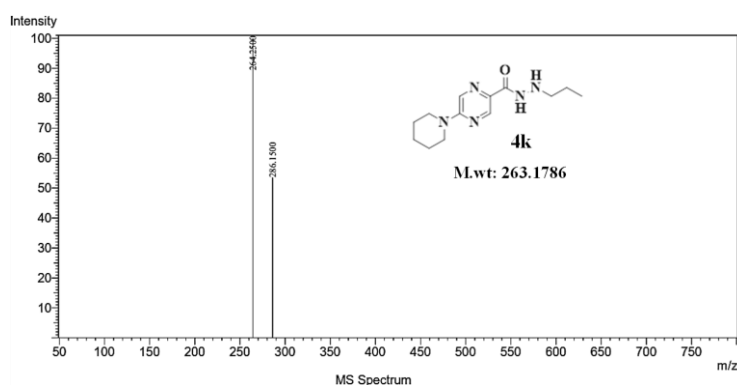


Spectra 4.63: ¹³C NMR Spectra for compound 4k.

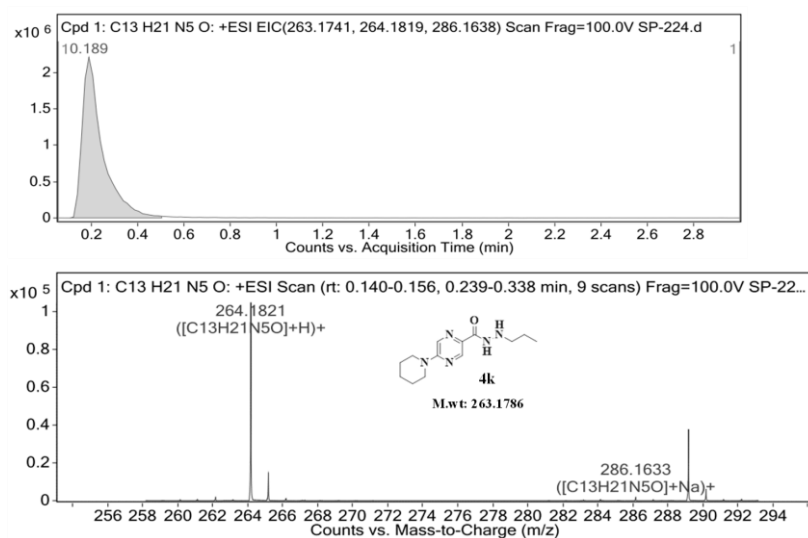
Chapter 4: Pyrazino hydrazides as HDAC3 selective inhibitors



Spectra 4.64: HPLC traces of compound 4k.



Spectra 4.65: LC-MS Spectra for the compound 4k.



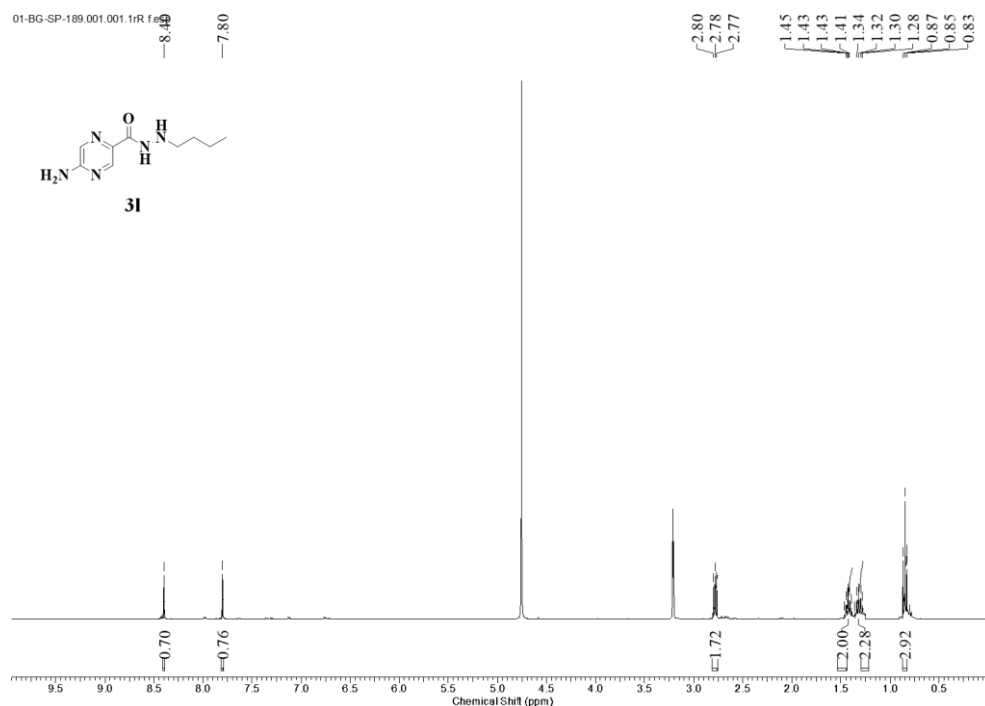
Spectra 4.66: HRMS Spectra for the compound 4k.

4.3.1.25. Preparation of 5-amino-N'-butylpyrazine-2-carbohydrazide (3l)

N'-butyl-5-((4-methoxybenzyl)amino)pyrazine-2-carbohydrazide (**3i**) (500 mg, 1.52 mmol) was dissolved in 5 mL of dry DCM and to these 3 equivalents of trifluoroacetic acid

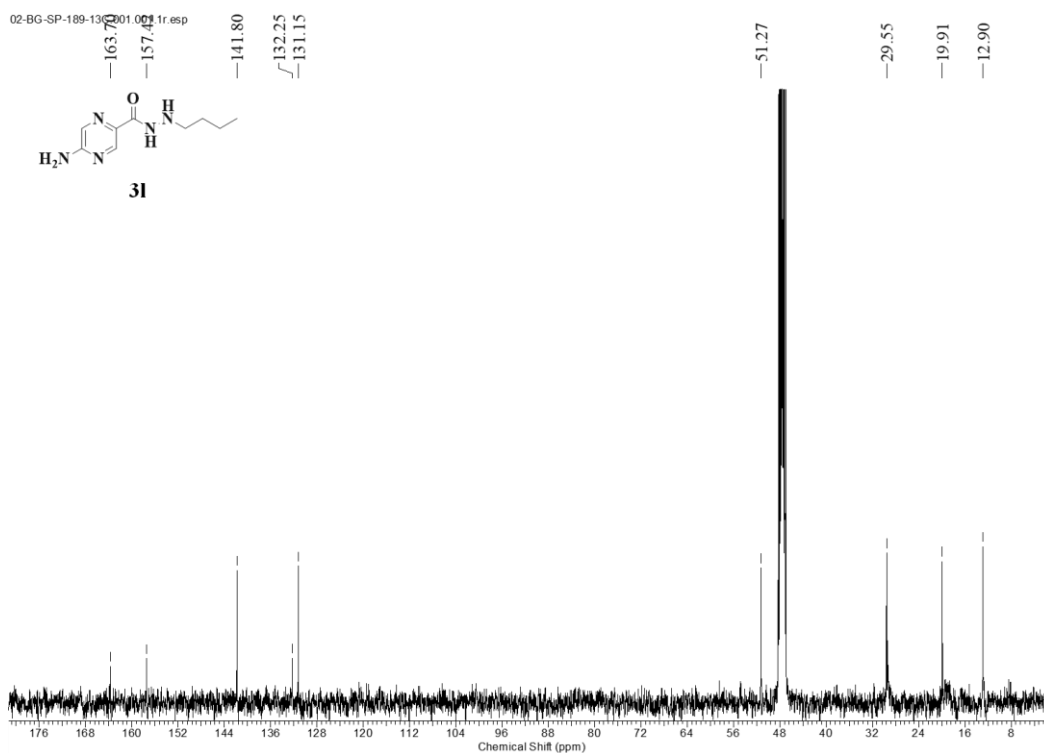
Chapter 4: Pyrazino hydrazides as HDAC3 selective inhibitors

(0.348 mL, 4.55 mmol) was added and stirred at 90 °C for 2 h. The reaction completion was monitored by TLC and once the reaction is complete, the excess solvent was evaporated under a rota evaporator. The crude reaction mixture was then neutralized with aqueous sodium bicarbonate solution and then dissolved in ethyl acetate and washed with water three times and the organic layer was separated. The organic layer containing the compound was then dried over anhydrous sodium sulphate and the excess solvent was removed under vacuum. The crude reaction mixture was then column purified and the pure compound **31** was eluted from the column using 65% ethyl acetate and 35% hexane as solvents. The obtained compound **31** in the form of yellow powder of about 41% yield. ¹H NMR (400 MHz, methanol-*d*₄) δ 8.40 (d, *J* = 1.38 Hz, 1H), 7.80 (d, *J* = 1.38 Hz, 1H), 2.77 - 2.81 (m, 2H), 1.38 - 1.47 (m, 2H), 1.28 - 1.36 (m, 2H), 0.83 - 0.87 (t, *J* = 7.32 Hz, 3H). ¹³C NMR (101 MHz, methanol-*d*₄) δ 163.7, 157.4, 141.8, 132.3, 131.2, 51.3, 29.6, 19.9, 12.9. HRMS (APESI) *m/z* calcd for C₉H₁₅N₅O. [M+H]⁺: 210.1297; found 210.1348.

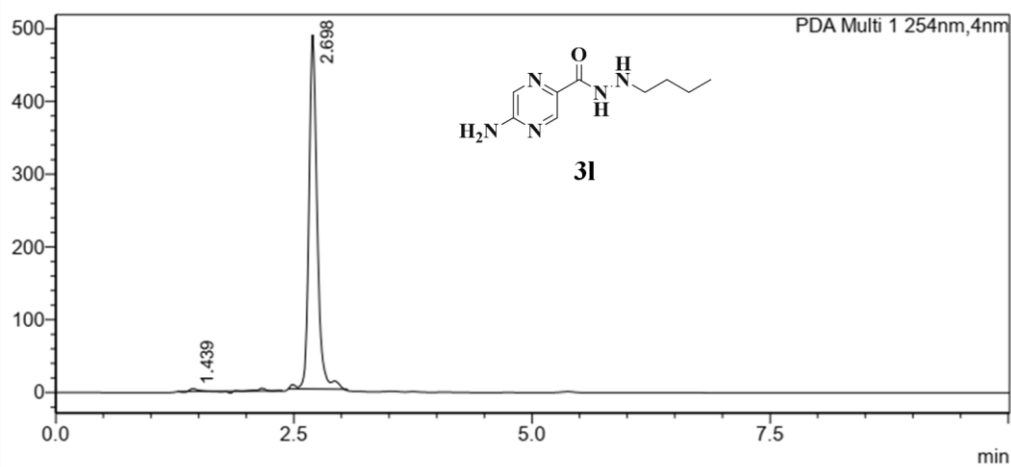


Spectra 4.67: ¹H NMR Spectra for the compound **31**.

Chapter 4: Pyrazino hydrazides as HDAC3 selective inhibitors



Spectra 4.68: ^{13}C NMR Spectra for compound 31.

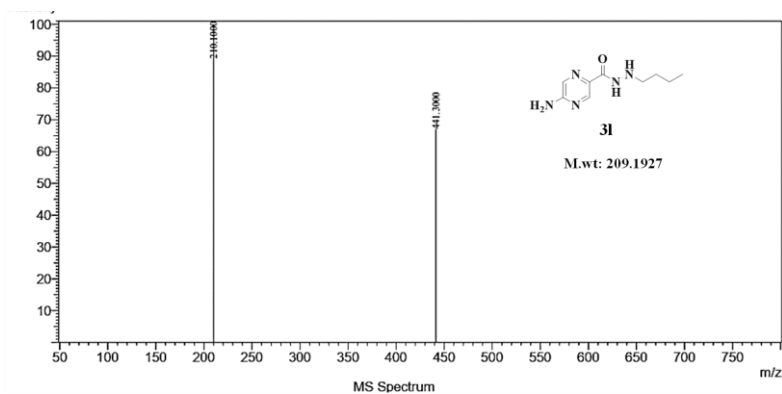


PDA Ch1 254nm

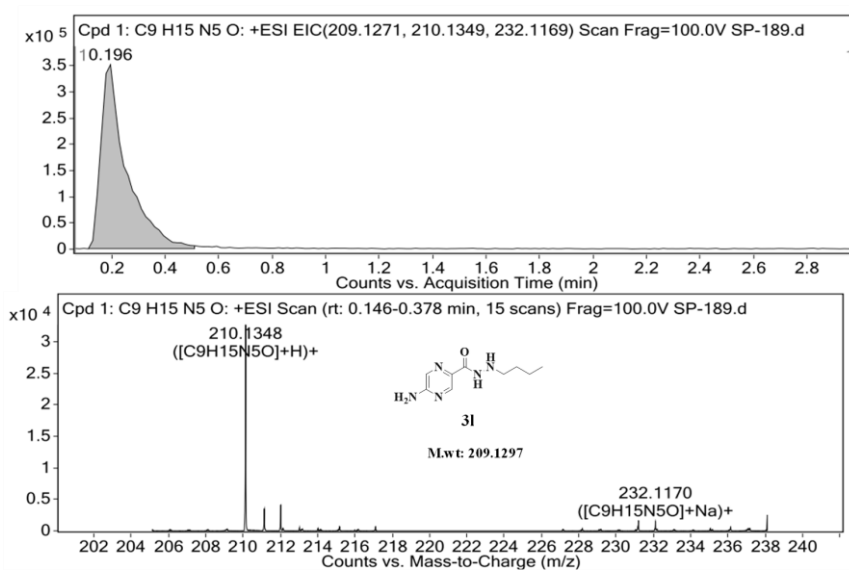
Peak#	Ret. Time	Area	Height	Area%
1	1.439	27266	3683	0.923
2	2.698	2926710	486533	99.077
Total		2953977	490216	100.000

Spectra 4.69: HPLC traces of compound 31.

Chapter 4: Pyrazino hydrazides as HDAC3 selective inhibitors



Spectra 4.70: LC-MS Spectra for the compound 31.

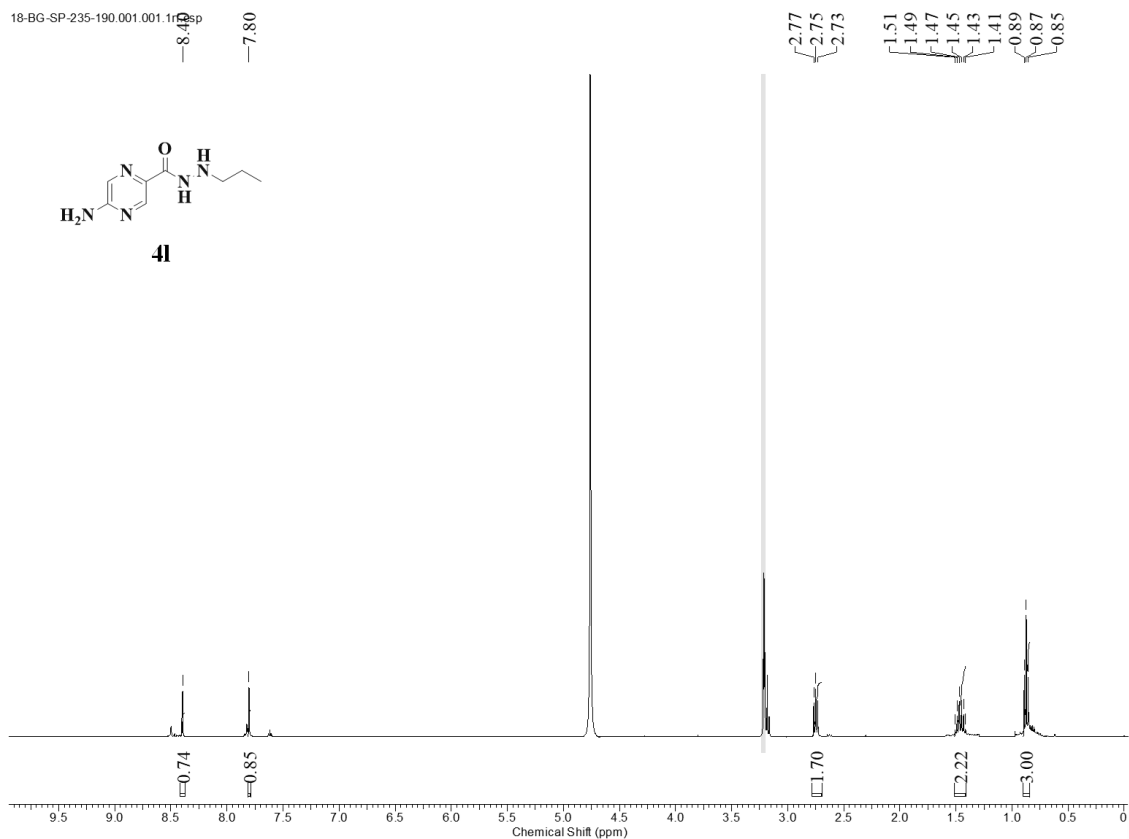


Spectra 4.71: HRMS Spectra for the compound 31.

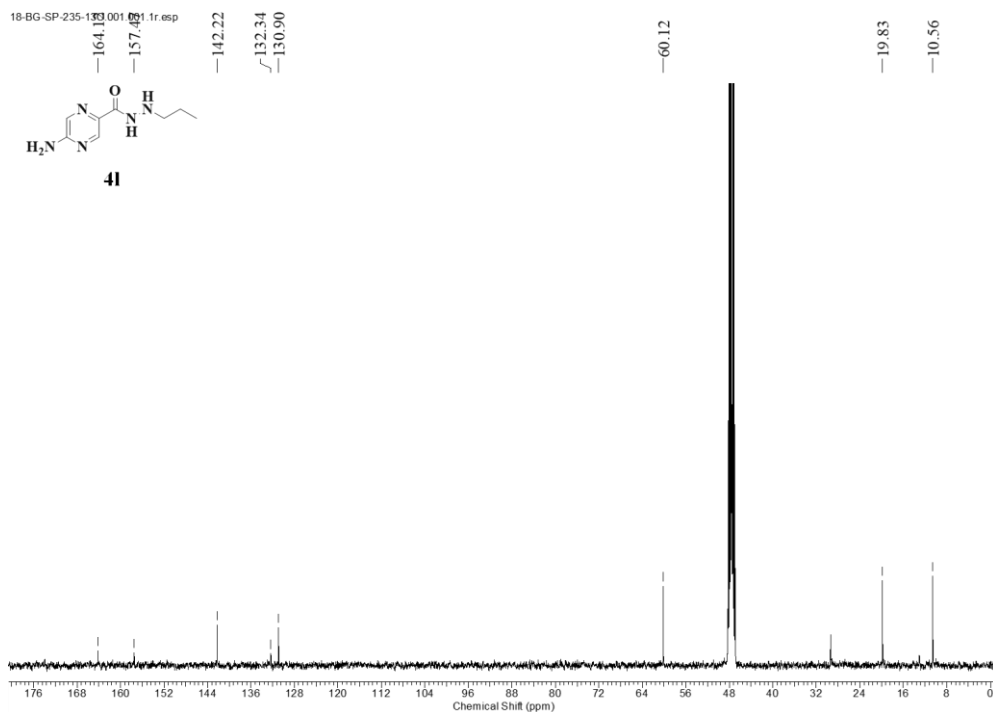
4.3.1.26. Preparation of 5-amino-*N*¹-propylpyrazine-2-carbohydrazide (**4l**)

Following the synthetic procedure of **3l**, starting materials **4i** and trifluoroacetic acid gave **4l** as a yellow powder in 45% yield. ¹H NMR (400 MHz, methanol-*d*₄) δ 8.40 (d, J = 1.38 Hz, 1H), 7.80 (d, J = 1.38 Hz, 1H), 2.73 - 2.77 (m, 2H), 1.42 - 1.51 (m, 2H), 0.85 - 0.89 (t, J = 7.44 Hz, 3H). ¹³C NMR (101 MHz, methanol-*d*₄) δ 164.1, 157.5, 142.2, 132.34, 130.9, 60.1, 19.8, 10.6. HRMS (APESI) m/z calcd for C₈H₁₃N₅O. [M+H]⁺: 196.114; found 196.119.

Chapter 4: Pyrazino hydrazides as HDAC3 selective inhibitors

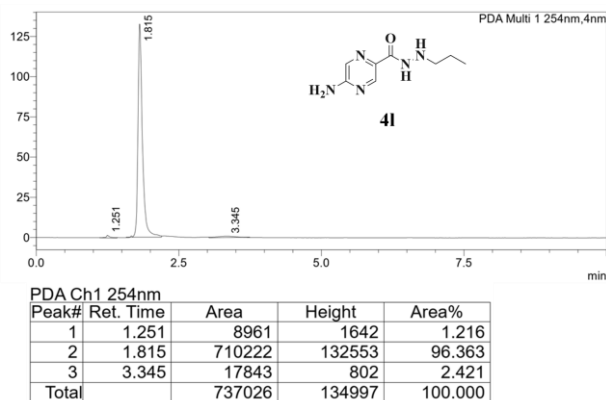


Spectra 4.72: ¹H NMR Spectra for the compound 4l.

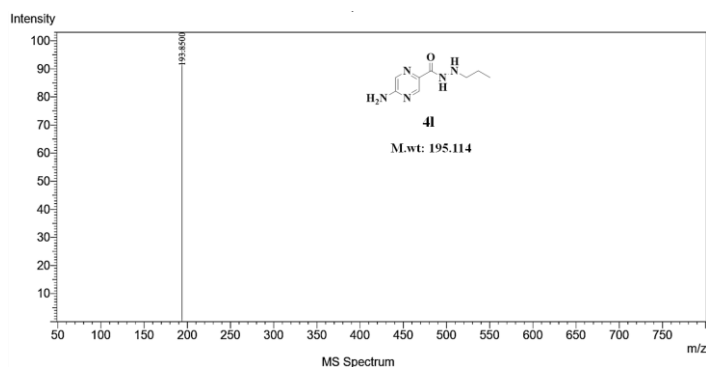


Spectra 4.73: ¹³C NMR Spectra for compound 4l.

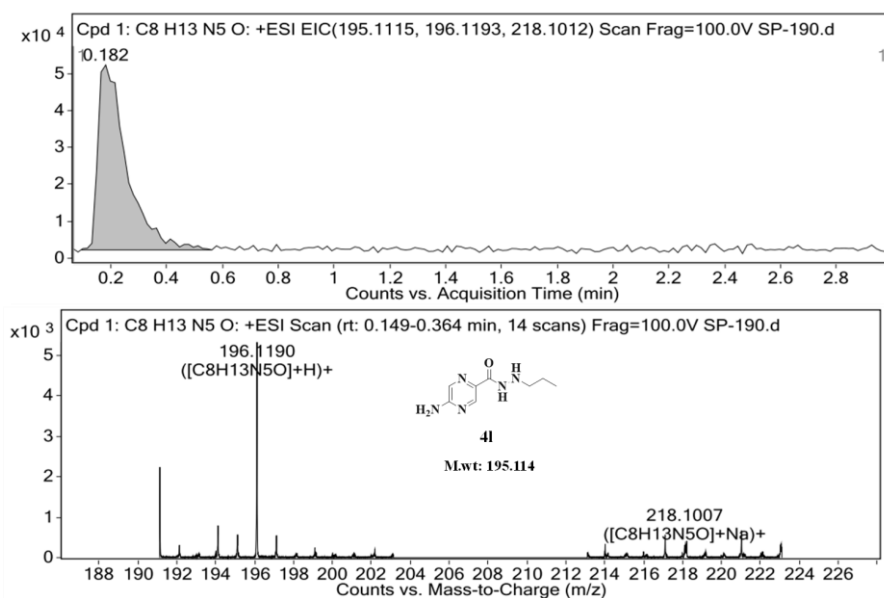
Chapter 4: Pyrazino hydrazides as HDAC3 selective inhibitors



Spectra 4.74: HPLC traces of compound 41.



Spectra 4.75: LC-MS Spectra for the compound 41.



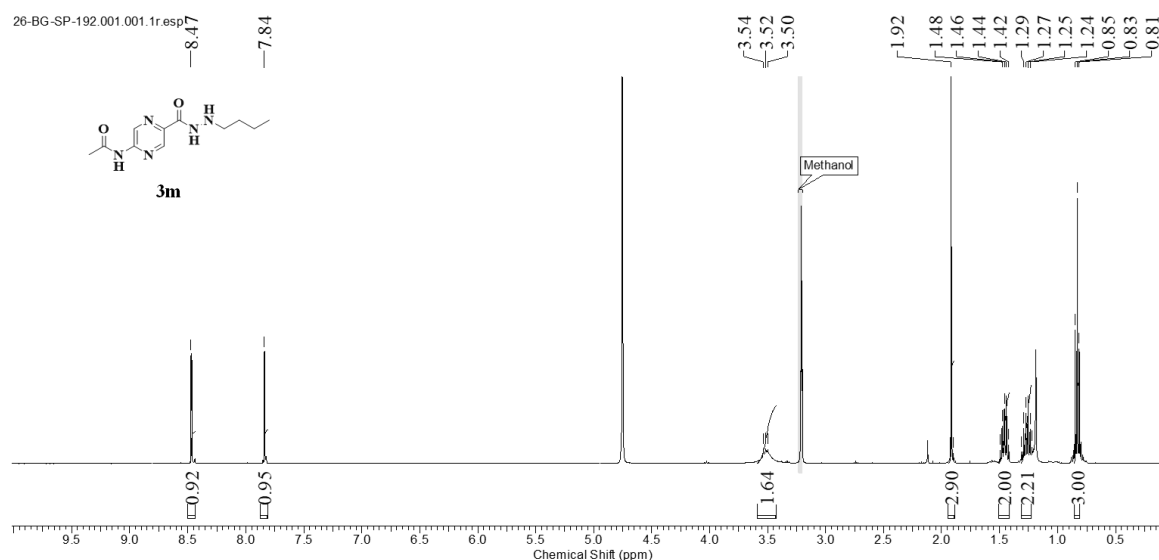
Spectra 4.76: HRMS Spectra for the compound 41.

4.3.1.27. Preparation of *N*-(5-(2-butylhydrazine-1-carbonyl)pyrazin-2-yl)acetamide (**3m**)

5-amino-*N*'-butylpyrazine-2-carbohydrazide (**3l**) (100 mg, 0.477 mmol) was dissolved in 5

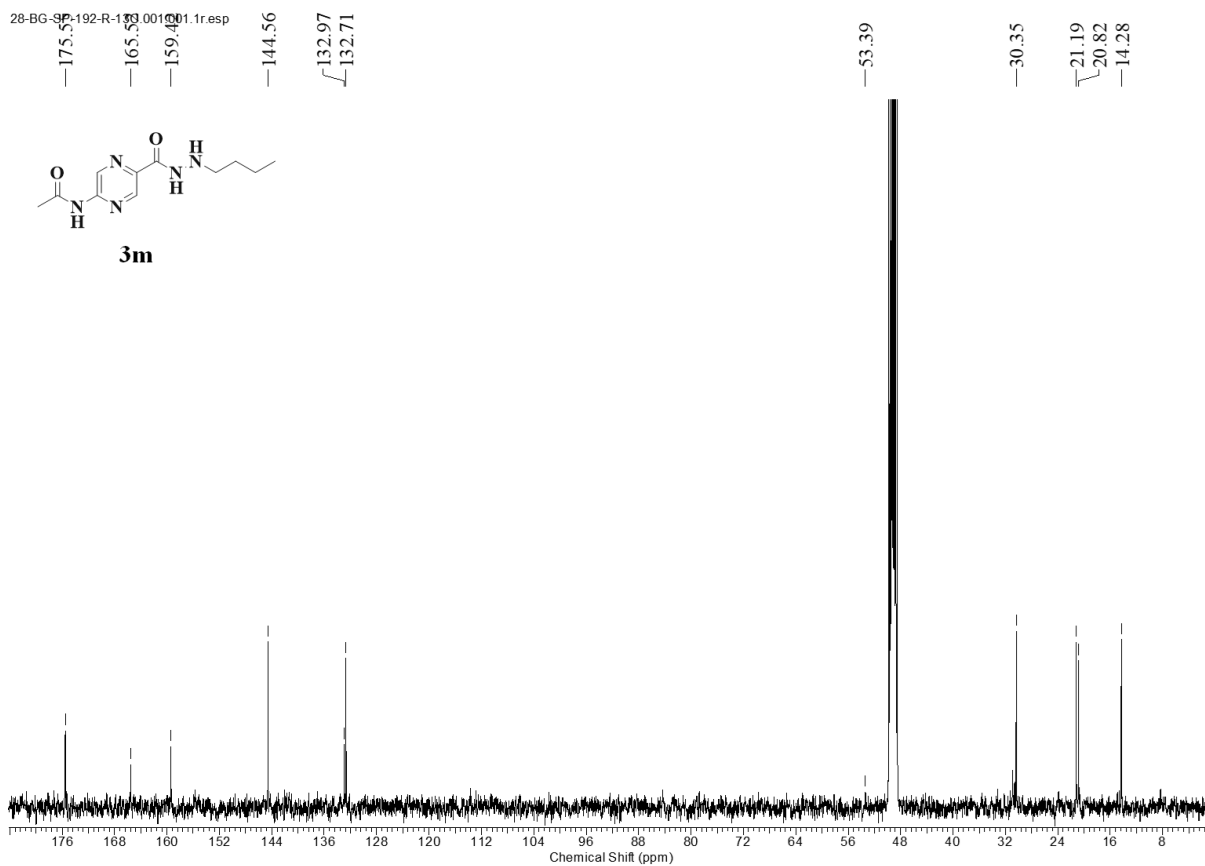
Chapter 4: Pyrazino hydrazides as HDAC3 selective inhibitors

mL of dry DCM and to these 3 equivalents of triethylamine (0.190 mL, 1.43 mmol) was added at 0 °C. To this acetyl chloride (51.15 μ L, 0.716 mmol) was added dropwise and the reaction mixture was left for stirring at room temperature for 6 h. The reaction completion was monitored by TLC and once the reaction is complete, the excess solvent was evaporated under a rota evaporator. The crude reaction mixture was then neutralized with aqueous sodium bicarbonate solution and then dissolved in ethyl acetate and washed with water three times and the organic layer was separated. The organic layer containing the compound was then dried over anhydrous sodium sulphate and the excess solvent was removed under vacuum. The crude reaction mixture was then column purified and the pure compound **3m** was eluted from the column using 70% ethyl acetate and 30% hexane as solvents. The obtained compound **3m** in the form of a white powder of about 53% yield. ^1H NMR (400 MHz, methanol- d_4) δ 8.47 (s, 1H), 7.84 (s, 1H), 3.50 - 3.54 (m, 2H), 1.92 (s, 3H), 1.42 – 1.50 (m, 2H), 1.22 – 1.31 (m, 2H), 0.81 – 0.85 (t, $J = 7.32$ Hz, 3H). ^{13}C NMR (101 MHz, methanol- d_4) δ 175.6, 165.5, 159.4, 144.6, 133.0, 132.7, 53.4, 30.4, 21.2, 20.8, 14.3. HRMS (APESI) m/z calcd for $\text{C}_{11}\text{H}_{17}\text{N}_5\text{O}_2$. $[\text{M}+\text{H}]^+$: 252.1401; found 252.1453.

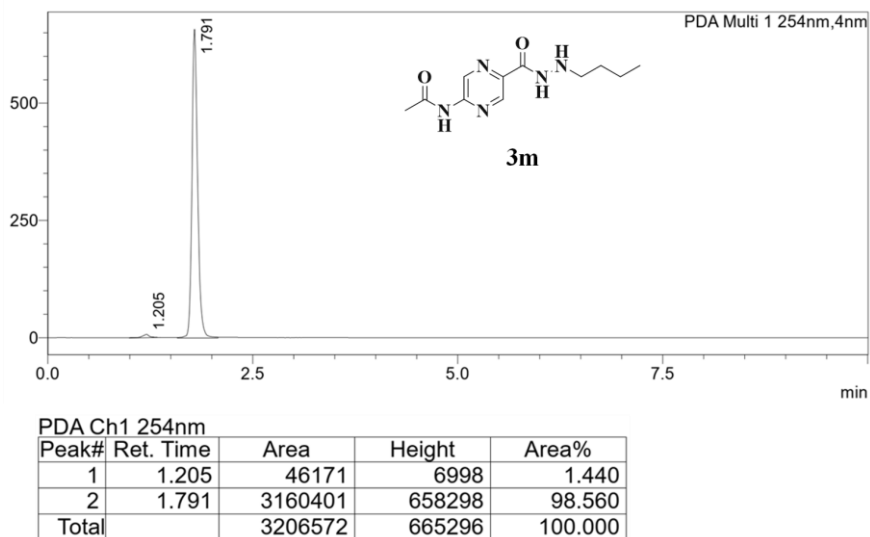


Spectra 4.77: ^1H NMR Spectra for the compound **3m**.

Chapter 4: Pyrazino hydrazides as HDAC3 selective inhibitors

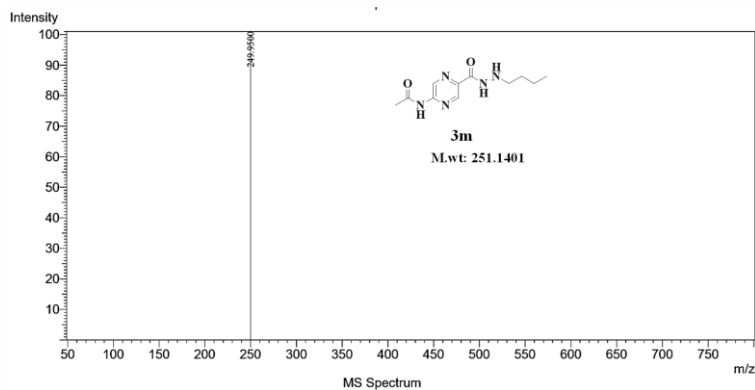


Spectra 4.78: ^{13}C NMR Spectra for compound **3m**.

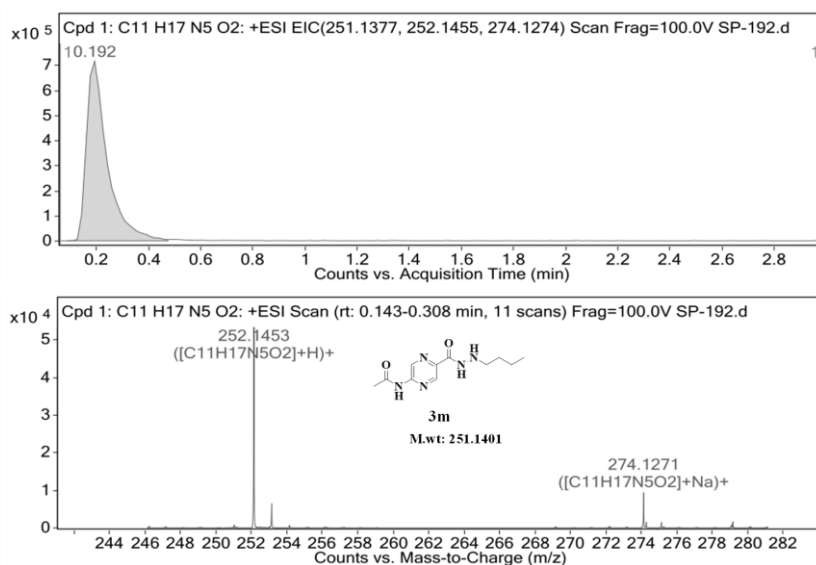


Spectra 4.79: HPLC traces of compound **3m**.

Chapter 4: Pyrazino hydrazides as HDAC3 selective inhibitors



Spectra 4.80: LC-MS Spectra for the compound 3m.

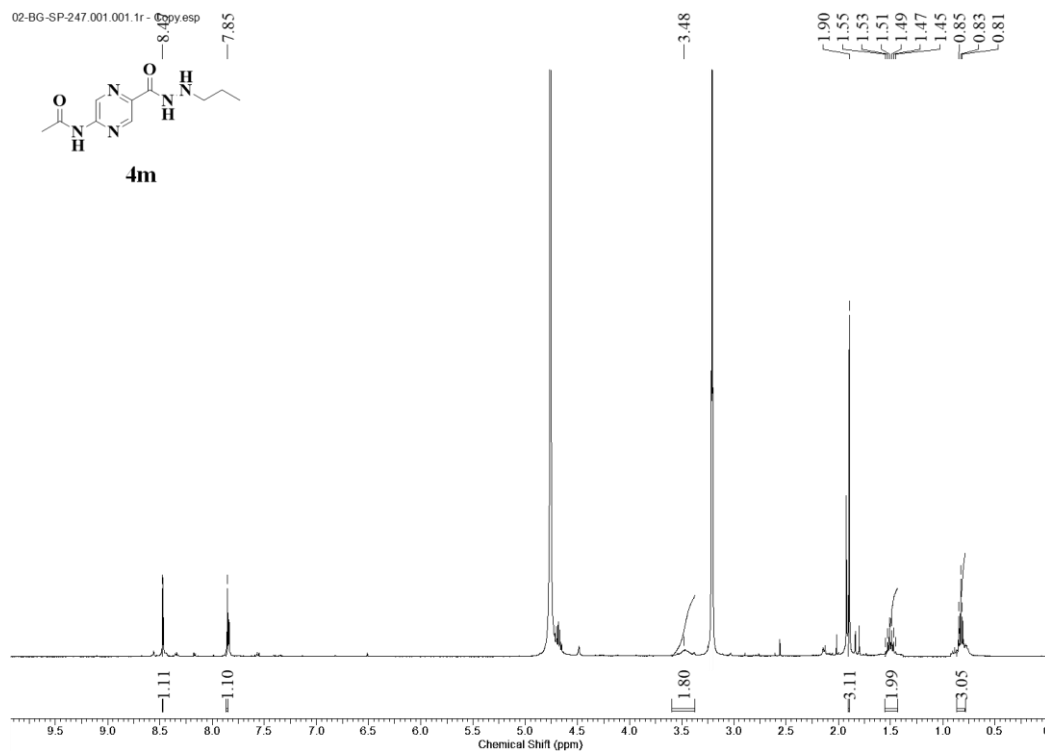


Spectra 4.81: HRMS Spectra for the compound 3m.

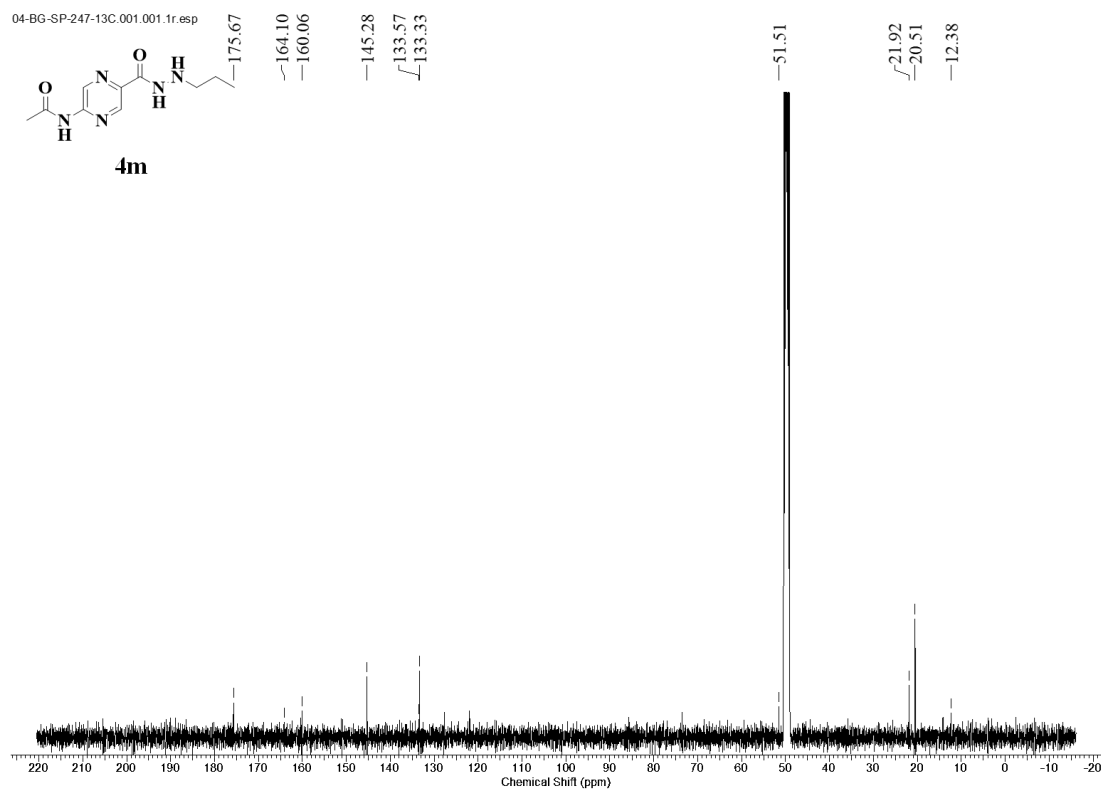
4.3.1.28. Preparation of *N*-(5-(2-propylhydrazine-1-carbonyl)pyrazin-2-yl)acetamide (**4m**)

Using the synthetic procedure of **3m**, starting materials **4l** and acetyl chloride gave **4m** as a white powder in 48% yield. ¹H NMR (400 MHz, methanol-*d*₄) δ 8.47 (s, 1H), 7.86 (s, 1H), 3.45 – 3.49 (m, 2H), 1.90 (s, 3H), 1.45 – 1.55 (m, 2H), 0.81 – 0.85 (t, J = 7.44 Hz, 3H). ¹³C NMR (101 MHz, methanol-*d*₄) δ 175.7, 164.1, 160.1, 145.3, 133.6, 133.3, 51.5, 21.9, 20.5, 12.4. HRMS (APESI) m/z calcd for C₁₀H₁₅N₅O₂. [M+H]⁺: 238.1246; found 238.1293.

Chapter 4: Pyrazino hydrazides as HDAC3 selective inhibitors

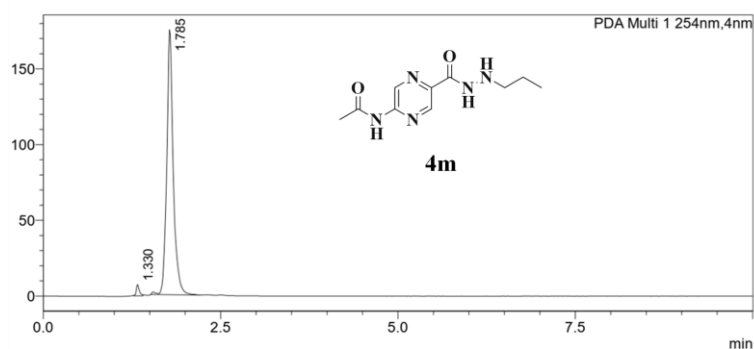


Spectra 4.82: ¹H NMR Spectra for the compound 4m.



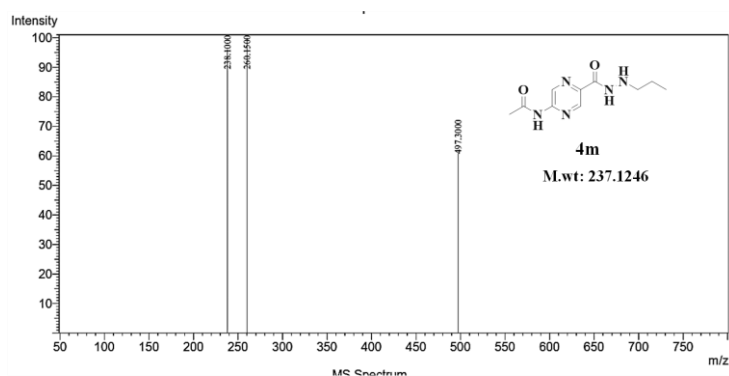
Spectra 4.83: ¹³C NMR Spectra for compound 4m.

Chapter 4: Pyrazino hydrazides as HDAC3 selective inhibitors

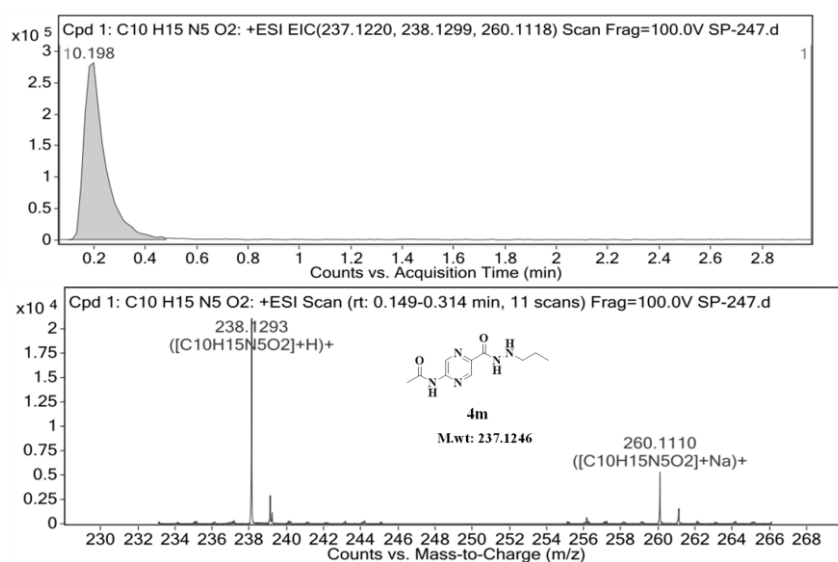


Peak#	Ret. Time	Area	Height	Area%
1	1.330	22736	7476	2.001
2	1.785	1113329	174960	97.999
Total		1136065	182436	100.000

Spectra 4.84: HPLC traces of compound 4m.



Spectra 4.85: LC-MS Spectra for the compound 4m.



Spectra 4.86: HRMS Spectra for the compound 4m.

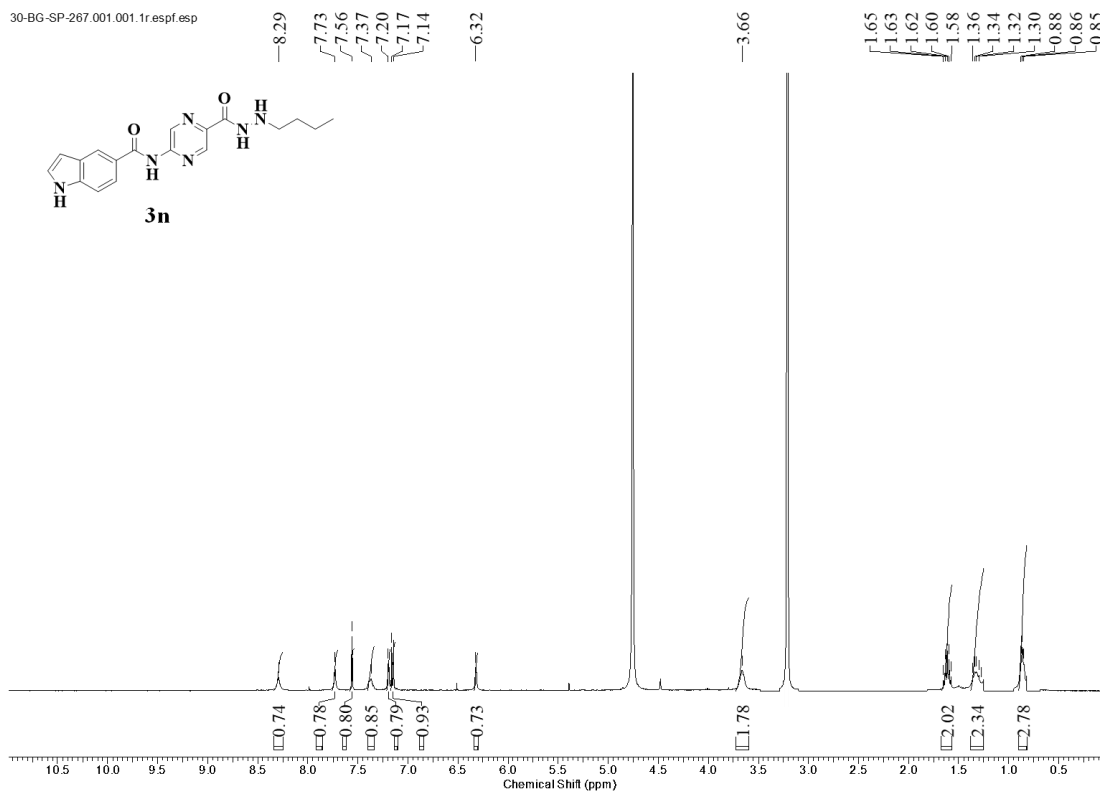
4.3.1.29. Preparation of *N*-(5-(2-butylhydrazine-1-carbonyl)pyrazin-2-yl)-1*H*-indole-5-

Chapter 4: Pyrazino hydrazides as HDAC3 selective inhibitors

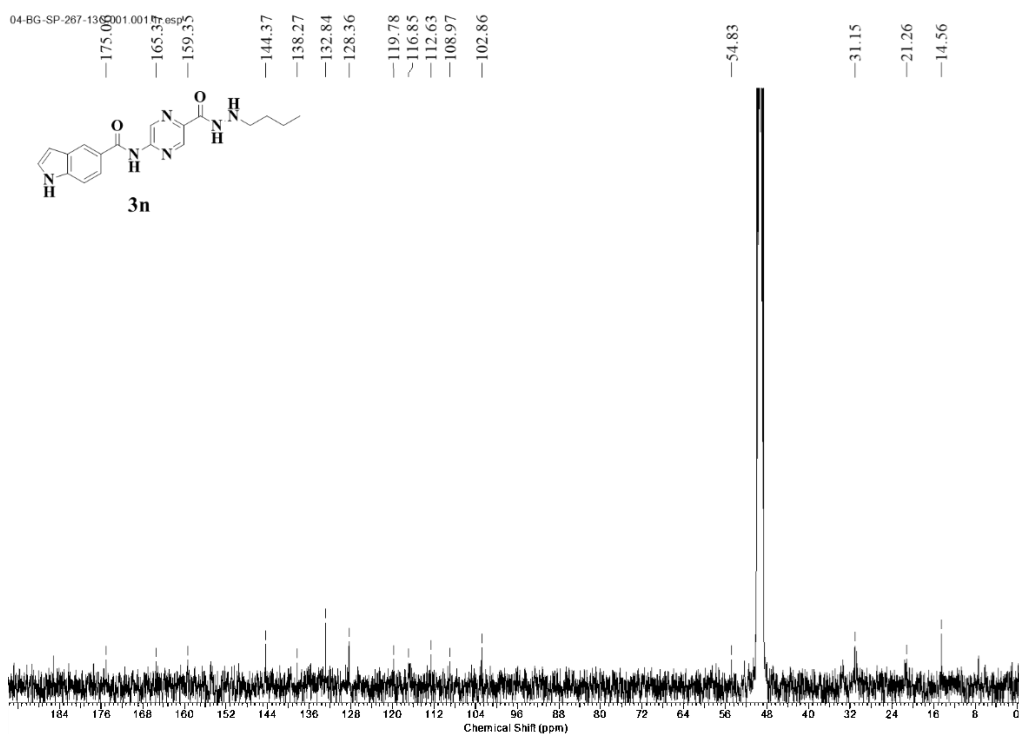
carboxamide (3n)

5-amino-N'-butylpyrazine-2-carbohydrazide (**3l**) (100 mg, 0.477 mmol) was dissolved in 5 mL of dry DCM and to these 2 equivalents of pyridine (76.99 μ L, 1.43 mmol) was added at 0 °C. To this, 1-ethyl-3-(3-dimethylaminopropyl) carbodiimide hydrochloride (EDCI, 183.23 mg, 0.955 mmol), 1-hydroxybenzotriazole (HOBT, 96.86 mg, 0.716 mmol), and indole-5-carboxylic acid (92.42 mg, 0.752 mmol) was added and the reaction mixture was left for stirring at room temperature overnight. The reaction completion was monitored by TLC and once the reaction is complete, the excess solvent was evaporated under a rota evaporator. The crude reaction mixture was then dissolved in ethyl acetate and washed with water three times and the organic layer was separated. The organic layer containing the compound was then dried over anhydrous sodium sulphate and the excess solvent was removed under vacuum. The crude reaction mixture was then column purified and the pure compound **3n** was eluted from the column using 75% ethyl acetate and 25% hexane as solvents. The obtained compound **3n** in the form of brown powder of about 49% yield. ¹H NMR (400 MHz, methanol-*d*₄) δ 8.29 (s, 1H), 7.73 (s, 1H), 7.56 (s, 1H), 7.37 – 7.39 (d, *J* = 8.88 Hz, 1H), 7.13 - 7.23 (m, 2H), 6.32 (s, 1H), 3.67 (m, 2H), 1.58 – 1.65 (m, 2H), 1.30 – 1.36 (m, 2H), 0.85 – 0.88 (t, *J* = 6.38 Hz, 3H). ¹³C NMR (101 MHz, methanol-*d*₄) δ 174.8, 165.1, 159.1, 144.2, 141.4, 138.0, 132.6, 128.1, 119.6, 116.6, 112.4, 108.7, 102.6, 54.6, 30.9, 21.0, 14.3. HRMS (APESI) *m/z* calcd for C₁₈H₂₀N₆O₂. [M+H]⁺: 353.1668; found 353.1718.

Chapter 4: Pyrazino hydrazides as HDAC3 selective inhibitors

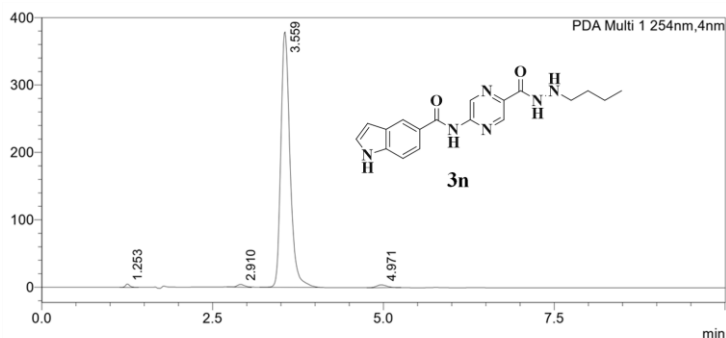


Spectra 4.87: ^1H NMR Spectra for the compound **3n**.



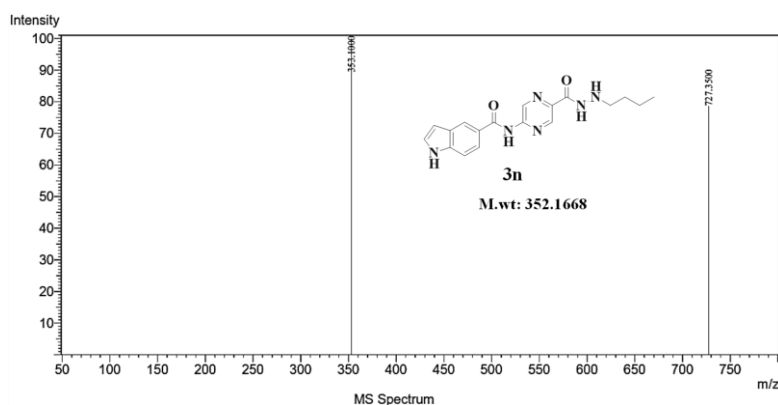
Spectra 4.88: ^{13}C NMR Spectra for compound **3n**.

Chapter 4: Pyrazino hydrazides as HDAC3 selective inhibitors

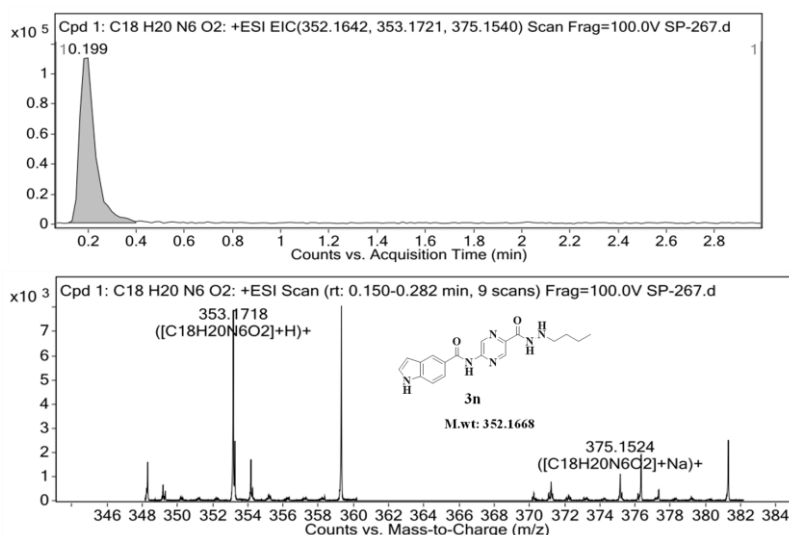


Peak#	Ret. Time	Area	Height	Area%
1	1.253	25239	5134	0.692
2	2.910	32473	4119	0.890
3	3.559	3548281	378834	97.253
4	4.971	42499	4121	1.165
Total		3648493	392207	100.000

Spectra 4.89: HPLC traces of compound 3n.



Spectra 4.90: LC-MS Spectra for the compound 3n.



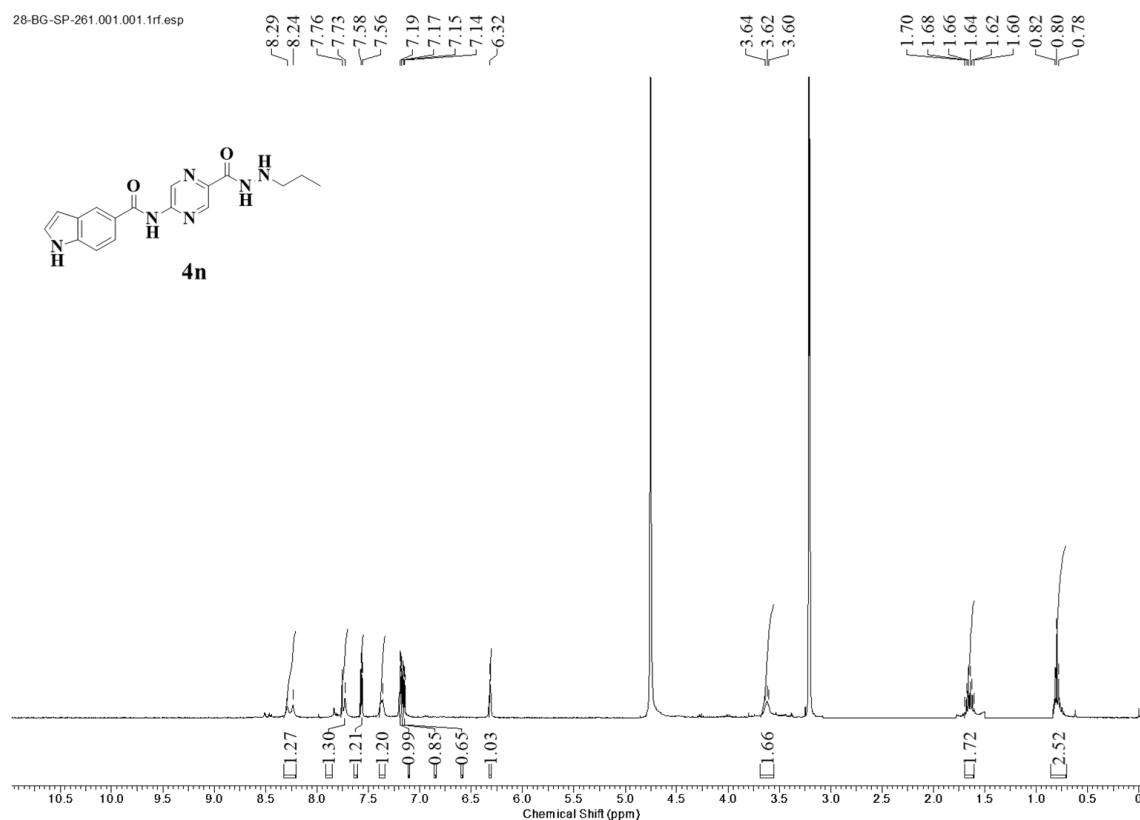
Spectra 4.91: HRMS Spectra for the compound 3n.

4.3.1.30. Preparation of *N*-(5-(2-propylhydrazine-1-carbonyl)pyrazin-2-yl)-1*H*-indole-5-

Chapter 4: Pyrazino hydrazides as HDAC3 selective inhibitors

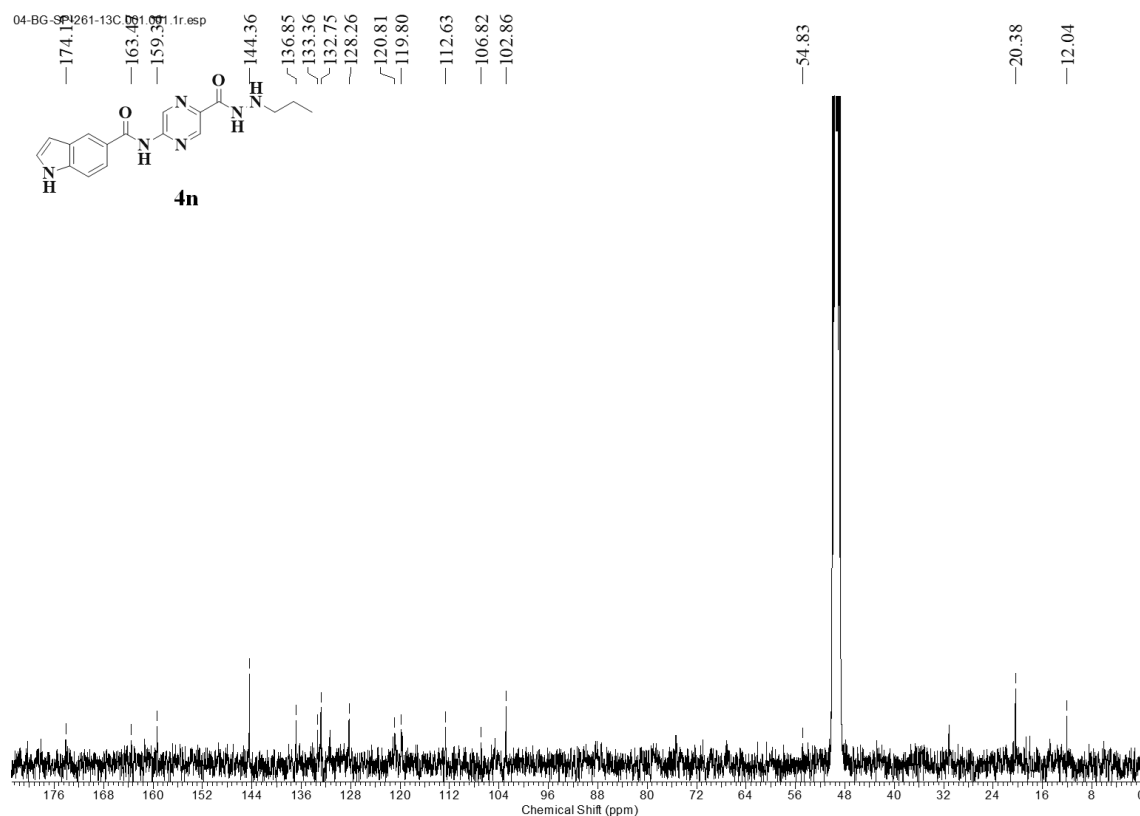
carboxamide (4n)

Following the synthetic procedure of **3n**, starting materials **3l** and indole-5-carboxylic acid gave **4n** as a brown powder in 53% yield. ^1H NMR (400 MHz, methanol- d_4) δ 8.29 (s, 1H), 7.73 - 7.76 (m, 1H), 7.56 - 7.58 (m, 1H), 7.36 - 7.38 (m, 1H), 7.19 (s, 1H), 7.17 - 7.18 (m, 1H), 7.14 - 7.16 (m, 1H), 6.31 - 6.32 (d, $J = 2.88$ Hz, 1H), 3.62 (m, 2H), 1.60 - 1.69 (m, 2H), 0.78 - 0.82 (t, $J = 7.07$ Hz, 3H). ^{13}C NMR (101 MHz, methanol- d_4) δ 174.1, 163.5, 159.3, 144.4, 136.9, 133.4, 132.7, 128.3, 120.8, 119.8, 112.6, 106.8, 102.9, 54.8, 20.4, 12.0. HRMS (APESI) m/z calcd for $\text{C}_{17}\text{H}_{19}\text{N}_6\text{O}_2$. $[\text{M}+\text{H}]^+$: 339.1501; found 339.1553.

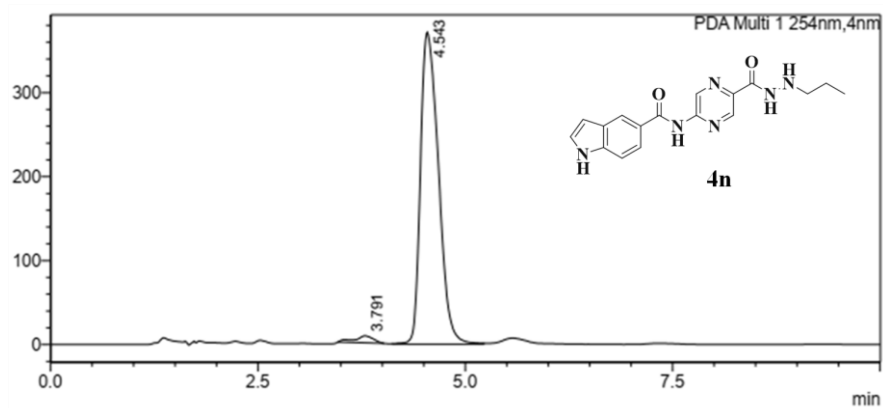


Spectra 4.92: ^1H NMR Spectra for the compound **4n**.

Chapter 4: Pyrazino hydrazides as HDAC3 selective inhibitors



Spectra 4.93: ^{13}C NMR Spectra for compound **4n**.

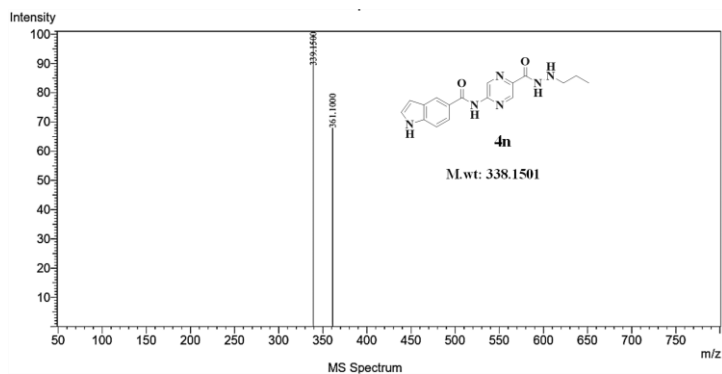


PDA Ch1 254nm

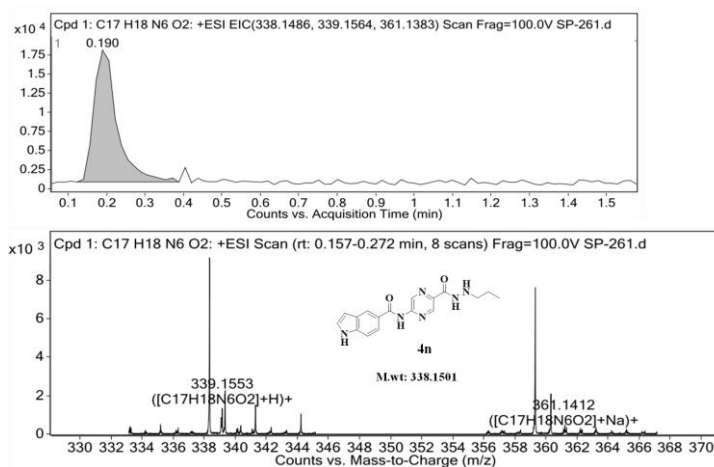
Peak#	Ret. Time	Area	Height	Area%
1	3.791	129839	8337	2.257
2	4.543	5622208	371620	97.743
Total		5752047	379958	100.000

Spectra 4.94: HPLC traces of compound **4n**.

Chapter 4: Pyrazino hydrazides as HDAC3 selective inhibitors



Spectra 4.95: LC-MS Spectra for the compound 4n.

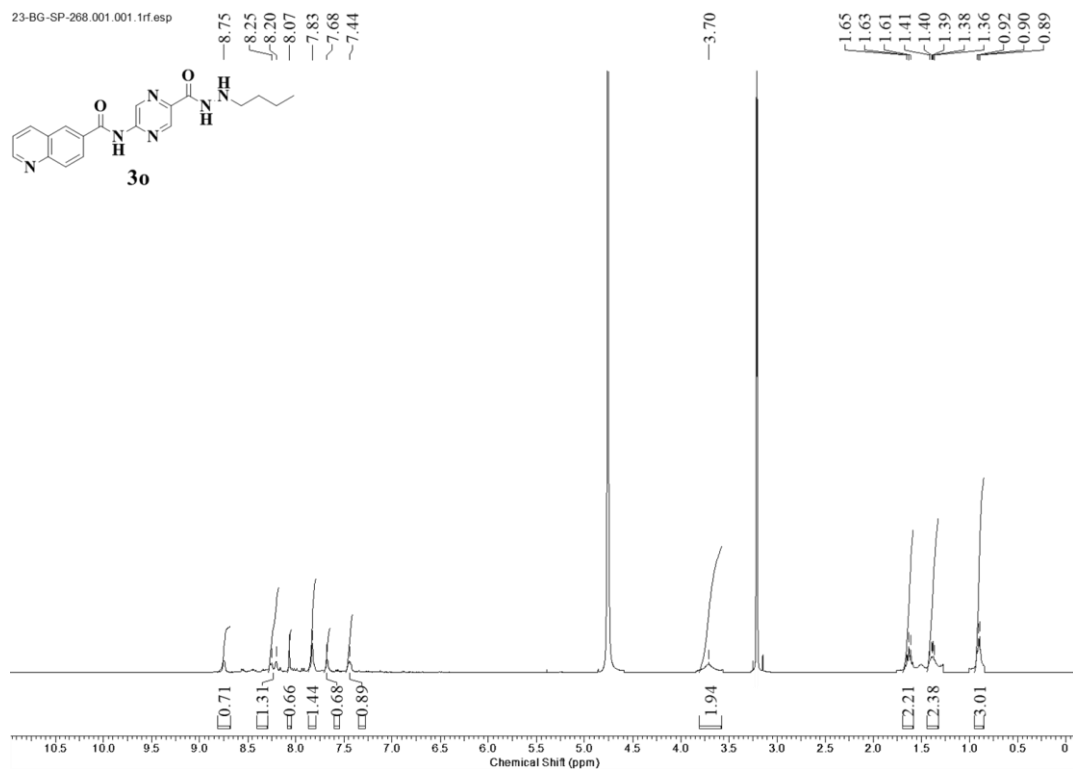


Spectra 4.96: HRMS Spectra for the compound 4n.

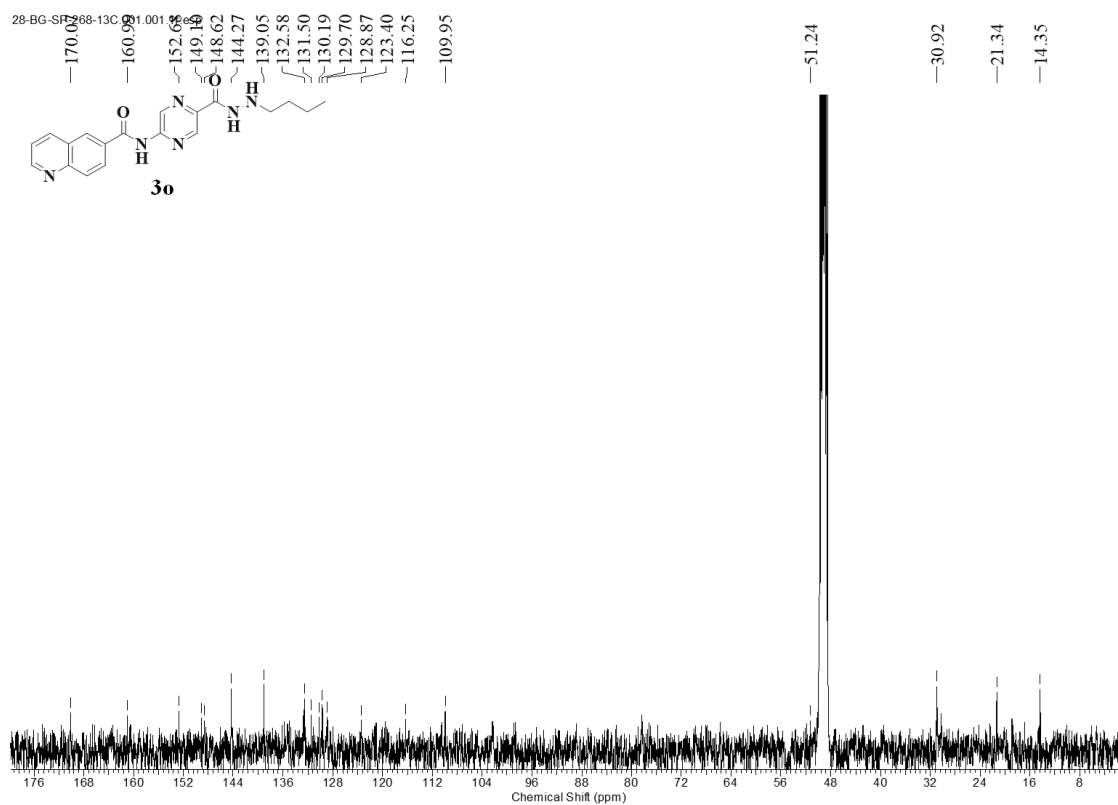
4.3.1.31. Preparation of *N*-(5-(2-butylhydrazine-1-carbonyl)pyrazin-2-yl)quinoline-6-carboxamide (**3o**)

Following the synthetic procedure of **3n**, starting materials **3l** and quinoline-6-carboxylic acid gave **3o** as a brown powder in 61% yield. ^1H NMR (400 MHz, methanol- d_4) δ 8.75 (br. s., 1H), 8.25 – 8.27 (d, $J = 8.38$ Hz, 1H), 8.20 (br. s., 1H), 8.07 (s, 1H), 7.83 (br. s., 2H), 7.68 (br. s., 1H), 7.43 - 7.46 (m, 1H), 3.71 (br. s., 2H), 1.61 – 1.67 (m, 2H), 1.36 – 1.41 (m, 2H), 0.89 - 0.92 (m, 3H). ^{13}C NMR (101 MHz, methanol- d_4) δ 170.1, 161.0, 152.7, 149.1, 148.6, 144.3, 139.1, 132.6, 131.5, 130.2, 129.7, 128.9, 123.4, 116.3, 109.9, 51.2, 30.9, 21.3, 14.3. HRMS (APESI) m/z calcd for $\text{C}_{19}\text{H}_{20}\text{N}_6\text{O}_2$. $[\text{M}+\text{H}]^+$: 365.1668; found 365.1711.

Chapter 4: Pyrazino hydrazides as HDAC3 selective inhibitors

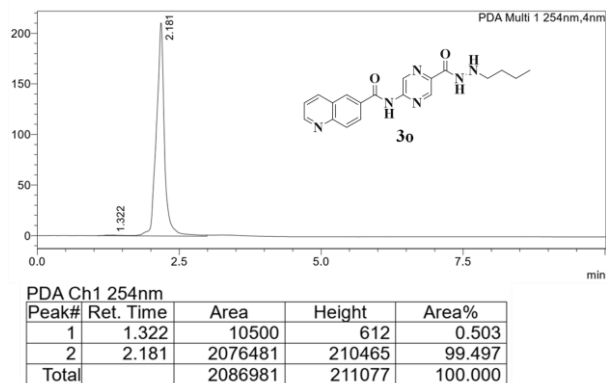


Spectra 4.97: ^1H NMR Spectra for the compound **30**.

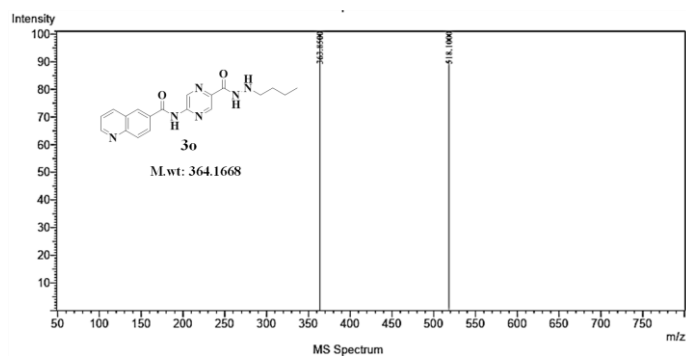


Spectra 4.98: ^{13}C NMR Spectra for compound **30**.

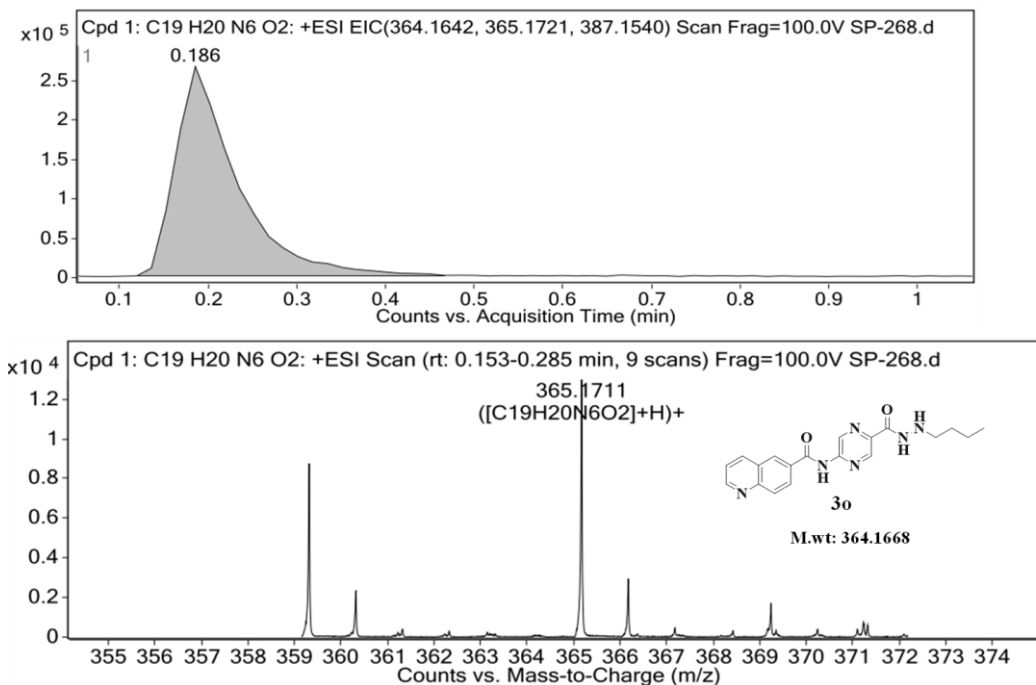
Chapter 4: Pyrazino hydrazides as HDAC3 selective inhibitors



Spectra 4.99: HPLC traces of compound 30.



Spectra 4.100: LC-MS Spectra for the compound 30.



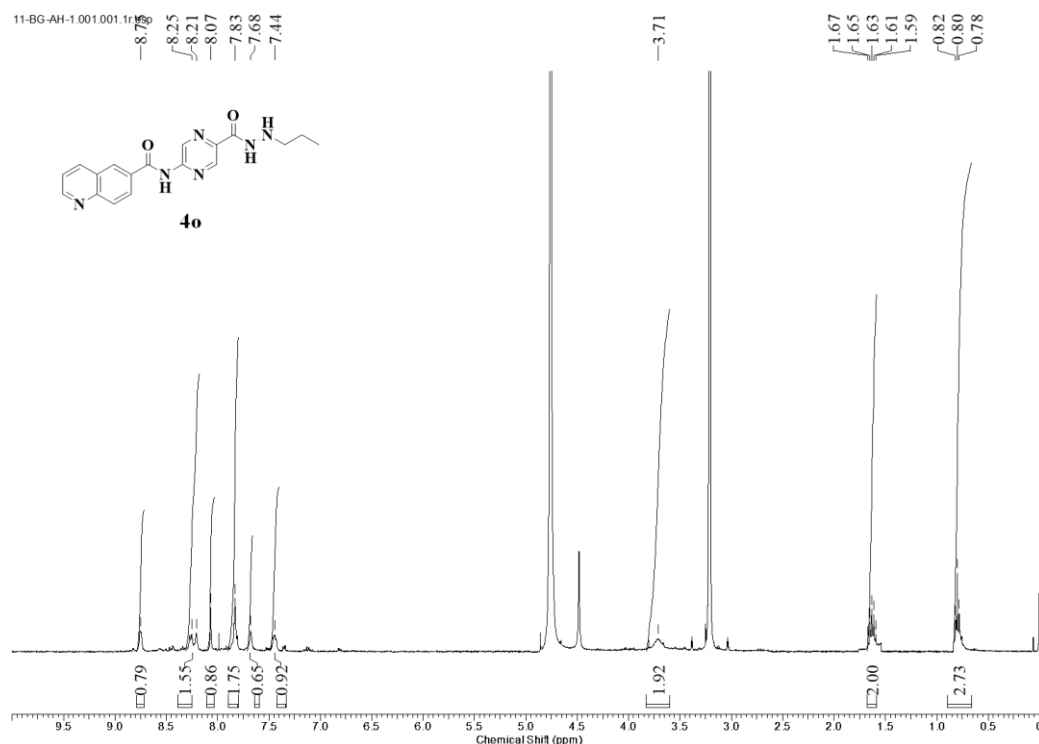
Spectra 4.101: HRMS Spectra for the compound 30.

4.3.1.32. Preparation of *N*-(5-(2-propylhydrazine-1-carbonyl)pyrazin-2-yl)quinoline-6-

Chapter 4: Pyrazino hydrazides as HDAC3 selective inhibitors

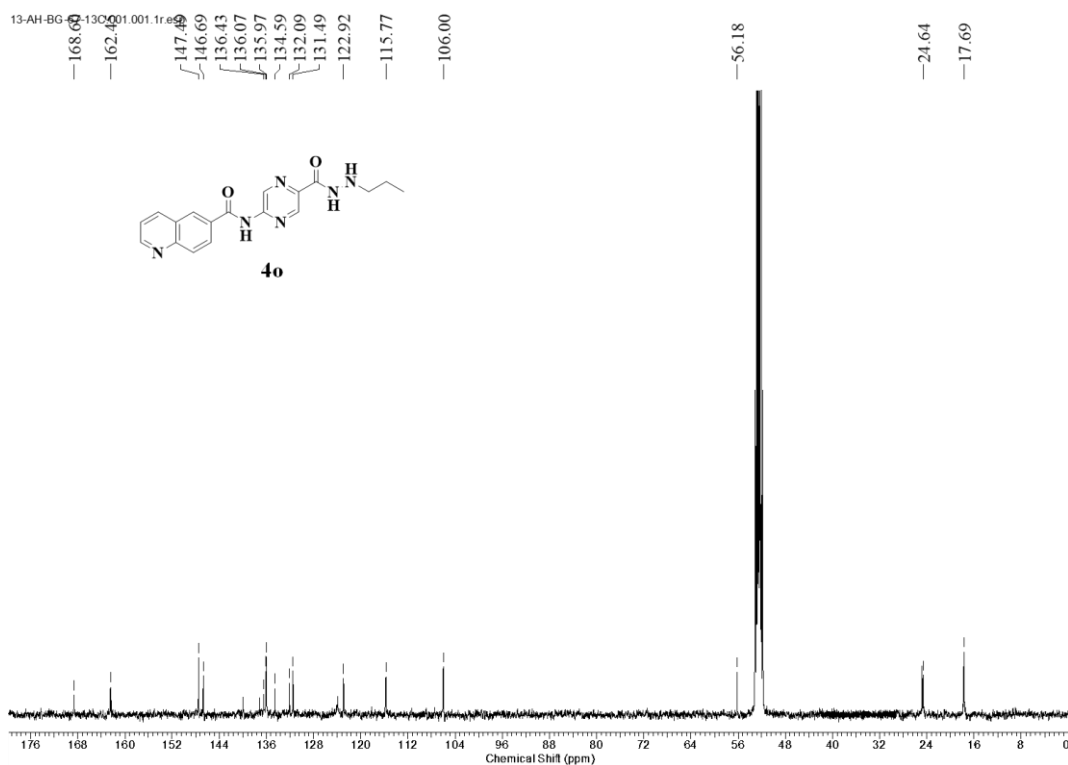
carboxamide (4o)

Following the synthetic procedure of **3n**, starting materials **4l** and quinoline-6-carboxylic acid gave **4o** as a brown powder in 58% yield. ^1H NMR (400 MHz, methanol- d_4) δ 8.75 (br. s., 1H), 8.25 – 8.27 (d, $J = 8.38$ Hz, 1H), 8.20 (br. s., 1H), 8.07 (s, 1H), 7.83 (br. s., 2H), 7.68 (br. s., 1H), 7.43 - 7.46 (m, 1H), 3.71 (br. s., 2H), 1.36 – 1.41 (m, 2H), 0.89 - 0.92 (m, 3H). ^{13}C NMR (101 MHz, methanol- d_4) δ 170.1, 161.0, 152.7, 149.1, 148.6, 144.3, 139.1, 132.6, 131.5, 130.2, 129.7, 128.9, 123.4, 116.3, 109.9, 51.2, 21.3, 14.3. HRMS (APESI) m/z calcd for $\text{C}_{18}\text{H}_{18}\text{N}_6\text{O}_2$. $[\text{M}+\text{H}]^+$: 351.1501; found 351.1557.

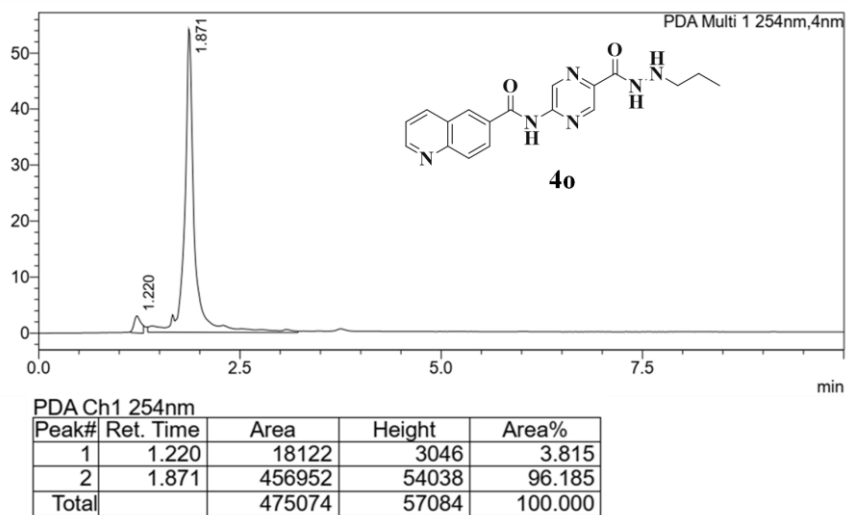


Spectra 4.102: ^1H NMR Spectra for the compound **4o**

Chapter 4: Pyrazino hydrazides as HDAC3 selective inhibitors

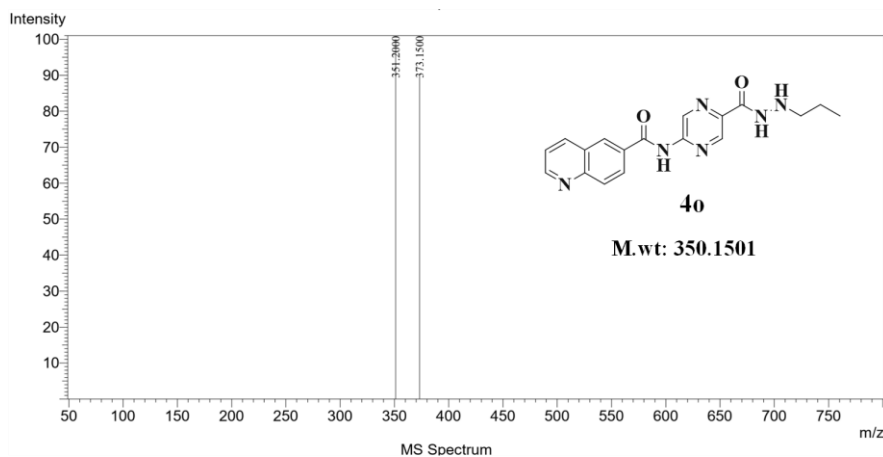


Spectra 4.103: ^{13}C NMR Spectra for compound **4o**

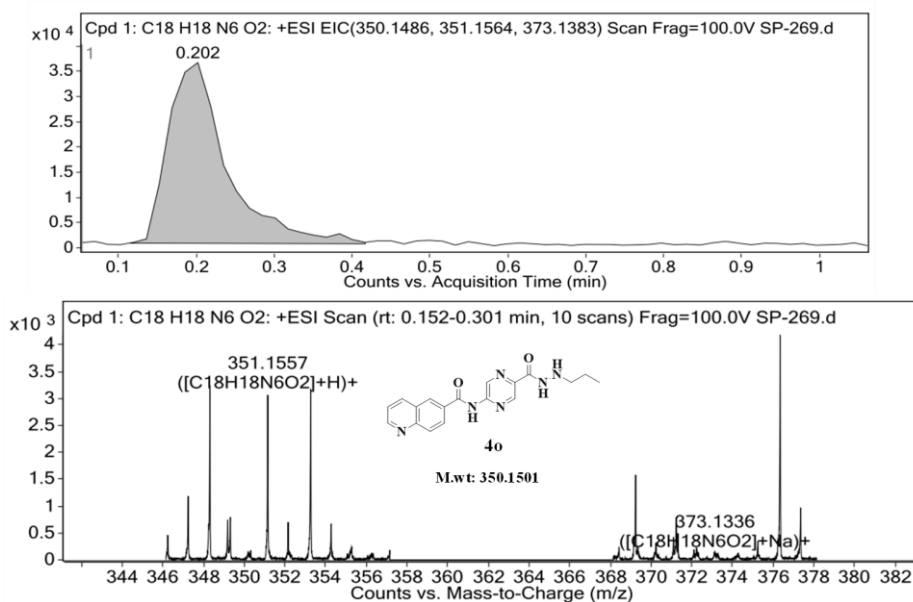


Spectra 4.104: HPLC traces of compound **4o**.

Chapter 4: Pyrazino hydrazides as HDAC3 selective inhibitors



Spectra 4.105: LC-MS Spectra for the compound 4o.

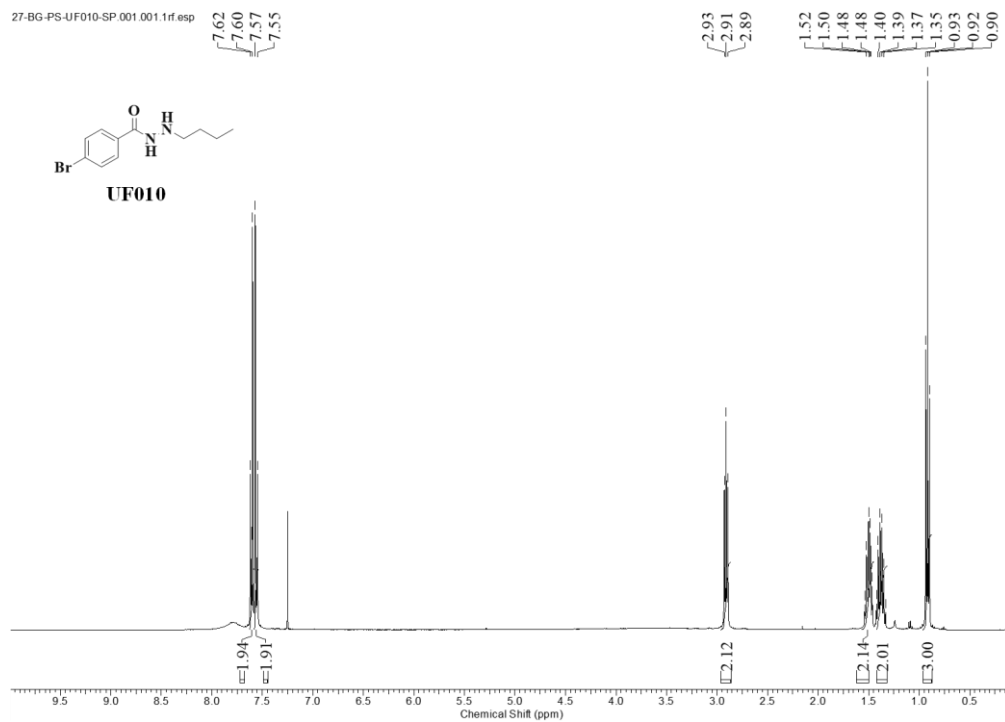


Spectra 4.106: HRMS Spectra for the compound 4o.

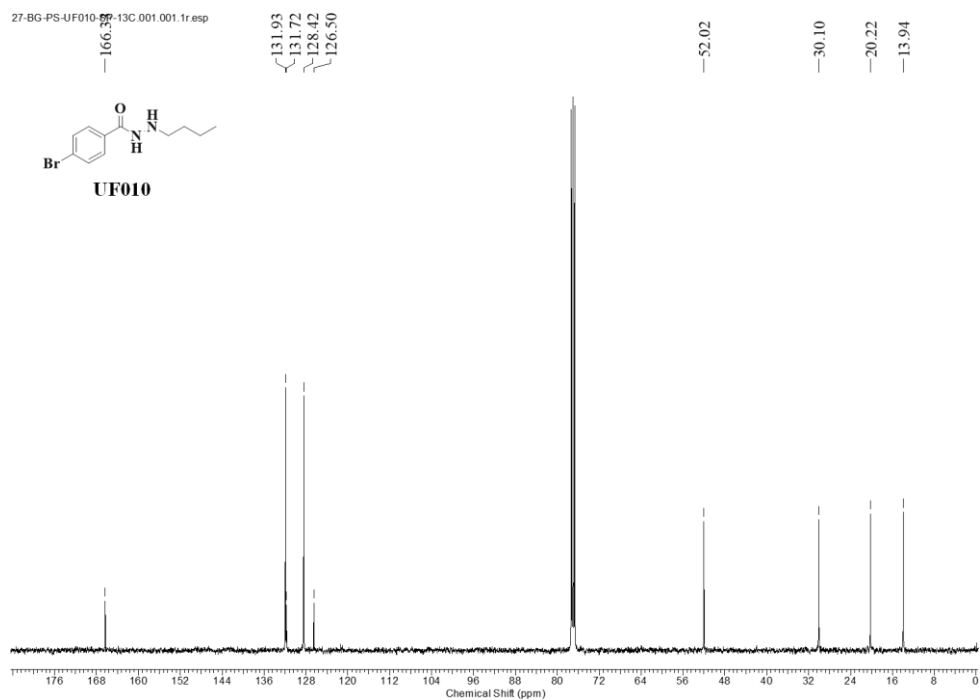
4.3.1.33. Preparation of UF010

The reference compound UF010 was synthesized in-house as per the reported protocol. (Pulya et al., 2022) The percentage yield obtained was 68%. ¹H NMR (400 MHz, CDCl₃) δ 7.55 - 7.62 (m, 4H), 2.89 - 2.93 (t, *J* = 7.19 Hz, 2H), 1.46 - 1.54 (m, 2H), 1.33 - 1.42 (m, 2H), 0.90 - 0.93 (t, *J* = 7.32 Hz, 3H). ¹³C NMR (101 MHz, CDCl₃) δ 166.3, 131.9, 131.7, 128.4, 126.5, 52.0, 30.1, 20.2, 13.9. HRMS (APESI) *m/z* calcd for C₁₁H₁₅BrN₂O. [M+H]⁺: 271.0368; found 271.0417.

Chapter 4: Pyrazino hydrazides as HDAC3 selective inhibitors

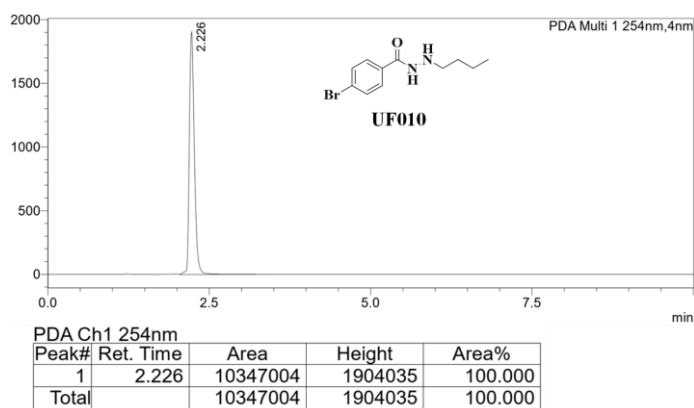


Spectra 4.107: ^1H NMR Spectra for the compound UF010.

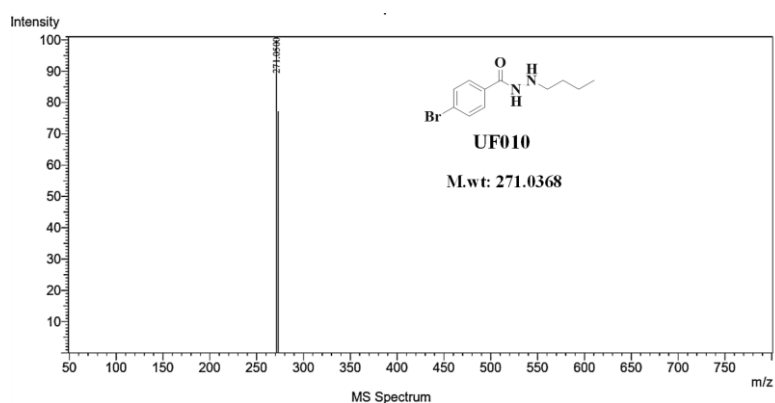


Spectra 4.108: ^{13}C NMR Spectra for compound UF010.

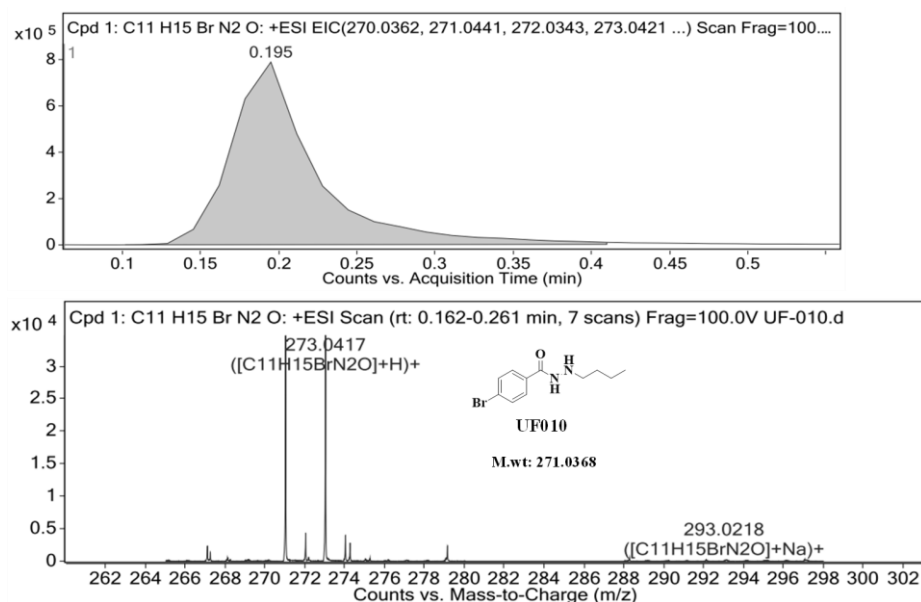
Chapter 4: Pyrazino hydrazides as HDAC3 selective inhibitors



Spectra 4.109: HPLC traces of compound UF010.



Spectra 4.110: LC-MS Spectra for the compound UF010.



Spectra 4.111: HRMS Spectra for the compound UF010.

4.3.2. *In vitro* cytotoxicity and cell culture studies

The *in vitro* cytotoxicity of the final compounds was evaluated in different subtypes of

Chapter 4: Pyrazino hydrazides as HDAC3 selective inhibitors

breast cancer cell lines and also over normal human cell lines following the MTT assay procedure.(Pulya et al., 2022)

The MTT assay was performed over a mouse triple-negative breast cancer cell line (4T1), human luminal A breast cancer cell line (MCF-7), human triple-negative breast cancer (TNBC) cell line (MDA-MB-231), human epidermal growth factor receptor 2+ (HER2+) breast cancer cell line (MDA-MB-453) along with three normal human cell lines, human breast cell line (MCF-10A), human embryonic kidney (HEK-293) cell line and human corneal epithelial cell line (HCEC). All the cell lines were procured from National Centre for Cell Science (NCCS, Pune, India). 4T1, MCF-7, MDA-MB-231, MDA-MB-453, MCF-10A and HEK-293 cell lines were primarily cultured in DMEM (Dulbecco's modified eagle medium, high glucose media: AL007S) and HCEC cell line was primarily cultured in DMEM/F-12 (Dulbecco's Modified Eagle Medium /Nutrient Mixture F12 Ham, AT140A, DMEM/F-12, 1:1 mixture) enriched with 10% fetal bovine serum (FBS) and 1% antibiotic (Pen strep: A001). The cultures were incubated at 37 °C under a 5% CO₂ atmosphere during the experiment. MTT [3-(4,5-dimethylthiazol-2-yl)-2,5-diphenyltetrazolium bromide], a yellow dye was used for determining the cell viability. All the required reagents were directly purchased from Himedia Laboratories Pvt. Ltd., Mumbai, India.

4.3.3. Chemicals and antibodies.

The DMSO stock solutions at 100 mM concentration of the final compounds were prepared and were stored at 4 °C. Histone deacetylase enzyme inhibition assays were carried out using HDAC fluorometric drug discovery assay kits such as HDAC1 (BML-AK-511-0001), HDAC2 (BML-AK-512-0001), HDAC3 (BML-AK-531-0001), HDAC6 (BML-AK-516-0001), and HDAC8 (BML-AK-518-0001), purchased from Enzo life sciences, Delhi and HDAC4 (cat #50064) and HDAC5 (cat #50065) purchased from Bps Biosciences, Mumbai. Staining solutions for nuclear staining assay such as DAPI, Acridine

Chapter 4: Pyrazino hydrazides as HDAC3 selective inhibitors

Orange and for cell cycle analysis, propidium iodide and RNase were directly purchased from Sigma-Aldrich. Apoptosis assay was performed using TACs Annexin-V/FITC – PI assay kit that was purchased from Bio-legend. For western blot analysis, the primary and secondary antibodies were all purchased from Cell Signalling Technology and the details along with catalogue numbers are as follows: rabbit mAb H3K9 acetylated histone H3 (cat#9649), H4K12 acetylated histone H4 (cat#13944), H3K27 acetylated histone H3 (cat#4353), alpha- Tubulin K40 acetylated (cat#3971), Caspase-3 (cat#9662), Caspase-7 (cat#12827), Bcl-2 (cat#3498), EGFR (cat#2132), CD44 (cat#3578), cytochrome *c* (cat#4280), Ki-67 (cat#9129S) and mouse mAb beta-actin primary antibodies (cat#58169) and the secondary antibodies – anti-rabbit HRP linked antibody (cat#7074), and anti-mouse IgG HRP-Linked antibody (cat#7076). The primary antibody, acetylated SMC3 (Lys105/106), clone 21A7 (cat#MABE1073) was purchased from Merck Sigma.

4.3.4. Pan-HDAC inhibition assay

Pan-HDAC inhibition of the compounds was carried out by using HDAC colorimetric assay kit (cat#BML-AK500-0001) containing HeLa nuclear extract and followed the protocol reported earlier.(Pulya et al., 2022) To the 96-well plate, 5 µL of HeLa nuclear extract, 10 µL of assay buffer, and 10 µL of 5 µM final concentration of the sample solution. The addition of 25 µL of the Color de Lys® substrate initiated the reaction and the microtiter plate was incubated for 30 min at room temperature. In the end, the reaction was terminated using 50 µL of the developer stop solution and the plate was further incubated for 15 min at 37°C. The absorbance was measured at 405 nm. The assay was carried out in duplicate and the results were analyzed using GraphPad Prism™ version 8.0.1.

4.3.5. HDAC3/NCOR1 inhibition assay

HDAC3 enzyme inhibition of the compounds was carried out by using HDAC3/NCOR1 fluorimetric drug discovery kit (cat#BML-AK531-0001) containing

Chapter 4: Pyrazino hydrazides as HDAC3 selective inhibitors

human recombinant HDAC3 enzyme and following the protocol reported earlier.(Pulya et al., 2022) The reaction mixture containing 15 μL of diluted HDAC3 complex enzyme solution, 10 μL of 1 μM concentration of the sample solution, and 25 μL of the Fluor de Lys® substrate solution was added for each sample and the microtiter plate was incubated for 15 min at room temperature for the reaction to proceed. Following this step, 50 μL of Fluor de Lys® developer II and Trichostatin A stop solution was added the plate was further incubated for 45 min at 37 °C. The fluorescence intensity was recorded at 360 nm/ 460 nm (excitation/emission) wavelengths. Following the same protocol, the IC₅₀ values were determined using the concentration range of 3.9 nM to 1000 nM for **4i** in duplicate. Analysis was done using the non-linear regression analysis method using GraphPad Prism™ version 8.0.1 and the corresponding graphs were plotted.

4.3.6. HDAC1 inhibition assay

HDAC1 inhibition of the compounds was carried out by using HDAC1 fluorimetric drug discovery kit (cat#BML-AK511-0001) containing recombinant HDAC1 enzyme and following the protocol reported earlier.(Pulya et al., 2022) The reaction mixture containing 15 μL of diluted HDAC1 complex enzyme solution, 10 μL of 1 μM concentration of the sample solution, and 25 μL of the Fluor de Lys® substrate solution was added for each sample and the microtiter plate was incubated for 15 min at room temperature for the reaction to proceed. Following this step, 50 μL of Fluor de Lys® developer II and Trichostatin A stop solution was added the plate was further incubated for 45 min at 37 °C. The fluorescence intensity was recorded at 360 nm/ 460 nm (excitation/emission) wavelengths. Following the same protocol, the IC₅₀ values were determined using the concentration range of 0.005 μM to 50 μM for **4i** in duplicate. Analysis was done using the non-linear regression analysis method using GraphPad Prism™ version 8.0.1 and the corresponding graphs were plotted.

Chapter 4: Pyrazino hydrazides as HDAC3 selective inhibitors

4.3.7. HDAC2 inhibition assay

HDAC2 inhibition of the compounds was carried out by using HDAC2 fluorimetric drug discovery kit (cat#BML-AK512-0001) containing recombinant HDAC2 enzyme and following the protocol reported earlier.(Pulya et al., 2022) The reaction mixture containing 15 μ L of diluted HDAC2 complex enzyme solution, 10 μ L of 1 μ M concentration of the sample solution, and 25 μ L of the Fluor de Lys® substrate solution was added for each sample and the microtiter plate was incubated for 30 min at room temperature for the reaction to proceed. Following this step, 50 μ L of Fluor de Lys® developer II and Trichostatin A stop solution was added the plate was further incubated for 15 min at 37 °C. The fluorescence intensity was recorded at 485 nm/ 530 nm (excitation/emission) wavelengths. Following the same protocol, the IC₅₀ values were determined using the concentration range of 0.005 μ M to 50 μ M for **4i** in duplicate. Analysis was done using the non-linear regression analysis method using GraphPad Prism™ version 8.0.1 and the corresponding graphs were plotted.

4.3.8. HDAC8 inhibition assay

HDAC8 inhibition of the compounds was carried out by using HDAC8 fluorimetric drug discovery kit (cat#BML-AK518-0001) containing recombinant HDAC8 enzyme and following the protocol reported earlier.(Pulya et al., 2022) The reaction mixture containing 15 μ L of diluted HDAC8 complex enzyme solution, 10 μ L of 1 μ M concentration of the sample solution, and 25 μ L of the Fluor de Lys® substrate solution was added for each sample and the microtiter plate was incubated for 15 min at room temperature for the reaction to proceed. Following this step, 50 μ L of Fluor de Lys® developer II and Trichostatin A stop solution was added the plate was further incubated for 45 min at 37 °C. The fluorescence intensity was recorded at 360 nm/ 460 nm (excitation/emission) wavelengths. Following the same protocol, the IC₅₀ values were determined using the

Chapter 4: Pyrazino hydrazides as HDAC3 selective inhibitors

concentration range of 0.005 μM to 125 μM for **4i** in duplicate. Analysis was done using the non-linear regression analysis method using GraphPad Prism™ version 8.0.1 and the corresponding graphs were plotted.

4.3.9. HDAC6 inhibition assay

HDAC6 inhibition of the compounds was carried out by using HDAC6 fluorimetric drug discovery kit (cat#BML-AK516-0001) containing recombinant HDAC6 enzyme and following the protocol reported earlier.(Pulya et al., 2022) The reaction mixture containing 15 μL of diluted HDAC6 complex enzyme solution, 10 μL of 10 μM concentration of the sample solution, and 25 μL of the Fluor de Lys® substrate solution was added for each sample and the microtiter plate was incubated for 10 min at room temperature for the reaction to proceed. Following this step, 50 μL of Fluor de Lys® developer II and Trichostatin A stop solution was added the plate was further incubated for 40 min at 37 °C. The fluorescence intensity was recorded at 360 nm/ 460 nm (excitation/emission) wavelengths. Following the same protocol, the IC₅₀ values were determined using the concentration range of 0.005 μM to 125 μM for **4i** in duplicate. Analysis was done using the non-linear regression analysis method using GraphPad Prism™ version 8.0.1 and the corresponding graphs were plotted.

4.3.10. HDAC4 inhibition assay

HDAC4 enzyme inhibition of the compounds was carried out by using HDAC4 fluorogenic kit containing recombinant HDAC4 enzyme and following the protocol reported earlier.(Pulya et al., 2022) The reaction mixture containing 5 μL of 20 μM substrate solution, 5 μL of 1mg/mL BSA solution, 30 μL of HDAC buffer, and 5 μL of 20 μM concentration of the sample solution were added and to this 5 μL of HDAC4 enzyme of 0.012 ng/ μL concentration was added to initiate the reaction. The microtiter plate was incubated for 30 min at room temperature for the reaction to proceed. Following this step,

Chapter 4: Pyrazino hydrazides as HDAC3 selective inhibitors

50 µL of undiluted developer stop solution was added the plate was further incubated for 15 min at 37 °C. The fluorescence intensity was recorded at 380 nm/ 480 nm (excitation/emission) wavelengths. Analysis was done using GraphPad Prism™ version 8.0.1 and the corresponding graphs were plotted.

4.3.11. HDAC5 inhibition assay

HDAC5 inhibition of the compounds was carried out by using HDAC5 fluorogenic kit containing recombinant HDAC5 enzyme and following the protocol reported earlier. (Pulya et al., 2022) The reaction mixture containing 5 µL of 20 µM substrate solution, 5 µL of 1mg/mL BSA solution, 30 µL of HDAC buffer, and 5 µL of 20 µM concentration of the sample solution were added and to this 5 µL of HDAC5 enzyme of 0.06 ng/µL concentration was added to initiate the reaction. The microtiter plate was incubated for 30 min at room temperature for the reaction to proceed. Following this step, 50 µL of undiluted developer stop solution was added the plate was further incubated for 15 min at 37 °C. The fluorescence intensity was recorded at 380 nm/ 480 nm (excitation/emission) wavelengths. Analysis was done using GraphPad Prism™ version 8.0.1 and the corresponding graphs were plotted.

In vitro cytotoxicity studies

4.3.12. MTT assay procedure

MTT assay procedure was followed for determining the *in vitro* cytotoxicity of the final compounds against different subtypes of breast cancer cell lines and their selectivity over normal human and breast cell lines. Cells were sub-cultured as per the ATCC protocol in their respective complete media and were subsequently seeded in a sterile 96-well plate with about 100 µL/well with a cell density of about 1×10^4 cells per well and were incubated overnight. The following day, the medium was aspirated and adhered the cells were treated with two different concentrations at 10 µM and 100 µM of the DMSO stock of final

Chapter 4: Pyrazino hydrazides as HDAC3 selective inhibitors

compounds in 150 µL of the respective media and were incubated for 72 h in the growth medium. Post-treatment period, the media was aspirated and to this 50 µL of 5 mg/mL of MTT solution in phenol red-free media was added and was incubated for about 3 h for the formation of formazan crystals. The MTT solution was removed and to the wells, 150 µL of DMSO was added for the dissolution of the formed crystals. The absorbance was measured at 570 nm and 650 nm wavelengths. The % cell viability was calculated as follows:

$$\frac{\text{Absorbance of treated cells}}{\text{Absorbance of untreated cells}} \times 100$$

Similarly, IC₅₀ values of the final compounds were determined using the MTT assay procedure described above. Dilutions at different concentrations were prepared from the DMSO stock solutions of the compounds in the respective media. The serial dilution method was followed and the dilutions were prepared from 200 µM to 0.781 µM concentrations with a control solution of 1% DMSO in the respective media. The treatment of the cells was carried out using the dilutions and the plate was incubated for 72 h. The % cell viability was determined and the obtained results were depicted as the dose-response curve for the IC₅₀ analysis using GraphPad Prism™ version 8.0.1.

In the case of the MCF-10A, HEK-293 and HCEC cell lines, the MTT assay was followed the same as previously described. (Pulya et al., 2022) Serial dilution method was followed and the dilutions were prepared from 2000 µM to 7.81 µM concentrations with a control solution of 1% DMSO in the respective media. The % cell viability was determined and the obtained results were depicted as the dose-response curve for the IC₅₀ analysis using GraphPad Prism™ version 8.0.1.

Generation of oxaliplatin-resistant cells and in vitro cytotoxicity study of 4i, UF010 and oxaliplatin (internal standard) in MDA-MB-231 sensitive and resistant cells

Following a low-concentration treatment method, drug resistance in the MDA-MB-231

Chapter 4: Pyrazino hydrazides as HDAC3 selective inhibitors

cells was built by gradually raising the drug concentration with the procedure reported previously. (Itoo et al., 2022) Cells were first cultured in T-25 flasks supplemented with free oxaliplatin (1 μ M). The oxaliplatin concentration was slowly increased to 10 μ M for 6 months of continuous culturing. To determine the chemosensitizing properties of **4i**, the compounds **4i**, **UF010**, **oxaliplatin** and a combination of equimolar ratio concentrations of **4i+oxaliplatin** were treated in both WT and OXPtR MDA-MB-231 cells for 72 h following MTT assay procedure. The % cell viability was determined and the obtained results were depicted as the dose-response curve for the IC₅₀ analysis using GraphPad Prism™ version 8.0.1.

4.3.13. Apo-ONE® Homogeneous Caspase-3/7 Assay

Caspase 3/7 assay was performed using Apo-ONE® Homogeneous Caspase-3/7 Assay kit (Promega, USA, catalogue no: G7792) following vendor's protocol. Briefly, 1×10^4 4T1 cells were seeded in 96-well plate and incubated overnight. The following day, cells were treated with IC₅₀ concentrations of compound **4i** and **UF010** in 4T1 cells for 72 h. Apo-ONE® Homogeneous Caspase-3/7 reagent was prepared by mixing Caspase Substrate Z-DEVD-R110 (100X) and Apo-ONE® Homogeneous Caspase-3/7 Buffer. After the treatment period, the media was aspirated and to this, 100 μ L of reagent was added and mixed by shaking it on plate shaker for 30 seconds at 300 rpm. Then plate was incubated for 40 mins at room temperature and fluorescence intensity was measured at 485 nm excitation wavelength and 527 nm emission wavelength using Spectramax M4 (Molecular Devices, USA).

4.3.14. Apoptosis assay

Apoptosis assay was performed using TACs/ Annexin V kit from Biolegend, US in 4T1 and MDA-MB-231 cells. A flat-bottomed 12-well plate was taken and 4T1 and MDA-MB-231 cells were seeded with a cell density of 0.5 million per well and were left overnight for

Chapter 4: Pyrazino hydrazides as HDAC3 selective inhibitors

attachment. This was followed by media aspiration and the subsequent treatment with **4i** and **UF010** was carried out at their *in vitro* IC₅₀ values in 4T1 and MDA-MB-231 cells in triplicate for 72 h. In another set of experiment, three different concentrations of the compounds **4i** and **UF010** were taken namely, C1 (lower), C2 (IC₅₀) and C3 (higher) and the 4T1 cells were treated as described previously. The cells were then washed twice with ice-cold PBS and then trypsinized. Further, the trypsinized cells were collected, centrifuged and the obtained cell pellet was again washed with ice-cold PBS and was resuspended in 100 µL Annexin V reagent freshly prepared that includes 10 µL of 10X binding buffer, 1 µL of FITC, 10 µL of PI and made up to 100 µL with double distilled water. These samples were incubated in dark for 30 min and were further diluted to 500 µL using 400 µL of 1X binding buffer. After the incubation, the samples were finally analyzed by flow cytometry (BD Aria™ III), BD biosciences.

4.3.15. Cell cycle analysis

Cell cycle analysis for the compound **4i** and **UF010** was carried out by flow cytometry using BD Aria™ III, BD biosciences instrument, and the obtained data were analyzed using *Flow Jo* software. For this purpose, 1 million cells per well of 4T1 and MDA-MB-231 were seeded into 12 well plates and were incubated overnight. The other day, the media was aspirated and to this, the required concentrations of **4i** and **UF010** were added and the treatment was continued up to 72 h. In another set of experiment, three different concentrations of the compounds **4i** and **UF010** were taken namely, C1 (lower), C2 (IC₅₀) and C3 (higher) and the 4T1 cells were treated as described previously. After the treatment, the sample wells were washed with ice-cold PBS followed by trypsinization and were collected in the form of a cell pellet. The pellet was washed twice with ice-cold PBS and the single-cell suspension was obtained by dropwise addition of 70% ice-cold ethanol by gentle vortexing. The fixed cells were left at -20 °C overnight. Subsequently, the samples were centrifuged and the cell pellet thus obtained was resuspended in

Chapter 4: Pyrazino hydrazides as HDAC3 selective inhibitors

500 µL of the staining solution prepared by 20% w/v RNase, 2% w/v PI in about 0.1% v/v of triton X 100 solution in PBS. The dissolved samples were incubated for 30 min in dark at room temperature and were subsequently analyzed by flow cytometry in BD Aria™ III, BD biosciences. The data were plotted in the form of a dot plot with PI width vs PI area on the X-axis and Y-axis respectively. The % population of DNA was analyzed from the histogram that was plotted with PI area vs count on X-axis and Y-axis respectively. The data were analyzed using *Flow Jo_V10.7.1_CL* software to measure the percentage of cells in each cell cycle phase.

4.3.16. Nuclear staining assay

Nuclear staining assay was performed with the lead compound **4i** and the reference compound **UF010** in 4T1 and MDA-MB-231 cells to determine the extent of disintegration of the cancer cells. Flat-bottomed 12 well plates were seeded with 4T1 and MDA-MB-231 cells and left overnight for attachment, followed by media aspiration and treatment with **control** of 1% DMSO solution, **4i** and **UF010** as per their *in vitro* IC₅₀ concentrations in the respective cell lines. Post-treatment, the 12-well plate was incubated for 72 h. The cells were fixed by using a 4% paraformaldehyde solution and then subsequently stained with DAPI and acridine orange. The extent of nuclear staining was visualized under a Laser Scanning Confocal Microscope (LSCM) DMI8 (Leica microsystems, Germany) on 63x Magnification. The quantification of the % apoptosis was done using *Image J* software. Significance was analyzed using one-way ANOVA analysis and the graph was plotted in GraphPad Prism™ version 8.0.1.

4.3.17. In vitro metabolic stability study using rat liver microsomes

The incubation mixtures were prepared and conducted in duplicates in freshly prepared 50 mM potassium phosphate buffer (pH 7.4) in Eppendorf. Firstly, to study NaDPH dependant oxidative metabolism, 25 µL of compound **4i** and **propranolol** (internal standard) were taken and to this 55 µL of pooled rat liver microsomal solution prepared in potassium

Chapter 4: Pyrazino hydrazides as HDAC3 selective inhibitors

phosphate buffer at a concentration of 0.5 mg/mL was added, and further incubated for 5 min at 37 °C. Further, the reaction was initiated by adding 20 µL of NADPH solution prepared to a final assay concentration of 1 mM in buffer was added to all the samples at different predetermined time points of 5 min, 15 min, 30 min, and 60 min except to the 0 min sample and were incubated at 37 °C for the designated time. In the case of 0 min, time point sample, the stopping solution ice-cold methanol containing internal standard was added followed by NADPH solution, and the reaction was terminated. For all the other samples, after the reaction periods, the reaction was stopped using 100 µL ice-cold methanol. Further, the samples were centrifuged at 13000 rpm for 10 min and the supernatant was collected and subjected to HPLC analysis. Data analysis was done using GraphPad Prism™ version 8.0.1 software. The degradation half-life ($t_{1/2}$) for the microsomal stability studies was calculated using the equation: $t_{1/2} = 0.693/k$, where k is the first-order elimination rate constant. The elimination rate constant (k) was estimated by one-phase exponential decay using nonlinear regression analysis of the degradation time course data in GraphPad Prism™ version 8.0.1. The graph was plotted with time (min) on the X-axis and concentration of the compound (µg/mL) on the Y-axis. Intrinsic clearance (Cl_{int} , µL/min/mg) was calculated using the equation: $Cl_{int} = V * 0.693/t_{1/2}$. [where V = volume of incubation (µL)/ microsomal mass (mg)].

4.3.18. Animals

The *in vivo* experiments were conducted following the CPCSEA guidelines of the protocol approval number (BITS-Hyd/IAEC/2021/26) approved by IAEC (Institutional animal ethics committee), Department of Pharmacy, BITS Pilani, Hyderabad campus, Hyderabad. Regarding the *in vivo* pharmacokinetic study, we have procured male Wistar rats of weight ~220 g of about 7 – 8 weeks age-old. For the *in vivo* tumor xenograft mice model study, we have purchased female Balb/c mice of weight 20 – 22 g of about 6 – 8 weeks age-old

Chapter 4: Pyrazino hydrazides as HDAC3 selective inhibitors

from the National Centre for Laboratory Animal Sciences, National Institute of Nutrition (Hyderabad, India). Once received all the animals were housed and separated into groups and kept in cages as per the experimental requirements. These cages were kept in the animal house in the department with the room temperature and conditions maintained at 23 ± 2 °C and at $60\pm 10\%$ relative humidity in a 12 h light/ 12 h dark cycle. All the animals were taken proper care of by providing them with standard food and water.

In vivo biological evaluation

4.3.19. Pharmacokinetic study

The pharmacokinetic study was carried out using 5 mg/kg and 15 mg/kg of **4i** and 15 mg/kg of **UF010** in 12 male Wistar rats, each grouped into 3 mice per group into 4 groups including the control. The intraperitoneal administration of control (5% DMSO in saline), **4i** (20 mg/mL), and **UF010** (20 mg/mL) solution in saline containing 5% DMSO was carried out. At different pre-determined time points of pre-dose, 0.25 h, 0.5 h, 1 h, 2 h, 4 h, 6 h, 8 h, 12 h, and 24 h about 500 μ L of blood samples were collected from the retro-orbital plexus of the rats under anesthetic conditions. The blood samples were collected and centrifuged and the supernatant plasma was taken and stored at -20 °C for further analysis. This was followed by the protein precipitation method using methanol, and the compound solutions **4i** and **UF010** were extracted from the plasma and subsequently analyzed by HPLC Shimadzu. The linear trapezoidal rule was used for the calculation of the area under the concentration and time curve (AUC values). Non-compartmental analysis was used to obtain the pk parameters. The clearance was estimated as $CL = \text{Dose}/AUC_{inf}$; $MRT = AUMC_{inf}/AUC_{inf}$. Data obtained represents the mean \pm standard deviation of the mean for $n = 3$.

4.3.20. In vivo antitumor activity by the 4T1-Luc xenograft mouse model

For the *in vivo* animal study experiment, 4T1-Luc cells were cultured in RPMI media as

Chapter 4: Pyrazino hydrazides as HDAC3 selective inhibitors

per ATCC guidelines. After 3 days of purchasing animals, they were inoculated subcutaneously with 1.0 million cells suspended in 100 μ L of sterile PBS into the dorsal flank region of the female Balb/c mice for tumor implantation. After 8 days post-injection of the cells, tumors sign was observed. Using a digital vernier caliper, tumor volume was measured and calculated as tumor volume = $[(\text{length} \times \text{width}^2) \div 2]$. Once the tumor volume reached 50 mm³, treatment was initiated. 48 animals were divided into 4 groups, 12 mice in each group treated with **Control**, **UF010** (reference compound-15 mg/kg), **4i** (5 mg/kg), and **4i** (15 mg/kg). The formulation to be injected was prepared by dissolving **UF010** and **4i** in 5% DMSO, 20% PEG and 75% saline at their respective doses. Treatment was given to animals once every 3 days (0, 3, 6, 9, 12, 15, 18, 21) for 21 days, and 4 groups of mice were treated with vehicle alone, 75 μ L of **UF010** at 15mg/kg dose, and 75 μ L and 62.5 μ L of **4i** at 15 mg/kg and 5 mg/kg dose respectively. Body weights and tumor volumes were recorded every alternate day. Tumor weights were measured on the 7th day and 14th day by sacrificing 3 mice from each group, and %Tumor Growth Inhibition was calculated using %Tumor Growth Inhibition = $[1 - (\text{MTW of treated} \div \text{MTW of Control})] * 100$. At the end of the experiment, the remaining 4 mice were sacrificed, and the tumors were removed and weighed.

4.3.21. Bioluminescence image analysis in the treated 4T1-Luc tumor xenograft mice

The growth of the tumors was monitored periodically by *in vivo* imaging technique using IVIS® Lumina III, PerkinElmer, USA, to carry out bioluminescence analysis. To anesthetize the mice, they were placed in the induction chamber with the flow of O₂ and 2% isoflurane continuously. Subsequently, Luciferin D (50 μ L, 150 mg/kg dissolved in sterile PBS) was injected intraperitoneally. Mice were then placed inside the imaging facility after 2 min. Four from each group of mice were selected randomly and were monitored for tumor growth on days 5, 10, 15, and day 21 of the treatment period and the

Chapter 4: Pyrazino hydrazides as HDAC3 selective inhibitors

images were acquired. Around the tumor area, the region of interest was selected and the bioluminescence signals were analyzed in the units of photons/sec/cm²/sr (maximum photons per second per centimeter square per steradian).

At the end of the study, the mice were sacrificed and tumors along with the major organs were isolated for further study and were stored at -80 °C in tissue freezing media. The tumor tissue was lysed using ice-cold 1X RIPA lysis buffer, 0.5 mM PMSF, and protease inhibitor and stored at -80 °C for western blot analysis. Using cryotome (Leica Biosystems, Germany), the isolated tumors of all groups were sectioned into 5 µm thicknesses. These tumor and organ tissue sections were further used for immunohistochemical analysis.

4.3.22. Evaluation of reactive oxygen species (ROS) generation in vivo

DCFH-DA probe was used for the evaluation of ROS generation. Mice were anesthetized (n = 4) and DCFH-DA (50 µL, 25 µM) was injected intratumorally on day 21 of the treatment. Images were obtained with IVIS® Lumina III, PerkinElmer, USA. By selecting the region of interest, the fluorescence intensity [(p/sec/cm²/sr)/µW/cm²] was quantified. After 30 min, the tumors were surgically isolated and the tumor sections were observed using a fluorescence microscope under the FITC channel (ex/em = 495/519 nm). The fluorescence intensities were evaluated and compared using *Image J* software.

4.3.23. Terminal deoxynucleotidyl transferase dUTP nick end labeling (TUNEL) assay on tumor tissue sections

The frozen tumor sections in the OCT media were cryo-sectioned to a thickness of 4 µm using a cryotome (Leica Biosystems, Germany). The assay was conducted according to the procedure previously described.(Pulya et al., 2022) Accordingly, the tumor tissues were stored at 37 °C, along with the terminal deoxynucleotidyl transferase (TdT) enzyme, for 1 h. To the fixed tissue slides, the TUNEL reaction mixture was added and kept in the dark, humid environment at 37 °C for another hour. Further, it was washed thrice using 1X PBS

Chapter 4: Pyrazino hydrazides as HDAC3 selective inhibitors

and stained using DAPI for 5 min. The slides were imaged under the fluorescence microscope. *Image J* software was used to process and analyze the obtained images.

4.3.24. Ki-67 staining of the tumor cryosections

Immunohistochemical analysis of the tumor sections was carried out by utilizing the biomarker Ki-67 to examine cell proliferation. The tissue sections were fixed with 4% paraformaldehyde onto the slides and were blocked for 1 h. The primary antibody of Ki-67 with a dilution of 1: 500 was used for incubation at 4 °C. The tumor sections were washed with 1X PBS, after overnight incubation and were further incubated with a secondary antibody for 2 h at 25 °C in dark. The tissue sections were washed with 1X PBS twice, and the coverslip was placed onto the sections. The results depict the extent of proliferation indicated by Ki-67 positively stained cells by fluorescence microscopy.

4.3.25. Histological evaluation of the tumor cryosections by H&E staining assay

The immunohistochemical examination of various organ sections and tumor sections was carried out in accordance with the procedure described. (Pulya et al., 2022) Briefly, tissue sections of 4 µm thickness were fixed on glass slides and treated with xylene and ethyl alcohol (100 % - 30 %), followed by washing with 1X PBS and water. Hematoxylin and eosin were used to stain the nuclei and cytoplasm, respectively. The tissue sections were then dehydrated using ethyl alcohol (30 % -100 %), followed by a xylene wash. The sections were finally fixed using mounting media and visualized with 10X magnification under a fluorescent microscope.

4.3.26. Study of lung metastasis

After the treatment period, the mice were anesthetized using ketamine/xylazine; the tumor was surgically removed and weighed. The animals were revived and monitored for 7 days, post-surgery. On day 7, the mice were imaged using intraperitoneally injected Luciferin D (50 µL, 150 mg/kg dissolved in sterile PBS). Further, the mice were sacrificed and the lungs

Chapter 4: Pyrazino hydrazides as HDAC3 selective inhibitors

were excised, weighed, and observed for metastasis. Images were obtained with IVIS® Lumina III, PerkinElmer, USA.

4.3.27. Western blot analysis of various biomarkers in vitro and in vivo

For the western blot analysis *in vitro*, the 4T1 cells were plated in a flat-bottomed 12 -well plate and they were subsequently treated with 1 μ M concentrations of **4i**, **UF010**, **BG-45** and **SAHA**. Further for another set of experiment, the plated 4T1 cells were treated with **4i** and **UF010** at 500 nM and 2 μ M concentrations. For the western blot analysis *in vivo*, 6 mg of the tumor tissue from the treated mice from all groups including control. After the treatment *in vitro*, the cells and *in vivo*, the tumor tissue was homogenized with 100 μ L 1X RIPA lysis buffer (Millipore, Billerica, MA, USA), supplemented with 0.5 mM phenylmethylsulfonyl fluoride (PMSF), and protease inhibitor. Protein quantification was done using the DC protein assay reagents (#5000116). 20 μ L (10 μ g) of tumor proteins with 5X loading buffer (5 μ L) were denatured at 95 °C for 5 min. The denatured proteins were then separated using sodium dodecyl sulfate-polyacrylamide gel electrophoresis. Gels were transferred to the polyvinylidene fluoride membranes (Bio-Rad, Laboratories, Inc.) and using 5% bovine serum albumin (#9048-46-8, Himedia Laboratories Pvt. Ltd) in tris-buffered saline with 1% Tween 20 (TBST), the membranes were blocked and incubated overnight at 4°C with Rabbit mAb H3K9 acetylated histone H3 (#9649S), Rabbit mAb H3K27 acetylated histone H3 (#8173), H4K12 acetylated histone H4 (#13944S), alpha-Tubulin K40 acetylated (cat#3971), acetylated SMC3 (Lys105/106), clone 21A7 (cat#MABE1073), Caspase-3 (cat#9662), Caspase-7 (#12827), Bcl-2 (#3498), EGFR (#2132), CD44 (#3578), Cytochrome *c* (#4280), Ki-67 (#9129) and Mouse mAb beta-Actin (#3700) as an internal control and primary antibodies (Cell Signalling Technology, Inc.). The following day, the membranes were washed twice with TBST and were further incubated with the corresponding secondary antibodies of anti-rabbit HRP linked antibody

Chapter 4: Pyrazino hydrazides as HDAC3 selective inhibitors

(cat#7074), and anti-mouse IgG HRP-Linked antibody (cat#7076) for 1 h at room temperature. After the secondary antibody incubation, the membranes were washed twice with TBST for 10 min each and were detected using a chemiluminescence kit (cat#170-5060, Bio-Rad, Laboratories, Inc.), for visualization and were exposed using a Fusion plus 6 Imaging System (Vilber Lourmat, France). The blots were quantified using *Image J* software and the graphs were plotted using GraphPad Prism™ version 8.0.1. software.

4.3.28. Statistical analysis

All the experiments were performed in triplicates, and data were represented as mean±SD (mean ± standard deviation). One-way ANOVA and student's t-test were performed using GraphPad Prism™ version 8.0.1. software between the groups to determine the significance. *p < 0.05, **p < 0.01, ***p < 0.001, ****p < 0.0001, significantly different from the control group and these were all considered statistically significant.

4.3.29. Molecular docking analysis

To know the binding mode of interactions of these compounds, all these molecules were docked into the X-ray crystallographic structures of the HDAC isoforms (i.e., HDAC1, HDAC2, HDAC3, HDAC6, and HDAC8) as per our earlier reported protocol(Pulya et al., 2022) All these X-ray crystallographic data were obtained from the Protein Data Bank.(Bank, n.d.) Here, for the molecular docking study, the *GLIDE* module of the Schrodinger Maestro v12.1 software was utilized.("Schrödinger Suite, Schrödinger, LLC, New York, USA, 2019. <http://www.schrodinger.com/glide.>," n.d.) Initially, the '*Protein Preparation Wizard*' of the Maestro v12.1 software("Schrödinger Suite, Schrödinger, LLC, New York, USA, 2019. <http://www.schrodinger.com/glide.>," n.d.) was used for the optimization and preparation of these HDACs including the addition of missing hydrogen atoms, generation of states, and refinement.(Pulya et al., 2022; "Schrödinger Suite, Schrödinger, LLC, New York, USA, 2019. <http://www.schrodinger.com/glide.>," n.d.) In

Chapter 4: Pyrazino hydrazides as HDAC3 selective inhibitors

this protein preparation process, the OPLS_2005 force field was used for the restrained minimization of the proteins. After the protein preparation, the ‘*Receptor Grid Generation*’ module from Maestro v12.1 was used to locate the active site and to prepare the receptor grid for molecular docking analysis.(Pulya et al., 2022) The hydrazide molecules were prepared with the help of the ‘*Ligprep*’ module of Maestro v12.1 using the OPLS_2005 force field. Finally, the molecular docking was executed with the extra precision (XP) method using the *GLIDE* module.(Pulya et al., 2022; “Schrödinger Suite, Schrödinger, LLC, New York, USA, 2019. [http://www.schrodinger.com/glide.](http://www.schrodinger.com/glide),” n.d.) The post-docking results produced different docking poses of these compounds with different docking scores. These docked conformations were studied and ranked depending on their docking scores and binding interactions at the active site of these HDACs.(Pulya et al., 2022)

4.4. CONCLUSION

Breast cancer is the most common cancer among women worldwide and TNBC accounts for about 15 – 20% of breast cancer types. TNBC is one of the most aggressive breast cancer types with chemotherapy as the only choice of treatment. Hence, targeted and efficient therapy for TNBC is the need of the hour for better prognosis and improving the survival rates of the patients. Especially, HDAC3 is one of the most promising targets for breast cancer therapy due to its abnormal expression in TNBC. Thus, developing highly selective and potent HDAC3is might offer an alternative strategy for TNBC therapeutics. In this work, we have developed a series of novel *pyrazino*-hydrazide scaffold containing highly potent and selective HDAC3 inhibitors with the lead compound **4i** exhibiting potent antitumor efficacy *in vitro* and *in vivo*. We have designed this novel chemotype containing *pyrazine* as the linker scaffold with various aryl, heteroaryl or heteroaroyl substituents at the *para*-amino group of the pyrazine moiety employing the hybrid structure strategy from the previous lead compounds of our group. Among the series, **4i** was identified as the lead

Chapter 4: Pyrazino hydrazides as HDAC3 selective inhibitors

compound inhibiting HDAC3 at $IC_{50} = 14$ nM with a minimum of 120-fold and 1500-fold selectivity over other class I HDAC isoforms and representative class II HDACs respectively. Significant cytotoxicity was exhibited by all the compounds against various subtypes of breast cancer cell lines and the highest potency was demonstrated against 4T1 and MDA-MB-231 cells *in vitro*. All the compounds were also prominently selective towards breast cancer cell lines over normal human cell lines including breast cells tested. **4i** also demonstrated the highest potency with 550 nM and 741 nM IC_{50} values against 4T1 and MDA-MB-231 cells respectively with more than 286-fold selectivity over HEK-293 and HCEC cell lines tested and 385-fold selectivity over MCF-10A cells. **4i** induced 63.5% of total apoptosis and caused G2/M phase arrest in the TNBC cell lines tested *in vitro*. For the first time, a hydrazide-based HDAC3 inhibitor was tested against a chemoresistant MDA-MB-231 cell line and interestingly, **4i** has retained its *in vitro* cytotoxicity suggesting a possible therapeutic strategy for chemoresistant TNBC. **4i** exhibited good metabolic stability with a $t_{1/2}$ value of 38.33 min when studied in rat liver microsomes and this was also well reflected with a $t_{1/2}$ value of 7.20 h in the *in vivo* pharmacokinetic analysis, when **4i** was intraperitoneally administered at 5 mg/kg and 15 mg/kg. Excellent *in vivo* antitumor potential was exhibited by **4i** at both the doses tested (5 mg/kg and 15 mg/kg) in the 4T1-Luc tumor bearing mouse model. Significant reduction in the growth of tumor volume and about 97.92% of tumor growth inhibition rate percentage was exhibited by **4i** at 15 mg/kg dose when treated with only 7 doses once in every 3 days for a treatment period of 21 days. **4i** also exhibited good biosafety as evidenced by the stable body weight of mice all through the treatment period and histological staining of the major organs isolated from the mice post-treatment period. Significant apoptotic activity induced by **4i** treatment was seen *in vivo* mediated by reactive oxygen species generation which was further evidenced by the upregulation of apoptotic proteins caspase-3, caspase-7, cytochrome *c*, and the

Chapter 4: Pyrazino hydrazides as HDAC3 selective inhibitors

downregulation of Bcl-2. Furthermore, the reduced metastatic potential of 4T1-Luc tumors was demonstrated in the **4i** treated mice with fewer tumor nodules in the lungs supported by the downregulation of CD44, a surface adhesion marker in tumor cells. The immunohistochemical analysis of the treated tissue samples with Ki-67 indicated significant antiproliferative activity also indicated by the downregulation of EGFR and Ki-67 through western blot analysis. Overall, we could identify a potent HDAC3 selective drug-able inhibitor **4i** as a promising therapeutic for the treatment of TNBC with excellent *in vitro* and *in vivo* therapeutic properties and it might also offer a perspective in the treatment of chemoresistant therapies of triple-negative breast cancer.

Chapter 5
Conclusions

Cancer is one of the leading causes of death worldwide and the growing incidence of cancer has urged the researchers across the globe to identify a promising treatment for cancer. Epigenetic alterations leading to the changes in the gene expression is one of the key research areas with wide applicability in developing precision therapeutics for different life-threatening diseases including cancer. Cancer is a complex disease that is characterised by various signalling pathways and can readily develop drug resistance, mostly due to both genetic and epigenetic factors contributing to its pathogenesis and progression. Histone deacetylases (HDACs), one of the key epigenetic enzymes has become an attractive therapeutic target, due to its overexpression in at various stages of cancer progression. In the recent past, epigenetic drug discovery, particularly histone deacetylase inhibitors (HDACis), targeting HDACs has shown some promising anticancer activity and six HDACis are currently in the clinic against different haematological cancers. Since then, various HDACis have been studied clinically and preclinically either alone or in combination with other anticancer drugs against different cancers. Most of the HDACis are non-selective towards different HDAC isoforms, thus causing severe side-effects, dose-related toxicities and in some cases death of the patients during clinical trials. Therefore, the discovery of isoform-selective HDACis is the most sought-after challenge as selectively inhibiting individual isoforms might reduce the off-target effects thus improving their overall clinical outcome.

The thesis aimed at identifying isoform specific HDACis, in particular HDAC3is with improved potency and selectivity as promising anticancer agents. In this direction, we have developed some potent small molecule HDAC3 selective inhibitors including novel chemotypes of benzoyl and *pyrazino* linked hydrazides with improved pharmacokinetic profile and promising antitumor efficacy *in vivo* in 4T1-Luc tumor xenograft mouse model.

Chapter 5: Conclusions

As discussed in **chapter 3**, our first objective included the design and synthesis of some novel small molecule benzoyl hydrazides with different acetyl, aryl or aroyl substituents in the cap region as potent and selective HDAC3is. Compound **4e** was identified as the lead molecule with 15.41 nM HDAC3 IC₅₀ and more than 18-fold HDAC3 isoform selectivity over other class I HDACs and more than 3000-fold selectivity over HDAC4, HDAC5 and HDAC6. All the compounds were significantly cytotoxic against different cancer cell lines such as 4T1, B16F10, MCF-7, A549 and were significantly less toxic against the normal cell lines such as HEK-293, HCEC and Raw 264.7. **4e** exhibited the highest potency against 4T1 cells with 1.92 μM IC₅₀ and over 80-fold selectivity for cancer cells over normal cells. Moreover, the *in vivo* pharmacokinetic study of compound **4e** in male wistar rats revealed the t_{1/2} of 2.19 h and 2.62 h when tested intravenously and with the t_{1/2} of 3.41 h and 4.54 h when tested intraperitoneally with 15 mg/kg and 25 mg/kg body weight dose respectively, thus demonstrating an improved pharmacokinetic profile. We, for the first time studied the *in vivo* antitumor efficacy in 4T1-Luc tumor xenograft mouse model in female Balb/c mice for selective HDAC3 inhibitors with hydrazide as ZBG. The lead compound **4e** has exhibited promising antitumor activity *in vivo* at 15 mg/kg and 25 mg/kg after 21 days of treatment (5 days/week). The significant reduction in the tumor volume with no general toxicity in the major organs was noted during the treatment period. Enhanced acetylation levels on H3K9 and H4K12 residues were found both *in vitro* and *in vivo* experiments upon treatment with **4e**. **4e** treatment induced significant apoptosis and reduced the proliferation and metastasis as evidenced by the western blot analysis of the treated tumor tissue. The cell cycle arrest at G2/M phase in 4T1 cells suggested the programmed cell death mechanism leading to apoptosis. Further, apoptotic activity was visualised by performing immunohistochemical analysis by TUNEL assay and ROS generation assay. Altogether, our aim to identify benzoyl hydrazide based

Chapter 5: Conclusions

HDAC3 selective inhibitors with potent anticancer activity has resulted in the identification of compound **4e** as the lead molecule to be developed into a promising compound for anticancer therapy in future.

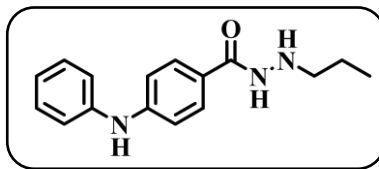


Figure 5.1. Structure of the lead compound **4e** from the series of benzoyl hydrazides as HDAC3 selective inhibitors. (Chapter 3)

Further, in our second objective discussed in **chapter 4**, we have successfully designed and developed a series of *pyrazino*-hydrazide based small molecules with modified cap groups as novel chemotypes of HDAC selective inhibitors. These compounds incorporated pyrazine as the linker scaffold with hydrazide as ZBG, with various aryl or heteroaryl or heteroaroyl substituents at the *para*-amino group of pyrazine moiety employing the hybrid structure strategy from previous lead compounds of our group. The lead compound **4i** has demonstrated significant potency and excellent selectivity against HDAC3 over other HDAC isoforms tested with HDAC3 IC₅₀ at 14 nM exhibiting about 120-fold and 1500-fold selectivity over other class I HDAC isoforms and representative class II HDACs respectively. As HDAC3 is one of the most promising targets of breast cancer, we tested these series of compounds against different subtypes of breast cancer cell lines for their cytotoxicity evaluation *in vitro*. Notably, all the compounds exhibited potent cytotoxicity against 4T1 and MDA-MB-231 breast cancer cells and among those the lead compound, **4i** has exhibited about 550 nM and 741 nM IC₅₀ respectively with more than 286-fold selectivity over HEK-293 and HCEC cell lines. **4i** induced more than 50% of total apoptosis and caused G2/M cell cycle arrest in 4T1 and MDA-MB-cell lines *in vitro*. Further, **4i** has displayed good metabolic stability with a t_{1/2} value of 38.33 min when studied in rat liver microsomes and also a t_{1/2} of 7.2 h in the *in vivo* pharmacokinetic

Chapter 5: Conclusions

analysis, where **4i** was intraperitoneally administered at 5 mg/kg and 15 mg/kg. It is noteworthy, that **4i** has retained its cytotoxicity in the oxaliplatin resistant MDA-MB-231 cells and also demonstrated its chemosensitizing properties by improving the cytotoxicity profile of the oxaliplatin when treated in combination. When treated *in vivo*, **4i** displayed excellent therapeutic efficacy in 4T1-Luc tumor xenograft mouse model in female Balb/c mice with about 97.92% of tumor growth inhibition rate at 15 mg/kg dose with a much shorter dosage regimen of 7 doses, once every 3 days for a treatment period of 21 days. The therapeutic efficacy of **4i** *in vivo* can be attributed to the apoptotic mechanism mediated by ROS generation and also due to modulation of pro-apoptotic and anti-apoptotic proteins which was demonstrated by western blot analysis. The reduced metastatic potential of the tumors *in vivo* along with the decreased proliferative activity upon treatment has further suggested the excellent potential of **4i** as anti-breast cancer therapeutic. This study described in **chapter 4**, identified **4i**, as a potent and selective HDAC3 inhibitor consisting of *pyrazino*-hydrazide scaffold as the novel chemotype with excellent *in vitro* and *in vivo* antitumor potential for the treatment of triple-negative breast cancer and the results obtained also suggested a perspective to explore the HDAC3 inhibitor, **4i** towards the treatment of chemoresistant therapies in case of breast cancer.

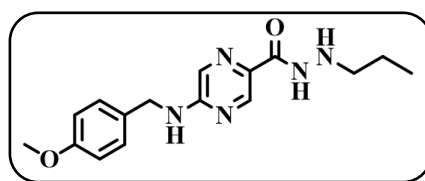


Figure 5.2. Structure of the lead compound **4i** from the series of pyrazino hydrazides as HDAC3 selective inhibitors. (**Chapter 4**)

Chapter 6
Future perspectives

Chapter 6: Future Perspectives

The role of epigenetics in cancer has been well established and the over expression of histone deacetylases (HDACs) has been characterised in the pathogenesis of different cancers. The role of histone deacetylase inhibitors (HDACis) in the treatment of different cancers has been explored with six of them being clinically approved for the treatment of different haematological cancers by FDA. Even though, HDACis have shown great potential as anticancer agents, still there is a lot of room for clinical optimisation as there is no HDACi approved since a decade as an anticancer therapeutic. Although, several HDACis have been tested preclinically and clinically, none of them have displayed promising clinical outcome due to their non-selectivity against different HDAC isoforms leading to off-target effects, severe dose limiting toxicities and poor pharmacokinetic profile. Also, the exact role and biological functions of HDACs is still not clear, and therefore, isoform selective HDACis with target specific activity might deliver promising therapeutic effects than non-selective HDACis. Since past decade numerous HDACis with modifications on different pharmacophoric regions have been carried out to enhance the potency and selectivity towards specific HDAC isoforms.

In this work, we have designed and developed molecules with nanomolar potency and selectivity towards HDAC3 isoform. The structure activity relationship information and the detailed *in vitro*, *in vivo* biological evaluation data can provide valuable insights for future development of these molecules. These molecules can be further studied for their specific mechanism of action and pathway elucidation by performing detailed pharmacological evaluation. Further, structural modifications can be performed to enhance their potency and antitumor efficacy. With the encouraging preliminary results of these molecules, they can be further explored in the development of multi-functional hybrid anticancer drug conjugates as well as in combination with other anticancer drugs. These

Chapter 6: Future Perspectives

molecules can be also developed by employing various drug delivery systems, thus enhancing their target specific delivery.

Altogether, these HDAC3 selective inhibitor leads have larger scope to be developed into anticancer therapeutics with greater capacity to be translated into the clinic in the near future.

Bibliography

Bibliography

- Acharya, M.R., Karp, J.E., Sausville, E.A., Hwang, K., Ryan, Q., Gojo, I., Venitz, J., Figg, W.D., Sparreboom, A., 2006. Factors affecting the pharmacokinetic profile of MS-275, a novel histone deacetylase inhibitor, in patients with cancer. *Invest New Drugs* 24, 367–375. <https://doi.org/10.1007/s10637-005-5707-6>
- Adhikari, N., Amin, S.A., Trivedi, P., Jha, T., Ghosh, B., 2018. HDAC3 is a potential validated target for cancer: An overview on the benzamide-based selective HDAC3 inhibitors through comparative SAR/QSAR/QAAR approaches. *Eur J Med Chem* 157, 1127–1142. <https://doi.org/10.1016/j.ejmech.2018.08.081>
- Adhikari, N., Jha, T., Ghosh, B., 2021. Dissecting Histone Deacetylase 3 in Multiple Disease Conditions: Selective Inhibition as a Promising Therapeutic Strategy. *J. Med. Chem.* 64, 8827–8869. <https://doi.org/10.1021/acs.jmedchem.0c01676>
- Ahmad Ganai, S., Ramadoss, M., Mahadevan, V., 2016. Histone Deacetylase (HDAC) Inhibitors - Emerging Roles in Neuronal Memory, Learning, Synaptic Plasticity and Neural Regeneration. *Curr Neuropharmacol* 14, 55–71. <https://doi.org/10.2174/1570159X13666151021111609>
- Amin, Sk.A., Adhikari, N., Kotagiri, S., Jha, T., Ghosh, B., 2019. Histone deacetylase 3 inhibitors in learning and memory processes with special emphasis on benzamides. *European Journal of Medicinal Chemistry* 166, 369–380. <https://doi.org/10.1016/j.ejmech.2019.01.077>
- André, F., Zielinski, C.C., 2012. Optimal strategies for the treatment of metastatic triple-negative breast cancer with currently approved agents. *Annals of Oncology, Triple-negative breast cancer in focus: From biology to novel therapeutics* 23, vi46–vi51. <https://doi.org/10.1093/annonc/mds195>
- Arrowsmith, C.H., Bountra, C., Fish, P.V., Lee, K., Schapira, M., 2012. Epigenetic protein families: a new frontier for drug discovery. *Nat Rev Drug Discov* 11, 384–400. <https://doi.org/10.1038/nrd3674>

Bibliography

- Asfaha, Y., Schrenk, C., Alves Avelar, L.A., Lange, F., Wang, C., Bandolik, J.J., Hamacher, A., Kassack, M.U., Kurz, T., 2020. Novel alkoxyamide-based histone deacetylase inhibitors reverse cisplatin resistance in chemoresistant cancer cells. *Bioorganic & Medicinal Chemistry* 28, 115108. <https://doi.org/10.1016/j.bmc.2019.115108>
- Balasubramanian, S., Verner, E., Buggy, J.J., 2009. Isoform-specific histone deacetylase inhibitors: The next step? *Cancer Letters, HDAC Inhibitors for the Treatment of Cancer* 280, 211–221. <https://doi.org/10.1016/j.canlet.2009.02.013>
- Banerjee, S., Adhikari, N., Amin, S.A., Jha, T., 2019. Histone deacetylase 8 (HDAC8) and its inhibitors with selectivity to other isoforms: An overview. *European Journal of Medicinal Chemistry* 164, 214–240. <https://doi.org/10.1016/j.ejmech.2018.12.039>
- Bank, R.P.D., n.d. RCSB PDB: Homepage [WWW Document]. URL <https://www.rcsb.org/> (accessed 8.27.20).
- Bannister, A.J., Kouzarides, T., 2011. Regulation of chromatin by histone modifications. *Cell Research* 21, 381–395. <https://doi.org/10.1038/cr.2011.22>
- Barbarotta, L., Hurley, K., 2015. Romidepsin for the Treatment of Peripheral T-Cell Lymphoma. *J Adv Pract Oncol* 6, 22–36.
- Barter, J.D., Foster, T.C., 2018. Aging in the Brain: New Roles of Epigenetics in Cognitive Decline. *Neuroscientist* 24, 516–525. <https://doi.org/10.1177/1073858418780971>
- Berger, S.L., 2002. Histone modifications in transcriptional regulation. *Current Opinion in Genetics & Development* 12, 142–148. [https://doi.org/10.1016/S0959-437X\(02\)00279-4](https://doi.org/10.1016/S0959-437X(02)00279-4)
- Bhaskara, S., Knutson, S.K., Jiang, G., Chandrasekharan, M.B., Wilson, A.J., Zheng, S., Yenamandra, A., Locke, K., Yuan, J., Bonine-Summers, A.R., Wells, C.E., Kaiser, J.F., Washington, M.K., Zhao, Z., Wagner, F.F., Sun, Z.-W., Xia, F., Holson, E.B., Khabele, D., Hiebert, S.W., 2010. Hdac3 Is Essential for the Maintenance of Chromatin Structure and Genome Stability. *Cancer Cell* 18, 436–447. <https://doi.org/10.1016/j.ccr.2010.10.022>

Bibliography

- Bianchini, G., De Angelis, C., Licata, L., Gianni, L., 2022. Treatment landscape of triple-negative breast cancer — expanded options, evolving needs. *Nat Rev Clin Oncol* 19, 91–113. <https://doi.org/10.1038/s41571-021-00565-2>
- Biel, M., Wascholowski, V., Giannis, A., 2005. Epigenetics—An Epicenter of Gene Regulation: Histones and Histone-Modifying Enzymes. *Angewandte Chemie International Edition* 44, 3186–3216. <https://doi.org/10.1002/anie.200461346>
- Biswas, S., Rao, C.M., 2017. Epigenetics in cancer: Fundamentals and Beyond. *Pharmacology & Therapeutics* 173, 118–134. <https://doi.org/10.1016/j.pharmthera.2017.02.011>
- Bolden, J.E., Shi, W., Jankowski, K., Kan, C.-Y., Cluse, L., Martin, B.P., MacKenzie, K.L., Smyth, G.K., Johnstone, R.W., 2013. HDAC inhibitors induce tumor-cell-selective pro-apoptotic transcriptional responses. *Cell Death Dis* 4, e519–e519. <https://doi.org/10.1038/cddis.2013.9>
- Boyault, C., Zhang, Y., Fritah, S., Caron, C., Gilquin, B., Kwon, S.H., Garrido, C., Yao, T.-P., Vouret-Craviari, C., Matthias, P., Khochbin, S., 2007. HDAC6 controls major cell response pathways to cytotoxic accumulation of protein aggregates. *Genes Dev.* 21, 2172–2181. <https://doi.org/10.1101/gad.436407>
- Bradner, J.E., West, N., Grachan, M.L., Greenberg, E.F., Haggarty, S.J., Warnow, T., Mazitschek, R., 2010. Chemical phylogenetics of histone deacetylases. *Nat Chem Biol* 6, 238–243. <https://doi.org/10.1038/nchembio.313>
- Brancolini, C., Gagliano, T., Minisini, M., 2022. HDACs and the epigenetic plasticity of cancer cells: Target the complexity. *Pharmacology & Therapeutics* 238, 108190. <https://doi.org/10.1016/j.pharmthera.2022.108190>
- Brentnall, M., Rodriguez-Menocal, L., De Guevara, R.L., Cepero, E., Boise, L.H., 2013. Caspase-9, caspase-3 and caspase-7 have distinct roles during intrinsic apoptosis. *BMC Cell Biology* 14, 32. <https://doi.org/10.1186/1471-2121-14-32>

Bibliography

- Buckley, M.T., Yoon, J., Yee, H., Chiriboga, L., Liebes, L., Ara, G., Qian, X., Bajorin, D.F., Sun, T.-T., Wu, X.-R., Osman, I., 2007. The histone deacetylase inhibitor belinostat (PXD101) suppresses bladder cancer cell growth in vitro and in vivo. *Journal of Translational Medicine* 5, 49. <https://doi.org/10.1186/1479-5876-5-49>
- Butler, K.V., Kalin, J., Brochier, C., Vistoli, G., Langley, B., Kozikowski, A.P., 2010. Rational Design and Simple Chemistry Yield a Superior, Neuroprotective HDAC6 Inhibitor, Tubastatin A. *J. Am. Chem. Soc.* 132, 10842–10846. <https://doi.org/10.1021/ja102758v>
- Cao, F., Zwinderman, M.R.H., Dekker, F.J., 2018. The Process and Strategy for Developing Selective Histone Deacetylase 3 Inhibitors. *Molecules* 23, 551. <https://doi.org/10.3390/molecules23030551>
- Cao, J., Zhang, M., Wang, B., Zhang, L., Zhou, F., Fang, M., 2021. Chemoresistance and Metastasis in Breast Cancer Molecular Mechanisms and Novel Clinical Strategies. *Front Oncol* 11, 658552. <https://doi.org/10.3389/fonc.2021.658552>
- Carew, J.S., Giles, F.J., Nawrocki, S.T., 2008. Histone deacetylase inhibitors: Mechanisms of cell death and promise in combination cancer therapy. *Cancer Letters* 269, 7–17. <https://doi.org/10.1016/j.canlet.2008.03.037>
- Chen, X., Zhao, S., Li, H., Wang, X., Geng, A., Cui, H., Lu, T., Chen, Y., Zhu, Y., 2019. Design, synthesis and biological evaluation of novel isoindolinone derivatives as potent histone deacetylase inhibitors. *European Journal of Medicinal Chemistry* 168, 110–122. <https://doi.org/10.1016/j.ejmech.2019.02.032>
- Chen, Yufeng, He, R., Chen, Yihua, D'Annibale, M.A., Langley, B., Kozikowski, A.P., 2009. Studies of Benzamide- and Thiol-Based Histone Deacetylase Inhibitors in Models of Oxidative-Stress-Induced Neuronal Death: Identification of Some HDAC3-Selective Inhibitors. *ChemMedChem* 4, 842–852. <https://doi.org/10.1002/cmdc.200800461>

Bibliography

- Chi, F., Liu, J., Brady, S.W., Cosgrove, P.A., Nath, A., McQuerry, J.A., Majumdar, S., Moos, P.J., Chang, J.T., Kahn, M., Bild, A.H., 2021. A 'one-two punch' therapy strategy to target chemoresistance in estrogen receptor positive breast cancer. *Translational Oncology* 14, 100946. <https://doi.org/10.1016/j.tranon.2020.100946>
- Cho, M., Choi, E., Yang, J.S., Lee, C., Seo, J.J., Kim, B.S., Oh, S.J., Kim, H.M., Lee, K., Park, S.-K., Kwon, H.J., Han, G., 2013. Discovery of Pyridone-Based Histone Deacetylase Inhibitors: Approaches for Metabolic Stability. *ChemMedChem* 8, 272–279. <https://doi.org/10.1002/cmdc.201200529>
- Conboy, K., Henshall, D.C., Brennan, G.P., 2021. Epigenetic principles underlying epileptogenesis and epilepsy syndromes. *Neurobiology of Disease* 148, 105179. <https://doi.org/10.1016/j.nbd.2020.105179>
- Connolly, R.M., Rudek, M.A., Piekarz, R., 2017. Entinostat: a promising treatment option for patients with advanced breast cancer. *Future Oncology* 13, 1137–1148. <https://doi.org/10.2217/fon-2016-0526>
- Cui, H., Hong, Q., Wei, R., Li, H., Wan, C., Chen, X., Zhao, S., Bu, H., Zhang, B., Yang, D., Lu, T., Chen, Y., Zhu, Y., 2022. Design and synthesis of HDAC inhibitors to enhance the therapeutic effect of diffuse large B-cell lymphoma by improving metabolic stability and pharmacokinetic characteristics. *European Journal of Medicinal Chemistry* 229, 114049. <https://doi.org/10.1016/j.ejmech.2021.114049>
- Cui, Z., Xie, M., Wu, Z., Shi, Y., 2018. Relationship Between Histone Deacetylase 3 (HDAC3) and Breast Cancer. *Med Sci Monit* 24, 2456–2464. <https://doi.org/10.12659/MSM.906576>
- Cuttini, E., Goi, C., Pellarin, E., Vida, R., Brancolini, C., 2023. HDAC4 in cancer: A multitasking platform to drive not only epigenetic modifications. *Frontiers in Molecular Biosciences* 10.

Bibliography

- Czabotar, P.E., Lessene, G., Strasser, A., Adams, J.M., 2014. Control of apoptosis by the BCL-2 protein family: implications for physiology and therapy. *Nat Rev Mol Cell Biol* 15, 49–63. <https://doi.org/10.1038/nrm3722>
- Das, C., Kundu, T., 2005. Transcriptional Regulation by the Acetylation of Nonhistone Proteins in Humans - A New Target for Therapeutics. *IUBMB Life* 57, 137–149. <https://doi.org/10.1080/15216540500090629>
- Dasgupta, T., Antony, J., Braithwaite, A.W., Horsfield, J.A., 2016. HDAC8 Inhibition Blocks SMC3 Deacetylation and Delays Cell Cycle Progression without Affecting Cohesin-dependent Transcription in MCF7 Cancer Cells. *J Biol Chem* 291, 12761–12770. <https://doi.org/10.1074/jbc.M115.704627>
- De Simone, A., Milelli, A., 2019. Histone Deacetylase Inhibitors as Multitarget Ligands: New Players in Alzheimer's Disease Drug Discovery? *ChemMedChem* 14, 1067–1073. <https://doi.org/10.1002/cmdc.201900174>
- Dokmanovic, M., Clarke, C., Marks, P.A., 2007. Histone Deacetylase Inhibitors: Overview and Perspectives. *Mol Cancer Res* 5, 981–989. <https://doi.org/10.1158/1541-7786.MCR-07-0324>
- Duan, H., Wang, C., Zhou, K., Wang, T., Li, Y., Qiu, D., Li, Q., Zhang, Y., Hua, Y., 2017. The effect of histone deacetylase inhibition on the expression of P-glycoprotein in human placental trophoblast cell lines. *Placenta* 49, 37–47. <https://doi.org/10.1016/j.placenta.2016.11.011>
- Dupont, C., Armant, D.R., Brenner, C.A., 2009. Epigenetics: Definition, Mechanisms and Clinical Perspective. *Semin Reprod Med* 27, 351–357. <https://doi.org/10.1055/s-0029-1237423>
- Fatma, H., Maurya, S.K., Siddique, H.R., 2022. Epigenetic modifications of c-MYC: Role in cancer cell reprogramming, progression and chemoresistance. *Seminars in Cancer*

Bibliography

- Biology, Epigenetic Regulation of Cancer Progression: Promises and Progress 83, 166–176. <https://doi.org/10.1016/j.semcancer.2020.11.008>
- Finnin, M.S., Donigian, J.R., Cohen, A., Richon, V.M., Rifkind, R.A., Marks, P.A., Breslow, R., Pavletich, N.P., 1999. Structures of a histone deacetylase homologue bound to the TSA and SAHA inhibitors. *Nature* 401, 188–193. <https://doi.org/10.1038/43710>
- Fraga, M.F., Ballestar, E., Villar-Garea, A., Boix-Chornet, M., Espada, J., Schotta, G., Bonaldi, T., Haydon, C., Ropero, S., Petrie, K., Iyer, N.G., Pérez-Rosado, A., Calvo, E., Lopez, J.A., Cano, A., Calasanz, M.J., Colomer, D., Piris, M.Á., Ahn, N., Imhof, A., Caldas, C., Jenuwein, T., Esteller, M., 2005. Loss of acetylation at Lys16 and trimethylation at Lys20 of histone H4 is a common hallmark of human cancer. *Nat Genet* 37, 391–400. <https://doi.org/10.1038/ng1531>
- Frühauf, A., Meyer-Almes, F.-J., 2021. Non-Hydroxamate Zinc-Binding Groups as Warheads for Histone Deacetylases. *Molecules* 26, 5151. <https://doi.org/10.3390/molecules26175151>
- Gallinari, P., Marco, S.D., Jones, P., Pallaoro, M., Steinkühler, C., 2007. HDACs, histone deacetylation and gene transcription: from molecular biology to cancer therapeutics. *Cell Res* 17, 195–211. <https://doi.org/10.1038/sj.cr.7310149>
- Gantt, S.L., Gattis, S.G., Fierke, C.A., 2006. Catalytic activity and inhibition of human histone deacetylase 8 is dependent on the identity of the active site metal ion. *Biochemistry* 45, 6170–6178. <https://doi.org/10.1021/bi060212u>
- Gao, L., Cueto, M.A., Asselbergs, F., Atadja, P., 2002. Cloning and functional characterization of HDAC11, a novel member of the human histone deacetylase family. *J. Biol. Chem.* 277, 25748–25755. <https://doi.org/10.1074/jbc.M111871200>
- Glozak, M.A., Sengupta, N., Zhang, X., Seto, E., 2005. Acetylation and deacetylation of non-histone proteins. *Gene* 363, 15–23. <https://doi.org/10.1016/j.gene.2005.09.010>

Bibliography

- Goldberg, A.D., Allis, C.D., Bernstein, E., 2007. Epigenetics: A Landscape Takes Shape. *Cell* 128, 635–638. <https://doi.org/10.1016/j.cell.2007.02.006>
- Gräff, J., Tsai, L.-H., 2013. Histone acetylation: molecular mnemonics on the chromatin. *Nature Reviews Neuroscience* 14, 97–111. <https://doi.org/10.1038/nrn3427>
- Gray, S.G., Ekström, T.J., 2001. The human histone deacetylase family. *Exp. Cell Res.* 262, 75–83. <https://doi.org/10.1006/excr.2000.5080>
- Grozinger, C.M., Hassig, C.A., Schreiber, S.L., 1999. Three proteins define a class of human histone deacetylases related to yeast Hda1p. *Proc. Natl. Acad. Sci. U.S.A.* 96, 4868–4873. <https://doi.org/10.1073/pnas.96.9.4868>
- Grunstein, M., 1997. Histone acetylation in chromatin structure and transcription. *Nature* 389, 349–352. <https://doi.org/10.1038/38664>
- Gryder, B.E., Pomella, S., Sayers, C., Wu, X.S., Song, Y., Chiarella, A.M., Bagchi, S., Chou, H.-C., Sinniah, R.S., Walton, A., Wen, X., Rota, R., Hathaway, N.A., Zhao, K., Chen, J., Vakoc, C.R., Shern, J.F., Stanton, B.Z., Khan, J., 2019a. Histone hyperacetylation disrupts core gene regulatory architecture in rhabdomyosarcoma. *Nat Genet* 51, 1714–1722. <https://doi.org/10.1038/s41588-019-0534-4>
- Gryder, B.E., Wu, L., Woldemichael, G.M., Pomella, S., Quinn, T.R., Park, P.M.C., Cleveland, A., Stanton, B.Z., Song, Y., Rota, R., Wiest, O., Yohe, M.E., Shern, J.F., Qi, J., Khan, J., 2019b. Chemical genomics reveals histone deacetylases are required for core regulatory transcription. *Nat Commun* 10, 3004. <https://doi.org/10.1038/s41467-019-11046-7>
- Guenther, M.G., Barak, O., Lazar, M.A., 2001. The SMRT and N-CoR Corepressors Are Activating Cofactors for Histone Deacetylase 3. *Molecular and Cellular Biology* 21, 6091–6101. <https://doi.org/10.1128/MCB.21.18.6091-6101.2001>

Bibliography

- Haberland, M., Montgomery, R.L., Olson, E.N., 2009. The many roles of histone deacetylases in development and physiology: implications for disease and therapy. *Nat Rev Genet* 10, 32–42. <https://doi.org/10.1038/nrg2485>
- Hai, R., He, L., Shu, G., Yin, G., 2021. Characterization of Histone Deacetylase Mechanisms in Cancer Development. *Frontiers in Oncology* 11.
- Hai, R., Yang, D., Zheng, F., Wang, W., Han, X., Bode, A.M., Luo, X., 2022. The emerging roles of HDACs and their therapeutic implications in cancer. *European Journal of Pharmacology* 931, 175216. <https://doi.org/10.1016/j.ejphar.2022.175216>
- Hamoud, M.M.S., Pulya, S., Osman, N.A., Bobde, Y., Hassan, A.E.A., Abdel-Fattah, H.A., Ghosh, B., Ghanim, A.M., 2020. Design, synthesis, and biological evaluation of novel nicotinamide derivatives as potential histone deacetylase-3 inhibitors. *New J. Chem.* 44, 9671–9683. <https://doi.org/10.1039/D0NJ01274B>
- Han, J., Lim, W., You, D., Jeong, Y., Kim, S., Lee, J.E., Shin, T.H., Lee, G., Park, S., 2019. Chemoresistance in the Human Triple-Negative Breast Cancer Cell Line MDA-MB-231 Induced by Doxorubicin Gradient Is Associated with Epigenetic Alterations in Histone Deacetylase. *Journal of Oncology* 2019. <https://doi.org/10.1155/2019/1345026>
- Hanigan, T.W., Aboukhatwa, S.M., Taha, T.Y., Frasor, J., Petukhov, P.A., 2017. Divergent JNK Phosphorylation of HDAC3 in Triple-Negative Breast Cancer Cells Determines HDAC Inhibitor Binding and Selectivity. *Cell Chemical Biology* 24, 1356-1367.e8. <https://doi.org/10.1016/j.chembiol.2017.08.015>
- Harbeck, N., Penault-Llorca, F., Cortes, J., Gnant, M., Houssami, N., Poortmans, P., Ruddy, K., Tsang, J., Cardoso, F., 2019. Breast cancer. *Nat Rev Dis Primers* 5, 1–31. <https://doi.org/10.1038/s41572-019-0111-2>
- He, J., Wang, S., Liu, X., Lin, R., Deng, F., Jia, Z., Zhang, C., Li, Z., Zhu, H., Tang, L., Yang, P., He, D., Jia, Q., Zhang, Y., 2020. Synthesis and Biological Evaluation of HDAC Inhibitors

Bibliography

- With a Novel Zinc Binding Group. *Frontiers in Chemistry* 8, 256.
<https://doi.org/10.3389/fchem.2020.00256>
- He, X., Hui, Z., Xu, L., Bai, R., Gao, Y., Wang, Z., Xie, T., Ye, X.-Y., 2022. Medicinal chemistry updates of novel HDACs inhibitors (2020 to present). *European Journal of Medicinal Chemistry* 227, 113946. <https://doi.org/10.1016/j.ejmech.2021.113946>
- Hess-Stumpp, H., Bracker, T.U., Henderson, D., Politz, O., 2007. MS-275, a potent orally available inhibitor of histone deacetylases—The development of an anticancer agent. *The International Journal of Biochemistry & Cell Biology, Molecular Pathways in Cancer: From Innovative Technologies to Novel Therapies* 39, 1388–1405.
<https://doi.org/10.1016/j.biocel.2007.02.009>
- Ho, T.C.S., Chan, A.H.Y., Ganesan, A., 2020. Thirty Years of HDAC Inhibitors: 2020 Insight and Hindsight. *J. Med. Chem.* 63, 12460–12484.
<https://doi.org/10.1021/acs.jmedchem.0c00830>
- Hsieh, H.-Y., Chuang, H.-C., Shen, F.-H., Detroja, K., Hsin, L.-W., Chen, C.-S., 2017. Targeting breast cancer stem cells by novel HDAC3-selective inhibitors. *European Journal of Medicinal Chemistry* 140, 42–51. <https://doi.org/10.1016/j.ejmech.2017.08.069>
- Hu, E., Chen, Z., Fredrickson, T., Zhu, Y., Kirkpatrick, R., Zhang, G.F., Johanson, K., Sung, C.M., Liu, R., Winkler, J., 2000. Cloning and characterization of a novel human class I histone deacetylase that functions as a transcription repressor. *J. Biol. Chem.* 275, 15254–15264.
<https://doi.org/10.1074/jbc.M908988199>
- Hubeek, I., Comijn, E.M., Van der Wilt, C.L., Merriman, R.L., Padron, J.M., Kaspers, G.J.L., Peters, G.J., 2008. CI-994 (N-acetyl-dinaline) in combination with conventional anti-cancer agents is effective against acute myeloid leukemia in vitro and in vivo. *Oncology Reports* 19, 1517–1523. <https://doi.org/10.3892/or.19.6.1517>

Bibliography

- Inwald, E.C., Klinkhammer-Schalke, M., Hofstädter, F., Zeman, F., Koller, M., Gerstenhauer, M., Ortman, O., 2013. Ki-67 is a prognostic parameter in breast cancer patients: results of a large population-based cohort of a cancer registry. *Breast Cancer Res Treat* 139, 539–552. <https://doi.org/10.1007/s10549-013-2560-8>
- Ito, A.M., Paul, M., Ghosh, B., Biswas, S., 2022. Oxaliplatin delivery via chitosan/vitamin E conjugate micelles for improved efficacy and MDR-reversal in breast cancer. *Carbohydrate Polymers* 282, 119108. <https://doi.org/10.1016/j.carbpol.2022.119108>
- Jablonka, E., Lamb, M.J., 2002. The Changing Concept of Epigenetics. *Annals of the New York Academy of Sciences* 981, 82–96. <https://doi.org/10.1111/j.1749-6632.2002.tb04913.x>
- Jenuwein, T., Allis, C.D., 2001. Translating the histone code. *Science* 293, 1074–1080. <https://doi.org/10.1126/science.1063127>
- Ji, X., Lu, Y., Tian, H., Meng, X., Wei, M., Cho, W.C., 2019. Chemoresistance mechanisms of breast cancer and their countermeasures. *Biomedicine & Pharmacotherapy* 114, 108800. <https://doi.org/10.1016/j.biopha.2019.108800>
- Jiang, Y., Xu, J., Yue, K., Huang, C., Qin, M., Chi, D., Yu, Q., Zhu, Y., Hou, X., Xu, T., Li, M., Chou, C.J., Li, X., 2022. Potent Hydrazide-Based HDAC Inhibitors with a Superior Pharmacokinetic Profile for Efficient Treatment of Acute Myeloid Leukemia In Vivo. *J. Med. Chem.* 65, 285–302. <https://doi.org/10.1021/acs.jmedchem.1c01472>
- Jin, X., Fang, Y., Hu, Y., Chen, J., Liu, W., Chen, G., Gong, M., Wu, P., Zhu, T., Wang, S., Zhou, J., Wang, H., Ma, D., Li, K., 2017. Synergistic activity of the histone deacetylase inhibitor trichostatin A and the proteasome inhibitor PS-341 against taxane-resistant ovarian cancer cell lines. *Oncol Lett* 13, 4619–4626. <https://doi.org/10.3892/ol.2017.6032>
- Jin, X., Mu, P., 2015. Targeting Breast Cancer Metastasis. *Breast Cancer (Auckl)* 9, 23–34. <https://doi.org/10.4137/BCBCR.S25460>

Bibliography

- Johnstone, R.W., 2002. Histone-deacetylase inhibitors: novel drugs for the treatment of cancer. *Nature Reviews Drug Discovery* 1, 287–299. <https://doi.org/10.1038/nrd772>
- Juhás, M., Zitko, J., 2020. Molecular Interactions of Pyrazine-Based Compounds to Proteins. *J. Med. Chem.* 63, 8901–8916. <https://doi.org/10.1021/acs.jmedchem.9b02021>
- Kang, S.P., Ramirez, J., House, L., Zhang, W., Mirkov, S., Liu, W., Haverfield, E., Ratain, M.J., 2010. A pharmacogenetic study of vorinostat glucuronidation. *Pharmacogenet Genomics* 20, 638–641. <https://doi.org/10.1097/FPC.0b013e32833e1b37>
- Kao, H.Y., Downes, M., Ordentlich, P., Evans, R.M., 2000. Isolation of a novel histone deacetylase reveals that class I and class II deacetylases promote SMRT-mediated repression. *Genes Dev.* 14, 55–66.
- Kao, H.-Y., Lee, C.-H., Komarov, A., Han, C.C., Evans, R.M., 2002. Isolation and characterization of mammalian HDAC10, a novel histone deacetylase. *J. Biol. Chem.* 277, 187–193. <https://doi.org/10.1074/jbc.M108931200>
- Karagianni, P., Wong, J., 2007. HDAC3: taking the SMRT-N-CoRrect road to repression. *Oncogene* 26, 5439–5449. <https://doi.org/10.1038/sj.onc.1210612>
- Karagiannis, D., Rampias, T., 2021. HDAC Inhibitors: Dissecting Mechanisms of Action to Counter Tumor Heterogeneity. *Cancers (Basel)* 13, 3575. <https://doi.org/10.3390/cancers13143575>
- Karthik, S., Sankar, R., Varunkumar, K., Ravikumar, V., 2014. Romidepsin induces cell cycle arrest, apoptosis, histone hyperacetylation and reduces matrix metalloproteinases 2 and 9 expression in bortezomib sensitized non-small cell lung cancer cells. *Biomedicine & Pharmacotherapy* 68, 327–334. <https://doi.org/10.1016/j.biopha.2014.01.002>
- Kashyap, K., Kakkar, R., 2020. Exploring structural requirements of isoform selective histone deacetylase inhibitors: a comparative in silico study. *Journal of Biomolecular Structure and Dynamics* 0, 1–16. <https://doi.org/10.1080/07391102.2019.1711191>

Bibliography

- Khan, O., Thangue, N.B.L., 2012. HDAC inhibitors in cancer biology: emerging mechanisms and clinical applications. *Immunology & Cell Biology* 90, 85–94. <https://doi.org/10.1038/icb.2011.100>
- Kim, H.-J., Bae, S.-C., 2011. Histone deacetylase inhibitors: molecular mechanisms of action and clinical trials as anti-cancer drugs. *Am J Transl Res* 3, 166–179.
- Kim, J.Y., Cho, H., Yoo, J., Kim, G.W., Jeon, Y.H., Lee, S.W., Kwon, S.H., 2022. Pathological Role of HDAC8: Cancer and Beyond. *Cells* 11, 3161. <https://doi.org/10.3390/cells11193161>
- Konsoula, Z., Cao, H., Velená, A., Jung, M., 2009. Pharmacokinetics-pharmacodynamics and antitumor activity of mercaptoacetamide-based histone deacetylase inhibitors. *Mol Cancer Ther* 8, 2844–2851. <https://doi.org/10.1158/1535-7163.MCT-09-0629>
- Kornberg, R.D., 1974. Chromatin Structure: A Repeating Unit of Histones and DNA. *Science* 184, 868–871. <https://doi.org/10.1126/science.184.4139.868>
- Kummar, S., Gutierrez, M., Gardner, E.R., Donovan, E., Hwang, K., Chung, E.J., Lee, M.-J., Maynard, K., Kalnitskiy, M., Chen, A., Melillo, G., Ryan, Q.C., Conley, B., Figg, W.D., Trepel, J.B., Zwiebel, J., Doroshow, J.H., Murgo, A.J., 2007. Phase I Trial of MS-275, a Histone Deacetylase Inhibitor, Administered Weekly in Refractory Solid Tumors and Lymphoid Malignancies. *Clin Cancer Res* 13, 5411–5417. <https://doi.org/10.1158/1078-0432.CCR-07-0791>
- Kwak, S.-M., Seo, J., Hwang, J.-T., Sung, G.-J., Song, J.-H., Jeong, J.-H., Lee, S.-H., Yoon, H.-G., Choi, H.-K., Choi, K.-C., 2019. EGFR–c-Src-Mediated HDAC3 Phosphorylation Exacerbates Invasion of Breast Cancer Cells. *Cells* 8, 930. <https://doi.org/10.3390/cells8080930>

Bibliography

- Lawrence, M., Daujat, S., Schneider, R., 2016. Lateral Thinking: How Histone Modifications Regulate Gene Expression. *Trends in Genetics* 32, 42–56. <https://doi.org/10.1016/j.tig.2015.10.007>
- Lee, H.S., Park, S.B., Kim, S.A., Kwon, S.K., Cha, H., Lee, D.Y., Ro, S., Cho, J.M., Song, S.Y., 2017. A novel HDAC inhibitor, CG200745, inhibits pancreatic cancer cell growth and overcomes gemcitabine resistance. *Sci Rep* 7, 41615. <https://doi.org/10.1038/srep41615>
- Lee, H.-Z., Kwitkowski, V.E., Del Valle, P.L., Ricci, M.S., Saber, H., Habtemariam, B.A., Bullock, J., Bloomquist, E., Li Shen, Y., Chen, X.-H., Brown, J., Mehrotra, N., Dorff, S., Charlab, R., Kane, R.C., Kaminskas, E., Justice, R., Farrell, A.T., Pazdur, R., 2015. FDA Approval: Belinostat for the Treatment of Patients with Relapsed or Refractory Peripheral T-cell Lymphoma. *Clin. Cancer Res.* 21, 2666–2670. <https://doi.org/10.1158/1078-0432.CCR-14-3119>
- Lehrmann, H., Pritchard, L.L., Harel-Bellan, A., 2002. Histone acetyltransferases and deacetylases in the control of cell proliferation and differentiation, in: *Advances in Cancer Research*. Academic Press, pp. 41–65. [https://doi.org/10.1016/S0065-230X\(02\)86002-X](https://doi.org/10.1016/S0065-230X(02)86002-X)
- Leoni, F., Zaliani, A., Bertolini, G., Porro, G., Pagani, P., Pozzi, P., Donà, G., Fossati, G., Sozzani, S., Azam, T., Bufler, P., Fantuzzi, G., Goncharov, I., Kim, S.-H., Pomerantz, B.J., Reznikov, L.L., Siegmund, B., Dinarello, C.A., Mascagni, P., 2002. The antitumor histone deacetylase inhibitor suberoylanilide hydroxamic acid exhibits antiinflammatory properties via suppression of cytokines. *Proceedings of the National Academy of Sciences* 99, 2995–3000. <https://doi.org/10.1073/pnas.052702999>
- Li, D., Marchenko, N.D., Moll, U.M., 2011. SAHA shows preferential cytotoxicity in mutant p53 cancer cells by destabilizing mutant p53 through inhibition of the HDAC6-Hsp90 chaperone axis. *Cell Death & Differentiation* 18, 1904–1913. <https://doi.org/10.1038/cdd.2011.71>

Bibliography

- Li, X., Jiang, Y., Peterson, Y.K., Xu, T., Himes, R.A., Luo, X., Yin, G., Inks, E.S., Dolloff, N., Halene, S., Chan, S.S.L., Chou, C.J., 2020. Design of Hydrazone-Bearing HDACIs Based on Panobinostat and Their p53 and FLT3-ITD Dependency in Antileukemia Activity. *Journal of Medicinal Chemistry*. <https://doi.org/10.1021/acs.jmedchem.0c00442>
- Li, X., Peterson, Y.K., Inks, E.S., Himes, R.A., Li, J., Zhang, Y., Kong, X., Chou, C.J., 2018. Class I HDAC Inhibitors Display Different Antitumor Mechanism in Leukemia and Prostatic Cancer Cells Depending on Their p53 Status. *J. Med. Chem.* 61, 2589–2603. <https://doi.org/10.1021/acs.jmedchem.8b00136>
- Li, Y., Seto, E., 2016. HDACs and HDAC Inhibitors in Cancer Development and Therapy. *Cold Spring Harb Perspect Med* 6. <https://doi.org/10.1101/cshperspect.a026831>
- Liao, B., Sun, Q., Yuan, Y., Yin, Y., Qiao, J., Jiang, P., 2020. Histone deacetylase inhibitor MGCD0103 causes cell cycle arrest, apoptosis, and autophagy in liver cancer cells. *J Cancer* 11, 1915–1926. <https://doi.org/10.7150/jca.34091>
- Liu, J., Wang, T., Wang, X., Luo, L., Guo, J., Peng, Y., Xu, Q., Miao, J., Zhang, Y., Ling, Y., 2017. Development of novel β -carboline-based hydroxamate derivatives as HDAC inhibitors with DNA damage and apoptosis inducing abilities. *Med. Chem. Commun.* 8, 1213–1219. <https://doi.org/10.1039/C6MD00681G>
- Liu, S.-S., Wu, F., Jin, Y.-M., Chang, W.-Q., Xu, T.-M., 2020. HDAC11: a rising star in epigenetics. *Biomed Pharmacother* 131, 110607. <https://doi.org/10.1016/j.biopha.2020.110607>
- Lo, H.-W., Hsu, S.-C., Hung, M.-C., 2006. EGFR signaling pathway in breast cancers: from traditional signal transduction to direct nuclear translocation. *Breast Cancer Res Treat* 95, 211–218. <https://doi.org/10.1007/s10549-005-9011-0>

Bibliography

- LoRusso, P.M., Demchik, L., Foster, B., Knight, J., Bissery, M.-C., Polin, L.M., Leopold, W.R., Corbett, T.H., 1996. Preclinical antitumor activity of CI-994. *Invest New Drugs* 14, 349–356. <https://doi.org/10.1007/BF00180810>
- Lu, X., Ning, Z., Li, Z., Cao, H., Wang, X., 2016. Development of chidamide for peripheral T-cell lymphoma, the first orphan drug approved in China. *Intractable Rare Dis Res* 5, 185–191. <https://doi.org/10.5582/irdr.2016.01024>
- Luger, K., Mäder, A.W., Richmond, R.K., Sargent, D.F., Richmond, T.J., 1997. Crystal structure of the nucleosome core particle at 2.8 Å resolution. *Nature* 389, 251–260. <https://doi.org/10.1038/38444>
- Luo, H., Zhou, Z., Huang, S., Ma, M., Zhao, M., Tang, L., Quan, Y., Zeng, Y., Su, L., Kim, J., Zhang, P., 2021. CHFR regulates chemoresistance in triple-negative breast cancer through destabilizing ZEB1. *Cell Death Dis* 12, 1–11. <https://doi.org/10.1038/s41419-021-04114-8>
- Luo, X., Cai, G., Guo, Y., Gao, C., Huang, W., Zhang, Z., Lu, H., Liu, K., Chen, J., Xiong, X., Lei, J., Zhou, X., Wang, J., Liu, Y., 2021. Exploring Marine-Derived Ascochlorins as Novel Human Dihydroorotate Dehydrogenase Inhibitors for Treatment of Triple-Negative Breast Cancer. *J. Med. Chem.* 64, 13918–13932. <https://doi.org/10.1021/acs.jmedchem.1c01402>
- M, H., S, M., G, C., G, F., M, Adib, F, M., M, Amanlou, 2022. Epigenetic-based cancer therapeutics: new potential HDAC8 inhibitors. *Journal of biomolecular structure & dynamics* 40. <https://doi.org/10.1080/07391102.2020.1813203>
- Ma, Y., Yue, Y., Pan, M., Sun, J., Chu, J., Lin, X., Xu, W., Feng, L., Chen, Y., Chen, D., Shin, V.Y., Wang, X., Jin, H., 2015. Histone deacetylase 3 inhibits new tumor suppressor gene DTWD1 in gastric cancer. *Am J Cancer Res* 5, 663–673.

Bibliography

- Maccallini, C., Ammazalorso, A., De Filippis, B., Fantacuzzi, M., Giampietro, L., Amoroso, R., 2022. HDAC Inhibitors for the Therapy of Triple Negative Breast Cancer. *Pharmaceuticals* 15, 667. <https://doi.org/10.3390/ph15060667>
- Mahmud, I., Liao, D., 2015. Microarray gene expression profiling reveals potential mechanisms of tumor suppression by the class I HDAC-selective benzoylhydrazide inhibitors. *Genom Data* 5, 257–259. <https://doi.org/10.1016/j.gdata.2015.06.019>
- Mai, A., Massa, S., Rotili, D., Cerbara, I., Valente, S., Pezzi, R., Simeoni, S., Ragno, R., 2005. Histone deacetylation in epigenetics: An attractive target for anticancer therapy. *Medicinal Research Reviews* 25, 261–309. <https://doi.org/10.1002/med.20024>
- Manal, M., Chandrasekar, M.J.N., Gomathi Priya, J., Nanjan, M.J., 2016. Inhibitors of histone deacetylase as antitumor agents: A critical review. *Bioorganic Chemistry* 67, 18–42. <https://doi.org/10.1016/j.bioorg.2016.05.005>
- Mann, B.S., Johnson, J.R., Cohen, M.H., Justice, R., Pazdur, R., 2007. FDA approval summary: vorinostat for treatment of advanced primary cutaneous T-cell lymphoma. *Oncologist* 12, 1247–1252. <https://doi.org/10.1634/theoncologist.12-10-1247>
- Marek, L., Hamacher, A., Hansen, F.K., Kuna, K., Gohlke, H., Kassack, M.U., Kurz, T., 2013. Histone Deacetylase (HDAC) Inhibitors with a Novel Connecting Unit Linker Region Reveal a Selectivity Profile for HDAC4 and HDAC5 with Improved Activity against Chemoresistant Cancer Cells. *J. Med. Chem.* 56, 427–436. <https://doi.org/10.1021/jm301254q>
- Marks, P.A., Jiang, X., 2005. Histone Deacetylase Inhibitors in Programmed Cell Death and Cancer Therapy. *Cell Cycle* 4, 549–551. <https://doi.org/10.4161/cc.4.4.1564>
- Marks, P.A., Richon, V.M., Rifkind, R.A., 2000. Histone Deacetylase Inhibitors: Inducers of Differentiation or Apoptosis of Transformed Cells. *J Natl Cancer Inst* 92, 1210–1216. <https://doi.org/10.1093/jnci/92.15.1210>

Bibliography

- McClure, J.J., Inks, E.S., Zhang, C., Peterson, Y.K., Li, J., Chundru, K., Lee, B., Buchanan, A., Miao, S., Chou, C.J., 2017. Comparison of the Deacylase and Deacetylase Activity of Zinc-Dependent HDACs. *ACS Chem. Biol.* 12, 1644–1655. <https://doi.org/10.1021/acscchembio.7b00321>
- McClure, J.J., Zhang, C., Inks, E.S., Peterson, Y.K., Li, J., Chou, C.J., 2016. Development of Allosteric Hydrazide-Containing Class I Histone Deacetylase Inhibitors for Use in Acute Myeloid Leukemia. *J. Med. Chem.* 59, 9942–9959. <https://doi.org/10.1021/acs.jmedchem.6b01385>
- McLeod, A.B., Stice, J.P., Wardell, S.E., Alley, H.M., Chang, C., McDonnell, D.P., 2018. Validation of histone deacetylase 3 as a therapeutic target in castration-resistant prostate cancer. *The Prostate* 78, 266–277. <https://doi.org/10.1002/pros.23467>
- Melesina, J., Simoben, C.V., Praetorius, L., Bülbül, E.F., Robaa, D., Sippl, W., 2021. Strategies To Design Selective Histone Deacetylase Inhibitors. *ChemMedChem* 16, 1336–1359. <https://doi.org/10.1002/cmdc.202000934>
- Minami, J., Suzuki, R., Mazitschek, R., Gorgun, G., Ghosh, B., Cirstea, D., Hu, Y., Mimura, N., Ohguchi, H., Cottini, F., Jakubikova, J., Munshi, N.C., Haggarty, S.J., Richardson, P.G., Hideshima, T., Anderson, K.C., 2014. Histone deacetylase 3 as a novel therapeutic target in multiple myeloma. *Leukemia* 28, 680–689. <https://doi.org/10.1038/leu.2013.231>
- Mulder, G.J., Meerman, J.H., 1983. Sulfation and glucuronidation as competing pathways in the metabolism of hydroxamic acids: the role of N,O-sulfonation in chemical carcinogenesis of aromatic amines. *Environ Health Perspect* 49, 27–32.
- Negi, L.M., Talegaonkar, S., Jaggi, M., Ahmad, F.J., Iqbal, Z., Khar, R.K., 2012. Role of CD44 in tumor progression and strategies for targeting. *Journal of Drug Targeting* 20, 561–573. <https://doi.org/10.3109/1061186X.2012.702767>

Bibliography

- Nepali, K., Chang, T.-Y., Lai, M.-J., Hsu, K.-C., Yen, Y., Lin, T.E., Lee, S.-B., Liou, J.-P., 2020. Purine/purine isoster based scaffolds as new derivatives of benzamide class of HDAC inhibitors. *European Journal of Medicinal Chemistry* 196, 112291. <https://doi.org/10.1016/j.ejmech.2020.112291>
- Newbold, A., Falkenberg, K.J., Prince, H.M., Johnstone, R.W., 2016. How do tumor cells respond to HDAC inhibition? *The FEBS Journal* 283, 4032–4046. <https://doi.org/10.1111/febs.13746>
- Ng, H.-H., Adrian, B., 1999. DNA methylation and chromatin modification. *Current Opinion in Genetics & Development* 9, 158–163. [https://doi.org/10.1016/S0959-437X\(99\)80024-0](https://doi.org/10.1016/S0959-437X(99)80024-0)
- Ning, Z.-Q., Li, Z.-B., Newman, M.J., Shan, S., Wang, X.-H., Pan, D.-S., Zhang, J., Dong, M., Du, X., Lu, X.-P., 2012. Chidamide (CS055/HBI-8000): a new histone deacetylase inhibitor of the benzamide class with antitumor activity and the ability to enhance immune cell-mediated tumor cell cytotoxicity. *Cancer Chemother Pharmacol* 69, 901–909. <https://doi.org/10.1007/s00280-011-1766-x>
- Novotny-Diermayr, V., Hart, S., Goh, K.C., Cheong, A., Ong, L.-C., Hentze, H., Pasha, M.K., Jayaraman, R., Ethirajulu, K., Wood, J.M., 2012. The oral HDAC inhibitor pracinostat (SB939) is efficacious and synergistic with the JAK2 inhibitor pacritinib (SB1518) in preclinical models of AML. *Blood Cancer Journal* 2, e69–e69. <https://doi.org/10.1038/bcj.2012.14>
- Núñez-Álvarez, Y., Suelves, M., 2022. HDAC11: a multifaceted histone deacetylase with proficient fatty deacylase activity and its roles in physiological processes. *The FEBS Journal* 289, 2771–2792. <https://doi.org/10.1111/febs.15895>
- Oie, S., Matsuzaki, K., Yokoyama, W., Murayama, A., Yanagisawa, J., 2013. HDAC3 regulates stability of estrogen receptor α mRNA. *Biochemical and Biophysical Research Communications* 432, 236–241. <https://doi.org/10.1016/j.bbrc.2013.02.007>

Bibliography

- O'Reilly, E.A., Gubbins, L., Sharma, S., Tully, R., Guang, M.H.Z., Weiner-Gorzal, K., McCaffrey, J., Harrison, M., Furlong, F., Kell, M., McCann, A., 2015. The fate of chemoresistance in triple negative breast cancer (TNBC). *BBA Clinical* 3, 257–275. <https://doi.org/10.1016/j.bbacli.2015.03.003>
- Park, M., Kim, D., Ko, S., Kim, A., Mo, K., Yoon, H., 2022. Breast Cancer Metastasis: Mechanisms and Therapeutic Implications. *Int J Mol Sci* 23, 6806. <https://doi.org/10.3390/ijms23126806>
- Park, S.-H., Kim, H., Kwak, S., Jeong, J.-H., Lee, J., Hwang, J.-T., Choi, H.-K., Choi, K.-C., 2020. HDAC3–ER α Selectively Regulates TNF- α -Induced Apoptotic Cell Death in MCF-7 Human Breast Cancer Cells via the p53 Signaling Pathway. *Cells* 9, 1280. <https://doi.org/10.3390/cells9051280>
- Park, S.-Y., Kim, J.-S., 2020. A short guide to histone deacetylases including recent progress on class II enzymes. *Experimental & Molecular Medicine* 52, 204–212. <https://doi.org/10.1038/s12276-020-0382-4>
- Parra, M., 2015. Class IIa HDACs – new insights into their functions in physiology and pathology. *The FEBS Journal* 282, 1736–1744. <https://doi.org/10.1111/febs.13061>
- Patel, V.K., Shirbhate, E., Tiwari, P., Kore, R., Veerasamy, R., Mishra, A., Rajak, H., 2023. Multi-targeted HDAC Inhibitors as Anticancer Agents: Current Status and Future Prospective [WWW Document]. <https://doi.org/10.2174/0929867329666220922105615>
- Portela, A., Esteller, M., 2010. Epigenetic modifications and human disease. *Nat Biotechnol* 28, 1057–1068. <https://doi.org/10.1038/nbt.1685>
- Prince, H.M., Bishton, M.J., Johnstone, R.W., 2009. Panobinostat (LBH589): a potent pan-deacetylase inhibitor with promising activity against hematologic and solid tumors. *Future Oncology* 5, 601–612. <https://doi.org/10.2217/fon.09.36>

Bibliography

- Pulya, S., Amin, Sk.A., Adhikari, N., Biswas, S., Jha, T., Ghosh, B., 2020. HDAC6 as privileged target in drug discovery: A perspective. *Pharmacological Research* 105274. <https://doi.org/10.1016/j.phrs.2020.105274>
- Pulya, S., Mahale, A., Bobde, Y., Routholla, G., Patel, T., Swati, Biswas, S., Sharma, V., Kulkarni, O.P., Ghosh, B., 2021. PT3: A Novel Benzamide Class Histone Deacetylase 3 Inhibitor Improves Learning and Memory in Novel Object Recognition Mouse Model. *ACS Chem. Neurosci.* <https://doi.org/10.1021/acchemneuro.0c00721>
- Pulya, S., Patel, T., Paul, M., Adhikari, N., Banerjee, S., Routholla, G., Biswas, S., Jha, T., Ghosh, B., 2022. Selective inhibition of histone deacetylase 3 by novel hydrazide based small molecules as therapeutic intervention for the treatment of cancer. *European Journal of Medicinal Chemistry* 238, 114470. <https://doi.org/10.1016/j.ejmech.2022.114470>
- Quina, A.S., Buschbeck, M., Di Croce, L., 2006. Chromatin structure and epigenetics. *Biochemical Pharmacology, Special Issue: Cell Signalling, Transcription and Translation as Therapeutic Targets* 72, 1563–1569. <https://doi.org/10.1016/j.bcp.2006.06.016>
- Raedler, L.A., 2016. Farydak (Panobinostat): First HDAC Inhibitor Approved for Patients with Relapsed Multiple Myeloma. *Am Health Drug Benefits* 9, 84–87.
- Rahbari, R., Rasmi, Y., Khadem-Ansari, M.H., Abdi, M., 2022. The role of histone deacetylase 3 in breast cancer. *Med Oncol* 39, 84. <https://doi.org/10.1007/s12032-022-01681-4>
- Ramaiah, M.J., Tangutur, A.D., Manyam, R.R., 2021. Epigenetic modulation and understanding of HDAC inhibitors in cancer therapy. *Life Sciences* 277, 119504. <https://doi.org/10.1016/j.lfs.2021.119504>
- RHODES, L.V., NITSCHKE, A.M., SEGAR, H.C., MARTIN, E.C., DRIVER, J.L., ELLIOTT, S., NAM, S.Y., LI, M., NEPHEW, K.P., BUROW, M.E., COLLINS-BUROW, B.M., 2012. The histone deacetylase inhibitor trichostatin A alters microRNA expression profiles

Bibliography

- in apoptosis-resistant breast cancer cells. *Oncol Rep* 27, 10–16.
<https://doi.org/10.3892/or.2011.1488>
- Richa, S., Dey, P., Park, C., Yang, J., Son, J.Y., Park, J.H., Lee, S.H., Ahn, M.-Y., Kim, I.S., Moon, H.R., Kim, H.S., 2020. A New Histone Deacetylase Inhibitor, MHY4381, Induces Apoptosis via Generation of Reactive Oxygen Species in Human Prostate Cancer Cells. *Biomol Ther (Seoul)* 28, 184–194. <https://doi.org/10.4062/biomolther.2019.074>
- Ropero, S., Esteller, M., 2007. The role of histone deacetylases (HDACs) in human cancer. *Mol Oncol* 1, 19–25. <https://doi.org/10.1016/j.molonc.2007.01.001>
- Rosato, R.R., Almenara, J.A., Dai, Y., Grant, S., 2003. Simultaneous activation of the intrinsic and extrinsic pathways by histone deacetylase (HDAC) inhibitors and tumor necrosis factor-related apoptosis-inducing ligand (TRAIL) synergistically induces mitochondrial damage and apoptosis in human leukemia cells. *Mol Cancer Ther* 2, 1273–1284.
- Rosato, R.R., Grant, S., 2005. Histone deacetylase inhibitors: insights into mechanisms of lethality. *Expert Opinion on Therapeutic Targets* 9, 809–824.
<https://doi.org/10.1517/14728222.9.4.809>
- Routholla, G., Pulya, S., Patel, T., Abdul Amin, Sk., Adhikari, N., Biswas, S., Jha, T., Ghosh, B., 2021a. Synthesis, biological evaluation, and molecular docking analysis of novel linker-less benzamide based potent and selective HDAC3 inhibitors. *Bioorganic Chemistry* 114, 105050. <https://doi.org/10.1016/j.bioorg.2021.105050>
- Routholla, G., Pulya, S., Patel, T., Adhikari, N., Abdul Amin, Sk., Paul, M., Bhagavatula, S., Biswas, S., Jha, T., Ghosh, B., 2021b. Design, synthesis and binding mode of interaction of novel small molecule o-hydroxy benzamides as HDAC3-selective inhibitors with promising antitumor effects in 4T1-Luc breast cancer xenograft model. *Bioorganic Chemistry* 117, 105446. <https://doi.org/10.1016/j.bioorg.2021.105446>

Bibliography

- Ruefli, A.A., Ausserlechner, M.J., Bernhard, D., Sutton, V.R., Tainton, K.M., Kofler, R., Smyth, M.J., Johnstone, R.W., 2001. The histone deacetylase inhibitor and chemotherapeutic agent suberoylanilide hydroxamic acid (SAHA) induces a cell-death pathway characterized by cleavage of Bid and production of reactive oxygen species. *Proceedings of the National Academy of Sciences* 98, 10833–10838. <https://doi.org/10.1073/pnas.191208598>
- Saito, A., Yamashita, T., Mariko, Y., Nosaka, Y., Tsuchiya, K., Ando, T., Suzuki, T., Tsuruo, T., Nakanishi, O., 1999. A synthetic inhibitor of histone deacetylase, MS-27-275, with marked in vivo antitumor activity against human tumors. *PNAS* 96, 4592–4597. <https://doi.org/10.1073/pnas.96.8.4592>
- Saito, K., Funayama, T., Yokota, Y., Murakami, T., Kobayashi, Y., 2017. Histone Deacetylase Inhibitors Sensitize Murine B16F10 Melanoma Cells to Carbon Ion Irradiation by Inducing G1 Phase Arrest. *Biological and Pharmaceutical Bulletin* 40, 844–851. <https://doi.org/10.1248/bpb.b16-01025>
- Sambucetti, L.C., Fischer, D.D., Zabludoff, S., Kwon, P.O., Chamberlin, H., Trogani, N., Xu, H., Cohen, D., 1999. Histone Deacetylase Inhibition Selectively Alters the Activity and Expression of Cell Cycle Proteins Leading to Specific Chromatin Acetylation and Antiproliferative Effects *. *Journal of Biological Chemistry* 274, 34940–34947. <https://doi.org/10.1074/jbc.274.49.34940>
- Sanderson, L., Taylor, G.W., Aboagye, E.O., Alao, J.P., Latigo, J.R., Coombes, R.C., Vigushin, D.M., 2004. Plasma Pharmacokinetics and Metabolism of the Histone Deacetylase Inhibitor Trichostatin a After Intraperitoneal Administration to Mice. *Drug Metab Dispos* 32, 1132–1138. <https://doi.org/10.1124/dmd.104.000638>

Bibliography

- Sarkar, R., Banerjee, S., Amin, S.A., Adhikari, N., Jha, T., 2020. Histone deacetylase 3 (HDAC3) inhibitors as anticancer agents: A review. *European Journal of Medicinal Chemistry* 192, 112171. <https://doi.org/10.1016/j.ejmech.2020.112171>
- Schölz, C., Weinert, B.T., Wagner, S.A., Beli, P., Miyake, Y., Qi, J., Jensen, L.J., Streicher, W., McCarthy, A.R., Westwood, N.J., Lain, S., Cox, J., Matthias, P., Mann, M., Bradner, J.E., Choudhary, C., 2015. Acetylation site specificities of lysine deacetylase inhibitors in human cells. *Nat Biotechnol* 33, 415–423. <https://doi.org/10.1038/nbt.3130>
- Schrödinger Suite, Schrödinger, LLC, New York, USA, 2019. <http://www.schrodinger.com/glide>, n.d.
- Seto, E., Yoshida, M., 2014. Erasers of histone acetylation: the histone deacetylase enzymes. *Cold Spring Harb Perspect Biol* 6, a018713. <https://doi.org/10.1101/cshperspect.a018713>
- Shah, R.R., 2019. Safety and Tolerability of Histone Deacetylase (HDAC) Inhibitors in Oncology. *Drug Saf* 42, 235–245. <https://doi.org/10.1007/s40264-018-0773-9>
- Shahbazian, M.D., Grunstein, M., 2007. Functions of Site-Specific Histone Acetylation and Deacetylation. *Annual Review of Biochemistry* 76, 75–100. <https://doi.org/10.1146/annurev.biochem.76.052705.162114>
- Shao, Y., Gao, Z., Marks, P.A., Jiang, X., 2004. Apoptotic and autophagic cell death induced by histone deacetylase inhibitors. *Proc Natl Acad Sci U S A* 101, 18030–18035. <https://doi.org/10.1073/pnas.0408345102>
- Sharma, S., Kelly, T.K., Jones, P.A., 2010. Epigenetics in cancer. *Carcinogenesis* 31, 27–36. <https://doi.org/10.1093/carcin/bgp220>
- Shultz, M., Fan, J., Chen, C., Cho, Y.S., Davis, N., Bickford, S., Buteau, K., Cao, X., Holmqvist, M., Hsu, M., Jiang, L., Liu, G., Lu, Q., Patel, C., Suresh, J.R., Selvaraj, M., Urban, L., Wang, P., Yan-Neale, Y., Whitehead, L., Zhang, H., Zhou, L., Atadja, P., 2011. The design, synthesis and structure–activity relationships of novel isoindoline-based histone

Bibliography

- deacetylase inhibitors. *Bioorganic & Medicinal Chemistry Letters* 21, 4909–4912.
<https://doi.org/10.1016/j.bmcl.2011.06.015>
- Siegel, R.L., Miller, K.D., Fuchs, H.E., Jemal, A., 2022. Cancer statistics, 2022. *CA: A Cancer Journal for Clinicians* 72, 7–33. <https://doi.org/10.3322/caac.21708>
- Singh, A., Chang, T.-Y., Kaur, N., Hsu, K.-C., Yen, Y., Lin, T.E., Lai, M.-J., Lee, S.-B., Liou, J.-P., 2021. CAP rigidification of MS-275 and chidamide leads to enhanced antiproliferative effects mediated through HDAC1, 2 and tubulin polymerization inhibition. *European Journal of Medicinal Chemistry* 215, 113169.
<https://doi.org/10.1016/j.ejmech.2021.113169>
- Singh, T.R., Shankar, S., Srivastava, R.K., 2005. HDAC inhibitors enhance the apoptosis-inducing potential of TRAIL in breast carcinoma. *Oncogene* 24, 4609–4623.
<https://doi.org/10.1038/sj.onc.1208585>
- Soliman, N.A., Yussif, S.M., 2016. Ki-67 as a prognostic marker according to breast cancer molecular subtype. *Cancer Biol Med* 13, 496–504. <https://doi.org/10.20892/j.issn.2095-3941.2016.0066>
- Son, S.I., Cao, J., Zhu, C.-L., Miller, S.P., Lin, H., 2019. Activity-Guided Design of HDAC11-Specific Inhibitors. *ACS Chem. Biol.* 14, 1393–1397.
<https://doi.org/10.1021/acscchembio.9b00292>
- Spiller, S.E., Ravanpay, A.C., Hahn, A.W., Olson, J.M., 2006. Suberoylanilide hydroxamic acid is effective in preclinical studies of medulloblastoma. *J Neurooncol* 79, 259–270.
<https://doi.org/10.1007/s11060-006-9142-0>
- Spurling, C.C., Godman, C.A., Noonan, E.J., Rasmussen, T.P., Rosenberg, D.W., Giardina, C., 2008. HDAC3 overexpression and colon cancer cell proliferation and differentiation. *Molecular Carcinogenesis* 47, 137–147. <https://doi.org/10.1002/mc.20373>

Bibliography

- Stenzel, K., Hamacher, A., Hansen, F.K., Gertzen, C.G.W., Senger, J., Marquardt, V., Marek, L., Marek, M., Romier, C., Remke, M., Jung, M., Gohlke, H., Kassack, M.U., Kurz, T., 2017. Alkoxyurea-Based Histone Deacetylase Inhibitors Increase Cisplatin Potency in Chemoresistant Cancer Cell Lines. *J. Med. Chem.* 60, 5334–5348. <https://doi.org/10.1021/acs.jmedchem.6b01538>
- Strahl, B.D., Allis, C.D., 2000. The language of covalent histone modifications. *Nature* 403, 41–45. <https://doi.org/10.1038/47412>
- Su, W., Zeng, L., Chen, W., 2021. Moscatilin Suppresses the Breast Cancer Both In Vitro and In Vivo by Inhibiting HDAC3. *Dose-Response* 19, 15593258211001252. <https://doi.org/10.1177/15593258211001251>
- Subbaiah, M.A.M., Meanwell, N.A., 2021. Bioisosteres of the Phenyl Ring: Recent Strategic Applications in Lead Optimization and Drug Design. *J. Med. Chem.* <https://doi.org/10.1021/acs.jmedchem.1c01215>
- Subramanian, S., Bates, S.E., Wright, J.J., Espinoza-Delgado, I., Piekarz, R.L., 2010. Clinical Toxicities of Histone Deacetylase Inhibitors. *Pharmaceuticals (Basel)* 3, 2751–2767. <https://doi.org/10.3390/ph3092751>
- Sun, Y., Bao, X., Ren, Y., Jia, L., Zou, S., Han, J., Zhao, M., Han, M., Li, H., Hua, Q., Fang, Y., Yang, J., Wu, C., Chen, G., Wang, L., 2019. Targeting HDAC/OAZ1 axis with a novel inhibitor effectively reverses cisplatin resistance in non-small cell lung cancer. *Cell Death Dis* 10, 1–13. <https://doi.org/10.1038/s41419-019-1597-y>
- Suresh, P.S., Devaraj, V.C., Srinivas, N.R., Mullangi, R., 2017. Review of bioanalytical assays for the quantitation of various HDAC inhibitors such as vorinostat, belinostat, panobinostat, romidepsin and chidamine. *Biomedical Chromatography* 31, e3807. <https://doi.org/10.1002/bmc.3807>

Bibliography

- Taunton, J., Hassig, C.A., Schreiber, S.L., 1996. A mammalian histone deacetylase related to the yeast transcriptional regulator Rpd3p. *Science* 272, 408–411. <https://doi.org/10.1126/science.272.5260.408>
- Telles, E., Seto, E., 2012. Modulation of Cell Cycle Regulators by HDACs. *Front Biosci (Schol Ed)* 4, 831–839.
- Thakur, A., Tawa, G.J., Henderson, M.J., Danchik, C., Liu, S., Shah, P., Wang, A.Q., Dunn, G., Kabir, M., Padilha, E.C., Xu, X., Simeonov, A., Kharbanda, S., Stone, R., Grewal, G., 2020. Design, Synthesis, and Biological Evaluation of Quinazolin-4-one-Based Hydroxamic Acids as Dual PI3K/HDAC Inhibitors. *J Med Chem* 63, 4256–4292. <https://doi.org/10.1021/acs.jmedchem.0c00193>
- Thaler, F., Mercurio, C., 2014. Towards Selective Inhibition of Histone Deacetylase Isoforms: What Has Been Achieved, Where We Are and What Will Be Next. *ChemMedChem* 9, 523–536. <https://doi.org/10.1002/cmdc.201300413>
- Thomas, M., Clarhaut, J., Tranoy-Opalinski, I., Gesson, J.-P., Roche, J., Papot, S., 2008. Synthesis and biological evaluation of glucuronide prodrugs of the histone deacetylase inhibitor CI-994 for application in selective cancer chemotherapy. *Bioorg Med Chem* 16, 8109–8116. <https://doi.org/10.1016/j.bmc.2008.07.048>
- Timmermann, S., Lehrmann, H., Poleskaya, A., Harel-Bellan, A., 2001. Histone acetylation and disease. *CMLS, Cell. Mol. Life Sci.* 58, 728–736. <https://doi.org/10.1007/PL00000896>
- Tr, H., Aw, T., C, C.-R., 1988. A direct link between core histone acetylation and transcriptionally active chromatin. *The EMBO journal* 7.
- Trivedi, P., Adhikari, N., Amin, S.A., Bobde, Y., Ganesh, R., Jha, T., Ghosh, B., 2019. Design, synthesis, biological evaluation and molecular docking study of arylcarboxamido piperidine and piperazine-based hydroxamates as potential HDAC8 inhibitors with

Bibliography

- promising anticancer activity. *Eur J Pharm Sci* 138, 105046.
<https://doi.org/10.1016/j.ejps.2019.105046>
- Trivedi, P., Adhikari, N., Amin, S.A., Jha, T., Ghosh, B., 2018. Design, synthesis and biological screening of 2-aminobenzamides as selective HDAC3 inhibitors with promising anticancer effects. *Eur J Pharm Sci* 124, 165–181. <https://doi.org/10.1016/j.ejps.2018.08.030>
- Turner, B.M., 2000. Histone acetylation and an epigenetic code. *BioEssays* 22, 836–845.
[https://doi.org/10.1002/1521-1878\(200009\)22:9<836::AID-BIES9>3.0.CO;2-X](https://doi.org/10.1002/1521-1878(200009)22:9<836::AID-BIES9>3.0.CO;2-X)
- Wagner, F.F., Weïwer, M., Lewis, M.C., Holson, E.B., 2013. Small Molecule Inhibitors of Zinc-dependent Histone Deacetylases. *Neurotherapeutics* 10, 589–604.
<https://doi.org/10.1007/s13311-013-0226-1>
- Wang, H., Huang, C., Zhao, L., Zhang, H., Yang, J.M., Luo, P., Zhan, B.-X., Pan, Q., Li, J., Wang, B.-L., 2016. Histone deacetylase inhibitors regulate P-gp expression in colorectal cancer via transcriptional activation and mRNA stabilization. *Oncotarget* 7, 49848–49858.
<https://doi.org/10.18632/oncotarget.10488>
- Wang, H., Shi, L., Wang, Z., 2021. A Novel Hydroxamic Acid-Based Curcumin Derivative as Potent Histone Deacetylase Inhibitor for the Treatment of Glioblastoma. *Frontiers in Oncology* 11.
- Wang, L.-Z., Ramírez, J., Yeo, W., Chan, M.-Y.M., Thuya, W.-L., Lau, J.-Y.A., Wan, S.-C., Wong, A.L.-A., Zee, Y.-K., Lim, R., Lee, S.-C., Ho, P.C., Lee, H.-S., Chan, A., Ansher, S., Ratain, M.J., Goh, B.-C., 2013. Glucuronidation by UGT1A1 Is the Dominant Pathway of the Metabolic Disposition of Belinostat in Liver Cancer Patients. *PLoS One* 8, e54522.
<https://doi.org/10.1371/journal.pone.0054522>
- Wang, Yunfei, Stowe, R.L., Pinello, C.E., Tian, G., Madoux, F., Li, D., Zhao, L.Y., Li, J.-L., Wang, Yuren, Wang, Yuan, Ma, H., Hodder, P., Roush, W.R., Liao, D., 2015. Identification of histone deacetylase inhibitors with benzoylhydrazide scaffold that

Bibliography

- selectively inhibit class I histone deacetylases. *Chem. Biol.* 22, 273–284.
<https://doi.org/10.1016/j.chembiol.2014.12.015>
- Watson, P.J., Fairall, L., Santos, G.M., Schwabe, J.W.R., 2012. Structure of HDAC3 bound to co-repressor and inositol tetraphosphate. *Nature* 481, 335–340.
<https://doi.org/10.1038/nature10728>
- Wawruszak, A., Luszczki, J.J., Kalafut, J., Okla, K., Halasa, M., Rivero-Muller, A., Stepulak, A., 2019. Additive Pharmacological Interaction between Cisplatin (CDDP) and Histone Deacetylase Inhibitors (HDIs) in MDA-MB-231 Triple Negative Breast Cancer (TNBC) Cells with Altered Notch1 Activity—An Isobolographic Analysis. *International Journal of Molecular Sciences* 20, 3663. <https://doi.org/10.3390/ijms20153663>
- Wei, H., Ma, W., Lu, X., Liu, H., Lin, K., Wang, Y., Ye, Z., Sun, L., Huang, Z., Pan, T., Zhou, Z., Cheng, E.Y., Zhang, H., Gao, P., Zhong, X., n.d. KDELR2 promotes breast cancer proliferation via HDAC3-mediated cell cycle progression. *Cancer Communications* n/a.
<https://doi.org/10.1002/cac2.12180>
- Wilson, A.J., Byun, D.-S., Popova, N., Murray, L.B., L'Italien, K., Sowa, Y., Arango, D., Velcich, A., Augenlicht, L.H., Mariadason, J.M., 2006. Histone Deacetylase 3 (HDAC3) and Other Class I HDACs Regulate Colon Cell Maturation and p21 Expression and Are Deregulated in Human Colon Cancer *. *Journal of Biological Chemistry* 281, 13548–13558.
<https://doi.org/10.1074/jbc.M510023200>
- Witt, O., Deubzer, H.E., Milde, T., Oehme, I., 2009. HDAC family: What are the cancer relevant targets? *Cancer Letters* 277, 8–21. <https://doi.org/10.1016/j.canlet.2008.08.016>
- Wong, N.-S., Seah, E.Z., Wang, L.-Z., Yeo, W.-L., Yap, H.-L., Chuah, B., Lim, Y.-W., Ang, P.C., Tai, B.-C., Lim, R., Goh, B.-C., Lee, S.-C., 2011. Impact of UDP-gluconoryltransferase 2B17 genotype on vorinostat metabolism and clinical outcomes in Asian women with

Bibliography

- breast cancer. *Pharmacogenet Genomics* 21, 760–768.
<https://doi.org/10.1097/fpc.0b013e32834a8639>
- Xu, W.S., Parmigiani, R.B., Marks, P.A., 2007. Histone deacetylase inhibitors: molecular mechanisms of action. *Oncogene* 26, 5541–5552. <https://doi.org/10.1038/sj.onc.1210620>
- Yang, F., Zhao, N., Ge, D., Chen, Y., 2019. Next-generation of selective histone deacetylase inhibitors. *RSC Adv.* 9, 19571–19583. <https://doi.org/10.1039/C9RA02985K>
- Yang, J., Gong, C., Ke, Q., Fang, Z., Chen, X., Ye, M., Xu, X., 2021. Insights Into the Function and Clinical Application of HDAC5 in Cancer Management. *Frontiers in Oncology* 11.
- Yang, M., Dang, X., Tan, Y., Wang, M., Li, X., Li, G., 2018. I-7ab inhibited the growth of TNBC cells via targeting HDAC3 and promoting the acetylation of p53. *Biomedicine & Pharmacotherapy* 99, 220–226. <https://doi.org/10.1016/j.biopha.2018.01.063>
- Yang, W.-M., Inouye, C., Zeng, Y., Bearss, D., Seto, E., 1996. Transcriptional repression by YY1 is mediated by interaction with a mammalian homolog of the yeast global regulator RPD3. *PNAS* 93, 12845–12850. <https://doi.org/10.1073/pnas.93.23.12845>
- Yang, W.M., Yao, Y.L., Sun, J.M., Davie, J.R., Seto, E., 1997. Isolation and characterization of cDNAs corresponding to an additional member of the human histone deacetylase gene family. *J. Biol. Chem.* 272, 28001–28007. <https://doi.org/10.1074/jbc.272.44.28001>
- Yang, X.-J., Grégoire, S., 2005. Class II Histone Deacetylases: from Sequence to Function, Regulation, and Clinical Implication. *Mol Cell Biol* 25, 2873–2884. <https://doi.org/10.1128/MCB.25.8.2873-2884.2005>
- Yang, X.-J., Seto, E., 2007. HATs and HDACs: from structure, function and regulation to novel strategies for therapy and prevention. *Oncogene* 26, 5310–5318. <https://doi.org/10.1038/sj.onc.1210599>
- Yin, Y., Zhang, M., Dorfman, R.G., Li, Y., Zhao, Z., Pan, Y., Zhou, Q., Huang, S., Zhao, S., Yao, Y., Zou, X., 2017. Histone deacetylase 3 overexpression in human cholangiocarcinoma

Bibliography

- and promotion of cell growth via apoptosis inhibition. *Cell Death & Disease* 8, e2856–e2856. <https://doi.org/10.1038/cddis.2016.457>
- You, D., Richardson, J.R., Aleksunes, L.M., 2020. Epigenetic Regulation of Multidrug Resistance Protein 1 and Breast Cancer Resistance Protein Transporters by Histone Deacetylase Inhibition. *Drug Metab Dispos* 48, 459–480. <https://doi.org/10.1124/dmd.119.089953>
- Yu, S., Gong, X., Ma, Z., Zhang, M., Huang, L., Zhang, J., Zhao, S., Zhu, T., Yu, Z., Chen, L., 2020. Endocrine resistant breast cancer cells with loss of ER α expression retain proliferative ability by reducing caspase7-mediated HDAC3 cleavage. *Cell Oncol.* 43, 65–80. <https://doi.org/10.1007/s13402-019-00439-x>
- Yu, X., Yang, F., Jiang, H., Fan, L., 2020. RGFP966 Suppresses Tumor Growth and Migration Through Inhibition of EGFR Expression in Hepatocellular Carcinoma Cells in vitro. *Drug Des Devel Ther* 14, 121–128. <https://doi.org/10.2147/DDDT.S234871>
- Yue, K., Qin, M., Huang, C., James Chou, C., Jiang, Y., Li, X., 2022. Comparison of three zinc binding groups for HDAC inhibitors – A potency, selectivity and enzymatic kinetics study. *Bioorganic & Medicinal Chemistry Letters* 70, 128797. <https://doi.org/10.1016/j.bmcl.2022.128797>
- Zhang, Lei, Zhang, J., Jiang, Q., Zhang, Li, Song, W., 2018. Zinc binding groups for histone deacetylase inhibitors. *J Enzyme Inhib Med Chem* 33, 714–721. <https://doi.org/10.1080/14756366.2017.1417274>
- Zhang, Y., Li, N., Caron, C., Matthias, G., Hess, D., Khochbin, S., Matthias, P., 2003. HDAC-6 interacts with and deacetylates tubulin and microtubules in vivo. *EMBO J* 22, 1168–1179. <https://doi.org/10.1093/emboj/cdg115>
- Zhao, W.-N., Ghosh, B., Tyler, M., Lalonde, J., Joseph, N.F., Kosaric, N., Fass, D.M., Tsai, L.-H., Mazitschek, R., Haggarty, S.J., 2018. Class I Histone Deacetylase Inhibition by

Bibliography

- Tianeptinaline Modulates Neuroplasticity and Enhances Memory. *ACS Chem Neurosci* 9, 2262–2273. <https://doi.org/10.1021/acschemneuro.8b00116>
- Zhou, M., Yuan, M., Zhang, M., Lei, C., Aras, O., Zhang, X., An, F., 2021. Combining histone deacetylase inhibitors (HDACis) with other therapies for cancer therapy. *European Journal of Medicinal Chemistry* 226, 113825. <https://doi.org/10.1016/j.ejmech.2021.113825>
- Zhou, X., Richon, V.M., Rifkind, R.A., Marks, P.A., 2000. Identification of a transcriptional repressor related to the noncatalytic domain of histone deacetylases 4 and 5. *Proc Natl Acad Sci U S A* 97, 1056–1061.

Appendix

List of publications (Thesis work)

1. Selective HDAC3 Inhibitors with Potent *In Vivo* Antitumor Efficacy against Triple-Negative Breast Cancer. **Sravani Pulya**; Himaja A; Paul, M; Adhikari, N.; Banerjee, S.; Routholla, G.; Biswas, S.; Jha, T.; Ghosh, B*. *Journal of Medicinal Chemistry* **2023**, 66 (17), 12033-12058.
2. Selective Inhibition of Histone Deacetylase 3 by Novel Hydrazone Based Small Molecules as Therapeutic Intervention for the Treatment of Cancer: **Sravani Pulya**; Patel, T.; Paul, M.; Adhikari, N.; Banerjee, S.; Routholla, G.; Biswas, S.; Jha, T*; Ghosh, B*. *European Journal of Medicinal Chemistry* **2022**, 238, 114470.
3. Chapter 23 - Epigenetics of Memory Processes: **Sravani Pulya**, Balaram Ghosh*: Editor(s): Trygve O. Tollefsbol, Handbook of Epigenetics (Third Edition), Academic Press, **2023**, 443-464, ISBN 9780323919098.
4. HDAC6 as privileged target in drug discovery: A perceptive: **Sravani Pulya**, Sk. Abdul Amin, Nilanjan Adhikari, Swati Biswas, Tarun Jha*, Balaram Ghosh*. *Pharmacological Research* 163 (2021) 105274.
5. Histone Deacetylase 8 as an Emerging Target in Drug Discovery with Special Emphasis on Medicinal Chemistry. Srinidhi Rajaraman, Ranjani Balakrishnan, Dhruv Deshmukh, Abhiram Ganorkar, Swati Biswas, **Sravani Pulya***, Balaram Ghosh*. Invited review article. *Future medicinal chemistry* **2023**, 15 (10), 885-908.
6. PT3: A Novel Benzamide Class Histone Deacetylase 3 Inhibitor Improves Learning and Memory in Novel Object Recognition Mouse Model: **Sravani Pulya[#]**; Mahale, A[#]; Bobde, Y.; Routholla, G.; Patel, T.; Swati; Biswas, S.; Sharma, V.; Kulkarni, O. P*; Ghosh, B*. *ACS Chemical Neuroscience*. **2021**, 12, 5, 883–892.
7. Design, Synthesis, and Biological Evaluation of Novel Nicotinamide Derivatives as Potential Selective Histone Deacetylase-3 Inhibitors: Mohamed M.S. Hamoud[#], **Sravani**

Pulya #, Nermine A. Osman, Yamini Bobde, Abdalla E. A. Hassan, Hanan A. Abdel-Fattah, Balaram Ghosh* Amany M. Ghanim*. *New Journal of Chemistry* **2020**, 44 (23), 9671.

List of publications (others)

1. Estrogenicity of Tetrazole Bisphenols: Computational studies, Synthesis and *In vitro* assessment: Gadgoli, Umesh; Y.C, Sunil; Kumar, Deepak; Pai*, Maya; **Sravani Pulya**; Ghosh, Balaram; Kulkarni, Onkar. *Journal of Chemical Information and Modeling (ACS)* **2022**, 62(4), 854-873.
2. Design, Synthesis and SAR Studies of Novel Spirochromanone hydrochloride Analogues as Anticancer Agents: Surendar Chitti#, **Sravani Pulya**#, Adinarayana N, Tarun Patel, Banoth Karan Kumar, Sankaranarayanan M, Balaram Ghosh*, KVG Chandra Sekhar*. *Future Medicinal Chemistry* **2022**, 14 (5), 325-342.
3. Design, Synthesis and Binding Mode of Interaction of Novel Small Molecule *o*-Hydroxy Benzamides as HDAC3-Selective Inhibitors with Promising Antitumor Effects in 4T1-Luc Breast Cancer Xenograft Model: Ganesh Routholla, **Sravani Pulya**, Tarun Patel, Nilanjan Adhikari, Sk. Abdul Amin, Milan Paul, Srividya Bhagavatula, Swati Biswas, Tarun Jha*, Balaram Ghosh*. *Bioorganic Chemistry* **117**, **2021**, 105446.
4. Synthesis, Biological Evaluation, and Molecular Docking Analysis of Novel Linker-less Benzamide Based Potent and Selective HDAC3 Inhibitors: Ganesh Routholla#, **Sravani Pulya** #, Tarun Kumar Patel, Sk. Abdul Amin, Nilanjan Adhikari, Swati Biswas, Tarun Jha*, Balaram Ghosh*. *Bioorganic Chemistry* **114**, **2021**, 105050.
5. Design, Synthesis and Biological Evaluation of 7-(5-((Substituted - Amino)-Methyl)-Thiophen-2-Yl)-Spiro-[Chroman-2,4'-Piperidin]-4-One Hydrochloride Analogues as Anticancer Agents: Chitti, S.#; **Sravani Pulya**#; Nandikolla, A.; Kumar Patel,

T.; Karan Kumar, B.; Murugesan, S.; Ghosh, B*; Venkata Gowri Chandra Sekhar, K*. *Bioorganic Chemistry* 112, 2021, 104865.

6. Discovery of 1, 2, 3-triazole based quinoxaline-1, 4-di-N-oxide derivatives as potential anti-tubercular agents: S Srinivasarao, Adinarayana N, A Suresh, Ewa, Agnieszka Głogowska, Balaram G, Banoth Karan Kumar, Sankaranarayanan M, **Sravani Pulya**, Himanshu A, Kondapalli Venkata Gowri Chandra Sekhar*. *Bioorganic Chemistry* 100, 2020, 103955.

7. Structure activity relationship of Human Carbonic Anhydrase II inhibitors: Detailed Insight for future development as anti-glaucoma agents: Soumajit Ghorai, **Sravani Pulya**, Partha sarathi Panda, Balaram Ghosh* and Shovanlal Gayen*. *Bioorganic Chemistry* 95, 2020, 103557.

8. Quinoline Consists of 1H-1,2,3-Triazole Hybrids: Design, Synthesis and Anticancer Evaluation: Sivarami Reddy Gangireddy Venkata, Umesh C. Narkhede, Vinod D Jadhav, Challa Gangu Naidu*, Ramakrishnam Raju Addada, **Sravani Pulya**, Balaram Ghosh. *Chemistry Select*, 4 (48), 2019, 14184-14190.

9. Fused Chromeno-Thieno/Furo-Pyridines as Potential Analogs of Lamellarin D and their Anticancer Activity Evaluation: T Uday Kumar, Yamini Bobde, **Sravani Pulya**, Krishnan Rangan, Balaram Ghosh, Anupam Bhattacharya*. *Chemistry Select*, 4 (36), 2019, 10726-10730.

10. Design, synthesis and biological evaluation of 1, 2, 3-triazole based 2-aminobenzimidazoles as novel inhibitors of LasR dependent quorum sensing in *Pseudomonas aeruginosa*: S Srinivasarao, Adinarayana N, Shashidhar N, Tsz Tin Yu, **Sravani Pulya**, Balaram G, Sankaranarayanan M, Naresh Kumar, Kondapalli Venkata Gowri Chandra Sekhar*. *RSC Advances*, 2019, 9, 50, 29273–29292.

List of Indian Patents

1. Histone deacetylase isoform 3 (hdac3) enzyme inhibiting compounds and methods of synthesizing the same: Dr. Balaram Ghosh, Dr. Swati Biswas, Mr. Adhikari Nilanjan, **Sravani Pulya**, Mr. Paul Milan, Ms. Himaja Ambati; Patent Authority BITS-Pilani: Indian Patent Application Number 202311011366. Filed on 20/02/2023.
2. Hydrazide based HDAC3 selective inhibitors: Dr. Balaram Ghosh, Dr. Swati Biswas, **Sravani Pulya**, Ganesh Routholla, Tarun Kumar Patel. Patent Authority BITS-Pilani: Indian Patent Application Number 202111022553, Filed on 20/05/2021. **Granted Patent No. 450418 on 11.09.2023**
3. Benzamide Based HDAC3 Selective Inhibitors: Dr. Balaram Ghosh, Dr. Swati Biswas, Ganesh Routholla, **Sravani Pulya**; Patent Authority BITS-Pilani: Indian Patent Application Number 202011056177. Filed on 23/12/2020. **Granted patent No. 448419 on 30.08.2023.**

Book chapters

1. Histone Deacetylase Inhibitors in Alzheimer's disease: Design, Synthesis, and Biological Evaluation: **Sravani Pulya**, Abhiram Ganorkar, Swati Biswas, **Balaram Ghosh***: Book entitled "Natural product-based synthetic drug molecules in Alzheimer's Disease - Therapeutic & Theranostic agents": *Springer* 2022. (Submitted).
2. Epigenetics of Memory Processes: **Sravani Pulya** and Balaram Ghosh* for "Hand Book of Epigenetics", 3rd Edition: Edited by Prof. Trygve Tollefsbol: *Elsevier*; 2021: The New Molecular and Medical Genetics, **2023**, Pages 443-464. doi.org/10.1016/B978-0-323-91909-8.00018-9.

Biography of Sravani Pulya

Mrs. Sravani Pulya completed her Bachelor of Pharmacy (2011) from Andhra University, Visakhapatnam, Andhra Pradesh, India. She completed her Master of Pharmacy in pharmaceutical chemistry (2013) from Vellore Institute of Technology, Tamil Nadu, India. Later, she worked as a Project assistant-II at National Chemical Laboratory (2014 – 2017). Mrs. Sravani Pulya, joined Dr. Balaram Ghosh's epigenetic research laboratory at Birla Institute of Technology and Science, Pilani, Hyderabad Campus for her doctoral studies. She has been awarded Senior Research Fellowship (SRF) by Council of Scientific and Industrial Research (CSIR), India from 2018 – 2021 for her PhD work. Later, she has received institution fellowship from Birla Institute of Technology and Science-Pilani, Hyderabad from 2021 – till date to continue her PhD work. Her doctoral research work involved the design, synthesis and biological evaluation of histone deacetylase – 3 inhibitors as potent anticancer agents. Mrs. Sravani has co-authored 17 scientific peer reviewed publications in international journals, 2 book chapters and she is one of the inventors for 3 Indian patents filed.

Biography of Dr. Balaram Ghosh

Dr. Balaram Ghosh is presently working as an Associate Professor, in the Department of Pharmacy, Birla Institute of Technology and Science, Pilani, Hyderabad Campus. Recently, he got appointed as Associate Investigator (Non-Resident), Molecular Medicine Institute [MMI], Boston, USA. He received his B. Pharm degree (1998) and M.Pharm (2000) from Jadavpur University, India. He was awarded his Ph.D. in Pharmaceutical Sciences in the year 2009 from Wayne State University, Michigan, USA. After completion of doctoral studies, he pursued his postdoctoral studies at the Centre for Human Genetic Research (CHGR), Harvard Medical School, Harvard University, USA (2013). He has been involved in research for the last 19 years. He has published more than 150 research publications, three US patents and 16 Indian Patents. He has authored 10 book chapters. One of the research molecules (BG-45) developed by him at Harvard Medical School has been commercialized with Sigma-Aldrich. He has successfully completed many sponsored projects and currently handling projects sponsored by SERB, CSIR, ICMR, DBT Government of India. Currently seven students are pursuing their Ph.D. research under his guidance.